



TECHNISCHE
UNIVERSITÄT
WIEN
Vienna University
of Technology

DISSERTATION

Diffusion and Distribution of Grain-Growth Inhibitors in Hardmetals

ausgeführt zum Zwecke der Erlangung des akademischen Grades eines Doktors der
technischen Wissenschaften unter der Leitung von

Ao. Univ. Prof. Dipl.-Ing. Dr. techn. Walter Lengauer
am
Institut 164-CT für
Chemische Technologien und Analytik

eingereicht an der Technischen Universität Wien
Fakultät für Technische Chemie

von
Dipl.-Ing. Christoph Buchegger, BSc.
Matrikelnummer: 0625592
Hofaustraße 5/6
5230 Mattighofen
Österreich

Wien, im Jänner 2016

Kurzfassung

Hartmetalle sind Verbundwerkstoffe, bestehend aus einem Hartstoff und einer zähen, metallischen Bindephase. Die außergewöhnliche Kombination aus Härte und Zähigkeit macht diesen Werkstoff seit Jahrzehnten unverzichtbar für eine Reihe industrieller Schlüsselanwendungen, etwa zur Metallbearbeitung, im Bergbau, im Straßen- und Tunnelbau oder in der Elektronikindustrie. Dem Trend zur Nanotechnologie folgend, liegt ein aktueller Fokus der Hartmetallforschung darauf, die Korngröße des wichtigsten Hartstoffs WC auf unter 100–300 nm zu senken. Die Herstellung von Hartmetallen erfolgt pulvermetallurgisch durch Flüssigphasensintern bei Temperaturen von 1380–1500°C, wobei ab ca. 1300°C eine stationäre flüssige Phase durch eine eutektische Reaktion des Hartstoffs und des Bindermetalls auftritt. In konventionellen Hartmetallen mit Korngrößen $>1\ \mu\text{m}$ zeigt das WC während des Flüssigphasensinterns eine Tendenz zum Kornwachstum, die mit abnehmender Korngröße zunimmt. Dieses Wachstum kann durch die Zugabe sogenannter Kornwachstumsinhibitoren (KWH) verringert werden, wobei V, Cr, Ta und Mo als wichtigste Inhibitoren zu nennen sind. Moderne Hartmetalle mit deutlich geringeren Korngrößen zeigen allerdings ein wesentlich stärker ausgeprägtes Wachstum, welches nicht erst während des Flüssigphasensinterns, sondern bereits bei deutlich tieferen Temperaturen ab ca. 1000°C beginnt. Während dieser frühen Sinterstadien müssen sich die Kornwachstumsinhibitoren allerdings erst durch Diffusion im Material verteilen. Bislang liegen noch keine experimentellen Daten vor, ob dies in ausreichender Geschwindigkeit erfolgt und welche Diffusionsmechanismen ratenbestimmend für die Verteilung sind. Während der frühen Sinterstadien läuft eine Vielzahl an Prozessen simultan ab, unter anderem die Benetzung des Hartstoffs durch die Bindephase, Verdichtung, Teilchenumordnung und -desintegration, carbothermische Reduktion der Oberflächenoxide, partielles Auflösen der Hartstoffe in der Bindephase und Kornwachstum. Diese Prozesse zeigen zum Teil wechselseitige Abhängigkeiten und beeinflussen die Verteilung der Kornwachstumsinhibitoren im Hartmetall. Die vorliegende Arbeit zielt daher auf ein tieferes Verständnis des Einflusses einer Reihe von Parametern wie Kohlenstoffpotential, Sinteratmosphäre, Bindephasenchemie, Korngröße, Nitride, Sinterzeit, Sintertemperatur und Gründichte auf die Verteilung der wichtigsten Kornwachstumshemmer Cr, V und Mo im Temperaturbereich von 950 – 1360°C ab.

Als Hauptmethode kommt dabei die Diffusionspaar-Technik zum Einsatz. Dazu werden je zwei Proben vom Typ WC-Binder und WC-KWH-Binder kontaktiert und im gewünschten Temperaturbereich geglüht. Aufgrund des chemischen Gradienten diffundiert der Kornwachstumshemmer aus dem WC-KWH-Binder-Bereich des Diffusionspaars in den WC-Binder-Bereich. Nach metallographischer Präparation werden die so erhaltenen KWH-Konzentrationsprofile mittels wellenlängendispersiver Elektronenstrahl-Mikroanalyse analysiert. Aus diesen Daten kann mittels Kurvenanpassung ein Transportparameter als Kennzahl für das Diffusionsverhalten errechnet werden.

Mittels Transmissionselektronenmikroskopie werden KWH-Segregationen an den WC/Co Interfaces analysiert. Vanadium ist bereits bei 1150°C messbar an den Interfaces angereichert, während bei Chrom keine derartigen Segregationen nachgewiesen wurden. Mittels Simultan-Thermoanalyse konnten detaillierte Einblicke in thermochemische Prozesse während früher Sinterstadien gewonnen werden. Unterstützt wurden die Ergebnisse durch lichtoptische und elektronenmikroskopische Gefügeanalysen.

Durch Kombination dieser Methoden konnte gezeigt werden, dass die Ausbildung eines durchgehenden Netzwerks an Binderphase ratenbestimmend für die Verteilung der Kornwachstumshemmer in einem Hartmetall ist. Dieses Netzwerk bildet sich durch die Benetzung der WC-Körner ab ca. 800°C aus. Die Binderschicht auf dem WC ist dabei zunächst verhältnismäßig dünn. Dadurch erhält sie korngrenzenartigen Charakter, was eine äußerst schnelle Diffusion ermöglicht. Die Transportfaktoren in den Hartmetall-Grünkörpern lagen in der Regel 1–2 Größenordnungen über den Literaturwerten für Diffusion in Bulk-Bindemetallen. Auf Basis der ermittelten kinetischen Daten konnte in weiterer Folge abgeschätzt werden, dass die kommerziell erhältlichen Korngrößen für Kornwachstumshemmer von ca. 1 µm aufgrund der schnellen Verteilung der KWH ausreichend fein für die Herstellung von flüssigphasengesinterten Hartmetallen mit WC-Korngrößen <300 nm sind. Die Dissertation stellt die erste quantitative Untersuchung des Einflusses kinetischer und thermodynamischer Faktoren auf die Verteilung von Kornwachstumshemmern in Hartmetallen während früher Stadien des Sintervorganges dar.

Abstract

Ultrafine grained hardmetals denote a class of composite materials with high potential for a variety of industrial key applications. They are produced via powdermetallurgical methods by liquid-phase sintering in the range 1380–1500°C, where stationary liquid phase appears at 1200 – 1360°C. The major challenge upon the production of ultrafine grades is control of the WC grain growth upon sintering. A number of so called grain-growth inhibitors, where vanadium, chromium and tantalum are the most important, were successfully applied in industry for decades in order to suppress the grain growth. While for conventional hardmetal grades grain growth before the appearance can be neglected, modern ultrafine or even near-nano grades show a strong growth tendency already at the initial sintering stages >900°C. Since growth inhibitors are added as powders to the initial mixture their distribution upon the sintering process is critical. This work aims to get deep insight in the distribution mechanism of grain-growth inhibitors chromium, vanadium and molybdenum upon the initial sintering stages. Thermal analysis and the diffusion couple technique were used in order to characterise a large number of possible influences on the inhibitor distribution such as temperature, binder phase composition, carbon potential, heating rate, sintering atmosphere, green density, reduction of surface oxides or addition of carbides and nitrides. The findings are supported by means of microstructural analysis. It was found the GGI distribution is very fast already upon initial sintering stages around 1000–1150°C and is not critical for the inhibiting effect in slowly heated and liquid-phase sintered hardmetals. The main distribution mechanism is diffusion via the binder network formed by wetting on WC grains. The so formed binder networks are fine lamellas with high tensions which allow fast diffusion. The transport factors of GGIs in hardmetals green bodies were found to be by 1–2 orders of magnitude higher as compared to bulk diffusion in pure binder metals. Using the determined kinetic data it was estimated that commercially available inhibitor powder grades of ~1 µm are sufficient for preparation of ultrafine, liquid-phase sintered hardmetal grades. Due to the fast diffusion there is no major benefit from finer grades

Danksagung

Die Erarbeitung und Abfassung einer Dissertation ist ein arbeits- und zeitintensives unterfangen, welches nicht ohne tatkräftige Unterstützung seitens Familie, Freunden und Kollegen zu bewältigen ist.

Ein besonderes Dankeschön gilt daher allen voran Prof. Walter Lengauer, welcher nicht nur die Finanzierung des zugrunde liegenden Projektes erst ermöglichte sondern stets mit fachlichem Rat zur Seite stand und mir tiefgehendes Wissen auf dem Gebiet der Hartmetalle und verwandter Themen vermittelte.

Besonderer Dank gilt auch meiner Kollegin Dr. Sabine Wawrzik die mir nicht nur als fachkundige Kollegin, sondern auch als Freundin in Erinnerung bleibt.

Weiterer Dank gilt meiner Kollegin Viktoria Schwarz für ihre tatkräftige Unterstützung bei der Durchführung vieler Experimente.

Johannes Bernardi, Jakob Gruber und Karin Whitmore vom USTEM an der TU Wien danke ich für die kompetente Unterstützung bei der Durchführung elektronenmikroskopischer Untersuchungen.

Jessica Langlade vom IFREMER in Brest und Franz Kiraly vom der Fakultät für Geowissenschaften an der Universität Wien möchte ich für die Hilfestellung bei der Elektronenstrahlmikroanalyse danken.

Ein langer vorangegangener Bildungsweg ist nötig, um überhaupt bis zu Dissertation zu gelangen. Ich möchte mich daher an dieser Stelle meinen Eltern Andreas und Theresia Buchegger bedanken, die keine Kosten und Mühen gescheut haben, mir diesen Weg zu ermöglichen und die stets an mich geglaubt haben.

Nicht zuletzt erfordert eine Dissertation auch Geduld. Nicht nur meinerseits, sondern noch viel mehr von jenen Menschen, die durchgearbeitete Wochenenden, an der Uni verbrachte Abende und häufige schlechte Laune geduldig ertragen. Mein größter Dank gilt daher meiner Frau Sabine, die mir während der letzten Jahre nicht nur häufige Abwesenheit nachgesehen hat, sondern mich auch stets in allen Belangen vorbehaltlos und liebevoll gestützt hat. Ohne dich hätte ich diese Arbeit wohl nicht fertigstellen können.

List of Abbreviations

BSE	Backscattered Electrons
Det. Lim.	Detection limit
DSC	Differential Scanning Calorimetry
DTA	Differential Thermal Analysis
EGA	Evolving Gas Analysis
EPMA	Electron-probe microanalysis
FIB	Focussed Ion Beam
GGI	Grain-growth inhibitor (Cr, V, Mo)
GGI-X	Grain-growth inhibitor compound , X=carbide, nitride or boride
LOM	Light-optical microscopy
SEM	Scanning electron microscopy
SPS	Spark-Plasma-Sintering
STA	Simultaneous thermal analysis
TEM	Transmission-electron microscope
TG	Thermogravimetric analysis
WDS-EPMA	Wavelength-dispersive electron-probe microanalysis

List of formula symbols

Symbol	Unit	Description
T	°C	Temperature
K_{IC}	$\text{MPa}\cdot\text{m}^{-0.5}$	Fracture toughness (Palmqvist-Shetty)
T_M	°C	Temperature of melt formation
HV	kg/mm^2	Vickers Hardness
l	m	Length
MS	$\mu\text{T}\cdot\text{m}^3/\text{kg}$	Magnetic saturation
E_a	$\text{J}\cdot\text{mol}/\text{K}$	Activation energy
H_c	kA/m	Coercive force
F	N	Force
$d_{m,WC}$	μm	Arithmetic mean WC grain-size
$d_{0,WC}$	μm	WC grain size from log. Normal fit
D	cm^2/s	Transport factor
d_{c-GGI}	μm	Critical diameter of GGIX grains
x_{GGI-WC}	μm	Maximum distance of GGIX and a particular WC grain in a hardmetal green body
c_0	wt%	Interface concentration of GGIs in diffusion couples
t	s	Time
c	wt%	Concentration

Content

1	Introduction	1
2	State of Knowledge	2
2.1	Terminology.....	2
2.2	The early stages of sintering near-nano and ultrafine hardmetals	4
2.2.1	Densification and microstructural evolution.....	5
2.2.2	WC grain growth at early sintering stages	7
2.3	Grain-growth inhibition.....	11
2.3.1	Mechanism of grain-growth inhibition.....	17
2.3.2	Grain-growth inhibitors and sintering behaviour.....	22
2.4	Phase Equilibria in hardmetals	23
2.5	Solubilities of hardmetal constituents	28
2.6	Distribution of hardmetal constituents.....	30
3	Materials and Methods.....	34
3.1	Raw materials.....	34
3.1.1	Preparation of the grade DS50m	34
3.1.2	Preparation of (W,V)C for thermal analyses.....	34
3.2	Preparation of hardmetal mixtures.....	36
3.3	Sintering	36
3.3.1	Induction furnace	36
3.3.2	Spark Plasma Sintering	38
3.4	Preparation of diffusion couples	39
3.4.1	G-type couples.....	41
3.4.2	H-type couples	43
3.4.3	M-type couples.....	44
3.5	Samples for SPS	53
3.6	Samples for grain growth experiments	53
3.7	Samples for thermal analyses	54
3.8	Microstructure.....	59
3.8.1	Metallographic sample preparation	59
3.8.2	Light-optical microscopy	59
3.8.3	Scanning electron microscopy and grain size analysis	60
3.8.4	Transmission electron microscopy.....	60
3.9	Mechanical properties	61
3.9.1	Hardness HV30.....	61
3.9.2	Fracture toughness	62
3.10	Magnetic properties	62
3.10.1	Coercive force.....	62
3.10.2	Magnetic saturation.....	63
3.11	Concentration Profiles (WDS-EPMA)	64
3.12	Thermal analysis	65
3.13	Calculation of transport parameters.....	67

4	Results	70
4.1	Determination of diffusion parameters	70
4.2	Reproducibility and error	74
4.2.1	Diffusion couples.....	75
4.2.2	Grain-size analyses	81
4.2.3	Thermal analyses.....	84
4.2.4	Transmission electron microscopy (TEM)	85
4.2.5	Summary of main findings regarding error estimation:.....	86
4.3	G-type diffusion couples	87
4.3.1	G-type diffusion couples with Cr, low carbon potential.....	87
4.3.2	G-type diffusion couples with Cr, mid carbon potential	93
4.3.3	G-type diffusion couples with Cr, high carbon potential	99
4.3.4	G-type diffusion couples with Cr ₃ C ₂ and nano-cobalt.....	107
4.3.5	G-type diffusion couples with Cr ₃ C ₂ and varying green density	112
4.3.6	G-type diffusion couples with CrB	114
4.3.7	G-type diffusion couples with Cr ₂ N	116
4.3.8	G-type diffusion couples with Cr annealed in N ₂ atmosphere	118
4.3.9	G-type diffusion couples with Cr annealed in CO atmosphere.....	121
4.3.10	G-type diffusion couples with VC, low carbon potential	123
4.3.11	G-type diffusion couples with VC, mid carbon potential	126
4.3.12	G-type diffusion couples with VC, high carbon potential	128
4.3.13	G-type diffusion couples with VC and nano-Co.....	136
4.3.14	G-type diffusion couples with varying compaction pressures.....	137
4.3.15	G-type diffusion couples with VC annealed in N ₂ or CO atmosphere .	140
4.3.16	G-type diffusion couples with alternative binder alloys.....	142
4.3.17	G-type couples with GGI=molybdenum and cobalt binder	145
4.3.18	G-type couples with Cr ₃ C ₂ +VC and Co binder	147
4.4	M-type diffusion couples.....	152
4.4.1	M-type couples with Cr and Co binder	152
4.4.2	M-type couples with V and Co binder	154
4.4.3	M-type couples with Cr and Fe/Co/Ni-binder	155
4.4.4	M-type couples with V and Fe/Co/Ni-binder.....	158
4.4.5	M-type couples with Cr and Fe/Ni-binder	160
4.5	H-type diffusion couples	162
4.5.1	H-type diffusion couples with Co binder	162
4.5.2	H-type diffusion couples with Fe/Co/Ni binder	164
4.5.3	H-type diffusion couples with Fe/Ni binder	166
4.5.4	H-type diffusion couples with Fe/Ni binder	170
4.6	Thermal Analyses.....	172
4.6.1	Diffusion couple components	172
4.6.2	Hardmetals with varying GGI/W ratio	184
4.6.3	WC-Co hardmetals with small amounts of dopants	194
4.7	Grain-size analyses	200
4.7.1	G-type diffusion couples	201
4.7.2	GGI-doped hardmetals with varying outgassing dwells	204

4.7.3	Spark plasma sintered samples (SPS)	217
4.8	Interface chemistry	219
4.8.1	VWC-Co-VC, 1050°C.....	220
4.8.2	WC-VC-Co, 1150°C	221
4.8.3	WC-Co-Cr ₃ C ₂ , 1150°C.....	225
4.8.4	WC-Co-Cr ₃ C ₂ -VC, 1150°C.....	230
5	Discussion.....	232
5.1	Thermal Analyses.....	232
5.1.1	Thermal analyses of the diffusion couple components	232
5.1.2	Thermal reactions in chromium doped hardmetals	237
5.1.3	Thermal reactions in vanadium doped hardmetals	242
5.2	Activation Energy.....	246
5.3	Diffusion in hardmetal binder phase (M-type).....	249
5.4	Diffusion in sintered hardmetals (H-type)	252
5.5	Diffusion in hardmetal green bodies (G-type)	255
5.5.1	Annealing time	255
5.5.2	Carbon potential.....	257
5.5.3	Initial cobalt grain-size	260
5.5.4	Binder phase composition.....	264
5.5.5	Green density.....	265
5.5.6	Nitrogen and CO	269
5.5.7	Diffusion of borides	274
5.5.8	Cr/V interdependency	277
5.6	GGI transport mechanisms.....	279
5.7	Effectiveness of GGIs at early sintering stages	285
5.8	Impact of results on hardmetal production.....	289
6	Summary.....	295
6.1	General Aspects	295
6.2	Thermal analyses	296
6.3	Parameters influencing GGI distribution	299
6.4	Efficiency of GGIs at initial sintering stages.....	302
6.5	Transport mechanisms of GGIs upon sintering	303
6.6	Conclusions for hardmetal production	304
7	Literature.....	305
8	Annex.....	320
8.1	Device settings for EPMA.....	320
8.2	Activation energies	322
8.3	DSC and TG analyses.....	324
8.3.1	Diffusion couple components with cobalt binder	324
8.3.2	Diffusion couple components with Fe/ Ni 15/85wt% binder	328
8.3.3	Diffusion couple components with Fe/Co/Ni 40/20/40wt% binder.....	331

8.3.4	Varying Cr/W ratio.....	332
8.3.5	Varying V/W ratio	334
8.3.6	Varying Mo/W ratio	337
8.3.7	Chromium-doped hardmetals.....	339

1 Introduction

Cemented carbides are composites of a hard phase, mainly WC and a tough, metallic binder phase. Their predominant characteristic is a unique combination of high hardness and reasonable toughness, which makes cemented carbides indispensable for a wide range of industrial applications. The main parameters influencing the properties of a particular grade are the binder volume fraction and the WC grain-size. The latter was subject to extended research activities due to a recent trend to ultrafine and near-nano grades. The development of such grades allowed increasing hardness without negative consequences on the toughness. The main challenge for realising such grades is to control the strong grain-growth tendency as compared to conventional grades. For this purpose a number of grain-growth inhibitors are available where VC and Cr_3C_2 are the most widely used. Their use was industrial standard for decades since they successfully suppress grain growth upon liquid-phase sintering process from 1380–1500°C. However in ultrafine or near-nano grades WC coarsening is known to initiate already upon early solid-state sintering around 1000°C. Sufficient growth inhibition is thus of particular relevance already at these temperatures. Inhibitors are commonly applied by adding powders of 1–5 μm grain size to hardmetal mixtures. Upon heat up they dissolve in the hardmetal binder phase and distribute in the hardmetal binder phase. Until now, not much attention was drawn to this process since it is fast once liquid phase appears at range 1290–1360°, where the inhibiting effect is needed. Anyway, at 1000°C it is not yet clear whether inhibitors are already distributed or dissolved, if they are as effective in solid-state as in liquid-state and by which mechanisms they are distributed. These questions are also relevant for advanced, modern sintering techniques such as SPS where now homogenising liquid-phase appears upon the entire sintering process.

This thesis aims to answer these questions and to gain deeper knowledge and understanding on the distribution of grain-growth inhibitors at the initial stages of sintering cemented carbides. The knowledge will help to further improve the production of ultrafine and near-nano hardmetals and make their outstanding properties accessible for a new generation of cutting tools.

2 State of Knowledge

2.1 Terminology

The term cemented carbide denotes a metal matrix composite based on a carbide hard phase and a metallic, tough binder phase. Cemented carbides are usually produced by liquid-phase sintering at temperatures ranging from 1300–1500°C. The hard phase is based on transition metal carbides or carbonitrides, respectively. The most important are WC, TiC, Ti(C,N), TiC, NbC, TaC, VC and Cr₃C₂. Composites based on WC are usually referred to as hardmetals, whereas TiC or Ti(C,N) based composites are usually referred to as cermets. Note that the term cermet can also refer to other composite materials based on both a ceramic and a metallic phase. Carbides other than WC or TiC, respectively are usually used in small amounts only in order to improve some specific properties, although for some particular applications cemented carbides based on NbC were reported [15WOY].

The binder phase provides the toughness required for the specific applications since the pure carbides would be too brittle. Binder metals have to meet some requirements, amongst others especially a good wettability on the carbide grains which is usually given for iron-group metals. In hardmetals cobalt turned out to have the best combination of properties and thus it is widely used in cermets Co/Ni alloys are commonly applied. Although hardmetals with cobalt binder reveals the best combination of properties in hardmetals some concerns on its use arose in recent years. Currently about 40% of the global cobalt production is located in the Democratic Republic of Congo. Due to the politic instability a high supply risk, accompanied by price jumps, appears. The British Geological Survey [12BGS] ranked cobalt with a score of 7.6 in a supply risk chart ranging from 1–10 where 1 denotes no supply risk and 10 high supply risk, see Table 2-1. From this list it can as well be seen that tungsten has an extraordinarily high supply risk which currently draws increasing attention to both cermets and recycling techniques. Besides the supply risk there are also some concerns about health issues with cobalt [07GRI, 07GRI1] and concerns about the relatively high and volatile price of 30\$/kg. Thus, in recent years cobalt-free binders based on Fe, Ni and alloys thereof and cobalt reduced Fe/Co/Ni alloys gained greater importance. Although they don't show the

widespread application range of cobalt they reveal some specific advantages for particular applications, as the works of e.g. Prakash et al. [79PRA, 09PRA, 14PRA], Sailer [01SAI, 02SAI], Gries [09GRI], Wagner [11WAG], Buchegger et al. [12BUC, 13BUC, 13BUC2] or Schubert et al. [15SCH] show. Such cobalt-free or cobalt-reduced binder alloys are usually referred to as alternative binders in literature.

A variety of classification systems exist for hardmetals. Besides systems regarding the fields of application they are usually categorised by their mean grain size. The classification suggested by the Fachverband Pulvermetallurgie e.V. (FPM) is nowadays de-facto standard, but other notations were for example suggested by Roebuck [95ROE] or Spriggs [95SPR]. An overview over these classifications is listed in Table 2-2. The notations in this work refer to the FPM classification.

Table 2-1: Supply risk of Fe, Co, Ni and W according to the Risk List 2012 of the British Geological Survey. Scale ranging from 1–10; 1 = low risk, 10 = high risk; DRC = Democratic Republic of the Congo [12BGS].

Element	Supply risk	Top producer	Top reserve holder
tungsten	9.5	China	China
cobalt	7.6	DRC	DRC
nickel	6.2	Russia	Australia
iron	5.2	China	Australia

Table 2-2: Classification systems suggested for hardmetals. All values in μm .

FPM		[95ROE]		[95SPR]	
Grain size	Notation	Grain size	Notation	Grain size	Notation
<0.2	Nano	<0.5	Ultra-fine	0.02 – 0.05	nano
0.2 – 0.5	Ultrafine	0.5 – 0.9	Extra-fine	0.1 – 0.5	ultrafine
0.5 – 0.8	Submicron	0.9 – 1.3	Fine	0.5 – 1.0	submicron
0.8 – 1.3	Fine	1.3 – 2.0	Medium	>1.0	conventional fine grained
1.3 – 2.5	Medium	2.0 – 4.0	Medium/ Coarse		
2.5 – 6.0	Coarse	>4.0	Coarse		
>6.0	Extra coarse				

2.2 The early stages of sintering near-nano and ultrafine hardmetals

The main factors influencing the properties of hardmetals are, besides dopants, the WC grain size and the binder phase content. A proper combination leads to a hardness/toughness combination which is ideal for a particular combination [95ROE]. A reduction of the WC grain size can increase both hardness and toughness and thus lead to superior properties for particular applications such as metal cutting [05GRE, 06VIL] or micro-drilling of printed circuit boards [02GIL, 07FU]. Thus, in recent years there was a focus on the development of hardmetals with nano-grained microstructure. Sintering of such materials reveals some specific problems which are described in the chapters below. Consequently, a large number of studies were conducted on these issues. Most of them are subject to liquid-phase sintered hardmetals. Since the focus of this work is on grain-growth inhibition during the early solid-state stages of sintering the following chapters will give an overview of the research published on the latter and no further attention will be drawn to liquid-phase sintering.

As compared to coarser grades the WC in near-nano or ultrafine hardmetals has a substantially higher specific surface. As a consequence some related physical parameters such as surface energy or diffusivities are increased. Thus, the driving force for grain coarsening is substantially higher and kinetic processes promoting both densification and grain growth upon sintering are proceeding significantly faster. Furthermore, particle rearrangement is much easier for small particles. Consequently, the densification of the material is almost completed already upon

solid-state sintering. Both the early densification and rapid sintering processes were subject to a number of studies which are described below.

2.2.1 Densification and microstructural evolution

Porat et al. [96POR] found by dilatometric analysis that full densification in near-nano WC-Co hardmetals can already be achieved upon solid-state sintering.

Da Silva et al. [01SIL, 03MAC] found that wetting of cobalt binder on WC grains initiates at temperatures around 800°C. This behaviour is related to the carbothermic reduction of surface oxides on WC particles [97GIL, 01ALL]. Simultaneously shrinkage of an ultrafine hardmetal initiated, whereas for a coarse grade the onset was found around 1100°C. Hence, densification processes such as particle rearrangement are more promoted in ultrafine grades. Similar results were obtained by Allibert [01ALL].

Maheswari et al. [07MAH] compared the shrinkage of various WC-Co grades from nano to coarse. By increasing grain-size the densification onset shifts from <800°C to 1000°C. For nano grades a densification of 90% was already achieved at 1200°C while it was 20% for the coarse grade. A graph taken from Fig. 1 in [07MAH] illustrating this relationship can be found in Figure 2-1.

Bounhoure et al. [09BOU, 14BOU] recently published results on non-conventional effects upon solid-state sintering of cemented carbides. They found that the shrinkage rate upon heat up decreases once a compact packaging due to particle rearrangement driven by spreading of the binder on WC is reached. Further solid-state densification requires additional mechanisms such as grain boundary sliding or Ostwald ripening. SEM-micrographs of the microstructural evolution upon solid-state densification taken from Fig.3 in [14BOU] can be found in Figure 2-2. The spreading of cobalt was found to be influenced by the C/W ratio. In low-carbon hardmetals (low C/W ratio) the shrinkage initiates at lower temperature as compared to high-carbon alloys (high C/W ratio). As a possible explanation they state the transition from ferromagnetic to paramagnetic state happens at lower temperatures in low-carbon hardmetals which decreases the WC/Co interfacial energy. From TEM studies they observed a morphology change of WC-grains to faceted. Furthermore, they found the

formation of a cubic WC_{1-x} film on some WC grains although it was not related to carbon potential and it was not clear whether it forms upon annealing or cooling. A number of authors such as Schubert et al. [95SCH, 99SCH], Haglund et al. [98HAG], Arato et al. [98ARA], Gille et al. [02GIL] or Petersson et al. [05PET] conducted solid-state densification experiments upon sintering of hardmetals, but the basic findings reveal the same as described above.

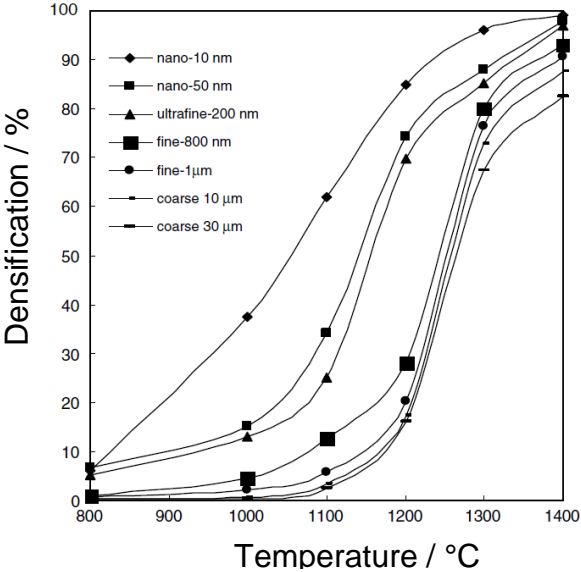


Figure 2-1: Shrinkage of various WC-Co grades upon continuous heating as provided in Fig. 1 in [07MAH].

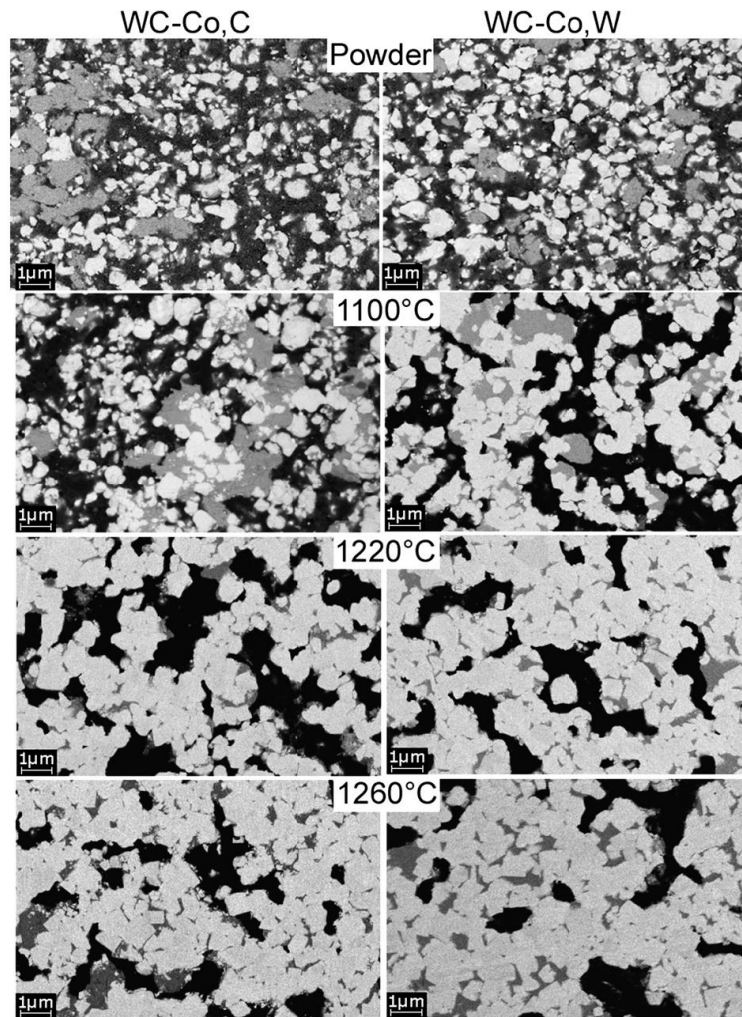


Figure 2-2: Microstructural evolution of WC-Co upon solid-state sintering as published in Fig.3 of Ref [14BOU].

2.2.2 WC grain growth at early sintering stages

Especially the pronounced grain growth is limiting efforts of producing nano and ultrafine hardmetal grades. Most studies on grain growth of conventional hardmetals focus on liquid-phase sintering since almost no coarsening happens upon solid-state. In contrast, the special features of finer grades require a more detailed understanding on solid-state coarsening. Thus, a number of studies on this subject were published in recent years.

A first comprehensive study on the sintering behaviour and grain growth of ultrafine WC-Co was provided by Schubert et al. [95SCH]. Based on interrupted-sintering experiments they found that already at 1100°C–1200°C significant grain growth

occurs. The latter appears concurrent to a change of grain morphology to prismatic grains. As a main growth mechanism in solid-state they reported coalescence of WC-particles and a solution-precipitation process promoted by a thin cobalt film covering the WC grains. Furthermore, they state a strong dependency of solid-state growth on the gross carbon content with a promoted growth at high carbon activities. As a special feature of ultrafine and nano grades, respectively they describe discontinuous grain growth such as local giant or nest-like growth, see also the work of Gille et al. [02GIL]. A number of explanations were provided for this phenomenon such as imbalances originating from powder manufacturing processes or agglomeration of very fine particles. In doped grades they state an insufficient distribution of inhibitors as a possible explanation.

In further works [04SCH] approaching interrupted sintering experiments for hardmetals with an initial WC grain-size of 150 nm they found that the coercive force, which is related to the binder mean free path and subsequently the WC grain size (see 3.7.1), drops at temperatures higher than 1000°C indicating WC grain growth. The growth rate rose with increasing carbon content. They furthermore found that fast heating rates cannot suppress this early growth process [99SCH].

They also provided information on the formation of particular large WC-crystals upon sintering ultrafine WC-Co [02SOM]

In a further study [06ADO] a decrease of coercivity was found upon temperatures higher than 1150°C for undoped samples.

Studies similar to these of Schubert were conducted by Fang and Eason [95FAN] who focussed on the densification behaviour during liquid-phase sintering from 1360–1480°C. They found a significant coarsening already at the beginning of the sintering plateaus, indicating grain growth upon the earlier sintering stages.

Later [05FAN] they reported on the microstructural evolution of hardmetals with nano-scaled WC-powders by interrupted sintering experiments.

In a further study of their research group [07MAH] they published their findings on the solid-state grain growth and densification behaviour of hardmetals with 10 nm initial WC crystallite size obtained by Attritor-milling of micron WC. They found that WC-grains tend to form agglomerates below 1100°C, which are transformed into larger single WC-grains with prismatic morphology upon 1200°C.

In a more detailed experimental study [08WAN] they focused on the grain growth of WC with initial grain size 10, 20 and 50 nm, respectively in WC-Co hardmetals upon both linear heat up and isothermal annealing. They found that grain growth occurs by three characteristic stages. The first stage (I) was described as “*initial slow stage*”, followed by a “*rapid grain-growth stage*” (II) until a “*latter stage*” (III) is reached.

In a further work [09WAN] they reported their results on the influence of the heating rate on solid-state grain growth. Starting from 10 nm WC grain size they conducted linear heat-up experiments with rates of 10 and 200 K/min, respectively. They found that within the temperature range of 810–1100°C the size of both agglomerates as well as crystallites within agglomerates increased almost independent from the heating rate accompanied by a smoothing of the particle surface morphology. The authors explain this effect by oriented coalescence. For micron size powders they state these changes occur at temperatures higher than 1200°C, although they do not provide a source for this statement. When a rapid heating rate was applied they observed no significant suppression of the initial growth mechanisms but a finer grain size as compared to the slow heating rate when reaching 1300°C. The latter seems natural with their experimental set-up since with faster heating the sample is exposed to temperatures where grain growth occurs for only 1/20 of the time as compared to the slow heating rate.

A review concerning various effects in sintering nano-scaled cemented carbides, involving some of the publications mentioned above was provided by Fang et al. [09FAN].

Lay et al. [03LAY] found by means of EBSD measurements that formation of WC-clusters, often observed within submicron hardmetals which may also lead to coalescence effects, is related to the presence of special grain boundary types such as $\Sigma 1$ and $\Sigma 2$ already within the initial powder mixture.

Sanchez et al. [05SAN] found a decrease in hardness upon post-sinter hot isostatic pressing of undoped ultrafine WC-Co hardmetals at solid-state temperatures which they relate to Ostwald-ripening.

A theoretical study on the coarsening behaviour of hardmetals was published by Sun et al. [07SUN] in terms of so called grain growth diagrams which are calculated graphs describing the relationship between WC grain size, isothermal annealing time and annealing temperature upon solid-state sintering. It should be considered that

these maps are not based on experimental data but constructed by theoretical calculations based on the concept of Oswald ripening and diffusion data of W, C and Co, respectively within the Co binder phase for stoichiometric W:C ratio. The experimental proof of their concept is based on measuring the grain growth of a WC-11Co hardmetal with 80 nm initial WC grain size at four temperatures of 900, 1100, 1200 and 1300°C, respectively. However, they do not provide any information on annealing time, heating rate or carbon content of the samples making the proof questionable. Nevertheless, they state that their calculations are “*basically coincident*” with experimental data provided by Wang et al. [05WAN]. Figure 2-3(a) illustrates the grain growth maps and (b) the corresponding experimental data provided by the authors.

Summarising the results published on the solid-state grain growth it turns out that especially for nano scaled grades significant coarsening is already observed at temperatures below 1000°C driven by a coalescence mechanism of agglomerated grains. The growth rate increases rapidly at temperatures around 1100–1200°C, depending on the initial grain-size, carbon potential and the particular experimental setups. An overview over experimental grain growth data provided by several authors can be found in Figure 2-4.

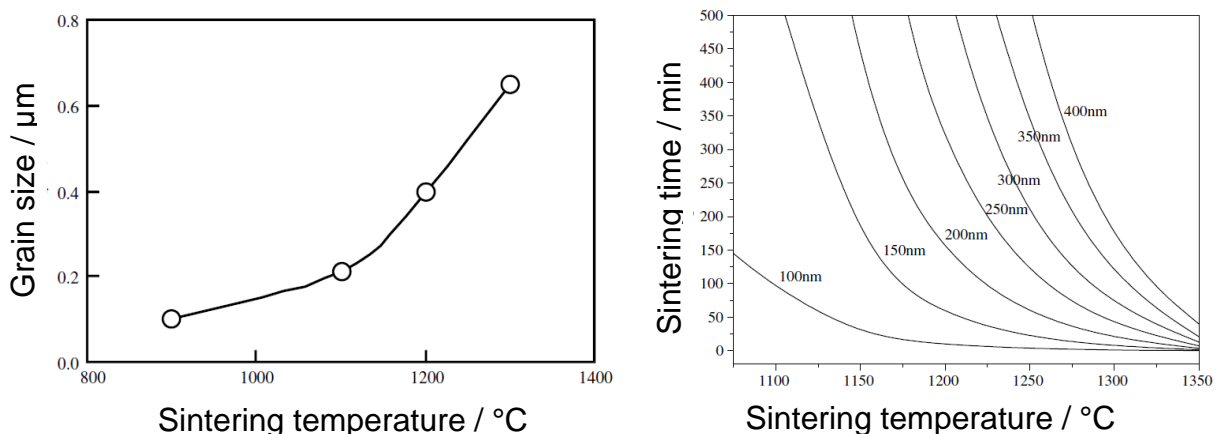


Figure 2-3: Grain size of WC grains in WC-11Co as function of sintering temperature (a) experimental results (Fig. 6 in [07SUN]) and (b) calculated grain growth maps (Fig. 5 in [07SUN]).

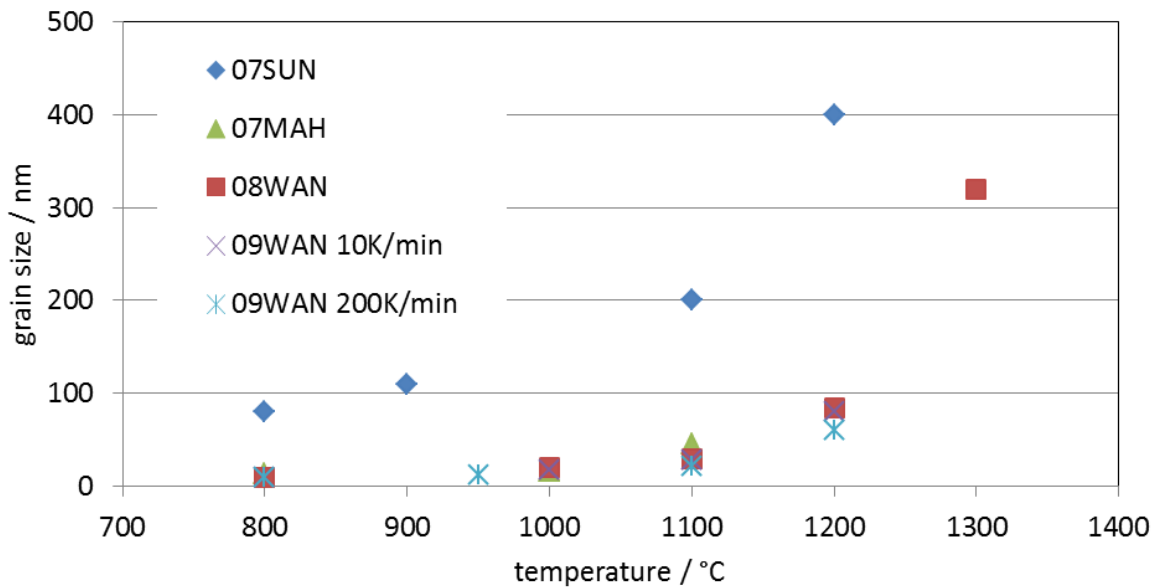


Figure 2-4: Grain growth curves upon heat-up of hardmetals with nano WC reconstructed from references [07SUN], [07MAH], [08WAN] and [09WAN].

2.3 Grain-growth inhibition

Based on the findings on solid-state grain growth it is evident that near-nano or ultrafine hardmetal grades can only be realised when sufficient growth inhibiting mechanisms are available already upon the early sintering stages.

Nowadays the use of grain-growth inhibitors in amounts below 1 wt% is industrial standard. The inhibiting effect of group 4–6 transition metals is known for decades by means of empirical findings. In a first comprehensive study Hayashi et al. [72HAY] tested the ranges for maximum effectiveness of various transition metal carbide additions. VC turned out to be the most effective inhibitor; sufficient effects were as well found for NbC and TaC additions. Cr₃C₂ and Mo₂C reveal their potential only at relatively high concentrations. Nevertheless Cr₃C₂ in a typical amount of <1 wt% and VC <0.4 wt% are nowadays the most common inhibitors [91FUK, 13RIC] since a high mobility as well as a sufficient solubility within the binder phase is observed already at relatively low temperatures [05MOR]. Although the maximum inhibiting effect is observed at relatively high concentrations an addition higher than the maximum solubility degrades the fracture toughness by formation of brittle precipitations [98ZAC, 13TOU] and should thus be avoided. A combination of both VC and Cr₃C₂

was found to further improve the effect, in particular yielding a narrower grain-size distribution as compared to VC single doping [99CAR, 10BRI1]

Almond and Robuck [87ALM] conducted comprehensive experiments on the effects of VC, Cr₃C₂ and (Ta,Nb)C on the grain growth and resulting properties such as hardness, toughness wear, creep and oxidation.

Besides these standard dopants Cha et al. [01CHA] found that 0.7 wt% TaC/VC is superior in terms of the final grain-size as compared to 0.7 wt% Cr₃C₂/VC doping. Lengauer, Lauter and Brieseck et al. [06LAU, 09BRI, 10LEN] showed by choosing proper inhibitor combinations such as Cr₃C₂/VC/TaC not only the grain size but also mechanic properties and the Weibull parameter can be significantly improved. They also reported benefits from replacing Cr₃C₂ by Cr₂N regarding the appearance of abnormal grown grains [09BRI, 10BRI].

A further growth reduction by adding a mixed carbonitride of composition (Cr_{0.8}V_{0.2})₂(C,N) was found by Xie et al. [14XIE]. They conclude a clear hardness improvement as compared to nitrogen-free carbide, which they relate to lower stability and hence faster solution in the binder phase. However, their reported values of 1690 and 1680 HV₃₀ for the carbonitrides and the carbide respectively, are equal within the error range. Similar findings apply to TRS (3800 vs. 3600 MPa) and K_{IC} (9.9 vs. 10.2 MPa.m^{0.5}) which are equal within usual error ranges for these methods. Thus, their conclusions are questionable. They furthermore state that the nitrogen from the carbonitrides reduces the W solubility in the binder phase of the sintered and cooled hardmetal from 38.5 to 22.7 wt% (EDX-analysis). This interpretation is as well questionable since the amount of nitrogen introduced by 0.5 wt% carbonitrides doping is small and the main part will escape to the atmosphere upon dissolution. Also the measured W concentrations seem unrealistically high and are meaningless without information on the carbon potential.

Especially when added in high concentrations molybdenum reveals a significant inhibition potential (Figure 2-5). Koos et al. [10KOO, 13BUC] found that addition of molybdenum nitride yields a slightly finer microstructure as compared to carbide. Genga et al. [13GEN] reported a significant improvement of mechanical properties of SPSed WC-Ni hardmetals by addition of Mo₂C which they assume to enhance the wetting properties of Ni on WC.

Dalbauer and Jewett [14DAL] found a significant “rounding” of WC grains in Mo-doped hardmetals but no significant hardness increase.

Rare earth oxides such as CeO_2 or Y_2O_3 were suggested as alternative inhibitors by Lin et al. [05LIN] and Liu et al. [06LIU]. They found that such additions can potentially yield a narrower grain-size distribution, whether they are used as single doping or combined with more common inhibitors such as VC.

In recent years the effects of GGI-addition in WC-Co hardmetals seem to be of rising interest as suggested by an increasing number of publications. However, some of them such as [14JIA, 14LIU, 15ALA, 15BAO, 16FAB] don't really expand the understanding of hardmetals but deliver findings which have already been state-of-the-art for several years.

Besides the addition of inhibitors grain growth in undoped hardmetals can as well be controlled by adjusting the binder phase chemistry. The latter is influenced by two main factors: the composition of the binder alloy and/or the adjustment of the carbon content.

The gross carbon content has a strong impact on the binder phase composition since an increase in carbon reduces the tungsten solubility as can be seen from the tungsten-rich corner of the W-C-Co diagram [98HAG] in Figure 2-6. At 1200°C the solubility of tungsten in the binder ranges from 2.5 – 9.0 at% within the WC+Co two phase area of the system. In hardmetals with nickel binders the concentration range is even wider, from a W:C atomic ratio of 1:2 to 3:1 [02WIT]. The adjustment of the carbon potential changes the binder phase composition only within the two-phase area. When the carbon content is too low, eta phase is formed, when it is too high carbon precipitations appear. In both cases the composition of the binder phase is fixed and does not change upon a further adjustment of the carbon concentration. It was found by several authors, e.g. [03CHA, 09DEL, 13BOR] that high carbon potential and, hence, low tungsten concentrations promote grain growth while it is less pronounced at low potentials. Chabretou et al. [03CHA] suggest the nucleation is more activated in C-rich alloys by precipitation of carbon at the WC/binder interface.

The second method for growth control in undoped samples is to change the composition of the binder metal. Wittmann et al. [02WIT] found that hardmetals with nickel binder exhibit much higher growth rates as compared to cobalt while almost no

growth is observed in iron binders. Richter et al. [13RIC] found that in hardmetals with alternative Fe/Co/Ni-40/20/40 wt% binder grain growth of WC is retarded as compared to hardmetals with cobalt binder.

However, the findings on grain-growth inhibitors discussed above are mostly subject to liquid-phase sintered hardmetals. Information on the solid-state efficiency of GGIs became available in recent years from a number of investigations based on the SPS technique, amongst others by Huang et al. [07HUA], SUN et al. [07SUN, 07SUN1, 11SUN], Bonache et al. [11BON], Espinosa-Fernández et al. [13ESP] or Al-Aqeeli et al. [14ALA, 15 ALA, 15ALA1]. Unfortunately it is hard to extract suitable data from these publications since most of them are biased by substantial methodical shortcomings. Most authors conducted their experiments in a temperature range of 1200–1300°C. Especially for chromium-doped, and by less extent also for vanadium-doped hardmetals the liquid-phase formation temperature is somewhere within this range, depending on the carbon potential and the GGI concentration. At a certain temperature a chromium-doped hardmetal can hence be in liquid-state, while the binder phase of VC-doped and undoped hardmetals is still solid. Subsequently Conclusions on the efficiency, the densification and the mechanical properties of such publications are questionable. Some authors also provided no information on the carbon potential. Since SPS dies are commonly produced from graphite the samples are in direct, pressured contact with carbon upon sintering and will likely form a carbon gradient. The problem with liquid-phase upon SPS is that the binder phase is by some extent squeezed out which influences the resulting properties of the material.

As stated, most of the authors fail to comment on one or more of these effects. Nevertheless, some information regarding the efficiency of GGIS at lower temperatures can be read by the following publications.

Huang et al. [07HUA] investigated the influence of 0.9 wt% of VC, NbC or Cr₃C₂ doping on the grain size and the mechanical properties of WC-Co hardmetals SPSed at 1240°C for 2 min at 60 MPa. They found almost no inhibiting effect of NbC, a certain effect of Cr₃C₂ and a strong effect of VC. The cumulated frequency after SPS, taken from Fig. 4 of [07HUA] is shown in Figure 2-7. However, no information on the carbon potential was provided. With 0.9 wt% Cr₃C₂ and direct contact to graphite the

binder phase is expected to be in liquid phase at least close to sample surface, while it is solid for the undoped sample (compare solidus temperatures in Table 2-3)

Bonache et al. [11BON] found that is significantly more effective at 1100°C as compared to chromium, which has only slight inhibiting effect. At this temperature binder phase is in solid state for any sample.

Al-Aqeeli et al. [14ALA, 15ALA1] found by SPSing WC-Co hardmetals based on WC with 10 nm initial grain-size that VC is more effective than Cr₃C₂. The sintering temperature range was 1200-1300°C, which results in above mentioned liquid-phase issue. Also no carbon potential was mentioned.

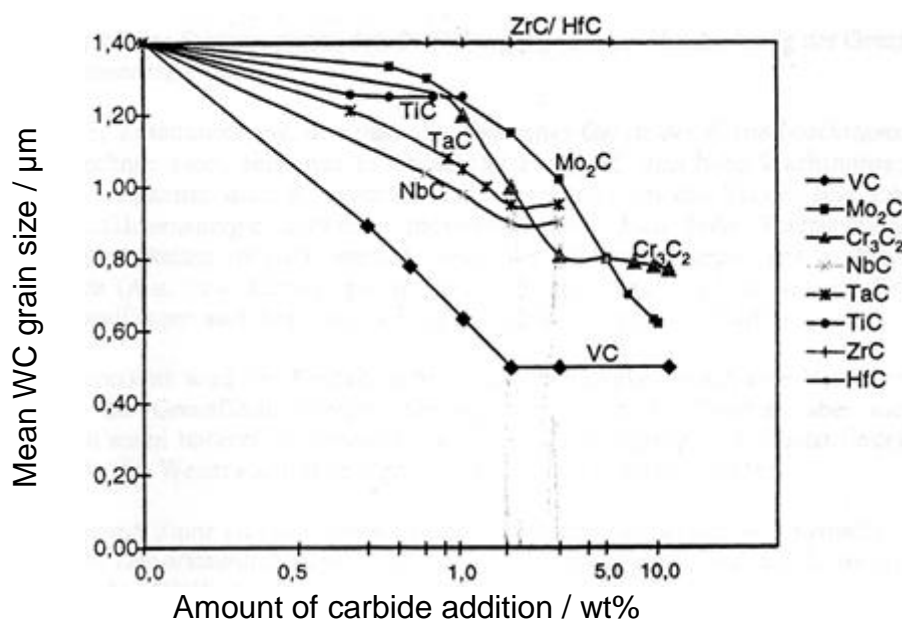


Figure 2-5: Inhibition effect of various grain-growth inhibitors as published by [72HAY].

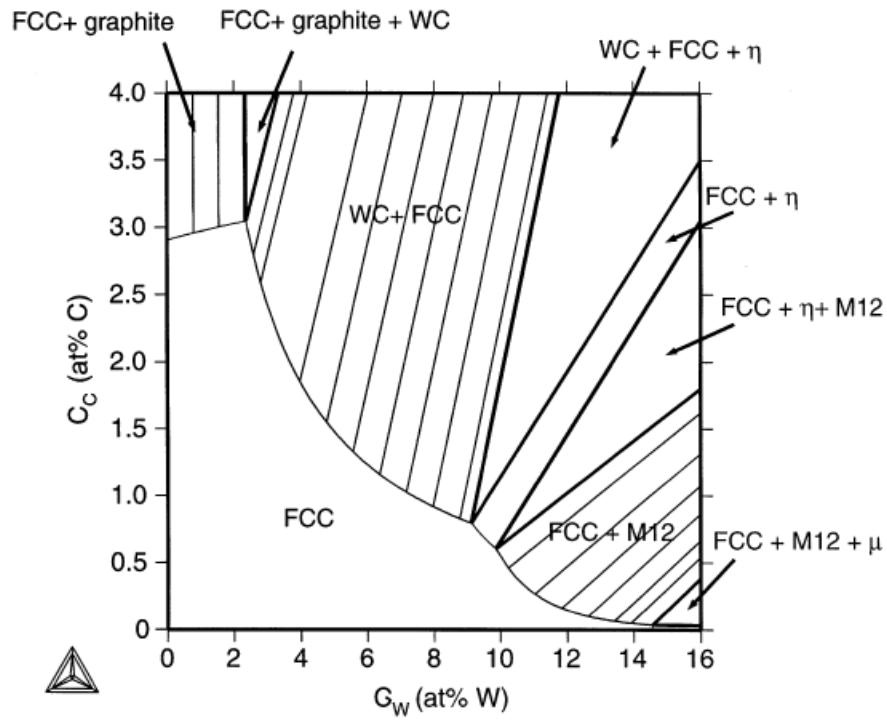


Figure 2-6: Co-rich corner of the C-Co-W system at 1200°C taken from Fig. 1 in ref [98HAG].

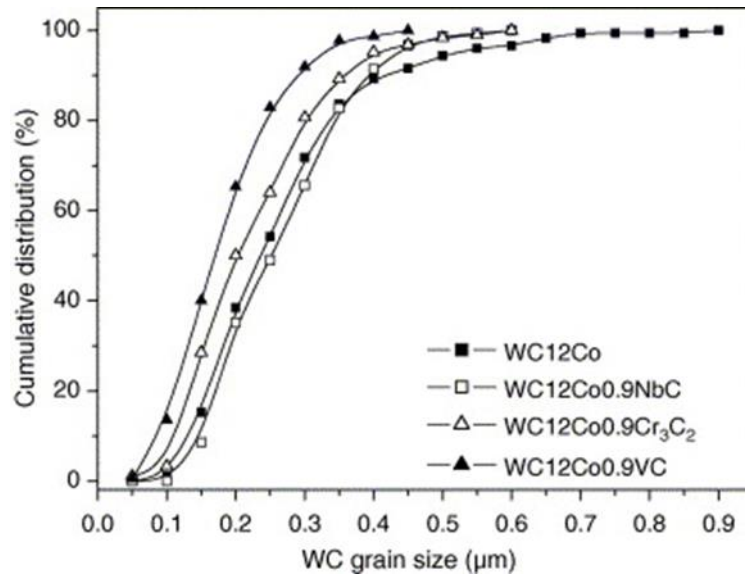


Figure 2-7: Cumulative grain-size distribution of WC in SPSed hardmetals with 0.9 wt% of NbC, VC or Cr₃C₂ doping as published in Fig.4 of ref. [07HUA].

2.3.1 Mechanism of grain-growth inhibition

Once the inhibiting effect of GGIs was discovered the question on the underlying mechanism arose. Despite various efforts the inhibiting mechanisms are not yet clarified which might be attributed to the fact that processes at high temperatures are not accessible for in-situ observations and thus limited to cooled-down samples (04SCH). Upon cooling thermodynamic parameters such as solubilities change and thus the composition and constitution of WC grains, the binder phase, WC/binder and WC/WC grain boundaries does not necessarily represent the high temperature state. The inhibition effect can origin from two basic mechanisms: A reduction of interfacial energy and thus the thermodynamic driving force or by influencing the growth kinetics. Subsequently, the following possible mechanisms were suggested by several authors:

- (1) A reduction of the tungsten diffusional flow through the binder phase caused by reduced tungsten solubility in presence of inhibitors.
- (2) The formation of a cubic $(GGI,W)C_x$ layer at WC/Binder grain boundaries acting as a barrier for WC dissolution and reprecipitation
- (3) A reduction of the interfacial energy of WC grains by formation of $(GGI,W)C_x$ layers or GGI segregation at the grain boundaries and a subsequent reduction of the driving force for grain growth
- (4) The temporary blocking of active growth sites on WC grains by temporary incorporation of GGIs
- (5) The reduction of the effective carbon activity within the binder phase by formation of GGI-C clusters limiting the carbon available for WC formation.

Seo et al. [06SEO] reported a strong influence of various GGI additions on the solubility of W in the liquid binder phase which they relate to the inhibiting effect according to (1). However, Exner et al. [73GRE] identified a reaction step within the solution-reprecipitation process as rate controlling, thus they state (1) and (2) cannot be the main inhibiting mechanisms. These findings seem legit since VC has a much stronger inhibiting effect as compared to Cr_3C_2 but a significantly lower solubility and hence a lower influence on the W-content of the binder phase [06LAU].

A number of studies are subject to the formation of interfacial layers upon sintering of WC-Co hardmetals. Yamamoto et al. [00YAM] found that vanadium-rich mixed carbide segregates at the WC-Co interface after liquid-phase sintering. Supported by TEM-EDS-scans they assume that $(W,V)_2C$ is formed since $(W,V)C$ reveals only a limited W solubility of 25 at%. The amount of the segregated mixed carbide depends on the habit of the WC grain at the interface. A HRTEM picture and the corresponding TEM-EDS scans (Fig.11 and Fig.12 in [00YAM]) towards the WC-Co interface can be found in Figure 2-8. A sample quenched from 1200°C revealed no mixed carbide layers but an enrichment of vanadium at the interface within the cobalt binder and faceting of the WC grains. They conclude that WC grain growth is retarded by a reduction of W solubility by V-addition according to (1) and a reduction of the solution-precipitation process due to the V-segregation.

Lay et al. [01LAY, 02LAY, 03LAY, 12LAY] found $(W,V)C$ and $(W,V)_2C$ precipitations on WC steps with orientation that allows a near-coincidence relationship. They furthermore found $(W,V)C_x$ layers within WC grains. They conclude that such layers already exist upon liquid-phase sintering and relate them to the inhibiting effect of VC which will refer to mechanism (2) or (3). Their findings were confirmed by Sugiyama et al. [12SUG] who found that $(W,V)C_x$ layers exist within WC grains several nanometres from the WC/Co interface. Figure 2-9(a) shows a HRTEM image of such a layer while b) shows the corresponding EDS scan, taken from Fig.4 in [12SUG].

Similar results were reported by Warbichler et al. [01WAR], Lee et al. [03LEE], Kawakami et al. [04KAW, 05KAW, 06KAW] and Weidow et al. [10WEI] although some of them draw different conclusions.

In chromium-doped samples Yamamoto et al. [01YAM] observed a lower influence on the WC grain shape as compared to vanadium and no formation of a mixed carbide layer at the WC/Co interface. However, they found an enrichment of chromium at the interface. A HRTEM micrograph of a chromium-doped hardmetal and the corresponding TEM-EDS line scan (Fig. 2 and 4 in [01YAM]) can be found in Figure 2-4(c) and (d). Elfving and Norgren [05ELF] confirmed both the enrichment of Cr at the interface and the absence of intergranular carbide layers. However, Brieseck et al. proved the existence of such a $(W,Cr)C_x$ phase by means of a WC/Cr₃C₂ diffusion couple [10BRI].

Delanoë and Lay [04DEL] found a metastable (W,Cr)C film forming on WC grains upon cooling from liquid phase. Chromium enrichment at the interface was already observed at 1200°C [09DEL1] which they assume to be associated with a change in interfacial energy. They furthermore found an interdependency of both the chromium content and the carbon potential on the evolution of the grain morphology upon liquid-phase sintering. In a recent publication [15BOU] they analysed the Co binder and the WC/Co interface of a chromium-doped hardmetal at 1220°C by TEM-EDX point analyses. While the Cr/Co ratio was 3.7 at% in the binder phase it was 5.6 at% at the interface, which they interpret as chromium enrichment at the interface.

Kawakami et al. [05KAW] compared the interface formation in VC single doped and VC+Cr₃C₂ double doped hardmetals. They found a higher V-concentration at the interface of the double doped sample. As inhibiting mechanism they suggest the blocking of active WC-growth sites by GGIs according to mechanism (4). With higher V-concentrations the average duration of stay at the site increases, leading to enhanced inhibition potential. However, they state that no strict correlation exists between the inhibiting effect and the amount of segregations. From experiments with varying cooling rates they conclude that interfacial segregation layers are formed upon cooling due to the decreasing solubility at lower temperatures and, hence, they are not responsible for the inhibiting effect.

In a further work [06KAW] they investigated the interfacial segregation of Ti and Ta and again found no correlation between the layer thickness of interfacial mixed carbides and the inhibiting effect, from which they conclude that such layers are not responsible for the inhibiting effect. In a further work [15KAW] they provide a model for the formation of a (W,V)C_x layer on WC(0001) upon cooling from sintering temperature.

Li et al. [07LI] claimed that the inhibition effect in Cr+V-doped hardmetals is based on reduction of the W solubility by GGIs and the subsequent retardation of the solution-precipitation process according to mechanism (1).

Poetschke et al. [12POE, 13POE, 14POE] found that VC and Cr₃C₂ can efficiently suppress grain growth in binderless WC. Thus, the binder phase is not necessarily required in order to explain the inhibition mechanism of these carbides. However, they used hardmetal linings to mechanically activate their powder prior to sintering.

The subsequent wear provided a certain amount of Co subsequently a phase of high mobility in the WC-powder. Therefore these materials are not strictly binderless.

As mentioned above an in-situ observation of interfacial processes is not possible which draws attention to theoretical considerations and simulations. Such studies were recently published by Johansson et al. [10JOH, 12JOH] by means of first principal calculations on VC-doped hardmetals. They state the existence of a $(W,V)C_x$ layer on WC grains over a large temperature range which is related to the inhibiting effect. According to their results a few atomic layers of cubic $(W,V)C$ are stable on WC even when $(W,V)C$ is unstable according to the phase diagram.

A reduction of the carbon activity in the binder phase by formation of stable metal-carbon clusters was suggested as a mechanism for the strong growth inhibiting effect of iron based binder alloys [04SCH] according to mechanism (5). This mechanism can as well be valid for other metals since all effective inhibitors are stable carbide formers, although there is no experimental proof of such clusters in a hardmetal binder alloy at sintering temperatures.

It has to be remarked when reading the publications mentioned above one may find an inconsistent use of the term “segregation”, which for some authors means the enrichment of GGIs at the interface excluding interfacial mixed carbide layers while other authors include these layers.

Summarising the various studies no clear picture on the inhibiting mechanism can be drawn. Recent experimental and theoretical findings suggest the existence of a $(W,V)C_x$ layer at the WC/Co interface which is related to the inhibiting effect of VC. However, no such mixed carbide layer was found for chromium which as well acts as an inhibitor. The inhibiting effect of Cr_3C_2 (and to a certain extent of VC) was related to enrichment in the binder phase adjacent to the interface. It was shown that the formation of such enrichments depends on the cooling rate and thus they do not necessarily exist upon sintering. Furthermore it was shown that the thickness of interfacial layers for various GGIs cannot be related to the effectiveness of the inhibition. However, it is very likely that a combination of at least some of the mechanisms (1) – (5) is required in order to explain the efficiency of GGIs.

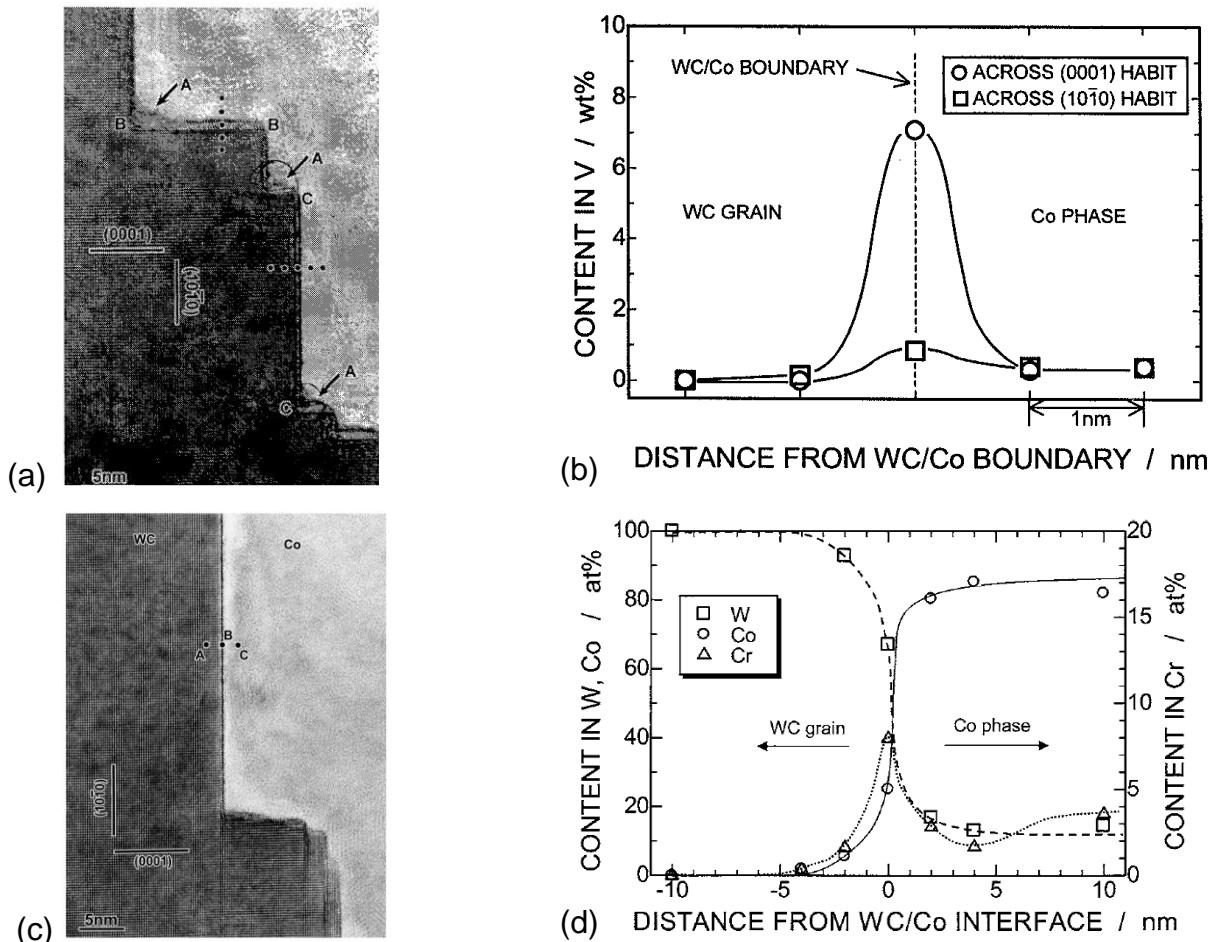


Figure 2-8: a) HRTEM image of the WC/Co interface of a VC-doped hardmetal and (b) corresponding TEM-EDS scans as provided in Figs. 11 and 12 of ref. [00YAM] (c) HRTEM image of the WC/Co interface of a Cr₃C₂-doped hardmetal and d) corresponding TEM-EDS scans as provided in Figs. 2 and 4 in [01YAM]

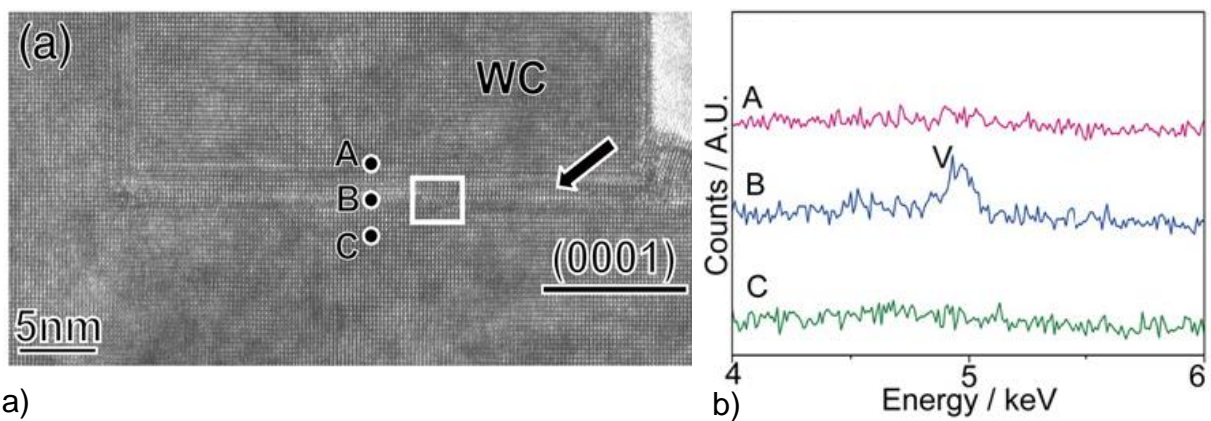


Figure 2-9: (a) HRTEM image of a (W,V)_x layer within a WC grain and (b) corresponding TEM-EDS scans as published in Fig.4 in [12SUG].

2.3.2 Grain-growth inhibitors and sintering behaviour

The addition of grain-growth inhibitors not only influences the final WC grain-size, but also the sintering kinetics of hardmetals. GGIs are known to change the composition and the wetting behaviour of the binder phase [06LAU]. Another important effect is that most GGIs form stable oxides. While the surface oxides of cobalt and WC are reduced below 900°C the oxides of Cr and V are stable up to 1000–1200°C, see e.g. [01ALL, 10BRI, 12BUC, 15WAN].

Comprehensive studies approaching the influence of GGIs on the densification of hardmetals were published by Leitner et al. [04LEI] and Gestrich et al. [06GES]. The onset of densification at 800°C was generally not influenced. Upon further heating the shrinkage was retarded as compared to an undoped hardmetal. The maximum of the shrinkage rate has higher amplitude in doped samples and is shifted to higher temperatures, as can be seen from Figure 2-10.

Caspers et al. [10CAS] reported on the densification of hardmetals with near-nano WC of BET=3.1 m²/g doped with 0.45 w% VC and 0.6 wt% Cr₃C₂. They found that up to 93% of the total solidification is reached below 1300°C within solid-state sintering range. They furthermore found the onset temperature of the maximum shrinking rate decreases by 30 °C for hardmetals with high carbon potential as compared to low potential within the two phase area.

Bounhoure et al. [07BOU, 09BOU, 14BOU] conducted detailed investigations on the influence of chromium on the microstructural evolution of WC-Co hardmetals with and without chromium doping.

Wang et al. [14WAN, 15WAN] performed detailed thermal analysis of Cr₃C₂-doped hardmetals. They claim the formation of (W,V)C and corresponding oxides upon the very first sintering stages <1100°C. The thermal analysis of doped hardmetals as published in [15WAN] is depicted in Figure 2-11.

Further studies on the influence of GGI on the densification were conducted e.g. by Gille et al. [02GIL] and Delanoë et al. [05DEL] which show similar results.

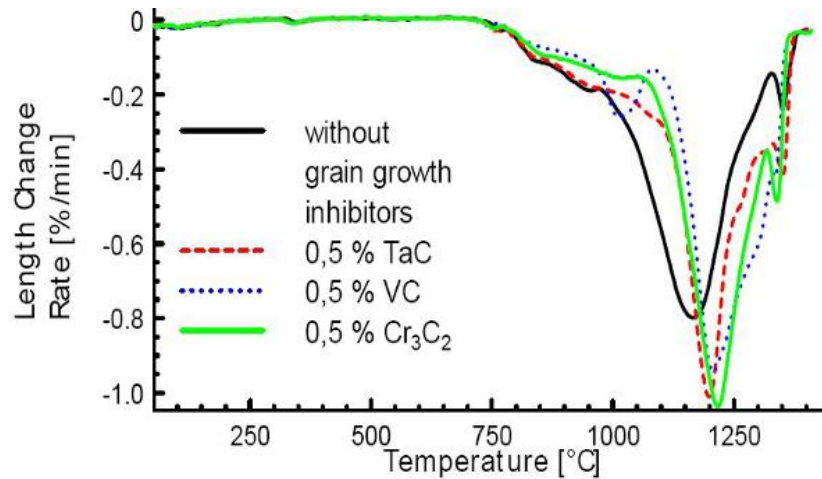


Figure 2-10: Influence of various GGI additions on the densification of WC-Co taken from [06GES].

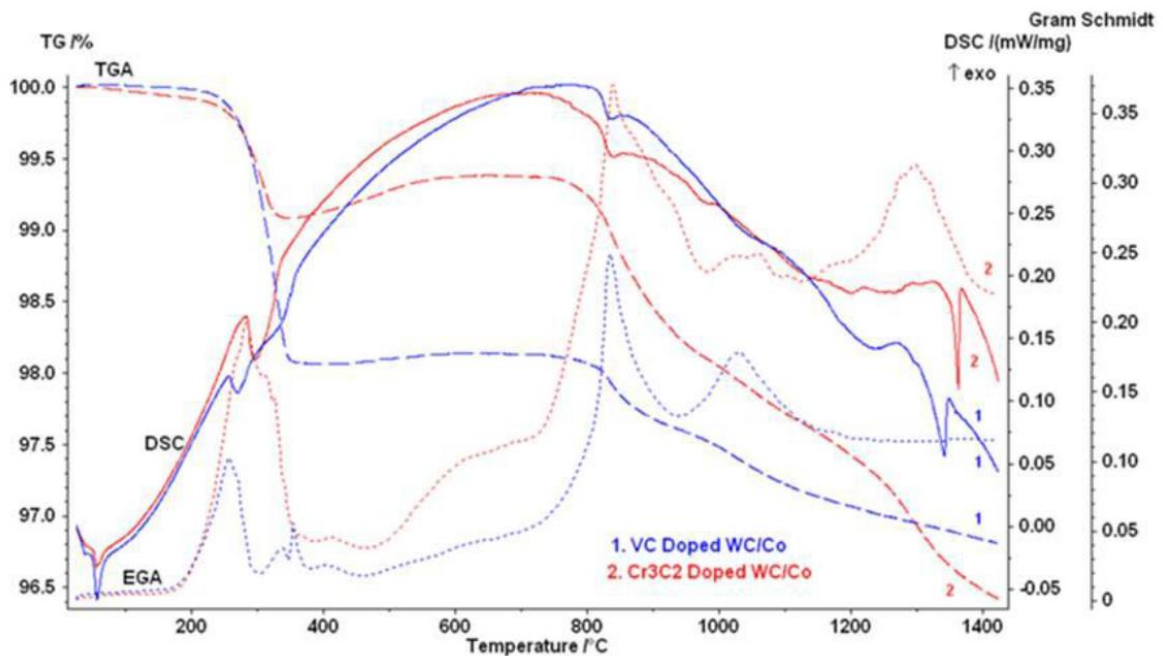


Figure 2-11: Thermal analysis of WC-Co hardmetals doped with 0.17 wt% VC or Cr_3C_2 as published in Figure 3 of Ref [15WAN].

2.4 Phase Equilibria in hardmetals

Due to its industrial importance thermodynamics of the W-C-Co system is well described. An isothermal section of the system is illustrated in Figure 2-12 (a) while (b) shows a corresponding isopleth at 20 wt% Co with varying carbon content taken

from refs. [15BON] and [16ZHO], respectively. The gross carbon content of hardmetals is usually adjusted within the so called carbon window denoting the area between the blue dots in Figure 2-12 (b) where only WC and fcc (binder phase) are present in equilibrium state. At higher carbon contents graphite precipitates accompanied by a decrease of both hardness and transverse rupture strength (TRS). At carbon contents below the two phase window M_6C (eta or η , where $M=Co$ or W) precipitates. Since these precipitates contain cobalt the binder fraction of the alloy decreases which increases the hardness but reduces toughness and TRS. Such M_6C precipitates are brittle and usually large as compared to the WC grains leading to further decreased toughness and fatigue strength. Hence, both carbon and M_6C precipitations are usually avoided. As it can be seen from Figure 2-12 (a) the two phase area WC + fcc becomes wider at higher cobalt content which makes the carbon adjustment easier.

First calculated phase diagrams of hardmetals with alternative binder alloys were published by Guillermet [88GUI]. A phase diagram of hardmetals with Fe/Co/Ni 40/20/40wt% binder was published by Schubert [15SCH]. However, improved phase diagrams for the alternative binder alloys Fe/Ni=15/85wt% and Fe/Co/Ni=40/20/40wt% used in this work were recently published by our group [16ZHO]. As illustrated in Figure 2-13 for WC with 20 wt% of (a) Fe/Co/Ni=40/20/40wt% and (b) Fe/Ni=15/85 wt% binder alloys the carbon window in such hardmetals is shifted as compared to the stoichiometric carbon content. The latter is illustrated by the red square on the horizontal axis.

The influence of chromium on the phase equilibria as a function of carbon potential can be read from the phase diagram in Figure 2-14(a) showing an isopleth of the system C-Co-Cr-W at fixed cobalt and chromium concentrations of 16 at% and 1.44 at%, respectively. Besides a reduction of the solidus temperature a melting range occurs as compared to the invariant reactions in the undoped system C-Co-W as shown in Figure 2-12(b). The phase field WC + fcc + liquid is significantly widened regarding the melting range. As a consequence, upon sintering of a chromium-doped hardmetal both fcc and liquid binder phase are present simultaneously over a wide temperature range of 800–1200°C with possible influences on the shrinkage behaviour or the homogeneity of the hardmetal. A detailed experimental-based

thermodynamic description of the system W-C-Cr-Co was recently published by Kaplan et al. [15KAP].

The temperatures of melt formation as published by several authors are listed in Table 2-3. While the phase equilibria liquid + WC + fcc + graphite and liquid + WC + fcc + M_6C are invariant for the W-C-Co system the addition of GGIs causes the formation of a melting range. The temperatures in Table 2-3 refer to the invariant temperatures where applicable, else they state the onset of liquid-phase formation (solidus temperature) upon heat up. Further information about the width of the melting range can be found in the corresponding references. The data of Hashiya et al. [09HAS] was determined from model alloys with 31 wt% of binder metal and 1.7 wt% of dopant (Cr_3C_2) or VC. Comparing to the solubility data listed in Table 2-4 it can be seen that the dopant concentrations are below the solubility limit. Since the influence of the melt formation is a function of the dopant concentration these data do not represent the maximum melting point reduction. It also has to be kept in mind that the solubility of dopants depends on the carbon potential of the hardmetal. Thus, the addition of a constant amount of dopants to hardmetals with varying carbon potential has different relative impact regarding the reduction of solidus temperature.

If chromium is added in an amount exceeding the solubility, as in in case of some diffusion couple components used in this work, cubic carbide precipitations such as M_7C_3 appear. Zackrisson et al. [98ZAC] and Kaplan et al. [14KAP, 14KAP1] reported a certain solubility of cobalt, especially in M_7C_3 where 21 wt% are soluble at 1250°C, which reduces the amount of cobalt available in diffusion couples. An overview of the results taken from Kaplan et al. is listed in Table 2-4.

Table 2-3: Liquid-phase formation temperatures in various hardmetal systems. Liq.= liquid phase, MC=metal carbide, gra.=graphite.

System	Equilibrium*	Melt formation** (°C)	Reference
W-C-Co	Liq. + WC + fcc + gra.	1298	01KRU
		1298	09HAS
		1290	05DEL
	Liq. + WC + fcc + M ₆ C.	1368	01KRU
		1368	09HAS
		1355	05DEL
W-C-Fe/Ni 15/85	Liq. + WC + fcc + gra.	1305	16ZHO
	Liq. + WC + fcc + M ₆ C.	1414	16ZHO
W-C-Fe/Co/Ni 40/20/40	Liq. + WC + fcc + gra.	1220	16ZHO
	Liq. + WC + fcc + M ₆ C.	1346	16ZHO
C-Co-V	Liq. + fcc + VC	1265	08FRI
W-C-Co-V	Liq.+ WC + fcc + MC + gra.	1254	05FRI
		1258	09HAS
	Liq.+ WC + fcc + MC + M ₆ C	1320	05FRI
		1329	09HAS
C-Cr-Co	Liq. + fcc + M ₇ C ₃ + gra.	1210	08FRI
W-C-Co-Cr	Liq. +WC + fcc + M ₇ C ₃ + gra.	1191	08FRI
W-C-Co-Cr-V	Liq. + fcc + WC + gra.	1226	09HAS
	Liq. + fcc + WC + M ₆ C	1278	09HAS

*Note that in doped systems the equilibrium Liq. + fcc + WC + M₆C is not invariant and hence the solidus temperature depends on the gross carbon content.

**For systems with a melting range the temperature of melt formation refers to the melting onset upon heat-up (solidus temperature)

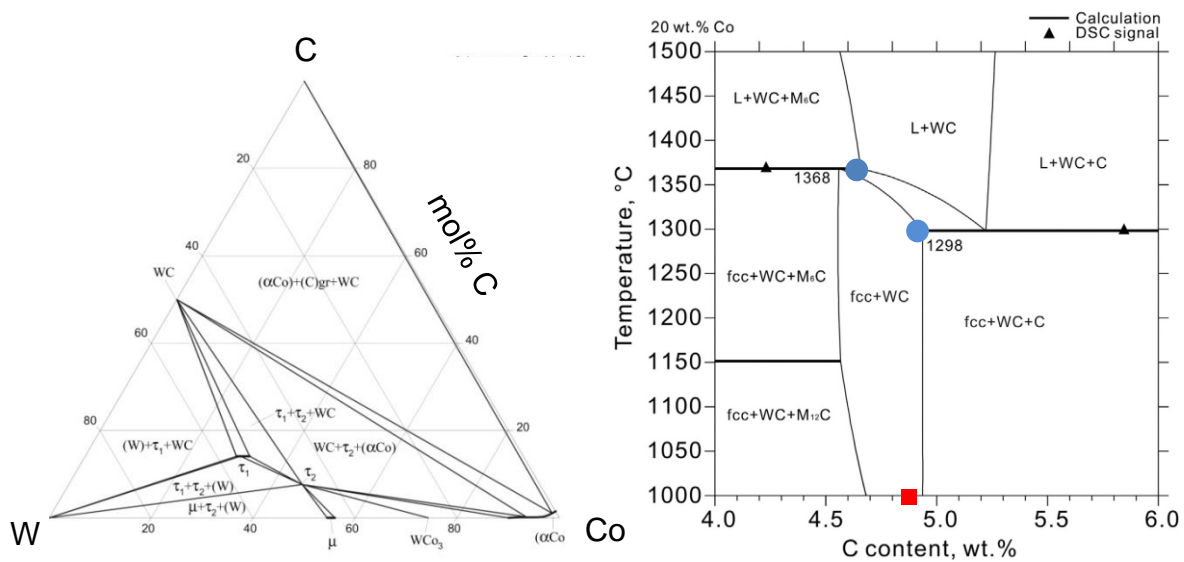


Figure 2-12: (a) isothermal section of the system W-C-Co at 1200°C [15BON] and (b) corresponding isopleth at 20 wt% Co [16ZHO]. Blue dots: border of sintering window; Red square: stoichiometric carbon.

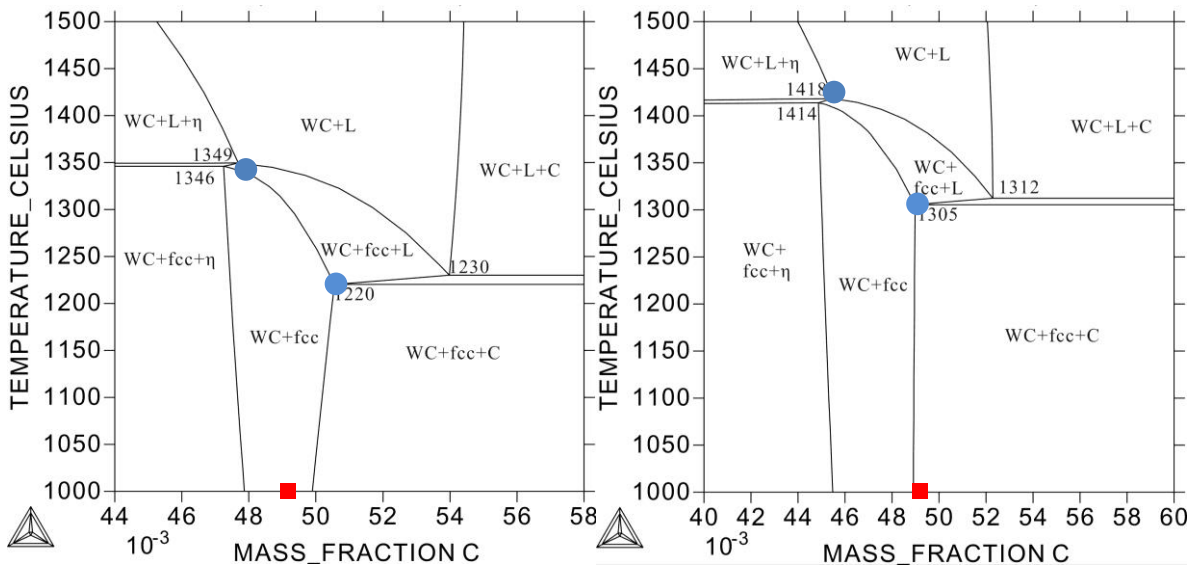


Figure 2-13: isopleths of the systems WC-20 wt% binder with (a) Fe/Co/Ni-40/20/40wt% and (b) Fe/Ni-15/85wt% binder alloys taken from [16ZHO]. Blue dots: borders of sinter-window; Red square: stoichiometric carbon.

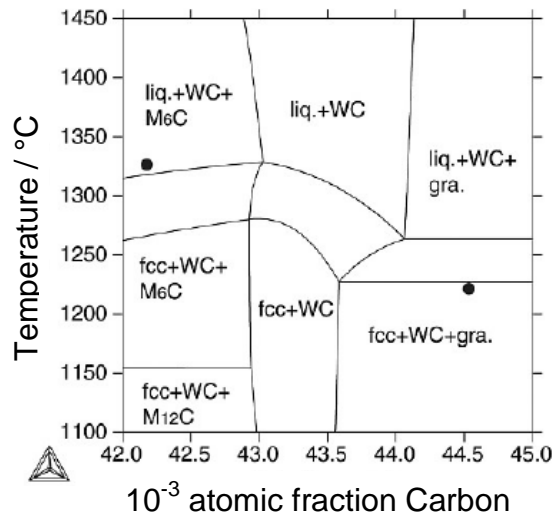


Figure 2-14: Isopleth of the system WC-Co with 0.65 at% Cr and 12.4 at% Co according to Fig. 2 in [08FRI].

2.5 Solubilities of hardmetal constituents

The solubility of grain-growth inhibitors in solid hardmetal binder phases shows a strong dependency on the temperature and the gross carbon content. Comprehensive data has been published by Obbard et al. [01OBB], Lauter et al. [06LAU] and Frisk [08FRI]. An overview on the data published in literature is listed in Table 2-4.

If chromium is added in an amount exceeding the solubility, as in in case of some diffusion couple components used in this work, cubic carbide precipitations such as M_7C_3 appear. Zackrisson et al. [98ZAC] and Kaplan et al. [14KAP, 14KAP1] reported a certain solubility of cobalt, especially in M_7C_3 where 21 wt% are soluble at 1250°C, which reduces the amount of cobalt available in diffusion couples. An overview of the results taken from Kaplan et al. is listed in Table 2-4a.

Table 2-4: Solubilities of Cr, V, Mo and W in hardmetal binder phases.

System	Equilibrium	Temperature [°C]	V [wt%]	Cr [wt%]	Mo [wt%]	W [wt%]	Reference
V-W-C-Co	fcc + MC + WC + gra.	1000	1.1	–	–	4.0	06LAU
		1200	1.3	–	–	6.4	01OBB
		1261	1.9	–	–	8.6	08FRI*
	Liq. + fcc + MC + WC + gra.	1262	4.1	–	–	11.4	08FRI*
		1300	4.6	–	–	12.1	08FRI*
	fcc + MC + WC + M ₆ C	1000	2.3	–	–	16.6	06LAU
1200		2.4	–	–	17.9	01OBB	
Cr-W-C-Co	fcc + M _x C _y + WC + gra.	1000	–	5.4	–	3.1	06LAU
		1190	–	6.9	–	6.2	08FRI*
	Liq. + fcc + M ₇ C ₃ + WC + gra.	1191	–	12.2	–	11.7	08FRI*
		1300	–	16.3	–	14.7	08FRI*
fcc + M _x C _y + WC + M ₆ C	1000	–	9.8	–	11.5	06LAU	
	1000	0.7	4.9	–	4.3	06LAU	
Cr-V-W-C-Co	fcc + M _x C _y + WC + gra.	1000	0.7	4.9	–	4.3	06LAU
		1000	1.3	6.2	–	10.0	06LAU
Mo-W-C-Co	fcc + M _x C _y + WC + gra.	1000	–	–	4.6	3.4	06LAU
		1000	–	–	3.9	8.6	06LAU

* Values originally published in at% and recalculated for this table

Table 2-4a: Solubility of cobalt in chromium carbides according to Kaplan et al. [14KAP1, 14KAP].

Equilibrium	Temperature [°C]	Phase	Co solubility [wt%]
liq.+M ₂₃ C ₆ +M ₇ C ₃	1350	M ₂₃ C ₆	17.6
		M ₇ C ₃	8.2
	1450	M ₂₃ C ₆	16.4
		M ₇ C ₃	6.1
M ₃ C ₂ +M ₇ C ₃ +C	1250	M ₃ C ₂	3.2
		M ₇ C ₃	21.1
	1450	M ₃ C ₂	3.4
		M ₇ C ₃	21.9

2.6 Distribution of hardmetal constituents

When sintering near-nano scaled hardmetals grain growth initiates already at relatively low temperatures as discussed in section 2.2.2. Hence, a sufficient distribution of GGIs before grain growth initiates is mandatory.

Brieseck et al. [12BRI] found by means of VC-Co/WC-Co diffusion couples that at 1050°C the diffusion depth of vanadium is already 40 µm and increases to 80 µm and 150–200 µm at 1150 and 1250°C, respectively. They furthermore found that the initial WC-grain size has no significant influence on the distribution of vanadium in WC-Co. The transport factor of vanadium at 1150°C was calculated $D=1.5 \cdot 10^{-10}$ cm²/s which indicates that the distribution of vanadium is fast already upon the early sintering stages before liquid-phase formation occurs. The maximum concentration of vanadium at VC-Co/WC-Co interface was measured around 0.8–1.0 wt%. Figure 2-15 shows the as-measured vanadium concentration profiles and the corresponding transport factors as published in Figure 6 of [12BRI].

Richter et al. [12RIC,13RIC] reported on GGI-doped hardmetals with ultrafine and near-nano WC-grades that chromium added as carbide is already sufficiently distributed in the hardmetal below the eutectic melt formation. Initiating dissolution and not further specified chemical changes of Cr₃C₂ were already observed at 700°C. Substantial interaction of the chromium carbide with the surrounding hardmetal components was reported at 1100°C. Upon the dissolution of GGIs pores formed. Due to the fast distribution they state that upper limit of the GGI grain-size is only determined by the size of the resulting pores. As long as they are in the size range of pores naturally formed in hardmetals (several µm) they will not negatively affect the resulting microstructure. Substantial dissolution of WC in Co was found at 1000°C by a decrease of magnetic saturation.

Li et al. [07LI] found by investigating WC-10Co-0.4VC-0.4Cr₃C₂ hardmetals that GGIs are mainly distributed in the binder phase after liquid-phase sintering and no GGI-based precipitations were detected

Collin and Norgren [05COL] realised hardness gradients by applying Cr₃C₂-powder on the surface of a WC-Co green body prior to liquid-phase sintering. A chromium gradient and subsequently a grain-size gradient formed at temperatures 1370°C and 1410°C. Besides the chromium gradient a cobalt gradient with depletion towards the

surface formed. Collin and Norgren attribute the gradient to local liquid-phase formation since the solidus temperature decreases with increasing chromium concentration. The results of both gradients taken from Fig. 6 and Fig. 7 of Ref. [05COL] are shown in Figure 2-16. They furthermore found no cubic carbide precipitates formed upon the diffusion experiment.

He et al. [07HE] conducted solid-state diffusion experiments of vanadium and tungsten in cobalt by means of V_8C_7 -Co and WC/ V_8C_7 -Co diffusion couples with high cobalt content. They compare their results to calculations, but provide no information on kinetic values such as diffusion coefficients.

In hardmetals not only dopants but also the binder phase has certain mobility in both solid and liquid state. Subsequently binder gradients can be formed due to gradients in carbon potential, GGI concentration or WC grain size. Comprehensive work on this topic was published by Konyashin et al. [09KON, 09KON1, 10KON, 12KON].

Preliminary results of this work regarding the distribution of chromium and vanadium in hardmetals with cobalt, Fe/Ni and Fe/Co/Ni binder alloys have already been published [13BUC, 15BUC]. An overview on diffusion data of various elements in fcc-cobalt is shown in Table 2-5.

Table 2-5: Diffusion parameters for various elements in fcc-cobalt.

Diffusing Element	E_a (kJ/mol)	Pre-exponential D_0 (cm ² /s)	Reference
W	282.1	0.7	[98HAG1]
W	320	6.6	[09NEU]
Co	260.5	0.17	[90CER]
C	149.3	0.872	[98HAG1]
C	174	0.21	[62LAN]
V	275.6	2.8	[07HE]
V	273	1	[09NEU]
Cr	266.1	0.44	[62LAN]

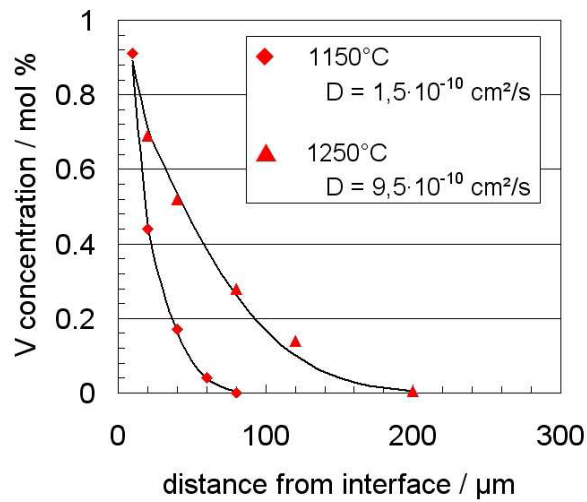


Figure 2-15: concentration profiles of vanadium in the WC-Co part in VC-Co-WC-Co diffusion couples as published in Figure 6 of [12BRI].

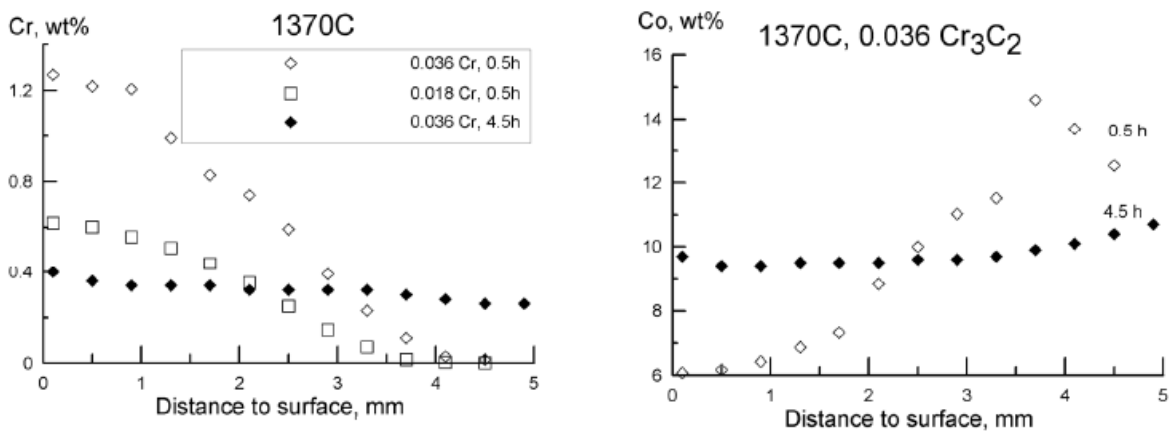


Figure 2-16: chromium (a) and cobalt (b) gradients formed by liquid-phase sintering of WC-Co with Cr_3C_2 applied on surface of the green body. Graphs taken from Fig. 6 and Fig. 7 of Ref. [05COL].

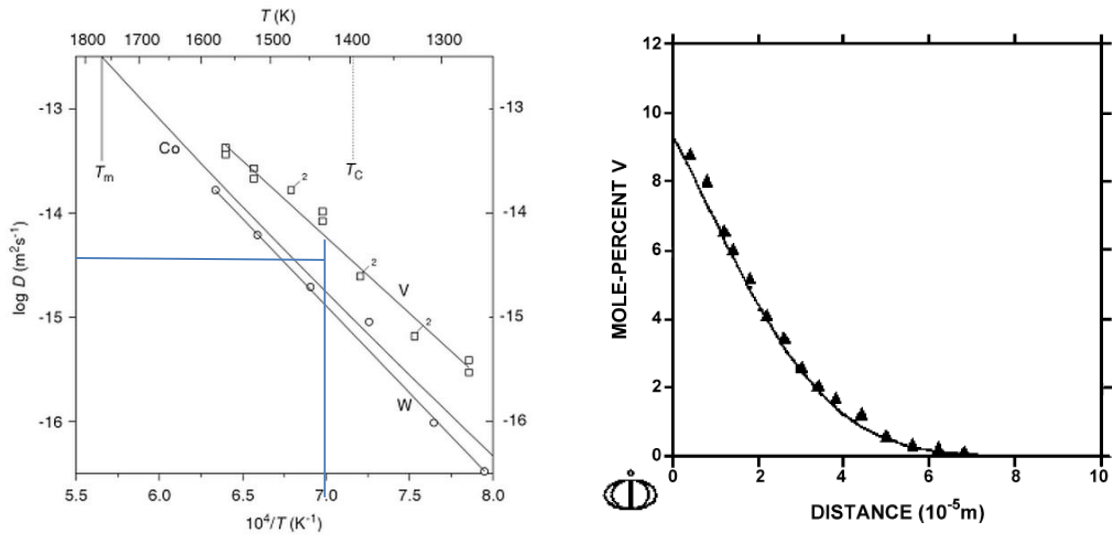


Figure 2-17: (a) Impurity diffusion of V, W and Co in fcc cobalt as published in Fig. 82.03 of [09NEU]; (b) concentration profile of V in Co determined by a $\text{V}_8\text{C}_7/\text{Co}$ diffusion couple annealed for 36 h at 1100°C as published by [07HE].

3 Materials and Methods

3.1 Raw materials

An overview of the raw materials used in this work is listed in Table 3-1.

Table 3-1: Characterisation of starting powders; TIAG=Treibacher Industrie AG.

Powder	Grade	Provider	FSSS	BET	O	C	Batch
			μm	m^2/g	wt.%	wt.%	
WC	DS50	H.C. Starck	0.55	2.1	1.2	6.14	
Cr_3C_2	100	TIAG	1.70	n.a.	0.62	13.03	L33247
VC	VC100	TIAG	1.00	n.a.	0.23	17.41	L33142
TaC	HGS	H.C. Starck	0.92	n.a.	0.15	6.24	
Mo_2C	fine	TIAG	1.6	n.a.	0.13	5.81	L13831
Cr_2N	Cr_2N	H.C. Starck	1.5	n.a.	0.48	0.02	74051
CrB	CrB	H.C. Starck	-	-	-	-	2595/01
MoB	MoB	H.C. Starck	-	-	-	-	2527/01/Rd
Cr_2O_3	Cr_2O_3	Riedl-deHaen	-	-	-	-	12233
V_2O_5	V_2O_5	H.C. Starck	-	-	-	-	53383
Co	Extra fine	Umicore	1.20	n.a.	0.36	0.0192	30033809
Co	Micron	Umicore	0.2	2.7	1.6	-	0.2 Micron
Fe/Co/Ni 40/20/40	Ampersint MAP A6050	H.C. Starck	1.00	1.62	1.11	0.0059	17048/08
Fe/Ni 15/85	Ampersint MAP A8500	H.C. Starck	2.43	n.a.	0.58	0.14	HL100
C	Luvocarb	H.C. Starck	n.a.	10.61	n.a.	-	UP030/M

3.1.1 Preparation of the grade DS50m

For preparation of the grade DS50m 100 g of WC DS50 were milled in an attritor of type Netzsch R41-25/4 with hardmetal linings in cyclohexane for 24 h. The powder was subsequently dried and granulated by means of a laboratory sieve.

3.1.2 Preparation of (W,V)C for thermal analyses

For thermal analysis samples doped with (W,V)C were prepared. The composition is listed in Table 3-2. It can be seen that two samples labelled (WV)C+C and (WV)C+W were synthesised. (WV)C_C is located in the phase field of cubic (V,W)C + C + WC

while (WV)C_W is located in the field $(V,W)_2C+(V,W)C$. The position of the samples in the W-V-C system is graphically illustrated in Figure 3-1.

The powder mixtures were compacted by uniaxial pressing at 40 MPa using a P/O Weber hydraulic laboratory press. The samples were subsequently annealed in vacuum for 10 h at 1500°C. The solid samples were crushed and used for preparing hardmetal samples.

Table 3-2: Composition of (W,V)C powders

Sample	Weighed portion (g)				Atomic ratio (at%)		
	WC	VC	C	W	V	W	C
(WV)C_C	60.875	39.127	1.523	-	32.4	16.2	51.4
(WV)C_W	60.873	39.127	-	1.857	34.5	17.8	47.6

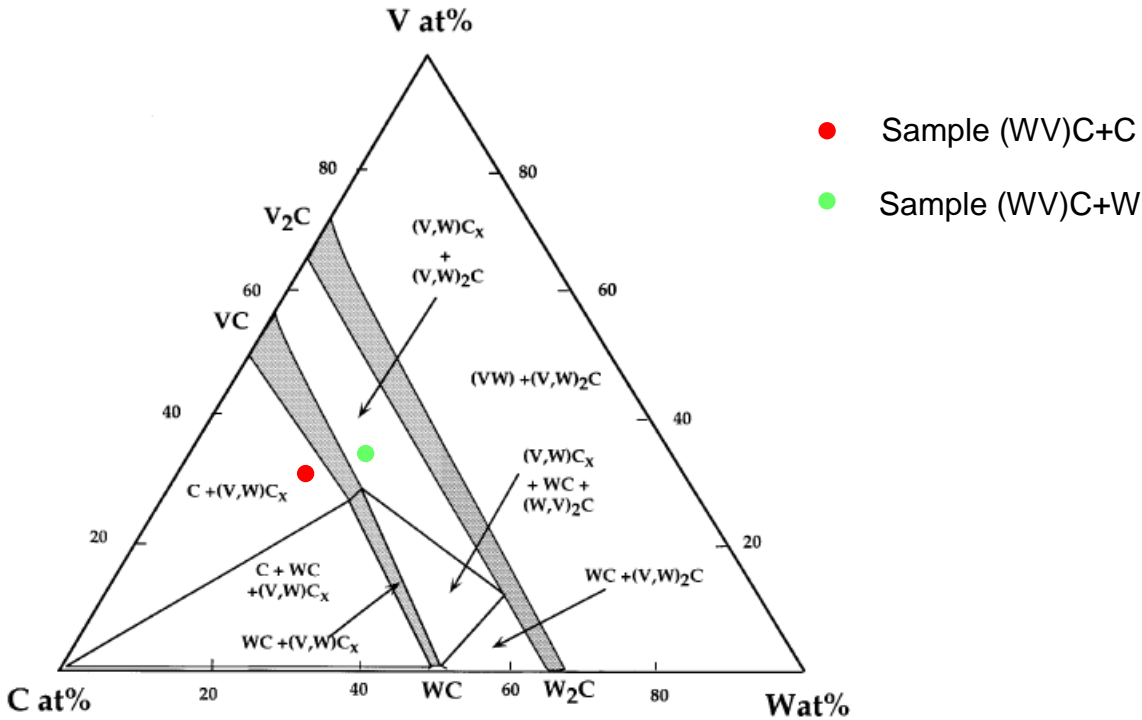


Figure 3-1: Isothermal section of phase diagram C-V-W at 1500°C; Graph taken from Fig. 2 of Ref. [01OBB].

3.2 Preparation of hardmetal mixtures

Hardmetal powder mixtures and mixtures for diffusion couple components were prepared by wet mixing. 30–150 g of powder mixture and hardmetal milling balls (6 mm in diameter) with a powder-to-ball weight ratio of 1:10 were filled in a 300 ml hardmetal drum. Cyclohexane was added as a milling aid. After milling for 24 h at 80 rpm the powder was dried and granulated by means of a laboratory sieve.

If carbon adjustment was required the powder+carbon or tungsten were dry-mixed using a Turbula-shaker for 3 h at 65 rpm.

For pressing green bodies 3–10 g of the powder mixtures were uniaxially compacted in a hardmetal die with diameter of 12.8 mm by applying a pressure of 240 MPa for 10 s using a P/O Weber laboratory press.

3.3 Sintering

3.3.1 Induction furnace

Annealing of the diffusion couples and grain growth experiments were conducted in an induction furnace. The experimental setup is schematically illustrated in Figure 3-2. For sintering and annealing of diffusion couples a carbon-crucible was used. In order to avoid diffusion of carbon into the hardmetals they were placed on a corundum plate. For evolving gas analysis a molybdenum crucible was used. The advantage of the induction setup is that fast heating rates of 300 K/min up to 1500°C can be realised. Since only the crucible is heated the cool-down is fast as well. The cooling curve in 100 mbar argon is shown in Figure 3-3.

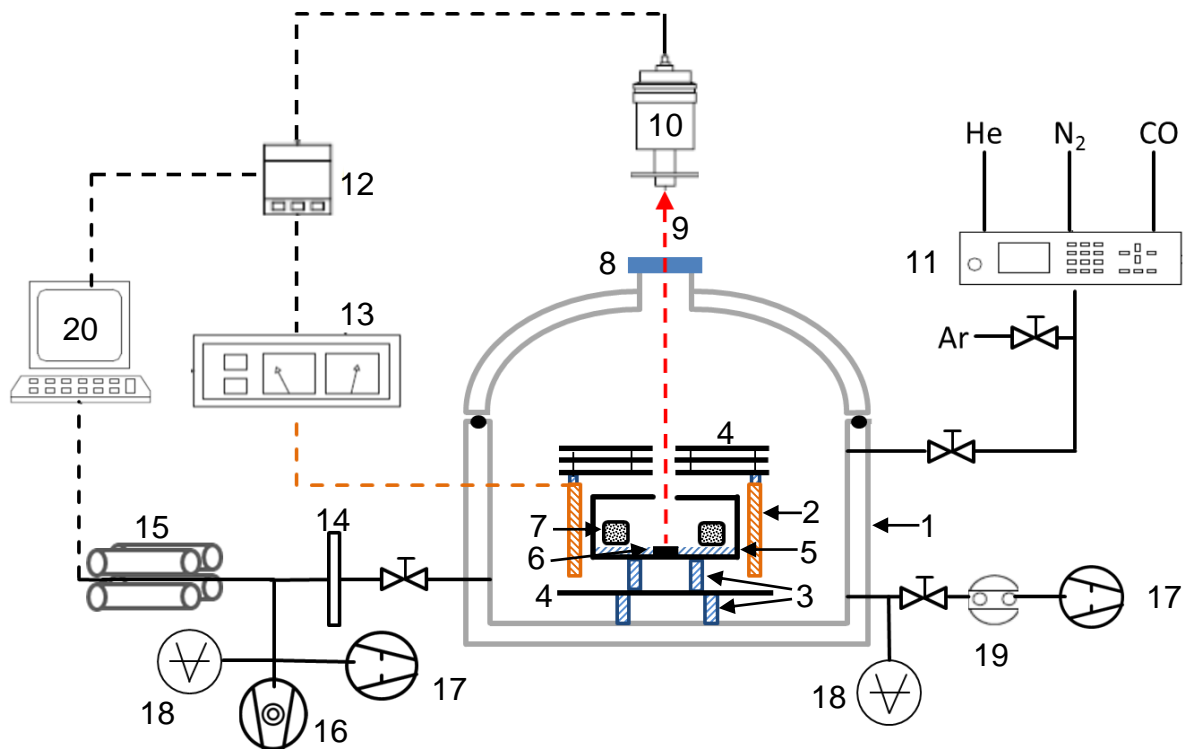


Figure 3-2: Schematic of the induction furnace. Solid connecting lines mark gas pipes. Dashed lines mark electronic connections. (1) water cooled, double walled stainless-steel recipient, volume ~30 l (2) Water-cooled copper induction coil (3) corundum support ring (4) Molybdenum radiation shield (5) Crucible: graphite for sintering, molybdenum for EGA (6) reference plate for pyrometer (7) sample (8) fused silica window (9) Pyrometer measurement path (10) Pyrometer (11) Mass flow controller (12) Eurotherm temperature control (13) Power generator EFD Induction PS12/18, 30 kHz (14) High-pressure interface for mass spectrometer (15) Pfeiffer PrismaPlus quadrupole mass spectrometer (16) Turbomolecular vacuum pump (17) Rotary vane pump (18) Pressure control (19) Diaphragm valve (20) Data recording.

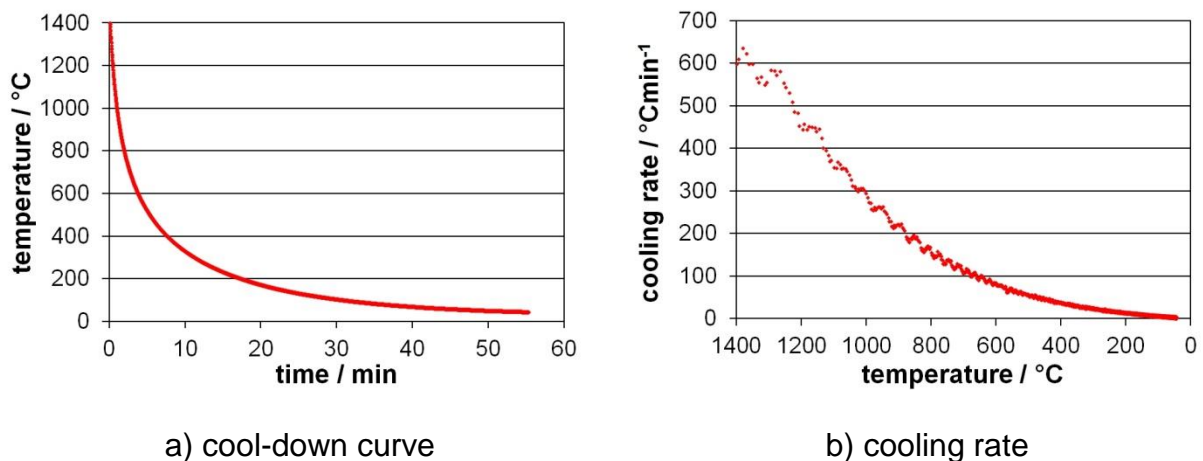


Figure 3-3: Cooling curve (a) and cooling rate (b) of a graphite crucible in 100 mbar argon in the induction furnace. Starting temperature: 1400°C.

3.3.2 Spark Plasma Sintering

Spark Plasma Sintering (SPS) is a sintering technique which allows sintering of hardmetals in solid binder state. Characteristics are the application of pressure upon sintering as well as fast heating and cooling rates. The latter are possible since the die is made from a conductive material (e.g. graphite) which is directly heated by a pulsed current flow. The fast heating and cooling as well as the pressure assistance make SPS interesting for producing near-nano and ultrafine hardmetal grades since sintering times are kept short. Furthermore SPS is commonly operated below the binder solidus temperature. These conditions help to retard grain growth. However, it has to be mentioned that a part of the hardmetal-community refuses to consider WC-Co obtained from SPS as “real” hardmetal since some of the special features such as grain shape or the characteristic microstructure require liquid phase to be formed. SPS experiments were conducted at the TU Bergakademie Freiberg (Germany) under supervision of Milan Dopita, PhD. using FCT HP D25/1 equipment. Graphite foil was used to separate the die from the powder to avoid sticking of the powder. The sintering conditions are summarised in Table 3-3. The powder mixtures for SPS experiments are listed in Table 3-15.

Table 3-3: SPS setup parameters.

Item	Value
Die	graphite
Diameter of die	20 mm
Heating rate	150°C/min
Annealing temperature	1150°C
Annealing time	15 min
Pre-compaction pressure	1 MPa
Sintering pressure	50 MPa
Initial powder mass	25 g
Finish sample height	5 mm
Program name	127WC-Co
Batch no.	2213–2220
Date of experiment	31.03.2014

3.4 Preparation of diffusion couples

Diffusion couples were prepared in order to study the diffusion of GGIs in WC-binder hardmetals. Therefore two materials of the type GGIX-WC-binder (X=carbide, nitride or boride) and WC-binder were contacted and annealed at testing temperature. The composition of the single constituents can be found in Table 3-7. Three different types of diffusion couples were prepared in order to gain insight into the mechanisms of diffusion upon hardmetal sintering cycles:

- **G-type** couples were prepared from hardmetal Green bodies
- **H-type** couples were prepared from pre-sintered Hardmetals
- **M-type** couples were prepared from pre-sintered Model alloys

For annealing the samples were placed on Al₂O₃ plates in a graphite-crucible and heated up in an induction furnace (see 3.3.1). The standard annealing time was 15 min, however, some of the samples were annealed for different times varying from 5–60 minutes in order to determine time-dependent effects on the diffusion of GGIs (see Table 3-10 – Table 3-12).

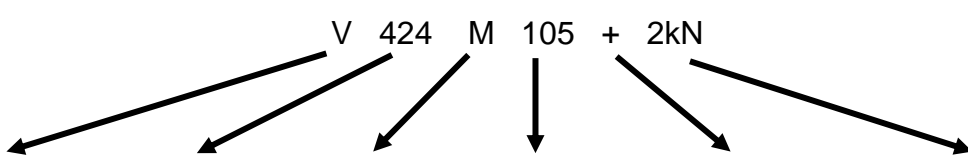
Driven by a gradient of the chemical potential GGIs diffuse from the GGIX-WC-binder towards the WC-binder part of the couple, yielding a GGI concentration profile which can be measured (see 3.11) and subsequently diffusion parameters can be calculated (see 3.13). A sketch of a diffusion couple, including the definition of the term “interface” is illustrated in Figure 3-4(a) whereas (b) shows a light-optical micrograph of the sample VCoG125+. The sample name VCoG125+ refers to a systematic nomenclature which was introduced for diffusion couples and is explained in Table 3-5. Diffusion experiments were conducted in the induction furnace. The applied temperature profiles are almost rectangularly shaped. After a fast heating rate of 100 K/min a typical dwell time of 15 min at 950–1360°C was chosen, followed by a fast cool-down according to the cooling curve in Figure 3-3(a). These conditions are close to typical SPS cycles of 100 K/min heating rate and 10–20 min dwell time at 1100-1250°C. Thus, the experiments gain insight into the distribution of GGIs upon fast sintering techniques, where a fast distribution of GGIs is essential. Following the idea of SPS-near experiments a set of experimental standard-parameters was chosen. These parameters are summarised in Table 3-4. However, according to

special requirements particular samples deviate from these conditions and have e.g. different annealing times. Such deviations are indicated by a suffix to the sample name as can be read from Table 3-5.

Table 3-4: Standard conditions for preparation of diffusion couples

Item	Value
Heating rate	100 K/min
Dwell time	15 min
Atmosphere	200 mbar Ar
Compaction pressure (green body)	240 MPa

Table 3-5: sample nomenclature of diffusion couples

					
GGIX	Binder	Couple type	Annealing temperature	Carbon potential of WC-binder	Suffix for G-type samples deviating from standard conditions
C = Cr ₃ C ₂	Co=Co	G= G-type	95=950°C	+ = +C	kN = pressing force in kN
V = VC	Co _n = nano-Co	H= H-type	100=1000°C	- =+eta	min= annealing time in min
CV= Cr ₃ C ₂ +VC	424= FeCoNi 40/20/40	M= M-type	105=1050°C	Blank = 2 phase	N= nitrogen atmosphere
CB=CrB	19=Fe/Ni 15/85		110=1100°C		CO=carbon monoxide
CN=Cr ₂ N			112=1125°C		Kmin=heating rate in K/min
M=Mo ₂ C			115=1150°C		
MB=MoB			120=1200°C		
			125=1250°C		
			136=1360°C		

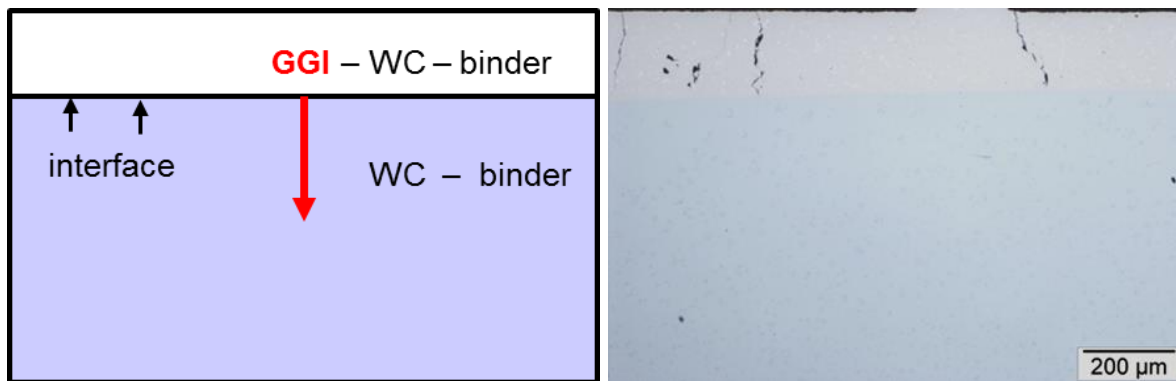


Figure 3-4: (a) Schematic of a diffusion couple and (b) LOM of the diffusion couple VCoG136+.

3.4.1 G-type couples

In G-type couples both the WC-binder and the GGI-X-binder parts of the diffusion couples (X=nitride, carbide or boride) were prepared from green bodies. An overview on the composition of the WC-binder mixtures is given in Table 3-7. The composition of the GGI-WC-binder parts is given in Table 3-8, in which the samples are listed in alphabetical order.

In a first step, the WC-binder body was compacted by uniaxially pressing 3 g of the powder mixture in a cylindrical hardmetal die with 12.8 mm in diameter. The resulting sample height was approximately 3 mm. Since the diffusion couples require a smooth interface between the two parts, the die was placed on a glass plate before pressing. The pressure was set to 240 MPa (30 kN) for the majority of the samples. However, in order to study the influence of the green density on the distribution behaviour a sample series with different press powers varying from 15–230 MPa was prepared. The green densities resulting from the various pressing conditions are listed in Table 3-6.

In a second step, the powder mixture for the GGI-part of the couple was applied on a glass plate as a layer of approximately 1 mm thickness. The WC-binder part, which was still remaining in the die, was positioned on this layer and pressed on it with a force of 1 kN (7 MPa). The result was a diffusion couple consisting of a WC-binder body with 3 mm thickness, covered with 100–200 μm of the GGI-WC-binder mixture.

In a third step, the samples were heated to the testing temperature and annealed for the particular dwell time. Besides the standard heating rate of 100 K/min one series

was prepared with a slow rate of 5 K/min. An overview on the used diffusion couple components and the particular testing conditions of G-type couples based on vanadium, chromium, vanadium+chromium double-doping and molybdenum is listed in Table 3-9, Table 3-10, Table 3-11 and Table 3-12, respectively. In these tables also the powder mixtures of the WC-binder parts according to Table 3-7 as well as of the GGI-WC-binder parts according to Table 3-8 are also listed. Some samples are based on the powder mixtures VA and CA, which are of type GGI-binder instead of GGI-WC-binder. The reason is that the very first samples in this project were of type GGI-binder. For chromium it turned out that the bonding of the diffusion couple parts is better when WC is added. Subsequently later samples were prepared as type GGI-WC-binder. To keep experimental conditions constant the vanadium based samples were as well prepared as type GGI-WC-Co. However, the resulting GGI concentration profiles in the WC-binder parts turned out to be comparable whether GGI-binder or GGI-WC-binder is used as a GGI source. Thus, the results determined from the GGI-binder based samples are further used in this project.

Table 3-6: Pressing conditions used to prepare the WC-binder part of G-type diffusion couples and resulting green densities.

Pressing force	Pressure	Green density
kN	MPa	g/cm ³
2	15	5.98
5	39	6.48
10	78	6.91
20	155	7.23
30	230	7.48

3.4.2 H-type couples

H-type couples are diffusion couples prepared from sintered hardmetals. That means in contrast to G-type the two parts were liquid-phase sintered separately (sintering cycle H_M_pre, see Figure 3-6). After sintering the samples were annealed at the intended testing temperature for 10 hours allowing equilibration of the binder phase. When preparing such diffusion couples out of two solid constituents clean and smooth contact areas are of particular importance. Impurities and/or poor contact can influence the resulting GGI concentration profile by restraining the mass transport towards the interface. Thus, the contacting surfaces were ground, polished to mirror (see Table 3-19 for conditions) and sonicated in ethanol (p.a. quality) to remove organic impurities. A tight contact during the annealing cycle was ensured by pressing the two parts together using the arrangement illustrated in Figure 3-5. The diffusion couples (A) were placed between two molybdenum washers (B) which were pressed together by a bolt (C) and nut (D). Molybdenum was chosen to avoid softening and subsequent loss of the pressing force of the washers at high temperatures. Since the sample would react with the molybdenum upon annealing corundum plates (E) were used as spacers. H-type diffusion couples were annealed according to the temperature profile M115 in Figure 3-7.

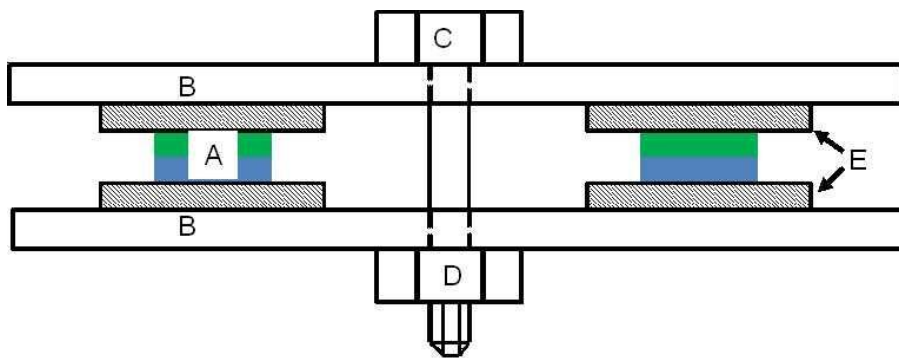
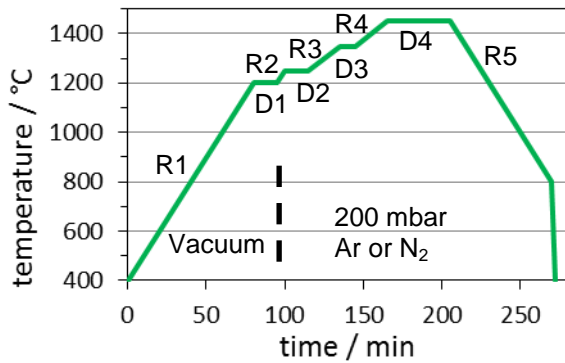


Figure 3-5: schematic of the arrangement for preparing H- and M-type diffusion couples.



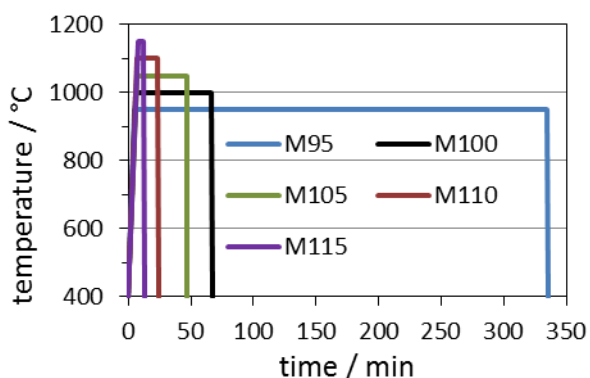
Item	Value
Rate R1	10 K/min
Dwell D1	1200°C, 15 min
Rate R2	10K/min
Dwell D2	1250°C, 10 min
Rate R3	5 K/min
Dwell D3	1300°C, 10 min
Rate R4	5K/min
Dwell D4	1450°C, 40 min
Rate R5	-10 K/min

Figure 3-6: Temperature profile H_M_pre for preparation of M- and H-type diffusion couple components. Gas application at end of D1. Cooling from end of R5 according to Figure 3-3(a).

3.4.3 M-type couples

The constituents of M-type couples are pre-sintered model alloys with a binder volume fraction of 50 vol% in the WC-binder body. Since large binder areas of approximately 100 μm in diameter appear in such samples they allow measuring the GGI diffusion in the equilibrated binder alloy. The preparation procedure is equal to H-type couples and can thus be found in 3.4.2.

As compared to G- and H-type couples lower annealing temperatures of 950°C and 1000°C were additionally chosen. Since the GGI diffusion is expected to be slow at such temperatures the annealing time was increased from up to 330 min, depending on the temperature. An overview of the testing conditions is given in Table 3-13. The corresponding annealing cycles are illustrated in Figure 3-7.



Cycle name	Temperature (°C)	Dwell time (min)
M95	950	330
M100	1000	60
M105	1050	40
M110	1100	15
M115	1150	5

Figure 3-7: Annealing cycles of M- and H-type diffusion couples. Heating rate is 100K/min. Cooling rate according to Figure 3-3(a).

Table 3-7: Powder compositions of the WC-binder diffusion couple parts.

Sample Name	Binder alloy	Binder volume fraction	Carbon	Co		WC		C	
		vol%		m (g)	wt%	m (g)	wt%	m (g)	wt%
W,A	Co	16.4	2 phase	15.003	10.00	134.55	89.71	0.434	0.29
W,B	Co	16.3	2 phase	14.99	9.96	135.04	89.76	0.424	0.28
W,C	Co	16.4	2 phase	14.02	10.01	125.75	89.79	0.286	0.20
W-C	Co	16.4	+eta	15.03	10.01	134.99	89.89	0.15	0.10
W+C,A	Co	16.3	+C	15.01	9.96	135.01	89.61	0.651	0.43
W+C,C	Co	16.4	+C	14.009	10.00	125.519	89.64	0.493	0.35
W+C,D	Co	16.3	+C	15.002	9.96	135.27	89.84	0.295	0.20
W+C,E	Co	16.4	+C	15.03	10.00	134.98	89.80	0.303	0.20
WCo _n	nano-Co	16.4	2 phase	6.04	10.01	54.03	89.58	0.242	0.40
WCo _n ,B	nano-Co	16.3	2 phase	9.9984	9.95	90.1701	89.73	0.3203	0.32
CoM+	Co	84.1	+C	44.994	74.62	14.99	24.86	0.31	0.51
424+	Fe/Co/Ni	15.6	+C	9.542	9.52	90.48	90.23	0.256	0.26
424M+	Fe/Co/Ni	85.9	+C	48.1	77.07	13.81	22.13	0.5	0.80
19+	Fe/Ni	16.1	+C	4.912	9.80	45.082	89.95	0.1276	0.25
19M+	Fe/Ni	84.1	+C	45.2	74.53	14.99	24.72	0.46	0.75

Table 3-8: Powder compositions of the GGI-WC-binder diffusion couple parts.

Sample Name	GGIX-1	GGIX-2	Binder fraction (vol%)	Binder Alloy			WC		GGI-X 1		GGI-X 2		C	
				Composition (wt%)	m (g)	wt%	m (g)	wt%	m (g)	wt%	m (g)	wt%	m (g)	wt%
CBWCo	CrB		16.2	Co	9.68	19.7	7.81	15.9	31.663	64.4			0.310	0.78
CCo	Cr ₃ C ₂		16.2	Co	12.31	20.5			47.7	79.5				
CNWCo	Cr ₂ N		16.3	Co	9.7	20.4	7.67	16.1	30.214	63.5			0.503	1.01
CVCo	Cr ₃ C ₂	VC	16.4	Co	13.22	22			23.43	39	23.5	39.1		
CW19+	Cr ₃ C ₂		16.7	Fe/Ni/15/85	9.11	18.6	8.92	18.2	30.91	63.2			0.327	0.67
CW19M+	Cr ₃ C ₂		43.1	Fe/Ni/15/85	25.15	42.6	14.88	25.2	19.05	32.2			0.243	0.41
CW424+	Cr ₃ C ₂		16.2	Fe/Co/Ni	5.12	17.6	5.4	18.5	18.63	63.9			0.076	0.26
CW424M+	Cr ₃ C ₂		45.1	Fe/Co/Ni	27.86	46.4	11.81	19.7	20.41	34			0.361	0.60
CWCo	Cr ₃ C ₂		16.6	Co	2.47	19.1	1.98	15.3	8.464	65.5				
CWCoM+	Cr ₃ C ₂		49	Co	27.74	47.7	15.24	26.2	15.19	26.1				
MBWCo	MoB		16.3	Co	7.99	15.7	6.51	12.8	36.33	71.5			0.137	0.30
MWCo	Mo ₂ C		16.7	Co	7.89	15.7	6.85	13.7	35.41	70.6			0.169	0.30
VCo	VC		16.3	Co	17.34	23.1			57.67	76.9				
VW19+	VC		16.4	Fe/Ni/15/85	10.27	20.5	7.96	15.9	31.81	63.6			0.324	0.65
VW19M+	VC		39.3	Fe/Ni/15/85	24.91	41.6	15.06	25.2	19.88	33.2			0.244	0.41
VW424+	VC		16.6	Fe/Co/Ni	6	20.5	4.09	14	19.13	65.5			0.076	0.26
VW424M+	VC		42.6	Fe/Co/Ni	27.95	46.5	12.13	20.2	19.98	33.3			0.345	0.57
VWCo	VC		16.5	Co	3.48	19.1	0.41	2.2	14.28	78.6			0.103	0.51
VWCo,B	VC		17.5	Co	4.29	21.5	4.07	20.4	11.59	58.1			0.106	0.52
VWCoM+	VC		43.7	Co	24.88	45.1	15.08	27.3	15.2	27.6			0.281	0.50

Table 3-9: Annealing conditions of G-type samples based on vanadium.

Sample Name	Binder alloy	WC-binder part	WC-GGIX-binder part	Carbon potential	Heating rate (K/min)	Compaction pressure (MPa)	Temperature (°C)	Isothermal annealing time (min)	Atmosphere
VCoG105-	Co	W-C	VCo	+eta	100	240	1050	15	200mbar Ar
VCoG110-_40min	Co	W-C	VWCo	+eta	100	240	1100	40	200mbar Ar
VCoG120-_7min	Co	W-C	VWCo	+eta	100	240	1200	7	200mbar Ar
VCoG125-	Co	W-C	VCo	+eta	100	240	1250	15	200mbar Ar
VCoG136-	Co	W-C	VCo	+eta	100	240	1360	15	200mbar Ar
VCoG105	Co	W,B	VCo	2 phase	100	240	1050	15	200mbar Ar
VCoG115	Co	W,B	VCo	2 phase	100	240	1150	15	200mbar Ar
VCoG120_7min	Co	W,B	VWCo	2 phase	100	240	1200	7	200mbar Ar
VCoG125	Co	W,B	VCo	2 phase	100	240	1250	15	200mbar Ar
VCoG136	Co	W,B	VCo	2 phase	100	240	1360	15	200mbar Ar
VCoG105+	Co	W+C,A	VCo	+C	100	240	1050	15	200mbar Ar
VCoG105+5Kmin	Co	W+C,D	VWCo,B	+C	5	240	1050	15	200mbar Ar
VCoG115+_5min	Co	W+C,D	VWCo,B	+C	100	240	1150	5	200mbar Ar
VCoG115+	Co	W+C,A	VWCo,B	+C	100	240	1150	15	200mbar Ar
VCoG115+_30min	Co	W+C,C	VWCo,B	+C	100	240	1150	30	200mbar Ar
VCoG125+	Co	W+C,A	VCo	+C	100	240	1250	15	200mbar Ar
VCoG136+	Co	W+C,A	VCo	+C	100	240	1360	15	200mbar Ar
VCoG115+2kN	Co	W+C,D	VWCo,B	+C	100	15	1150	30	200mbar Ar
VCoG115+6kN	Co	W+C,D	VWCo,B	+C	100	40	1150	30	200mbar Ar
VCoG115+10kN	Co	W+C,D	VWCo,B	+C	100	80	1150	30	200mbar Ar
VCoG115+20kN	Co	W+C,D	VWCo,B	+C	100	160	1150	30	200mbar Ar
VCo _n G105	nano-Co	WCo _n	VCo	2 phase	100	240	1050	15	200mbar Ar
VCo _n G110	nano-Co	WCo _n	VCo	2 phase	100	240	1100	15	200mbar Ar
VCo _n G115	nano-Co	WCo _n	VCo	2 phase	100	240	1150	15	200mbar Ar
V115CoG-N	Co	W-C,A	VWCo,B	+eta	100	240	1150	15	200mbar N ₂
V115CoG+N	Co	W+C,D	VWCo,B	+C	100	240	1150	15	200mbar N ₂
V115CoG+CO	Co	W+C,D	VWCo,B	+C	100	240	1150	15	200mbar CO
V19G115+	Fe/Ni	W19+	VW19+	+C	100	240	1150	15	200mbar Ar
V424G115+	Fe/Co/Ni	W424+	VW424+	+C	100	240	1150	15	200mbar Ar

Table 3-10: Annealing conditions of G-type samples based on chromium.

Sample Name	Binder alloy	WC-binder part	WC-GGI-binder part	Carbon potential	Heating rate (K/min)	Compaction pressure (MPa)	Temperature (°C)	Isothermal annealing time (min)	Atmosphere
CCoG100-_60min	Co	W-C	CWCo	+eta	100	240	1000	60	200mbar Ar
CCoG105-	Co	W-C	CA	+eta	100	240	1050	15	200mbar Ar
CCoG105-_5Kmin	Co	W-C	CWCo	+eta	5	240	1050	15	200mbar Ar
CCoG110-_40min	Co	W-C	CWCo	+eta	100	240	1100	40	200mbar Ar
CCoG115-_8min	Co	W-C	CWCo	+eta	100	240	1150	8	200mbar Ar
CCoG136-	Co	W-C	CA	+eta	100	240	1360	15	200mbar Ar
CCoG105	Co	W,A	CA	2 phase	100	240	1050	15	200mbar Ar
CCoG110	Co	W,B	CWCo	2 phase	100	240	1100	15	200mbar Ar
CCoG115	Co	W,A	CA	2 phase	100	240	1150	15	200mbar Ar
VCoG125	Co	W,A	CA	2 phase	100	240	1250	15	200mbar Ar
VCoG136	Co	W,A	CA	2 phase	100	240	1360	15	200mbar Ar
CCoG105+	Co	W+C,A	CA	+C	100	240	1050	15	200mbar Ar
CCoG105+5Kmin	Co	W+C,D	CWCo	+C	5	240	1050	15	200mbar Ar
CCoG112+	Co	W+C,D	CA	+C	5	240	1125	15	200mbar Ar
CCoG115+_5min	Co	W+C,D	CWCo	+C	100	240	1150	5	200mbar Ar
CCoG115+_A	Co	W+C,A	CWCo	+C	100	240	1150	15	200mbar Ar
CCoG115+_B	Co	W+C,D	CWCo	+C	100	240	1150	15	200mbar Ar
CCoG115+_30min_A	Co	W+C,D	CWCo	+C	100	240	1150	30	200mbar Ar
CCoG115+_30min_B	Co	W+C,E	CWCo	+C	100	240	1150	30	200mbar Ar
CCoG115+_60min	Co	W+C,D	CWCo	+C	100	240	1150	60	200mbar Ar
CCoG125+	Co	W+C,A	CWCo	+C	100	240	1250	15	200mbar Ar
CCoG136+	Co	W+C,A	CWCo	+C	100	240	1360	15	200mbar Ar
CCoG115+2kN	Co	W+C,D	CWCo	+C	100	15	1150	30	200mbar Ar
CCoG115+5kN	Co	W+C,D	CWCo	+C	100	40	1150	30	200mbar Ar
CCoG115+10kN	Co	W+C,D	CWCo	+C	100	80	1150	30	200mbar Ar
CCoG115+20kN	Co	W+C,D	CWCo	+C	100	160	1150	30	200mbar Ar

Continuation of Table 3-10.

Sample Name	Binder alloy	WC-binder part	WC-GGI-binder part	Carbon potential	Heating rate (K/min)	Compaction pressure (MPa)	Temperature (°C)	Isothermal annealing time (min)	Atmosphere
CCo _n G105	nano-Co	WCo _n	CWCo	2 phase	100	240	1050	15	200mbar Ar
CCo _n G110	nano-Co	WCo _n ,B	CWCo	2 phase	100	240	1100	15	200mbar Ar
CCo _n G115	nano-Co	WCo _n	CWCo	2 phase	100	240	1150	15	200mbar Ar
CCoG125	nano-Co	WCo _n	CWCo	2 phase	100	240	1250	15	200mbar Ar
CCoG136	nano-Co	WCo _n	CWCo	2 phase	100	240	1360	15	200mbar Ar
C115CoG-N	Co	W-C	CWCo	+eta	100	240	1150	15	200mbar N ₂
C115CoG+N	Co	W+C,E	CWCo	+C	100	240	1150	15	200mbar N ₂
C115CoG+CO	Co	W+C,E	CWCo	+C	100	240	1150	15	200mbar CO
C19G115+	Fe/Ni	W19+	CW19+	+C	100	240	1150	15	200mbar Ar
C424G115+	Fe/Co/Ni	W424+	CW424+	+C	100	240	1150	15	200mbar Ar
CN105CoG-5Kmin	Co	W-C	CNWC _o	+eta	5	240	1050	15	200mbar Ar
CN105CoG+5Kmin	Co	W+C,D	CNWC _o	+C	5	240	1050	15	200mbar Ar
CN115CoG+	Co	W+C,D	CNWC _o	+C	100	240	1150	15	200mbar Ar
CN115CoG+ 30min	Co	W+C,D	CNWC _o	+C	100	240	1150	30	200mbar Ar
CN115CoG-N	Co	W-C	CNWC _o	+eta	100	240	1150	15	200mbar N ₂
CN115CoG+N	Co	W+C,D	CNWC _o	+C	100	240	1150	15	200mbar N ₂
CB105CoG-5Kmin	Co	W+C,E	CBWC _o	+eta	5	240	1050	15	200mbar Ar
CB105CoG+5Kmin	Co	W+C,E	CBWC _o	+C	5	240	1050	15	200mbar Ar
CB115CoG+	Co	W+C,E	CBWC _o	+eta	100	240	1150	15	200mbar Ar

Table 3-11: Annealing conditions of G-type samples based on chromium and vanadium.

Sample Name	Binder alloy	WC-binder part	WC-GGI-binder part	Carbon potential	Heating rate (K/min)	Compaction pressure (MPa)	Temperature (°C)	Isothermal annealing time (min)	Atmosphere
CVCoG100_40min	Co	W,B	CVA	2 phase	100	240	1000	40	200mbar Ar
CVCoG105_60min	Co	W,B	CVA	2 phase	100	240	1050	60	200mbar Ar
CVCoG110_40min	Co	W,B	CVA	2 phase	100	240	1100	40	200mbar Ar
CVCoG115	Co	W,B	CVA	2 phase	100	240	1150	15	200mbar Ar
CCoG125	Co	W,B	CVA	2 phase	100	240	1150	8	200mbar Ar
CCoG136	Co	W,B	CVA	2 phase	100	240	1360	15	200mbar Ar

Table 3-12: Annealing conditions of G-type samples based on molybdenum.

Sample Name	Binder alloy	WC-binder part	WC-GGI-binder part	Carbon potential	Heating rate (K/min)	Compaction pressure (MPa)	Temperature (°C)	Isothermal annealing time (min)	Atmosphere
M105CoG-5Kmin	Co	W-C	MWCo	+eta	5	240	1050	15	200mbar Ar
M105CoG+5Kmin	Co	W+C,E	MWCo	+C	5	240	1050	15	200mbar Ar
M115CoG+	Co	W+C,E	MWCo	+C	100	240	1150	15	200mbar Ar
MB115CoG+	Co	W+C,E	MBWCo	+C	100	240	1150	15	200mbar Ar

Table 3-13: Sample compositions and annealing conditions of M-type diffusion couples.

Sample Name	Binder alloy	WC-binder part	GGIX part	carbon potential	heating rate	temper-ature	Isothermal annealing time	Atmosphere
					(°C/min)	(°C)	(min)	
CCoM95+	Co	CoM+	CCoM+	+C	100	950	330	Ar
CCoM105+	Co	CoM+	CCoM+	+C	100	1050	40	Ar
CCoM115+	Co	CoM+	CCoM+	+C	100	1150	5	Ar
VCoM95+	Co	CoM+	VCoM+	+C	100	950	330	Ar
VCoM115+	Co	CoM+	VCoM+	+C	100	1150	5	Ar
C424M95+	Fe/Co/Ni 40/20/40	424M+	C424M+	+C	100	950	330	Ar
C424M105+	Fe/Co/Ni 40/20/40	424M+	C424M+	+C	100	1050	40	Ar
C424M110+	Fe/Co/Ni 40/20/40	424M+	C424M+	+C	100	1100	15	Ar
C424M115+	Fe/Co/Ni 40/20/40	424M+	C424M+	+C	100	1150	5	Ar
V424M110+	Fe/Co/Ni 40/20/40	424M+	V424M+	+C	100	1050	15	Ar
V424M115+	Fe/Co/Ni 40/20/40	424M+	V424M+	+C	100	1150	5	Ar
V424M115+N	Fe/Co/Ni 40/20/40	424M+	V424M+	+C	100	1150	5	N ₂
C19M95+	Fe/Ni 15/85	19M+	C19M+	+C	100	950	330	Ar
C19M105+	Fe/Ni 15/85	19M+	C19M+	+C	100	1050	40	Ar
C19M110+	Fe/Ni 15/85	19M+	C19M+	+C	100	1100	15	Ar
C19M115+	Fe/Ni 15/85	19M+	C19M+	+C	100	1150	5	Ar

Table 3-14: Sample compositions and annealing conditions of H-type diffusion couples.

Sample Name	Binder alloy	WC-binder part	GGIX part	Carbon potential	Heating rate	Binder volume fraction	Temper-ature	Isothermal annealing time	Atmosphere
					°C/min		°C		
VCoH115+	Co	WCo+B	VWCo+	+C	300	16.3	1150	5	Ar
CCoH115+	Co	WCo+B	CWCo+	+C	300	16.3	1150	5	Ar
V424H115+	Fe/Co/Ni 40/20/40	W424+	VW424+	+C	300	16.3	1150	5	Ar
V424H115+N	Fe/Co/Ni 40/20/40	424+	VW424+	+C	300	16.3	1150	5	N ₂
C424H115+	Fe/Co/Ni 40/20/40	124+	CW124+	+C	300	16.3	1150	5	Ar
C424H115+N	Fe/Co/Ni 40/20/40	424+	CW424+	+C	300	16.3	1150	5	N ₂
V19H115+	Fe/Ni 15/85	19+	VW19+	+C	300	16.3	1150	5	Ar
C19H115+	Fe/Ni 15/85	19+	Cw19+	+C	300	16.3	1150	5	Ar

3.5 Samples for SPS

For preparing ultrafine hardmetals not only a fast distribution but also a high efficiency of GGIs is required. Since the known order $Cr+V > V > Cr$ is valid for liquid-phase sintered samples, SPS solid-state experiments were designed to check if this order can as well be applied to early solid-state sintering.

For this purpose samples are sintered at 1150°C for 15 min with parallel loading of uniaxial pressure. The exact conditions can be read from Table 3-3. The aim of this experiment was not to produce applicable hardmetals but to determine the maximum efficiency of the GGIs. Thus the samples were doped with a GGI-content slightly higher than usually used in hardmetals with a weight ratio of $c(GGI/Co)=0.08$ for chromium and 0.05 for vanadium. At these concentrations GGIs are not fully solvable in the hardmetals (compare literature data in Table 2-4). Also the carbon potential was fixed by presence of free carbon. The sample compositions are listed in Table 3-15.

3.6 Samples for grain growth experiments

Like the SPSed hardmetals discussed above this sample series aims to get information on the efficiency of GGIs upon early sintering stages. However, in contrast to SPS these samples series is based on liquid-phase sintered hardmetals. Upon liquid-phase sintering usually a degassing dwell at 1050–1200°C for 10–30 min is applied to allow quantitative reduction of surface oxides before the samples densify. The idea behind this series is that if GGIs show different activity at initial sintering stages, the exact conditions of the degassing dwell should influence the final grain-size distribution. Subsequently upon heat-up to liquid-phase sintering dwell at 1380°C for 40 min, three different degassing dwells at 1000°C for 15 min (100K), 1150°C for 15 min (115K) and 1150°C for 600 min (115L) were applied. The sintering profiles are illustrated in Figure 3-8.

Two classes of samples were prepared in this series. The first is based on conventional WC DS50, the second one on the attritor-milled grade DS50m. The compositions of the particular samples are listed in Table 3-16.

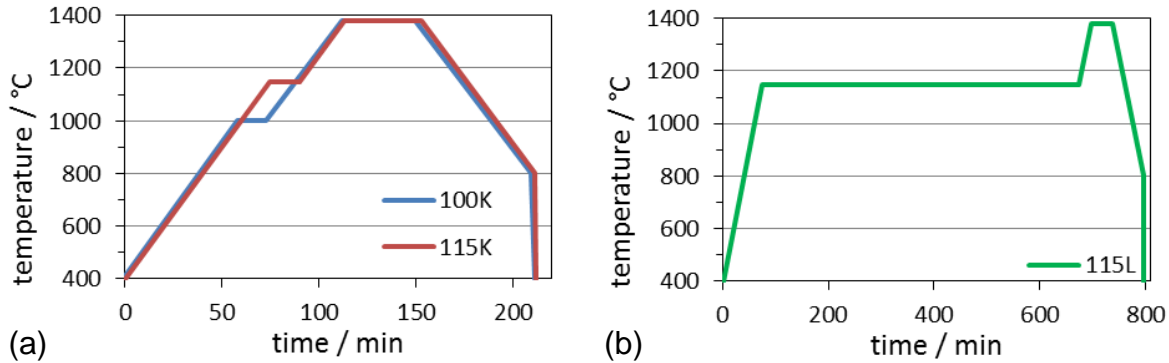


Figure 3-8: Annealing profiles (a) 100K, 115K and (b) 115L for grain growth experiments.

3.7 Samples for thermal analyses

Thermal analyses were conducted on a variety of samples. First of all, the components of G-type diffusion couples (see Table 3-7 and Table 3-8 for composition) were investigated in order to characterise a possible influence of surface oxides on the distribution of GGIs and to measure the solidus temperatures. However, the GGI-WC-binder parts have high GGI-X (X= boride, nitride, carbide) concentrations and low WC contents and have less in common with typical hardmetals.

Thus, in order to determine the influence of usual small amounts GGI-dopants on the thermal reactions of hardmetals, samples with a GGI weight ratio of $c(\text{GGI}/\text{Co})=0.05$ and low carbon potential were prepared. Their compositions are listed in Table 3-17. From literature (see section 2.3.2) it is known that the degassing characteristic of doped hardmetals is not only the sum of the particular powders, but determined by certain interactions. In order to identify these interactions three series of hardmetals doped with VC, Cr_3C_2 and Mo_2C were prepared with a fixed binder content of 16.3 vol% and varying atomic ratios of $c(\text{GGI}/\text{W})= 2/98, 10/90, 20/80$ and 50/50. From the specific change of peak positions and intensities conclusions on thermochemical reaction can be drawn. The compositions of the samples are listed in

Table 3-18. Additionally the samples of this series were liquid-phase sintered according to the temperature profile in Figure 3-9.

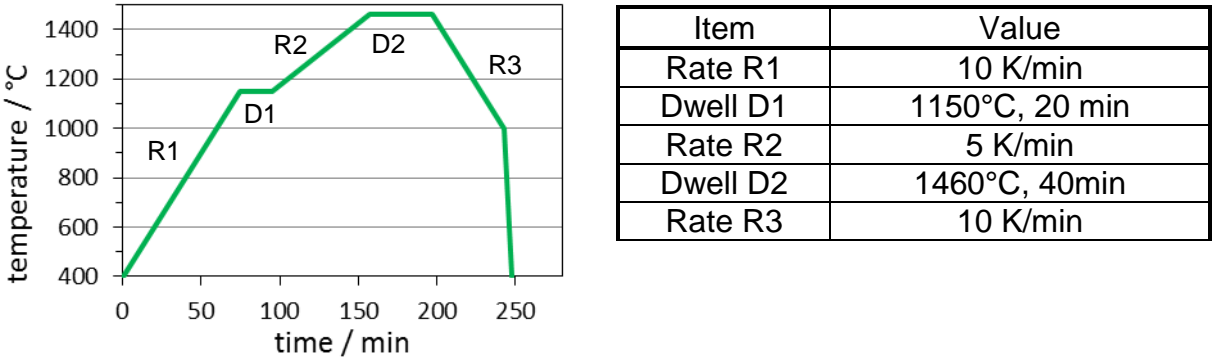


Figure 3-9: Temperature profile for sintering samples with varying GGI/W atomic ratio.

Table 3-15: Composition of SPS-samples.

Sample	GGI-X	GGI/Co (wt%/wt%)	Co standard		WC DS50		Cr ₃ C ₂		Cr ₂ N		VC		C	
			m (g)	wt%	m (g)	wt%	m (g)	wt%	m (g)	wt%	m (g)	wt%	m (g)	wt%
SP	none	-	15.071	10.04	135.041	89.96	-	-	-	-	-	-	0.18	0.120
SPC	Cr ₃ C ₂	0.089	9.998	9.99	89.05	88.98	1.029	1.03	-	-	-	-	0.062	0.062
SPCN	Cr ₂ N	0.088	9.99	9.99	89.005	89.01	-	-	1.001	1.00			0.127	0.127
SPV	VC	0.049	9.996	10.00	89.397	89.40	-	-	-	-	0.602	0.60	0.081	0.081
SPCV	Cr ₃ C ₂ +VC	0.084	10.032	10.02	89.068	88.98	0.597	0.60	-	-	0.399	0.40	0.061	0.061

Table 3-16: Composition of doped hardmetals for grain growth experiments (series MG).

Sample	GGI-X	WC-grade	Co		WC		Cr ₃ C ₂		VC		C	
			m (g)	wt%	m (g)	wt%	m (g)	wt%	m (g)	wt%	m (g)	wt%
MGRefU+	none	DS50	5.018	10.0	44.982	90.0					0.157	0.31
MGCU+	Cr ₃ C ₂	DS50	5.035	10.1	44.464	88.9	0.502	1.00			0.149	0.30
MGVU+	VC	DS50	4.998	10.0	44.698	89.4			0.30	0.61	0.160	0.32
MGCVU+	Cr ₃ C ₂ +VC	DS50	5.050	10.1	44.459	88.9	0.301	0.60	0.19	0.38	0.141	0.28
												0.00
MGRefU+	none	DS50m	4.994	10.0	45.007	90.0					0.156	0.31
MGCU+	Cr ₃ C ₂	DS50m	4.948	9.9	44.554	89.1	0.498	1.00			0.147	0.29
MGVU+	VC	DS50m	4.983	10.0	44.721	89.4			0.30	0.59	0.151	0.30
MGCVU+	Cr ₃ C ₂ +VC	DS50m	4.973	9.9	44.343	88.7	0.484	0.97	0.20	0.40	0.150	0.30

Table 3-17: Composition of doped hardmetals for thermal analysis.

Sample name	GGI-X	Weight ratio c(GGI)/c(Co)	Co		WC		C		GGI-X	
			m (g)	wt%	m (g)	wt%	m (g)	wt%	m (g)	wt%
HM_VC	VC	0.047	3.008	10.3	26.004	89.1	0.15	0.51	0.176	0.60
HM_Cr ₃ C ₂	Cr ₃ C ₂	0.050	3.010	10.0	26.829	89.4	0.15	0.50	0.174	0.58
HM_Cr ₂ N	Cr ₂ N	0.053	3.012	10.0	26.818	89.4	0.15	0.50	0.179	0.60
HM_CrB	CrB	0.050	3.004	10.0	26.894	89.4	0.15	0.50	0.182	0.61
HM_MoC	Mo ₂ C	0.050	3.003	10.0	26.842	89.5	0.15	0.50	0.159	0.53
HM_MoB	MoB	0.055	2.999	10.0	26.833	89.4	0.15	0.50	0.167	0.56
HM_Cr ₂ O ₃	Cr ₂ O ₃	0.050	2.998	10.0	26.799	89.3	0.356	1.17	0.221	0.74
HM_V ₂ O ₅	V ₂ O ₅	0.052	2.983	9.9	26.823	89.2	0.81	2.62	0.274	0.91

Table 3-18: Composition of samples with varying GGI/W atomic ratio for thermal analysis

Vanadium series	Binder alloy	Atomic ratio GGI/W	GGIX	Binder alloy		WC		GGI-X		C	
				mass (g)	wt%	mass (g)	wt%	mass (g)	wt%	mass (g)	wt%
WC-Co-2V	Co	2/98	VC	1.011	10.1	8.928	89.3	0.060	0.60	-	-
WC-Co-10V	Co	10/90	VC	1.067	10.7	8.626	86.2	0.312	3.12	-	-
WC-Co-20V	Co	20/80	VC	1.139	11.4	8.205	82.0	0.659	6.59	-	-
WC-Co-50V	Co	50/50	VC	1.441	14.4	6.478	64.8	2.084	20.83	-	-
WC-FeNi-20Vr	Fe/Ni	20/80	VC	1.139	11.4	8.201	82.0	0.659	6.59	-	-
WC-Co-2Cr	Co	2/98	Cr ₃ C ₂	1.023	10.2	8.9614	89.6	0.0201	0.20	0.001	0.011
WC-Co-10Cr	Co	10/90	Cr ₃ C ₂	1.071	10.7	8.6415	86.4	0.2911	2.91	0.020	0.201
WC-Co-20Cr	Co	20/80	Cr ₃ C ₂	1.141	11.4	8.2306	82.3	0.6314	6.31	0.042	0.420
WC-Co-50Cr	Co	50/50	Cr ₃ C ₂	1.451	14.5	6.541	65.5	2.0001	20.02	0.134	1.341
WC-FeNi-20Cr	Fe/Ni	20/80	Cr ₃ C ₂	1.142	11.4	8.229	82.3	0.63	6.30	0.042	0.418
WC-Co-2Mo	Co	2/98	Mo ₂ C	1.200	11.8	8.95	87.9	0.035	0.34	0.002	0.020
WC-Co-20Mo	Co	20/80	Mo ₂ C	1.049	10.5	8.582	85.9	0.365	3.65	0.022	0.220
WC-Co-50Mo	Co	50/50	Mo ₂ C	1.569	15.7	7.073	70.8	1.354	13.55	0.080	0.800
WC-FeNi-20Mo	Fe/Ni	20/80	Mo ₂ C	1.061	10.6	8.582	85.7	0.372	3.71	0.022	0.223

3.8 Microstructure

3.8.1 Metallographic sample preparation

For a sufficient microstructural characterisation of hardmetals metallographic preparation is required. In a first step samples were cut with a diamond cutting wheel in a high precision cutting machine of type Accutom 5 (Struers). One piece of the cut samples was embedded in a conductive phenolic resin (ConduFast, Struers) at 180°C using an embedding press (LaboPress-3, Struers). The embedded samples were ground and polished according to the conditions listed in Table 3-19 on aRotoPol-31 (Struers) polishing equipment. Step 5 was used for preparation of SEM-samples only, the preparation of samples for WDS-EPMA and LOM ended with step 4.

Table 3-19: Conditions for metallographic sample preparation.

	Step 1: grinding	Step 2: polishing	Step 3: polishing	Step 4: polishing	Step 5: polishing
Disc type	MD-Piano	MD-Largo	MD-Largo	MD-Dac	OP-Chem
Grinding agent	Diamond	DiaDuo-Suspension	DiaDuo-Suspension	DiaDuo-Suspension	OP-S Suspension
Graining	120 µm	9 µm	3 µm	1 µm	0.04 µm
Rpm	300	150	150	150	150
Cooling agent	Wasser	Lubricant-Blue	Lubricant-Blue	Lubricant-Blue	none
Force	30 N	25 N	25 N	20 N	10 N
Time	until planar	6 min	5 min	5 min	1 min

3.8.2 Light-optical microscopy

Light-optical microscopy (LOM) was performed using the bright field mode of either an Olympus GX51 or a Zeiss Observer.D1m reflecting microscope. Typically magnifications of 200x and 1000x were used in order to characterise the porosity and homogeneity of the samples.

3.8.3 Scanning electron microscopy and grain size analysis

A field-emission scanning electron microscope (SEM) in backscatter (BSE) mode provided by the USTEM of the Vienna University of Technology was used to generate pictures of the microstructure in a magnification up to 60000x. Such micrographs allow the determination of the average WC grain size by applying the linear intercept method (ASTM E112-96). The number of lines and the magnification used for the grain-size measurement depends on the grain size and was chosen case-by-case in a manner that at least 150 grains are measured in one picture. It was found [00ROE] that at least 150-200 grains should be measured in order to ensure a reasonable statistical error of the determined value.

Since such a SEM micrograph represents only a very small area of the sample, BSE-pictures of at least three different sample positions with a total number of >500 grains were analysed in order to increase the significance of the results.

3.8.4 Transmission electron microscopy

Transmission electron microscopy (TEM) analyses were conducted on G-type diffusion couples annealed at temperatures ranging from 1050–1360°C in order to gain insight into the WC/Co interface chemistry. Since the GGI-concentration is a function of the distance from interface, a method allowing precise spatial preparation is required, such as focussed ion beam (FIB) technique. The process of sample preparation using Quanta 200 3D DualBeam-FIB equipment is illustrated in Figure 3-10. In a first step the position of the later sample lamella 10 µm from the GGI-WC-Co/WC-Co interface was protected by four layers of Pt-coatings. In a second step the lamella was cut on three sides with a Ga-ion-beam (Figure 3-10a). After thinning to 500 nm (Figure 3-10b) the lamella were transferred to a copper sample holder by means of micro-manipulators (Figure 3-10b). The sample holder is the reason for a copper-signal detected in later EDX-analysis. Further thinning to 200 nm is principally required for TEM-observation but was challenging to impossible due to the high porosity and subsequent low mechanical stability of the samples. Thus, imaging and EDX-analyses were only possible at the bottom edge of the lamella where low thickness was reached by wedge-shaped thinning. Both imaging

and standardless EDX-analyses were made on several WC/Co interfaces for each sample using FEI TECNAI F20 equipment.

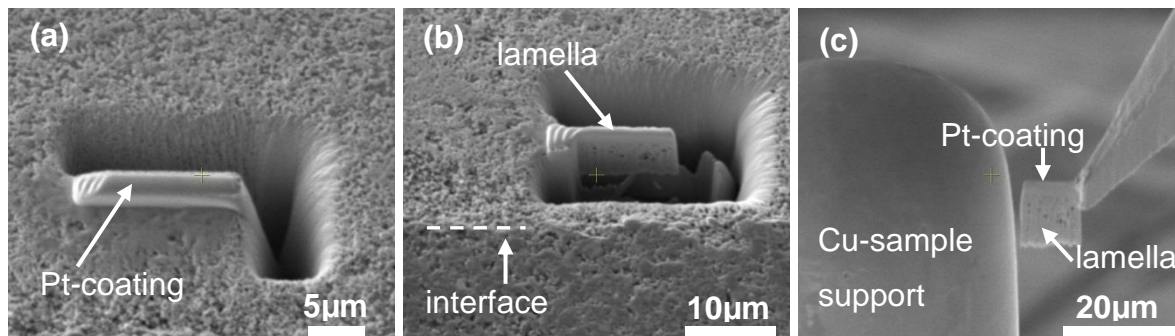


Figure 3-10: FIB preparation of lamellae for TEM-investigations.

3.9 Mechanical properties

3.9.1 Hardness HV30

The hardness of hardmetal samples was determined by the Vickers indentation method. Hardness tests were performed on a M4U-025 Tester (EMCO Test) with a load of 30 kg (294.3 N) in accordance to the ISO 3878 standard. The indentation time was 10 s. The length of the two indentation diagonals was measured by LOM. From the diagonals the hardness value can be calculated using Equation 1.

$$HV = \frac{1.854 * M}{d^2} \quad \text{Equation 1}$$

HV	Vickers hardness
M	Applied force [kg]
d	Mean length of the indentation diagonals [mm]

3.9.2 Fracture toughness

The fracture toughness was determined by the Palmqvist-Shetty method. Therefore the length of the cracks originating from the corners of a Vickers indentation is measured by LOM. According to Shetty [85SHE, 86SHE] the fracture toughness is estimated by Equation 2.

$$K_{Ic} = 0.0275 * \sqrt{\frac{HV * P}{L}} \quad \text{Equation 2}$$

K_{Ic}	Fracture toughness [MPa*m ^{0.5}]
HV	Vickers hardness [kg/mm ²]
P	Applied load [kg]
L	Sum of crack lengths [mm]

3.10 Magnetic properties

3.10.1 Coercive force

The coercive force allows conclusions on the sintering state of a hardmetal. It is dependent on the residual stress and subsequently on the mean free path of the binder phase in a sintered hardmetal. For a given binder phase composition it reaches a maximum at the ideal sintering time. A longer sintering time increases the binder mean free path by WC grain growth yielding lower residual stresses and a decreased coercive force. At shorter sintering times the binder phase is not ideally distributed within the material which is as well leading to a decreased coercive force value. However, it has to be noticed that the ideal value depends on a variety of material parameters such as the carbon potential, dopants or the initial WC grain size and is subsequently material-specific. Despite this drawback, the coercive force can be used to detect irregularities in otherwise constant production parameters of a particular hardmetal grade. For a known system also information on the average WC grain-size is accessible. The coercive force was measured using a Koerzimat 1.096 CS V3.09 (Foerster). The mean value of four single measurements at two different positions in the magnetic coil was considered to be statistically significant.

3.10.2 Magnetic saturation

The relative magnetic saturation (MS), also referred to as $4\pi\sigma$, allows an estimation of the carbon potential within the binder phase of a hardmetal. This is possible since the carbon potential is correlated to the amount of tungsten dissolved in the binder phase in a manner that higher carbon potential leads to lower tungsten solubility, see also Figure 2-6. Since dissolved tungsten atoms lower the mass-specific magnetic saturation of a ferromagnetic binder phase they allow an indirect carbon measurement. The correlation between the carbon potential and the magnetic saturation according to [07SCH] is shown in Equation 3. This equation also considers the influence of chromium additions on the magnetic saturation within the limitation that no chromium-based precipitations appear in the sample. Such precipitations have certain solubility for cobalt, see Table 2-4, and will hence affect the amount of magnetic cobalt binder. Vanadium and tantalum, both are common additives, are not considered in this equation. However, their solubility in the binder phase is low, so according to [07SCH] there is an agreement that their influence can be neglected in most cases.

$$4\pi\sigma = \frac{\sigma_s * 100}{2.02(Co - 0.876 * Cr_3C_2)} \quad \text{Equation 3}$$

$4\pi\sigma$	Relative magnetic saturation [%]
σ_s	Mass specific magnetic saturation [$\mu\text{T}\cdot\text{m}^3\cdot\text{kg}^{-1}$]
Co	Cobalt mass fraction [wt.%]
Cr_3C_2	Chromium mass fraction [wt.%]

Equation 3 is valid for cobalt binder only. However, within the Fe/Co/Ni binder systems such a relationship can be found for all austenitic binders. It was found by previous works, e.g. [79PRA, 11WAG, 13BUC2] that ferritic, ferritic+austenitic or partially martensitic iron based binder systems do not exhibit a carbon/magnetic saturation relationship suitable for an estimation of the carbon potential. In such a case information on the carbon content of a sample is only accessible by absolute carbon measurement such as the hot gas extraction.

The magnetic saturation was measured using a Koerzimat 1.096 CS V3.09 (Foerster). The mean of five single measurements was used in order to get a statistical significant value.

3.11 Concentration Profiles (WDS-EPMA)

The concentration profiles of GGIs, W, C and binder elements in diffusion couples were determined by wavelength-dispersive electron-probe microanalysis (WDS-EPMA) using Cameca SX100 Microprobe equipment.

An incident electron beam with energy of 20 keV stimulates element specific x-ray emission which is selected in monochromators and detected. The parameters used for the various analyses are listed in the annex section 8.1. Two different devices were used, one located at the IFREMER in Brest, France, the other one located at the Department of Lithospheric Research of the University of Vienna, Austria. For measuring concentration profiles within the WC-binder part of diffusion couples as a function of the distance from interface line-scans parallel to the interface were measured at certain distances. In order to achieve a statistically significant value for the concentration of the various elements at a particular distance from interface the lines-scans were of 15–20 points length with a distance of 2–10 μm between the particular spots. The concentration of the elements was subsequently defined as the mean of the particular points. This method allows determining concentration values in inhomogeneous microstructures. An illustration of a measurement on sample VCoH115+ and the corresponding concentration profile is depicted in Figure 3-11.

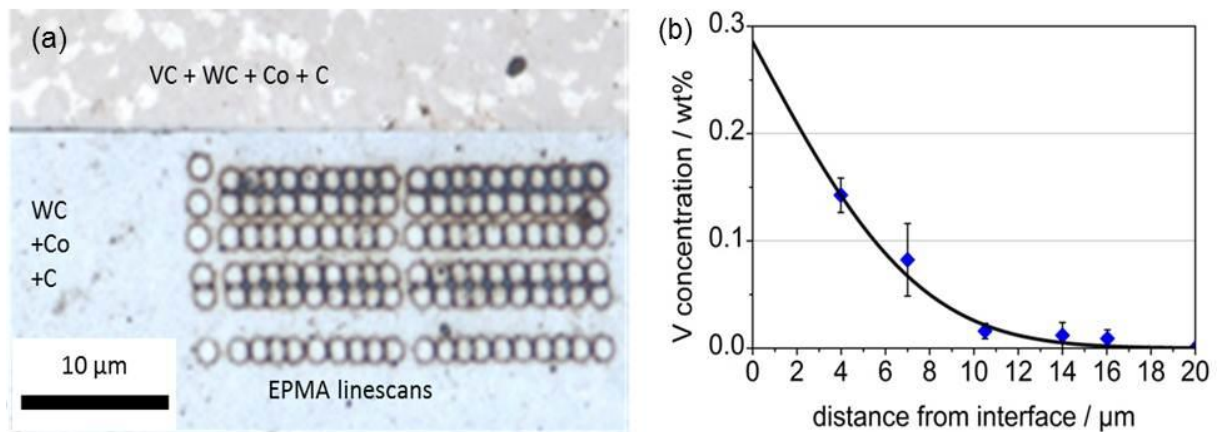


Figure 3-11: Sample VCoH115+; (a): LOM micrograph and position of EPMA linescans; (b) corresponding vanadium concentration (blue data points) and fitted concentration profile (black line) .

3.12 Thermal analysis

Differential Scanning Calorimetry (DSC) allows the detection of phase transitions (e.g. liquid ↔ solid) as a function of temperature.

Compacted powder mixtures are placed in a corundum crucible with a diameter of 5 mm and a height of 3 mm and covered with a corundum plate. Upon heating a powder mixture the detected phase reactions are not necessarily related to the equilibrium since they can be the results of non-equilibrium reactions of particular components. To overcome this issue the samples are heated in a so called “zigzag” profile as exemplarily shown for the mid-carbon WC-Co diffusion couple component WCo in Figure 3-12. Upon such a temperature cycle the sample is heated to a temperature higher than the expected liquid-phase transition and then cooled down below this temperature followed by a subsequent repeat of this profile. In the second heating step the binder phase of the hard material is expected to be in a homogeneous state and thus will deliver information on the equilibrium reaction. This is advantageous since within one experiment information on the behaviour during sintering (1st cycle) as well as on the equilibrium state (2nd cycle) can be obtained.

The information used in this work is the “onset” temperature which marks the beginning of the phase reaction. Additional information can be gained from the offset temperature and the peak maximum. However, in a hardmetal they depend on a

variety of parameters such as heating rate, amount of binder phase or the width of the melting interval which makes the interpretation difficult. Usually a hysteresis between the onset of the heating and cooling peak is observed. In the first heating cycle this can be explained by the non-equilibrium reactions during heating. In the second cycle the gap between the onset-temperatures can have two reasons:

- The finite heating rate: Due to kinetic effects (e.g. nucleation during cooling) the onset of the phase reaction can be shifted. An exact value could only be reached by an infinitely slow heating rate.
- A melting interval: If the sample shows a melting interval (e.g. the eutectic reaction of WC-10Co with 4.9 wt% carbon, compare Figure 2-12) the onset during heating marks the lower boundary of the interval while the cooling onset marks the upper boundary. In such a case an asymmetric or bimodal peak is usually observed.

Simultaneous to the calorimetric signal the mass loss of the sample is detected by thermal gravimetry (TG), see Figure 3-12. In hardmetals, besides desorption of water or organic compounds at low temperatures, the mass loss derives from the evolution of CO caused by the carbothermic reduction of surface oxides or N₂ the decomposition of nitrides, respectively. Thus, a reasonable TG signal is usually achieved upon the first heating cycle only. The first derivation of the mass signal can be compared to the results from the evolving gas analysis. The evolving gas analysis has a higher accuracy and allows the separation of N₂ and CO signals. However, the TG is useful since it allows a quantification of the mass change.

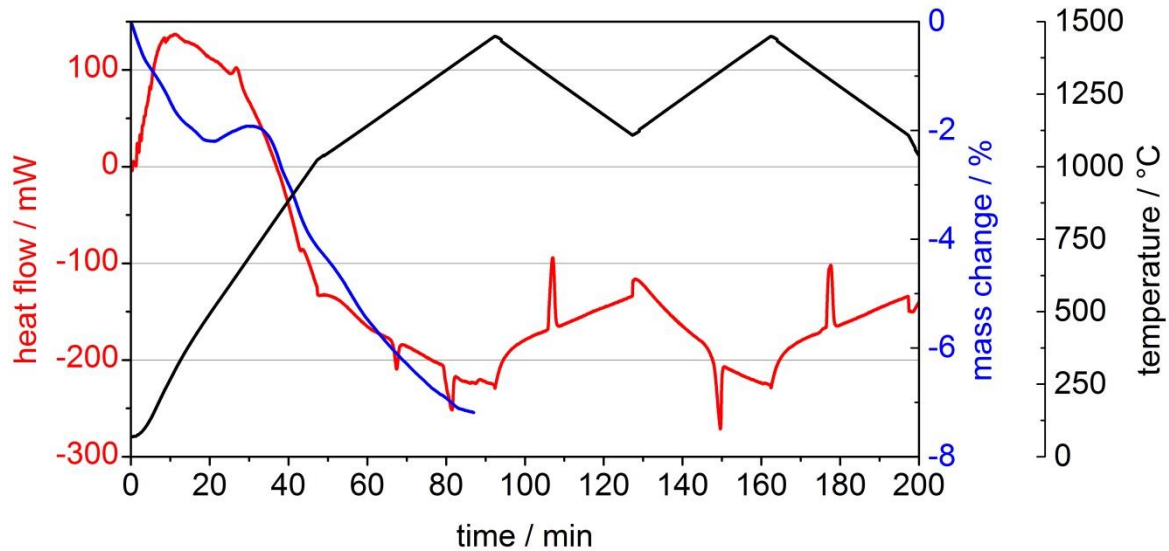


Figure 3-12: Typical results of thermal analysis. Black line: temperature; red line: DSC signal; blue line: TG signal.

3.13 Calculation of transport parameters

The diffusion coefficient D can be calculated from the measured concentration profiles by using a solution of Fick's 2nd law for a fixed interface concentration [07MEH] which was fitted to the experimental data, setting D as a fitting parameter. The concentration profile is given by

$$\frac{c - c_s}{c_0 - c_s} = 1 - \operatorname{erf}\left(\frac{x}{2\sqrt{D * t}}\right) \quad \text{Equation 4}$$

where c is the GGI concentration (wt%) in a distance x from the interface (cm), c_0 the interface concentration (wt%), $c_s=0$, D the diffusion coefficient (cm^2/s) and t the diffusion time (s). If the diffusion coefficient is measured for at least two different temperatures the activation energy Ea as well as the pre-exponential factor D_0 can be calculated using the Arrhenius equation:

$$D = D_0 * \exp\left(-\frac{Ea}{RT}\right) \quad \text{Equation 5}$$

where Ea is the activation energy for GGI diffusion (J/mol), T the temperature (K), R the gas constant (8.314 J/mol*K) and D_0 a pre-exponential factor (cm²/s).

Equation 4 allows the calculation of concentration profiles for a time independent diffusion coefficient D . During heat up the temperature and subsequently D changes continuously. The temperature dependency of D is given by the Arrhenius equation and for no isothermal diffusion D is set as $D(T)$. If the temperature change as a function of time is known T can be expressed by $T=T(t)$. For a linear heat up rate T can be expressed as

$$T(t)=T_s+r*t \quad \text{Equation 6}$$

where T_s is the starting temperature (K) and r the heating rate (K/s). The diffusivity then becomes

$$D(t) = D_0 * \exp\left(-\frac{Ea}{R(T_s + r * t)}\right) \quad \text{Equation 7}$$

According to [97FRA] a time dependent diffusivity can be introduced by defining an independent variable y , meeting the condition $dy=D(t)dt$ or

$$y = \int_0^{t'} D(t)dt \quad \text{Equation 8}$$

This equation is also true for isothermal diffusion, which can easily be verified by setting D time independent, which yields again $y=D*t$. To use y for calculating diffusion profiles Fick's second law must be rearranged to

$$\frac{\partial C}{\partial y} = \frac{\partial^2 c}{\partial^2 x} \quad \text{Equation 9}$$

Equation 9 can be solved in the same manner as Fick's second law, resulting in

$$\frac{c_x - c_S}{c_0 - c_S} = 1 - \operatorname{erf}\left(\frac{x}{2 * \sqrt{y}}\right) \quad \text{Equation 10}$$

Equation 9 allows the calculation of concentration profiles for linear heat up or cool down (with negative r values).

However, it has to be pointed out that the distribution of GGIs in hardmetals is not only determined by bulk diffusion. As it will be discussed in 5.6 a variety of parameters such as cobalt wetting on WC or WC particle rearrangement influence the measured concentration profiles. Hence, the application of Equation 4 is not physically correct. However, a satisfying correlation of the experimental data and the model was observed. The parameter D was hence not considered a diffusion coefficient but was introduced as a transport factor which is a measure for the distribution of GGIs in hardmetals.

Since the transport is not a pure diffusion no deeper investigation such as concentration dependent diffusion model or Boltzmann-Matano analysis was applied.

4 Results

The behaviour of Cr, V and Mo at early sintering stages is a function of temperature, carbon potential, sintering atmosphere, green density, binder-phase composition and heating rate as well as the investigation of interdependencies lead to a large number of 130 diffusion couples in total. Also a large number of microstructural and thermal analyses were conducted. For improving clearness it was decided to separate results and discussion in independent sections. In this chapter all experimental results are shown without discussing them in depth. Similar thoughts apply to the results of microstructural and thermal analyses. A detailed discussion which takes into account results from diffusion couples as well as microstructural, interfacial and thermal analyses is given in chapter 5.

4.1 Determination of diffusion parameters

The idea of the diffusion couple technique is to gain diffusion parameters from an experimental setup with fixed boundary conditions. As it was described in section 3.4.1 GGIs are expected to diffuse from the GGI-WC-binder part to the WC-binder part of the diffusion couple. The GGI amount available in the GGI-WC-binder part is by orders of magnitude higher than the amount expected to migrate into the WC-Co part during the experiment. Furthermore, based on previous works [12BRI] the main fraction of GGIs is expected to be transported via the binder phase. Binder volume fraction and carbon potential of the diffusion couple parts are kept constant in order to avoid gradients of carbon or binder metals. Based on these boundary conditions the GGIs are expected to be the only moving component and a thin layer of the GGI-WC-binder part will meet the conditions for an “unlimited source”. These two assumptions allow the application of Equation 4 in order to determine the diffusion coefficient of GGIs.

The application of the model to typical experimental data is shown in Figure 4-1 on the example of G-type diffusion couples annealed at 1150°C for 15 min. The dots represent the as-measured concentrations of chromium, vanadium or molybdenum determined from line scans of 30 µm length at a given distance from the interface

(see section 3.11). The solid lines represent a nonlinear fit of the model according to Equation 4, omitting data points below the detection limit or within a distance of 10 μm from the interface. The error bars represent the standard deviation of the experimental data obtained from one line scan. It has to be noted that the standard deviation in this case does not represent the uncertainty of the EPMA measurements but derives from a convolution of the uncertainty and the inhomogeneity of the microstructure. Since the uncertainty of the method itself should be approximately equal for each data point the error bars can be interpreted as a measure of the microstructural inhomogeneity within a single linescan.

The data points for chromium in Figure 4-1(a) show a relatively large scatter and especially close to the interface the correlation with the model is poor. For vanadium (b) a relatively smooth concentration profile is measured, but it does not correlate very well with the model data while for molybdenum (c) the empirical data fits well to the applied model.

Upon annealing of diffusion couples a variety of processes appear. In WC-Co the densification process is known to initiate around 800°C driven by cobalt spreading on the WC grains. As discussed in section 2.2.1 the wetting onset depends on the gross carbon potential and the presence of GGIs. Subsequently three processes influencing the microstructure appear simultaneously:

- (1) Migration of cobalt binder driven by wetting of WC grains depending on local GGI concentrations.
- (2) Densification of the green body due to wetting and subsequent particle rearrangement.
- (3) Formation of local inhomogeneities by non-uniform wetting.

The combination and interdependency of these fundamental processes make clear that the assumed boundary condition of GGIs as the only moving component is untenable. Since the application of Equation 4 requires these assumptions the influence of the effects (1)–(3) has to be eliminated.

When porous materials are measured by EPMA the total sum of the measured elements concentrations is below 100% if, like in our case, fully dense standards are

used for calibration. Subsequently, in a material with uniform GGI concentration higher porosity at a particular spot leads to lower measured GGI concentration values. This effect has to be eliminated in order to allow a comparison of measurements at local positions. Since higher porosity causes a lower signal and, hence, a lower total concentration, the latter can be used as a measure for the local porosity. Normalising the as-measured concentrations by the “total” will eliminate the influence of the porosity and in particular of local pore distribution inhomogeneities. The results of the normalisation are shown by the data points indicated by black squares in Figure 4-2. It turns out that this normalisation method does not significantly improve the scatter of the data points and the curves do not basically differ from Figure 4-1. It can be concluded that the porosity and, hence, the densification does not play a major role for the measurement of concentration profiles.

The migration of cobalt driven by wetting can lead to local inhomogeneities of the cobalt concentration. Since GGIs are expected to diffuse mainly via the cobalt phase, this will also lead to scatter in the as-measured GGI concentration. A normalisation of the GGI-concentration by the Co-concentration would eliminate this influence. As it can be seen from the red, diamond-shaped data points in Figure 4-2 the normalised concentration profiles become significantly smoother as compared to the as-measured profiles (Figure 4-1). This is a direct proof that the majority of the GGI diffuses via the binder phase. By this normalisation the concentration profiles become smoother and also show better correlation to the model as can be seen from the correlation coefficient R^2 in Table 4-1. From these findings it is clear that inhomogeneous cobalt distribution which is natural in green bodies at initial sintering stages can be compensated by the normalisation.

Based on the considerations above the comparisons of concentration profiles in this work are normalised by the corresponding cobalt concentration.

It can be seen from Figure 4-2(a) that the correlation between experimental data and model is quite good for chromium ($R^2=0.951$) after normalisation, the same applies to molybdenum (c) with $R^2=0.977$. For vanadium (b) the fit is still poor after normalisation ($R^2=0.828$). The findings are also representative for samples prepared

at other conditions, the fit of vanadium is usually poor while it is good for both chromium and molybdenum. The reasons are discussed in detail in section 5.6.

Summarising the results and considerations above it can be stated that the concentration profiles measured in diffusion couples not only depend on the diffusion of GGIs but are convolved with a variety of other effects such as spreading of the binder phase, particle rearrangement and subsequent densification, dissolution kinetics and carbothermic reactions of surface oxides. From such a point of view it is clear that the parameter D in Equation 4 is not a real diffusion coefficient and the application of Equation 4 is not physically correct in terms of the diffusion laws. On the other hand, as it was shown above the model applies quite well if the as-measured data is normalised by the local binder concentration, and it particularly fits well to the data far from the interface for all investigated GGIs, allowing a decent description of the diffusion depth.

For that reason the parameter D was used in this work as a measure of the GGI transport kinetics, but it has to be kept in mind that it is not a diffusion coefficient in a physically correct way. Nevertheless it can be considered as a transport parameter summarising all kinetic effects influencing the GGI transport.

Table 4-1: Transport factors D and correlation coefficients R² of the corresponding fit determined from as-measured and normalised data (see Figure 4-1 and Figure 4-2).

Sample	GGI	Correction method	D (10 ⁻¹⁰ cm ² /s)	R ²
CCoG115+	Cr	none	395	0.806
		total	389	0.730
		cobalt	342	0.951
VCoG115+	V	none	65	0.839
		total	77	0.896
		cobalt	121	0.828
MCoG115+	Mo	none	20.7	0.936
		total	22.7	0.993
		cobalt	15.5	0.977

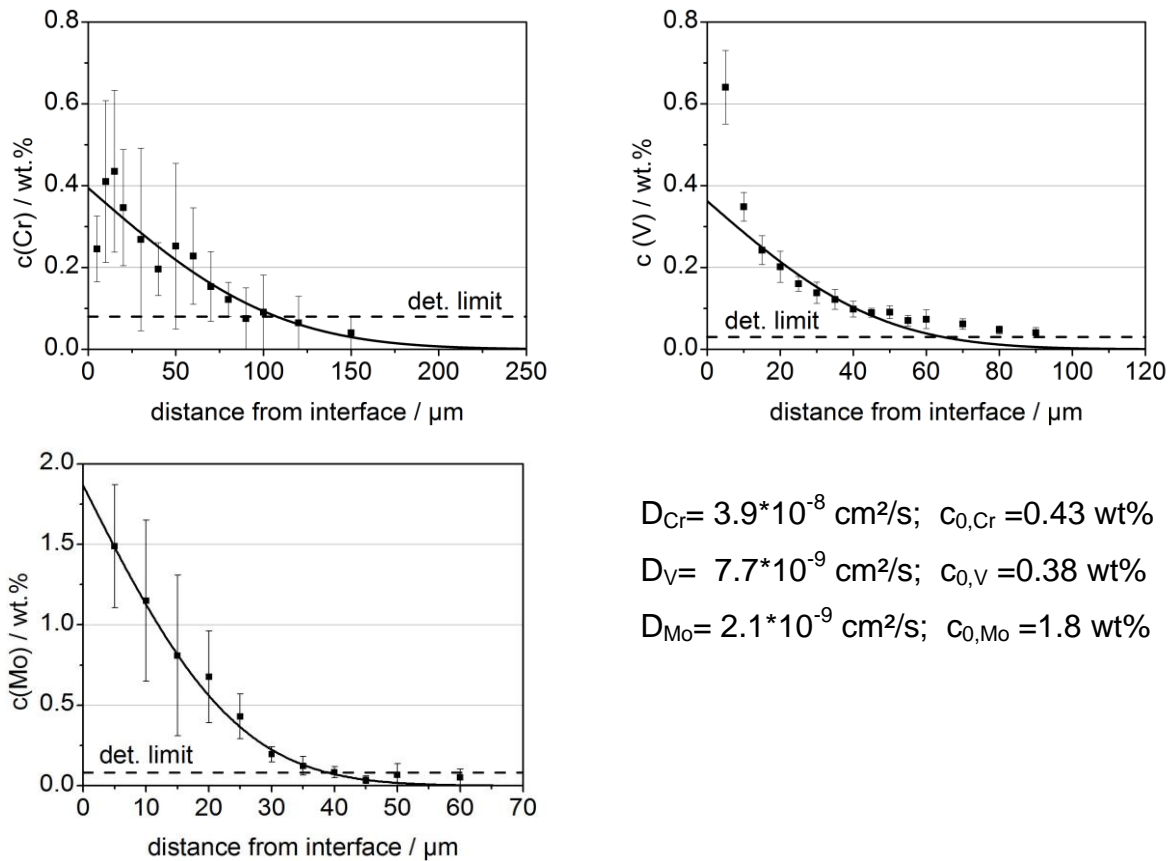


Figure 4-1: As-measured concentration profiles (data points) and corresponding fit of Equation 4 (solid lines) of (a) Cr, (b) V and (c) Mo in a G-type diffusion couple annealed at 1150°C for 15 min.

4.2 Reproducibility and error

In the following section the experimental methods used in this work are analysed on their reproducibility. Furthermore sources of error are discussed and quantified where applicable.

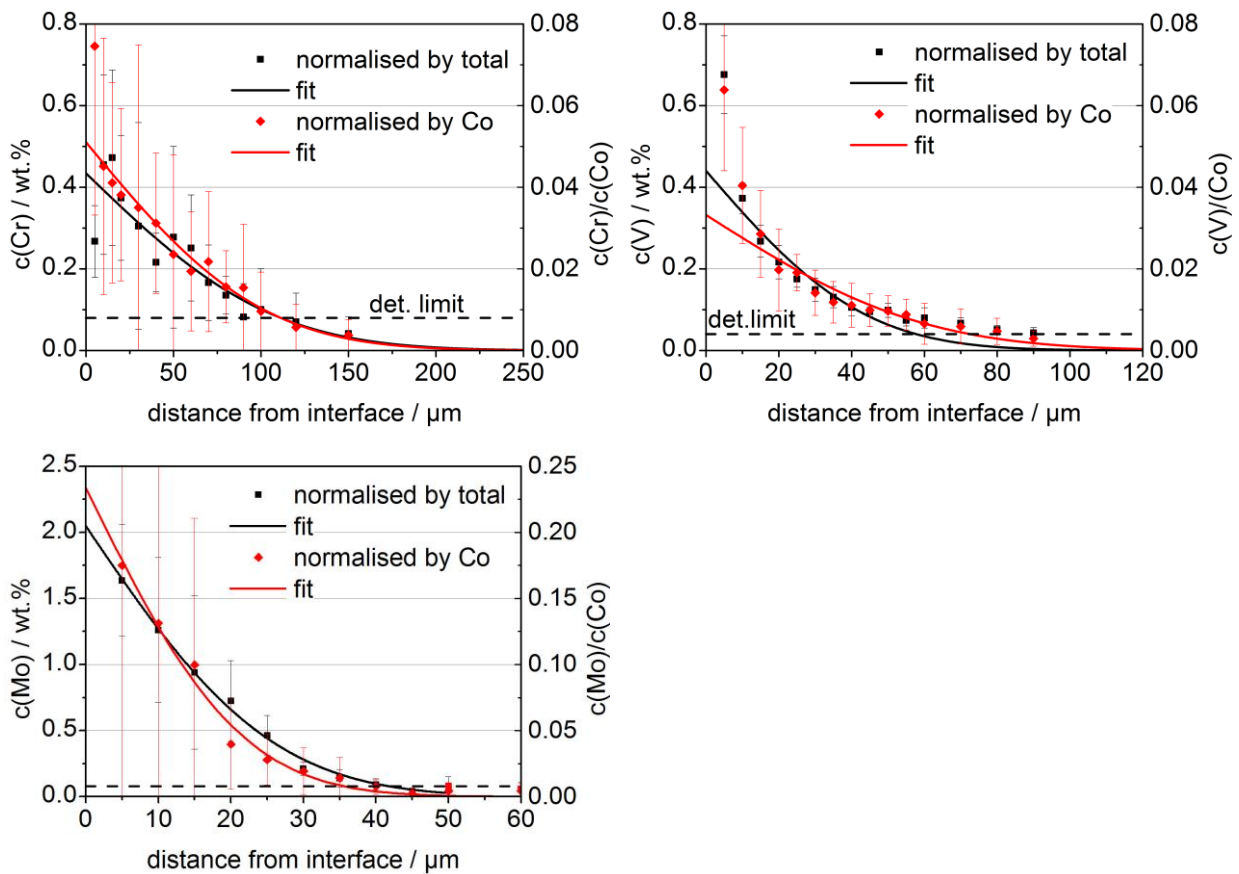


Figure 4-2: Comparison of normalised concentration profiles (data points) and corresponding fit of Equation 4 (solid lines) of (a) Cr, (b) V and (c) Mo in a G-type diffusion couple annealed at 1150°C for 15 min.

4.2.1 Diffusion couples

Upon preparation and analyses of diffusion couples a number of error sources appear. Some of them can be quantified as follows:

- The temperature dependency of diffusion is exponential as can be seen from Equation 5 (Arrhenius plot). Hence, slight deviations in temperature can cause a large error. By calibrating the furnace with combined thermocouple/pyrometer measurements the temperature deviation was measured +/- 2°C.

For example, the transport factor for chromium diffusion in cobalt binder was determined as

$$D_{Cr}^{Co,M} = 5.24 * \exp\left(-\frac{299600}{8.314 * T}\right)$$

At a temperature of 1150°C the transport factor is $D=5.26*10^{-11}$ cm²/s, at 1152°C it was measured $D=5.45*10^{-11}$ cm²/s. The error caused by temperature deviations is hence around 3.5% relative.

- The metallographic preparation of the samples involves cutting, embedding and polishing. Correct measurements require cutting strictly perpendicular to the interface. Deviations cause an error in the diffusion depth. The angular deviation of the sample holder of the cutting machine is around 3°, leading to an error regarding the diffusion depth of 1.5% relative.
- Selective polishing: Upon metallographic preparation the samples are polished to a smooth surface. However, due to the large hardness differences the soft cobalt phase might be selectively removed from the sample. Line-scans within the WC-Co part of the diffusion couples at a distance from interface where the microstructure is not influenced by GGIs can be found from the various G-type couples in section 4.3, e.g. Figure 4-9. In such a case the cobalt concentration scatters around the initial 10 wt%, hence such an effect is not significant and can be neglected.
- The position uncertainty of the EPMA-stage is +/- 1 µm.
- Since G-type couples are prepared from powders the interface is not perfectly smooth but has a certain roughness. The latter increases if the annealing temperature is lowered. A BSE image of the representative sample CVCoG105 which was annealed at a relatively low temperature of 1050°C is depicted in Figure 4-3. The interface roughness of this sample is 2–3 µm.

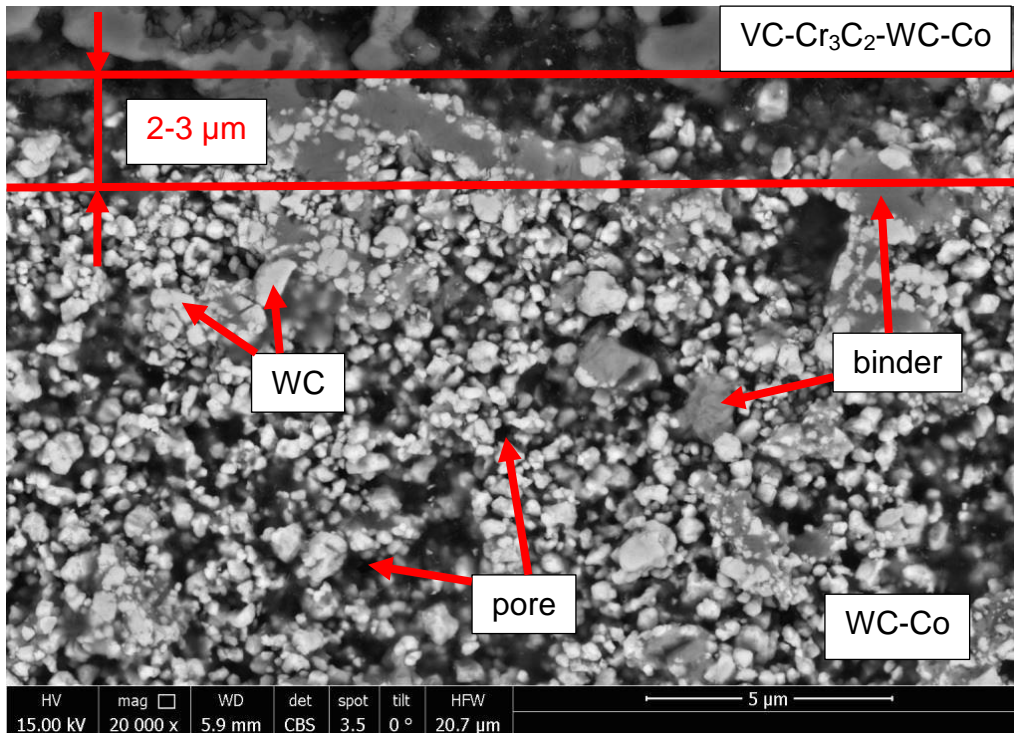


Figure 4-3: BSE image of the interface of sample CVC0G105, annealed at 1050°C.

Some error sources are terminated by the experimental setup, such as:

- Chemical composition: All samples of a particular carbon potential and binder alloy were prepared from the same initial powder mixture. Aging effects were eliminated by proper powder mixture storage in a vacuum desiccator.
- Organic Surface contaminations caused by sample handling or by traces of polishing agent in the pores were eliminated by applying oxygen plasma when introducing them into the EPMA chamber. No significant increase of the surface oxide concentration was detected.

A number of influences such as impurities of the furnace atmosphere, insufficient contact of the diffusion couple components, microstructural inhomogeneities or EPMA-beam deviations by local magnetism can hardly be quantified. Thus, some samples were reproduced in order to get an estimation of the summarised influence of all errors and of the reproducibility of the method.

Two samples of the G-type couple CCoG115+_30min, labelled with _A and _B were prepared independently starting from the preparation of the powder mixtures. From sample _B the chromium concentration profile was measured at two different spots of

the sample with a distance of 1 cm between them, labelled with _B1 and _B2, respectively. Subsequently the difference between A and B indicates the cumulated errors of the preparation and measurement processes, while the difference between _B1 and _B2 is a measure for the uncertainty of the EPMA-measurement, including the influence of microstructural features. The resulting normalised chromium concentration profiles are depicted in Figure 4-4(a). Both concentration profiles B1 and B2 are almost identical; the resulting transport factors of resp. $3.10 \cdot 10^{-8} \text{ cm}^2/\text{s}$ and $3.23 \cdot 10^{-8} \text{ cm}^2/\text{s}$ differ by 9% relative, see Table 4-2. When comparing A and B1 a larger difference of almost 40% appears, though the concentration profile doesn't look that much different.

In order to confirm this error a second sample (CCoG115+) was as well prepared two times, but the annealing time was 15 min. The resulting concentration profiles of chromium, labelled A and B, are shown in Figure 4-4(b). The particular data points do not show a large deviation. The fitted curves are slightly different due to random errors of the single data points. However, the corresponding transport factors of resp. $D=2.54 \cdot 10^{-8} \text{ cm}^2/\text{s}$ and $3.61 \cdot 10^{-8} \text{ cm}^2/\text{s}$ again differ by 40% confirming the value determined from CCoG115+_30min. Anyway, these considerations show that even small random deviations have large impact on the calculated transport factor, despite the optical indifference of the two as-measured curves.

Since the transport factors measured at different temperatures with at least 50°C step width differ by an order of magnitude (factor 10) an error of 40 % (factor 1.4) can be tolerated.

A more detailed discussion is required on the error of single line scans of diffusion couples. A particular line scan consists of 15–20 single points in a distance of 3–5 μm . The concentration at a given distance from the interface is defined by the mean of these 15–20 single points. The corresponding standard deviation is indicated by the error bars in all concentration profiles diffusion couple related figures of section 4. However, the information represented by these error bars depends on the type of diffusion couples. In M-type couples the particular points were measured within the equilibrated binder phase. The binder phase is homogeneous without porosity. The error is hence completely caused by measurement errors which are small around 10% rel., as exemplarily shown for a chromium based M-type couple at

1150°C in Figure 4-5(a). These considerations apply as well for H-type couples since they have a homogeneous ultrafine grained microstructure. However, for G-type couples the situation is more complex. As shown in Figure 4-5(b) the standard deviation is large by more than 100% relative. As mentioned above only 10% rel. can be explained by random errors, the majority of the error originates from a different source. As can be seen from Figure 4-3 the distribution of binder phase and WC at e.g. 1050°C is still extremely inhomogeneous in G-type couples. In a line scan of 20 data points of 1 µm diameter particular spots will hit cobalt grains while others will hit WC agglomerates. This inhomogeneity causes large concentration differences between the single spots of a scan. Since the majority of the GGI is dissolved in the binder phase these inhomogeneities are transferred to the GGI-concentration profile as well. Furthermore, precipitations of GGI-carbides will as well have such an effect. Consequently the standard deviation of line scans in G-type couples does not necessarily represent the error of the method but is a measure for the microstructural inhomogeneity and hence the homogeneity of the GGI-distribution in the hardmetal. One specific parameter influencing the concentration profiles and subsequently the transport factor was not quantified yet: the influence of densification. The green bodies will densify upon the diffusion experiments, which will influence the measured diffusion depth. However, the local densification at a given temperature is a function of the green density, the cobalt concentration, the carbon potential, the annealing time and especially the GGI concentration. All of these parameters not only change upon the experiments but are also interdependent. Their relationship is complex and not fully understood yet and can hence not be modelled or predicted. The usual linear densification of fully densified hardmetals is ~20% (see literature in 2.2.1). Since in solid-state experiments the samples will shrink only by 10–15% and densification appears during the whole period and not suddenly at the end of the annealing time the error on the distance from the interface can be estimated by 10%. The influence of the diffusion depth on the transport factor is parabolic which yields an error of ±21% for the transport factor D. This error is lower than the 40% estimated by the reproducibility experiments. However, this work revealed that at least the main part of the GGI is transported via the binder phase. Simultaneously to the densification the binder phase is more

homogeneously distributed which facilitates the diffusion and redistributes the GGI already resolved in the binder phase. This effect is further discussed in the results section and is specific for the GGI distribution. Hence, it is not considered as an error source.

Table 4-2: Reproducibility of transport factors determined by diffusion couples.

Sample	Conditions	D(Cr/Co) [10 ⁻⁸ cm ² /s]	Deviation	
			inter	intra
CCoG115+_30min_A	1150°C 30 min	2.23	39%	-
CCoG115+_30min_B1		3.10		9%
CCoG115+_30min_B2		3.39	-	
CCoG115+_A	1150°C 15 min	2.54	42%	-
CCoG115+_B		3.61		

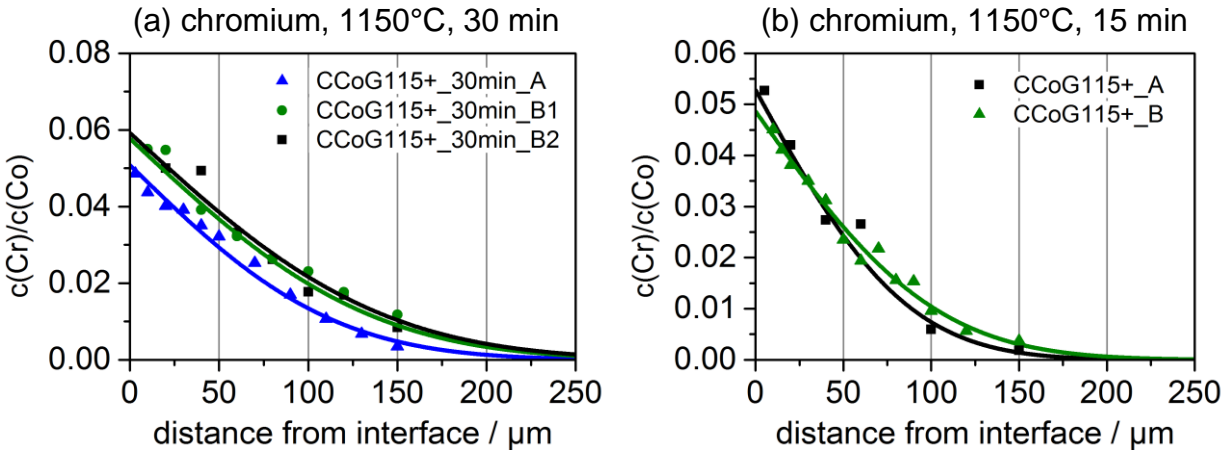


Figure 4-4: Reproducibility of as-measured and fitted chromium concentration profiles.

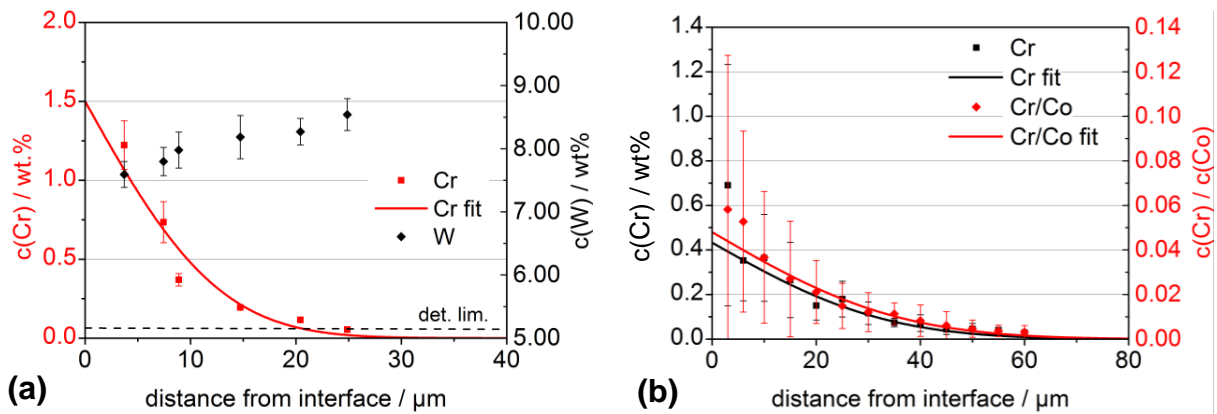


Figure 4-5: Concentration profiles of chromium at 1150°C in (a) M-type couple and (b) G-type couple.

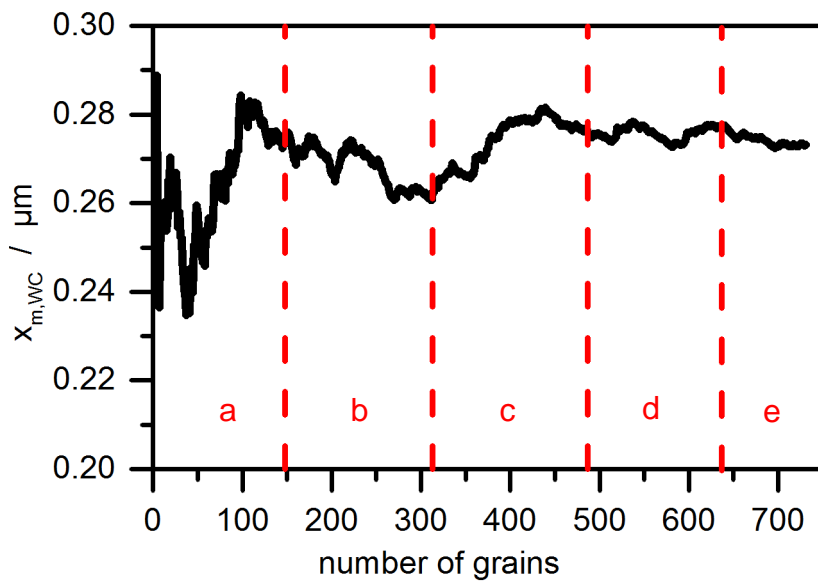
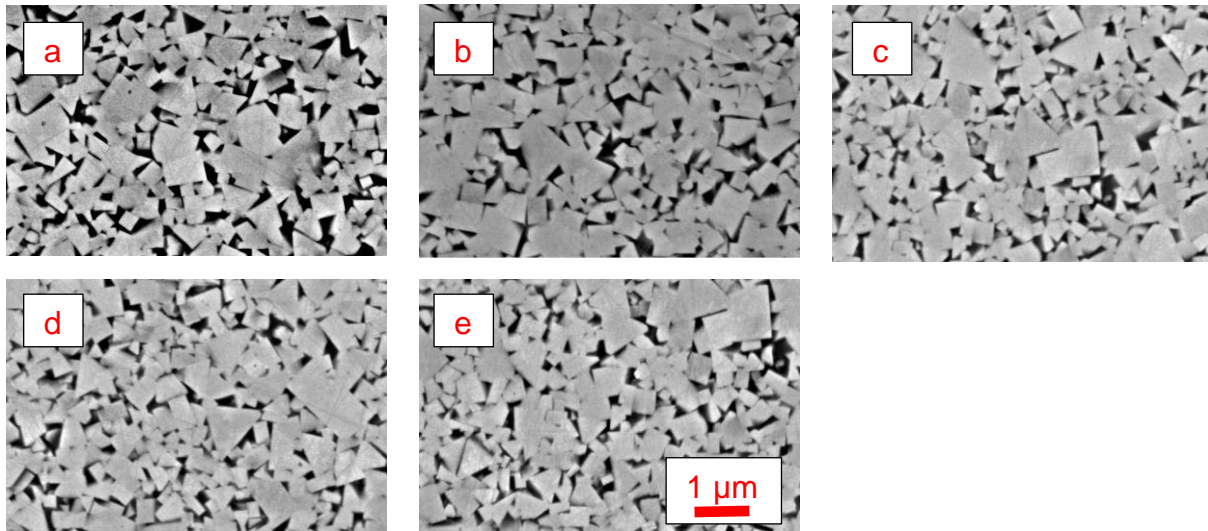
4.2.2 Grain-size analyses

It was already mentioned in the experimental section (3.8.3) that the standard deviation of the grain size measurement cannot be determined from a single image since this would be mainly influenced by the grain size distribution. Therefore the standard deviation w of the logarithmic normal distribution is introduced as a measure of the distribution width. However, there is still the question about the error range of the mean grain size $x_{m,WG}$. This error can be determined by analysing various image frames from different spots of one sample and calculating the standard deviations from the mean grain sizes $x_{m,WG}$. It was also mentioned in section 3.8.3 that at least 150–200 grains should be analysed to get a significant grain size value. However, this is only valid for a particular image frame. Microstructural inhomogeneities might deliver different values for different frames. Thus, the second question is how many image frames from a macroscopic homogeneous area (sample bulk) are required for a statistical significant grain size value? To answer these questions 5 image frames of the bulk of sample MGCV24+100K were taken at random spots. The resulting microstructures are shown in Figure 4-6 (a) – (e). The intercept length of ~ 150 grains was measured for each frame. The results are listed bottom right in Figure 4-6. From these five values the mean grain size and the standard deviation were calculated. Based on these results the error of the measurement is $\sigma_{inter} = \pm 0.02 \mu\text{m}$ absolute or $\pm 8\%$ relative. The standard deviations for all other samples of this project were found in a similar range.

To answer the minimum required amount of image frames the mean grain size was calculated from the first 2, 3, 4, and so on grains of frame (a). After the last grain of frame (a) the first grain of (b) was included in the same manner and so on. The results are plotted in Figure 4-6 bottom right. As expected the scatter is large when less grains are used and decreases with increasing grain number. With increasing grain number the scatter becomes smaller. However, a clear change in the trend can be found if a new image is applied. This can easily be explained: addition of frame (c) causes a rising trend since its average grain size is higher than the average size of (a)+(b). Starting from the end of frame (c) the addition of new frames has no further smoothing effect; the scatter within a particular frame is larger than of the differences of the grain size at the frame borders. Subsequently three frames are considered as sufficient for a statistical significant grain-size value.

The hardmetals analysed in this project were prepared from submicron WC-powder grades. Especially the attritor-milled grade DS50m has a high fraction of grains <100 nm. For such fine grains the resolution of the BSE imaging becomes important. The width of a typical frame of magnification 30000x is 15 μm , as exemplarily shown in Figure 4-7. An image resolution of 1024x786 pixels subsequently yields 14.6 nm/pixel. In very fine grained hardmetals, e.g. MGCV24+100K, a $d_{10}=59$ nm was measured. Since the uncertainty of 14.6 nm applies at both interfaces of an intercept line, an error of up to 30 nm must be taken into account. The fine-grained part of a grain-size distribution has therefore a bias of up to 30 nm. However, for larger grains the error can be neglected and the mean grain-size is not significantly influenced by the limited resolution since the error of ± 14.6 nm averages out.

Another effect of the limited resolution which has to be taken into account is the discretisation. The software used to determine the intercept length can only measure full pixels. Hence, the intercept values are multiples of 14.6 nm. This is relevant since the width of the histogram classes is only 50 nm. Subsequently either three or four length values are represented by one class which affects their frequency. The application of wider classes, e.g. 100 nm, turned out to be too coarse for fitting the logarithmic normal distribution. However, due to the large number of 25 classes the effect will average out upon fitting.



Sample	No. of grains	$x_{m,WC}$ [μm]
a	148	0.273
b	150	0.252
c	156	0.302
d	140	0.253
e	143	0.271
Mean $x_{m,WC}$		0.274
St. dev. σ_{inter}		0.020

Figure 4-6: Microstructures and corresponding mean grain size of sample MGCV24+100K analysed at 5 randomly chosen spots a-e of the bulk.

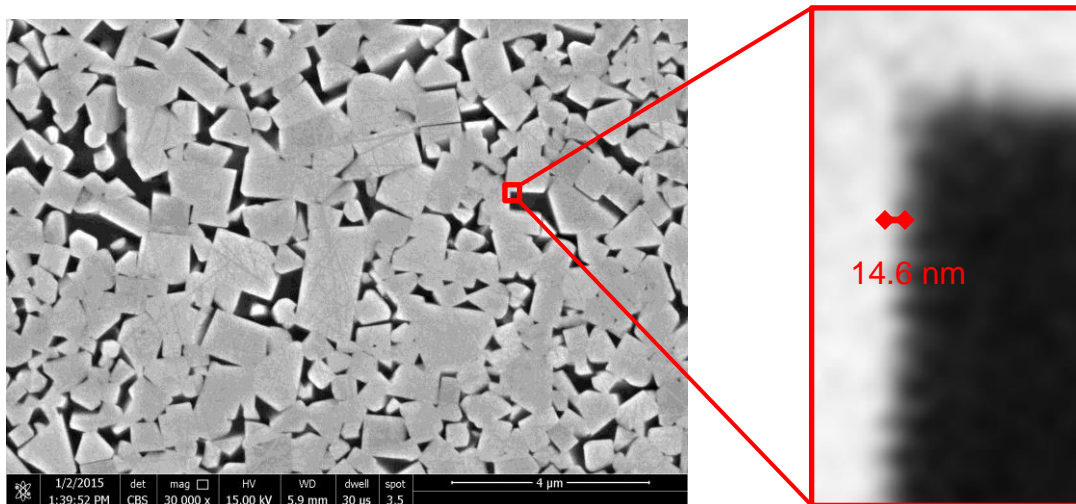


Figure 4-7: BSE-Image of the WC-Co hardmetal MGRRefU+115L.

4.2.3 Thermal analyses

The error of the DSC measurements was determined as $\pm 1^\circ\text{C}$ by earlier experiments. However, signals in the temperature range of $1000\text{--}1050^\circ\text{C}$ cannot be used since the heating rate was changed from 50 K/min to 10 K/min at 1000°C . This change caused an artefact which overrules possible signals from thermal reactions and cannot be completely compensated by a zero-curve correction.

The detection limit of the balance for thermogravimetric analysis is $0.1\ \mu\text{g}$. Taking into account the typical sample weight of 150 mg the resolution is 0.06% relative. Typical mass losses of particular reduction events are around $0.1\text{--}5\%$ relative, hence the resolution is suitable.

However, besides this theoretic limit TG is sensitive to vibrations and in the range of liquid-phase formation at $1200\text{--}1300^\circ\text{C}$ noisy signals are usually found. Also TG is performed in stationary atmosphere. The CO evolving from carbothermic reduction of surface oxides subsequently remains in the furnace. The CO partial pressure hence increases with increasing temperature, which shifts the peaks to higher temperatures. The evolving gas analysis is more precise since by a factor $50\text{--}100$ higher sample masses are used, dynamic atmosphere is applied and it is not sensitive to vibrations. EGA further allows discrimination of different evolving species while TG only measures total mass loss. However, TG has the advantage that the information is

gained simultaneously to the DSC experiment while EGA needs an extra measurement. A comparison of the differentiated TG signal and the EGA signal of WC-Co doped with 1 wt% VC is shown in Figure 4-8. As already discussed, EGA has a better resolution and a significantly smoother baseline. Especially in the high-temperature range $>1200^{\circ}\text{C}$ TG-noise is in the range of signal heights. Hence, TG is not really suitable at temperatures $>1200\text{--}1300^{\circ}\text{C}$. However, regarding the main degassing events the accordance is satisfying which makes TG a suitable method for characterising thermal reactions in hardmetals.

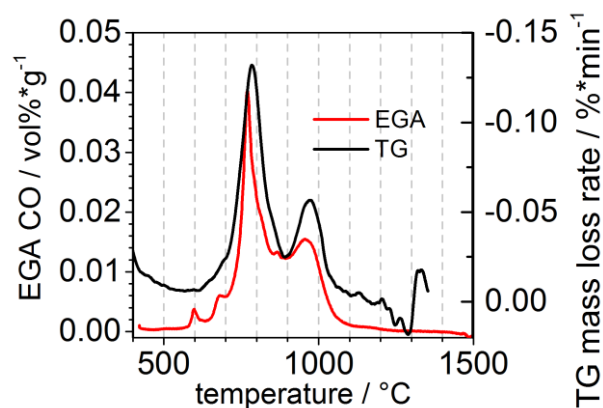


Figure 4-8: comparison of evolving gas analysis and thermogravimetric analysis of HM_WC-Co-VC. TG curve is depicted “upside down” for equal peak direction.

4.2.4 Transmission electron microscopy (TEM)

TEM-EDX measurements towards the WC/Co interfaces of diffusion couples were conducted in order to detect GGI enrichments at the interface. However, according to their thickness is just a few atomic layers, even in presence of segregates. The measured concentration will hence still be small. For vanadium, concentrations around 1 wt% are expected in the cobalt binder, with a possible slight increase at the interface. Since the detection limit is around 0.5 wt% the results from these measurements are only semi-quantitative.

4.2.5 Summary of main findings regarding error estimation:

- Data points within the first 10 μm from the interface are not used for curve fitting due to the interface roughness of 3 μm , the stage position uncertainty of 1 μm , the beam diameter of 1 μm and deviations caused by metallographic preparation.
- The reproducibility of the transport factor D determined from different scans within the same sample is $\pm 10\%$ relative.
- The reproducibility of the transport factor determined from 2 independently prepared samples is $\pm 40\%$ relative.
- The standard deviation determined from 10–20 data points of a particular line scan does not only reflect the error of the EPMA-measurement but is convolved with the microstructural inhomogeneity. The error bars of the GGI concentration profiles within this document are hence a measure for the microstructural homogeneity.
- The intercept length of single grains can be determined with a maximum resolution of ± 14.6 nm. The grain size distributions will hence be biased at low grain sizes. The difficulty of identifying WC/WC grain boundaries of very small grains will further intensify this effect.
- At least three different image frames with a total number of >500 grains are required in order to achieve a reasonable statistical validity of the mean grain size. The standard deviation of the means determined from 3–5 single frames with at least 150 grains each is $\pm 7\text{--}10\%$ relative.
- The DSC signal in the temperature range of 1000–1050°C cannot be used since it is convolved with a signal caused by change of the heating rate from 50 K/min to 10 K/min.
- TEM-measurements are only semi-quantitative

4.3 G-type diffusion couples

G-type diffusion couples are based on green-bodies which are annealed at various temperatures and times. The results of the analyses series are described sample-by-sample in the following section. For a particular sample usually four values obtained from EPMA-measurements are given as a function of the distance from the interface: the GGI concentration as-measured and normalised by the binder phase concentration (see 4.1), the weight ratio of the binder phase and the summarised total concentration of all EPMA-measurements. The concentration of carbon and tungsten were also measured for all samples but are not shown in this section. Their values are controlled by the local WC concentration which is the main constituent and equally distributed in the sample volume. Of course, the gradients of W and C in the binder phase would be of great interest, but their amounts are small as compared to the amounts of WC and get lost in the scatter of the W and C signals. The concentrations can be found in the tables listed in the appendix. As discussed in section 4.2.1 it has to be pointed out that the error bars do not only represent the error of the measurements but are convolved with microstructural inhomogeneities. Assuming the error of the method is constant for all samples the error bars can be interpreted as a measure of the homogeneity.

4.3.1 G-type diffusion couples with Cr, low carbon potential

In order to allow an estimation of the activation energy G-type diffusion couples with chromium and low carbon potential were prepared over a wide temperature range of 1000°C–1360°C. For sample CCoG100- annealed at 1000°C for 60 min a diffusion depth of 33 μm was measured, resulting in a transport factor of $D=7.8 \cdot 10^{-10} \text{ cm}^2/\text{s}$. The chromium concentration at the interface obtained from the fit was $\text{Cr}/\text{Co}=0.036$, see Figure 4-9(a).

Samples at 1050°C were prepared at different heating rates of 5 K/min and 100 K/min as illustrated in Figure 4-10 and Figure 4-11, respectively. It is shown that the heating rate has almost no influence on the diffusion depth which was 45 μm for both samples and the interfacial concentration which was $\text{Cr}/\text{Co}=0.044\text{--}0.046$. The

LOM-microstructure of the sample CCoG105- is presented in Figure 4-15(a). Initiating densification can be observed in the bulk of the WC-Co part of the diffusion couple. The “roundish” bright areas of 100–300 diameters are slightly denser as compared to the darker areas. At the interface no significant influence of chromium is observed, though between the interface (red dashed line) and the chromium diffusion depth (green dashed line) the hardmetal seems to be slightly brighter and, hence, denser. When increasing the temperature to 1100°C the diffusion depth increases to 62 µm after 15 min (Figure 4-12) and the interface concentration is Cr/Co=0.083. A significant densification appeared as compared to 1050°C, see Figure 4-15(b). Some large scale substructures are observed on millimetre-scale, but the roundish structures which were observed at 1050°C disappeared. The semicircle structure shown in the top row seems to originate from an area without direct contact of the diffusion couple components. Since the chromium diffusion depth is by a factor of 5 smaller than the structure it is rather caused by the influence of a local micro-atmosphere in the gap than by chromium.

At 1150°C an interfacial concentration of Cr/Co=0.11 and a diffusion depth of 95 µm were measured after 8 min annealing time for sample CCoG115-_8min (Figure 4-13), leading to a transport factor of $D=5.34 \cdot 10^{-8}$ cm²/s. The hardmetal is homogeneously densified and no substructures appear, but porosity is still observed.

The LOM-micrograph of the diffusion couple at 1250°C (CCoG125-) is shown in Figure 4-15(d). A tight contact of the two diffusion couple components is observed and the microstructure is homogeneous with some residual porosity. Some single η-carbide grains are observed, proving the low carbon potential. Due to a data conversion error no diffusion data is available at this temperature.

When annealed at 1360°C for 15 min such as sample CCoG136- in Figure 4-15(e) the binder phase is expected to be in liquid state. Subsequently diffusion is expected to be fast. Indeed, a diffusion depth of 2050 µm, see Figure 4-14(a), is measured giving a transport factor of $3.2 \cdot 10^{-6}$ cm²/s which is by two orders of magnitude higher than at 1150°C. A smooth interface and a dense, homogeneous microstructure without visible precipitations are observed.

For all samples of this series the fitting model according to Equation 4 delivers good accordance to the experimental data except within the first 10 µm from the interface,

which can be attributed to artefacts of the method, see section 4.1. For all samples annealed with solid binder phase the cobalt-concentration as a function of the distance from interface scatters around 10 wt% without any trend. The totals, which can be related to the porosity, are as well independent from the interface and, hence, from the Cr-concentration but show an increase with increasing temperature. An overview of measured and related calculated parameters is given in Table 4-3.

Table 4-3: Transport parameters and interface concentrations of chromium in G-type diffusion couples with Co binder and low carbon potential.

Sample	Diffusion depth (μm)	D ($10^{-10}\text{cm}^2/\text{s}$)	$c_0(\text{Cr}/\text{Co})$ (wt%)/ (wt%)
CCoG100-	33	7.8 ± 2.1	0.036 ± 0.004
CCoG105-	31	21.6 ± 3.8	0.056 ± 0.003
CCoG105-_5Kmin	34	28.7 ± 2.2	0.049 ± 0.002
CCoG110-	62	72.8 ± 5.7	0.086 ± 0.003
CCoG115-_8min	92	53.4 ± 2.89	0.084 ± 0.002
CCoG136-	2050	32452 ± 2803	0.78 ± 0.018

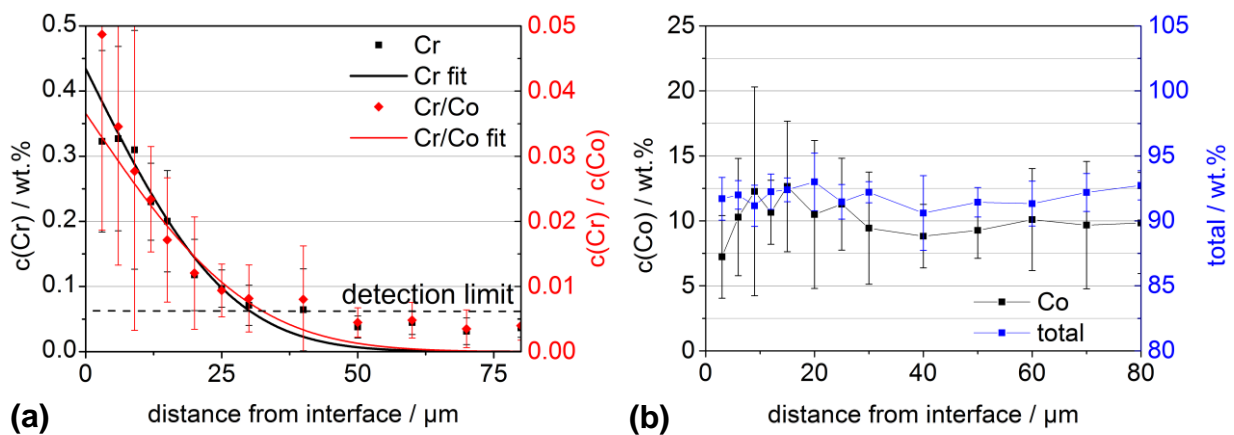


Figure 4-9: CCoG100–, annealed at 1000°C for 60 min, low carbon, (a) as-measured and normalised EPMA-concentration profiles of chromium, (b) concentration profile of Co and corresponding total of all measured elements.

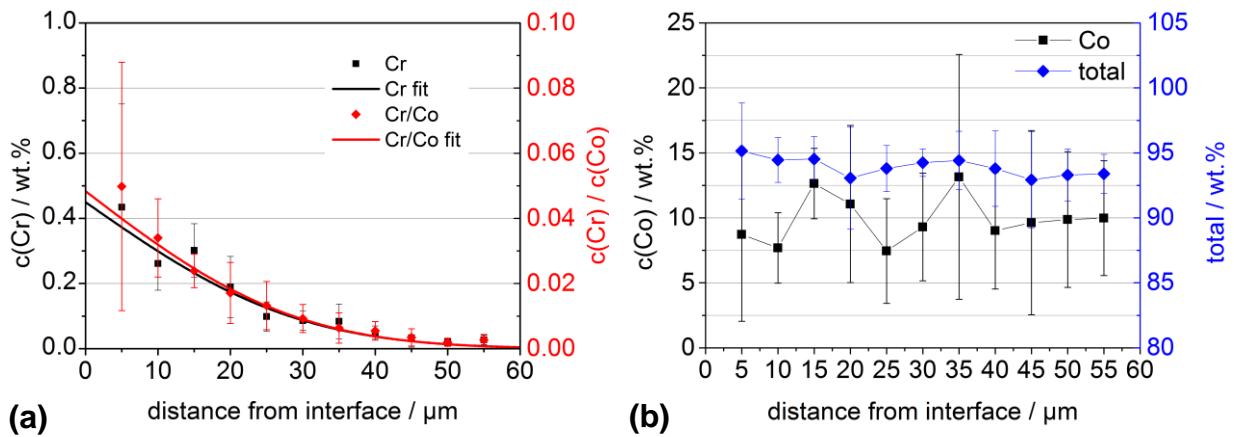


Figure 4-10: CCoG105–5Kmin, linear heat up to 1050°C with 5K/min, low carbon, (a) as-measured and normalised EPMA-concentration profiles of chromium, (b) concentration profile of Co and corresponding total of all measured elements.

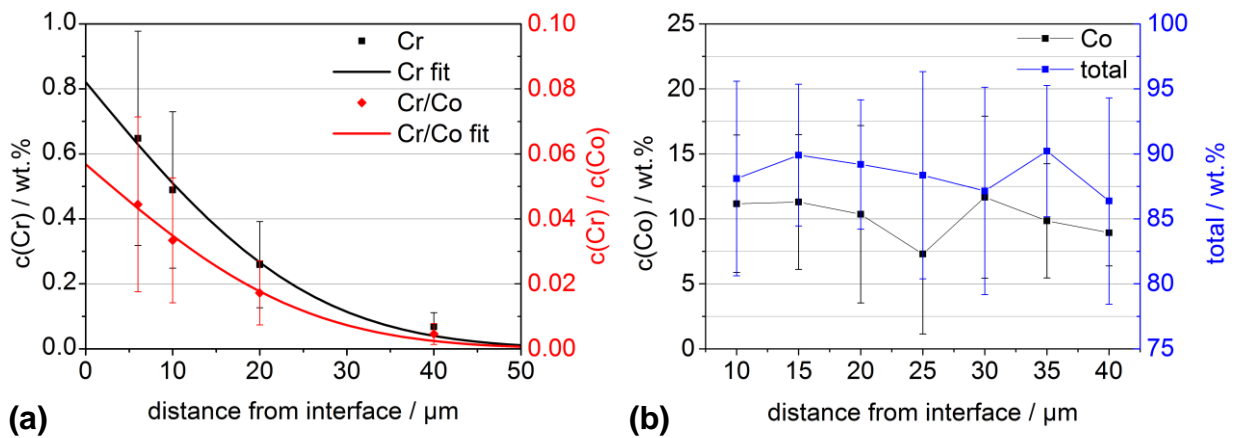


Figure 4-11: CCoG105–, annealed at 1050°C for 15 min, low carbon, (a) as-measured and normalised EPMA-concentration profiles of chromium, (b) concentration profile of Co and corresponding total of all measured elements.

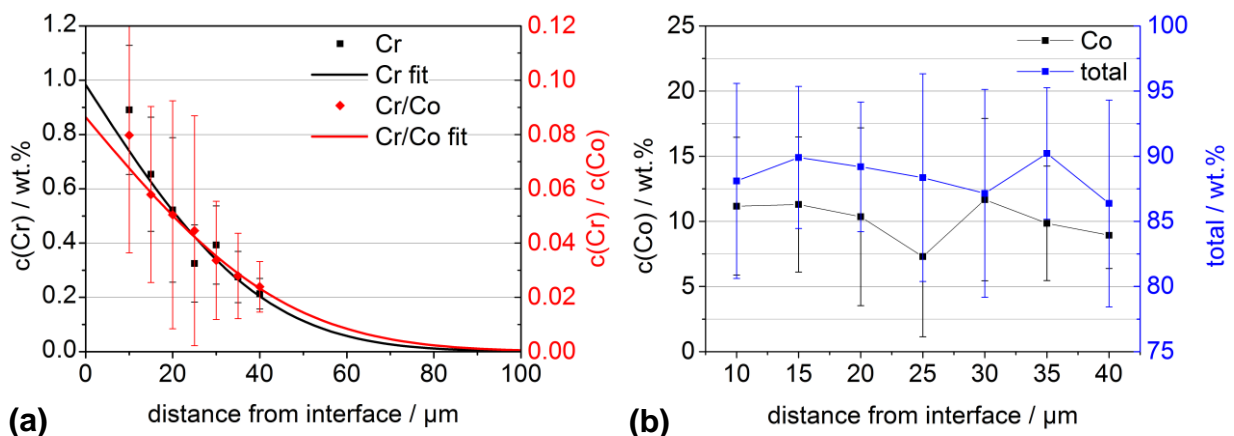


Figure 4-12: CCoG110–, annealed at 1100°C for 15 min, low carbon, (a) as-measured and normalised EPMA-concentration profiles of chromium, (b) concentration profile of Co and corresponding total of all measured elements.

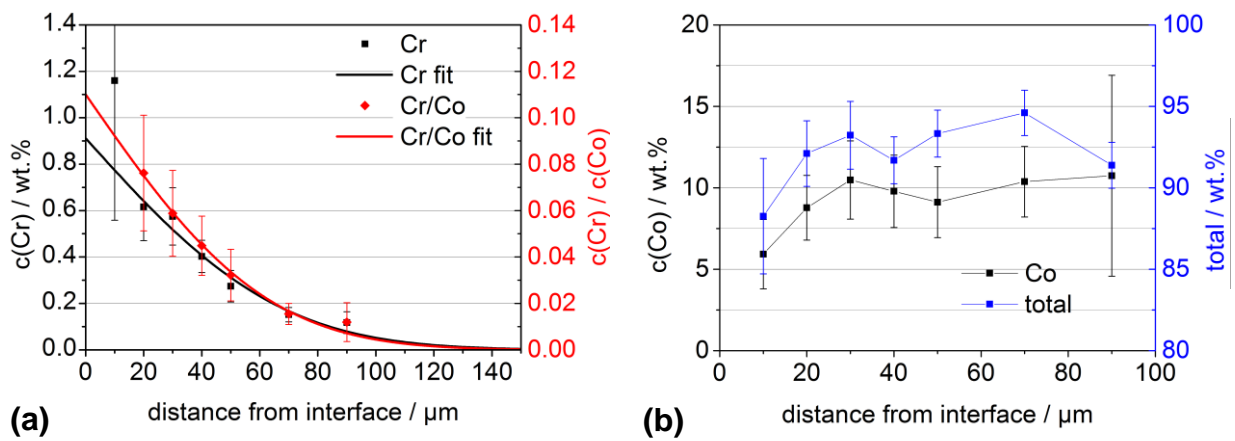


Figure 4-13: CCoG115–8min, annealed at 1150°C for 8 min, low carbon,
 (a) as-measured and normalised EPMA-concentration profiles of chromium,
 (b) concentration profile of Co and corresponding total of all measured elements.

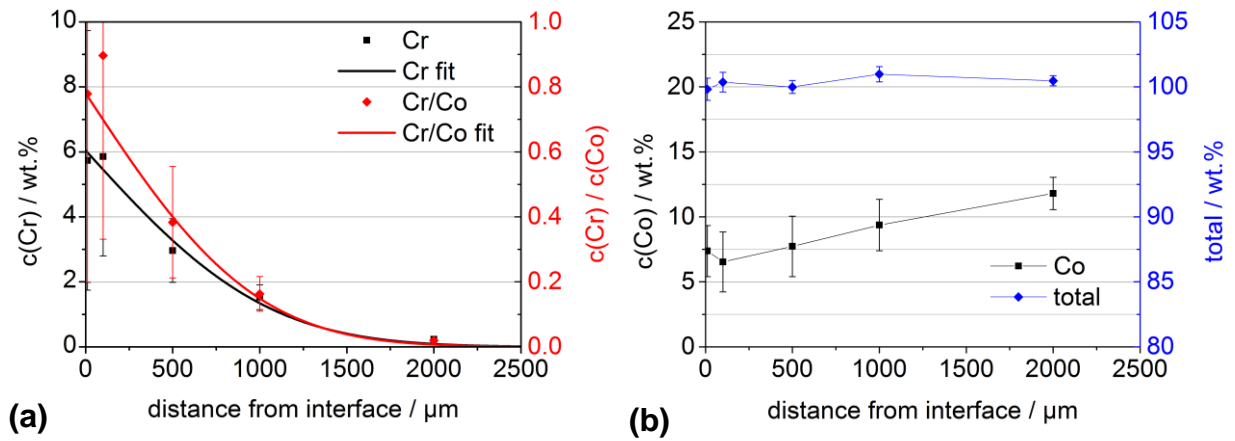


Figure 4-14: CCoG136–, annealed at 1360°C for 15 min, low carbon,
 (a) as-measured and normalised EPMA-concentration profiles of chromium,
 (b) concentration profile of Co and corresponding total of all measured elements.

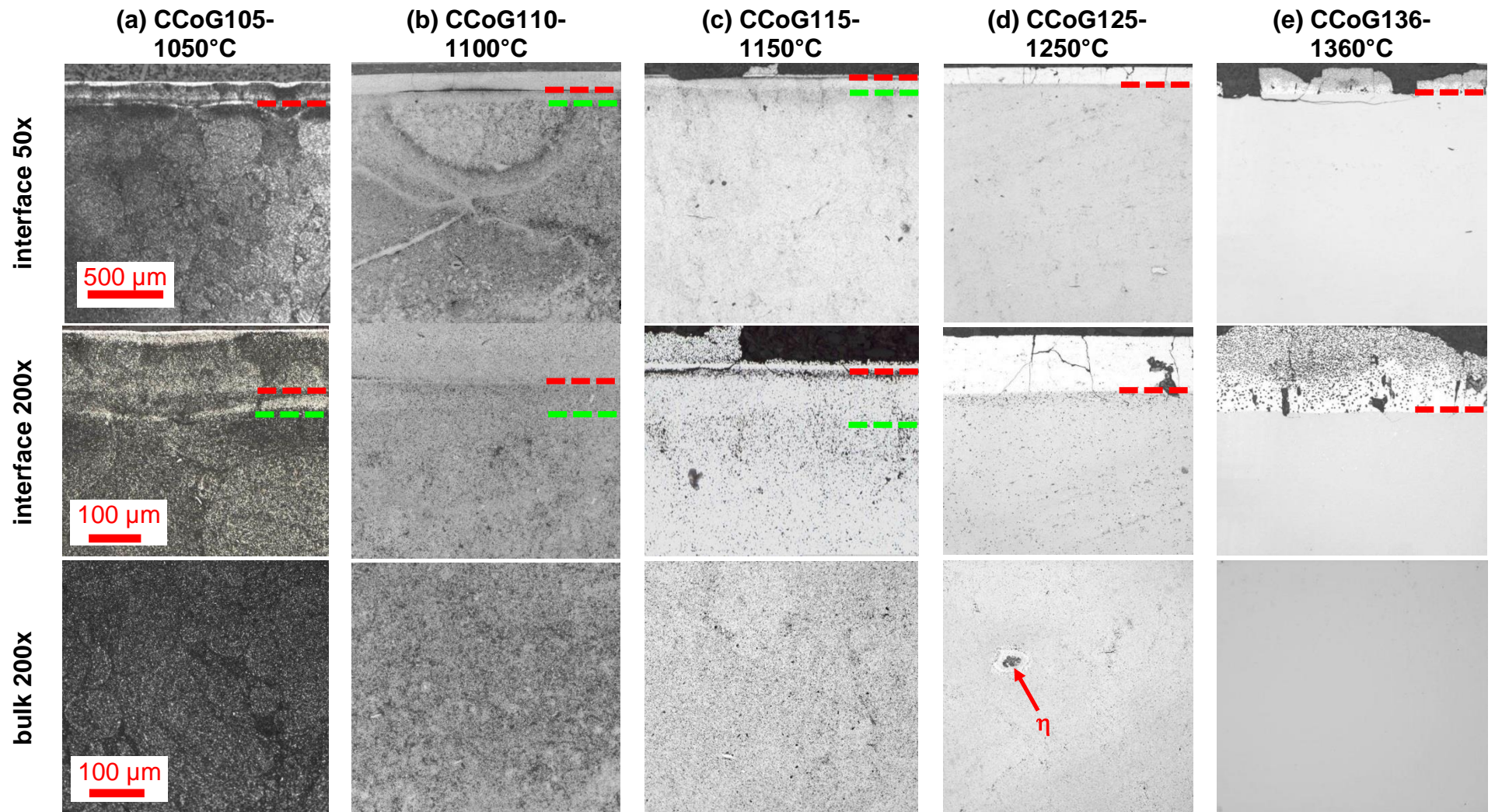


Figure 4-15: LOM of low-carbon chromium based G-type couples (CCoG-) annealed at various temperatures. Green lines mark the diffusion depth of chromium.

4.3.2 G-type diffusion couples with Cr, mid carbon potential

G-type couples with mid carbon potential were prepared in a temperature range from 1050°C–1360°C. All samples of this series show good accordance of the as-measured and the normalised experimental data with the fitting model given in Equation 4. The DTA analysis of the WC-Co-part of the couple (WCo), shown in Figure 4-129(a) (p.174), proves the carbon adjustment within the WC+fcc two phase area.

The normalised chromium diffusion depth of the sample CCoG105, annealed at 1050°C for 15 min was measured 42 µm, yielding a transport factor of $D=3.78 \cdot 10^{-9}$ cm²/s. A significant deviation of the normalised and the as-measured concentration profiles appears as shown in Figure 4-16(a), which can be related to a cobalt-depletion towards the interface (b). From the LOM-microstructure shown in Figure 4-21(a) a clear influence of chromium on the densification behaviour is observed. The influenced microstructure appears brighter as compared to the bulk, indicating a more propagated densification.

For sample CCoG110, annealed at 1100°C for 7 min a diffusion depth of 66 µm yielding a transport factor of $D=1.13 \cdot 10^{-8}$ cm²/s and a corresponding interface concentration of $c_0(\text{Cr/Co})=0.139$ were found, see Figure 4-17.

At 1150°C (CCoG115) the diffusion depth after 15 min is already 130 µm as shown in Figure 4-18. The corresponding fit of the normalised data yields $D=2.54 \cdot 10^{-8}$ cm²/s and $c_0(\text{Cr/Co})=0.110$. The corresponding LOM-micrographs in Figure 4-21(b) show again a clear influence of chromium on the densification. Within the diffusion depth of chromium the densification is more propagated and homogeneous. At distances higher than the chromium diffusion depth inhomogeneous, sub-structured densification is observed, likely caused by initial inhomogeneities of the WC and Co distribution.

When the temperature is increased by 100°C to 1250°C for 15 min the diffusion depth increases by a factor of 10 to 1300 µm and D by factor of 66 to $D=1.67 \cdot 10^{-6}$ cm²/s, see Figure 4-19. Taking into account the high interface concentration $c_0(\text{Cr/Co})=0.33$ and literature data (section 2.4) this dramatic increase indicates liquid binder phase. This finding is supported by the LOM-micrographs depicted in Figure 4-21(c). Three characteristic zones are observed. Within the first

150 μm from the interface almost no porosity appears. From 150–1300 μm slight porosity is observed. At >1300 μm porosity suddenly increases which is coincident with the measured diffusion depth of chromium. The liquid-phase formation of the bulk sets on around 1340°C as it was proved by DTA of the diffusion couple component WCo_n , see Figure 4-129(a) (p.174). Hence, the binder phase of the bulk is in solid-state at 1250°C. As it was discussed in section 2.4 chromium decreases the solidus temperature in a chromium-saturated hardmetal (presence of Cr-based carbide phases) to 1191–1230°C dependent on the carbon potential. For a hardmetal without graphite or M_6C precipitations the solidus temperature varies within this range. Subsequently the binder phase close to the interface, where the binder phase is chromium-saturated, is partially in liquid state at 1250°C. However, the exact carbon potential is unknown since diffusion of C simultaneously appears to chromium diffusion and the carbon state of the binder phase cannot be determined by EPMA analysis (91% of the carbon is located in the WC). The presence of liquid phase explains the almost full densification close to the interface. However, the solidus temperature not only depends on the carbon state but also on the chromium concentration. In a distance >150 μm from the interface the chromium concentration drops to a level where the binder is fully in solid-state and the porosity increases. The latter is, however, still lower than at a distance >1300 μm , where the hardmetal is not influenced by chromium. This finding is coincident with the densification-propagating effect of chromium in solid-state which was already observed at lower temperatures. A further temperature increase by 110°C to 1360°C yields a diffusion depth of 2600 μm already after 15 min related to a transport factor of $D=5.02 \cdot 10^{-6} \text{ cm}^2/\text{s}$ as shown for sample CCoG136 in Figure 4-20. The interface concentration of $c_0(\text{Cr/Co})=0.6$ is very high and clearly indicates the presence of liquid binder phase. From the LOM-micrograph in Figure 4-21(d) an almost pore-free zone is observed within 1.4 mm from the interface. At higher distances at a chromium concentration $<c(\text{Cr/Co})=0.09$ carbon precipitations appear. These precipitations are surprising since the DTA clearly suggests the carbon potential of WC-Co part of the couple is in the WC+fcc two phase area prior to annealing. Thus, the C-precipitations are formed by C-diffusion during the experiment. At 1360°C binder phase is supposed to be in liquid state even in the areas uninfluenced by chromium. Hence a medium for fast C-

transport towards the whole sample is available. As a carbon source the WC-Cr₃C₂-Co part of the diffusion couple is likely, since chromium was initially added as Cr₃C₂, but appears as carbon-poor M₇C₃ after the experiment, see section 5.1.2. As a consequence the real carbon potential is different from the potential initially intended. Since the carbon potential is a degree of freedom within the WC+fcc area of a mid-carbon hardmetal upon diffusion experiments this finding also applies for samples at lower temperatures though it cannot be directly observed due to porosity. Within a distance >1400 μm the carbon seems to be consumed by the formation of chromium based carbides which are also visible in the LOM-micrographs. It cannot be confirmed whether these chromium carbides are formed upon the diffusion annealing or if they precipitate upon cooling.

The as-measured cobalt concentrations and the total of all measured concentrations as illustrated in Figure 4-16(b) – Figure 4-20(b) show relatively large error bars and, hence, indicate a strong microstructural inhomogeneity. No specific trend can be confirmed upon samples in solid-state due to the large scatter. In liquid-phase at 1250 and 1360°C a cobalt-depletion towards the interface is observed, likely caused by migration of the liquid binder phase which is already described in literature by [09KON, 10KON]. An overview of the values determined from this sample series can be found in Table 4-4.

Table 4-4: Transport parameters and interface concentrations of chromium in G-type diffusion couples with Co binder and mid carbon potential.

Sample	Diffusion depth (μm)	D (10 ⁻¹⁰ cm ² /s)	c ₀ (Cr/Co) (wt%)/ (wt%)
CCoG105	31	37.8 ± 8.2	0.062 ± 0.003
CCoG110	66	113 ± 23	0.139 ± 0.020
CCoG115	130	254 ± 47	0.110 ± 0.010
CCoG125	1300	16700 ± 1380	0.334 ± 0.019
CCoG136	2600	50220 ± 2001	0.600 ± 0.036

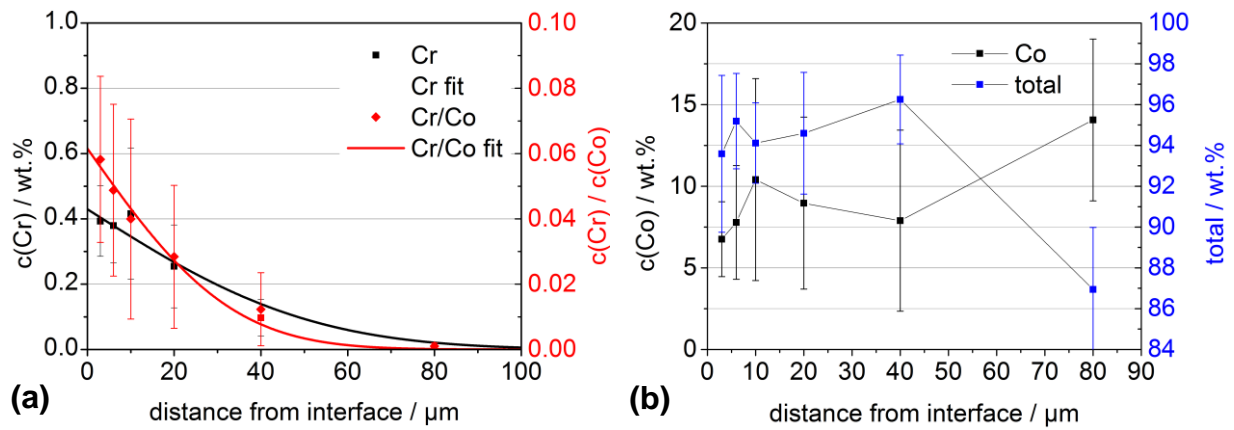


Figure 4-16: CCoG105, annealed at 1050°C for 15 min, mid carbon potential
 (a) as-measured and normalised EPMA-concentration profiles of chromium
 (b) concentration profile of Co and corresponding total of all measured elements

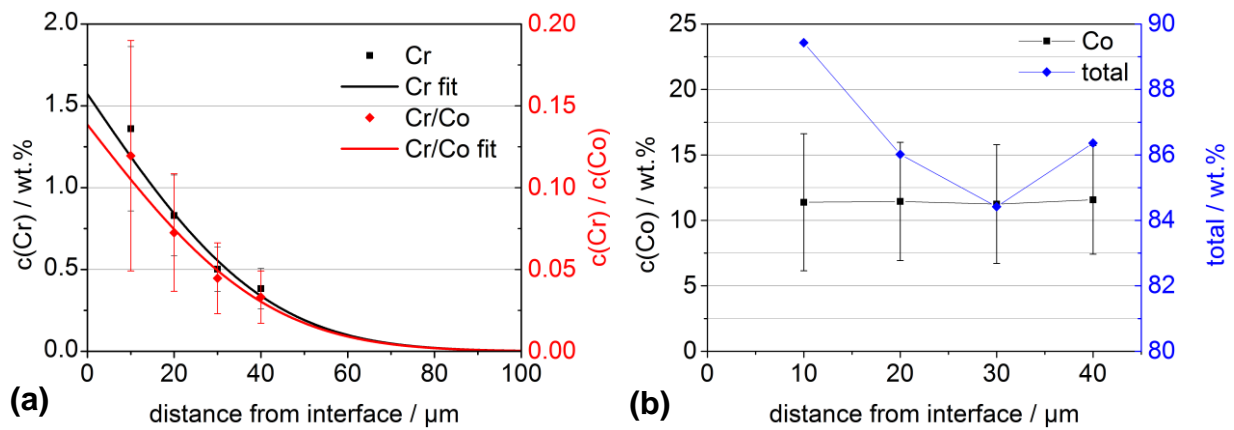


Figure 4-17: CCoG110, annealed at 1100°C for 15 min, mid carbon potential,
 (a) as-measured and normalised EPMA-concentration profiles of chromium,
 (b) concentration profile of Co and corresponding total of all measured elements.

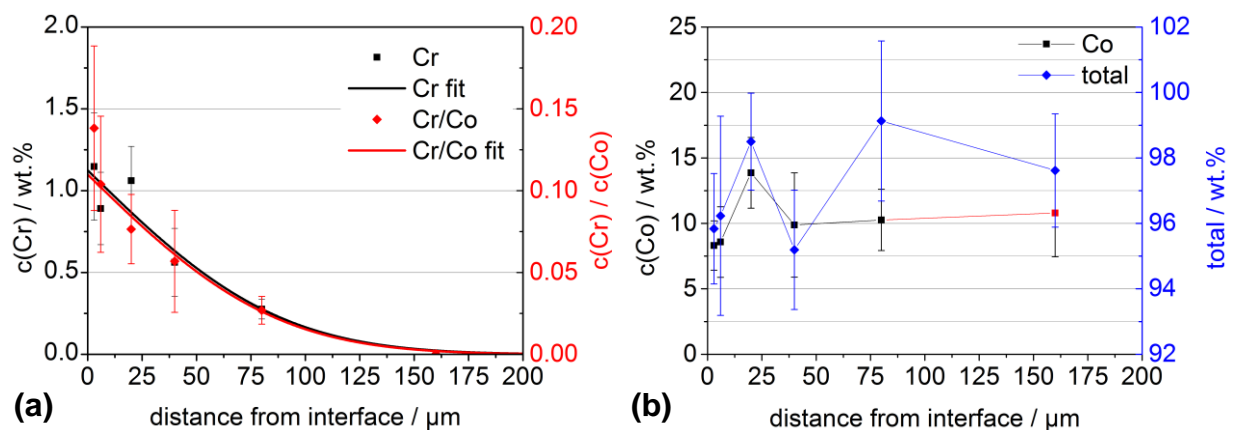


Figure 4-18: CCoG115, annealed at 1150°C for 15 min, mid carbon potential,
 (a) as-measured and normalised EPMA-concentration profiles of chromium,
 (b) concentration profile of Co and corresponding total of all measured elements.

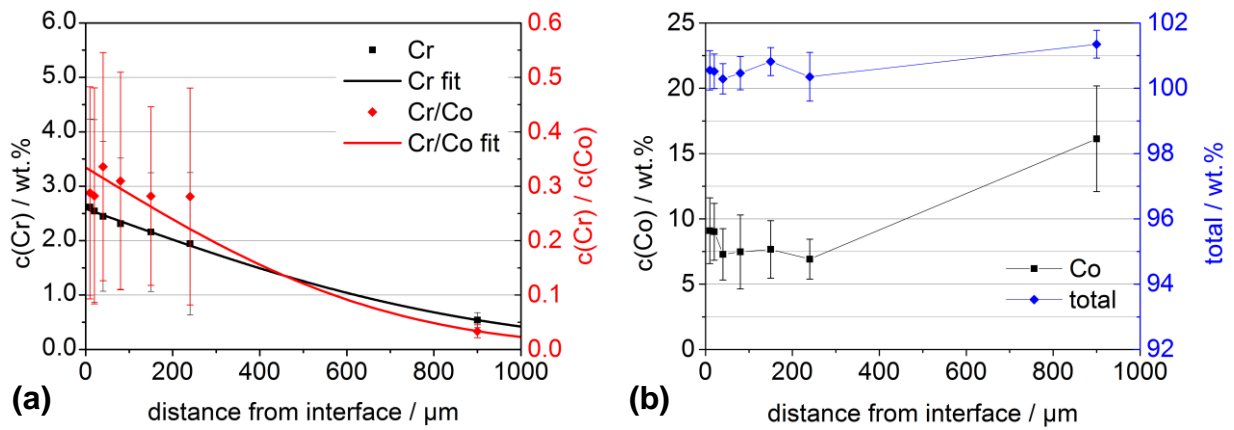


Figure 4-19: CCoG125, annealed at 1250°C for 15 min, mid carbon potential, (a) as-measured and normalised EPMA-concentration profiles of chromium, (b) concentration profile of Co and corresponding total of all measured elements.

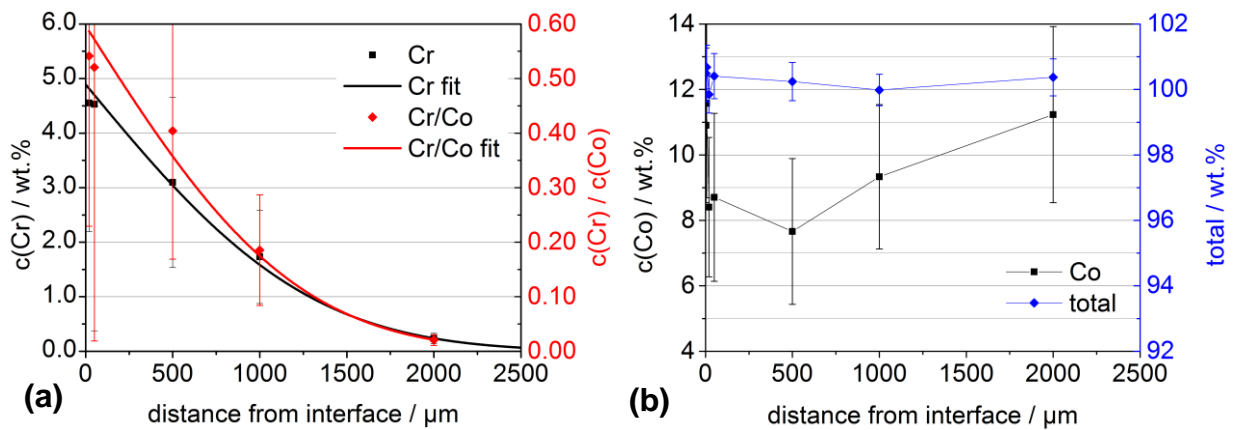


Figure 4-20: CCoG136, annealed at 1360°C for 15 min, mid carbon potential, (a) as-measured and normalised EPMA-concentration profiles of chromium, (b) concentration profile of Co and corresponding total of all measured elements.

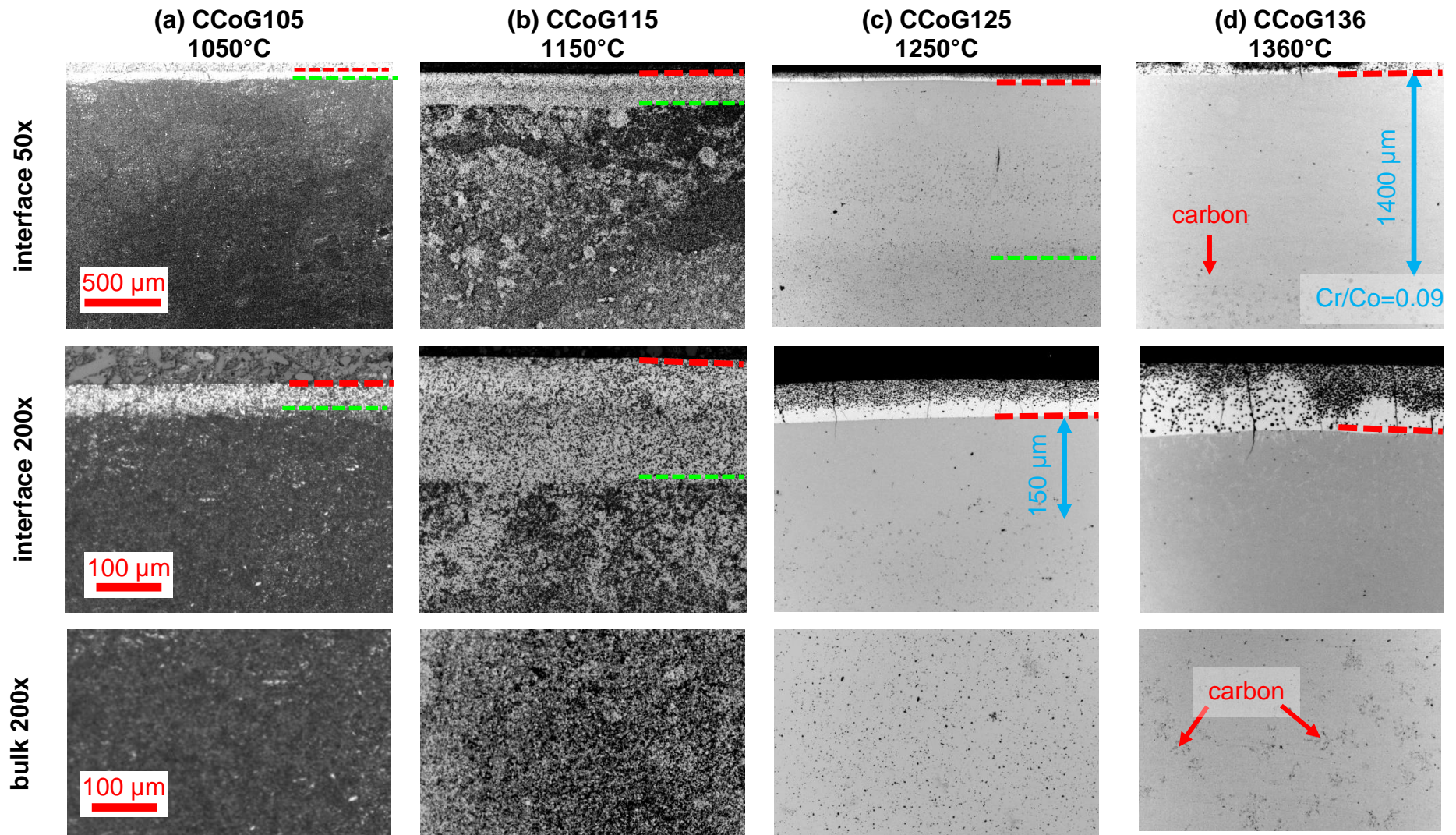


Figure 4-21: LOM of G-type couples CCoGxxx at annealed at various temperatures. Green lines mark the Cr diffusion depth.

4.3.3 G-type diffusion couples with Cr, high carbon potential

In the sample series of G-type couples with chromium, cobalt binder and high carbon potential a larger number of samples as compared to other series was prepared. Some of the samples at 1150°C were prepared and investigated several times at constant conditions in order to allow an estimation of the method's error.

At an annealing temperature of 1050°C two samples labelled CCoG105+5Kmin and CCoG105+ were annealed for 15 min with different heating rates of 5 K/min and 100 K/min, respectively. In case of the slow-heated sample as can be seen from Figure 4-22 a diffusion depth of 41 μm is reached while 43 μm are measured for the fast-heated sample in Figure 4-23, resulting in transport factors of $D=6.4 \cdot 10^{-9} \text{cm}^2/\text{s}$ and $D=4.4 \cdot 10^{-9} \text{cm}^2/\text{s}$, respectively. The interface concentrations of $c(\text{Cr}/\text{Co})=0.025$ and 0.048 for the slow and fast heated sample, respectively show a significant deviation which is caused by the dissolution kinetics of the hardmetal constituents as discussed in section 5.6. When annealed at 1125°C for 30 min chromium reaches a depth of 109 μm and a maximum concentration of $C(\text{Cr}/\text{Co})=0.15$ with a transport factor of $D=1.6 \cdot 10^{-8} \text{cm}^2/\text{s}$, see Figure 4-24.

At 1150°C the sample CCoG115+_5min (Figure 4-25) was prepared with a very short annealing time of 5 min, leading to a diffusion depth of 57 μm . The corresponding fit matches the experimental data and delivers results of $D=2.9 \cdot 10^{-8} \text{cm}^2/\text{s}$ and a maximum concentration of $c(\text{Cr}/\text{Co})=0.036$.

Two samples labelled CCoG115+ (Figure 4-26) and CCoG115+_A (Figure 4-27) were prepared at 1150°C with the standard annealing time of 15 min. Both show a comparable diffusion depth of 112 and 107 μm . However, a slight difference between calculated transport factors of $3.4 \cdot 10^{-8} \text{cm}^2/\text{s}$ and $2.5 \cdot 10^{-8} \text{cm}^2/\text{s}$ appears, while the interface solubilities of $c_0(\text{Cr}/\text{Co})=0.051$ and 0.053, respectively are almost equal.

When the annealing time is increased to 30 min as in case of samples CCoG115+_30min_A in Figure 4-28, CCoG115+_30min_B1 in Figure 4-29 and CCoG115+_30min_B2 in Figure 4-30 the diffusion depth increases to 180 μm , 140 μm and 161 μm , respectively. While CCoG115+_30min_B and CCoG115+_30min_C show equal transport factors of $D=2.2 \cdot 10^{-8} \text{cm}^2/\text{s}$ the value of $D=3.4 \cdot 10^{-8} \text{cm}^2/\text{s}$ for sample CCoG115+_30min_A is significantly higher. Since these three samples were

prepared with constant conditions equal values are expected. The reasons for the deviation are discussed in section 4.2.1.

A further increase of the annealing time to 60 min (CCoG115+_60min) yields a diffusion depth of 293 μm as shown in Figure 4-31(a). The transport factor and interface concentration were $D=4.3 \cdot 10^{-8} \text{ cm}^2/\text{s}$ and $c(\text{Cr}/\text{Co})=0.055$, respectively.

The sample CCoG120+ was annealed at 1200°C for 15 min. In chromium saturated high-carbon WC-Co the equilibrium solidus temperature is 1191°C (see Table 2-3), hence the cobalt phase is expected to be partially liquid at 1200°C, where the phase fraction of liquid binder depends on the local chromium concentration. As shown in Figure 4-32(a) the diffusion depth of 841 μm is significantly increased as compared to 1150°C. Also the transport factors of $7.28 \cdot 10^{-7} \text{ cm}^2/\text{s}$ and the jump in interface concentration to $c(\text{Cr}/\text{Co})=0.3$ point out a change in Cr transport. As a consequence the cobalt concentration (b) is around 7.5 wt% within at least 800 μm from the interface while it scattered around 10 wt% for the samples with solid binder phase as shown in Figure 4-22(b) – Figure 4-31(b).

By a further temperature increase of 50°C to 1250°C the binder is expected to be fully liquid, which dramatically increases the diffusion depth to 1450 μm as shown in Figure 4-33(a), with a corresponding transport factor of $1.9 \cdot 10^{-6} \text{ cm}^2/\text{s}$ and interface concentration of $c(\text{Cr}/\text{Co})=0.49$.

At 1360°C (CCoG136+) the diffusion depth is already 2300 μm after 15 min as can be seen from Figure 4-34(a) with a high interface concentration of $c(\text{Cr}/\text{Co})=0.58$ and $D=2.7 \cdot 10^{-6} \text{ cm}^2/\text{s}$. In both cases of 1250°C and 1360°C as can be seen from Figure 4-33(b) and Figure 4-34(b) the cobalt concentration at the interface is almost the initial 10 wt%, decreases to 7 wt% at 250 μm from the interface and again reaches 10 wt% after 600–800 μm .

The totals of all measured EPMA concentrations show an increasing tendency when annealing temperature and time are increased, indicating elimination of porosity. For the two samples with liquid binder phase at 1250°C and 1360°C totals around 100% were measured indicating almost full density.

Table 4-5: Transport parameters and interface concentrations of chromium in G-type diffusion couples with Co binder and high carbon potential.

Sample	Diffusion depth (μm)	D ($10^{-10}\text{cm}^2/\text{s}$)	$c_0(\text{Cr}/\text{Co})$ (wt%)/ (wt%)
CCoG105+5Kmin	41	63.7 ± 10.7	0.025 ± 0.002
CCoG105+	43	44.6 ± 6.5	0.048 ± 0.005
CCoG112+	109	156.1 ± 3.3	0.148 ± 0.003
CCoG115+_5min	57	178.5 ± 32.4	0.043 ± 0.004
CCoG115+_A	112	342.8 ± 32.6	0.051 ± 0.003
CCoG115+_B	107	254.3 ± 40.2	0.053 ± 0.010
CCoG115+_30min_A	180	339.2 ± 48.7	0.059 ± 0.003
CCoG115+_30min_B1	140	223.8 ± 24.1	0.073 ± 0.003
CCoG115+_30min_B2	161	223.0 ± 12.2	0.051 ± 0.002
CCoG115+_60min	293	428.7 ± 66.7	0.055 ± 0.002
CCoG120+	841	7280 ± 2790	0.300 ± 0.016
CCoG125+	1450	18698 ± 3687	0.491 ± 0.032
CCoG136+	2350	26829 ± 6690	0.576 ± 0.036

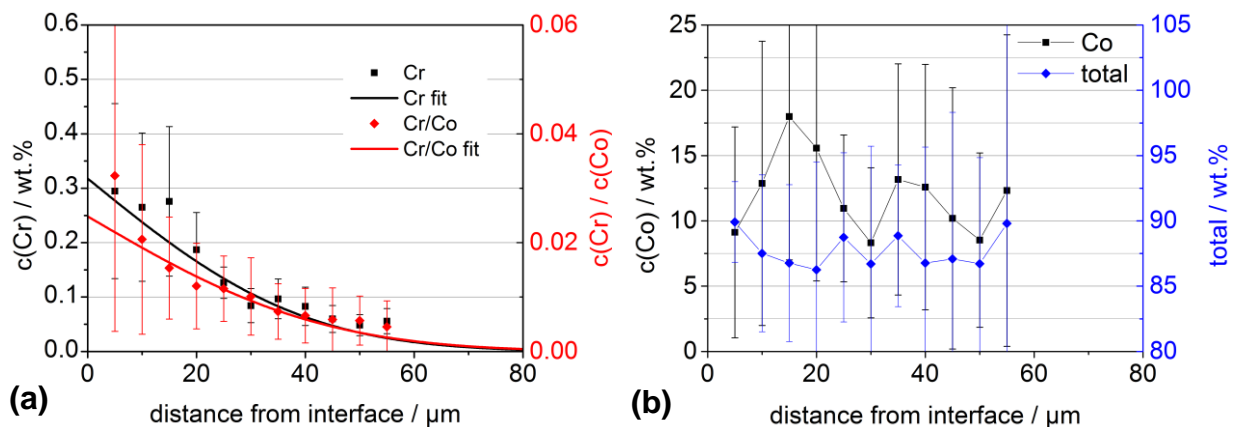


Figure 4-22: CCoG105+_5Kmin, linear heat-up to 1050°C with 5K/min, high carbon potential
 (a) as-measured and normalised EPMA-concentration profiles of chromium
 (b) concentration profile of Co and corresponding total of all measured elements

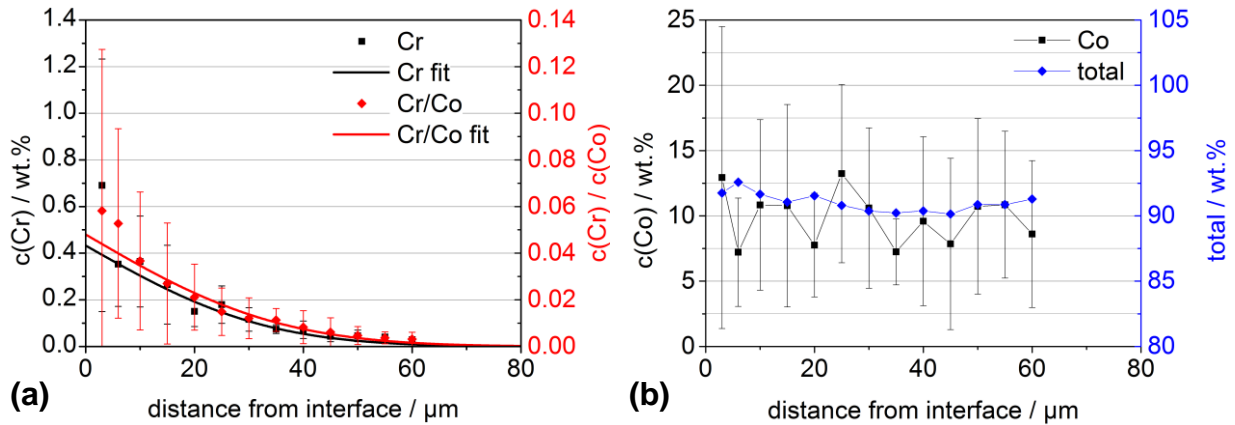


Figure 4-23: CCoG105+, annealed at 1050°C for 15 min, high carbon potential, (a) as-measured and normalised EPMA-concentration profiles of chromium, (b) concentration profile of Co and corresponding total of all measured elements.

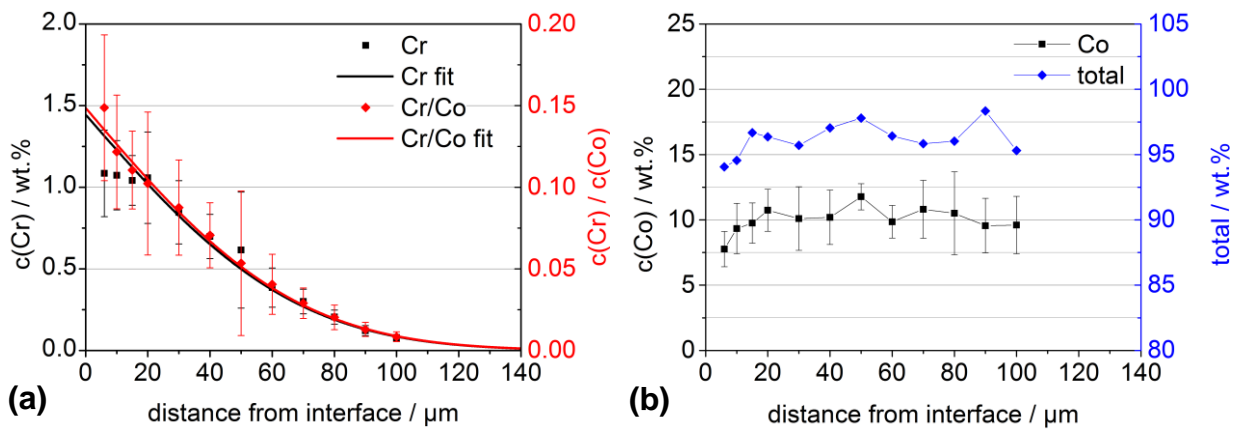


Figure 4-24: CCoG112+, annealed at 1125°C for 30 min, high carbon potential, (a) as-measured and normalised EPMA-concentration profiles of chromium, (b) concentration profile of Co and corresponding total of all measured elements.

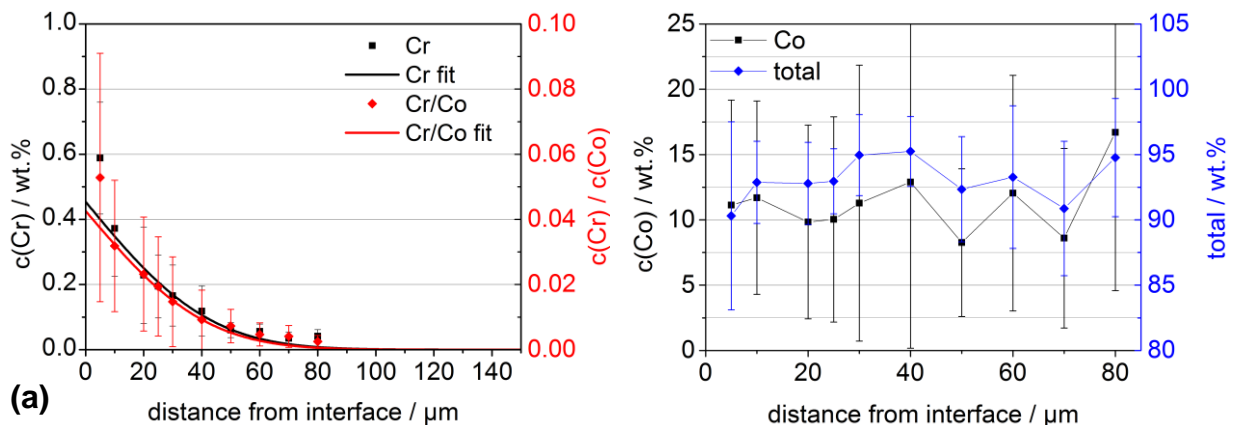


Figure 4-25: CCoG115+_5min, annealed at 1150°C for 5 min, high carbon potential, (a) as-measured and normalised EPMA-concentration profiles of chromium, (b) concentration profile of Co and corresponding total of all measured elements.

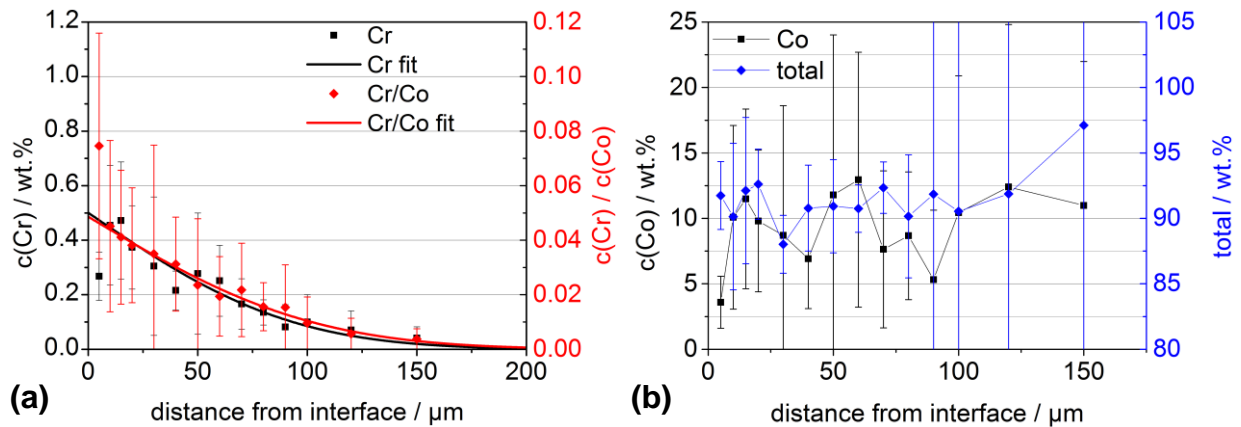


Figure 4-26: CCoG115+_A, annealed at 1150°C for 15 min, high carbon potential, (a) as-measured and normalised EPMA-concentration profiles of chromium, (b) concentration profile of Co and corresponding total of all measured elements.

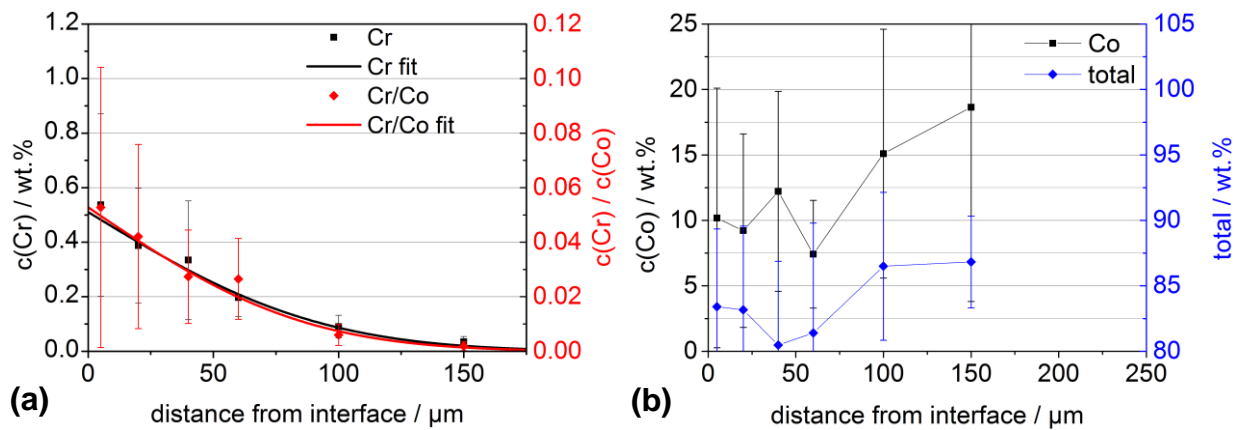


Figure 4-27: CCoG115+_B, annealed at 1150°C for 15 min, high carbon potential, (a) as-measured and normalised EPMA-concentration profiles of chromium, (b) concentration profile of Co and corresponding total of all measured elements.

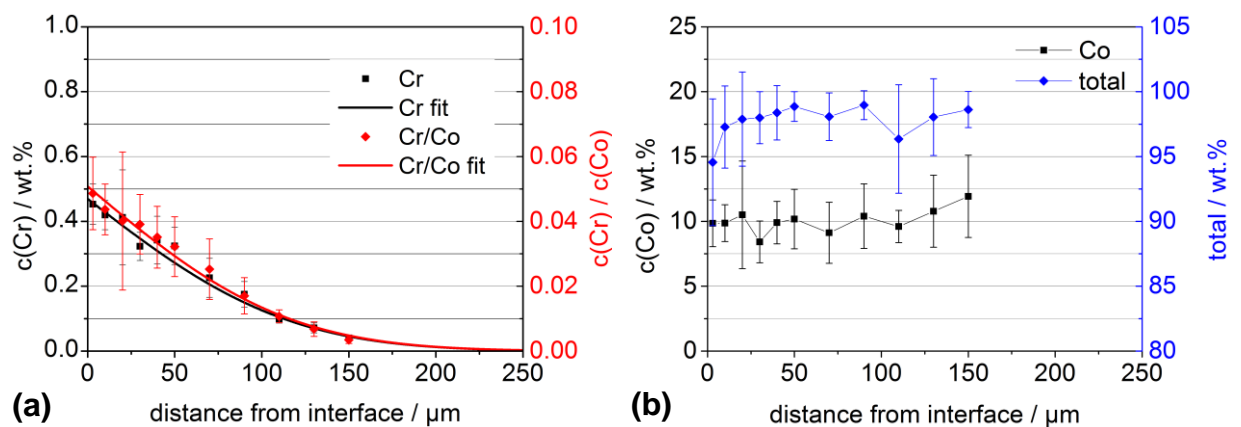


Figure 4-28: CCoG115+_30min_A, annealed at 1150°C for 30 min, high carbon potential, (a) as-measured and normalised EPMA-concentration profiles of chromium, (b) concentration profile of Co and corresponding total of all measured elements.

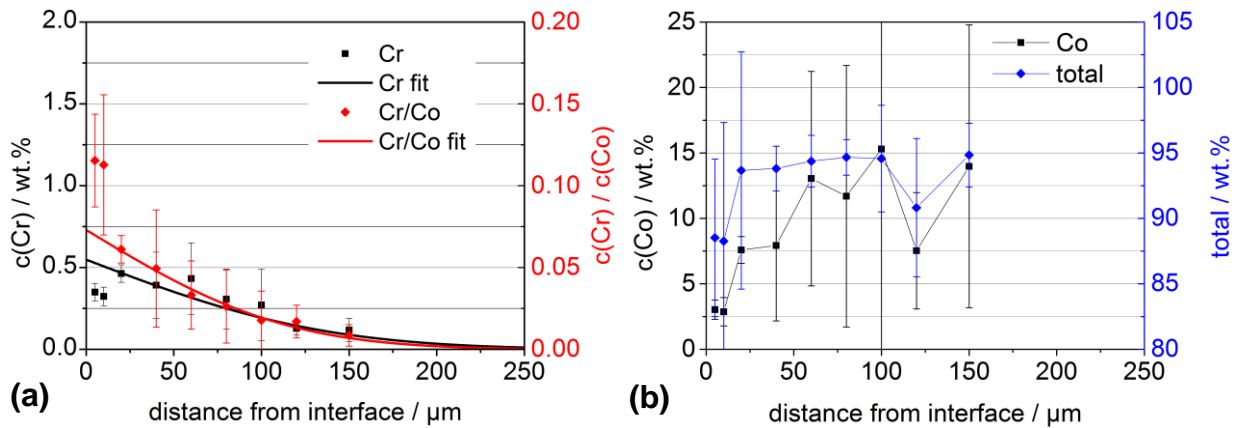


Figure 4-29: CCoG115+_30min_B1, annealed at 1150°C for 30 min, high carbon potential, (a) as-measured and normalised EPMA-concentration profiles of chromium, (b) concentration profile of Co and corresponding total of all measured elements.

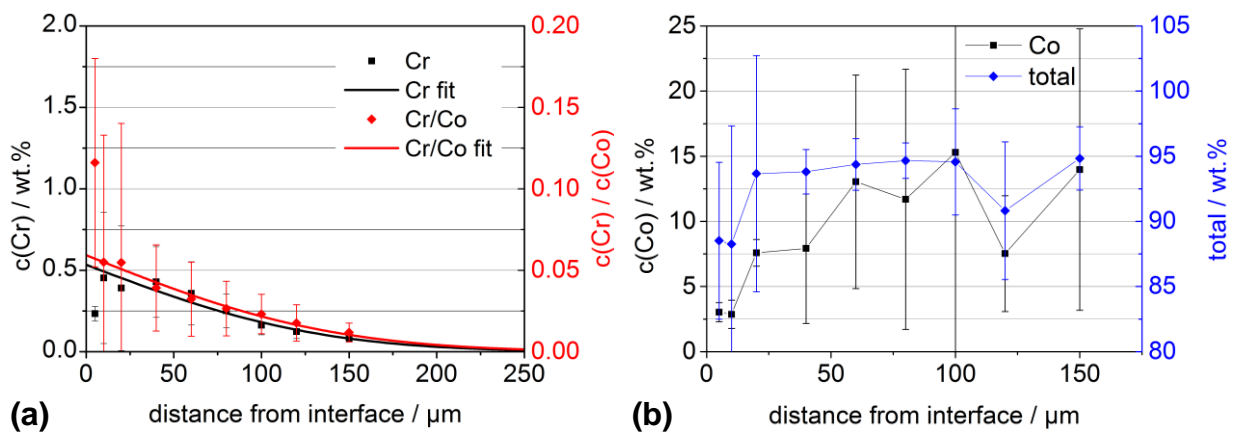


Figure 4-30: CCoG115+_30min_B2, annealed at 1150°C for 30 min, high carbon potential, (a) as-measured and normalised EPMA-concentration profiles of chromium, (b) concentration profile of Co and corresponding total of all measured elements.

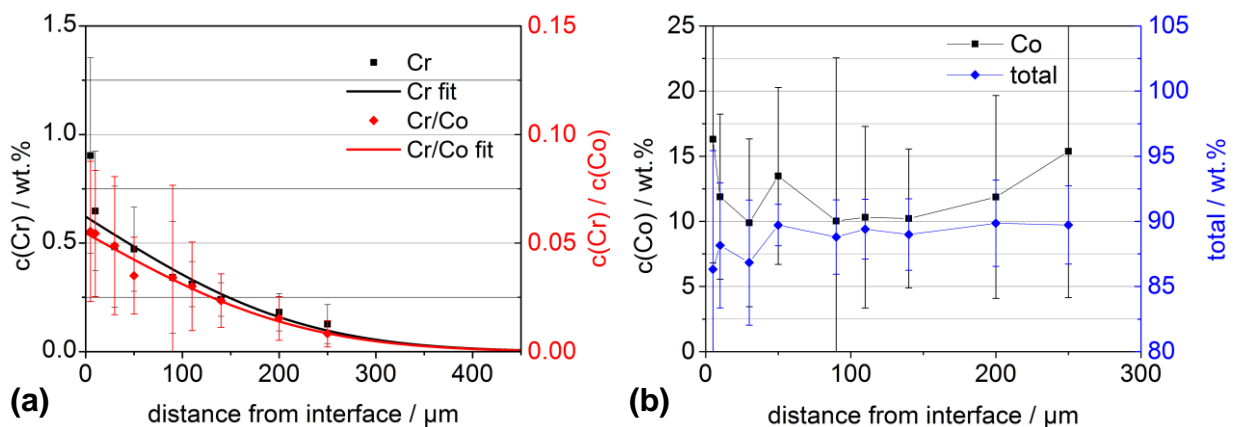


Figure 4-31: CCoG115+_60min, annealed at 1150°C for 60 min, high carbon potential, (a) as-measured and normalised EPMA-concentration profiles of chromium, (b) concentration profile of Co and corresponding total of all measured elements.

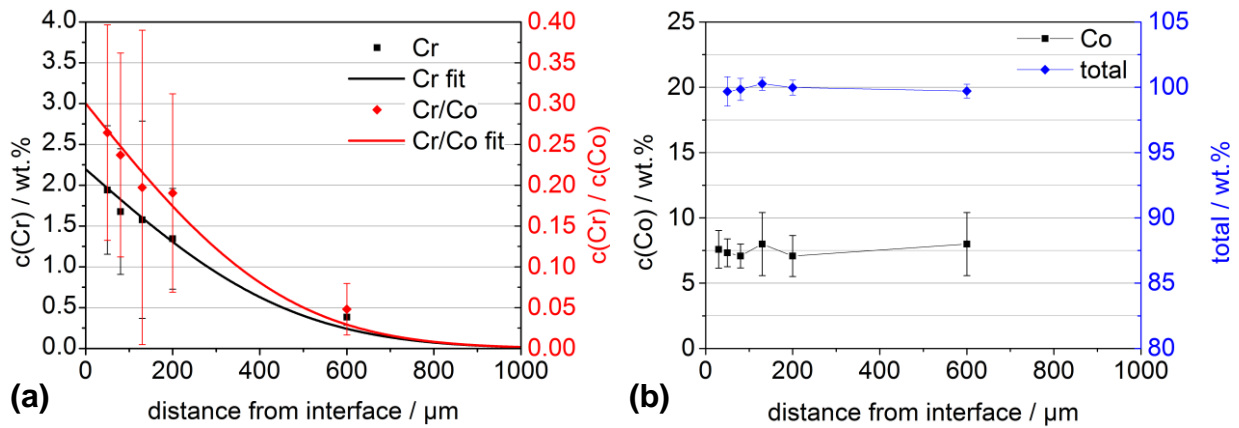


Figure 4-32: CCoG120+, annealed at 1200°C for 15 min, high carbon potential, (a) as-measured and normalised EPMA-concentration profiles of chromium, (b) concentration profile of Co and corresponding total of all measured elements.

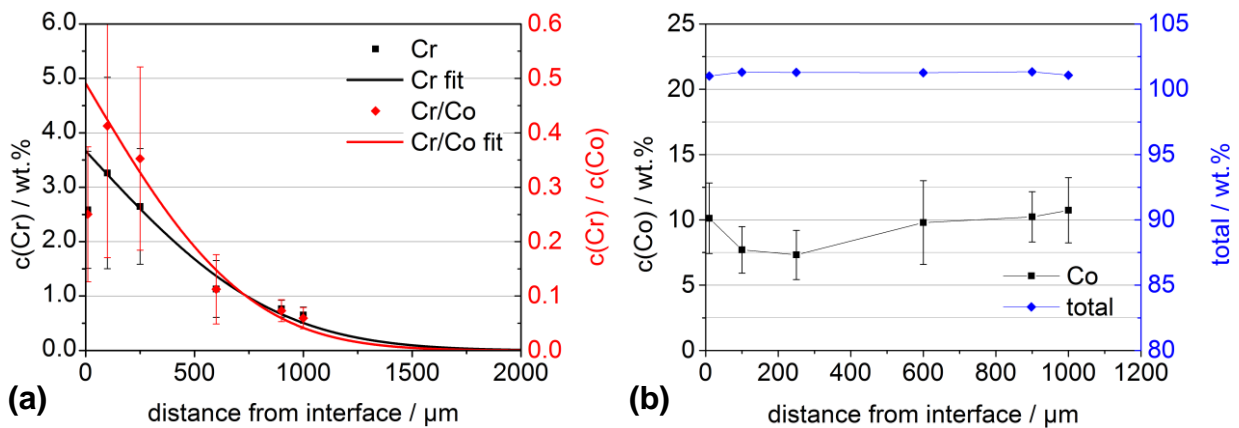


Figure 4-33: CCoG125+, annealed at 1250°C for 15 min, high carbon potential, (a) as-measured and normalised EPMA-concentration profiles of chromium, (b) concentration profile of Co and corresponding total of all measured elements.

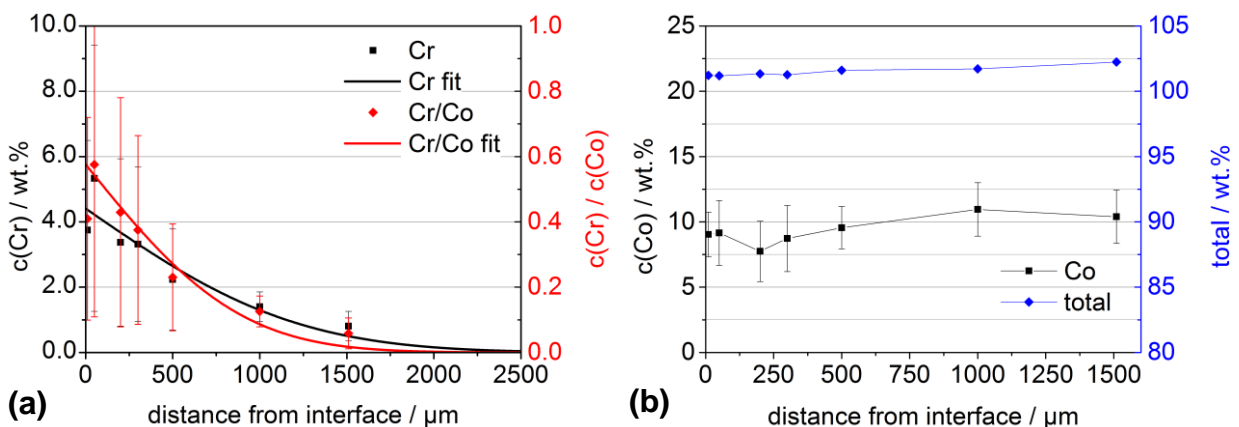


Figure 4-34: CCoG136+, annealed at 1360°C for 30 min, high carbon potential, (a) as-measured and normalised EPMA-concentration profiles of chromium, (b) concentration profile of Co and corresponding total of all measured elements.

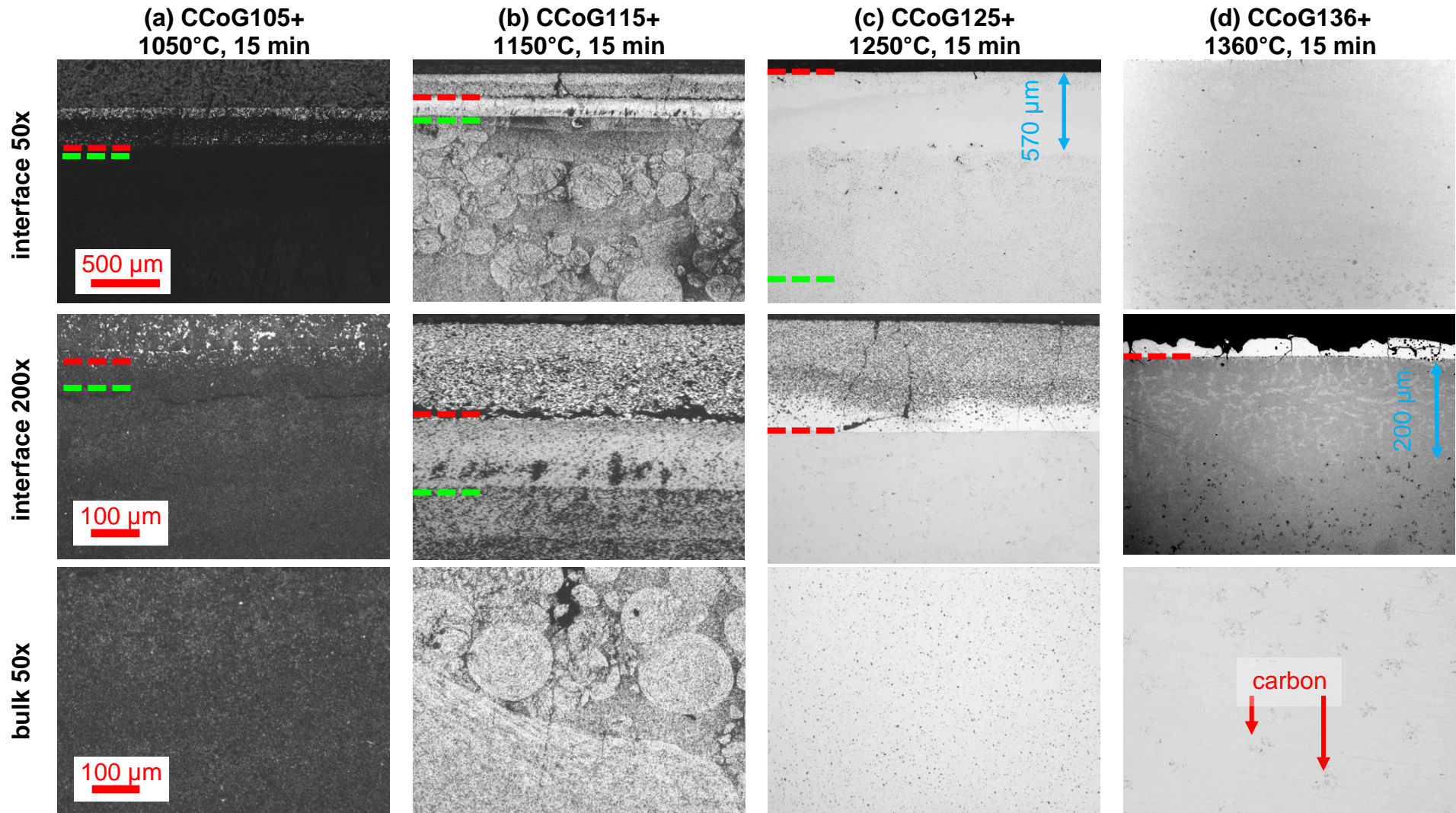


Figure 4-35: G-type sample series CCoG+: LOM of interface and bulk of the WC-Co part of the diffusion couple at various temperatures. Dashed red lines mark the interfaces, green lines the chromium diffusion depth

4.3.4 G-type diffusion couples with Cr₃C₂ and nano-cobalt

A series of WC-Co G-type diffusion couples with nano-cobalt grade in order to see the influence of the initial cobalt grain size on the distribution of chromium: The carbon potential was adjusted within the WC-binder two phase window, which is confirmed by DSC measurements, see Figure 4-131 (page 175). The sample CCo_nG105 was annealed for 15 min at 1050°C, yielding a chromium diffusion depth of 39 μm with corresponding transport factor and interface concentration of $D=2.9 \cdot 10^{-9}$ cm²/s and $c_0(\text{Cr/Co})=0.052$, respectively as shown in Figure 4-36. Due to the high porosity the LOM-microstructure of this sample is a more or less black area as shown in Figure 4-40(a). The diffusion depth of chromium is indicated by the dashed green line. The area influenced by chromium appears brighter, which is related to a higher densification activity.

At 1100°C the diffusion depth increases to 88 μm after 15 min for sample CCo_n110 in Figure 4-37(a) and 129 μm at 1150 °C for sample CConG115 in Figure 4-38(a). The corresponding transport factors are $D=1.5 \cdot 10^{-8}$ cm²/s and $D=3.0 \cdot 10^{-8}$ cm²/s, respectively. The interface concentrations show only a minor increase with temperature of $c_0(\text{Cr/Co})=0.067$ at 1100°C and $c_0(\text{Cr/Co})=0.074$ at 1150°C. The microstructure at 1150°C is shown in Figure 4-40(b). An inhomogeneous densification of the bulk is observed. Close to the interface a higher densification and a more homogeneous microstructure is induced by the presence of chromium. The cobalt concentration however scatters around the initial 10 wt%, see Figure 4-38(b). Hence, no significant gross cobalt migration occurs.

At 1250°C no suitable fit can be applied to the experimental data, see Figure 4-39(a). Within a distance from 0–300 μm from the interface the data points show no clear trend, and large differences between the as-measured and the normalised values appear. The standard deviation covers a wide range of +/-100% relative, indicating an inhomogeneous distribution of chromium and/or cobalt. At distances >350μm from the interface the data points show the expected concentration profiles, as-measured and normalised data are comparable and error bars are small. The cobalt concentration is around 5-8 wt% at <300 μm with a very small standard deviation and is around 10 wt% at >350 μm with a larger standard deviation. Thus, the large error bars of the standard deviation are not caused by cobalt but by an inhomogeneous

chromium distribution. The total is around 100 wt% at distances $<300\ \mu\text{m}$, indicating nearly full density and drops to 96 wt% at distances $>350\ \mu\text{m}$, indicating slight porosity. This finding is supported by the microstructure as shown in Figure 4-40(c). A dense microstructure is found within $320\ \mu\text{m}$ from the interface and porosity is observed at higher distances. This phenomenon can be explained by local chromium-induced liquid-phase formation. In a high-carbon hardmetal the liquid-phase formation appears at 1298°C (Table 2-4).

For the WC-Co-part of the diffusion couple this temperature was also confirmed by DTA analysis, see sample WCo_n in Figure 4-131(a), page 175. In a hardmetal with chromium-saturated binder alloy the solidus temperature decreases to 1191°C , see Table 2-3. This is the case at the interface of the diffusion couple. For lower chromium concentrations the solidus temperature is between $1191\text{--}1298^\circ\text{C}$. Within $0\text{--}320\ \mu\text{m}$ from the interface the chromium concentration is high enough for liquid-phase formation. At higher distances the chromium concentration is too low and the binder remains in solid-state. Upon cooling from liquid phase the chromium solubility decreases and $(\text{Cr},\text{Co})_y\text{C}_x$ precipitates, which explains the inhomogeneous chromium distribution at $x < 320\ \mu\text{m}$. The chromium concentration at the solid/liquid border is around $c(\text{Cr}/\text{Co})=0.2$. At 1191°C Frisk and Markström [08FRI] reported a chromium solubility in the liquid phase of the equilibrium $\text{fcc} + \text{liquid} + \text{WC} + \text{M}_7\text{C}_3$ of $c(\text{Cr}/\text{Co})=0.16$ and at 1300°C of $c(\text{Cr}/\text{Co})=0.$, see Table 2-4. A linear interpolation yields a solubility of $c(\text{Cr}/\text{Co})=0.2$ at the test temperature of 1250°C , which corresponds to the value measured in the diffusion couples.

At 1360°C no more porosity is observed, see Figure 4-40(d). At this temperature the binder phase is expected to be in liquid phase within the whole diffusion couple. Large precipitations of $10\ \mu\text{m}$ length are observed within the first $210\ \mu\text{m}$. From $210\text{--}560\ \mu\text{m}$ a dense microstructure without visible precipitations is observed. At distances $>560\ \mu\text{m}$ carbon precipitations appear. Thus, the carbon is very likely consumed by chromium based precipitates such as M_7C_3 at $x < 560\ \mu\text{m}$. Unfortunately, due to a data conversion error no diffusion data is available on this sample.

A remarkable feature of this series is that all samples with solid binder (1050 , 100 and 1150°C) have an extremely good accordance of the experimental data with the

fitted data. Furthermore, the normalised concentration profile is almost exactly 10% of the as-measured profile. Hence, the cobalt binder is very well distributed in this sample. The results of this sample series are summarised in Table 4-6.

Table 4-6: Transport parameters and interface concentrations of chromium in G-type diffusion couples with nano-Co binder and mid carbon potential.

Sample	Diffusion depth (μm)	D ($10^{-10}\text{cm}^2/\text{s}$)	$c_0(\text{Cr}/\text{Co})$ (wt%)/ (wt%)
CCo _n G105	39	29.8 ± 3.5	0.052 ± 0.003
CCo _n G110	90	151.1 ± 12.9	0.067 ± 0.004
CCo _n G115	129	201.0 ± 14.4	0.074 ± 0.002
CCo _n G125	800	n.a.	n.a.
CCo _n G136	n.a.	n.a.	n.a.

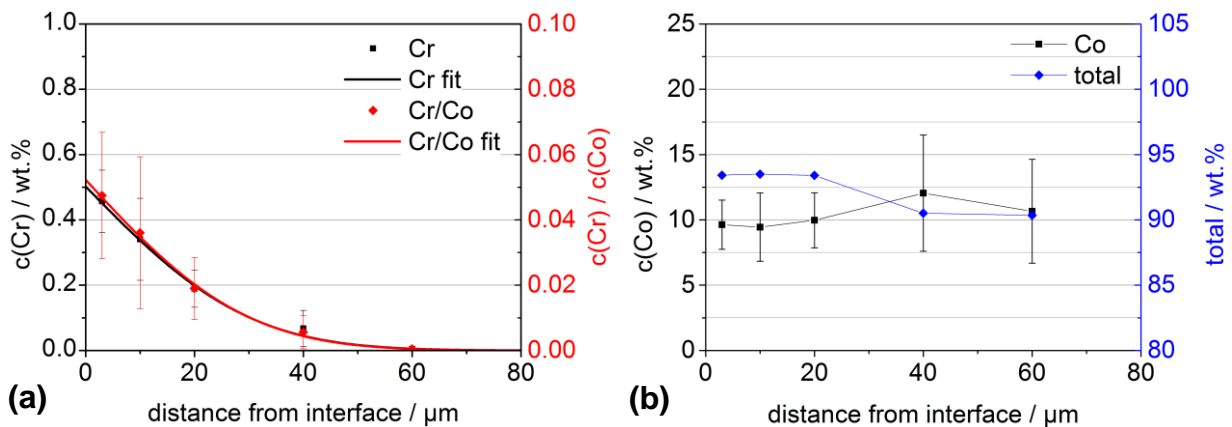


Figure 4-36: CCo_nG105, annealed at 1050°C for 15 min, mid carbon potential, nano-Co, (a) as-measured and normalised EPMA-concentration profiles of chromium, (b) concentration profile of Co and corresponding total of all measured elements.

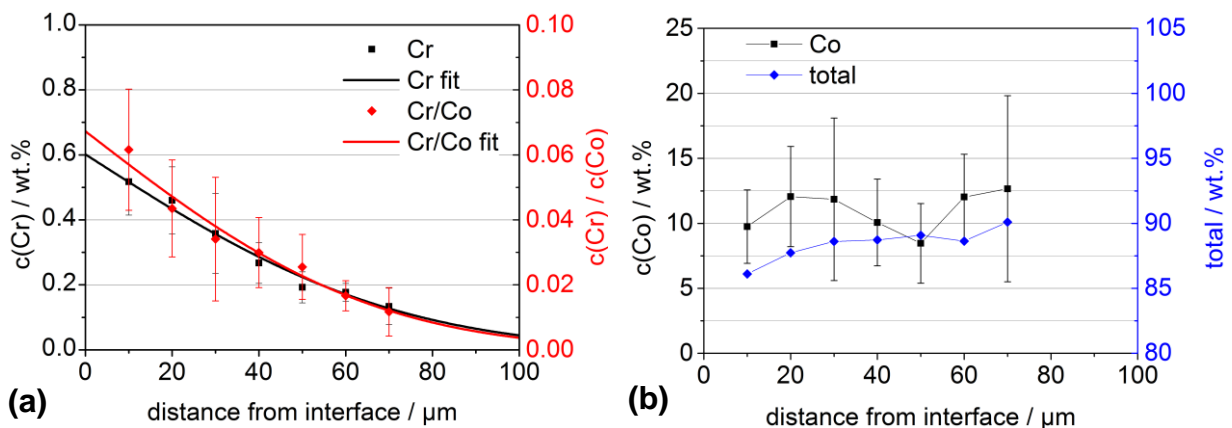


Figure 4-37: CCo_nG110, annealed at 1100°C for 15 min, mid carbon potential, nano-Co, (a) as-measured and normalised EPMA-concentration profiles of chromium, (b) concentration profile of Co and corresponding total of all measured elements.

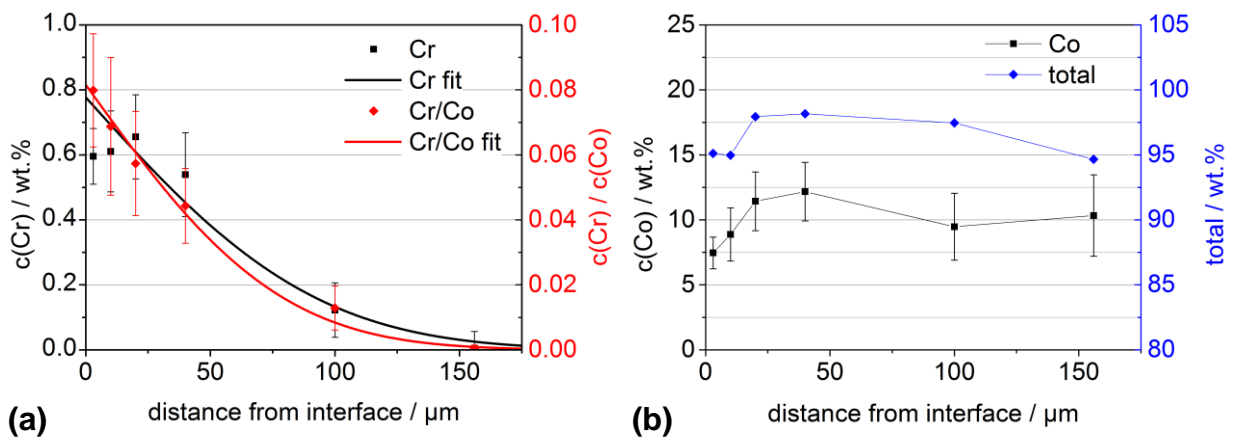


Figure 4-38: CCo_nG115, annealed at 1150°C for 15 min, mid carbon potential, nano-Co, (a) as-measured and normalised EPMA-concentration profiles of chromium, (b) concentration profile of Co and corresponding total of all measured elements.

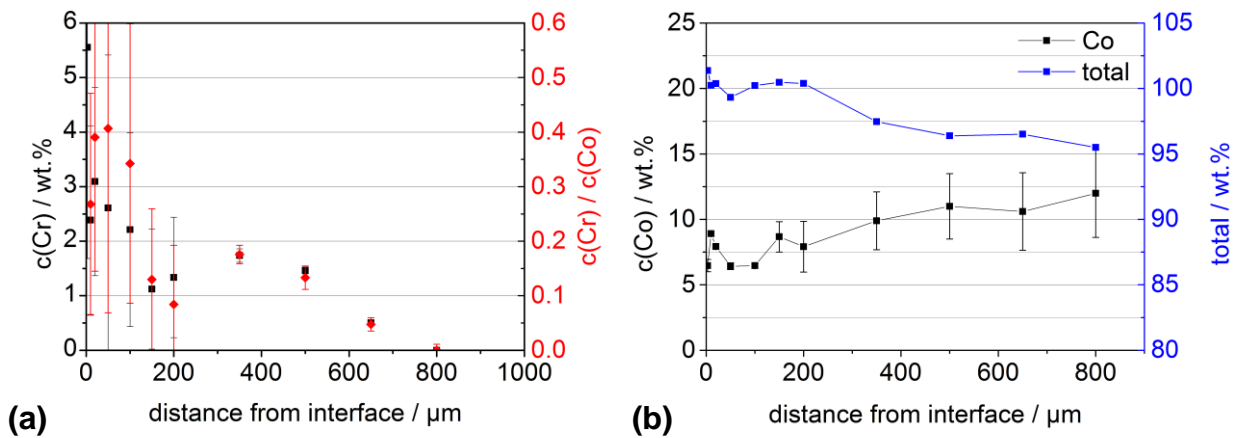


Figure 4-39: CCo_nG125, annealed at 1250°C for 15 min, mid carbon potential, nano-Co, (a) as-measured and normalised EPMA-concentration profiles of chromium, (b) concentration profile of Co and corresponding total of all measured elements.

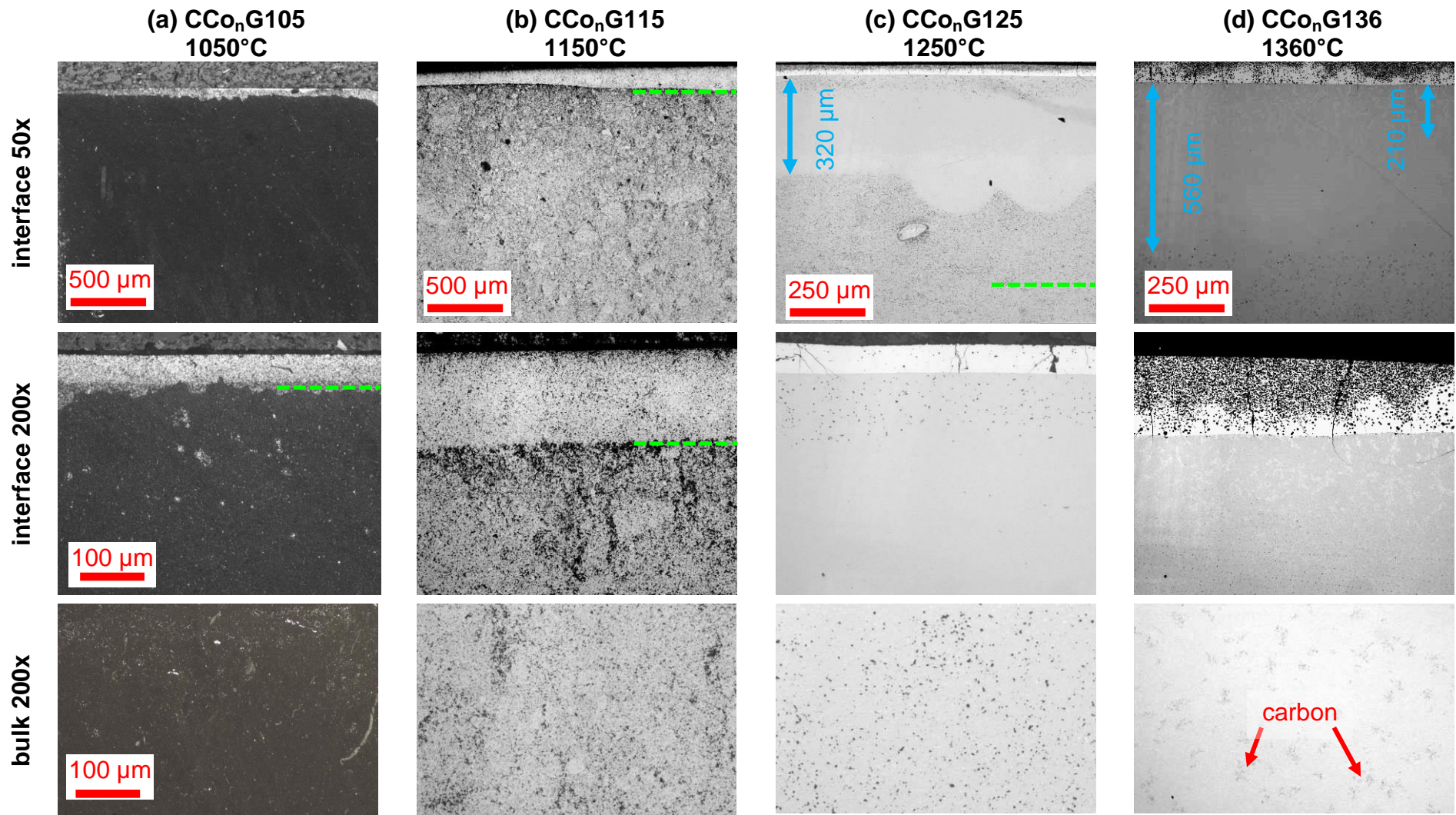


Figure 4-40: LOM of G-type diffusion couples with nano-Co and GGI=Cr, series CCo_nG, at various temperatures. Dashed green lines mark the diffusion depth of chromium.

4.3.5 G-type diffusion couples with Cr₃C₂ and varying green density

The green density of green bodies has impact on the amount and quality of pressing compacts and subsequently on the wetting of WC by cobalt and the activation of particle rearrangement. Hence, an influence on the distribution of chromium at early sintering stages is expected. All samples of this series were annealed for 30 min at 1150°C.

For the samples with low compaction forces of 2 kN (Figure 4-41(a)) and 5 kN (Figure 4-42(a)) it is particularly striking that the normalised concentration profiles $c(\text{Cr})/c(\text{Co})$ show expected diffusion profiles while the as-measured concentration drops to zero at the interface and reach a maximum around 50 μm from interface. The reason is a strong cobalt gradient as can be seen from Figure 4-41(b) and Figure 4-42(b).

This phenomenon is less promoted at a higher pressure of 10 kN, see Figure 4-43(a) and (b) and almost disappears at 20 kN, see Figure 4-44(a) and (b). However, regarding the transport factors D and interfacial concentration c_0 no clear trend can be deduced as shown in Table 4-7.

Table 4-7: Transport parameters and interface concentrations of chromium in G-type diffusion couples with high carbon potential and different green densities

Sample	diffusion depth (μm)	D ($10^{-10} \text{ cm}^2/\text{s}$)	c_0 [Cr(wt%)/Co(wt%)]
CCoG115+2kN	121	281.6 ± 36.2	0.065 ± 0.006
CCoG115+5kN	130	161.7 ± 19.3	0.069 ± 0.003
CCoG115+10kN	142	192.5 ± 8.06	0.068 ± 0.003
CCoG115+20kN	115	202.3 ± 7.8	0.033 ± 0.001

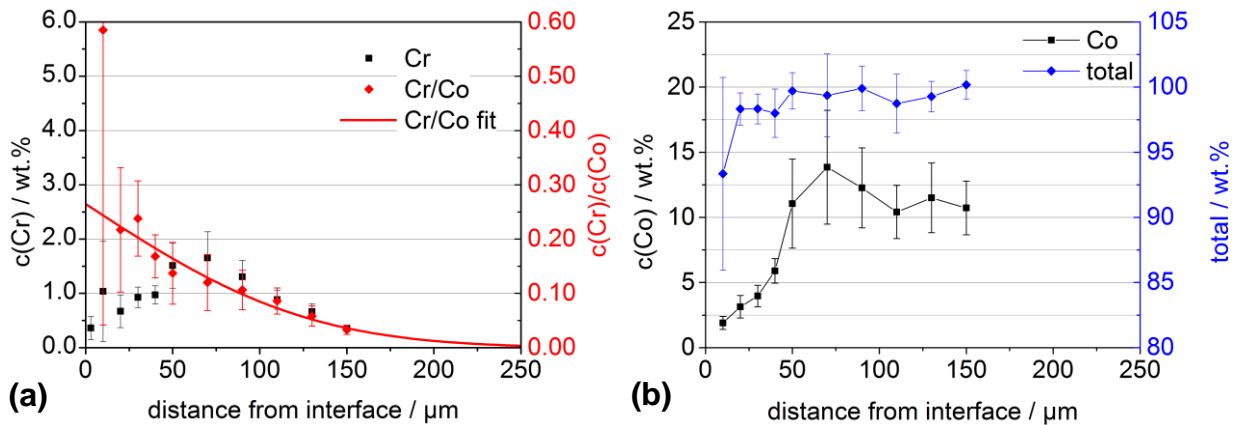


Figure 4-41: CCoG115+2kN, annealed at 1150°C for 30 min, 2kN pressing force, (a) as-measured and normalised EPMA-concentration profiles of chromium, (b) concentration profile of cobalt and corresponding total of all measured elements.

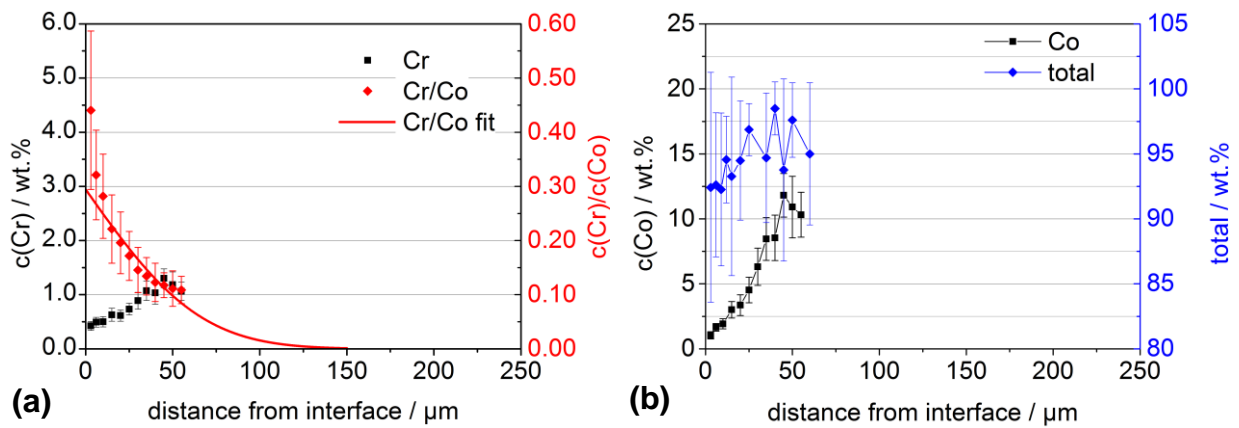


Figure 4-42: CCoG115+5kN, annealed at 1150°C for 30 min, 5kN pressing force, (a) as-measured and normalised EPMA-concentration profiles of chromium, (b) concentration profile of cobalt and corresponding total of all measured elements.

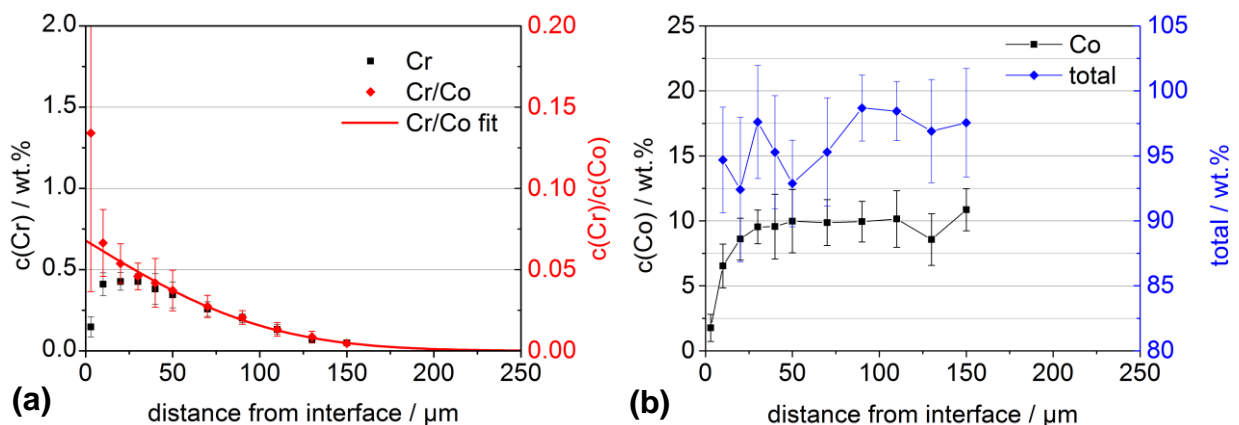


Figure 4-43: CCoG115+10kN, annealed at 1150°C for 30 min, 10kN pressing force, (a) as-measured and normalised EPMA-concentration profiles of chromium, (b) concentration profile of cobalt and corresponding total of all measured elements.

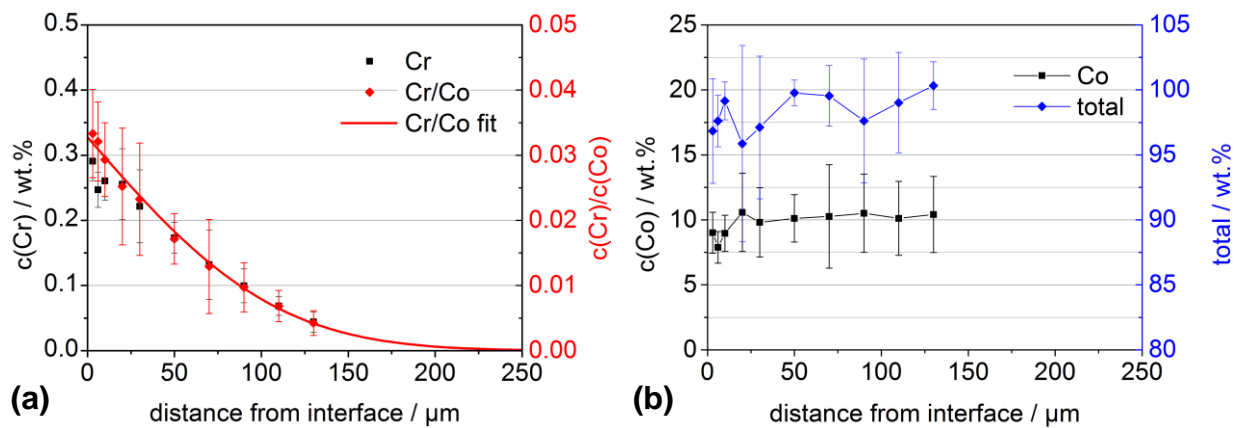


Figure 4-44: CCoG115+20kN, annealed at 1150°C for 30 min, 20kN pressing force, (a) as-measured and normalised EPMA-concentration profiles of chromium, (b) concentration profile of cobalt and corresponding total of all measured elements.

4.3.6 G-type diffusion couples with CrB

In this sample series chromium is added as boride in order to investigate an influence of boron on the chromium distribution in WC-Co hardmetals.

The samples CBCoG105+5Kmin and CBCoG105-5Kmin were prepared with high and low carbon potential, respectively and annealed for 15 min at 1050°C after heating up with a slow rate of 5K/min. As can be seen from Figure 4-45(a) for the high carbon hardmetal and Figure 4-46(a) for the low carbon hardmetal and the values given in Table 4-8 the distribution of chromium is slightly faster in low carbon ($D=4.9 \cdot 10^{-9} \text{ cm}^2/\text{s}$) than in high carbon ($D=3.6 \cdot 10^{-9} \text{ cm}^2/\text{s}$) samples. However, in presence of boron the maximum solubility of chromium seems to be higher in high-carbon hardmetals ($c_0(\text{Cr}/\text{Co})=0.151$) than in low-carbon ($c_0(\text{Cr}/\text{Co})=0.068$) samples. The cobalt concentration profiles Figure 4-45(b) and Figure 4-46(b) show large error bars, which in combination with the low total values indication indicates high porosity and microstructural inhomogeneity.

When annealed for 15 min at 1150°C as shown in Figure 4-47(a) it is particularly striking that no suitable concentration profile can be drawn from the as-measured values. However, normalised data matches the model provided in Equation 4 when the second data point is considered as an outlier. The reason can be found in the strong cobalt gradient as shown in Figure 4-47(b) which forms in presence of boron. The interface concentration obtained from the fit of $c_0(\text{Cr}/\text{Co})=0.217$ is surprisingly

high. For samples with Cr_3C_2 such values appear with liquid binder phase only (compare Table 4-5).

Table 4-8: Transport parameters and interface concentrations of chromium in G-type diffusion couples with CrB as a Cr-source

Sample	Diffusion depth (μm)	D ($10^{-10}\text{cm}^2/\text{s}$)	$c_0(\text{Cr}/\text{Co})$ (wt%)/(wt%)
CBCoG105+5Kmin	53	36.5 ± 4.5	0.151 ± 0.018
CBCoG105-5Kmin	74	49.4 ± 4.0	0.068 ± 0.004
CBCoG115+	115	150.3 ± 21.4	0.217 ± 0.017

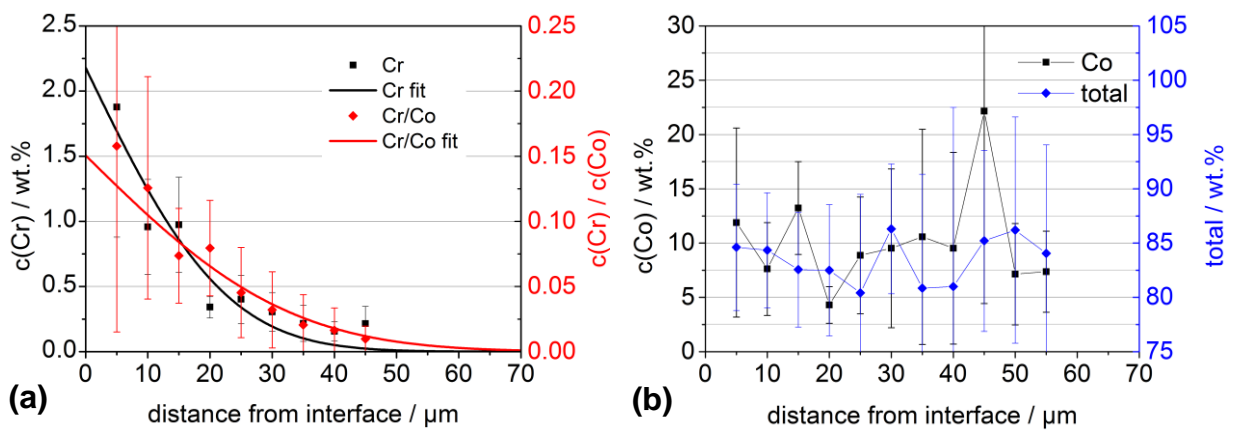


Figure 4-45: CBCoG105+5Kmin, linear heat-up to 1050 with 5K/min, high carbon potential, (a) as-measured and normalised EPMA-concentration profiles of chromium, (b) concentration profile of Co and corresponding total of all measured elements.

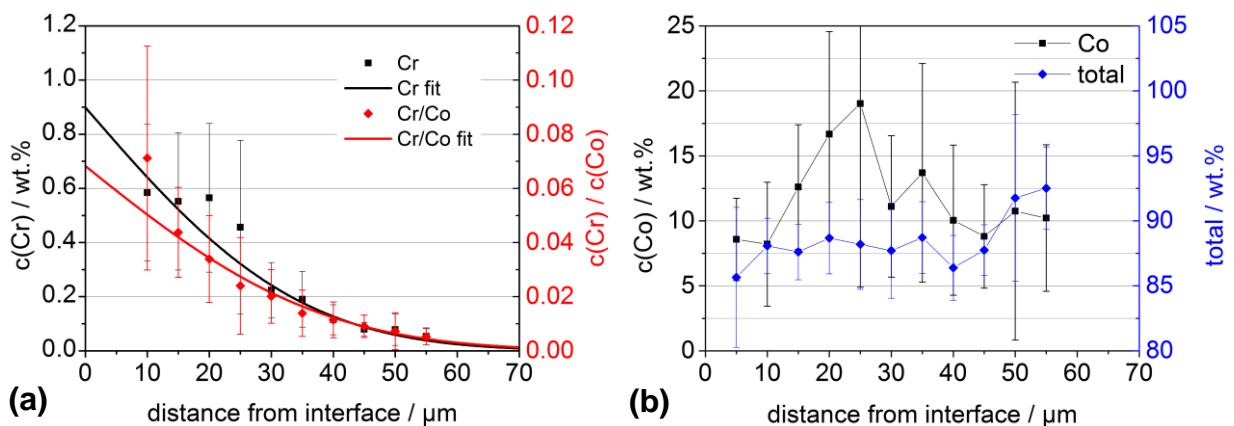


Figure 4-46: CBCoG105-5Kmin, linear heat-up to 1050 with 5K/min, low carbon potential, (a) as-measured and normalised EPMA-concentration profiles of chromium, (b) concentration profile of Co and corresponding total of all measured elements.

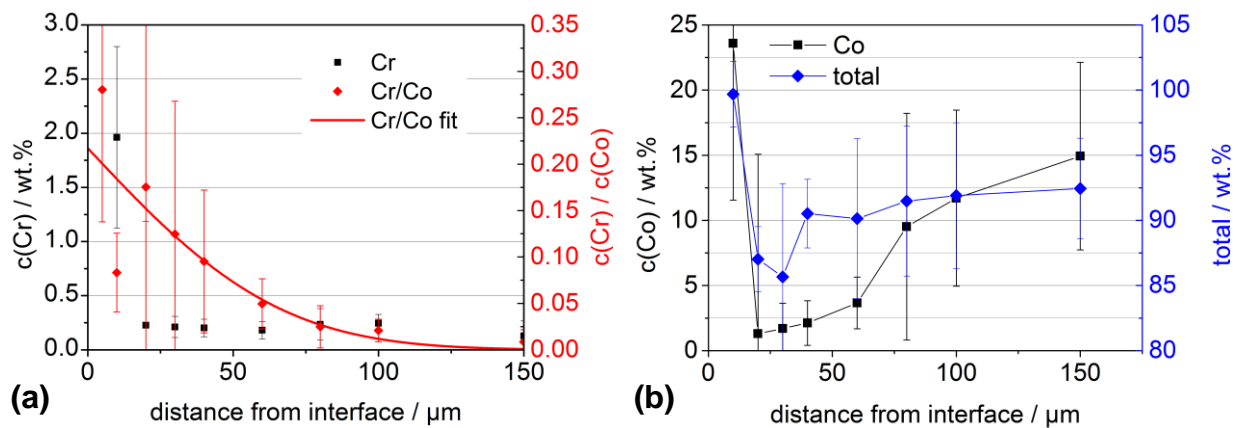


Figure 4-47: CBCoG115+, annealed at 1150°C for 15 min, high carbon potential, (a) as-measured and normalised EPMA-concentration profiles of chromium, (b) concentration profile of Co and corresponding total of all measured elements.

4.3.7 G-type diffusion couples with Cr_2N

Chromium was added as nitride in this series. Two samples CNCoG105+5Kmin (Figure 4-48) and CNCoG105-5Kmin (Figure 4-49) with high and low carbon potential, respectively were annealed at 1050°C for 15 min after slow heat-up with 5K/min. Both the high and the low carbon sample show comparable diffusion depths of 29 μm and 31 μm and transport factors of $D=2.2 \cdot 10^{-9} \text{ cm}^2/\text{s}$ and $2.0 \cdot 10^{-9} \text{ cm}^2/\text{s}$, respectively. The interface concentration of $c_0(\text{Cr}/\text{Co})=0.059$ for the low carbon and $c_0(\text{Cr}/\text{Co})=0.044$ for the high carbon alloy are equal within the error range.

At 1150°C sample CNCoG115+ and CNCoG115+30min were annealed for 15 min and 30 min, respectively. As can be seen from Figure 4-50 chromium reaches the detection limit at 101 μm after 15 min and 162 μm after 30 min as illustrated in Figure 4-51. With both annealing times transport factors equal within the error range of $D=2.2 \cdot 10^{-8} \text{ cm}^2/\text{s}$ and $D=2.0 \cdot 10^{-8} \text{ cm}^2/\text{s}$ were calculated. However, the interfacial concentration increases from $c_0(\text{Cr}/\text{Co})=0.058$ to 0.106 when increasing the annealing time from 15 to 30 min. The reason behind is the decomposition of the nitride and the subsequent appearance of metallic chromium. This effect is further discussed in section 5.5.7. Besides some insignificant deviations within 10 μm from the interface no trend for the cobalt concentration or the total was found as can be seen from Figure 4-48(b) – Figure 4-51(b). An overview of the calculated values can be found in Table 4-9.

Table 4-9: Transport parameters and interface concentrations of chromium in G-type diffusion couples with Cr₂N as a Cr-source.

Sample	Diffusion depth (μm)	D (10 ⁻¹⁰ cm ² /s)	c ₀ (Cr/Co) (wt%)/ (wt%)
CNCoG105+5Kmin	29	22.2 ± 3.9	0.044 ± 0.005
CNCoG105-5Kmin	31	19.7 ± 3.9	0.059 ± 0.010
CNCoG115+	101	217.8 ± 22.8	0.058 ± 0.030
CNCoG115+30min	162	198.4 ± 34.5	0.106 ± 0.016

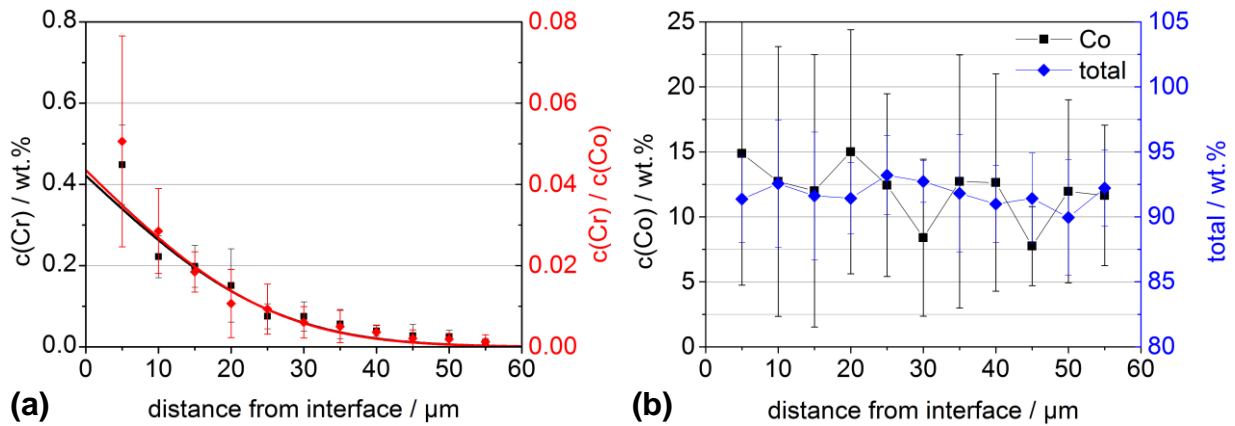


Figure 4-48: CNCoG105+5Kmin, linear heat-up to 1050 with 5K/min, high carbon potential, (a) as-measured and normalised EPMA-concentration profiles of chromium, (b) concentration profile of Co and corresponding total of all measured elements.

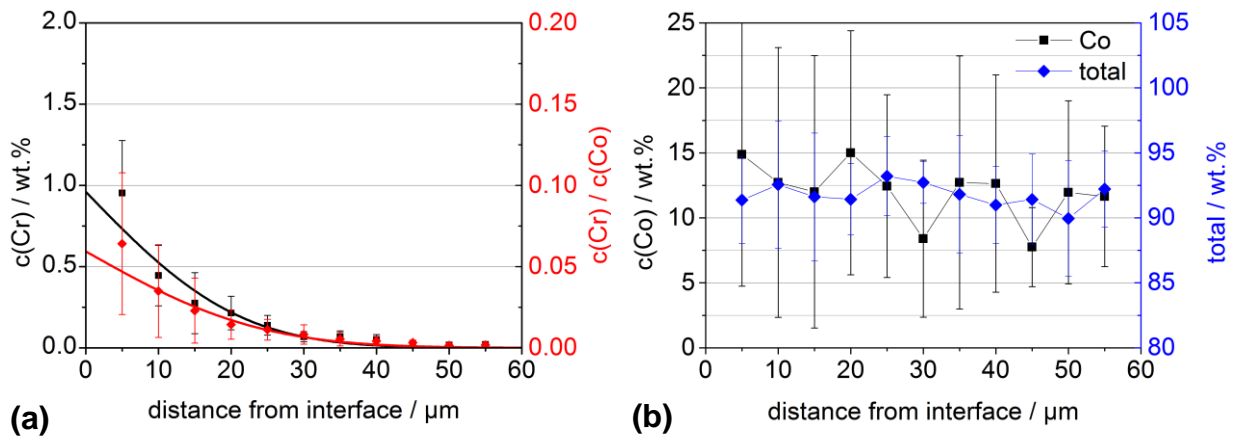


Figure 4-49: CNCoG105-5Kmin, linear heat-up to 1050 with 5K/min, low carbon potential, (a) as-measured and normalised EPMA-concentration profiles of chromium, (b) concentration profile of Co and corresponding total of all measured elements.

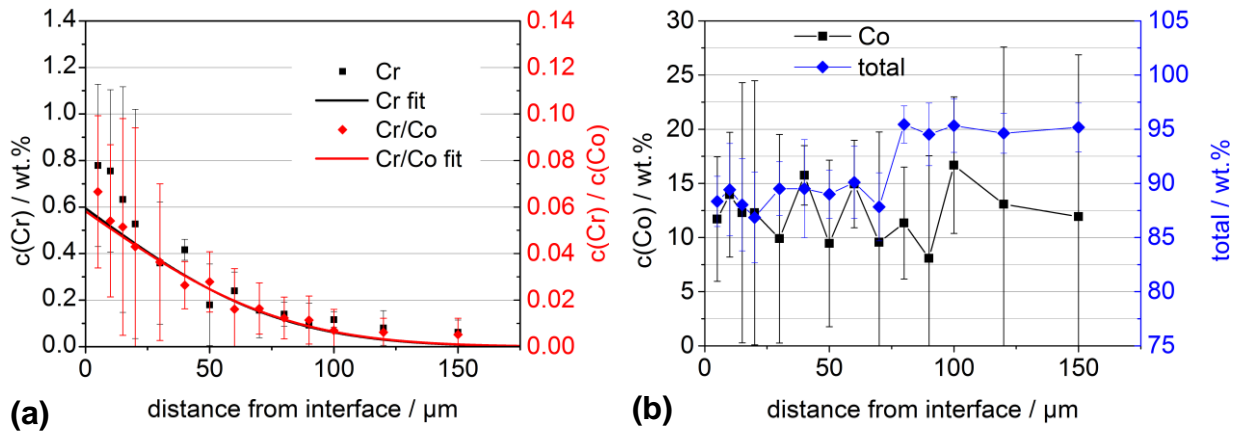


Figure 4-50: CNCoG115+, annealed at 1150°C for 15 min, high carbon potential, (a) as-measured and normalised EPMA-concentration profiles of chromium, (b) concentration profile of Co and corresponding total of all measured elements.

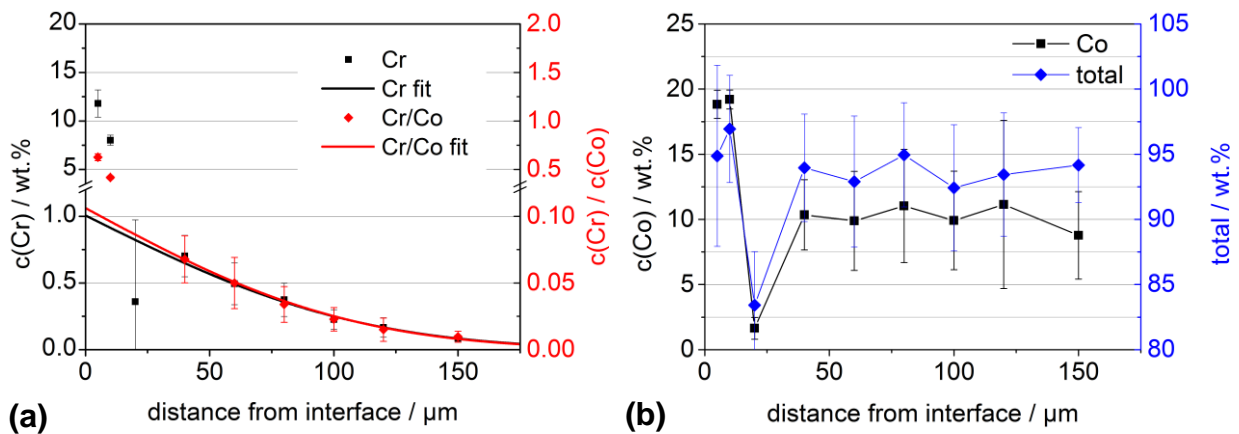


Figure 4-51: CNCoG115+30min, annealed at 1150°C for 30 min, high carbon potential, (a) as-measured and normalised EPMA-concentration profiles of chromium, (b) concentration profile of Co and corresponding total of all measured elements.

4.3.8 G-type diffusion couples with Cr annealed in N₂ atmosphere

Upon sintering hardmetals interaction with nitrogen atmosphere was reported as discussed in section 2.3. In this series a possible influence of nitrogen on the distribution of chromium at 1150°C is investigated. The chromium concentration profiles of the low-carbon sample CCoG115-N and the high-carbon sample CCoG115+N after 15 min annealing time are shown in Figure 4-52(a) and Figure 4-53(a), respectively. Both show a comparable diffusion depth of 65 and 71 μm with relatively low transport factors of $2.4 \cdot 10^{-9} \text{ cm}^2/\text{s}$ and $7.3 \cdot 10^{-9} \text{ cm}^2/\text{s}$, respectively which is by an order of magnitude lower than in Argon-atmosphere (compare Table

4-3 and Table 4-5) while the interface concentrations of $c(\text{Cr}/\text{Co})=0.27$ and 0.13 are surprisingly high.

The samples CNCoG115+N, see Figure 4-55 and CNCoG115-N, see Figure 4-54 are prepared with high and low carbon potential, respectively and Cr_2N as a chromium source instead of Cr_3C_2 . The transport factors of $D=9.0 \cdot 10^{-9} \text{ cm}^2/\text{s}$ and $D=8.1 \cdot 10^{-9} \text{ cm}^2/\text{s}$ are slightly higher than of the samples with carbide. The interfacial concentration of the low-carbon sample of $c(\text{Cr}/\text{Co})=0.11$ is high as compare to $c(\text{Cr}/\text{Co})=0.019$ of the high carbon sample. The reason for the low value of the high-carbon sample can be found in the poor quality of the fit and a lack of data points above the detection limit.

The totals of the EPMA measurements in Figure 4-52(b) – Figure 4-54(b) scatter around 98% for the samples prepared with Cr_3C_2 but is only around 92% for the samples with Cr_2N . Since all these samples were annealed within the same sintering cycle and prepared from the same WC-Co mixture the presence of nitrides seems to have a retarding effect on the shrinkage in N_2 atmosphere. No significant effect on the cobalt-distribution was observed. An overview on the calculated values of this series is given in Table 4-10.

Table 4-10: Transport parameters and interface concentrations of chromium in G-type diffusion couples annealed in N_2 atmosphere.

Sample	Diffusion depth (μm)	D ($10^{-10} \text{ cm}^2/\text{s}$)	$c_0(\text{Cr}/\text{Co})$ (wt%)/(wt%)
CCoG115-N	65	24.2 ± 7.6	0.272 ± 0.007
CCoG115+N	71	72.5 ± 2.1	0.13 ± 0.005
CNCoG115-N	84	90.0 ± 8.9	0.111 ± 0.006
CNCoG115+N	76	81.0 ± 46.4	0.019 ± 0.016

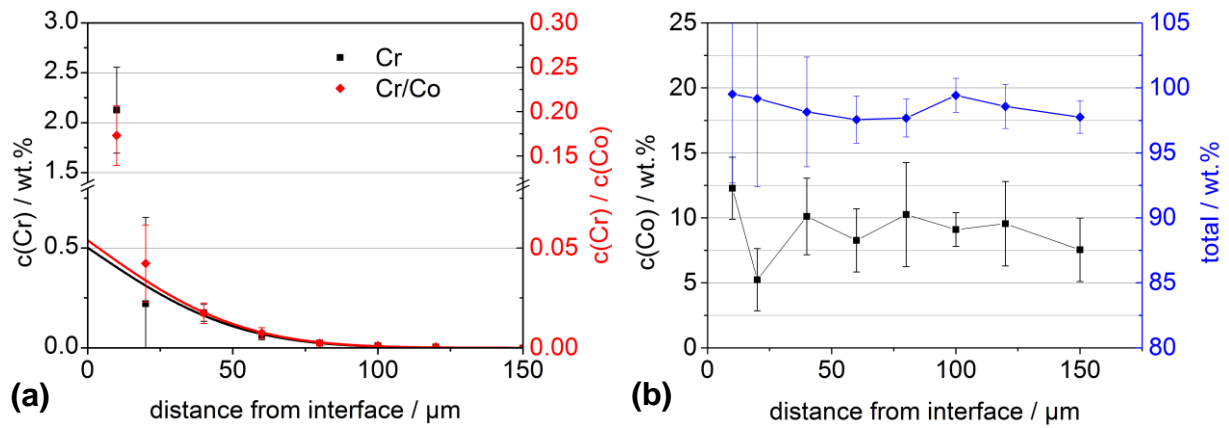


Figure 4-52: CCoG115-N, annealed at 1150°C for 15 min, low carbon, N₂ atmosphere, (a) as-measured and normalised EPMA-concentration profiles of chromium, (b) concentration profile of cobalt and corresponding total of all measured elements.

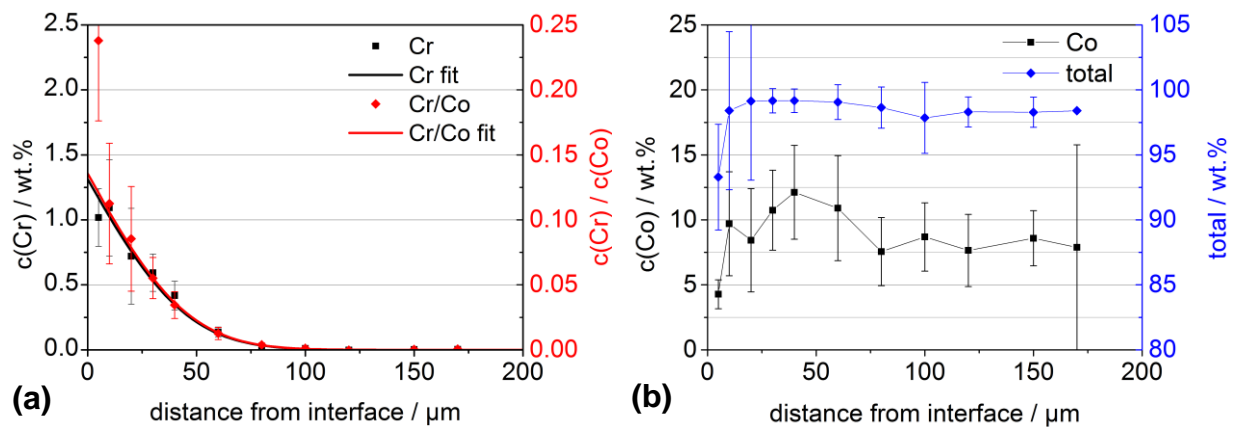


Figure 4-53: CCoG115+N, annealed at 1150°C for 15 min, low carbon, N₂ atmosphere, (a) as-measured and normalised EPMA-concentration profiles of chromium, (b) concentration profile of cobalt and corresponding total of all measured elements.

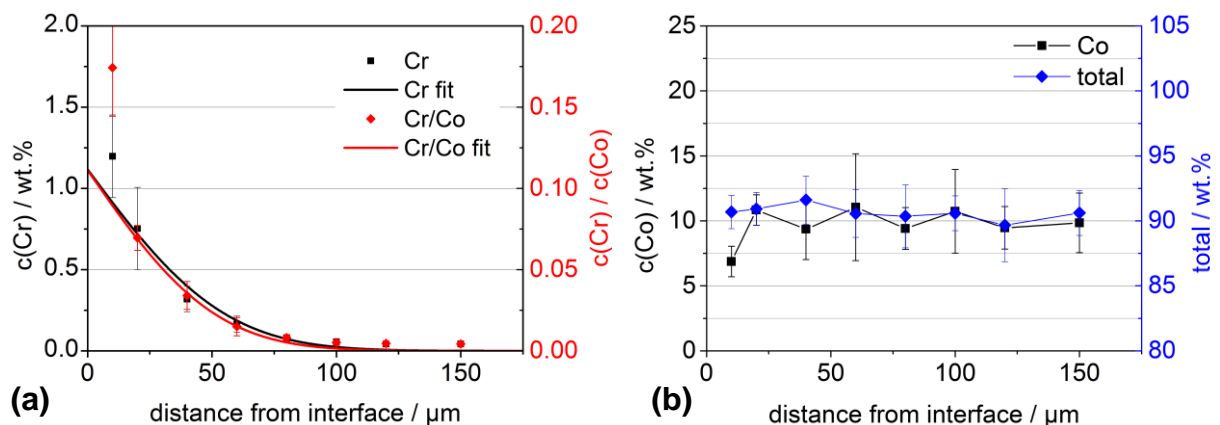


Figure 4-54: CNCCoG115-N, annealed at 1150°C for 15 min, low carbon, N₂ atmosphere, (a) as-measured and normalised EPMA-concentration profiles of chromium, (b) concentration profile of cobalt and corresponding total of all measured elements.

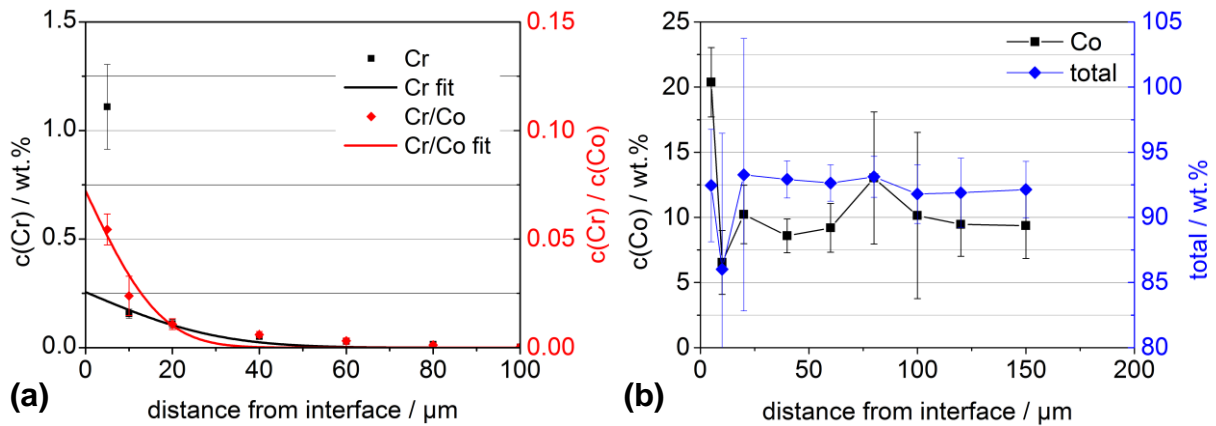


Figure 4-55: CNCrCoG115+N, annealed at 1150°C for 15 min, high carbon, N₂ atmosphere, (a) as-measured and normalised EPMA-concentration profiles of chromium, (b) concentration profile of cobalt and corresponding total of all measured elements.

4.3.9 G-type diffusion couples with Cr annealed in CO atmosphere

Carbon monoxide plays an interesting role when sintering hardmetals. It is formed in-situ by carbothermic reduction of surface oxides, which happens below 900°C for WC-Co. However, for GGIs the reduction happens between 1000–1200°C, see section 5.1. Below this temperature CO has oxidising potential on GGIs. It also acts carburising to the binder phase. In order to see its influence on the distribution of chromium in WC-Co the samples CCoG115+CO with Cr₃C₂ and CNCrCoG115+CO with Cr₂N as a chromium source were annealed for 15 min at 1150°C in 400 mbar CO atmosphere. The results can be seen in Figure 4-56(a) and Figure 4-57(a), respectively. Both samples show excellent accordance of measured and fitted data. The sample with Cr₃C₂ reveals significantly faster chromium transport of $D=2.8 \cdot 10^{-8} \text{ cm}^2/\text{s}$ as compared to $D=1.9 \cdot 10^{-8} \text{ cm}^2/\text{s}$ of the sample with Cr₂N and higher interface solubilities of $c(\text{Cr}/\text{Co})=0.12$ vs. 0.10, respectively. While the cobalt concentration scatters around 10 wt.% for the sample CCoG115+CO in Figure 4-56(b) a gradient with cobalt enrichment is formed in sample CNCrCoG115+CO, see Figure 4-57(b).

A summary of the calculated parameters is listed in Table 4-11.

Table 4-11: Transport parameters and interface concentrations of chromium in G-type diffusion couples annealed in CO atmosphere.

Sample	Diffusion depth (μm)	D ($10^{-10}\text{cm}^2/\text{s}$)	$c_0(\text{Cr}/\text{Co})$ (wt%)/(wt%)
CCoG115+CO	140	279.3 ± 25.3	0.121 ± 0.004
CNCoG115+CO	110	191.0 ± 8.2	0.100 ± 0.004

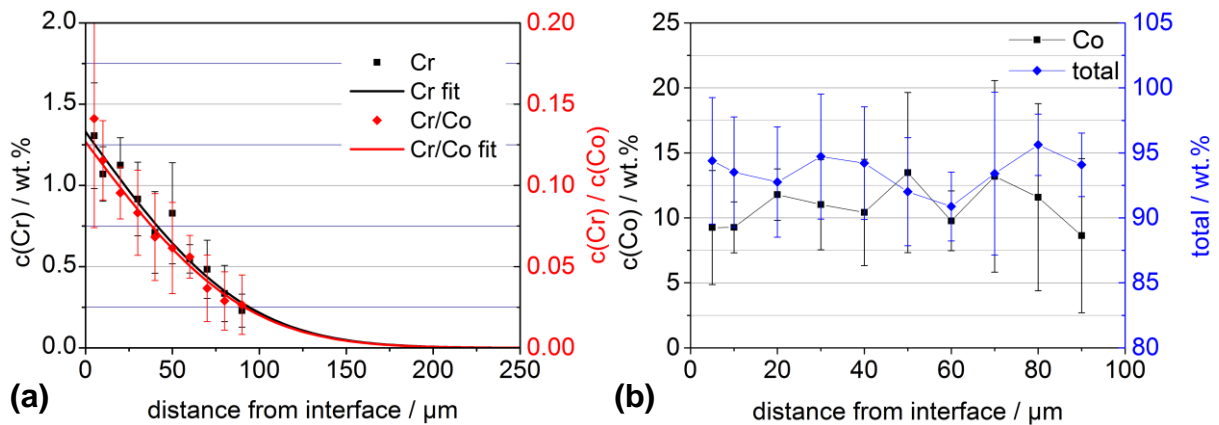


Figure 4-56: CCoG115+CO, annealed at 1150°C for 15 min, high carbon, CO atmosphere, (a) as-measured and normalised EPMA-concentration profiles of chromium, (b) concentration profile of cobalt and corresponding total of all measured elements.

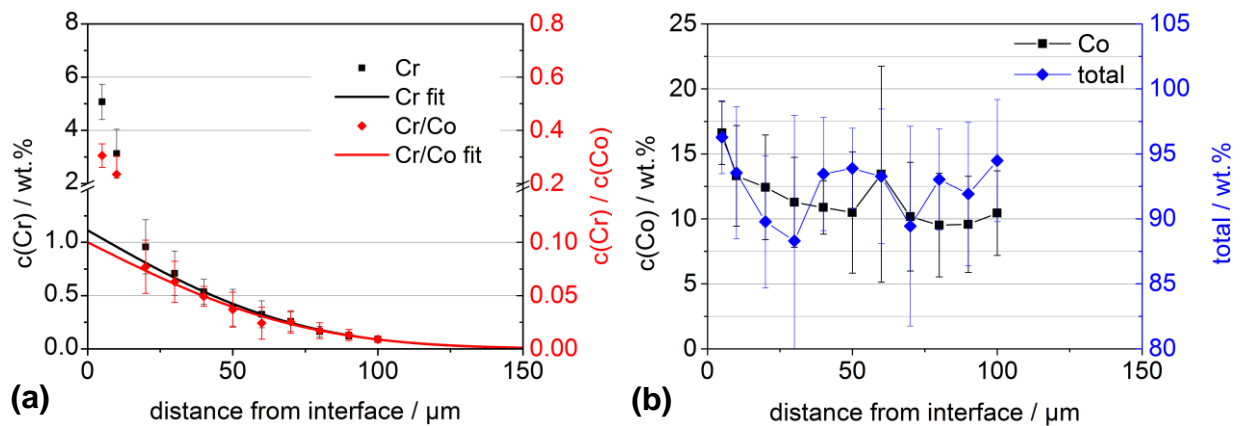


Figure 4-57: CNCoG115+CO, annealed at 1150°C for 15 min, low carbon, CO atmosphere, (a) as-measured and normalised EPMA-concentration profiles of chromium, (b) concentration profile of cobalt and corresponding total of all measured elements.

4.3.10 G-type diffusion couples with VC, low carbon potential

G-type samples with VC as a vanadium source and low carbon potential within the WC-Co part of the diffusion couple were prepared in a temperature range of 1050°C–1360°C.

At 1050°C in sample VCoG105- vanadium was transported to a depth of 22 μm within 15 min as shown in Figure 4-58(a) resulting in a transport factor of $D=3.3 \cdot 10^{-10} \text{ cm}^2/\text{s}$. This value is by an order of magnitude lower as compared to chromium in sample CCoG105- (Table 4-3) prepared under equal conditions.

At 1100°C the transport factor is increased to $D=3.3 \cdot 10^{-10} \text{ cm}^2/\text{s}$ as shown in Figure 4-59(a) for sample VCoG110-_40min where the diffusion depth is 45 μm after 40 min annealing time. At 1200°C a depth of 45 μm is reached already after 7 min as shown in Figure 4-60(a) for sample CCoG120-_7min resulting in a transport factor of $D=6.2 \cdot 10^{-9} \text{ cm}^2/\text{s}$.

Interestingly the interface concentrations of $c(\text{V}/\text{Co})=0.099$, 0.072 and 0.043 are declining with increasing temperature from 1050, 1100 and 1200°C, respectively.

The sample annealed at 1250°C (VCoG125-) for 15 min does not show a suitable concentration profile as illustrated in Figure 4-61(a). Since the solidus temperature of V-saturated low-carbon WC-Co is 1320°C, this sample is expected to be in solid-state. However, during the diffusion experiment the carbon state can change locally. Since the high-carbon solidus temperature is around 1250°C some local melting phenomenon could have occurred causing the present concentration profile.

The binder phase of sample VCoG136- which was annealed at 1360°C is expected to be liquid. As can be seen from Figure 4-62(a) no evaluable concentration profile is measured for this sample either. Since they were annealed within the same cycle as samples such as e.g. CCoG136- and VCoG136+, which yielded a concentration profile, this has to be some sample specific effect.

The total concentration values scatter around 90–94 wt% for the samples annealed in solid-state as shown in Figure 4-58(b) – Figure 4-60(b) At 1250 and 1360°C they are around 100 wt% as can be seen from Figure 4-61(b) and Figure 4-62(b), respectively.

An overview of the values calculated from this sample series is given in Table 4-12.

Table 4-12: Transport parameters and interface concentrations of vanadium in G-type diffusion couples with low carbon potential.

Sample	Diffusion depth (μm)	D ($10^{-10}\text{cm}^2/\text{s}$)	$c_0(\text{Cr}/\text{Co})$ (wt%)/(wt%)
VCoG105-	22	3.3 ± 0.2	0.099 ± 0.005
VCoG110-_40min	45	8.7 ± 0.9	0.072 ± 0.010
VCoG120-_7min	45	61.8 ± 11.4	0.043 ± 0.005
VCoG125-	n.a.	n.a.	n.a.
VCoG136-	n.a.	n.a.	n.a.

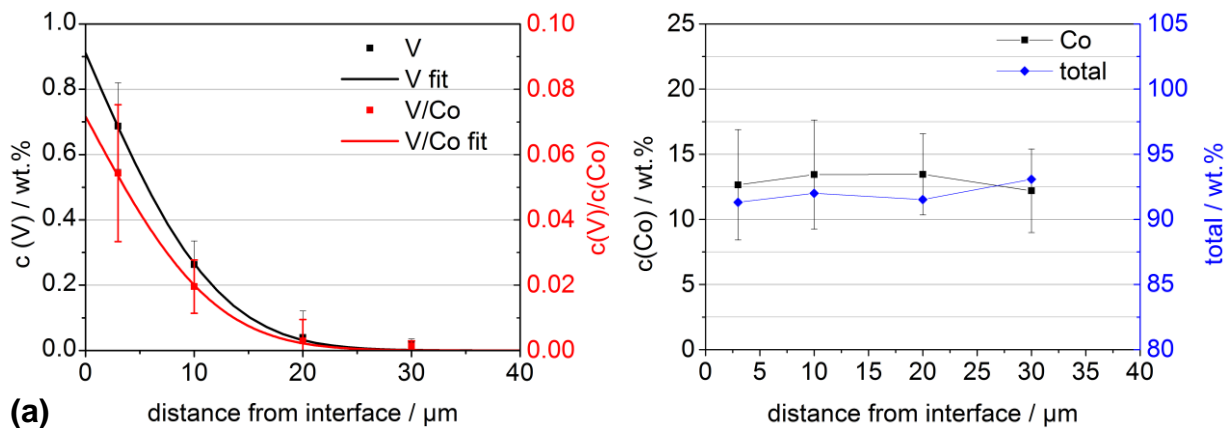


Figure 4-58: VCoG105-, annealed at 1100°C for 15 min, low carbon, (a) as-measured and normalised EPMA-concentration profiles of vanadium, (b) concentration profile of cobalt and corresponding total of all measured elements.

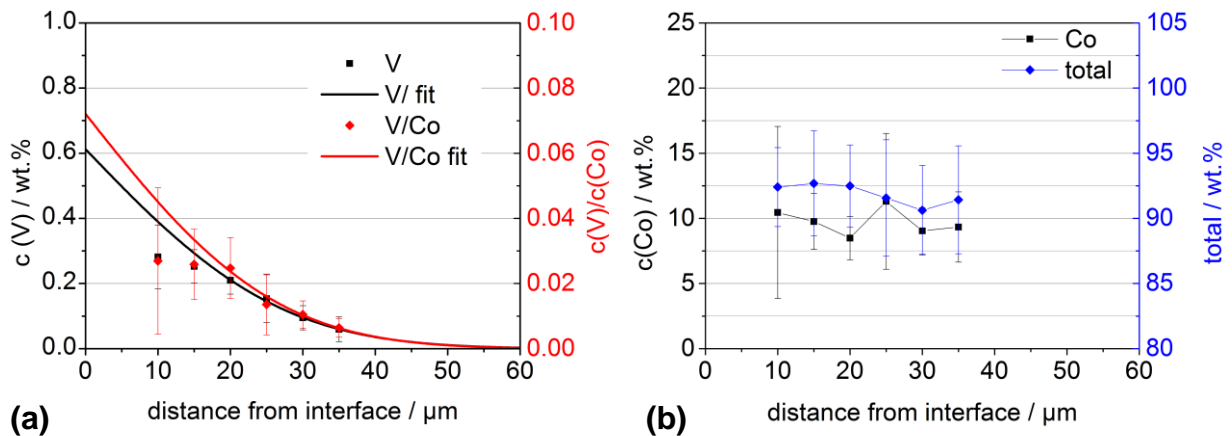


Figure 4-59: VCoG110-_40min, annealed at 1100°C for 40 min, low carbon, (a) as-measured and normalised EPMA-concentration profiles of vanadium, (b) concentration profile of cobalt and corresponding total of all measured elements.

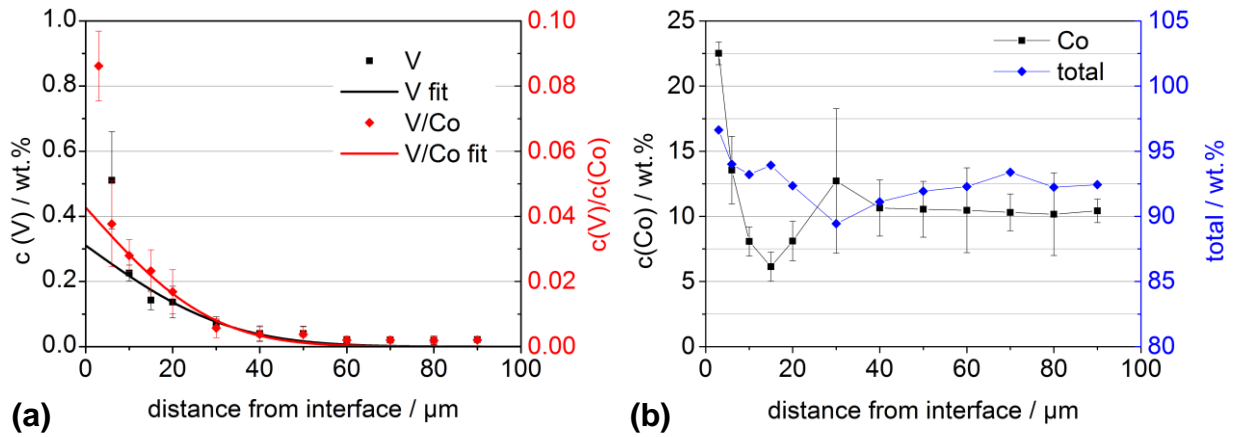


Figure 4-60: VCoG120-7min, annealed at 1200°C for 7 min, low carbon, (a) as-measured and normalised EPMA-concentration profiles of vanadium, (b) concentration profile of cobalt and corresponding total of all measured elements.

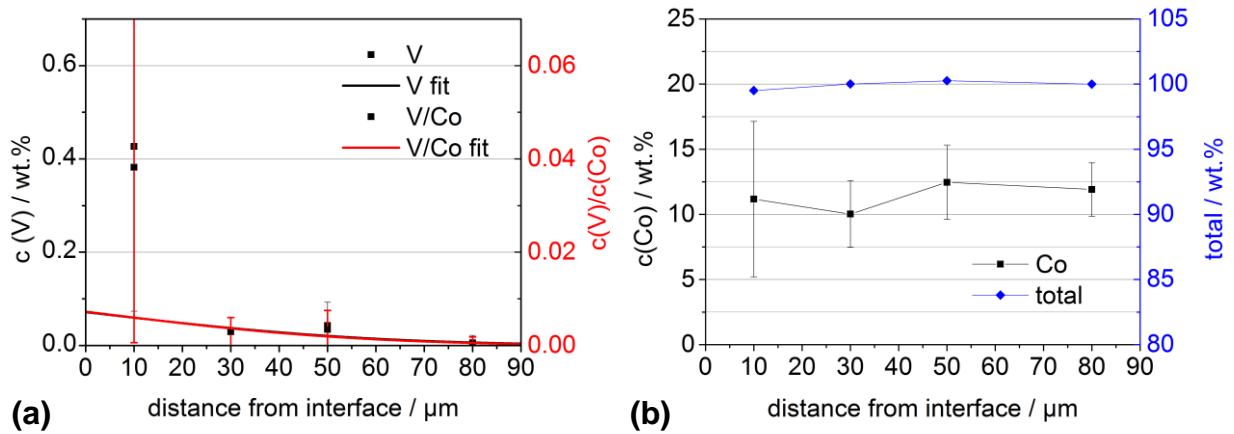


Figure 4-61: VCoG125-, annealed at 1250°C for 15 min, low carbon, (a) as-measured and normalised EPMA-concentration profiles of vanadium, (b) concentration profile of cobalt and corresponding total of all measured elements.

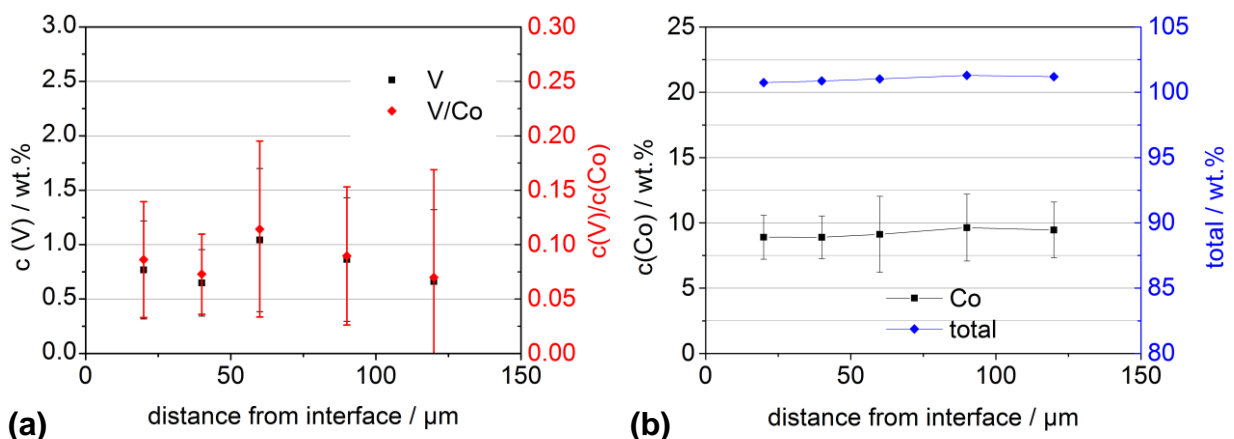


Figure 4-62: VCoG136-, annealed at 1360°C for 15 min, low carbon, (a) as-measured and normalised EPMA-concentration profiles of vanadium, (b) concentration profile of cobalt and corresponding total of all measured elements.

4.3.11 G-type diffusion couples with VC, mid carbon potential

The carbon potential of this sample series of G-type diffusion couples with VC and Co binder was adjusted within the WC+Co two-phase window. However, when interpreting the results it has to be kept in mind that the carbon potential can locally shift by the reaction of the two diffusion couple parts.

The sample VCoG105 was annealed at 1050°C for 15 min. As the results in Figure 4-63(a) show the diffusion depth is 30 μm yielding $D=1.09 \cdot 10^{-9} \text{ cm}^2/\text{s}$. For the sample VCoG115 annealed at 1150°C the diffusion depth and transport factor are increased to 80 μm and $D=6.6 \cdot 10^{-9} \text{ cm}^2/\text{s}$, respectively as shown in Figure 4-64(a). A further temperature increase to 1200°C delivers a transport factor of $D=1.18 \cdot 10^{-8} \text{ cm}^2/\text{s}$ which refers to a diffusion depth of 93 μm after 7 min annealing time as shown in Figure 4-65(a).

At 1250°C vanadium is transported by 207 μm after 15 min as shown for sample VCoG125 in Figure 4-66. For all the other evaluable samples in this project annealed at 1250°C much faster transport was measured, attributed to the –at least partially– liquid binder phase. But the transport factor of $D=4.96 \cdot 10^{-8} \text{ cm}^2/\text{s}$ clearly indicates solid phase diffusion since D would be by an order of magnitude higher in liquid phase.

For sample VCoG136, annealed at 1360°C for 15 min no evaluable concentration profile was measured as shown in Figure 4-67(a). Similar to the sample series with low carbon potential (see Table 4-12) a decline of the interface concentration with increasing temperature from $c(\text{V}/\text{Co})=0.077$ at 1050°C to $c(\text{V}/\text{Co})=0.042$ at 1250°C was measured as shown in Table 4-13. As can be seen from for the other samples in Figure 4-63(b) – Figure 4-67(b) no gradient formation was observed for any sample. At 1200°C the totals reach 100 wt% indicating samples with only minor residual porosity.

Table 4-13: Transport parameters and interface concentrations of vanadium in G-type diffusion couples with mid carbon potential.

Sample	Diffusion depth (μm)	D ($10^{-10} \text{ cm}^2/\text{s}$)	$c_0(\text{V}/\text{Co})$ (wt%)/(wt%)
VCoG105	30	10.9 ± 4.9	0.077 ± 0.023
VCoG115	80	65.7 ± 12.4	0.052 ± 0.005
VCoG120_7min	93	118.2 ± 9.7	0.049 ± 0.003
VCoG125	207	496.2 ± 69.5	0.042 ± 0.002
VCoG136	n.a.	n.a.	n.a.

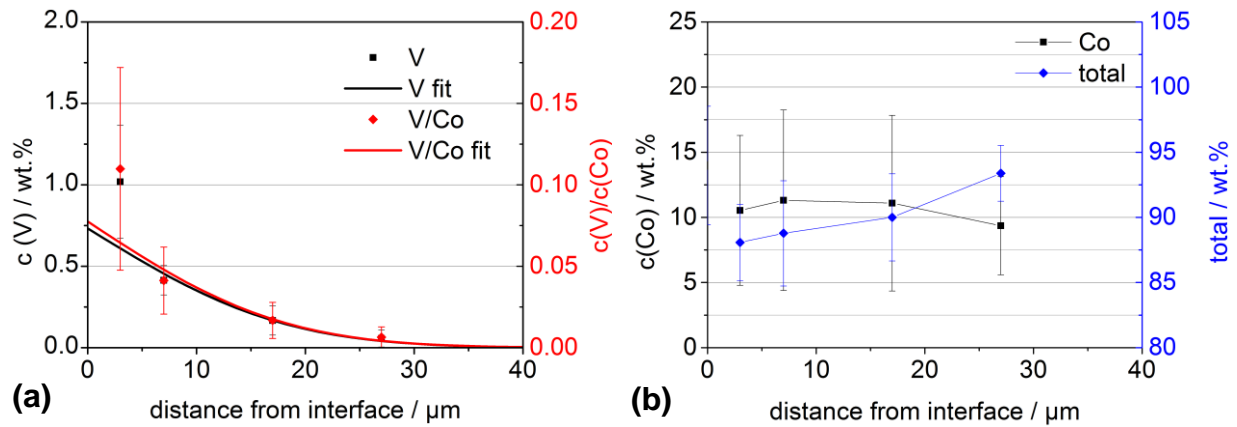


Figure 4-63: VCoG105, annealed at 1050°C for 15 min, mid carbon potential, (a) as-measured and normalised EPMA-concentration profiles of vanadium, (b) concentration profile of cobalt and corresponding total of all measured elements.

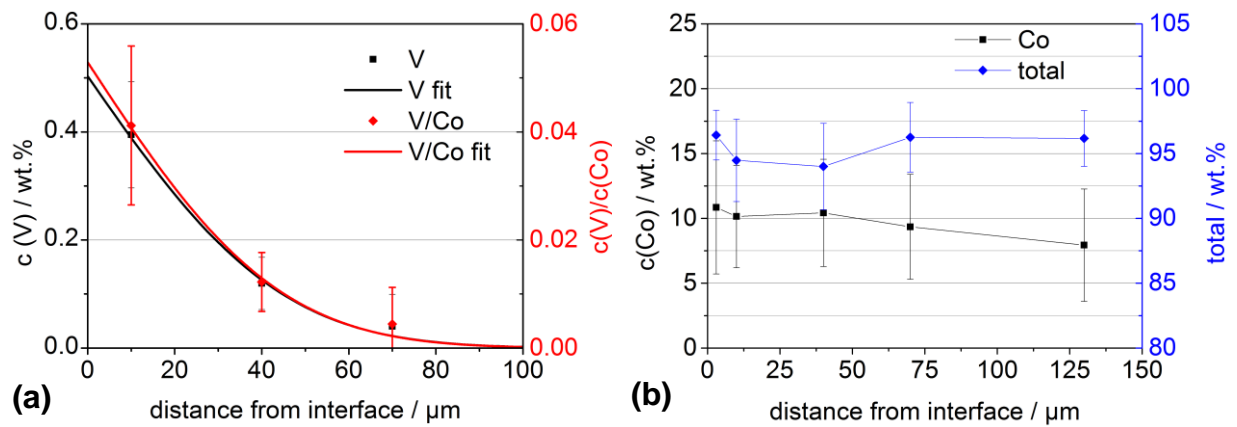


Figure 4-64: VCoG115, annealed at 1150°C for 15 min, mid carbon potential, (a) as-measured and normalised EPMA-concentration profiles of molybdenum, (b) concentration profile of cobalt and corresponding total of all measured elements.

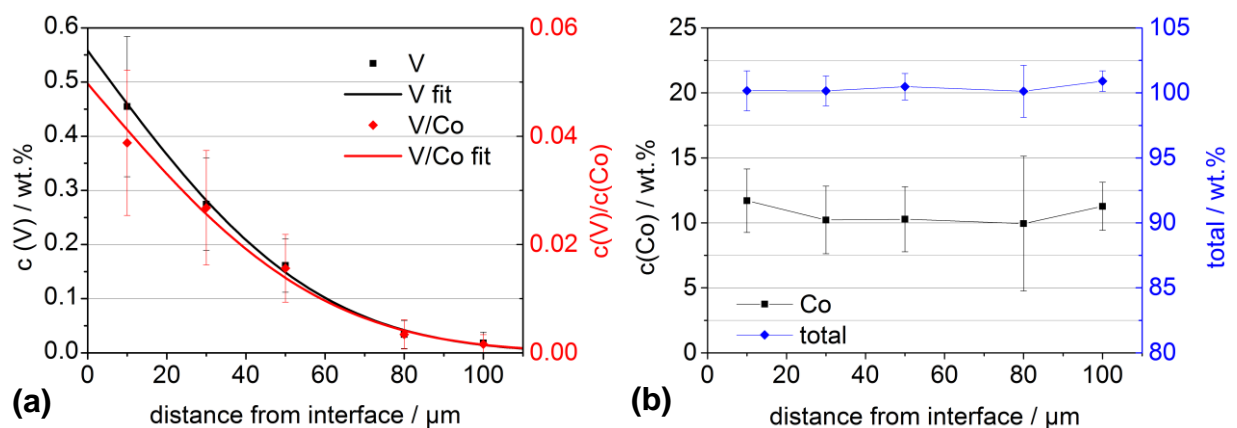


Figure 4-65: VCoG120_7min, annealed at 1200°C for 7 min, mid carbon potential, (a) as-measured and normalised EPMA-concentration profiles of molybdenum, (b) concentration profile of cobalt and corresponding total of all measured elements.

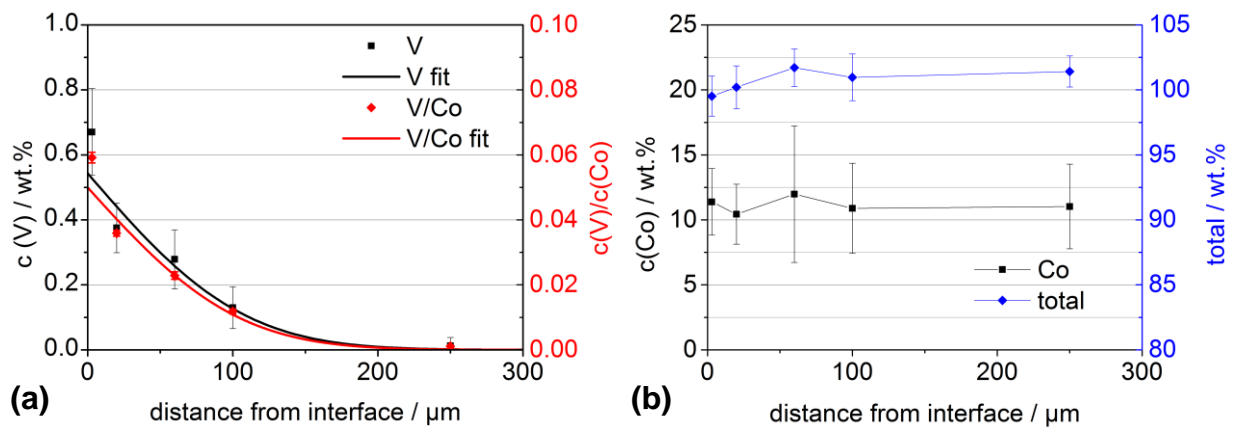


Figure 4-66: VCoG125, annealed at 1250°C for 15 min, mid carbon potential, (a) as-measured and normalised EPMA-concentration profiles of molybdenum, (b) concentration profile of cobalt and corresponding total of all measured elements.

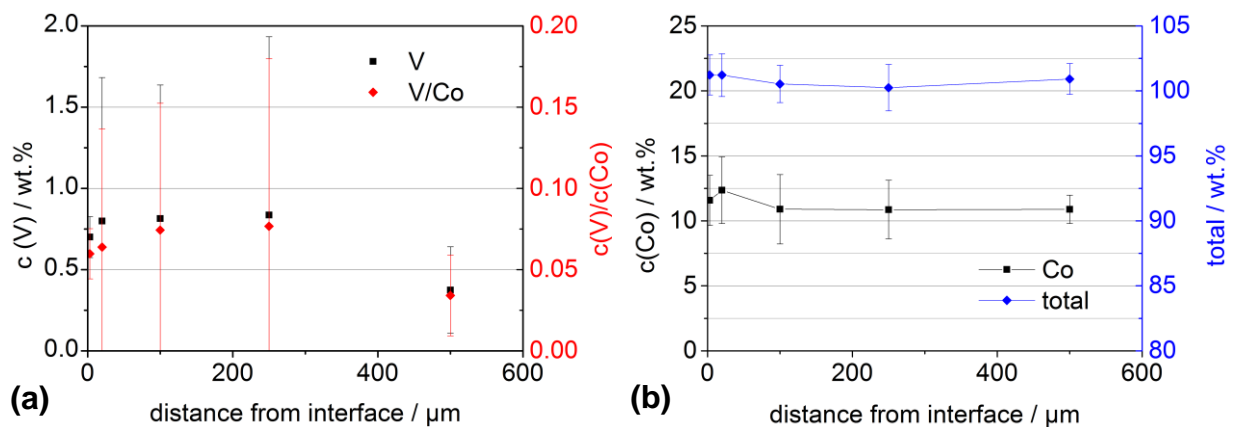


Figure 4-67: VCoG136, annealed at 1360°C for 15 min, mid carbon potential, (a) as-measured and normalised EPMA-concentration profiles of molybdenum, (b) concentration profile of cobalt and corresponding total of all measured elements.

4.3.12 G-type diffusion couples with VC, high carbon potential

This sample series of G-type diffusion couples was prepared with VC and Co binder. The carbon potential of the WC-Co part (WCo+) of the diffusion couple was fixed at high carbon potential. The latter refers to the presence of graphite phase after equilibrium formation. The carbon potential was confirmed by DTA, see section 4.6.1.1.

The sample VCoG105+ was annealed for 15 min at 1050°C. The resulting vanadium concentration profiles are depicted in Figure 4-68(a). The detection limit at these conditions is reached after 36 μm . The transport factor calculated from the normalised profile is $D=1.35 \cdot 10^{-9} \text{ cm}^2/\text{s}$. No large difference in the shape of the as-measured and the normalised profile appears. As can be seen from (b) the cobalt

concentration is around 10 wt% at all measured positions from interface. The particular line scans (data points) show a large standard deviation, which can be explained by the inhomogeneous cobalt distribution at such low temperatures. The LOM micrograph in Figure 4-76(a) appears dark, which is a sign for low reflection and hence high porosity of the sample. The first 40 μm from interface are more reflective, which is dedicated to higher density. This area exactly matches the diffusion depth of vanadium, represented by the green dashed line.

By sample VCoG105+_5Kmin a slower heating rate of 5 K/min was applied upon heat-up to 1050°C. The corresponding concentration profiles are shown in Figure 4-69(a). The transport factor determined from the profile is $D=1.2\cdot 10^{-9}$ cm²/s. This value is equal within the error range to the fast heated sample VCo105G+ as can be seen from Table 4-14. No cobalt gradient was found for this sample either (b). The total, however is slightly higher than for the fast heated sample, pointing to a higher densification.

Three samples at 1150°C were prepared with annealing times of 5 min, 15 min and 30 min. The concentration profiles after 5 min (sample VCoG115+_5min) can be seen in Figure 4-70(a). A strong deviation of the fitted model and the data points within 15 μm from the interface is observed. Such behaviour was as well found after 15 min (VCoG115+) and 30 min (VCoG115+_30min), see Figure 4-71(a) and Figure 4-72(a), respectively. The transport factors obtained from the three samples are in the range of $1.14 - 1.26\cdot 10^{-8}$ cm²/s and hence equal within the error range. The diffusion depth increases from 53 μm to 88 μm and 118 μm after 5, 15 and 30 min, respectively.

No formation of a cobalt gradient was observed as shown in Figure 4-70(b) – Figure 4-72(b). The microstructure after 15 min is illustrated by the LOM-micrograph in Figure 4-76(b). Especially the bulk shows an interesting behaviour. Roundish structures of 50–200 μm diameter are observed, which seem to have densified faster as compared to the darker areas between.

At 1200°C the vanadium is distributed by 146 μm already after an annealing time of 7 min, as depicted in Figure 4-73(a). The binder phase, even if saturated with vanadium, is still expected in solid-state (solidus temperature 1254°C). The transport factor was determined $3.21\cdot 10^{-8}$ cm²/s.

The annealing temperature of sample VCoG125+ is very close to the solidus temperature of a vanadium saturated hardmetal. The GGI-containing diffusion couple component VWCo is still in solid-state as proofed by DSC, see Figure 4-140. However, liquid phase at the interface cannot be completely excluded from these considerations. From the LOM-micrograph in Figure 4-76(c) it turns out that the microstructure at the interface is identical to the bulk. However, when comparing the interface solubilities c_0 a sudden decrease from $c_0(\text{Cr/Co})=0.043$ at 1200°C to $c_0(\text{Cr/Co})=0.15$ is observed which is a strong hint for the local presence of liquid phase. The concentration profile is shown in Figure 4-74(a), the corresponding transport factor was measured $1.58 \cdot 10^{-7} \text{ cm}^2/\text{s}$. Experimental data points are only available within the first $100 \mu\text{m}$, but the diffusion depth is $390 \mu\text{m}$. This causes a strong uncertainty of $\pm 60\%$ rel. in the fit of the concentration profile. Furthermore, since there is an indication for the appearance of local liquid phase more data points from $100\text{--}390 \mu\text{m}$ would be required in order to determine the real concentration profile. The sample is subsequently not used for the determination of the activation energy in (compare section 5.2).

For the sample at 1360°C (VCoG136+) the binder phase in both parts of the diffusion couple is expected to be in liquid state, independent from the vanadium concentration. However, upon heat-up the liquid phase forms earlier close to the interface as compared to the bulk. Due to the fast heating rate of $100\text{K}/\text{min}$ this influence was kept low. The microstructure of this sample is shown in Figure 4-76(d). No significant differences are observed between bulk and interface. However, a close look at the grain size reveals that even within the short annealing time of 15 min the significant WC grain growth is observed which is suppressed by vanadium close to the interface. The transport factor was calculated $D=2.92 \cdot 10^{-7} \text{ cm}^2/\text{s}$ from the corresponding vanadium concentration profile, compare Figure 4-75(a). As for the sample at 1250°C not enough data points are available for a sufficient description of the concentration profile, this value can only be a rough estimation of the vanadium diffusion at 1360°C . Also no conclusions can be drawn regarding a possible cobalt gradient due to the lack of data points.

When comparing the interface concentrations c_0 in Table 4-14 no clear trend as a function of temperature or annealing time can be found. Since the vanadium concentration is increasing with rising temperature the determined c_0 values do not

necessarily represent the solubilities of vanadium in cobalt binder phase. This effect is further discussed in section 5.6.

Table 4-14: Transport parameters and interface concentrations of vanadium in G-type diffusion couples with high carbon potential (series VCoG+).

Sample	Diffusion depth (μm)	D ($10^{-10}\text{cm}^2/\text{s}$)	$c_0(\text{V}/\text{Co})$ (wt%)/(wt%)
VCoG105+	36	13.5 ± 2.7	0.041 ± 0.005
VCoG105+5Kmin	26	12.2 ± 5.2	0.008 ± 0.002
VCoG115+_5min	53	114.3 ± 21.7	0.025 ± 0.003
VCoG115+	88	121.2 ± 26.5	0.033 ± 0.004
VCoG115+_30min	118	126.2 ± 58.4	0.025 ± 0.007
VCoG120+_7min	146	321.8 ± 73.8	0.043 ± 0.003
VCoG125+	390	1580 ± 880	0.152 ± 0.016
VCoG136+	570	2920 ± 930	0.139 ± 0.034

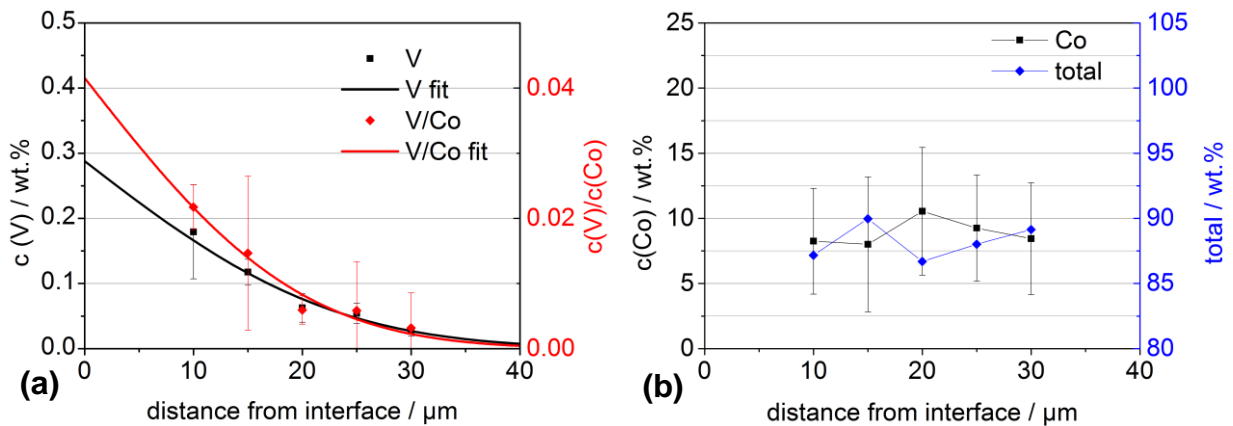


Figure 4-68: VCoG105+, annealed at 1050°C for 15 min, high carbon potential, (a) as-measured and normalised EPMA-concentration profiles of vanadium, (b) concentration profile of cobalt and corresponding total of all measured elements.

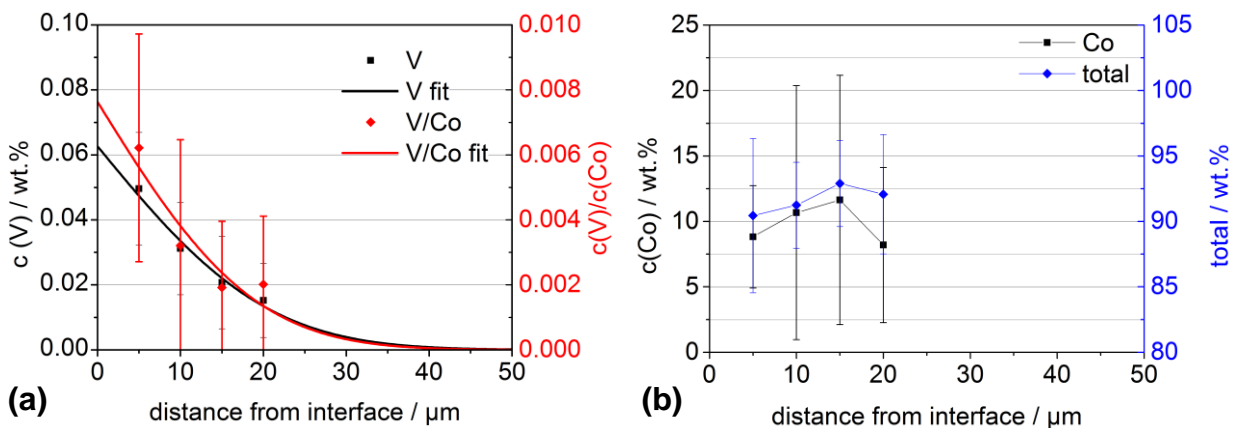


Figure 4-69: VCoG105+5Kmin, annealed at 1050°C for 15 min, 5K/min heating rate high, carbon potential; (a) as-measured and normalised EPMA-concentration profiles of vanadium, (b) concentration profile of cobalt and corresponding total of all measured elements.

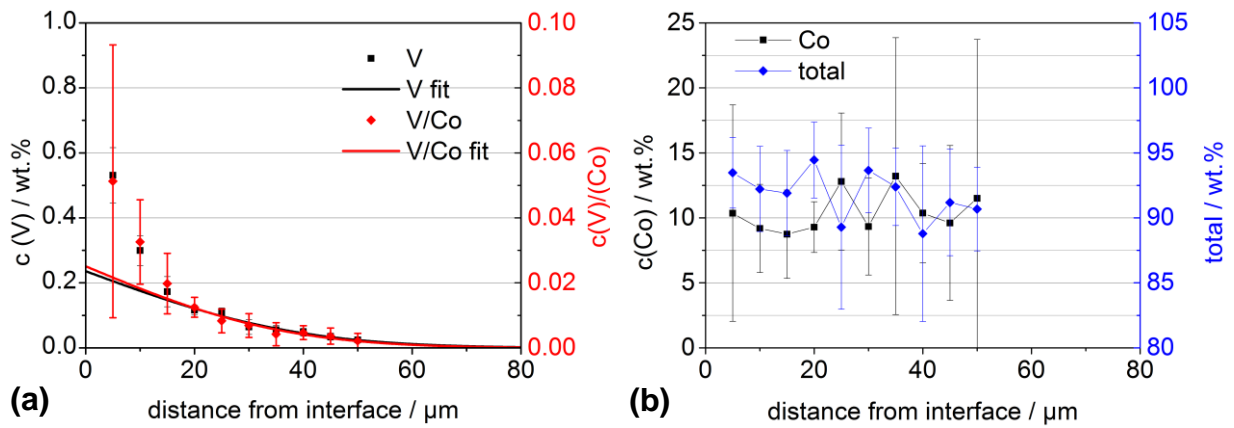


Figure 4-70: VCoG115+_5min, annealed at 1150°C for 5 min, high carbon potential, (a) as-measured and normalised EPMA-concentration profiles of vanadium, (b) concentration profile of cobalt and corresponding total of all measured elements.

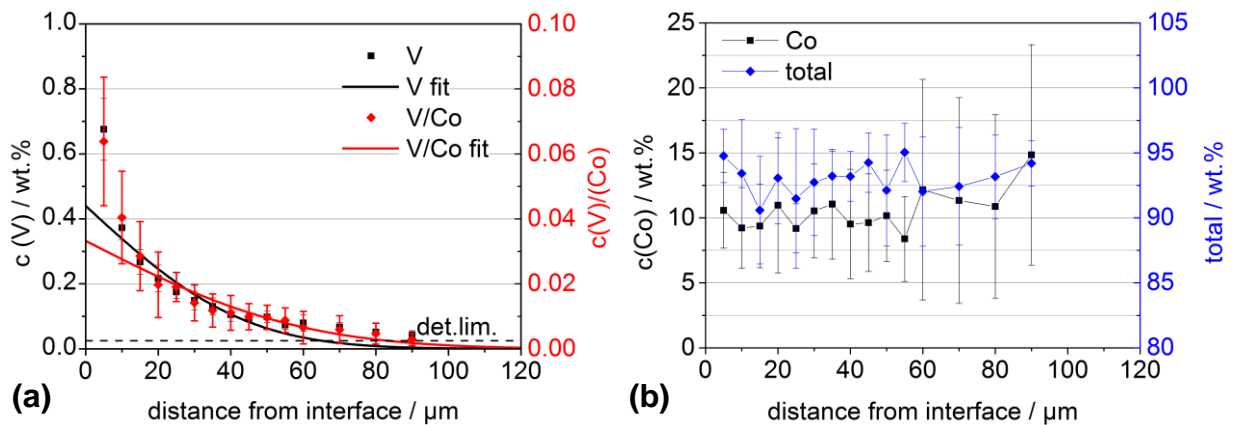


Figure 4-71: VCoG115+ annealed at 1150°C for 15 min, high carbon potential, (a) as-measured and normalised EPMA-concentration profiles of vanadium, (b) concentration profile of cobalt and corresponding total of all measured elements.

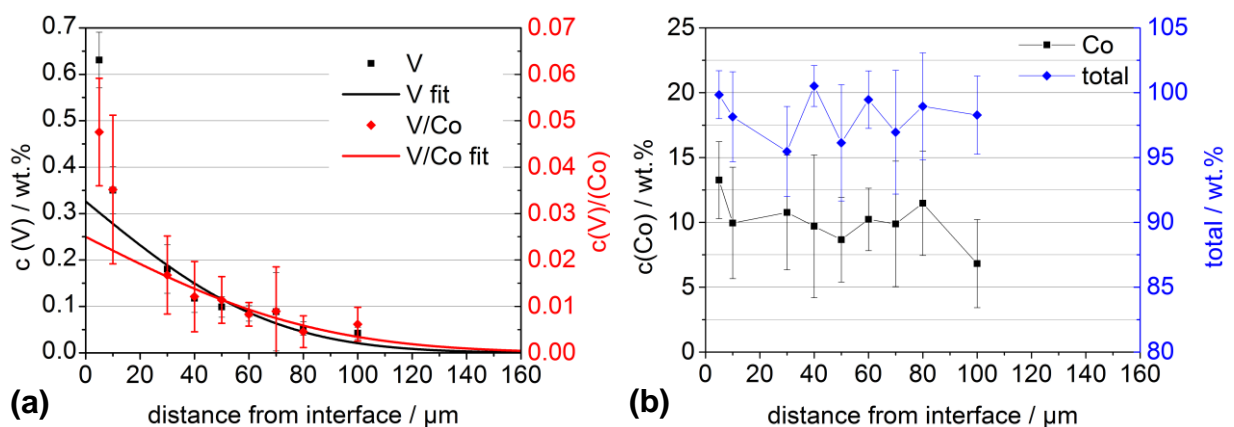


Figure 4-72: VCoG115+_30min, annealed at 1150°C for 30 min, high carbon potential, (a) as-measured and normalised EPMA-concentration profiles of vanadium, (b) concentration profile of cobalt and corresponding total of all measured elements.

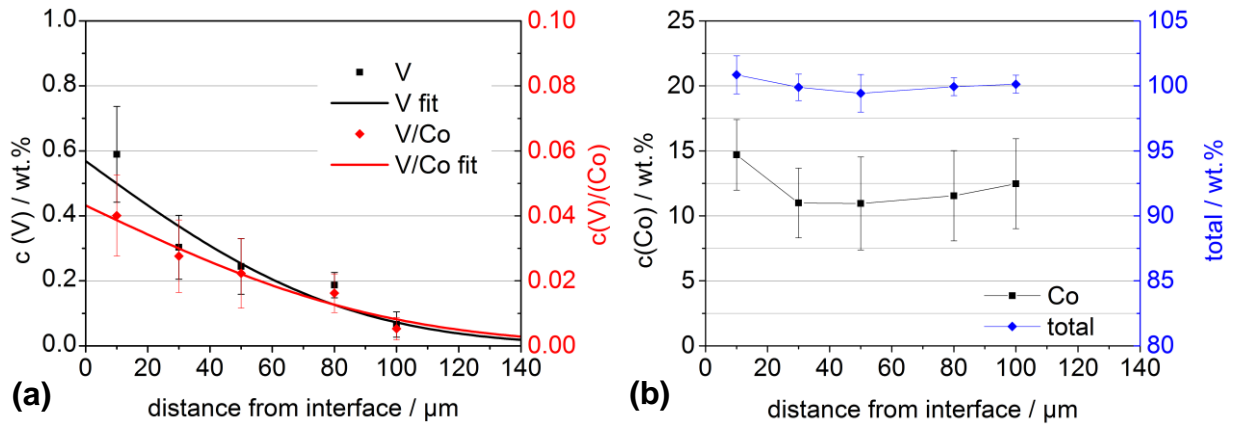


Figure 4-73: VCoG120+_7min, annealed at 1200°C for 7 min, high carbon potential, (a) as-measured and normalised EPMA-concentration profiles of vanadium, (b) concentration profile of cobalt and corresponding total of all measured elements.

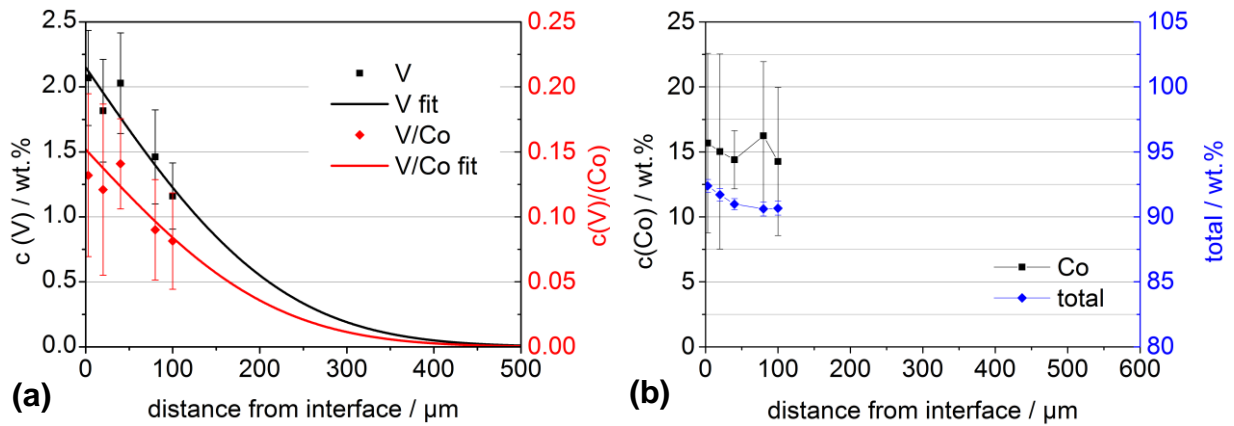


Figure 4-74: VCoG125+, annealed at 1250°C for 15 min, high carbon potential, (a) as-measured and normalised EPMA-concentration profiles of vanadium, (b) concentration profile of cobalt and corresponding total of all measured elements.

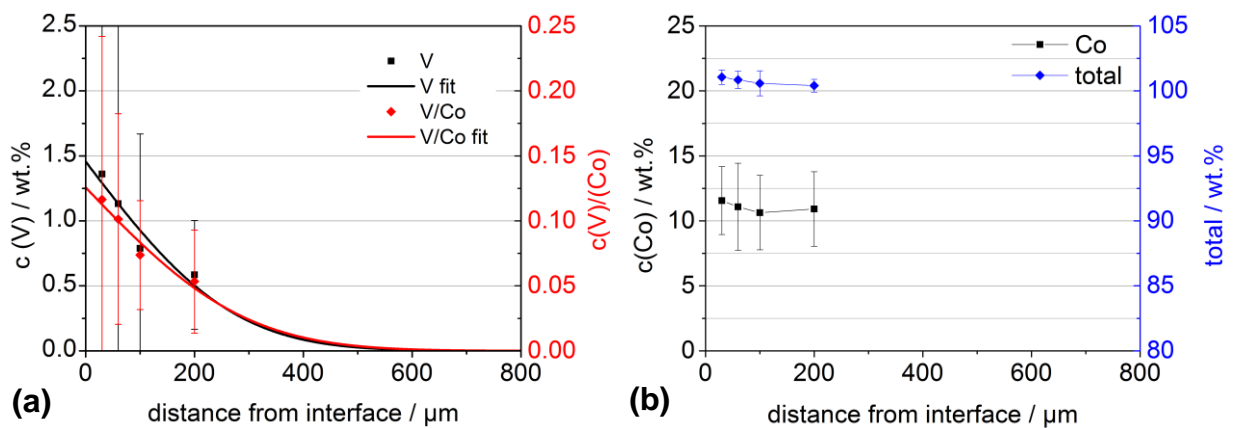


Figure 4-75: VCoG136+, annealed at 1360°C for 15 min, high carbon potential, (a) as-measured and normalised EPMA-concentration profiles of vanadium, (b) concentration profile of cobalt and corresponding total of all measured elements.

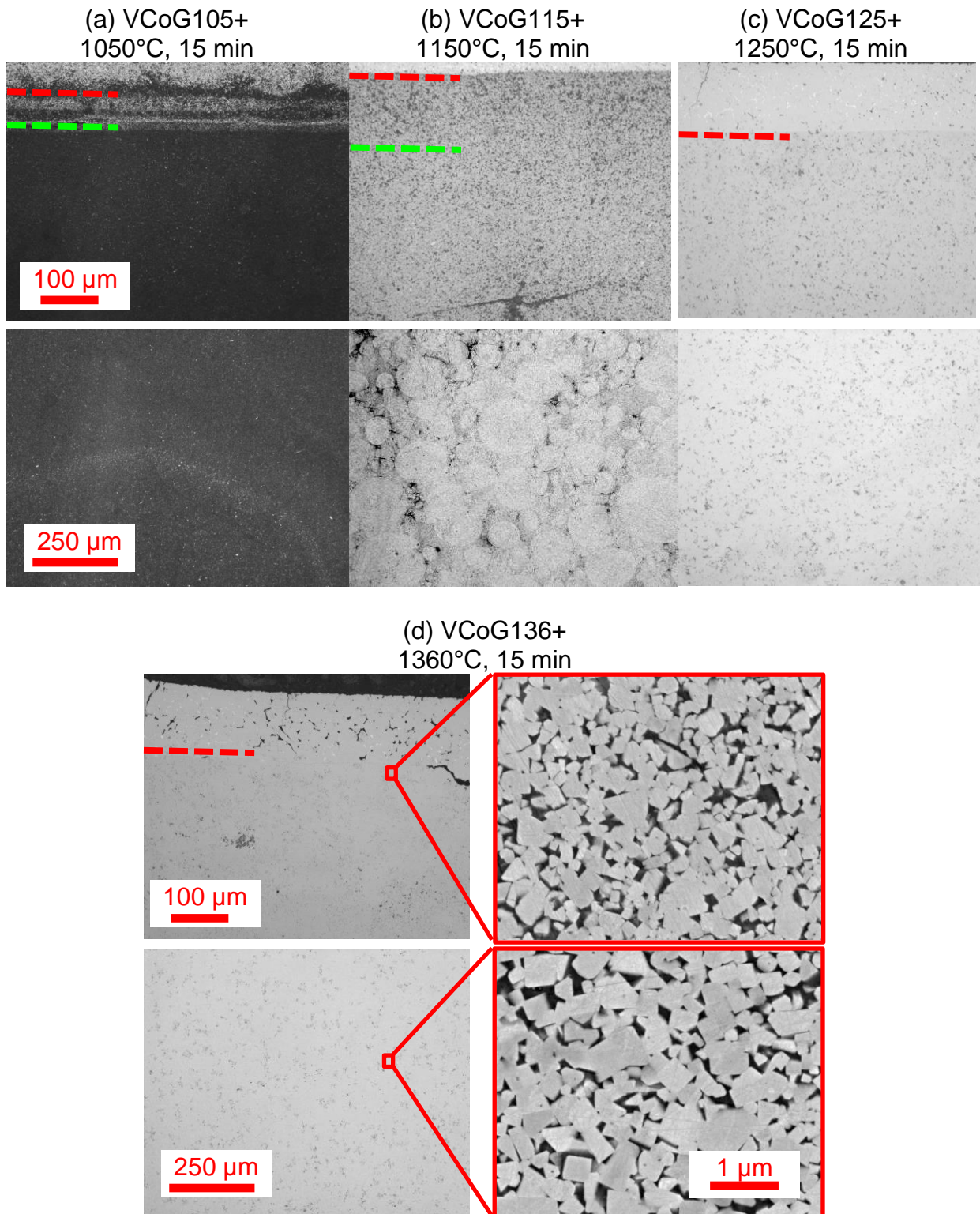


Figure 4-76: G-type diffusion couples VCoG+ at various temperatures: LOM and BSE micrographs of interface and bulk. Dashed red lines mark the interfaces, dashed green lines the diffusion depth of vanadium. At 1250 and 1360 °C the diffusion depth is larger than the image frame height.

4.3.13 G-type diffusion couples with VC and nano-Co

In this sample series G-type diffusion couples with GGI=vanadium were prepared with a nano-sized cobalt instead of the conventional grade. For all three samples annealed at 1050°C, 1100°C and 1150°C the vanadium concentration profiles show a good accordance of the model and the as-measured data as illustrated in Figure 4-77(a), Figure 4-78(a) and Figure 4-79(a), respectively. The transport factors increase from $3.4 \cdot 10^{-9}$ cm²/s at 1050°C to $4.4 \cdot 10^{-10}$ cm²/s at 1100°C and $1.9 \cdot 10^{-8}$ cm²/s at 1150°C. The fitted interface concentrations remain stable at $c(\text{V}/\text{Co})=0.040$. No cobalt gradients were formed as can be seen from cobalt concentrations in Figure 4-77(b) – Figure 4-79(b). The totals increase with rising temperature, indicating decreasing porosity. An overview of all samples is given in Table 4-15

Table 4-15: Transport parameters and interface concentrations of vanadium in G-type diffusion couples with nano-cobalt and mid carbon potential.

Sample	Diffusion depth (μm)	D (10 ⁻¹⁰ cm ² /s)	c ₀ (V/Co) (wt%)/(wt%)
VCo _n G105	36	34.4 ± 5.2	0.040 ± 0.006
VCo _n G110	54	44.4 ± 16.8	0.037 ± 0.010
VCo _n G115	78	96.0 ± 7.6	0.037 ± 0.002

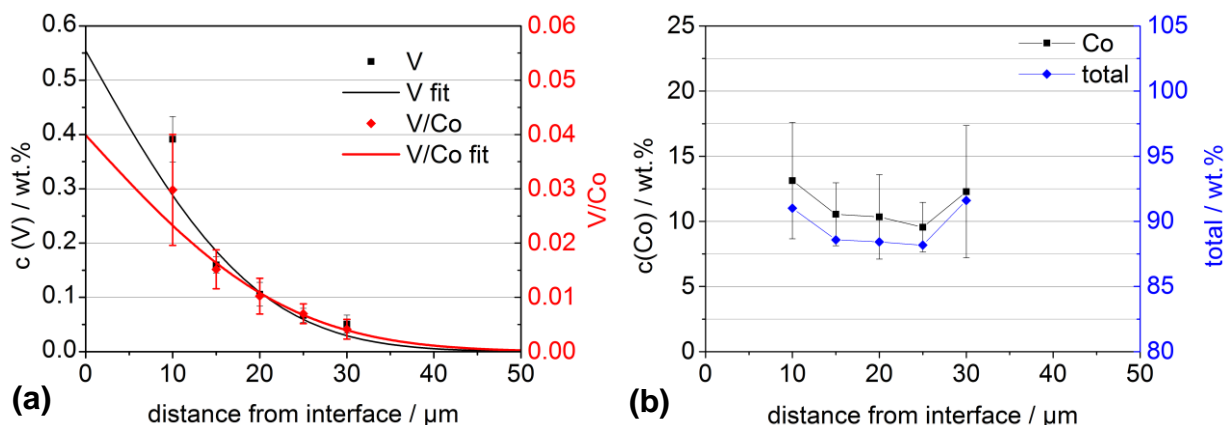


Figure 4-77: VCo_nG105, annealed at 1050°C for 15 min, mid carbon potential, nano-Co, (a) as-measured and normalised EPMA-concentration profiles of vanadium, (b) concentration profile of Co and corresponding total of all measured elements.

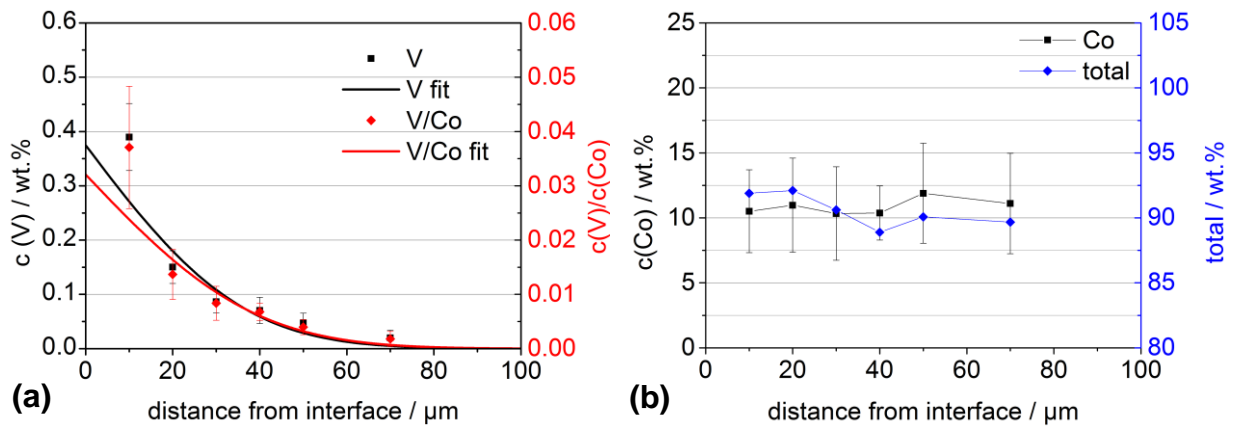


Figure 4-78: VCo_nG110, annealed at 1100°C for 15 min, mid carbon potential, nano-Co
 (a) as-measured and normalised EPMA-concentration profiles of vanadium
 (b) concentration profile of Co and corresponding total of all measured elements

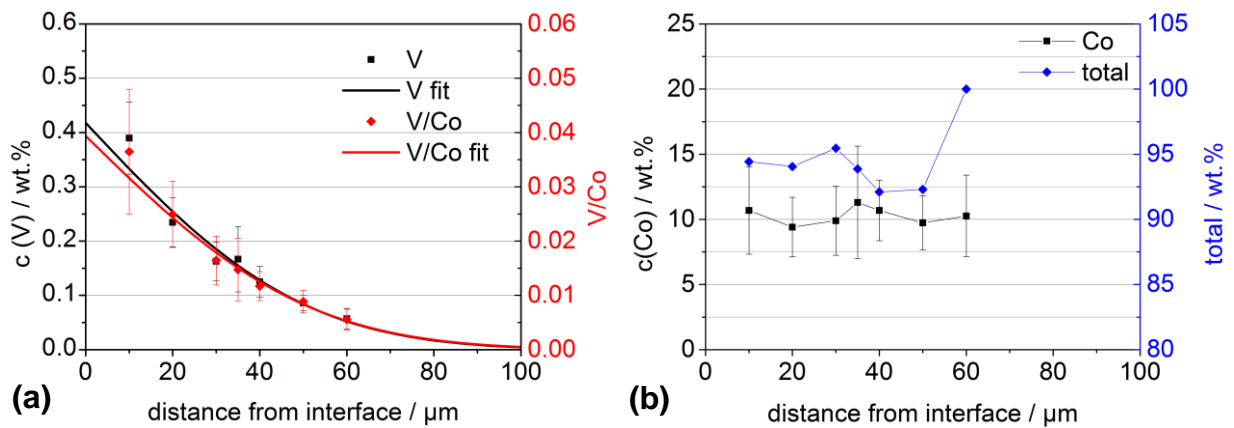


Figure 4-79: VCo_nG115, annealed at 1150°C for 15 min, mid carbon potential, nano-Co,
 (a) as-measured and normalised EPMA-concentration profiles of vanadium,
 (b) concentration profile of Co and corresponding total of all measured elements.

4.3.14 G-type diffusion couples with varying compaction pressures

While G-type samples of other series are prepared with a compaction pressure of 240 MPa in this series G-type couples with GGI=vanadium were prepared with reduced compaction pressures, resulting in reduced green densities. All samples were annealed at 1150°C for 30 min.

Samples VCoG115+2kN, VCoG115+5kN, VCoG115+10kN, VCoG115+20kN, prepared at compaction pressures of 15, 39, 78 and 155 MPa are shown in Figure 4-80(a), Figure 4-81(a), Figure 4-82(a) and Figure 4-83(a), respectively. The $c(V)/c(Co)$ concentration profiles are comparable for all compaction pressures. The transport factors of the samples 39, 78 and 155 MPa are around $D=8.7 \cdot 10^{-9} \text{ cm}^2/\text{s}$

and equal within the error range as can be seen from Table 4-16, whereas it is by 50% higher for the samples pressed at lowest pressure of 15 MPa. The same trend can be found for the diffusion depth, while the interface concentrations c_0 are equal within the error range for all samples. A drastic increase in interface concentration within the first 10 μm from the interface is observed for all samples which is an artefact of the method as discussed in section 4.1. No significant cobalt gradient was found for any of the samples as shown in Figure 4-80(b) – Figure 4-83(b). The totals and, subsequently the density tend to lower values towards the interface for samples at low compaction pressures of 15 and 39 MPa.

Table 4-16: Transport parameters and interface concentrations of vanadium in G-type diffusion couples with nano-cobalt and mid carbon potential.

Sample	Compaction pressure (MPa)	Diffusion depth (μm)	D ($10^{-10}\text{cm}^2/\text{s}$)	$c_0(\text{V}/\text{Co})$ (wt%)/ (wt%)
VCoG115+2kN	15	126	131.8 ± 14.0	0.030 ± 0.001
VCoG115+5kN	39	106	88.7 ± 3.5	0.034 ± 0.001
VCoG115+10kN	78	95	87.2 ± 2.5	0.023 ± 0.002
VCoG115+20kN	155	103	86.6 ± 27.9	0.032 ± 0.002

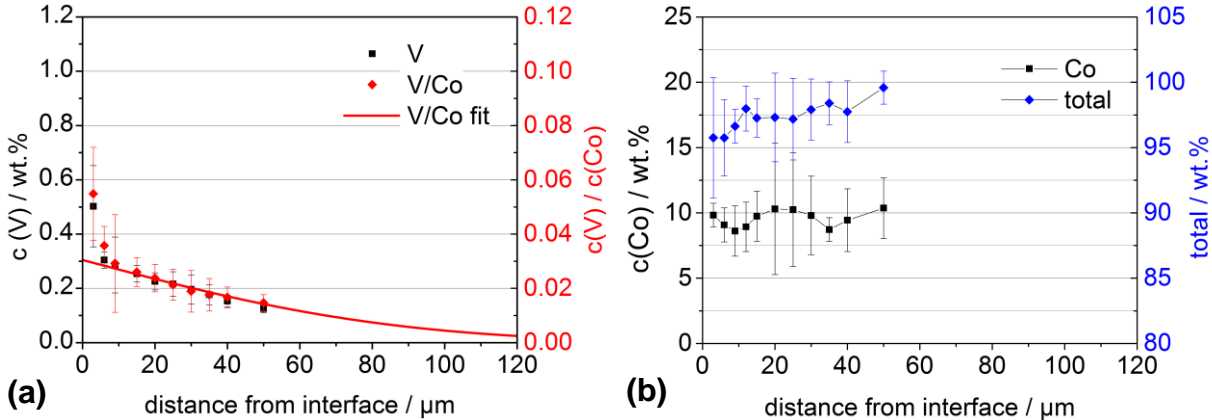


Figure 4-80: VCoG115+2kN, annealed at 1150°C for 30 min, 2kN pressing force, (a) as-measured and normalised EPMA-concentration profiles of vanadium, (b) concentration profile of cobalt and corresponding total of all measured elements.

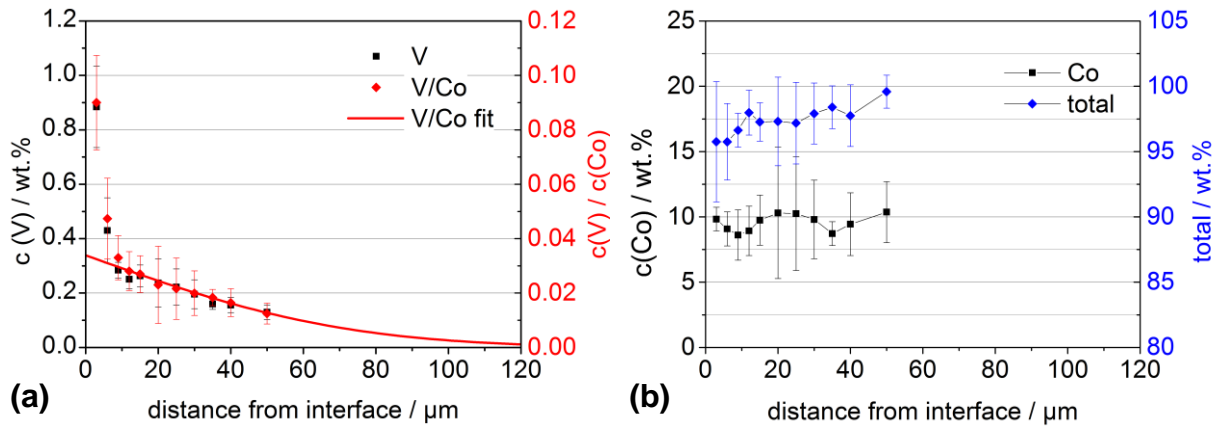


Figure 4-81: VCoG115+5kN, annealed at 1150°C for 30 min, 5kN pressing force, (a) as-measured and normalised EPMA-concentration profiles of vanadium, (b) concentration profile of cobalt and corresponding total of all measured elements.

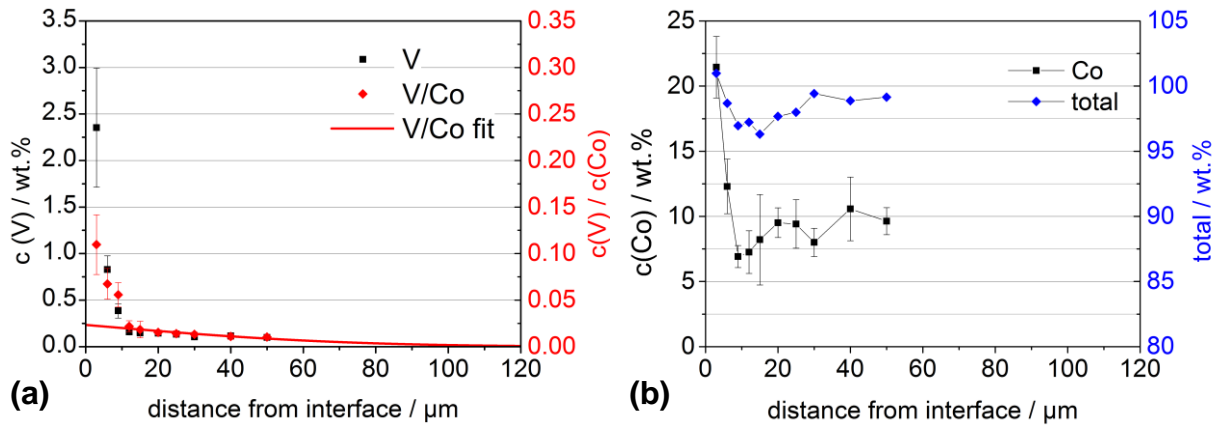


Figure 4-82: VCoG115+10kN, annealed at 1150°C for 30 min, 10kN pressing force, (a) as-measured and normalised EPMA-concentration profiles of vanadium, (b) concentration profile of cobalt and corresponding total of all measured elements.

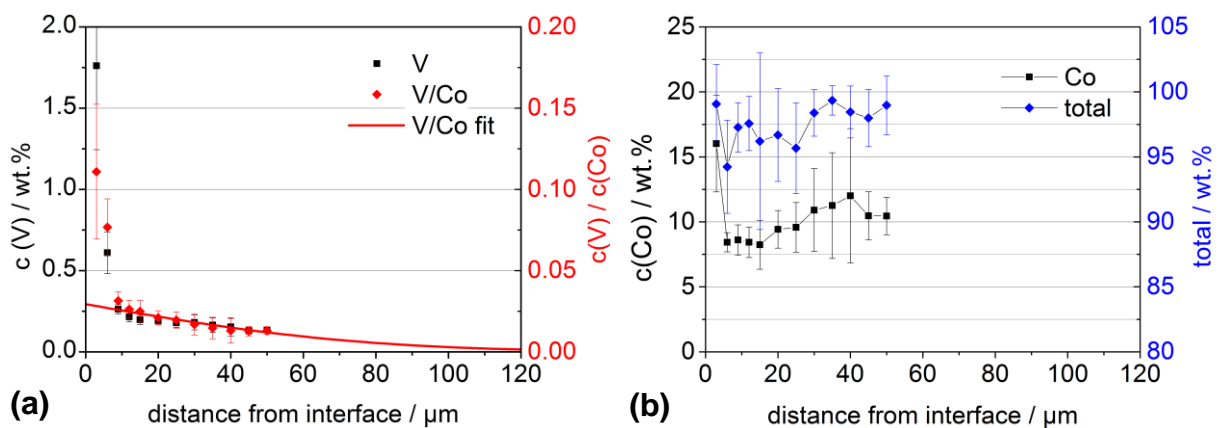


Figure 4-83: VCoG115+20kN, annealed at 1150°C for 30 min, 20kN pressing force, (a) as-measured and normalised EPMA-concentration profiles of vanadium, (b) concentration profile of cobalt and corresponding total of all measured elements.

4.3.15 G-type diffusion couples with VC annealed in N₂ or CO atmosphere

The samples VCoG115-N and VCoG115+N prepared with low and high carbon potential, respectively were annealed in 400 mbar nitrogen at 1150°C for 15 min. The resulting vanadium concentration profiles of the low-carbon sample are shown in Figure 4-84(a). It can be seen that both the normalised and the as-measured concentration profile have equal shape and no cobalt gradient is formed (b). The transport factor was measured $D=2.1 \cdot 10^{-9} \text{ cm}^2/\text{s}$ and the interface concentration is $c(\text{V}/\text{Co})=0.024$. While the interface concentration is slightly decreased to $c(\text{V}/\text{Co})=0.017$ for the high carbon sample the transport factor of $D=2.6 \cdot 10^{-9} \text{ cm}^2/\text{s}$ is equal within the error range as can be seen from the results in Figure 4-85(a). Also no significant cobalt gradient was formed (b).

When CO is used instead N₂ as in case of sample VCoG115+CO in Figure 4-86(a) the transport factor of $D=2.4 \cdot 10^{-9} \text{ cm}^2/\text{s}$ and interface concentration of $c(\text{V}/\text{Co})=0.019$ are comparable to those of the samples prepared in nitrogen. An overview of the corresponding values of this series is given in Table 4-17.

It has to be remarked that for all three samples only a few samples were used for fitting the model to the data, since data points within 10 μm from the interface and below the detection limit of 0.02 wt% were omitted. As a consequence the relative error ranges for the transport factors are up to ±30% as in case of sample VCoG115+N.

Table 4-17: Transport parameters and interface concentrations of vanadium in G-type diffusion couples annealed in 400 mbar CO or N₂ atmosphere.

Sample	Diffusion depth (μm)	D (10 ⁻¹⁰ cm ² /s)	c ₀ (V/Co) (wt%)/(wt%)
VCoG115-N	126	21.2 ± 3.2	0.024 ± 0.003
VCoG115+N	106	25.8 ± 7.2	0.017 ± 0.003
VCoG115+CO	95	24.3 ± 4.4	0.019 ± 0.002

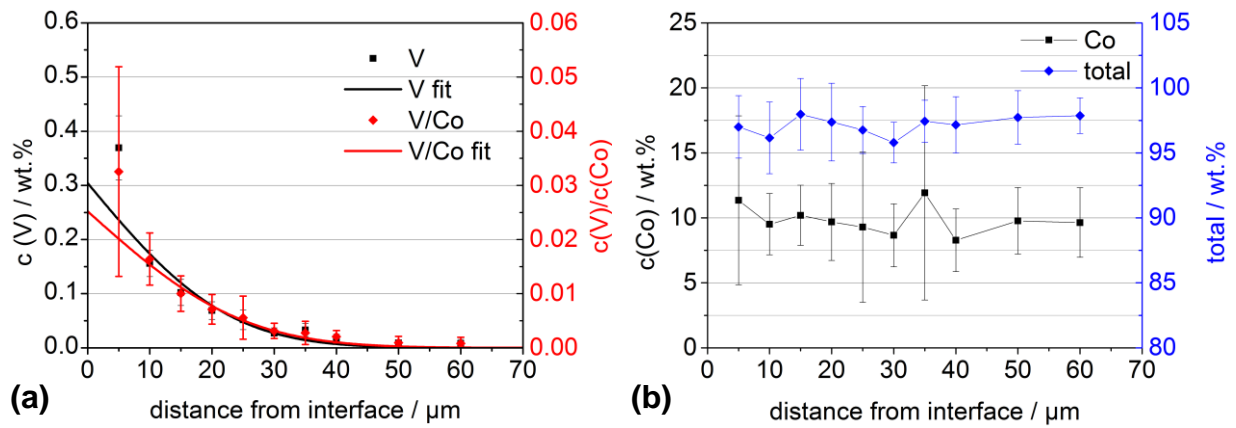


Figure 4-84: VCoG115-N, annealed at 1150°C for 15 min, low carbon, N₂ atmosphere, (a) as-measured and normalised EPMA-concentration profiles of vanadium, (b) concentration profile of cobalt and corresponding total of all measured elements.

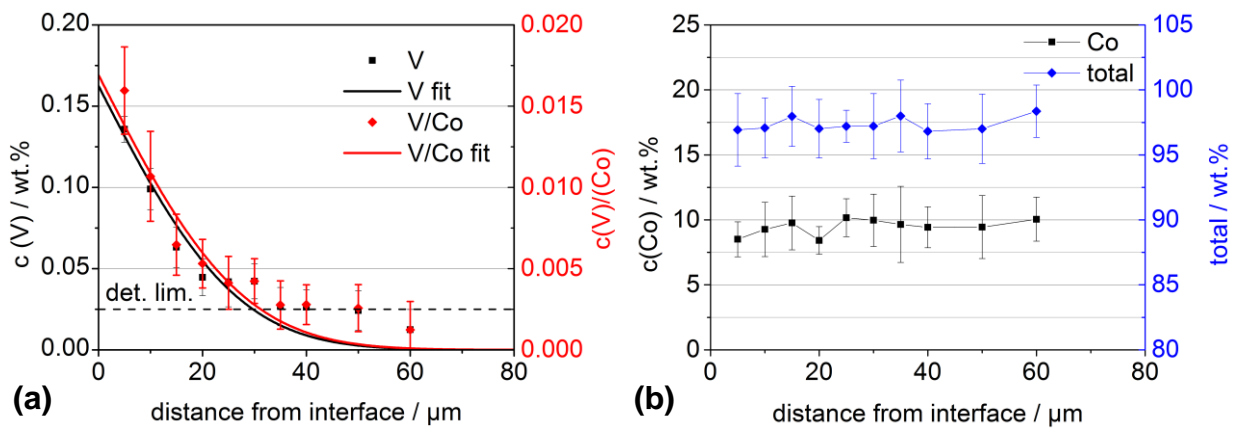


Figure 4-85: VCoG115+N, annealed at 1150°C for 15 min, high carbon, N₂ atmosphere, (a) as-measured and normalised EPMA-concentration profiles of vanadium, (b) concentration profile of cobalt and corresponding total of all measured elements.

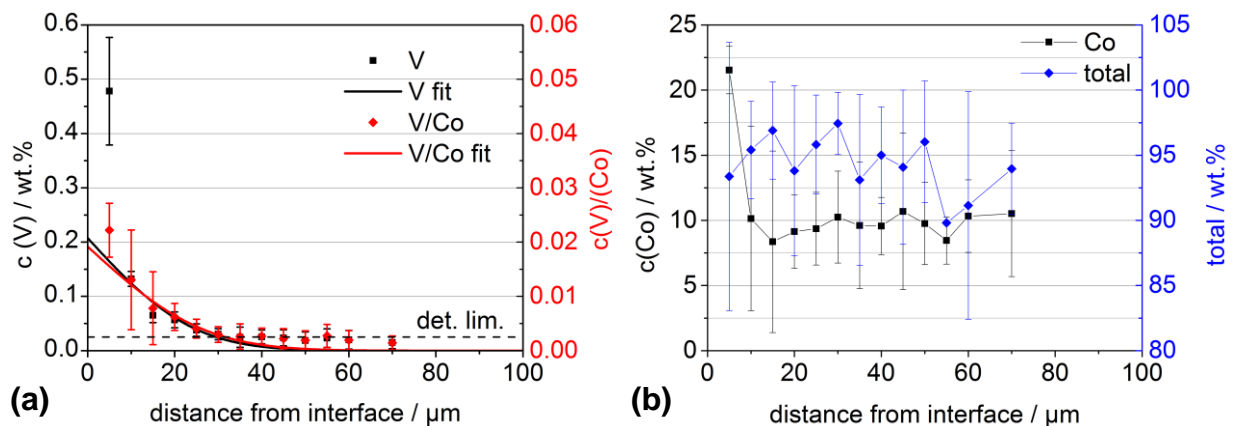


Figure 4-86: VCoG115+CO, annealed at 1150°C for 15 min, high carbon, CO atmosphere, (a) as-measured and normalised EPMA-concentration profiles of vanadium, (b) concentration profile of cobalt and corresponding total of all measured elements.

4.3.16 G-type diffusion couples with alternative binder alloys

A series of G-type diffusion couples was prepared with alternative binder alloys. All samples were annealed for 15 min at 1150°C.

The chromium concentration profiles of sample C19G115+ prepared with Fe/Ni binder are illustrated in Figure 4-87(a) while (b) shows the corresponding concentration profiles of Fe and Ni. A significant deviation of the as-measured and the normalised chromium profile is observed for this sample. However, the normalised profile shows excellent accordance with the fitted model while this is not the case for the as-measured data. The deviation of the as-measured data can be explained with a strong scatter of the binder concentrations. The latter is caused by a strong scatter of the total-value and, hence by microstructural inhomogeneity or porosity which can be seen by the correlation of the total and the nickel concentration. The transport factor was calculated $D=3 \cdot 10^{-8} \text{ cm}^2/\text{s}$ and the corresponding interface concentration $c_0(\text{Cr/binder})=0.065$.

When Fe/Co/Ni binder is used in case of sample C424G115+ the interface concentration is equal $c_0(\text{Cr/binder})=0.065$ as can be seen from Figure 4-88(a) while the transport factor of $4.3 \cdot 10^{-8} \text{ cm}^2/\text{s}$ is significantly higher as compared to Fe/Ni binder. An excellent accordance of the normalised and the as-measured data as well as the fitted model was observed. Consequently no significant scatter of the binder component concentrations or the total was observed as can be seen from Figure 4-88(b). However, while for distances higher than 100 μm from the interface equal concentrations for Fe and Ni were measured the concentration of nickel increases in relation to Fe for shorter distances from the interface. The reasons are further discussed in section 5.5.4.

The sample V19G115+ was prepared with vanadium as GGI and Fe/Ni binder. As illustrated in Figure 4-89(a) the interface concentration of $c(\text{V/binder})=0.02$ is significantly lower as compared to the sample with chromium, same applies for the transport factor of $D=6.7 \cdot 10^{-9} \text{ cm}^2/\text{s}$. Again a deviation of the normalised and the as-measured data was observed for this binder alloy. As can be seen from Figure 4-89 (b) a strong scatter of the nickel concentration was measured while almost no scatter of the total was observed.

Similar to the effects in chromium-containing samples the interface concentrations are equal within the error range while the transport factor of $D=1.2 \cdot 10^{-8} \text{ cm}^2/\text{s}$ is significantly higher for the sample V424G115+ with Fe/Co/Ni binder alloy as shown in Figure 4-90(a). The normalised concentrations are higher than expected when compared to the as-measured data. Though a binder phase gradient could explain this effect no such gradient was observed as shown in Figure 4-90(b). The reasons for the deviation are further discussed in section 5.6. While for the chromium-containing sample with Fe/Co/Ni binder a relative Ni/Fe gradient was observed this is not the case for V424G115+. An overview of the values calculated from the normalised chromium and vanadium concentrations is given in Table 4-18.

Table 4-18: Transport parameters and interface concentrations of vanadium and chromium in G-type diffusion couples with alternative binder alloys.

Sample	Binder alloy	Diffusion depth (μm)	D ($10^{-10} \text{ cm}^2/\text{s}$)	$c_0(\text{GGI}/\text{binder})$
C19G115+	Fe/Ni	122	301.2 ± 21.9	0.065 ± 0.002
C424G115+	Fe/Ni	145	430 ± 16.2	0.065 ± 0.001
V19G115+	Fe/Co/Ni	56	66.6 ± 3.8	0.020 ± 0.001
V424G115+	Fe/Co/Ni	75	121.1 ± 13.4	0.018 ± 0.001

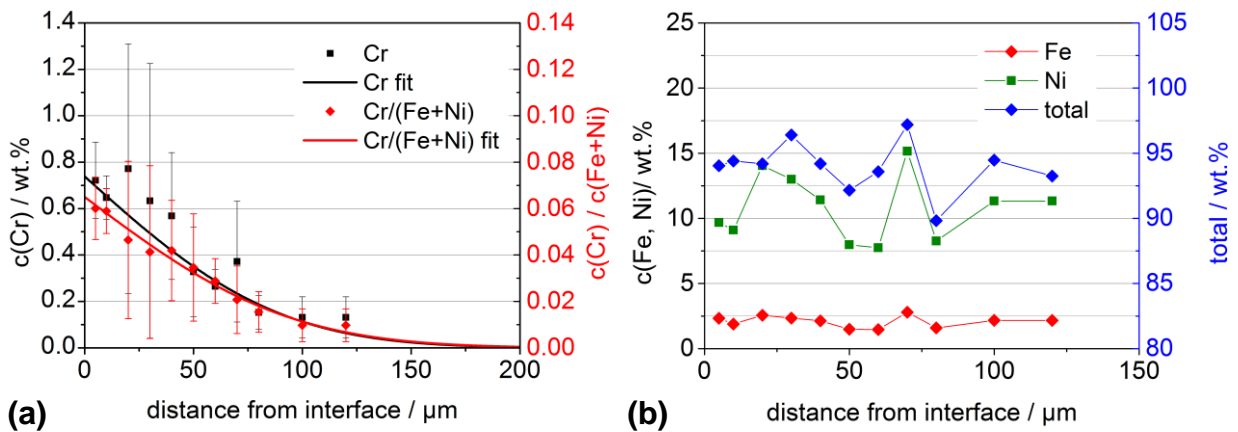


Figure 4-87: C19G115+, annealed at 1150°C for 15 min, Fe/Ni binder, (a) as-measured and normalised EPMA-concentration profiles of chromium, (b) concentration profile of Fe and Ni and corresponding total of all measured elements.

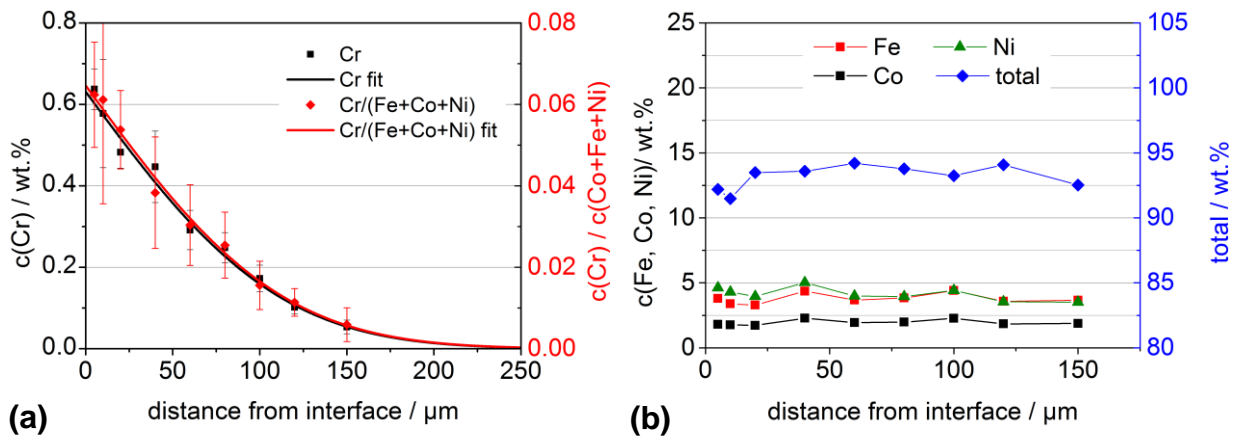


Figure 4-88: C424G115+, annealed at 1150°C for 15 min, Fe/Co/Ni binder, (a) as-measured and normalised EPMA-concentration profiles of chromium, (b) concentration profile of Fe, Ni and Co and corresponding total of all measured elements.

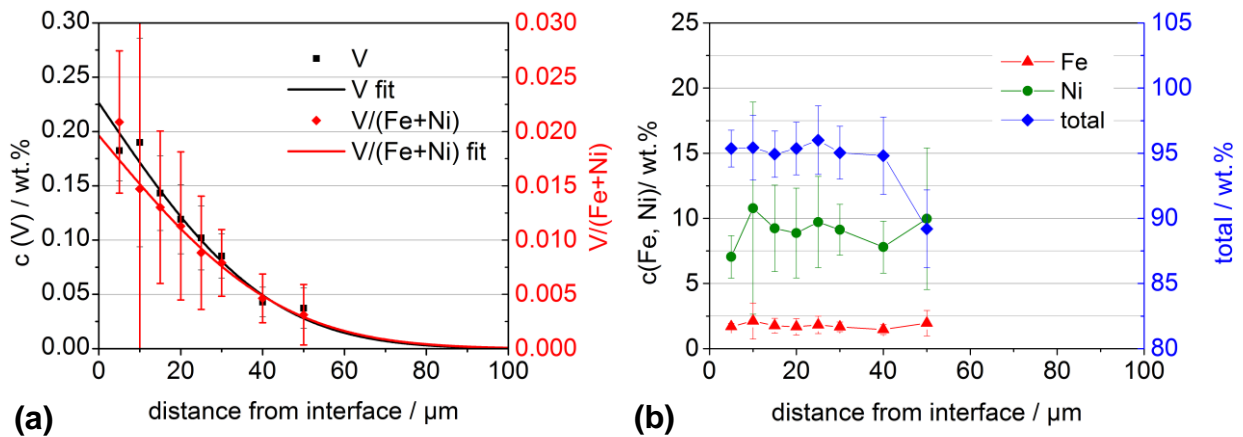


Figure 4-89: V19G115+, annealed at 1150°C for 15 min; Fe/Ni binder, (a) as-measured and normalised EPMA-concentration profiles of vanadium, (b) concentration profile of Fe and Ni and corresponding total of all measured elements.

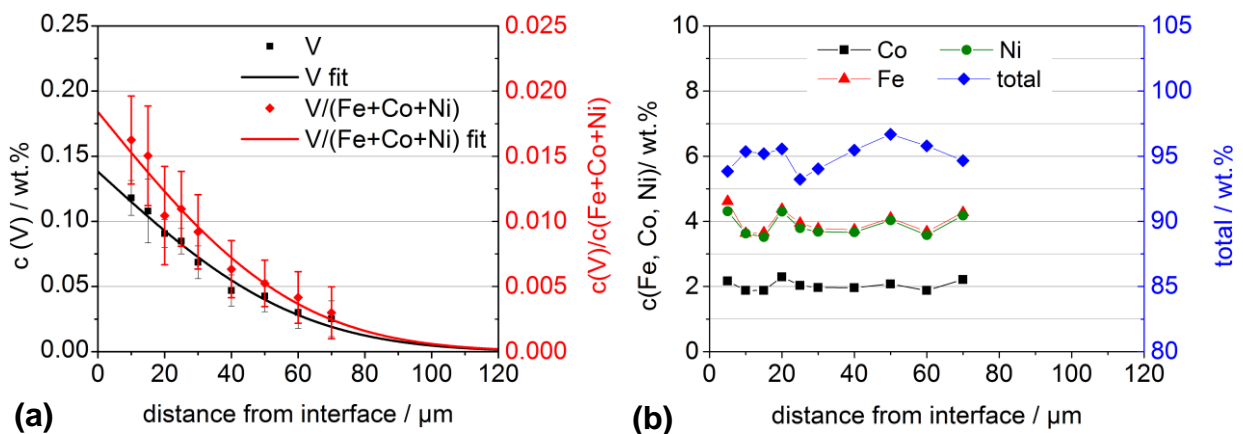


Figure 4-90: V424G115+, annealed at 1150°C for 15 min; Fe/Co/Ni binder (a) as-measured and normalised EPMA-concentration profiles of vanadium (b) concentration profile of Fe, Co and Ni and corresponding total of all measured elements

4.3.17 G-type couples with GGI=molybdenum and cobalt binder

A series of four G-type couples was prepared with molybdenum as a grain-growth inhibitor. The samples MCoG105-5Kmin and MCoG105+5Kmin were prepared with high and low carbon potential, respectively, heated-up with a slow rate of 5 K/min and annealed at 1050°C for 15 min. For the low-carbon sample as illustrated in Figure 4-91(a) the diffusion depth is very low since the detection limit of 0.08 wt% is already reached after 10 µm. Usually the data points within the first 10 µm or below the detection limit are omitted for data fitting, hence a fit is not significant. However, in order to get at least an approximate value for the distribution behaviour of molybdenum a fit was made which is basically coincident to the as-measured data. The scatter of the cobalt concentration and the corresponding error bars in Figure 4-91(b) are large which is attributed to high porosity and inhomogeneous component distribution at 1050°C.

Similar results were obtained for the high carbon alloy as can be seen from Figure 4-92. A strong scatter of the as-measured molybdenum concentration is observed when the detection limit is reached after 11 µm. Since no significant data points were achieved the fit is as well just an approximation and delivers a transport factor of $D=7.2 \cdot 10^{-10} \text{ cm}^2/\text{s}$. No gradient of the cobalt concentration but a strong microstructural inhomogeneity are as well observed in this sample. The estimated interface concentrations of $c(\text{Mo/Co})=0.027$ and $c(\text{Mo/Co})=0.032$ are equal within the error range for the low- and high-carbon sample, respectively.

The sample MCoG115+ was annealed for 15 min at 1150°C. The detection limit was reached after 40 µm, hence a sufficient number of data points above the detection limit is available as shown in Figure 4-93(a). The corresponding fit yields a transport factor of $1.4 \cdot 10^{-9} \text{ cm}^2/\text{s}$ and shows good accordance to the as-measured data. Interestingly the error bars within the first 15 µm are large indicating a strong inhomogeneity. The cobalt concentration in Figure 4-93(b) scatters around 10 wt% and shows no gradient.

When MoB is used instead of Mo₂C as a molybdenum source as for sample MBCoG115+ the concentration profile becomes flatter, see Figure 4-94(a) but the transport factor slightly increases to $D=2.0 \cdot 10^{-9} \text{ cm}^2/\text{s}$. A clear misfit in the shape of the as-measured and the normalised concentration profile is observed which is caused by a strong cobalt gradient as shown in Figure 4-94(b). The interface

concentration obtained from the fit of $c(\text{Mo}/\text{Co})=0.12$ is by 50% lower than of the Mo_2C sample. However, the real interface concentration might differ due to the strong gradient formation. All calculated values are listed in Table 4-19.

Table 4-19: Transport parameters and interface concentrations of molybdenum in G-type diffusion couples.

Sample	Diffusion depth (μm)	D ($10^{-10}\text{cm}^2/\text{s}$)	$c_0(\text{Mo}/\text{Co})$ (wt%/wt%)
MCoG105-5Kmin*	8	5.1 ± 0.7	0.027 ± 0.005
MCoG115+5Kmin*	11	7.2 ± 2.9	0.032 ± 0.021
MCoG115+	40	14.3 ± 2.3	0.251 ± 0.027
MBCoG115+	35	20.2 ± 4.2	0.123 ± 0.015

* Values are only approximate due to lack data points above detection limit.

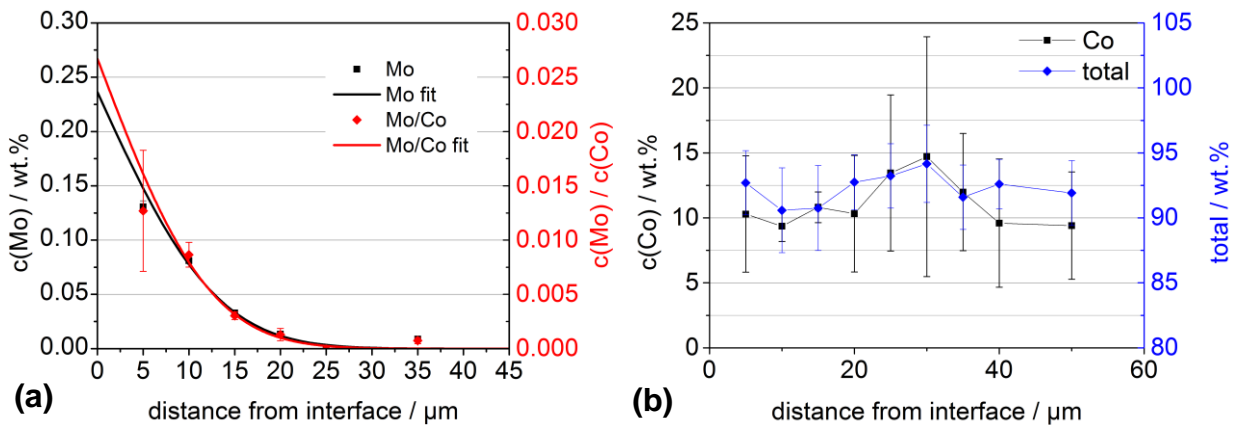


Figure 4-91: MCoG105-5Kmin, linear heat-up to ;1050°C with 5 K/min, low carbon potential, (a) as-measured and normalised EPMA-concentration profiles of molybdenum, (b) concentration profile of cobalt and corresponding total of all measured elements.

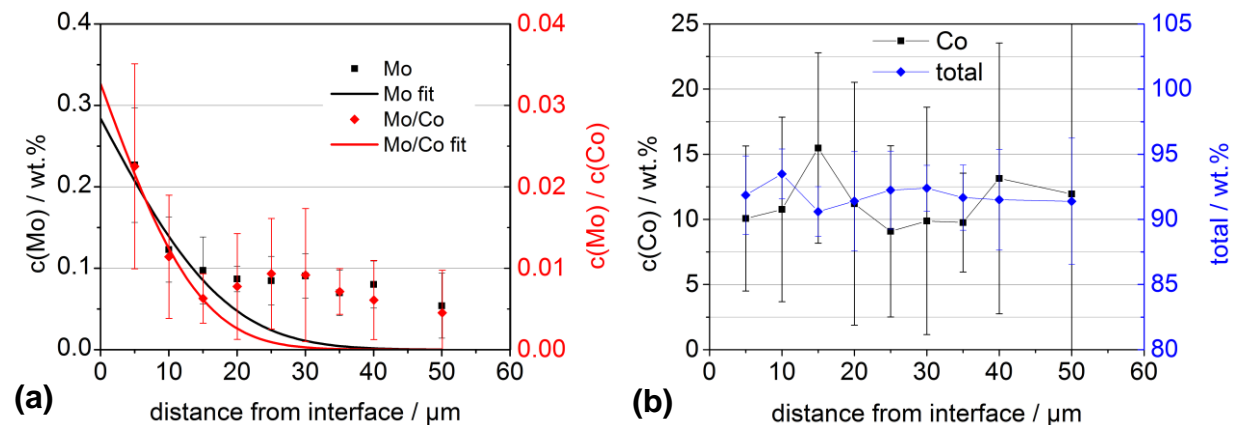


Figure 4-92: MCoG105+5Kmin, linear heat-up to 1050°C with 5 K/min, high carbon potential, (a) as-measured and normalised EPMA-concentration profiles of molybdenum, (b) concentration profile of cobalt and corresponding total of all measured elements.

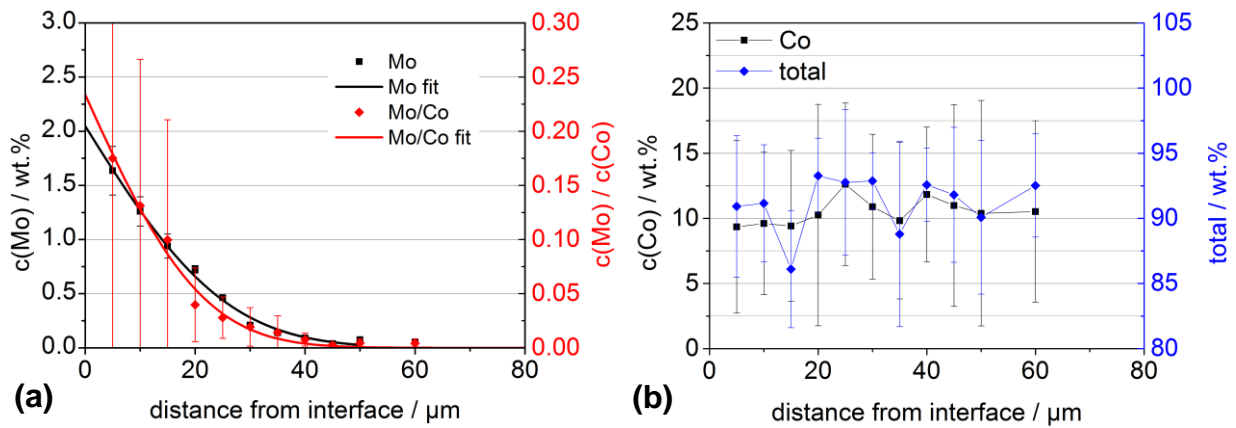


Figure 4-93: MCoG115+, annealed at 1150°C for 15 min, high carbon potential, (a) as-measured and normalised EPMA-concentration profiles of molybdenum, (b) concentration profile of cobalt and corresponding total of all measured elements.

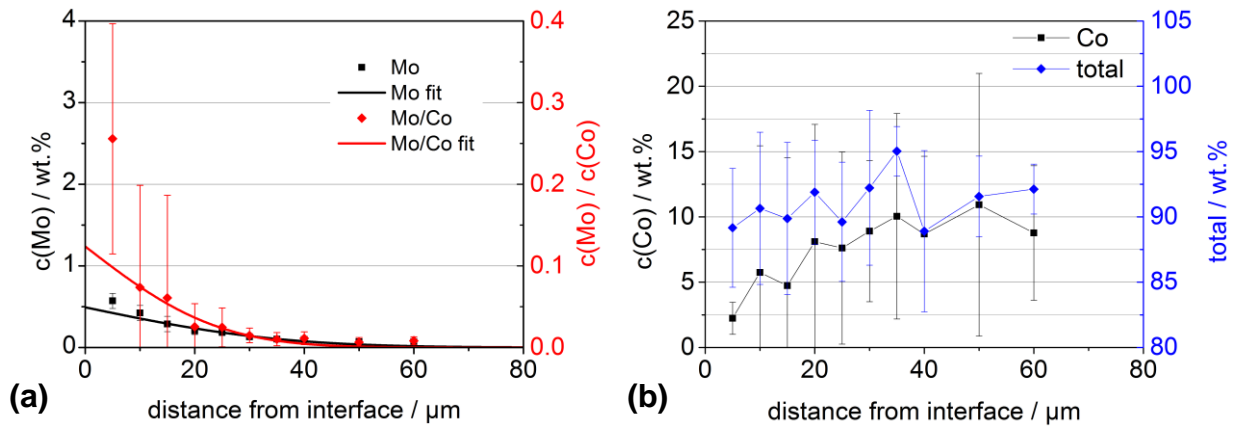


Figure 4-94: MBCoG115+, annealed at 1150°C for 15 min, Mo added as boride, (a) as-measured and normalised EPMA-concentration profiles of molybdenum, (b) concentration profile of cobalt and corresponding total of all measured elements.

4.3.18 G-type couples with Cr_3C_2 +VC and Co binder

In this series the interdependency of the chromium and vanadium diffusion in G-type couples with cobalt binder was investigated. The results for sample CVCoG100_40min, annealed for 40 min at 1000°C, are shown in Figure 4-95(a). It is particularly striking that the interfacial concentration of vanadium $c(\text{V}/\text{Co})=0.008$ is only 1/3 of chromium $c(\text{Cr}/\text{Co})=0.027$ which is attributed to the lower solubility of vanadium. As listed in Table 2-4 the solubility of Cr in Cr+V-doped hardmetals is 4.1wt% of $c(\text{Cr}/\text{Co})=0.046$ and of vanadium is 0.7 wt% or $c(\text{V}/\text{Co})=0.008$. While the calculated concentration of vanadium matches literature data the value of chromium is only 50% of literature data. A potential explanation is that Lauter et al. [06LAU]

determined their results from model alloys with high binder content which were prepared by long-time annealing of samples cooled down from liquid phase while the present sample has never been in liquid state, the constituents have to resolve in the binder phase and local concentrations are very likely not in equilibrium state. Not only the interface concentration but also the transport factor of $D=9.7 \cdot 10^{-10} \text{ cm}^2/\text{s}$ and $D=4.8 \cdot 10^{-10} \text{ cm}^2/\text{s}$ is higher for chromium as compared to vanadium, respectively.

By increasing temperature by 50°C as for sample CVCoG105+_60min both interface concentrations of chromium and vanadium increase to $c_0(\text{Cr/Co})=0.046$ and 0.017 , respectively, see Figure 4-96. The transport factor of chromium is $D=2.8 \cdot 10^{-9} \text{ cm}^2/\text{s}$ and for vanadium $D=1.0 \cdot 10^{-9} \text{ cm}^2/\text{s}$. A further increase by 50°C to 1100°C for sample CVCoG110_40min annealed for 40 min, as illustrated in Figure 4-97 delivers the same relative behaviour of chromium and vanadium, but the interface concentrations increase to $c_0(\text{Cr/Co})=0.080$ and $c_0(\text{V/Co})=0.021$ and the transport factors to $D=4.2 \cdot 10^{-9} \text{ cm}^2/\text{s}$ and $D=2.7 \cdot 10^{-9} \text{ cm}^2/\text{s}$, respectively.

At 1150°C the annealing time was reduced to 15 min as shown in Figure 4-98 for sample CVCoG115. However, both chromium and vanadium reach a diffusion depth comparable to those achieved at 1100°C for 15 min, resulting in transport factors of $D=1.9 \cdot 10^{-8} \text{ cm}^2/\text{s}$ for chromium and $D=9.0 \cdot 10^{-9} \text{ cm}^2/\text{s}$ for vanadium. The interface concentration of chromium is $c_0(\text{Cr/Co})=0.091$ and of vanadium $c_0(\text{V/Co})=0.031$.

No cobalt gradient was formed in any of the samples described above.

For all previous samples the binder phase is expected to be in solid-state upon the experiment. Since sample CVCoG136 was annealed at 1360°C for 15 min the binder phase is expected to be in liquid phase according to literature data (see Table 2-3). As shown in Figure 4-99 an interesting difference in the concentration profiles of chromium and vanadium is observed. While chromium reveals a typical shape both the as-measured and the normalised vanadium concentrations show a peak-shaped profile. A similar behaviour was found for the sample VCoG136 without chromium co-doping, see Figure 4-67. Since the effect was not observed for chromium within the same sample it has to be specific for vanadium. The reasons behind will be further discussed in section 5.6. The results of the calculated of this series are summarised in Table 4-20.

Table 4-20: Transport parameters and interface concentrations of chromium and vanadium in G-type diffusion couples; n.a.: No data available.

Sample	D (10^{-10} cm ² /s)		C ₀ wt%/wt%	
	Cr	V	Cr/Co	V/Co
CVCoG100_40min	9.7 ± 1.4	4.8 ± 0.9	0.027 ± 0.003	0.008 ± 0.001
CVCoG105_60min	28.3 ± 2.4	10.3 ± 1.8	0.046 ± 0.002	0.017 ± 0.002
CVCoG110_40min	50.9 ± 2.5	27.1 ± 1.7	0.080 ± 0.002	0.021 ± 0.001
CVCoG115	188.4 ± 14.3	90.2 ± 12.1	0.091 ± 0.002	0.031 ± 0.002
CVCoG125	1637 ± 374	2018 ± 1050	0.096 ± 0.003	0.024 ± 0.002
CVCoG136	54836 ± 11481	n.a.	0.187 ± 0.020	n.a.

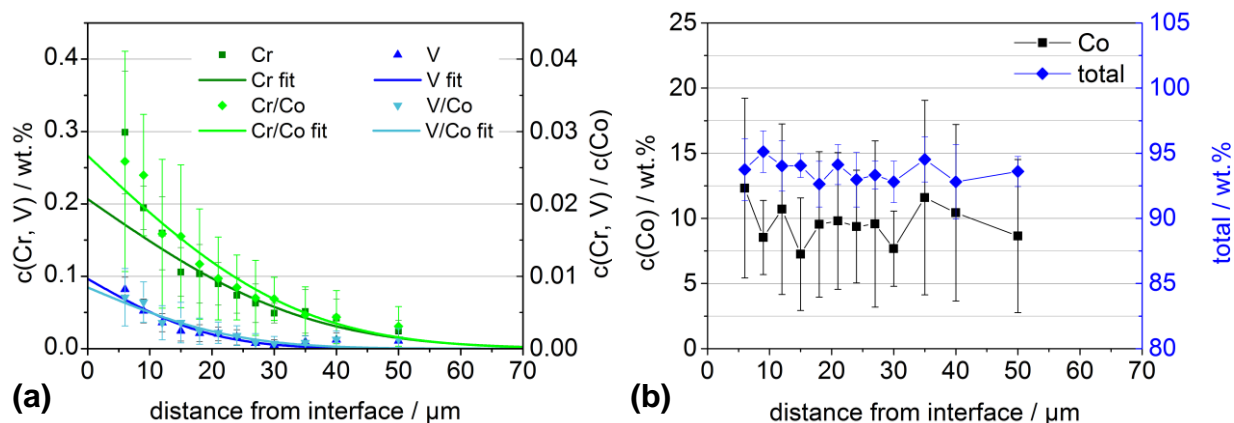


Figure 4-95: CVCoG100_40min, annealed at 1000°C for 40 min, mid carbon potential, (a) as-measured and normalised EPMA-concentration profiles of vanadium and chromium, (b) concentration profile of cobalt and corresponding total of all measured elements.

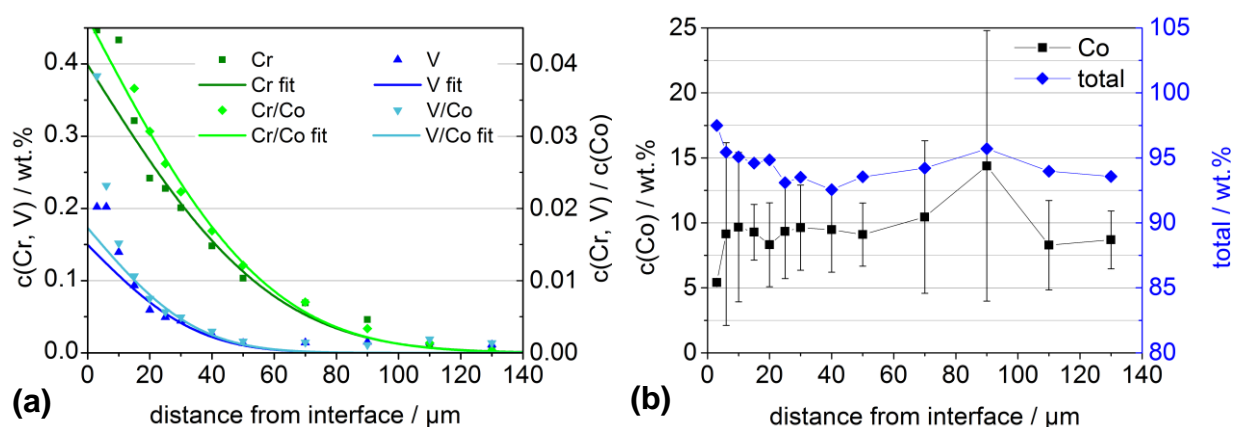


Figure 4-96: CVCoG105_60min, annealed at 1050°C for 60 min, mid carbon potential, (a) as-measured and normalised EPMA-concentration profiles of vanadium and chromium, (b) concentration profile of cobalt and corresponding total of all measured elements.

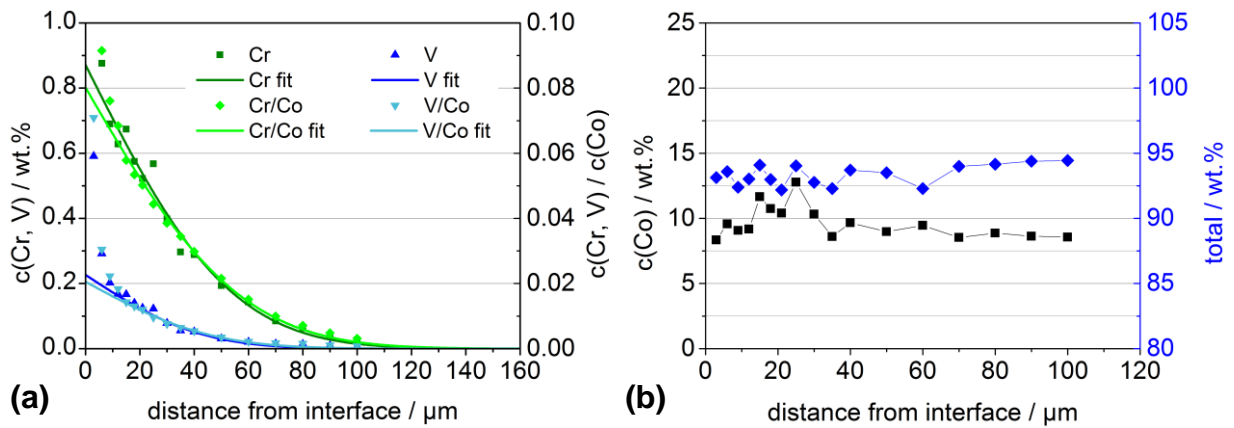


Figure 4-97: CVC0G110_40min, annealed at 1100°C for 40 min, mid carbon potential, (a) as-measured and normalised EPMA-concentration profiles of vanadium and chromium, (b) concentration profile of cobalt and corresponding total of all measured elements.

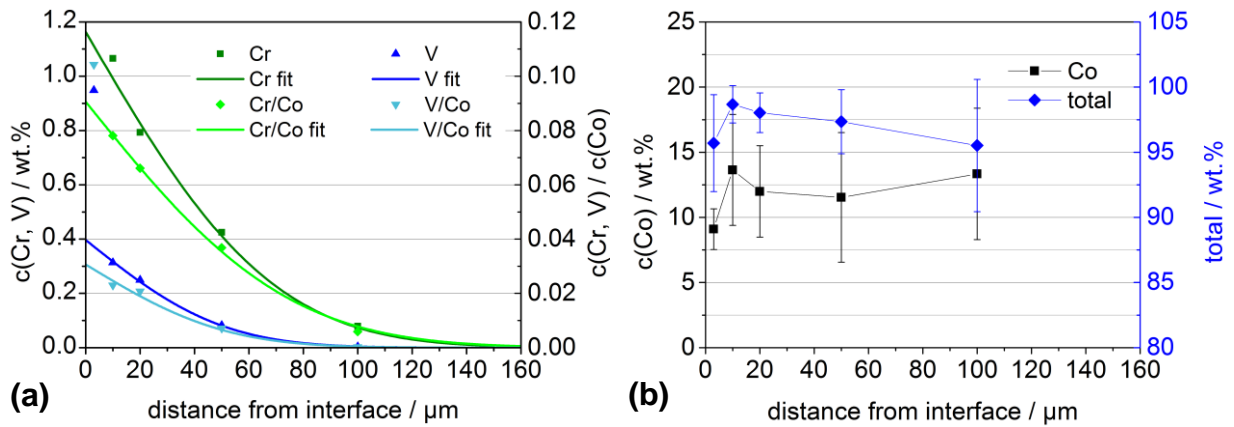


Figure 4-98: CVC0G115, annealed at 1150°C for 15 min, mid carbon potential, (a) as-measured and normalised EPMA-concentration profiles of vanadium and chromium, (b) concentration profile of cobalt and corresponding total of all measured elements.

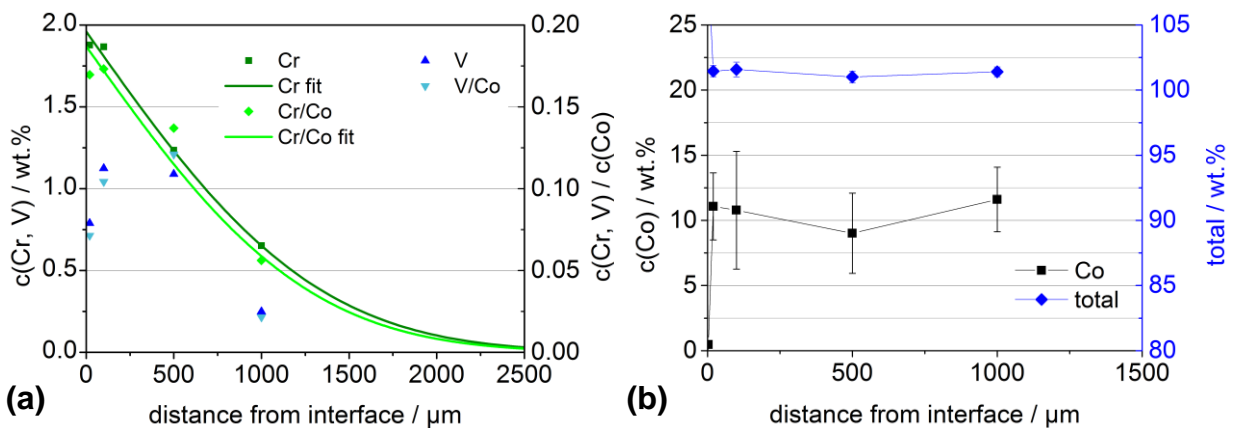


Figure 4-99: CVC0G136, annealed at 1360°C for 15 min, mid carbon potential, (a) as-measured and normalised EPMA-concentration profiles of vanadium and chromium, (b) concentration profile of cobalt and corresponding total of all measured elements.

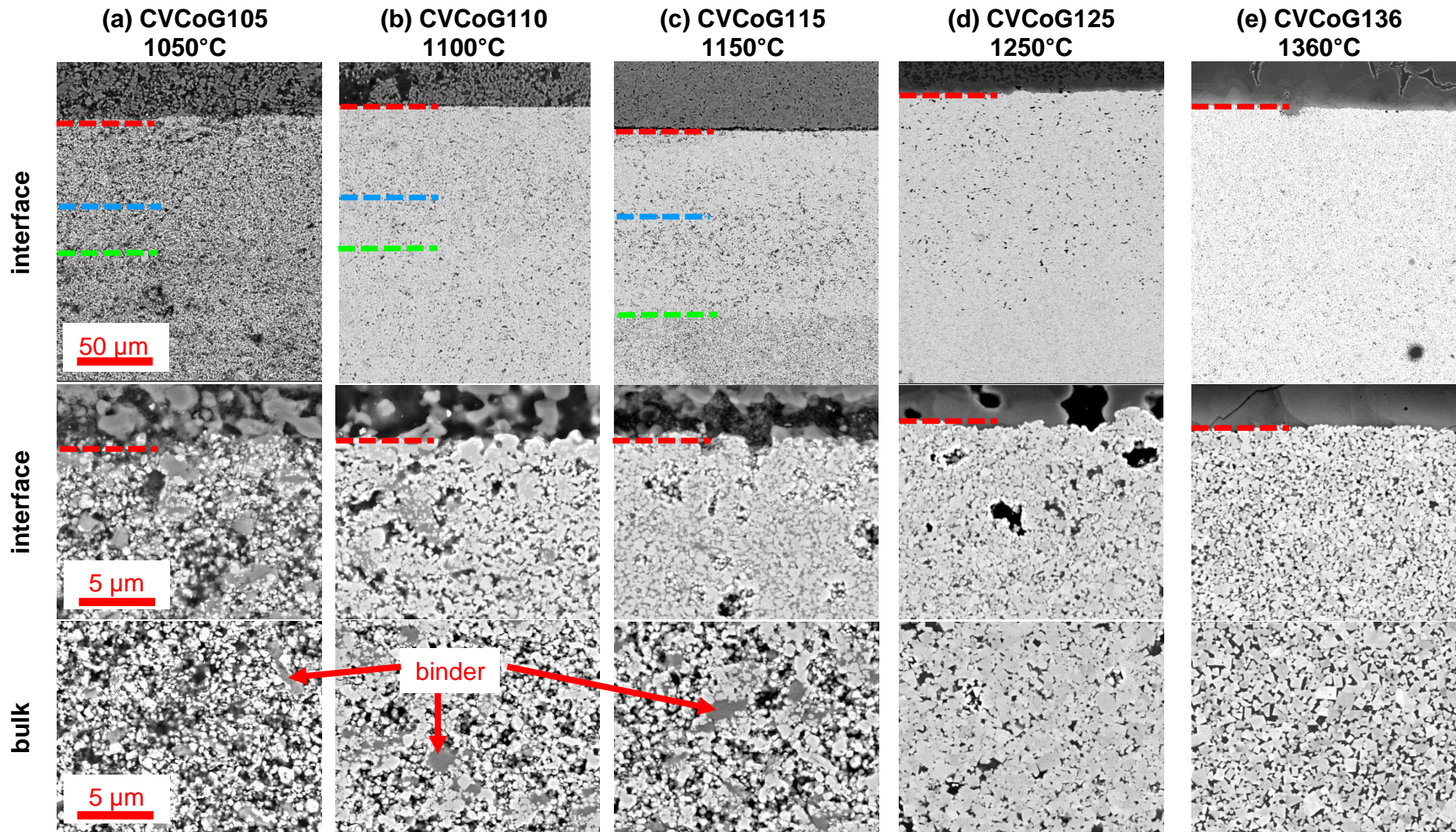


Figure 4-100: SEM-BSE micrographs of G-type diffusion couples at various temperatures. Red line: interface; Blue line: Diffusion depth of vanadium. Green line: diffusion depth of vanadium.

4.4 M-type diffusion couples

M-type diffusion couples were prepared with an initial binder volume fraction of 70%. EPMA line-scans were placed within the binder phase only. Subsequently the data represents the diffusion of GGIs in the equilibrated binder phase. Particular measuring points hitting carbide precipitations were omitted upon the subsequent data treatment.

Prior to the diffusion experiment the diffusion couple were annealed for 10 h at the intended testing temperature. Hence, the binder phase is close to equilibrium state and saturated with tungsten. However, in presence of GGIs the W solubility in the binder phase is lower. As a consequence GGIs can only be dissolved and diffuse into the binder phase when the tungsten concentration is simultaneously decreased. The figures in the following chapters show both, the GGI and the tungsten concentration profile. No normalised concentration was calculated since the results already show the diffusion in binder phase. Also no total value is given; it is around 100% for a fully dense material.

In case of alternative binder alloys the presence of GGIs was found to influence the local ratio of the binder phase elements. For such samples, the concentrations of the single binder constituents normalised by the total binder phase concentration are additionally presented.

In contrast to G-type couples the position of the EPMA-measurements was visible after the measurements in M-type couples, which allowed the exact determination of the line-scan positions. The data points in this section refer to this measured distance from interface.

In G-type couples the standard deviation is a convolution of both the measurement error and the microstructural inhomogeneity. In M-type samples the latter is not of significance, since the measurement is conducted in dense binder phase. Hence, the error bars in the figures are small as compared to G-type couples and are a direct measure for the scatter of the method.

4.4.1 M-type couples with Cr and Co binder

This series of M-type diffusion couples was prepared with chromium as a GGI and cobalt binder. The sample CCoM95+ was annealed for 330 min at 950°C. As can be

seen from Figure 4-101(a) the detection limit is reached within 14 μm despite the long annealing time. As a result the transport factor $D=3.1 \cdot 10^{-11} \text{ cm}^2/\text{s}$ is comparatively low, consequently chromium distribution in the binder phase at 950°C is slow. The calculated interface concentration $c_0(\text{Cr})=0.35 \text{ wt}\%$ is unexpectedly low while the tungsten concentration of $c(\text{W})\sim 9\%$ is unexpectedly high. Though no solubility data is available for $T=950^\circ\text{C}$ a comparison with data at 1000°C (Table 2-4) shows that the measured chromium concentration is only 10% of the solubility, but the tungsten concentration is by a factor of 3 higher. This means that the binder phase was not in equilibrium state but oversaturated with tungsten, which limits the chromium solubility and transport. It can be seen from Figure 4-101 that the tungsten concentration depletes simultaneously to increasing chromium concentration. The consequences are discussed in section 5.3. Similar findings apply for samples CCoM105+ (b) and CCoM115+ (c), annealed for 60 min at 1050°C and 5 min at 1150°C , respectively. As shown in Table 4-21 the interface concentrations increase to 0.48 wt% and 1.44 wt% while the transport factor rises to $D=2.8 \cdot 10^{-10} \text{ cm}^2/\text{s}$ and $1.7 \cdot 10^{-9} \text{ cm}^2/\text{s}$, respectively.

Table 4-21: Transport factor and interface concentrations of chromium in M-type diffusion couples with cobalt binder and high carbon potential.

Sample	$D_{Cr}^{Co,M} [10^{-10} \text{ cm}^2/\text{s}]$	$c_0(\text{Cr}) [\text{wt}\%]$
CCoM95+	0.31 ± 0.07	0.35 ± 0.06
CCoM105+	2.8 ± 0.7	0.48 ± 0.05
CCoM115+	16.9 ± 2.3	1.44 ± 0.53

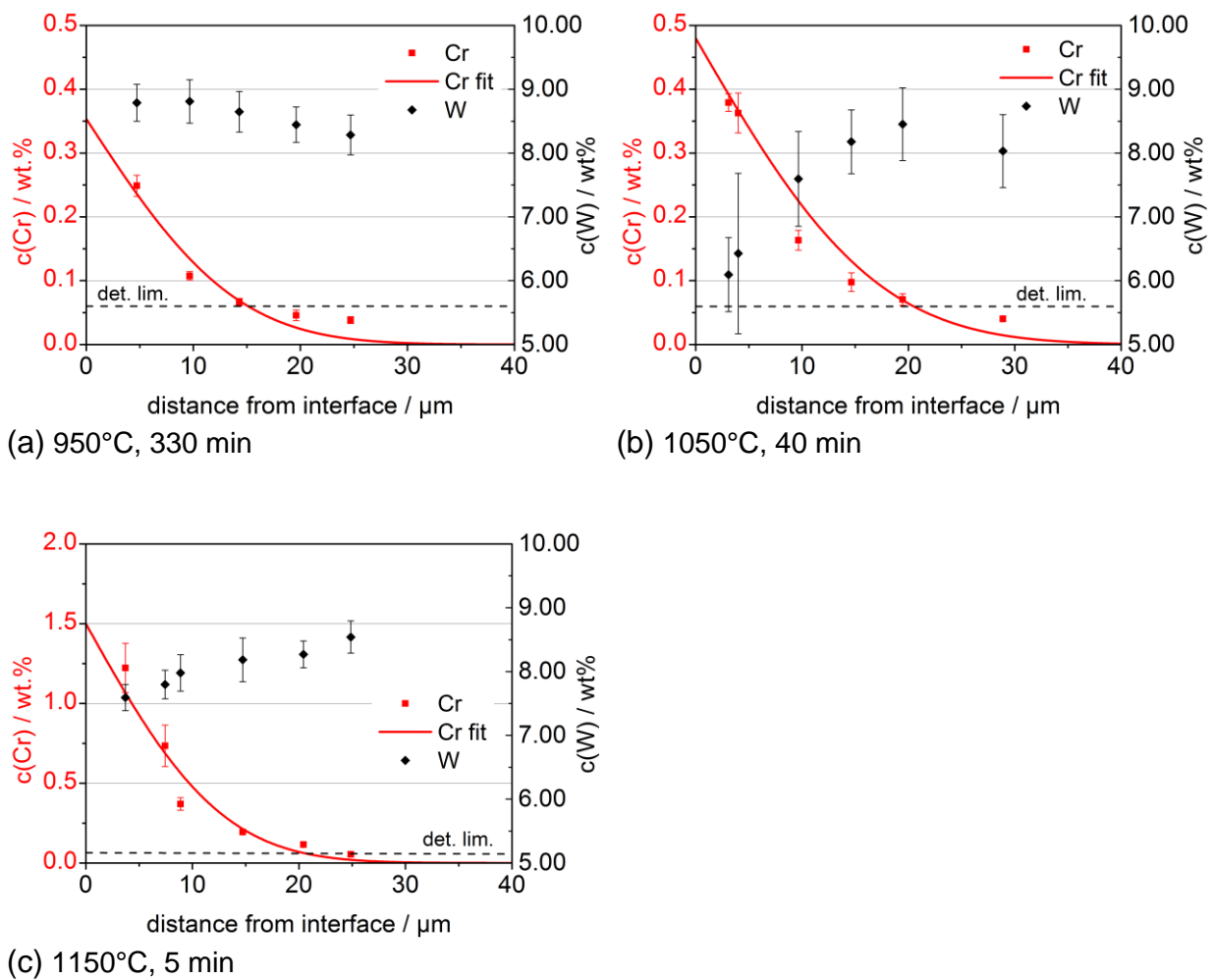


Figure 4-101: Chromium and tungsten concentration profiles in M-type diffusion couples with Co binder and high carbon potential (a) CCoM95+, (b) CCoM105+, (c) CCoM115+.

4.4.2 M-type couples with V and Co binder

The results for the series of M-type samples with GGI=vanadium and cobalt binder are shown in Figure 4-102(a) for VCoM95+, annealed at 950°C for 330 min and (b) for VCoM115+, annealed at 1150°C for 5 min. While the interface concentration was $c_0(V)=0.33$ wt% at 950°C it is just 0.14 wt% at 1150°C, which is clearly below the solubility at these temperatures. Especially at 1150°C a strong tungsten gradient was measured. The transport factors of $D=2.6 \cdot 10^{-11}$ cm²/s and $D=1.5 \cdot 10^{-9}$ cm²/s, respectively are almost equal to these of cobalt at the same temperature. The low number of data points above the detection limit causes some uncertainty of the

calculated data. However, there is a good accordance of the model with the experimentally determined data. The results are summarised in Table 4-22.

Table 4-22: Transport factor and interface concentrations of vanadium in M-type diffusion couples with cobalt binder and high carbon potential.

Sample	D (10^{-10} cm ² /s)	$c_0(\text{Cr})$ (wt%)
VCoM95+	0.26 ± 0.03	0.33 ± 0.02
VCoM115+	15.1 ± 2.8	0.14 ± 0.05

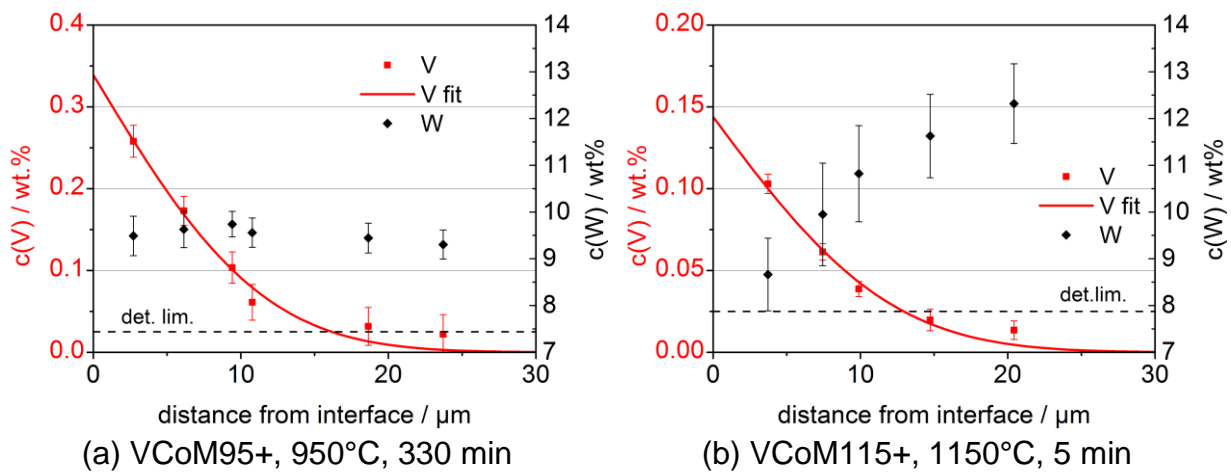


Figure 4-102: Vanadium and tungsten concentration profiles in M-type diffusion couples with Co binder.

4.4.3 M-type couples with Cr and Fe/Co/Ni-binder

This series aimed to investigate the chromium transport in the equilibrated Fe/Co/Ni=40/20/40 wt% binder phase with high carbon potential.

The sample C424M95+ was annealed for 330 min at 950°C. The resulting maximum concentration of chromium at the interface was measured $c_0=0.31$ wt% as shown in Figure 4-103(a). This value is low as compared to the solubility of chromium in cobalt, which is around 4 wt% as extrapolated from literature data in Table 2-4. In iron-rich binder alloys solubilities were reported to be up to 50% lower [11WAG], but not by more than an order of magnitude. Similar findings apply for all samples in this series. The reasons are discussed in section 5.6. A strong tungsten gradient was measured with depletion from 2 wt.% in the bulk to 1.4 wt.% at the interface.

The interface concentration of $c(\text{Cr})=0.29$ at 1050°C is equal within the error range, see results for sample C424M105+ in Figure 4-104(a). The corresponding transport factor of chromium was calculated $D=4.2 \cdot 10^{-10} \text{ cm}^2/\text{s}$. A tungsten gradient was measured as well, but in contrast to 950°C it has a higher concentration of 2.4 wt% at the interface which decreases to 1.8 wt% in the bulk. At 1100°C the transport factor increases to $D=8.1 \cdot 10^{-10} \text{ cm}^2/\text{s}$ and the interface concentration to $c(\text{Cr})=0.7 \text{ wt}\%$, see Figure 4-105(a). No significant W-gradient appears, the concentration remains at 1.7–1.8 wt%.

A sample at 1150°C (C424M115+) was prepared but no chromium profile was measured which was probably due to an insufficient contact of the diffusion couple components. Thus, no results are shown in this section. However, when annealed in nitrogen as in case of sample C424M115+N a chromium concentration profile was measured, see Figure 4-106(a). The fitted model shows good accordance to the as-measured data. The interface concentration $c(\text{Cr})=0.42 \text{ wt}\%$ is lower than for sample C424110+, though the latter was annealed at 50°C lower temperature. The tungsten concentration was constant at 2.2 wt% within the investigated distance from interface.

From Figure 4-103(b) – Figure 4-106(b) it can be seen that no significant change of the Fe/Co/Ni ratio occurred as a function of the local chromium concentration. The results of the curve fitting are summarised in Table 4-23.

Table 4-23: Transport factor and interface concentrations of chromium in M-type diffusion couples with Fe/Co/Ni binder and high carbon potential.

Sample	$D_{Cr}^{424,M} [10^{-10} \text{ cm}^2/\text{s}]$	$c_0(\text{Cr}), \text{wt}\%$
C424M95+	0.30 ± 0.04	0.31 ± 0.02
C424M105+	2.4 ± 0.9	0.39 ± 0.09
C424M110+	8.1 ± 0.7	0.70 ± 0.06
C424M115+N	23.8 ± 2.8	0.42 ± 0.02

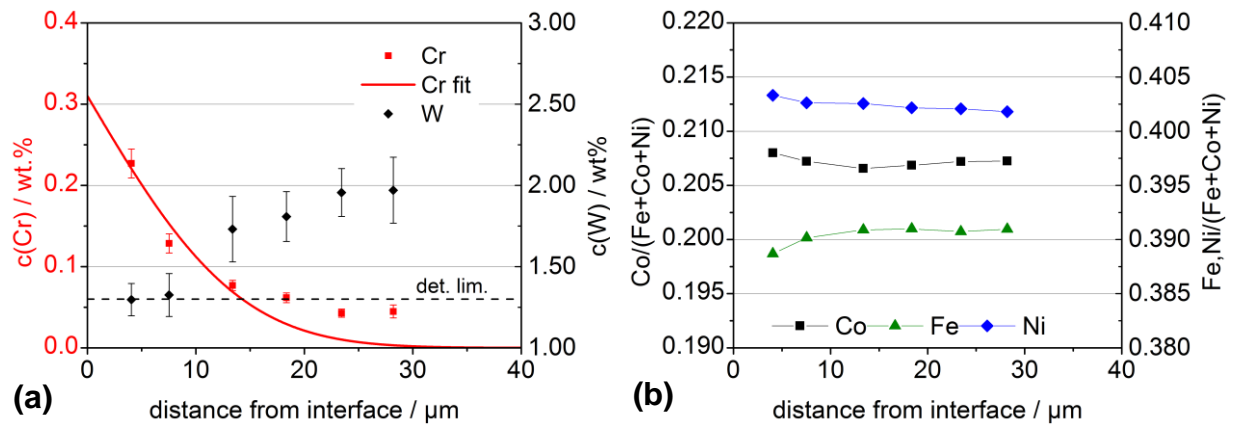


Figure 4-103: C424M95+, annealed at 950°C for 330 min; Fe/Co/Ni binder,
 (a) chromium and tungsten EPMA concentration profile,
 (b) concentration of Fe, Ni and Co normalised by total binder concentration.

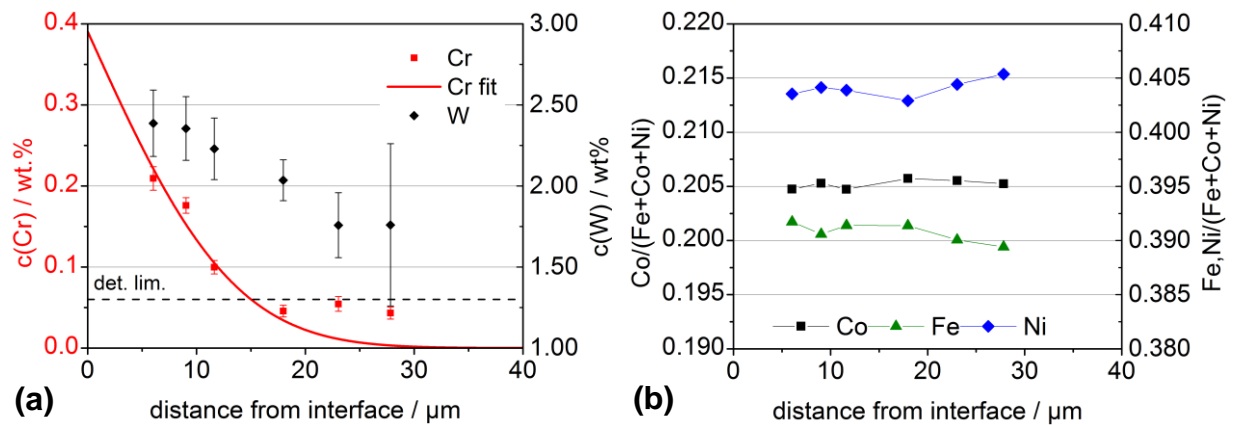


Figure 4-104: C424M105+, annealed at 1050°C for 60 min, Fe/Co/Ni binder,
 (a) chromium and tungsten EPMA concentration profile,
 (b) concentration of Fe, Ni and Co normalised by total binder concentration.

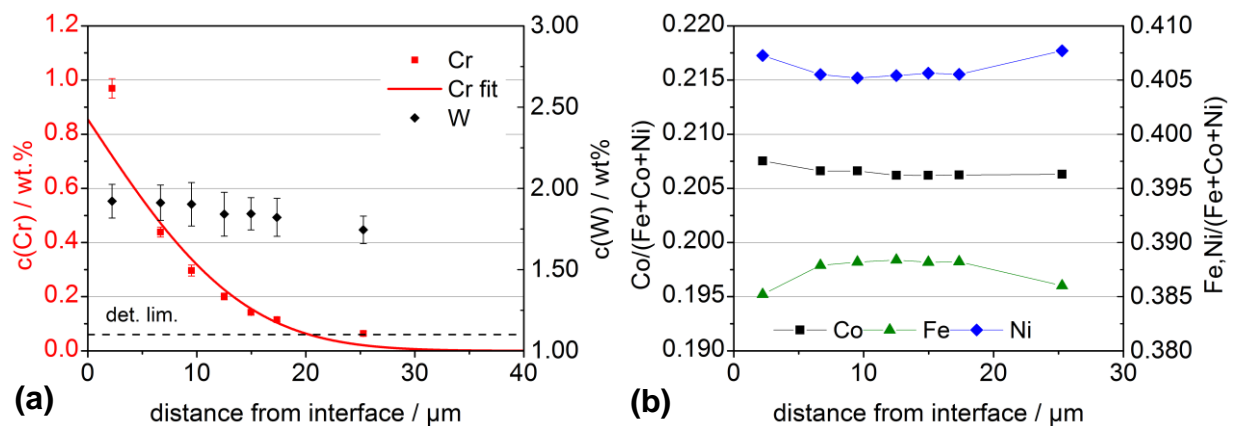


Figure 4-105: C424M110+, annealed at 1100°C for 40 min, Fe/Co/Ni binder,
 (a) chromium and tungsten EPMA concentration profile,
 (b) concentration of Fe, Ni and Co normalised by total binder concentration.

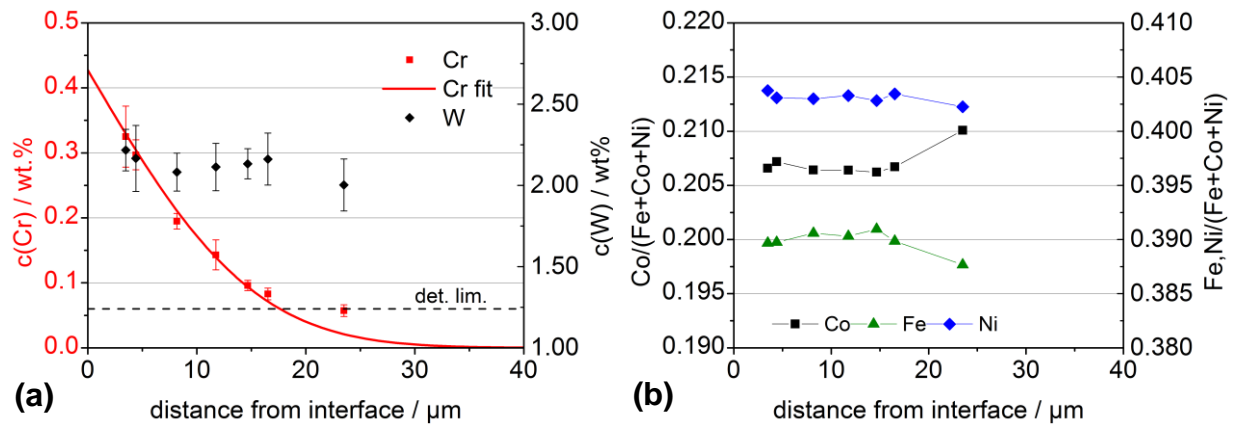


Figure 4-106: C424M115+N, annealed at 1150°C for 5 min, Fe/Co/Ni binder, N₂-atmosphere, (a) chromium and tungsten EPMA concentration profile, (b) concentration of Fe, Ni and Co normalised by total binder concentration.

4.4.4 M-type couples with V and Fe/Co/Ni-binder

The M-type diffusion samples in this series were prepared with GGI=vanadium and Fe/Co/Ni-40/20/40 wt% binder alloy. Sample V424M110+ was annealed for 15 min at 1100°C; the resulting vanadium concentration profile is shown in Figure 4-107(a). Excellent accordance of the model with the experimental data was possible, the resulting parameters are $D=5.6 \cdot 10^{-10}$ cm²/s and an interface concentration of $c(V)=1.28$ wt%. The tungsten concentration is constant $c(W)=1.8-2.0$ wt% without significant gradient. At 1150°C the W concentration slightly increases to $c(W)=2.2-2.3$ wt%, see sample V424M115+ in Figure 4-108(a). The transport factor increases to $D=1.5 \cdot 10^{-9}$ cm²/s. The chromium interface concentration, however, decreases to $c(Cr)=0.89$ wt% which is further discussed in section 5.3. When annealing in 400 mbar nitrogen at 1150°C as for sample V424M115+N in Figure 4-109(a) the transport is slightly decreased to $D=1.2 \cdot 10^{-9}$ cm²/s and the interface concentration decreases to 0.47 wt%. The tungsten concentration of $c(W)=2.1-2.2$ wt% is equal to that of the sample annealed in argon. From Figure 4-107(b) – Figure 4-109(b) it can be seen that no gradients in the Fe/Co/Ni ratio formed at 1150°C, but at 1100°C the nickel concentration is slightly increased from the initial $c(Ni/(Ni+Fe+Co))=0.40$ to 0.41 while the iron concentration is decreased by the same amount. The results calculated from the fit are summarised in Table 4-24.

Table 4-24: Transport factor and interface concentrations of vanadium in M-type diffusion couples with cobalt binder and high carbon potential.

Sample	$D_V^{424,M}$ [10^{-10} cm ² /s]	$c_0(V)$, wt%
V424M110+	6.1 ± 0.6	1.28 ± 0.08
V424M115+	15.2 ± 3.3	0.89 ± 0.07
V424M115+N	12.0 ± 1.9	0.47 ± 0.03

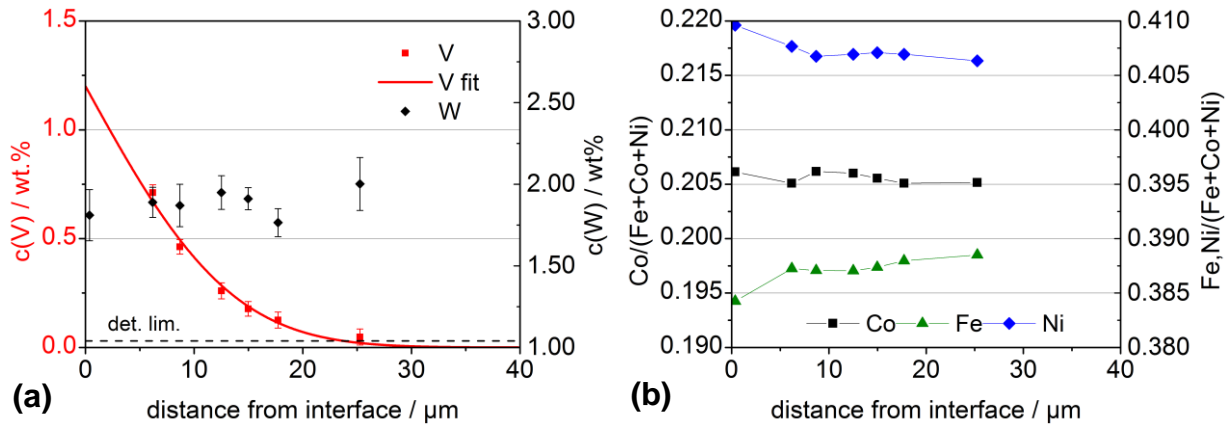


Figure 4-107: V424M110+, annealed at 1100°C for 15 min, Fe/Co/Ni binder, (a) chromium and tungsten EPMA concentration profile, (b) Fe, Ni and Co normalised by total binder concentration.

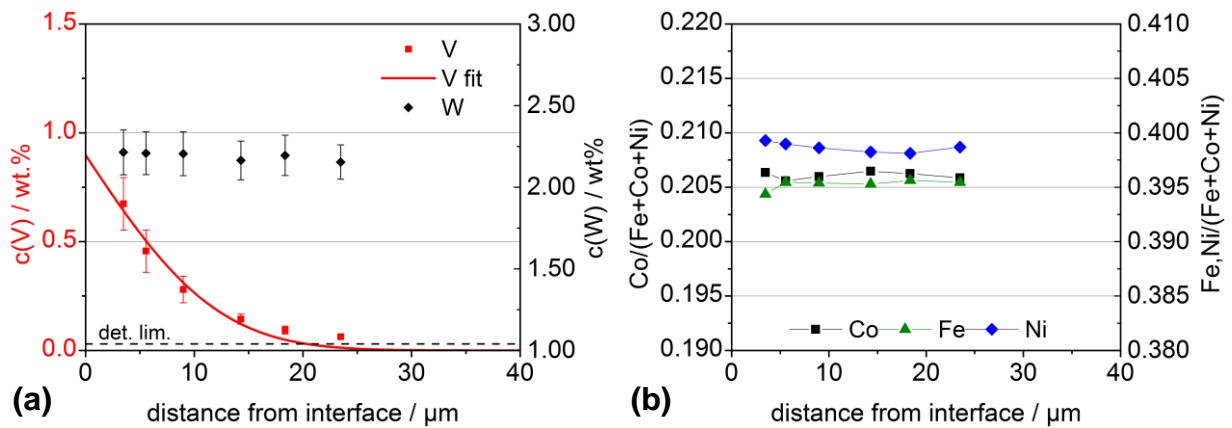


Figure 4-108: V424M115+, annealed at 1150°C for 15 min, Fe/Co/Ni binder, (a) vanadium and tungsten EPMA concentration profile, (b) Fe, Ni and Co normalised by total binder concentration.

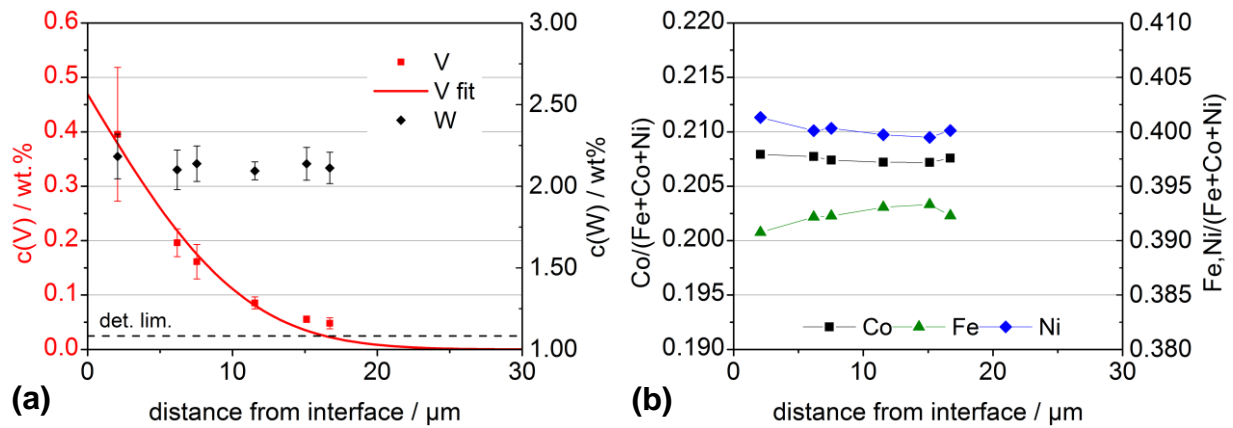


Figure 4-109: V424M115+N, annealed at 1150°C for 15 min, Fe/Co/Ni binder, N₂ atmosphere
 (a) vanadium and tungsten EPMA concentration profile,
 (b) Fe, Ni and Co normalised by total binder concentration.

4.4.5 M-type couples with Cr and Fe/Ni-binder

Four different M type-diffusion couples with GGI=chromium and Fe/Ni-15/85 wt% binder alloy were prepared in a temperature range from 950–1150°C.

Sample C19M95+ was annealed for 330 min at 950°C. The resulting chromium concentration profile is illustrated in Figure 4-110(a). The measured interface concentration $c_0(\text{Cr})=0.25 \text{ wt}\%$ is very low compared to the solubility of $c(\text{Cr})=4.9 \text{ wt}\%$ as extrapolated from literature data for cobalt binder. Though the binder alloy is different, the solubility should at least be within the same order of magnitude. The transport factor of chromium is $D=3.1 \cdot 10^{-11} \text{ cm}^2/\text{s}$.

Sample C19M105+ was annealed at 1050°C for 40 min, the results are shown in Figure 4-111(a). The interface concentration of $c_0(\text{Cr})=0.43 \text{ wt}\%$ is still low, the transport factor increased to $D=2.4 \cdot 10^{-10} \text{ cm}^2/\text{s}$. At 1100°C, see Figure 4-112(a), $c_0(\text{Cr})=0.64 \text{ wt}\%$ and $D=5.4 \cdot 10^{-10} \text{ cm}^2/\text{s}$ were calculated. At 1150°C the interface concentration dramatically increased to $c_0(\text{Cr})=3.28 \text{ wt}\%$ as illustrated in Figure 4-113(a), but is still below the expected solubility. The transport factor is $D=1.6 \cdot 10^{-9} \text{ cm}^2/\text{s}$. The tungsten concentration is around 4.4–5.0 wt% for all samples, the formation of a tungsten gradient was observed for none of the samples. At all temperatures a shift of the Fe/Ni ratio is observed as shown in Figure 4-110(a) – Figure 4-113(b), with a slight enrichment of nickel towards the interface.

The calculated results are summarised in Table 4-25.

Table 4-25: Transport factor and interface concentrations of chromium in M-type diffusion couples with Fe/Ni-15/85 wt% binder and high carbon potential.

Sample	$D_{Cr}^{19,M}$ [10^{-10} cm ² /s]	$c_0(\text{Cr})$, wt%
C19M95+	0.31 ± 0.06	0.25 ± 0.02
C19M105+	2.4 ± 0.4	0.43 ± 0.05
C19M110+	5.4 ± 0.8	0.64 ± 0.08
C19M115+	16.2 ± 1.0	3.28 ± 0.18

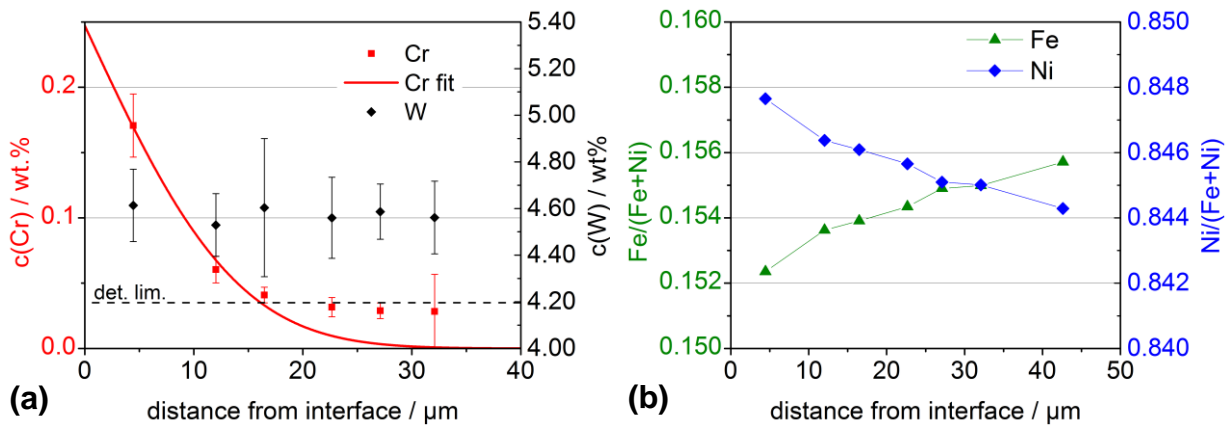


Figure 4-110: C19M95+, annealed at 950°C for 330 min, Fe/Ni binder
 (a) chromium and tungsten EPMA concentration profile; (b) Fe, Ni normalised by total binder concentration.

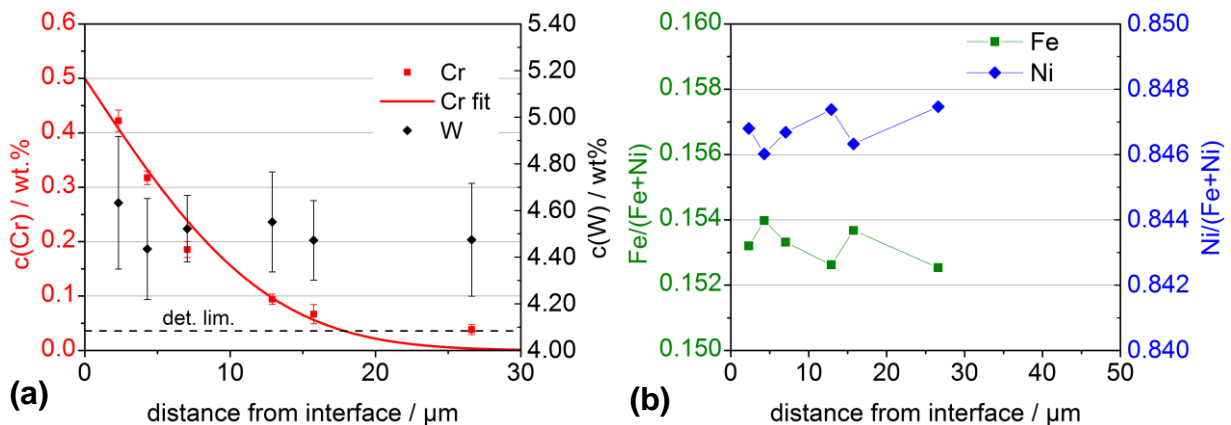


Figure 4-111: C19M105+, annealed at 1050°C for 40 min, Fe/Ni binder
 (a) chromium and tungsten EPMA concentration profile; (b) Fe, Ni normalised by total binder concentration.

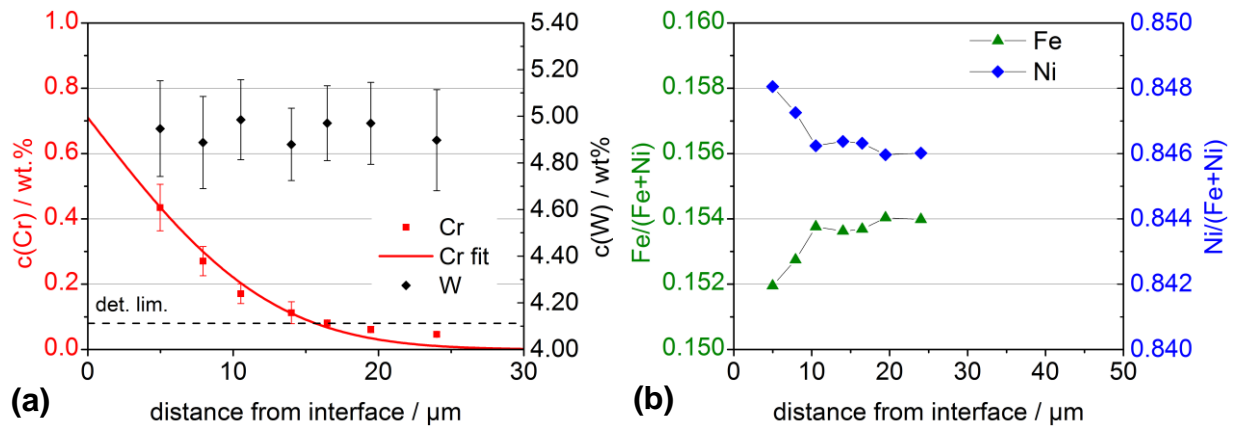


Figure 4-112: C19M110+, annealed at 1100°C for 15 min, Fe/Ni binder
 (a) chromium and tungsten EPMA concentration profile; (b) Fe, Ni normalised by total binder concentration.

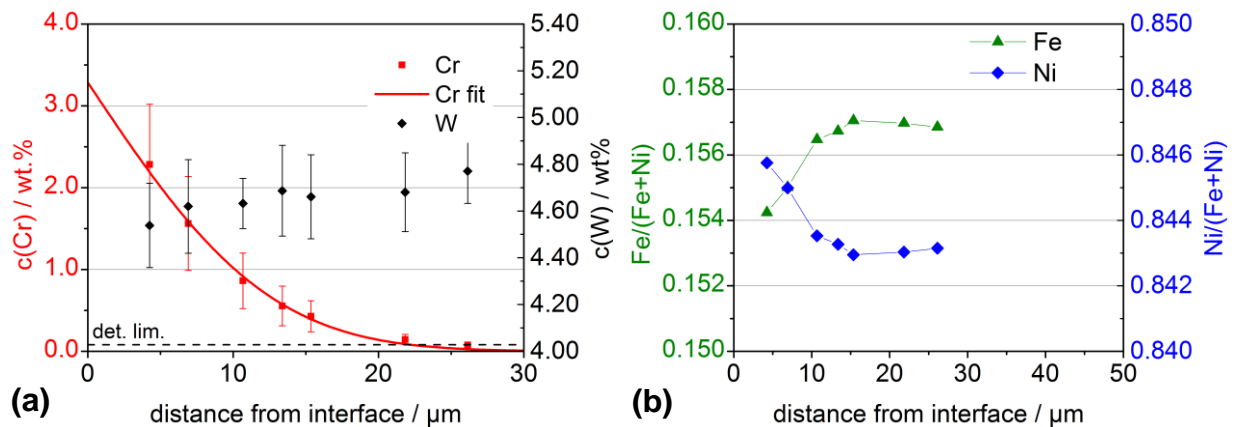


Figure 4-113: C19M115+, annealed at 1150°C for 15 min, Fe/ Ni binder
 (a) chromium and tungsten EPMA concentration profile; (b) Fe, Ni normalised by total binder concentration.

4.5 H-type diffusion couples

4.5.1 H-type diffusion couples with Co binder

The sample VCoH115+ is an H-type diffusion couple with cobalt binder and GGI=vanadium. As shown Figure 4-114(a) the detection limit is already reached after 25 μm . The normalised interface concentration $c_0(\text{V}/\text{Co})=0.031$ is by a factor of 2.5 higher than it is expected from the solubility data in literature, where $c(\text{V}/\text{Co})=0.012$ at 1150°C as interpolated from literature data in Table 2-4.

The reasons are further discussed in section 5.4. The transport factor was estimated to $D=2.05 \cdot 10^{-9} \text{ cm}^2/\text{s}$. No cobalt gradient was detected. An almost identical transport factor of $2.01 \cdot 10^{-9} \text{ cm}^2/\text{s}$ was measured for chromium transport.

Very large standard deviations were calculated as indicated by the error bars. The liquid phase sintering with the subsequent annealing caused significant WC grain growth with grain sizes larger than the EPMA bean size. Particular EPMA measuring points can thus hit single WC grains without detecting binder phase, while other points hit coarsened binder areas. The large standard deviation in this case is hence caused by grain coarsening. The totals (b), represented by the blue dots, scatter around $100 \pm 0.5 \text{ wt}\%$. Since the samples have no porosity the total confirms the accuracy of the EPMA measurements and the validity of the calibration.

Sample	$D [10^{-10} \text{ cm}^2/\text{s}]$	$c_0(\text{GGI}/\text{Co})$
CCoH115+	20.1 ± 3.1	0.061 ± 0.014
VCoH115+	20.5 ± 5.7	0.033 ± 0.008

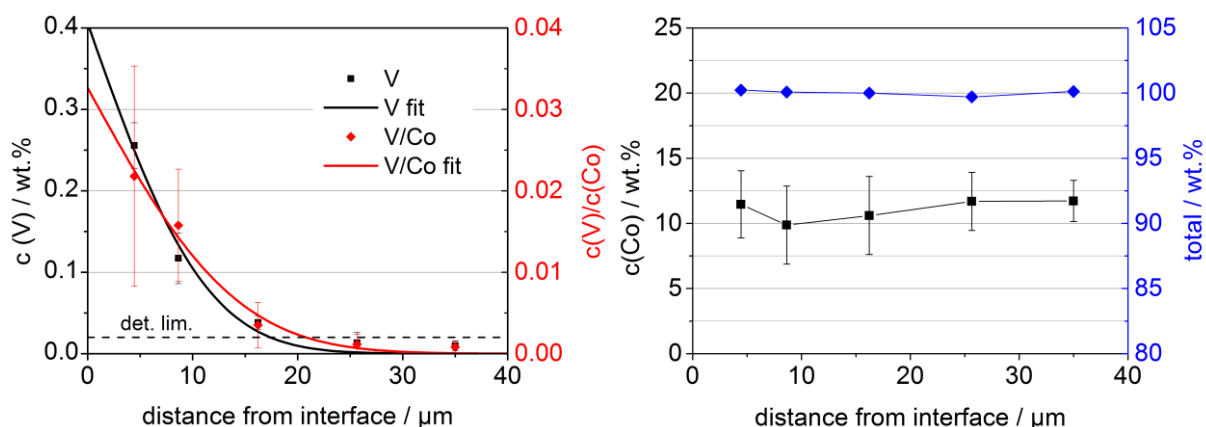


Figure 4-114: VCoH115+, annealed at 1150°C for 5 min; Co binder; as-measured and normalised EPMA-concentration profiles of vanadium.

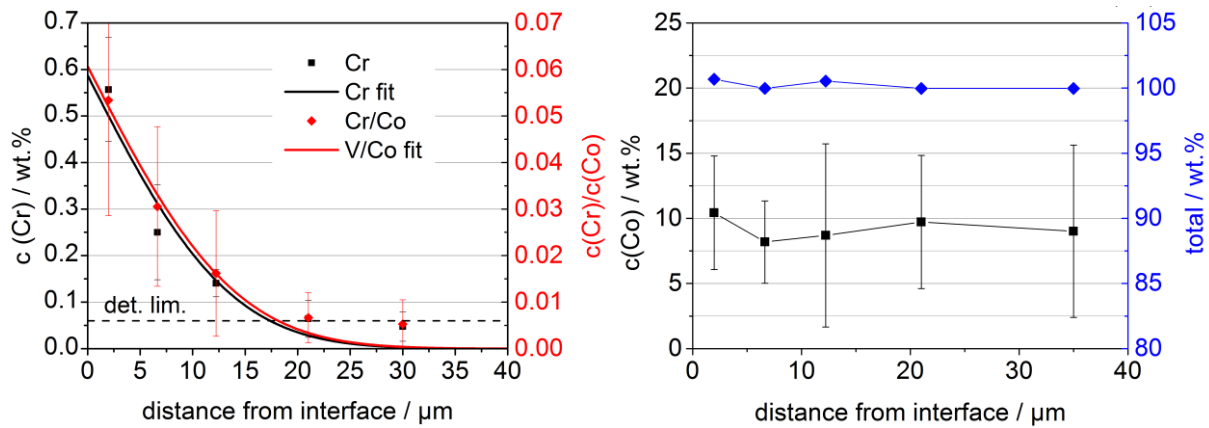


Figure 4-115: CCoH115+, annealed at 1150°C for 5 min; Co binder; as-measured and normalised EPMA-concentration profiles of vanadium.

4.5.2 H-type diffusion couples with Fe/Co/Ni binder

The as-measured and the normalised chromium concentration profiles of sample C424H115+ with Fe/Co/Ni-40/20/40 wt% binder are presented in Figure 4-122(a) while (b) shows the relative concentrations of Fe, Co and Ni. The normalised interface concentration of chromium is $c_0(\text{Cr}/\text{binder})=0.062$. No literature data for the solubility of chromium in Fe/Co/Ni binder alloy is available. However, by interpolating the literature data in Table 2-4 a solubility of chromium in cobalt binder is $c(\text{Cr}/\text{Co})\sim 0.07$ at 1150°C. Though the solubility in Fe/Co/Ni binder alloy is certainly different the measured chromium concentration is close to the solubility in cobalt. The corresponding transport factor was calculated to $D=1\cdot 10^{-9}$ cm²/s. Regarding the Fe/Co/Ni ratio no clear influence of chromium was found (b).

The transport factor of vanadium in V424H115+ of $D=9.6\cdot 10^{-10}$ cm²/s, see Figure 4-124(a) for the concentration profiles, is equal within the error range to chromium. The interface concentration of $c(\text{V}/\text{binder})=0.025$ is significantly lower as compared to chromium. In cobalt binder, the vanadium solubility is $c(\text{V}/\text{Co})=0.014$ at 1150°C as interpolated from the data in Table 2-4. Though the binder alloy is different a similar solubility is expected. According to [11WAG] it is even slightly lower in Fe-rich alloys.

Consequently the maximum vanadium concentration is above the solubility limit in the binder phase which will be further discussed in section 5.4. No clear influence of vanadium on the Fe/Co/Ni ratio was observed as illustrated in Figure 4-124(b). A summary of the calculated values is listed in Table 4-28.

Table 4-26: Transport factor and interface concentration of chromium and vanadium in H-type samples with Fe/Co/Ni-40/20/40 wt% binder alloy.

Sample	D [10^{-10} cm ² /s]	$c_0(\text{GGI/binder})$
C424H115+	10.1 ± 2.1	0.067 ± 0.007
C424H115+N	12.6 ± 1.4	0.027 ± 0.002
V424H115+	9.6 ± 3.7	0.025 ± 0.004
V424H115+N	13.0 ± 1.8	0.028 ± 0.005

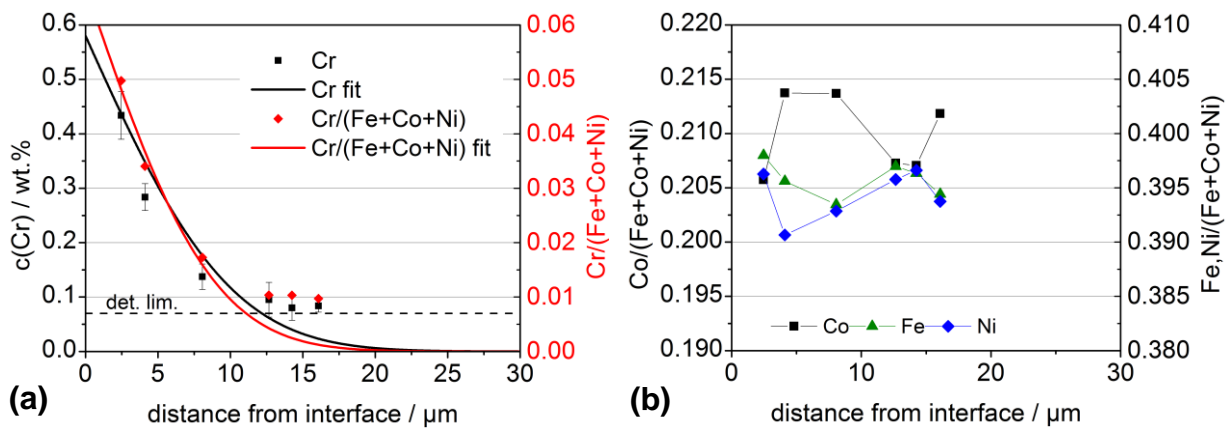


Figure 4-116: C424H115+, annealed at 1150°C for 15 min, Co binder.

(a) as-measured and normalised EPMA-concentration profiles of chromium, (b) Fe, Co, Ni normalised by total binder concentration.

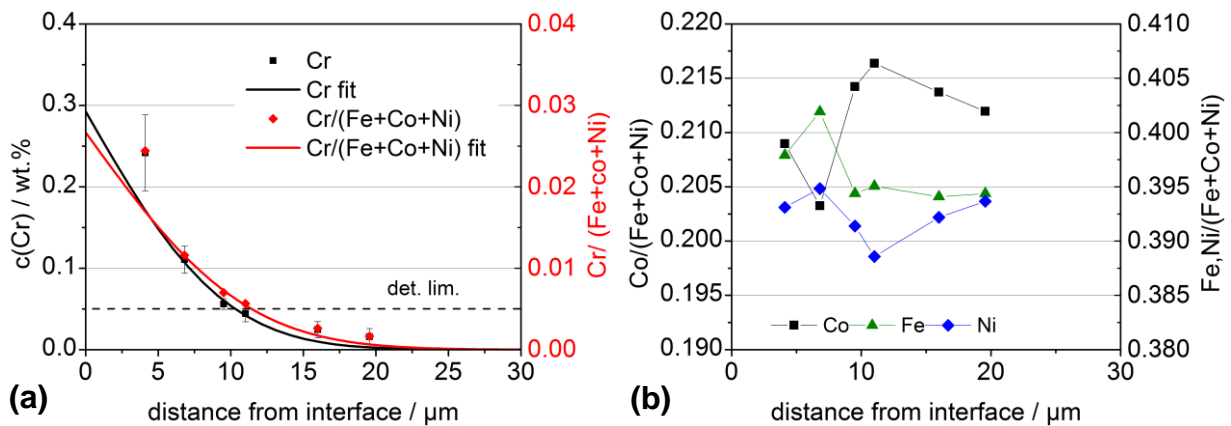


Figure 4-117: C424H115+N, annealed at 1150°C for 15 min in nitrogen, Co binder.

(a) as-measured and normalised EPMA-concentration profiles of chromium (b) Fe, Co, Ni normalised by total binder concentration.

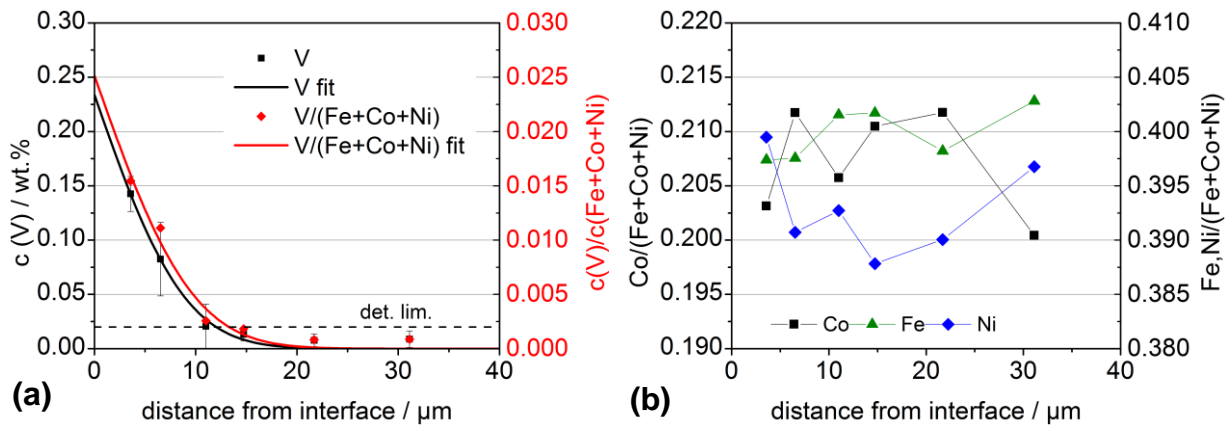


Figure 4-118: V424H115+, annealed at 1150°C for 15 min; Fe/Co/ Ni binder, (a) as-measured and normalised EPMA-concentration profiles of vanadium, (b) Fe, Co, Ni normalised by total binder concentration.

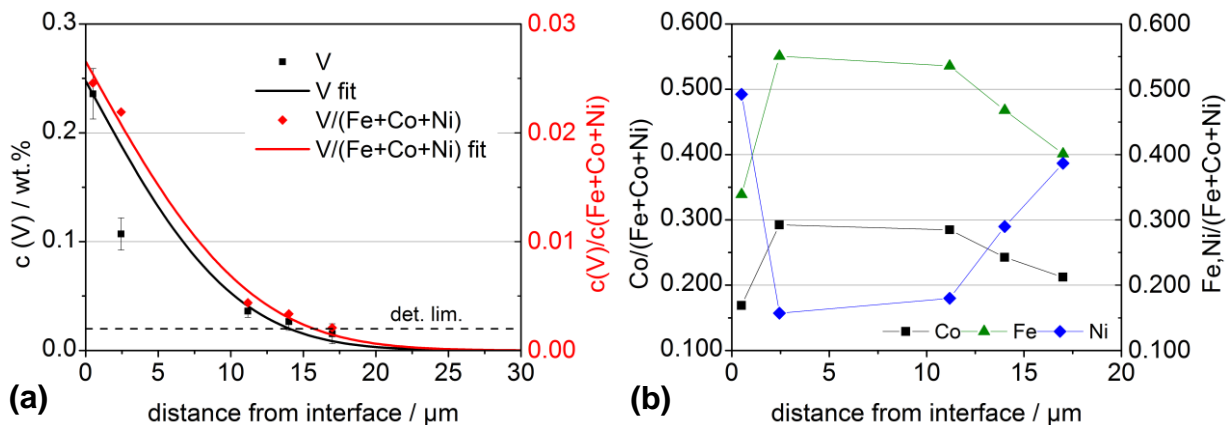


Figure 4-119: V424H115+N, annealed at 1150°C for 15 min in nitrogen, Co binder. (a) as-measured and normalised EPMA-concentration profiles of vanadium (b) Fe, Co, Ni normalised by total binder concentration.

4.5.3 H-type diffusion couples with Fe/Ni binder

The chromium concentration profiles for sample C19H115+ are shown in Figure 4-126(a). A chromium interface concentration of $c_0(\text{Cr}/(\text{Fe+Ni}))=0.041$ was measured, and the transport factor is $D=7.6 \cdot 10^{-10} \text{ cm}^2/\text{s}$. The transport factor of vanadium in sample V19H115+ of $D=4.8 \cdot 10^{-10} \text{ cm}^2/\text{s}$ is slightly lower while the interface concentrations are equal within the error range as can be seen from Figure 4-127(a) and Table 4-29. However, significant differences occur when comparing the Fe/Ni ratio in Figure 4-126(b) and Figure 4-127(b) for chromium and vanadium samples, respectively. In case of GGI=chromium a decrease of the iron concentration is observed close to the interface while no such gradient is found with vanadium.

Table 4-27: Transport factor and interface concentration of chromium and vanadium in H-type samples with Fe/Ni-15/85 wt% binder alloy.

Sample	$D_{GGI}^{19,H}$ [10^{-10} cm ² /s]	$c_0(\text{GGI/Co})$,
C19H115+	7.7 ± 1.7	0.041 ± 0.005
V19H115+	6.2 ± 0.8	0.037 ± 0.002

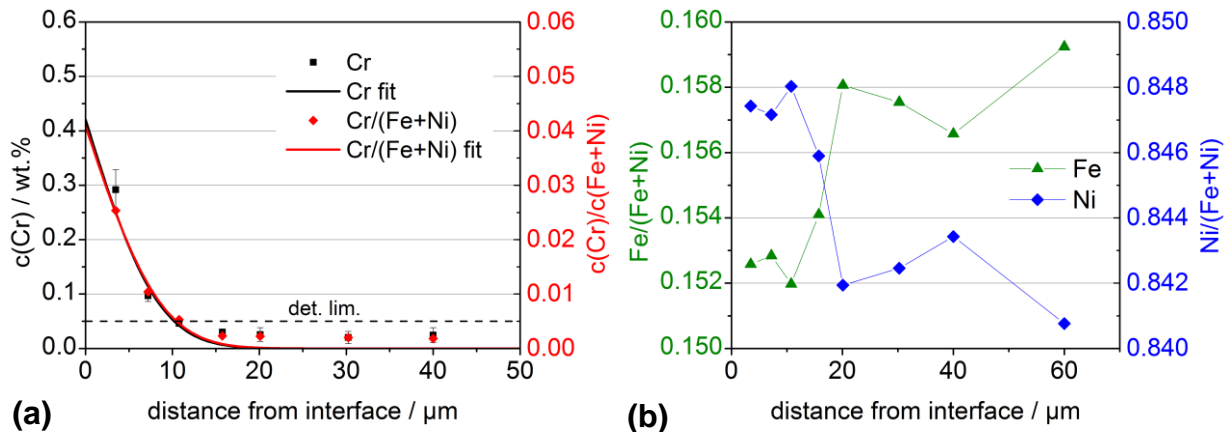


Figure 4-120: C19H115+, annealed at 1150°C for 15 min; Fe/ Ni binder, binder Ta-doped, (a) as-measured and normalised EPMA-concentration profiles of chromium, (b) Fe, Ni normalised by total binder concentration.

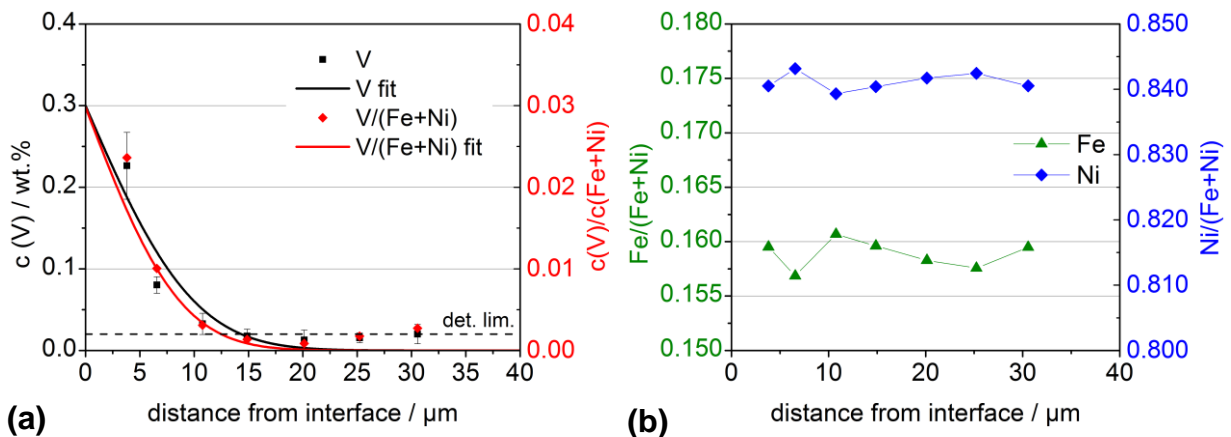


Figure 4-121: V19H115+, annealed at 1150°C for 15 min; Fe/Ni binder, binder Ta-doped, (a) as-measured and normalised EPMA-concentration profiles of vanadium, (b) Fe, Ni normalised by total binder concentration-

The two components of H-type diffusion couples are liquid-phase sintered hardmetals with subsequent annealing at 1150°C for 10 h. The binder phase is thus close to equilibrium state. The diffusion experiment was conducted at 1150°C for 5 min for all samples. Generally, the diffusion depths obtained for H-type couples are short

around 20 μm , since a significantly faster diffusion was expected prior to the experiment. Consequently, only a small number of data points above detection limit are available for curve fitting and the errors are larger than the differences between the samples. Nevertheless, they provide some important information which is discussed later. Some of the transport factors listed in this chapter differ slightly from those recently published in [15BUC]. These values were obtained from as-measured data, while the values presented here were obtained from normalised data. The normalisation was chosen to eliminate the errors by inhomogeneous binder distribution as discussed in section 4.1.

Though the binder alloy is different a similar solubility is expected. According to [11WAG] it is even slightly lower in Fe-rich alloys.

Consequently the maximum vanadium concentration is above the solubility limit in the binder phase which will be further discussed in section 5.4. No clear influence of vanadium on the Fe/Co/Ni ratio was observed as illustrated in Figure 4-124(b). A summary of the calculated values is listed in Table 4-28.

Table 4-28: Transport factor and interface concentration of chromium and vanadium in H-type samples with Fe/Co/Ni-40/20/40 wt% binder alloy.

Sample	D [10^{-10} cm ² /s]	$c_0(\text{GGI/binder})$
C424H115+	10.1 ± 2.1	0.067 ± 0.007
C424H115+N	12.6 ± 1.4	0.027 ± 0.002
V424H115+	9.6 ± 3.7	0.025 ± 0.004
V424H115+N	13.0 ± 1.8	0.028 ± 0.005

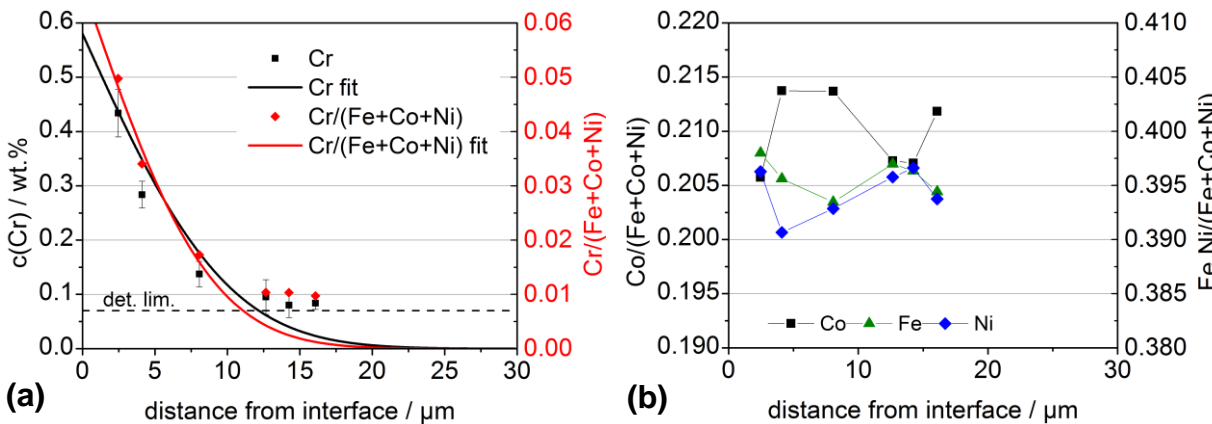


Figure 4-122: C424H115+, annealed at 1150°C for 15 min, Co binder. as-measured and normalised EPMA-concentration profiles of chromium (b) Fe, Co, Ni normalised by total binder concentration

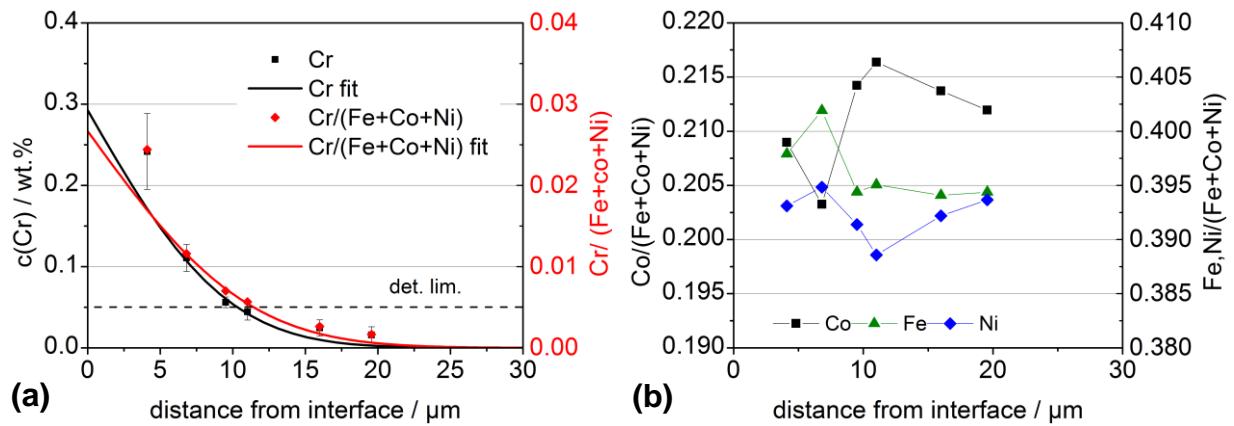


Figure 4-123: C424H115+N, annealed at 1150°C for 15 min in nitrogen, Co binder. (a) as-measured and normalised EPMA-concentration profiles of chromium (b) Fe, Co, Ni normalised by total binder concentration

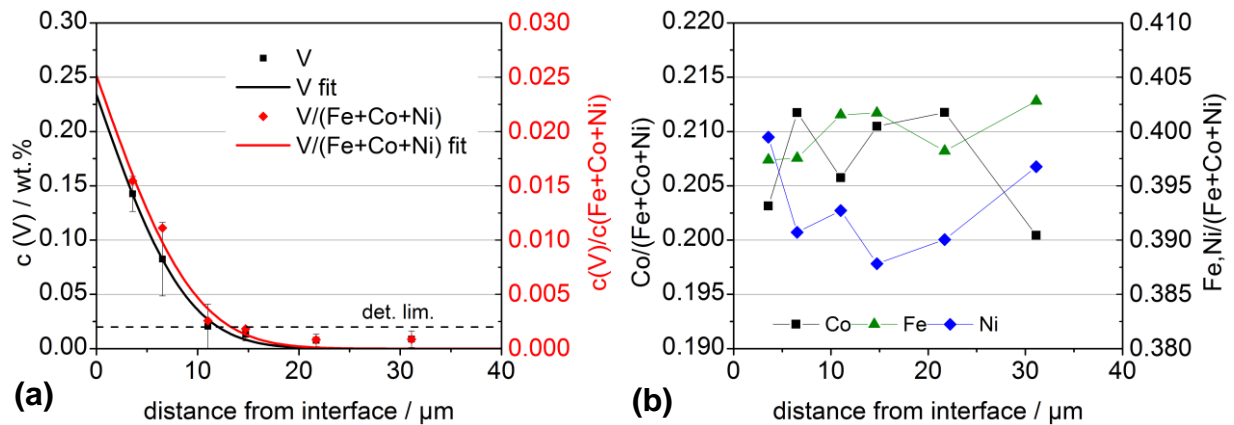


Figure 4-124: V424H115+, annealed at 1150°C for 15 min; Fe/Co/ Ni binder (a) as-measured and normalised EPMA-concentration profiles of vanadium (b) Fe, Co, Ni normalised by total binder concentration

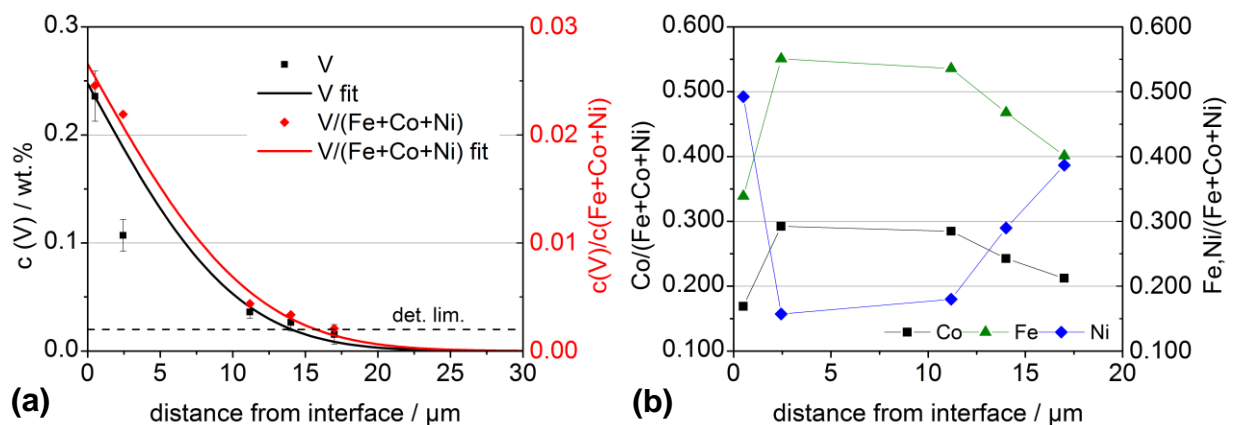


Figure 4-125: V424H115+N, annealed at 1150°C for 15 min in nitrogen, Co binder. (a) as-measured and normalised EPMA-concentration profiles of vanadium (b) Fe, Co, Ni normalised by total binder concentration

4.5.4 H-type diffusion couples with Fe/Ni binder

The chromium concentration profiles for sample C19H115+ are shown in Figure 4-126(a). A chromium interface concentration of $c_0(\text{Cr}/\text{Fe}+\text{Ni})=0.041$ was measured, and the transport factor is $D=7.6 \cdot 10^{-10} \text{ cm}^2/\text{s}$. The transport factor of vanadium in sample V19H115+ of $D=4.8 \cdot 10^{-10} \text{ cm}^2/\text{s}$ is slightly lower while the interface concentrations are equal within the error range as can be seen from Figure 4-127(a) and Table 4-29. However, significant differences occur when comparing the Fe/Ni ratio in Figure 4-126(b) and Figure 4-127(b) for chromium and vanadium samples, respectively. In case of GGI=chromium a decrease of the iron concentration is observed close to the interface while no such gradient is found with vanadium.

Table 4-29: Transport factor and interface concentration of chromium and vanadium in H-type samples with Fe/Ni-15/85 wt% binder alloy.

Sample	$D_{GGI}^{19,H} [10^{-10} \text{ cm}^2/\text{s}]$	$c_0(\text{GGI}/\text{Co}),$
C19H115+	7.7 ± 1.7	0.041 ± 0.005
V19H115+	6.2 ± 0.8	0.037 ± 0.002

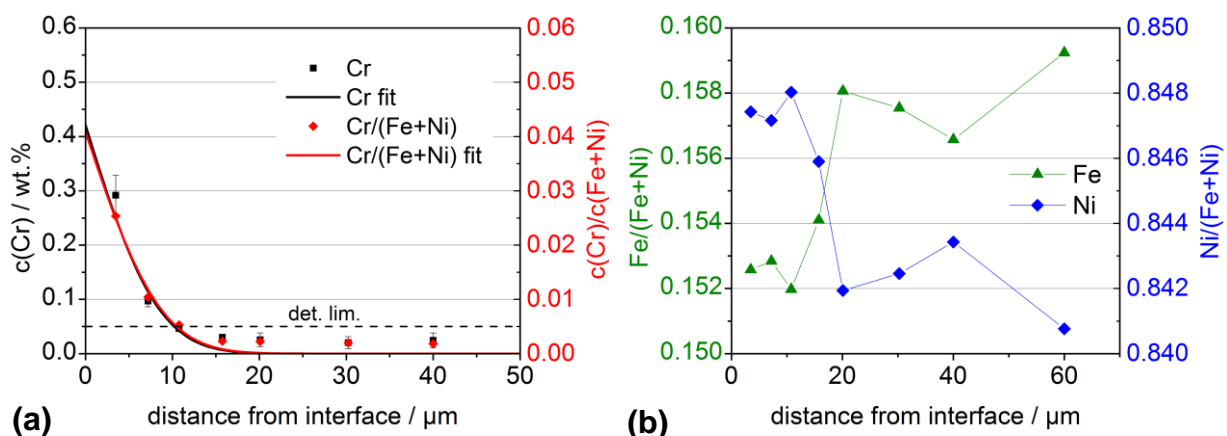


Figure 4-126: C19H115+, annealed at 1150°C for 15 min; Fe/ Ni binder, binder Ta-doped
 (a) as-measured and normalised EPMA-concentration profiles of chromium
 (b) Fe, Ni normalised by total binder concentration

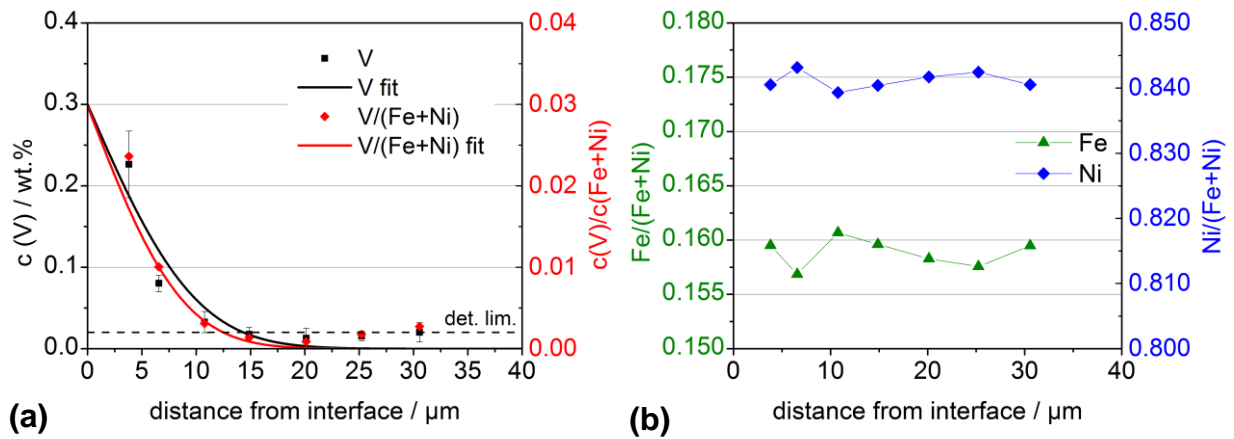


Figure 4-127: V19H115+, annealed at 1150°C for 15 min; Fe/Ni binder, binder Ta-doped, (a) as-measured and normalised EPMA-concentration profiles of vanadium, (b) Fe, Ni normalised by total binder concentration.

4.6 Thermal Analyses

Three different types of samples were investigated by means of thermal analyses. In the first series, phase reactions and degassing behaviour of the powder mixtures used to prepare G-type couples were analysed. The data allows answering questions on the phase reactions and degassing processes of the diffusion couple components upon annealing and possible influences on the GGI distribution. Furthermore it allows a confirmation of the intended carbon potential of the WC-binder diffusion couple parts.

The second sample type are series of hardmetal of type WC-GGI-binder (GGI=Cr, Mo, V) with varying GGI/W ratios ranging from 2/98–50/50 in order to identify reactions between the compounds upon heating a doped hardmetal.

The third sample type are doped hardmetals of type WC-GGI-Co with an application-related concentration of $c(\text{GGI})=0.9$ wt%. Cr, Mo and V were added as different compounds such as carbides, nitrides and borides in order to determine their influence on phase reactions.

4.6.1 Diffusion couple components

4.6.1.1 Undoped

The undoped samples represent the WC-binder-parts of the diffusion couples. All of the samples reveal only one specific DSC-peak upon heat-up and cool down, see Figure 4-128(a) – Figure 4-133(a). This peak marks the temperature of melt formation. The samples WCo_+ , WCo , WCo_- and WCo_n with cobalt binder reveal a relatively narrow peak and the onset temperatures of the first heat-up and cool-down cycles are close. In comparison, hardmetals with alternative binder alloys W424+ and W19+ show signals over a wider temperature range. While the peaks for the hardmetal with Fe/Co/Ni binder are unimodal but blurred over a relatively wide temperature range, see Figure 4-132(a), bimodal peaks were detected for the hardmetal with Fe/Ni-binder as shown in Figure 4-133(a). Both cases can be explained by the melt formation taking place in a temperature range instead of an invariant equilibrium as for cobalt. Such a melting range fits to literature data, see Figure 2-13.

The temperature of melt-formation can be used as an indicator for proper carbon potential adjustment when it is compared to the phase diagrams in section 2.4.

It can be seen from the DSC data as summarised in Table 4-30 that all WC-binder diffusion couple parts have the intended carbon potential since the measured data fits well to those read from the phase diagrams or literature data from Table 2-3.

From TG data in Figure 4-128(b) – Figure 4-133(b), a characteristic mass loss is observed around 700–900°C for all binder alloys. It has been proven in previous works, e.g. [06GES, 10BR11, 12BUC] that this mass loss can be attributed to the carbothermic reduction of surface oxides covering WC grains. As a consequence the WC-binder part of the diffusion couple is free of oxides at the diffusion experiment temperatures and no influence on the diffusion behaviour is expected.

Besides the WC-reduction peak at 700–900°C a second peak is observed around 350–650°C for the hardmetals with cobalt binder. It turns out that for the sample with nano-cobalt (WCo_n) the mass loss of this signal is significantly larger as compared to the sample with conventional cobalt (WCo). Since the nano-grade has a higher specific surface and, hence a higher oxygen-content this peak can be correlated to the carbothermic reduction of cobalt. In hardmetals with alternative binder alloys the binder reduction peak is multimodal and shifted to higher temperatures. For the hardmetal with Fe/Co/Ni binder three maxima are detected related to the three binder metals, Figure 4-132(b). The shift to higher temperatures is even more promoted for the hardmetal with Fe/Ni binder, where a bimodal peak partially overlaps with the WC peak as shown in Figure 4-133(b). An overview of the characteristic temperatures is given in Table 4-30.

Table 4-30: Onset of DSC and maximum of TG peaks of undoped WC-binder diffusion couple components upon first heat-up cycle. All values in °C.

Sample	Binder	Onset DSC signal	TG maximum binder	TG maximum WC
WCo+	Co	1298	604	757
WCo	Co	1324	450	780
WCo-	Co	1368	580	863
WCo _n	nano-Co	1314	460	700
W424+	Fe/Co/Ni	1290	370/600/690	810
W19+	Fe/Ni	1320	600/700	790

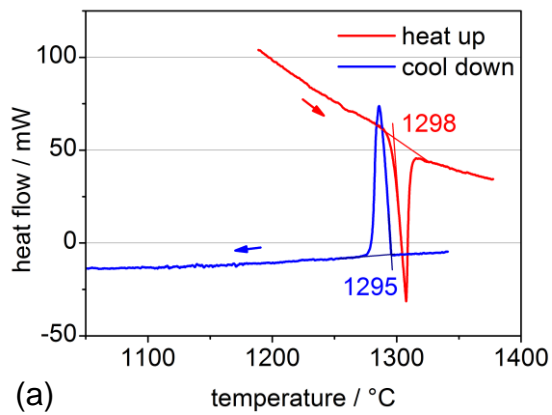


Figure 4-128: Thermal analysis of the diffusion couple component WCo+ with high carbon potential. (a) DSC signals of the first heating and cooling cycle. (b) TG analysis of first heat-up.

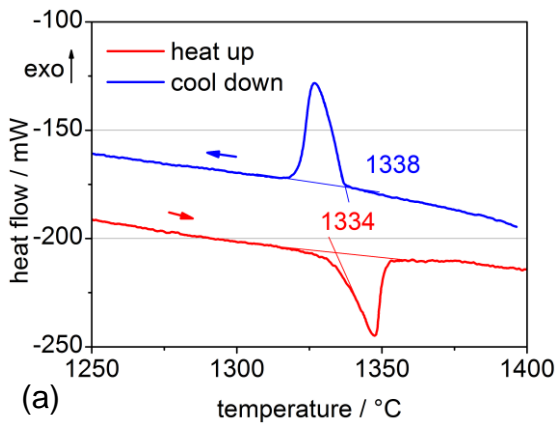


Figure 4-129: Thermal analysis of the diffusion couple component WCo with mid carbon potential. (a) DSC signals of the first heating and cooling cycle. (b) TG analysis of first heat-up.

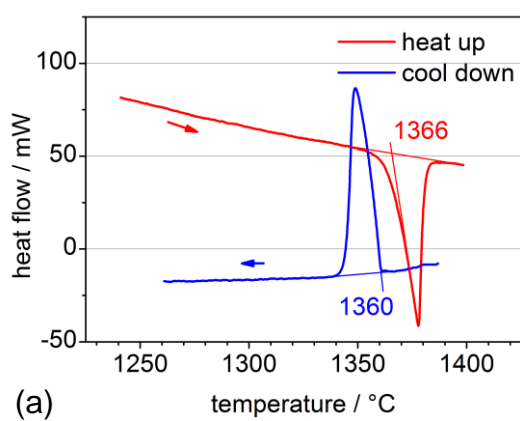


Figure 4-130: Thermal analysis of the diffusion couple component WCo- with low carbon potential. (a) DSC signals of the first heating and cooling cycle. (b) TG analysis of first heat-up.

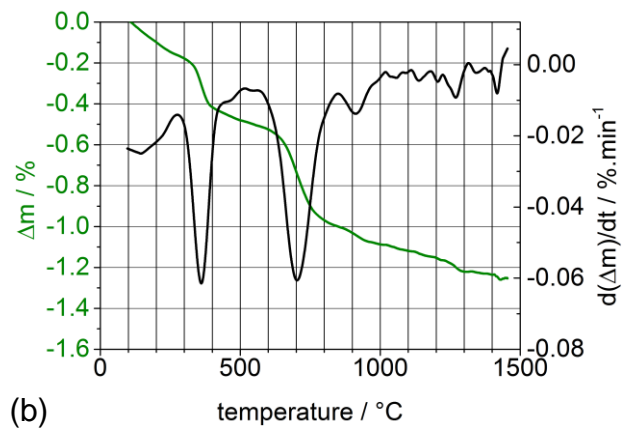
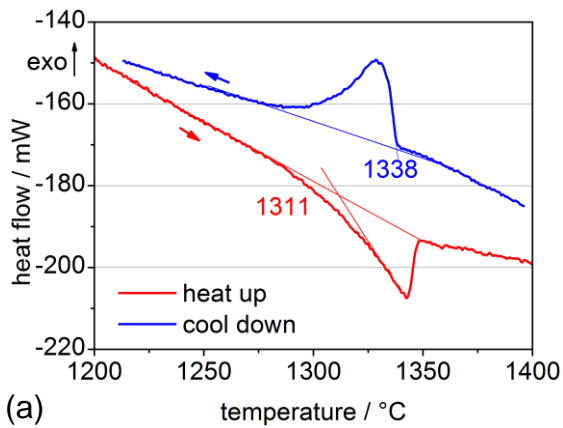


Figure 4-131: Thermal analysis of the diffusion couple component WCo_n : WC-Co(nano) mid-carbon hardmetal. (a) DSC signals of the first heating and cooling cycle. (b) TG analysis of first heat-up.

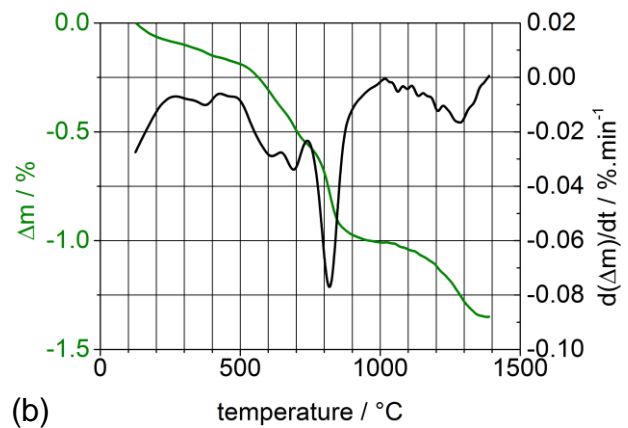
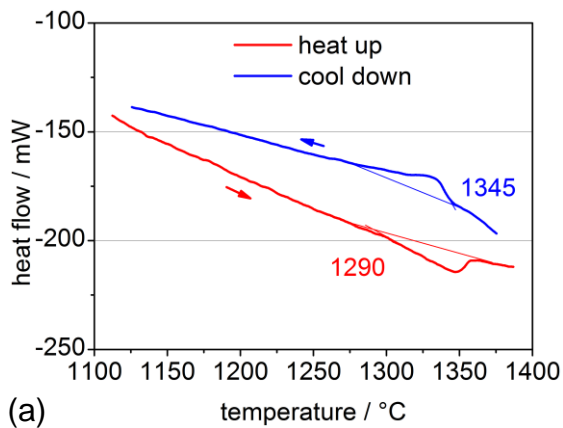


Figure 4-132: Thermal analysis of the diffusion couple component $W424+$: WC-Fe/Co/Ni 40/20/40 high-carbon hardmetal. (a) DSC signals of the first heating and cooling cycle; (b) TG analysis of first heat-up.

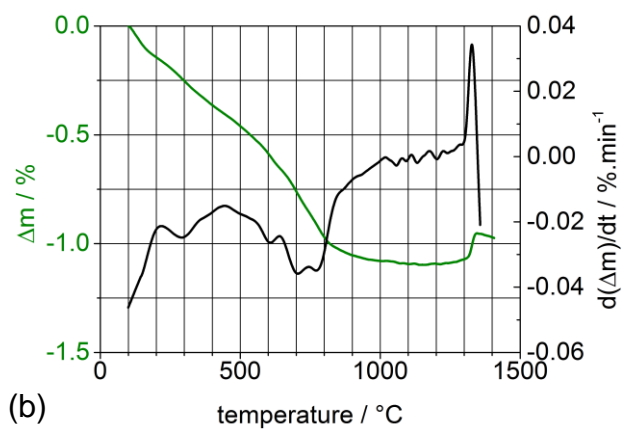
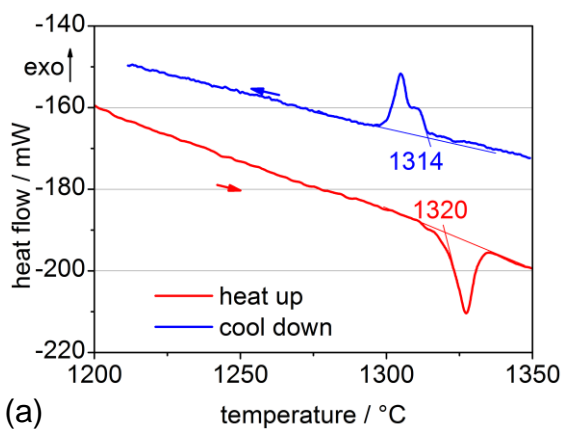


Figure 4-133: Thermal analysis of the diffusion couple component $W19+$: WC-Fe/Ni 15/85 high-carbon hardmetal. (a) DSC signals of the first heating and cooling cycle. (b) TG analysis of first heat-up.

4.6.1.2 Cr-based

The thermochemistry of the chromium-based parts of the diffusion couples is determined by its high chromium content of 70 wt%. Thus, its thermochemistry is not that of usual chromium-doped hardmetal but shows some significant deviations which are discussed below.

The chromium containing parts of diffusion couples with cobalt binder were produced in two different subtypes with and without WC addition represented by the samples CCo+ and CWCo+, respectively. The DSC results of CWCo+ are shown in Figure 4-136 (a) while the corresponding TG-signal is shown in (b). It is particularly striking that no liquid phase signal appears at temperatures around 1190°C as it would be expected from chromium-doped hardmetals with high carbon potential (see Table 2-3). For the tungsten-less system CCo+ (Figure 4-134) no liquid phase signal was detected either. In the latter case according to Kaplan et al. [14KAP] the given composition results in the phase equilibrium $M_3C_2 + M_7C_3 + C$ where indeed no liquid phase is expected within the investigated temperature range. The reason is a certain solubility of cobalt in chromium carbides. However, since the samples origin from powder mixtures it is remarkable that homogenisation takes place that fast already in the solid-state and no local non-equilibrium melting occurs. It has to be noted that the heating rate of 10 K/min upon DSC analysis is significantly lower as compared to the diffusion experiments (100 K/min). Due to the resulting shorter homogenisation time local melting phenomena are still possible within diffusion couples but cannot be verified by DSC.

In case of the W-containing sample CWCo+ similar considerations apply. Based on literature [14KAP, 15KAP] cobalt- and tungsten-containing mixed chromium carbides are expected to form.

When cobalt is replaced by the cobalt-reduced alternative binder Fe/Co/Ni=40/20/40 wt% in sample CW424+, it can be seen from Figure 4-137 (a) that an endothermic DSC signal upon heat-up and exothermic upon cool-down indicating melting of the binder phase is detected. Unlike in cobalt at least a part of the binder phase is not incorporated in the carbide phase. This can be explained by either a slower incorporation of iron and nickel or a lower solubility of the latter in the chromium carbide. If the first case applies the peak upon cool-down should disappear or at least be significantly smaller than the heat-up peak because the binder phase

has time to resolve in the time range where it is liquid and the presence of liquid phase should further boost the reaction.

It can be concluded that lower cobalt content in the sample leads to a stronger liquid phase signal upon DSC measurements indicating a higher amount of liquid phase present in the sample.

The temporary formation of $(\text{Co,Cr,W})_x\text{C}_y$ carbides might occur as well upon the early sintering stages of a doped hardmetal and can hence serve as a nucleus for microstructural inhomogeneities. This effect will be further discussed in section 5.1.1. Chromium carbides are known to form a stable oxide layer on their surface. Due to the large specific surface of micron-scaled powders a significant amount of oxygen is introduced in doped hardmetals. These oxides disappear by carbothermic reduction upon the first sintering stages. However, while in WC-binder hardmetals all oxides are reduced at temperatures below 900°C, chromium oxides are stable until 1000–1100°C see e.g. [06GES, 09BRI, 10BRI1, 12BUC, 15WAN]. Subsequently they will remain in diffusion couples tested below this temperature range. Thus, it is important to gain information on the carbothermic reduction kinetics which can be deduced from thermogravimetric analysis. The TG data of the samples with cobalt binder can be found in Figure 4-134(b) and Figure 4-136(b) for the tungsten-free sample CCo+ and the tungsten-containing sample CWCo+, respectively. For both samples a characteristic peak appears at 1000°C, which can be attributed to the reduction of chromium oxides. Below 450°C a smaller characteristic peak is caused by reduction of cobalt oxides. A similar picture is drawn for the alternative binder samples CW424+ in Figure 4-137(b) and CW19+ in Figure 4-138(b) where the chromium reduction peak appears as well around 1000°C. The binder specific peaks can be found around 400–500°C, though it is hard to spot whether the mass loss is caused by the binder phase or the decomposition of organic impurities. However, this temperature range is irrelevant for diffusion couple testing, thus no further experiments to separate binder signals from impurity signals were conducted. The chromium reduction is completed at temperatures below 1050°C, the peak maximum appears around 990°C independent from the binder alloy.

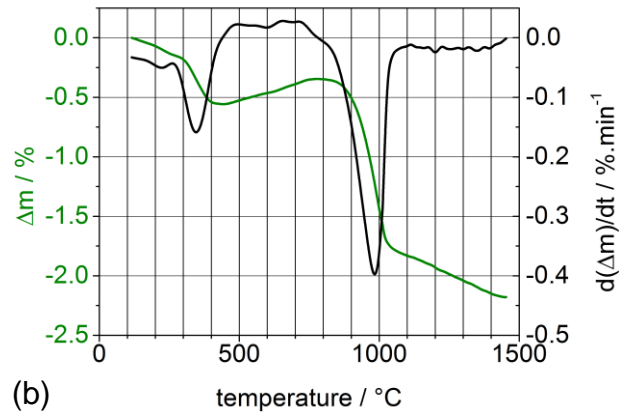
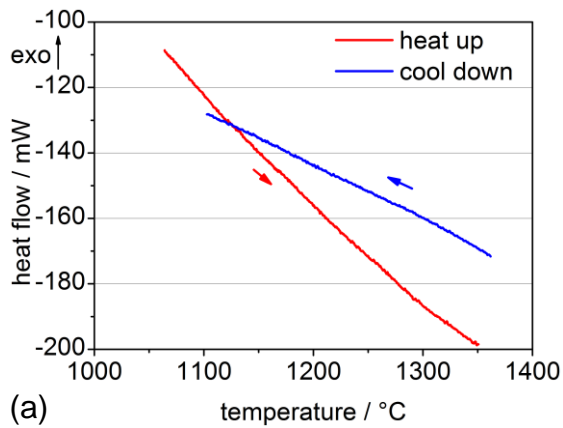


Figure 4-134: Thermal analysis of the diffusion couple component CCo+. (a) DSC signals of the first heating and cooling cycle. (b) TG analysis of first heat-up.

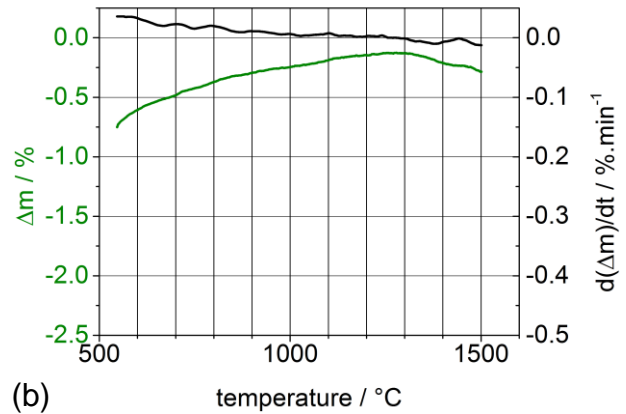
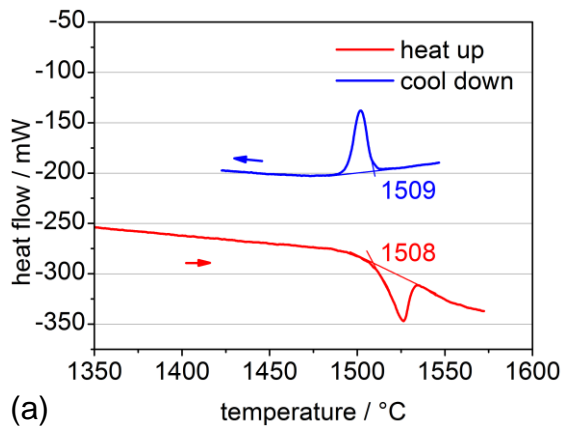


Figure 4-135: Thermal analysis of the diffusion couple component CCo+_in situ. (a) DSC signals of the first heating and cooling cycle. (b) TG analysis of first heat-up.

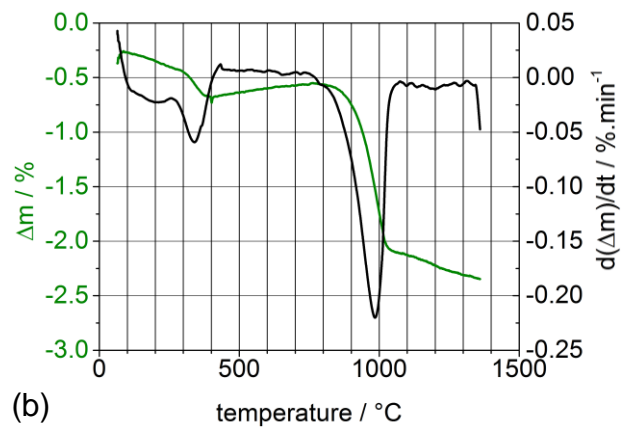
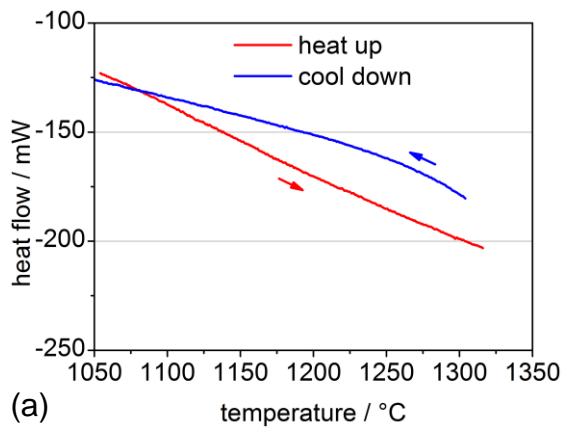


Figure 4-136: Thermal analysis of the diffusion couple component CWCo+. (a) DSC signals of the first heating and cooling cycle. (b) TG analysis of first heat-up.

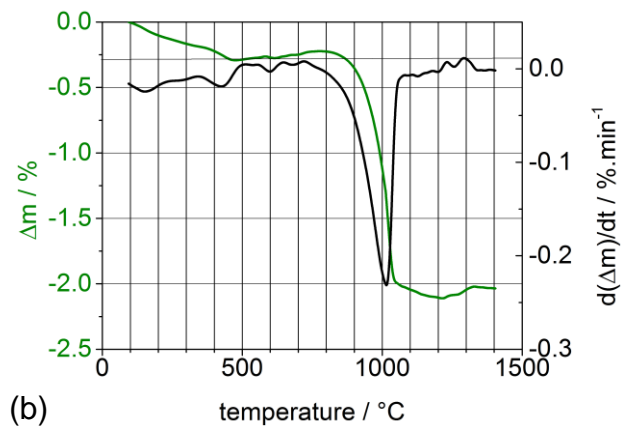
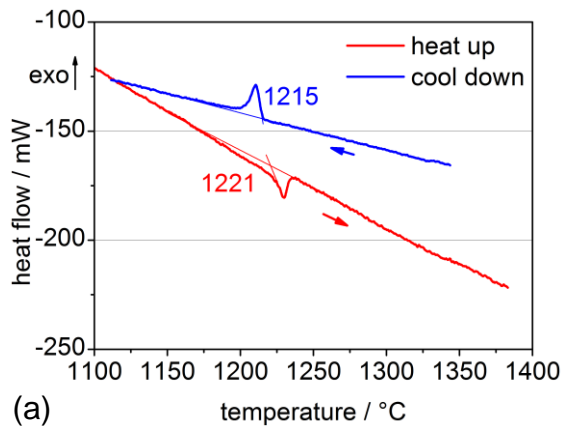


Figure 4-137: Thermal analysis of the diffusion couple component CW424+. (a) DSC signals of the first heating and cooling cycle. (b) TG analysis of first heat-up.

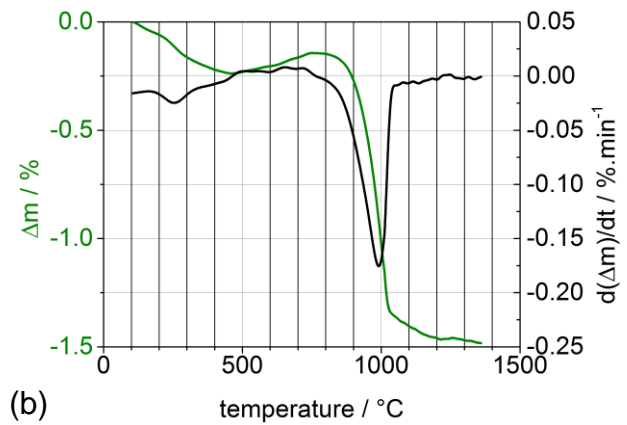
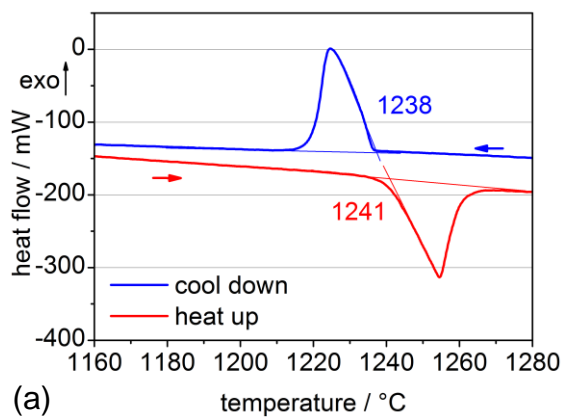


Figure 4-138: Thermal analysis of the diffusion couple component CW19+. (a) DSC signals of the first heating and cooling cycle. (b) TG analysis of first heat-up.

4.6.1.3 V-based

Four diffusion couple components based on VC were prepared. All of them show a strong TG signal below 400°C which is only observed in VC containing samples. Signals in this range likely origin from either water or organic impurities. However, the signal covers the binder specific mass loss, which is hence not further discussed in this section. Since this temperature range is irrelevant for diffusion couples it will not influence the GGI transport.

The sample VCo is a VC-Co cemented carbide with high carbon potential in order to avoid V₂C formation. The DSC upon the first heat-up cycle shows four characteristic peaks as depicted in Figure 4-139(a). A small peak is observed at 1198°C. The peak at 1246°C was found only upon heat-up and is not related to a mass loss event. The signal setting on at 1314°C is related to the VC-Co eutectic reaction appearing at 1330°C, compare Table 2-3. The earlier onset can be explained by non-equilibrium states upon the first heating cycle. The equilibrated signal (Appendix section, Figure 8-9), upon the second heating cycle delivers 1336°C onset temperature and the shape is unimodal instead of bimodal.

Interestingly, the signals of 1246°C upon heat-up and 1207°C upon cool-down are as well found in equilibrium state. As a consequence a second phase transition appears additionally to the VC/Co eutectic reaction. This is an important finding since diffusion couples with VC were also prepared at 1250°C where this phase transition takes place. The consequences on the GGI-distribution are discussed in section 5.1.1. The TG is shown in Figure 4-139(b). A bimodal peak setting on at 600°C with maxima at 913°C (A) and 1013°C (B) was detected. At 1143°C a signal overlapping with the main peak appears (C). The mass loss event with maximum at 1340°C (D) concurs with the liquid phase formation.

If 10 wt% of tungsten is added as in case of VWCo+ three DSC peaks are detected as shown in Figure 4-140(a). The signals at 1102°C and 1201°C are only detected upon heat-up, but not upon cool down or the second heating cycle. Hence, they are related to non-equilibrium reaction. A comparison to the TG data (b) shows that these peaks correlate with the mass-loss event (C). The liquid phase formation peak sets on at 1325°C and shows a long tailing, which disappears upon cool-down and is hence attributed to the non-equilibrium state of the mixture.

The carbothermic reduction of WC usually happens around 800°C, but no such peak is detected. Instead, a strong peak with maxima at 916°C and 1013°C is detected. Both were also found at the same temperatures in the tungsten-free sample VCo and are hence related to VC but not to WC. A small signal (D) was detected at 1408°C which matches the offset of the liquid-phase formation peak.

In sample VW424+ the Co is replaced by a Fe/Co/Ni. The DSC is depicted in Figure 4-141(a) and shows peaks at 1148°C, 1201°C and 1350°C. The latter marks the liquid-phase formation. The peak at 1201°C correlates with the mass-loss event (C) as it was already observed for cobalt-based sample WVCo at the same temperature. The TG peaks are as well similar to the cobalt based alloy but shifted by +20°C to higher temperatures. As can be seen from (b) their positions are 936°C (A), 1028°C (B) and 1168°C (C).

The sample VW19+ is based on Fe/Ni-15/85 wt% binder alloy. It can be seen from Figure 4-142(a) that three peaks appear upon the first heat-up cycle as already observed for the samples based on Co and Fe/Co/Ni binder alloy. The first sets on at 1170°C and overlaps with the second peak setting on at 1206°C. Both are not detected upon cool-down and hence non-equilibrium reactions. The signal 2 at 1206°C correlates with the mass-loss peak C as can be seen from Figure 4-138(b). The liquid phase signal appears at 1371°C. The TG again shows three characteristic signals at 929°C (A), 1023°C (B) and 1190°C (C).

A characteristic regarding the TG is that all of the WC-containing samples of this series show a constant mass loss of 0.05 %/min at temperatures >1000°C, which is not observed for the W-free sample VCo. This behaviour was found for V-based samples only. The reasons however could not be identified. The DSC as well as the TG data obtained from this sample series is summarised in Table 4-31.

Table 4-31: DSC and TG signals of V-based diffusion couple components upon first heat-up cycle.

Sample	DSC onset 1 st heat up (°C)				TG 1 st derivation peak maximum (°C)			
	1	2	3	4	A	B	C	D
VCo	1198	1246	1314	1356	916	1013	1080	1340
VWCo+	-	1102	1201	1325	916	1013	1143	1408
VW424+	-	1148	1201	1350	936	1028	1168	-
VW19+	-	1170	1206	1371	929	1023	1190	-

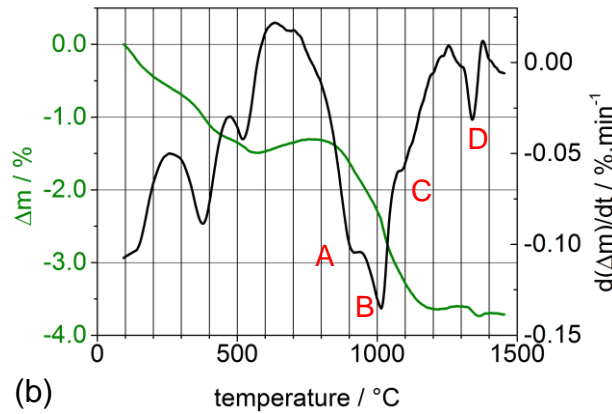
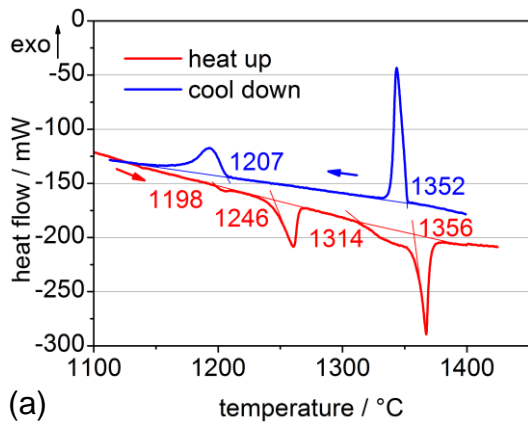


Figure 4-139: Thermal analysis of the diffusion couple component VCo. (a) DSC signals of the first heating and cooling cycle. (b) TG analysis of first heat-up.

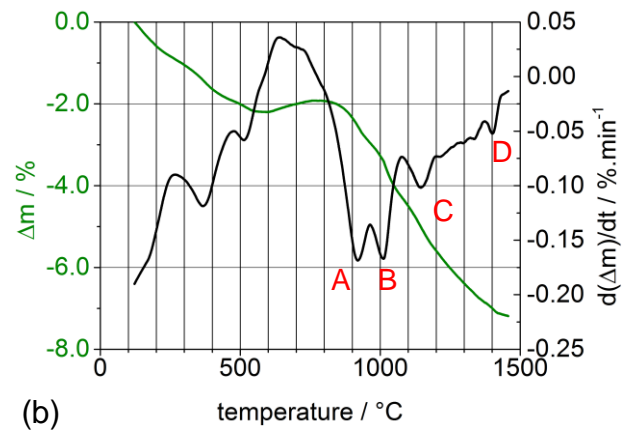
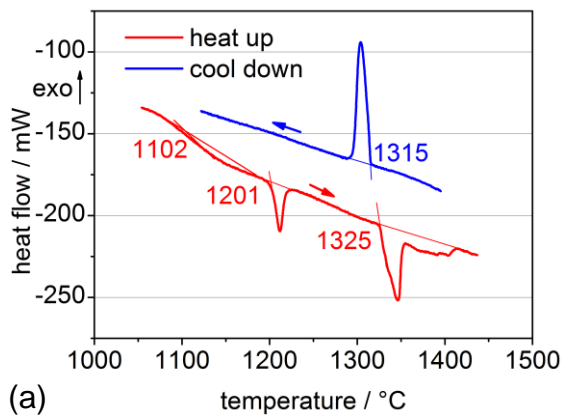


Figure 4-140: Thermal analysis of the diffusion couple component VWCo. (a) DSC signals of the first heating and cooling cycle. (b) TG analysis of first heat-up.

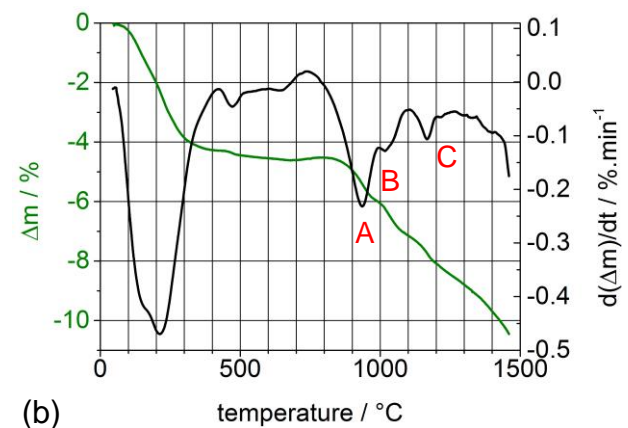
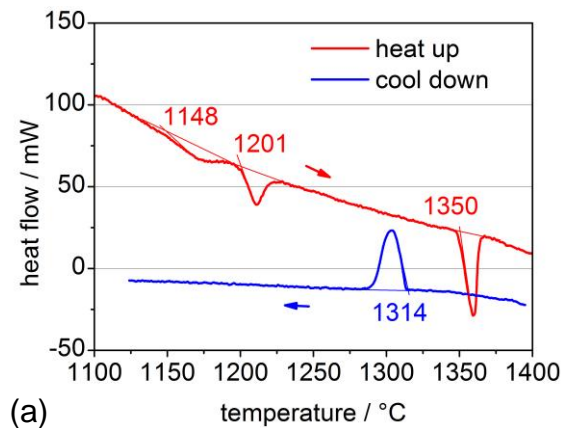


Figure 4-141: Thermal analysis of the diffusion couple component VW424. (a) DSC signals of the first heating and cooling cycle. (b) TG analysis of first heat-up.

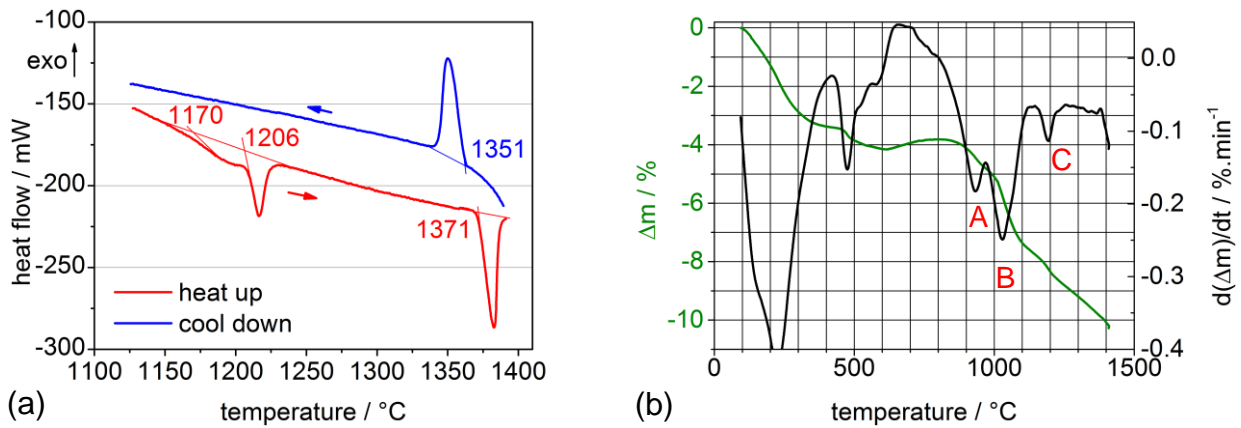


Figure 4-142: Thermal analysis of the diffusion couple component VW19. (a) DSC signals of the first heating and cooling cycle. (b) TG analysis of first heat-up.

4.6.1.4 Cr₃C₂+VC based diffusion couples components

The DSC of the diffusion couple component CVA is depicted in Figure 4-143(a). A single signal at 1254 °C appears at the temperature of melt formation. The bimodal shape indicates the appearance of a melting range. The TG signal (b) shows a bimodal peak with maxima at 990 °C and 1050 °C. A strong mass loss event <500 °C is caused by reduction of cobalt oxides.

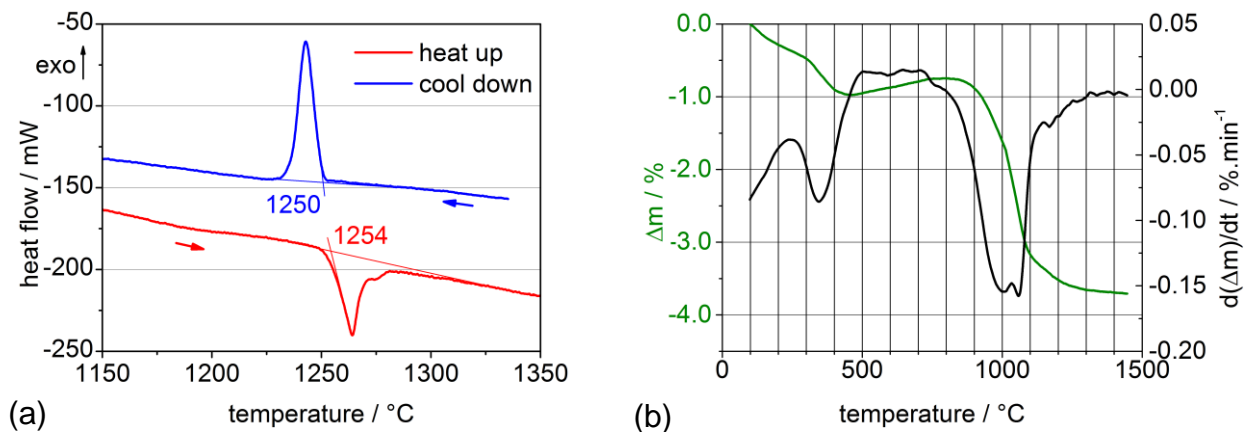


Figure 4-143: Thermal analysis of the diffusion couple component CVA; (a) DSC signals of the first heating and cooling cycle; (b) TG analysis of first heat-up.

4.6.2 Hardmetals with varying GGI/W ratio

4.6.2.1 WC-Co hardmetals with varying V/W ratio

The influence of vanadium on the thermal chemistry of hardmetals was studied by a series of WC-VC-Co hardmetals with an atomic ratio of $V/W=2/98-50/50$ and constant cobalt concentration of 16.3 vol%. A special feature of this sample series is that in the temperature range of 100–300°C strong mass-loss was observed for both samples with CO and Fe/Ni binder alloy. The WC powder was of the same batch as for the other, simultaneously prepared samples. Hence this mass loss is caused by VC. The low temperature onset of this signal points to desorption of H₂O. Since the signal is bimodal two different species have to be involved. It is also possible that the mass-loss is caused by evaporating or cracking organic impurities. However, the identity of the species cannot be clarified by the present data. This strong signal covers the cobalt-related mass loss, which can hence not be detected.

The sample WC-Co-2V was prepared with an atomic ratio of $V/W=2/98$. The corresponding DSC curve is shown in Figure 4-144(a). A small signal with onset at 1141°C appears which is absent upon cool-down and hence related to a non-equilibrium reaction. The peak at 1316°C is caused by melt formation. Upon the second heat-up cycle the equilibrium signal is found by the same temperature. This temperature correlates well to the equilibrium-temperature of 1320°C of a VC-doped WC-Co hardmetal, see Table 2-3. Two characteristic mass loss events (b) are detected: the carbothermic reduction of WC (W) with maximum at 862°C and a VC related mass-loss (V2) at 1062°C.

The DSC of sample WC-Co-10V with $V/W=10/90$ is depicted in Figure 4-145(a). A large peak at 1052°C is observed upon heat-up with a maximum at 1100°C. Both onset and maximum are correlated to the mass-loss event V2, see Figure 4-145(b).

The liquid phase DSC-signal appears at 1285°C. This temperature is lower than the equilibrium in a VC saturated low-carbon hardmetal. The C potential is thus expected to be between the WC+fcc+MC+eta and the WC+fcc+MC+graphite phase fields. The WC related mass-loss appears at 815°C, but the height is significantly lower than of the $V/W=2/98$ hardmetal. However, the main degassing (V2) appears at 1099°C. A shoulder close to the onset is observed at ~950°C. At 1150°C a bimodal peak set on

with maxima at 1201°C (V3) and 1295°C (V4). The latter is identical to the maximum of the DSC signal related to liquid-phase formation.

The effects of a further increase of the V/W ratio to 20/80 is shown by means of sample WC-Co-20V. The DSC analysis depicted in Figure 4-146(a) shows a broad signal setting on at 1055°C with a maximum at 1115°C. As can be seen from (b) both concur with the mass loss event V2. A further small peak is observed at 1176°C, while the liquid phase related signal appears at 1289°C. This temperature is identical to the sample with V/W=10/90, hence similar considerations apply. The WC-reduction peak is no more visible as a single peak but overlaps with the degassing events V1 and V2. Its maximum can be estimated at 809°C. A further signal V3 is detected at 1158°C. The appearance of V4 at a temperature of 1284°C is coincident with the formation of liquid phase.

In sample WC-FeNi-20V the cobalt binder is replaced by a Fe/Ni=15/85 wt% binder alloy. Upon DSC analyses a very broad but flat signal setting on at 1099°C and off at 1250°C is detected, see Figure 4-147(a). This range is related to the degassing event V3, see (b). The liquid phase formation sets on at 1381°C and thus at higher temperature than in a cobalt based hardmetal. This is in accordance to the generally higher phase transition temperatures of Fe/Ni-15/85 based hardmetals, compare Figure 2-12(b) and Figure 2-13(b). The WC reduction (W) peak at 807°C is overlapped by two peaks: the shoulder at the onset is caused by reduction of Fe, see [12BUC], while the event V1 is related to VC degassing. The Peak V2, which is the main peak in the chromium-based hardmetal, is small, while V3 at 1158°C is the strongest peak. Hence, the VC degassing events are dependent on the interaction with binder alloy metals. This effect is further discussed in section 5.1.3.

Sample WC-Co-50V has the highest V/W ratio of 50/50. The DSC curve is illustrated in Figure 4-148(a). Again a signal at 1146°C is observed which is related to the degassing-peak V3, see (b). The liquid phase formation onset was found at 1326°C. The peak upon cool-down is bimodal, indicating the existence of a melting range. The maximum of the WC reduction is found at 887°C (W). It overlaps with a strong VC-related peak ranging from 850–1250°C with several maxima at 1003°C (V1), 1098°C (V2), 1298°C (V4) and the strongest maximum at 1200°C (V3). The DSC and the TG data of this sample series is summarised in Table 4-32 and Table 4-33, respectively.

Table 4-32: DSC data of W-VC-Co hardmetals with varying V/W ratio.

Sample	1 st heat-up			1 st cool-down	Comment
	1	2	3		
WC-Co-2V	-	1141	1316	1317	
WC-Co-10V	1052	-	1285	1283	
WC-Co-20V	1055	1176	1289	1286	
WC-FeNi-20V	1099	-	1381	1296/1309	cool-down peak bimodal
WC-Co-50V	-	1146	1326	1371	peak 1 100°C wide and multimodal

Table 4-33: TG data of W-VC-Co hardmetals with varying V/W ratio.

Sample	WC	VC related peaks			
	W	V1	V2	V3	V4
WC-Co-2V	862	-	1062	-	-
WC-Co-10V	815	950	1099	1201	1295
WC-Co-20V	809	891	1113	1218	1284
WC-FeNi-20V	807	-	1004	1158	-
WC-Co-50V	887	1003	1095	1200	1298

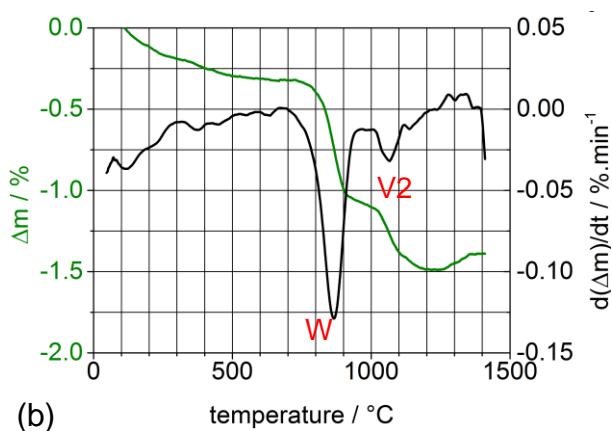
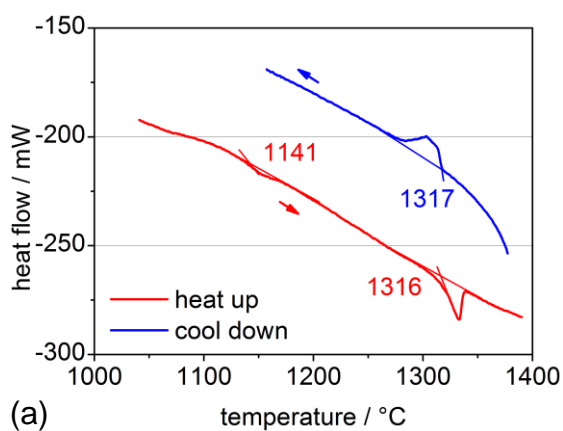
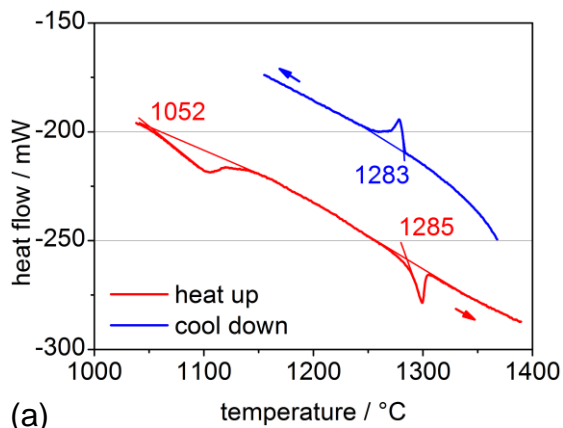
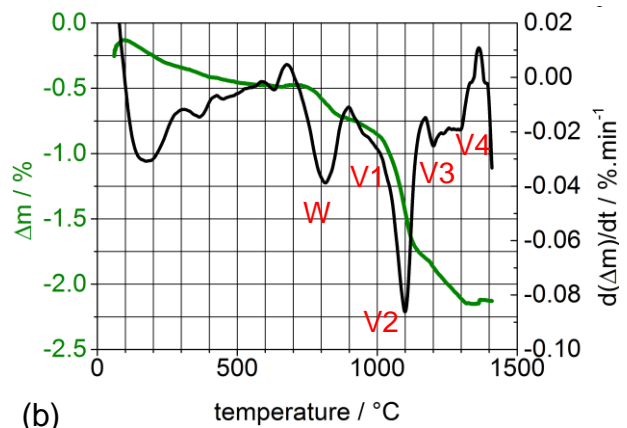


Figure 4-144: Thermal analysis of WC-Co-2V. (a) DSC signals of the first heating and cooling cycle. (b) TG analysis of first heat-up.

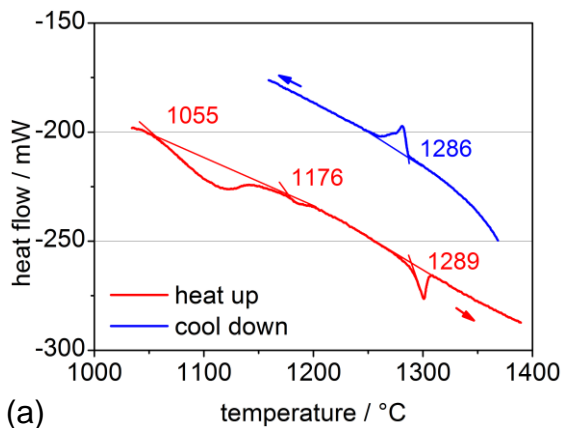


(a)

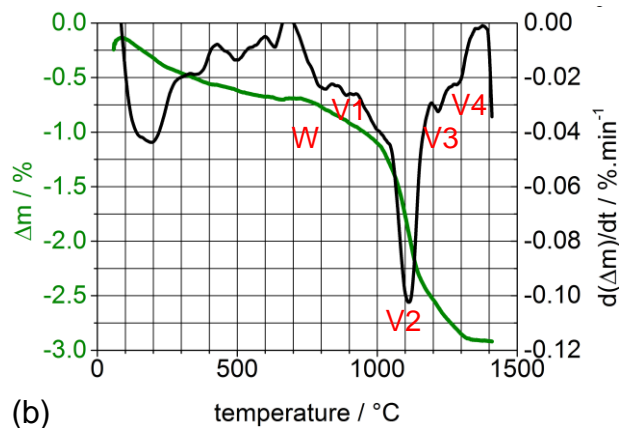


(b)

Figure 4-145: Thermal analysis of WC-Co-10V. (a) DSC signals of the first heating and cooling cycle. (b) TG analysis of first heat-up.

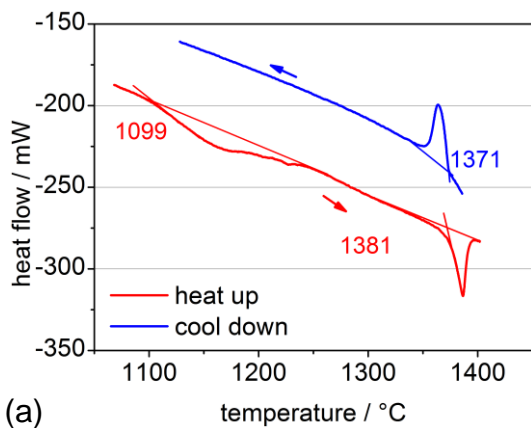


(a)

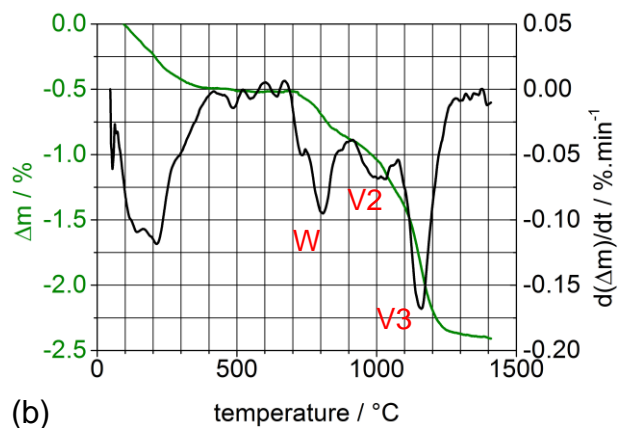


(b)

Figure 4-146: Thermal analysis of WC-Co-20V. (a) DSC signals of the first heating and cooling cycle. (b) TG analysis of first heat-up.



(a)



(b)

Figure 4-147: Thermal analysis of WC-Fe/Ni-20V. (a) DSC signals of the first heating and cooling cycle. (b) TG analysis of first heat-up.

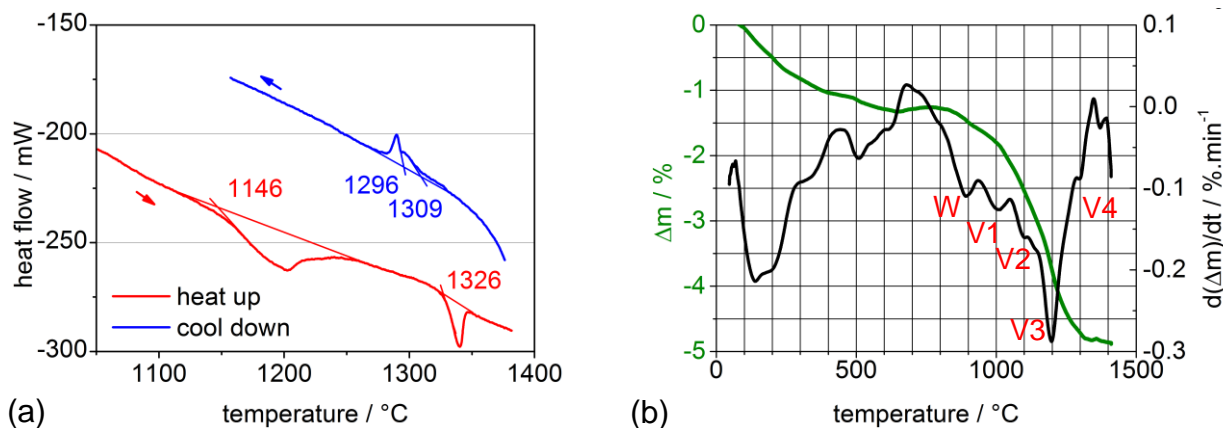


Figure 4-148: Thermal analysis of WC-Co-50V. (a) DSC signals of the first heating and cooling cycle. (b) TG analysis of first heat-up.

4.6.2.2 WC-Co hardmetals with varying Cr/W ratio

In this sample series the atomic ratio of Cr/W of a WC-Cr₃C₂-Co hardmetal was varied from 2/98 – 50/50. The cobalt concentration was kept constant at 16.3 vol%. The composition of sample WC-Co-2Cr is closest to common hardmetals. The DSC signal is shown in Figure 4-149(a). The endothermic main signal at 1336°C indicates the liquid phase formation which is confirmed by the exothermic signal at 1335°C upon cool-down. If the Cr/W ratio is increased to 10/90, see sample WC-Co-10Cr in Figure 4-150(a) three signals appear with onsets in the range of 1169–1213°C which are as well found upon cool down. Interestingly, by a further increase of the chromium concentration to Cr/W=20/80, see Figure 4-151(a), only one signal at 1192°C is detected, which is in accordance to the liquid-phase formation temperature of a chromium-doped high carbon hardmetal, see Table 2-3. However, upon cool-down two signals at 1244°C and 1197°C appear. These signals might be attributed to the melting range of a chromium-doped hardmetal (compare Figure 2-14) and hence mark the liquid- and solidus-temperature, respectively. A similar behaviour can be found if Fe/Ni binder is used instead of cobalt, see sample Figure 4-152(a). Upon heat up a single peak at 1242°C is observed, the shoulder close before offset indicates the presence of a melting range, which is confirmed by the bimodal peak upon cool-down. The onset temperatures are by 50°C higher which is in accordance to the generally higher solidus-temperatures in Ni-based binders, compare phase diagrams in section 2.4. By a further increase of the chromium atomic ratio to Cr/W=50/50, Figure 4-153(a), no DSC signal was detected, as already observed for

the Cr_3C_2 -Co diffusion couple component CCo_+ , compare Figure 4-134(a). Thus, the lack of a signal is sample specific and not a measurement error. However, a small signal is observed around 1183°C but its signal/noise ratio is too small to be significant.

A strong effect of the Cr/W ratio was not only observed on the liquid phase formation but also on the degassing characteristics. The sample with Cr/W=2/98 shows one main peak at $800\text{--}900^\circ\text{C}$ which can be attributed to WC and a small peak around 1050°C . If the chromium content is increased to Cr/W=10/90, Figure 4-150(b), the pattern becomes more complex. The main peak between $800\text{--}90^\circ\text{C}$ is slightly sifted to lower temperatures. A strong bimodal peak with maxima at 990°C and 1080°C is observed. Furthermore a peak around 1200°C with a sharp onset at 1213°C appears which is probably correlated to the DSC signal observed at the same temperature. At a chromium content of Cr/W=20/80 the signal at $800\text{--}900^\circ\text{C}$ becomes small. One strong peak ranging from $850\text{--}1100^\circ\text{C}$ with a maximum at 990°C is observed. At $1190\text{--}1200^\circ\text{C}$ a second strong peak appears which is again correlated to the DSC signal and hence liquid-phase formation. Interestingly this peak disappears when Fe/Ni binder is used instead of cobalt. The small peak at $800\text{--}900^\circ\text{C}$ and the main peak from $850^\circ\text{C}\text{--}1100^\circ\text{C}$ with the maximum at 990°C are almost equal to the sample with cobalt binder. The signal at 750°C can be attributed to iron reduction. At high chromium concentration of Cr/W=50/50, Figure 4-153(b), only one single peak with a maximum at 900°C is observed. The signal around 1200°C disappeared which might correlate with the absence of a liquid-phase signal in DSC measurements.

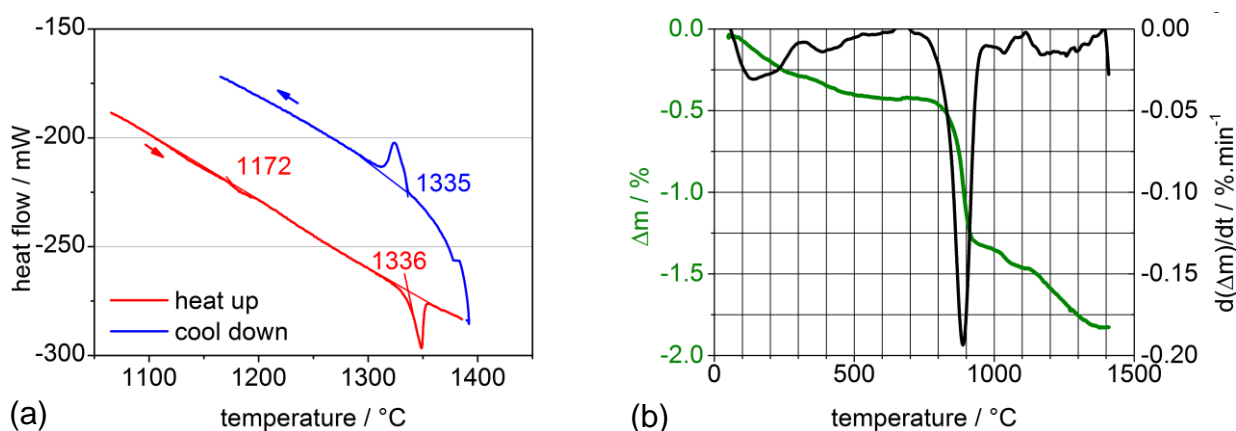


Figure 4-149: WC-Co-2Cr. (a) DSC signals of the first heating and cooling cycle. (b) TG analysis of first heat-up.

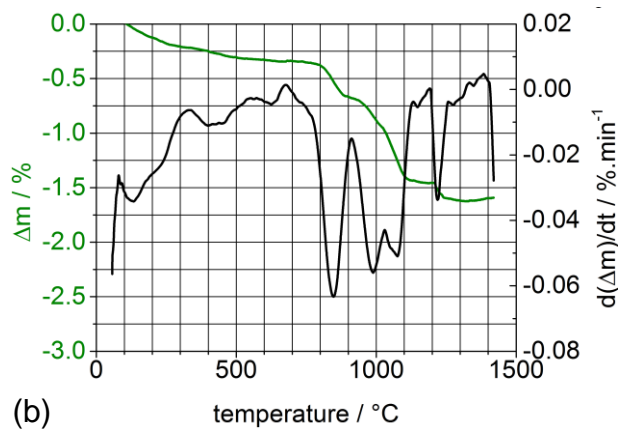
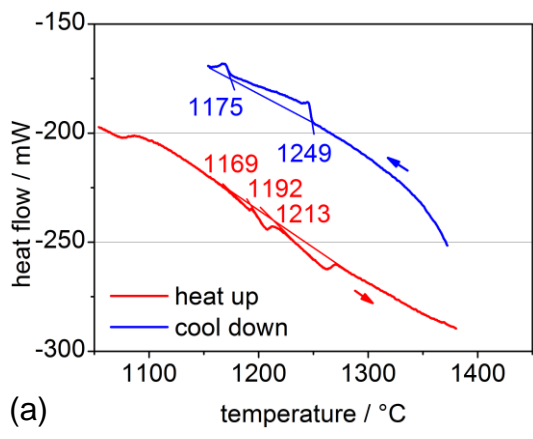


Figure 4-150: WC-Co-10Cr. (a) DSC signals of the first heating and cooling cycle. (b) TG analysis of first heat-up.

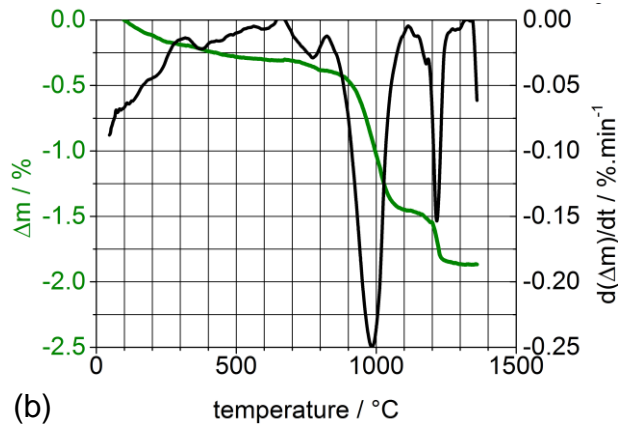
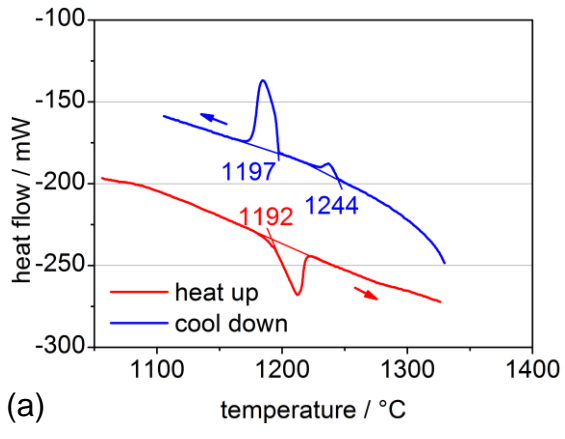


Figure 4-151: WC-Co-20Cr. (a) DSC signals of the first heating and cooling cycle. (b) TG analysis of first heat-up.

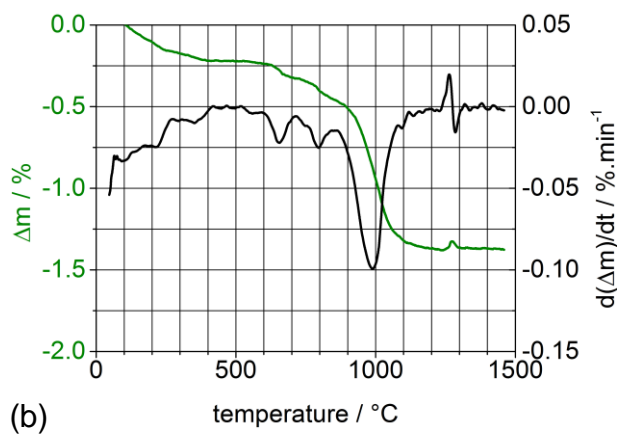
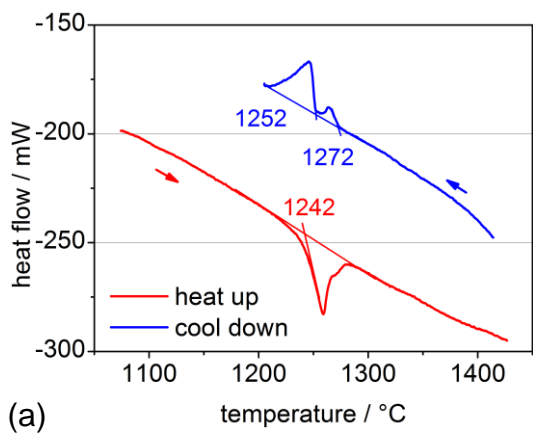


Figure 4-152: WC-Fe/Ni-20Cr. (a) DSC signals of the first heating and cooling cycle. (b) TG analysis of first heat-up.

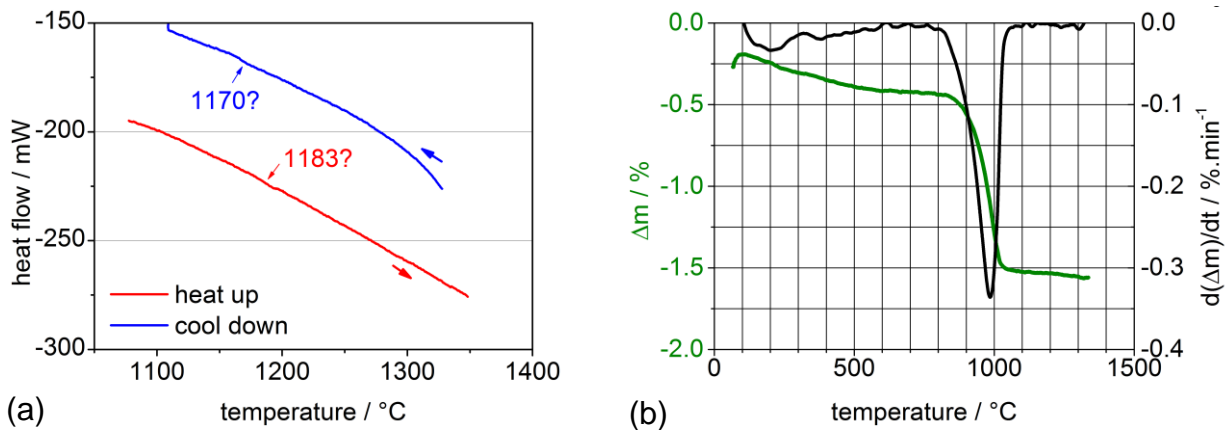


Figure 4-153: WC-Co-50Cr. (a) DSC signals of the first heating and cooling cycle. (b) TG analysis of first heat-up.

4.6.2.3 WC-Co hardmetals with varying Mo/W ratio

Hardmetals with molybdenum and cobalt binder were prepared with three different atomic ratios of Mo/W=2/98, 20/80 and 50/50. A sample with Mo/W=20/80 was additionally prepared with Fe/Ni binder instead of cobalt.

The DSC of hardmetal with Mo/W=2/98 is depicted in Figure 4-154(a). The liquid phase formation appears at 1347°C, which is confirmed by signal upon the cool-down. The irregular shape especially of the cool-down peak is rather due to the appearance of a melting range than to an invariant temperature. A small signal is observed at 1212°C, but only upon the first heat-up cycle. Since it is small, not related to a mass-loss event and also not observed at the other samples of this series it is likely just an artefact. The binder-phase related mass-loss appears around 400°C but is convolved with some noise. A small signal is observed at 630°C (1). The WC-reduction peak is setting on at 750°C with a maximum at 895°C. No further molybdenum related signal is observed.

At a higher ratio of Mo/W=20/80 as in sample WC-Co-20Mo the liquid phase signal is shifted to a lower temperature of 1301°C, see Figure 4-155(a). The TG (b) shows as well a strong peak setting on at 750°C with a maximum at 895°C (3) and a smaller peak (1) at 635°C.

If Fe/Ni binder is used as in case of WC-FeNi-20Mo the liquid phase appears at a higher temperature of 1363°C, see Figure 4-156(a). The onset of the TG signal (b) is

shifted to lower temperatures of 670°C and a shoulder is observed before the maximum is reached. The maximum however is again found around 900°C.

Sample WC-Co-50Mo has the highest Mo-concentration of Mo/W=50/50 at%. The liquid phase forms already at 1183°C. Upon cool-down a second peak at 1334°C is observed. Possibly this second peak also appears upon heat-up since a slight change of the DSC-curve is observed. However, this possible signal is too small to be significant. Regarding the mass loss (b) the maximum of the main peak is slightly shifted by 30°C to a lower temperature of 864°C. Additionally two small peaks are detected with maxima at 646°C (1) and 715°C (2). By the appearance of liquid phase at 1183°C the signal starts to scatter and a slight mass increase is observed.

Table 4-34: DSC and TG data of samples WC-Mo₂C-Co with varying Mo/W atomic ratio. DSC values represent onset temperatures, TG values represent peak maxima. All values in °C.

Sample	1 st heat-up		1 st cool-down		TG Peak			
	1	2	1	2	1	2	3	
							onset	max
WC-Co-2Mo	1212	1347	-	1348	630	-	753	901
WC-Co-20Mo	-	1301	-	1315	635	-	760	895
WC-FeNi-20Mo	-	1183	1216	1334	-	-	670	904
WC-Co-50Mo	-	1363	-	1376	646	715	760	864

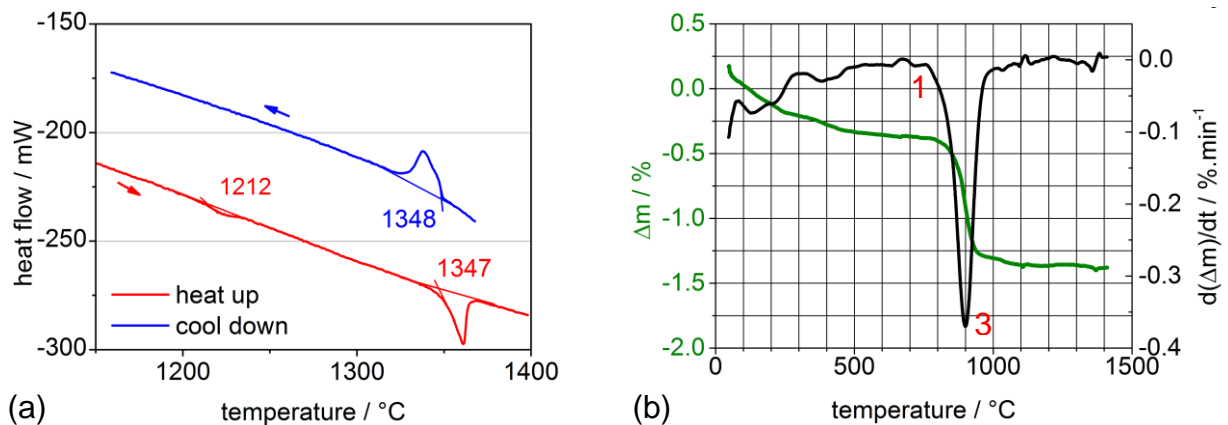


Figure 4-154: WC-Co-2Mo. (a) DSC signals of the first heating and cooling cycle. (b) TG analysis of first heat-up.

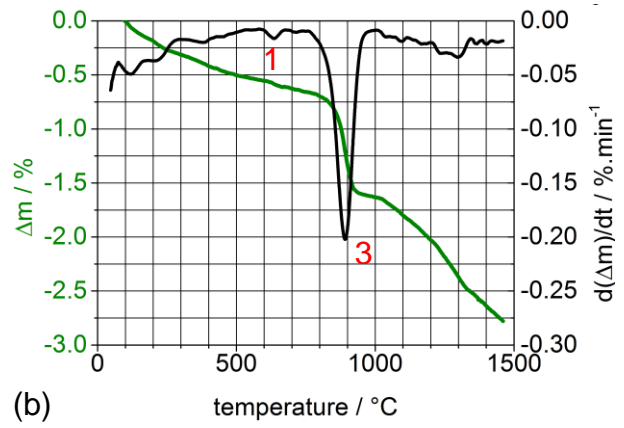
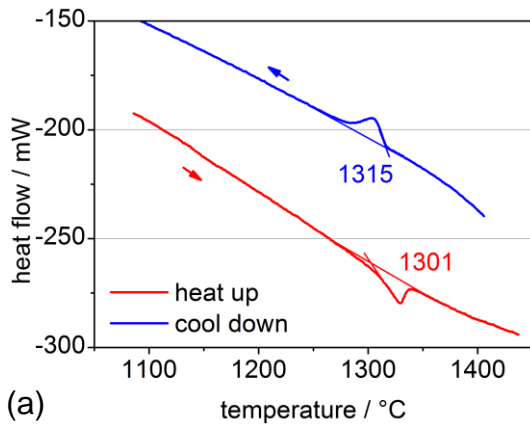


Figure 4-155: WC-Co-20Mo. (a) DSC signals of the first heating and cooling cycle. (b) TG analysis of first heat-up.

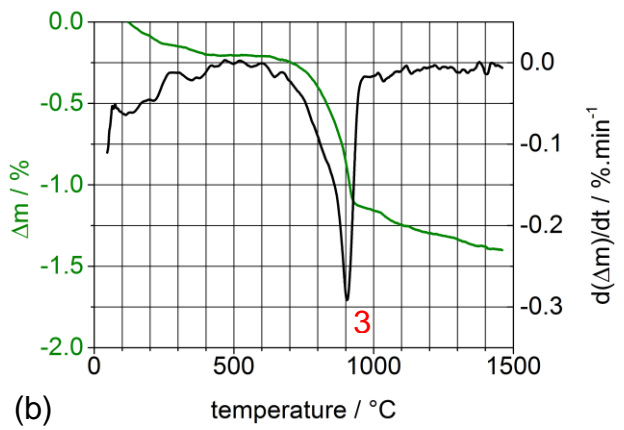
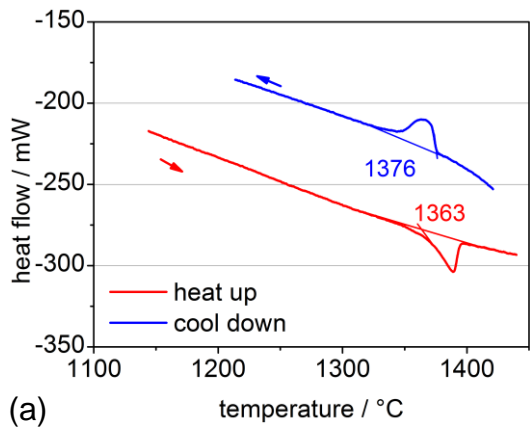


Figure 4-156: WC-Fe/Ni-20Mo. (a) DSC signals of the first heating and cooling cycle. (b) TG analysis of first heat-up.

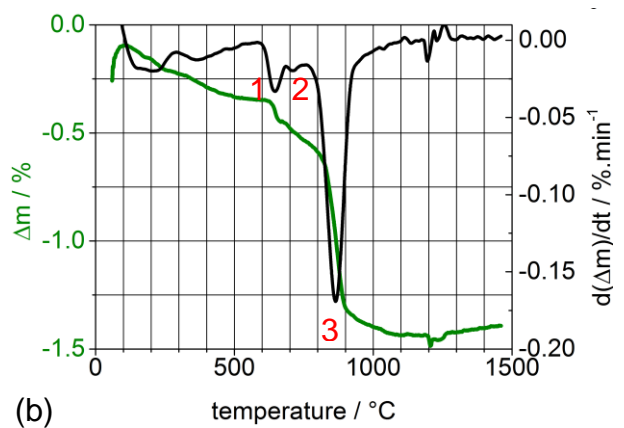
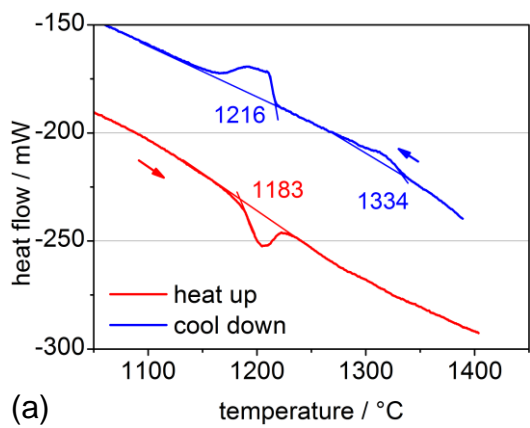


Figure 4-157: WC-Co-50Mo; (a) DSC signals of the first heating and cooling cycle; (b) TG analysis of first heat-up.

4.6.3 WC-Co hardmetals with small amounts of dopants

The samples discussed in above sections have higher GGI concentrations than usually applied in hardmetals. In this sample series WC-Co-GGI hardmetals with GGI concentrations of $c(\text{GGI}/\text{Co})=0.05$ (weight ratio) were analysed as they are used in common hardmetals, see Table 3-17 for particular compositions.

The hardmetal $\text{HM}_{\text{Cr}_3\text{C}_2}$ was doped with 0.6 wt% of Cr_3C_2 and prepared with low carbon potential. The latter is confirmed by the corresponding DSC signal in Figure 4-158(a). A single signal at 1314°C upon heat-up and 1330°C upon cool-down is observed. The TG signal (b) shows three characteristic peaks. The peaks at 370 and 787°C can be attributed to cobalt and WC reduction, respectively. The third reduction peak at 971°C is caused by the chromium addition.

In hardmetal $\text{HM}_{\text{Cr}_2\text{N}}$ the chromium carbide is replaced by a nitride. The resulting DSC signal is shown in Figure 4-159(a). A single signal at 1309°C upon heat-up and 1330°C upon cool-down is observed, which is comparable to the hardmetal with chromium carbide addition. The TG signal (b) is more complex, since not only CO but also N_2 evolves due to the decomposition of the nitride. The binder reduction peak is overruled by noise and not detectable. The WC reduction maximum appears at 830°C. The chromium-related signal is bimodal and sets on at 1020°C. The maxima of this bimodal peak were found at 1057 and 1288°C. A third chromium-induced mass-loss event with at 1290°C and maximum at 1300°C was detected. This signal fits well to the liquid phase formation temperature of 1309°C.

Since an influence of the carbon potential on the decomposition of nitrides is expected a chromium-doped hardmetal was as well prepared with high carbon potential, see $\text{HM}_{\text{Cr}_2\text{N}+}$ in Figure 4-160. The DSC signal (a) was detected at 1201°C which is by 108°C lower than of the low-carbon sample and a proof of the high carbon potential (compare solidus temperature from literature in Table 2-3). The binder reduction peak has its maximum at 584°C, the WC signal at 821°C. The GGI-related mass loss seems to be unimodal with a maximum at 926°C. However, the irregular shape of the peak suggests it is composed by two overlapping, neighboured signals. Interestingly, a sudden mass increase is detected at 1202°C which fits exactly to the occurrence of liquid phase. In consequence of this accordance it is rather a sample specific effect than a measurement error. Since the experiment was

carried out in static atmosphere it is possibly caused by a re-uptake of previously evolved nitrogen due to increased nitrogen solubility in liquid phase. The effect of boron was studied on a sample HM_CrB which was doped with 0.6 wt% chromium boride. The DSC signal in Figure 4-161(a) consists of two elongated, equally shaped signals setting on at 1200°C and 1248°C. These two peaks also appear upon cool-down. The mass loss (b) of cobalt and WC have their maxima at 373°C and 786°C, resp. Related to vanadium two signals are observed. The first one is setting on at 915°C and has a maximum at 1012°C, the second one at 1071°C. A mass increase is observed from 1100°C until the onset of the second DSC signal at 1248°C which is a hint of reaction between boron and the atmosphere, possibly the formation of boron oxide by CO from the furnace atmosphere after the CrB is dissolved in the binder phase.

The hardmetal HM_Cr₂O₃ was prepared with chromium-oxide in order to see its degassing characteristics in a hardmetal matrix. The sample was doped with carbon in an amount that allows the formation of Cr₃C₂ out of Cr₂O₃. The DSC signal in Figure 4-162(a) shows a broad peak with onset 1093°C which can be related to the carbothermic reduction of the chromium oxides, since it is not observed upon cool-down. A second signal setting on at 1323°C marks the beginning of the liquid phase formation. The mass-loss maxima (b) for cobalt and WC reduction appear at 601 and 820°C, respectively. The chromium related mass loss shows two strong peaks of comparable height. The first peak sets on at 878°C and has its maximum at 1017°C, while the second peak has its maximum at 1147°C. The appearance of two peaks is a hint that the reduction of Cr₂O₃ in hardmetals is at least a two step process. A third mass chromium-related mass loss event again appears at sets on at 1318°C and has its maximum at 1354°C. The onset of the peak is in good accordance to the liquid-phase signal at 1323°C.

The DSC of the hardmetal doped with 0.6 wt% of VC is depicted in Figure 4-163. A single signal at 1294°C is found. The literature liquid-phase formation temperature is 1320°C for a V-saturated low carbon hardmetal (compare Table 2-3), which means the carbon potential was not fixed in the eta-phase field for this sample. Of course the first heat-up cycle does not yield the equilibrium temperatures. However, the signal at the 2nd heat-up cycle sets on at 1309°C (compare Appendix section,), which is still below the equilibrium temperature. Nevertheless the carbon potential is still low, but

within the WC+fcc+MC phase field instead of WC+fcc+MC+eta. The TG (b) reveals a binder peak at 363°C and a WC peak maximum at 768°C.

Sample HM_V₂O₅ was prepared with 0.91 wt% vanadium oxide V₂O₅. Carbon was added to the mixture in order to allow the formation of VC by carbothermic reduction. The DSC, depicted in Figure 4-164(a), reveals a bimodal peak setting on at 1240°C. The equilibrium temperature from the 2nd heating cycle is 1249°C (see appendix) which points to high carbon potential (compare Table 2-3). The bimodal shape is confirmed by the cool-down curve. Regarding the TG (b), besides the cobalt and WC degasing at 388°C and 838°C, resp. only one significant vanadium-related peak with a maximum at 988°C was observed. Simultaneously to the appearance of liquid phase at 1240°C a mass increase by 0.3% was observed, related to a re-uptake of a component from the atmosphere. The static furnace atmosphere is composed by high-purity argon and CO formed upon previous reactions. Since no solubility for argon is reported in hardmetals binder phase the only possible component for a mass increase is CO. A measurement failure can be excluded due to the correlation of the signal to the appearance of liquid phase. A special feature of this composition is the low melting point of V₂O₅ of 690°C. However, no specific TG signal was detected at this temperature, thus V₂O₅ is not expected to escape to the furnace atmosphere.

The influence of molybdenum was studied with the 0.6 wt% MoC-doped sample HM_MoC. The DSC signal is depicted in Figure 4-165(a). A single peak with onset temperature 1240°C was detected, close to the solidus temperature of an undoped low-carbon hardmetal (1368°C). Since dopants usually lower the solidus temperature by some extent the low carbon potential can be considered as confirmed. The TG (b) shows the binder related mass loss at 365°C and the WC signal at 793°C. Only small Mo-specific signals were detected at 936°C and 1200°C.

The sample HM_09MoB was prepared with 0.53 wt% MoB addition. The DSC signal is shown in Figure 4-166(a). A number of very small peaks appear, the main peaks have onset temperatures of 1213 and 1291°C. These two peaks are also found upon cool-down. The effect is further discussed in section 5.5.7. The mass loss (b) of the cobalt binder and WC was detected at 366°C and 828°C, respectively. The MoB-related mass loss is characterised by the appearance of a number of small peaks in the temperature range of 950–1300°C. The main peaks have maxima at 1000°C, 1191°C and 1270°C.

Table 4-35: Onset temperatures of DSC signals of doped hardmetals with low carbon potential upon 1st heat-up and cool-down cycle.

Sample	1 st heat-up		1 st cool-down		Comment
	1	2	1	2	
HM_Cr ₃ C ₂	-	1314	-	1330	
HM_Cr ₂ N-	-	1309	-	-	
HM_Cr ₂ N+	-	1201	-	1253	high carbon potential
HM_Cr ₂ O ₃	1093	1323	-	1294	
HM_CrB	1200	1248	1208	1287	
HM_VC	-	1294	-	1320	carbon not fixed in eta-region
HM_V ₂ O ₅	-	1240	1247	1261	bimodal signals, high carbon
HM_MoC	-	1340	-	1352	
HM_MoB	1213	1291	1229	1313	noisy DSC curve upon heat up

Table 4-36: Thermal analysis of hardmetals doped with various GGIs.

Sample	Binder	WC	GGI peak number			Comment
	B	W	G1	G2	G3	
HM_Cr ₃ C ₂	370	787	-	-	-	
HM_Cr ₂ N	n.a.	844	979	1057	1288	
HM_Cr ₂ N+	584	821	926	-	-	mass increase at 1204°C
HM_Cr ₂ O ₃	601	820	1017	1147	1356	
HM_CrB	373	786	1012	1071		mass increase at 1112°C
HM_VC	363	768	969	-	-	
HM_V ₂ O ₅	388	838	988	-	-	mass increase at 1244°C
HM_MoC	365	793	936	1200	-	
HM_MoB	366	828	1100	1191	1270	numerous small peaks >1100°C

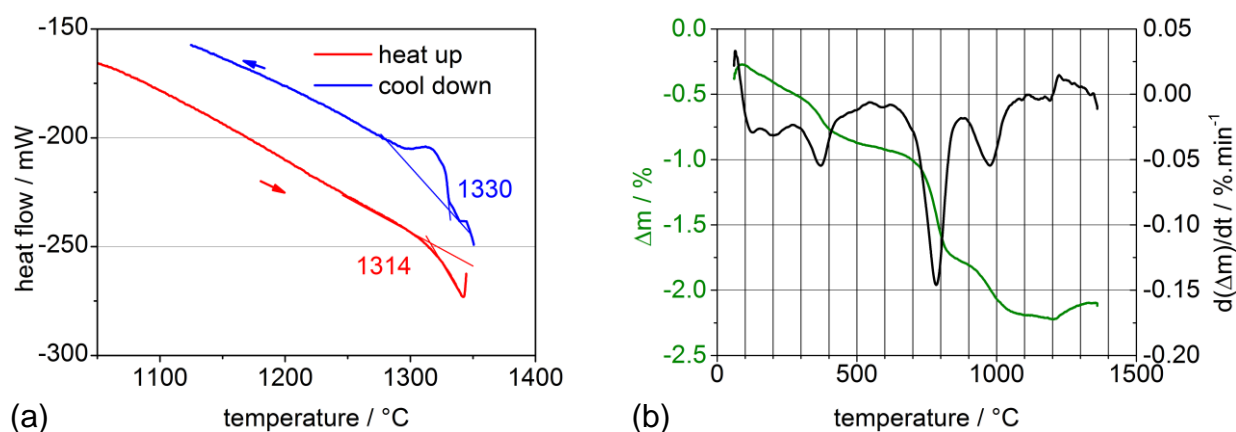
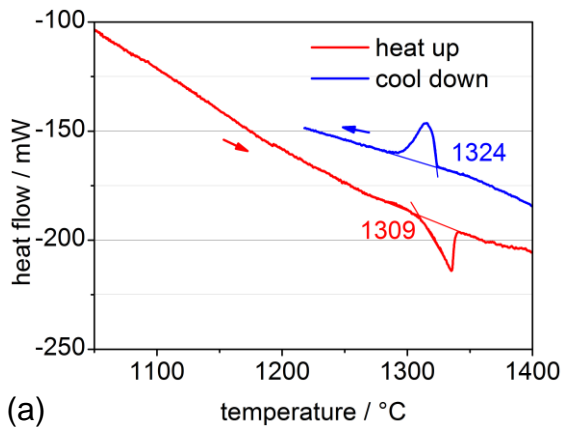
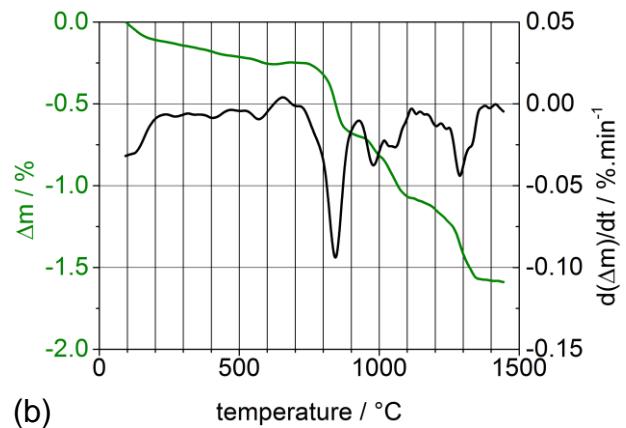


Figure 4-158: HM_Cr₃C₂, (a) DSC signals of the first heating and cooling cycle. (b) TG analysis of first heat-up.

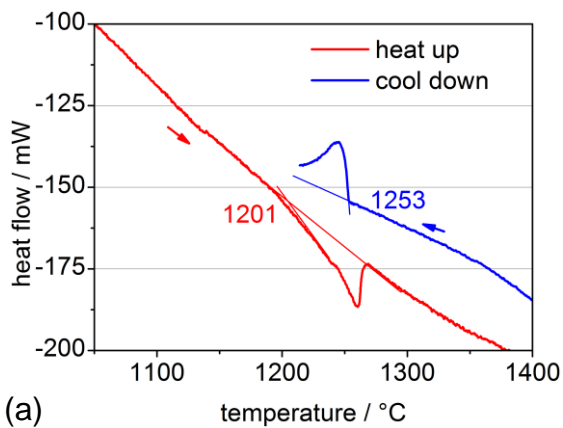


(a)

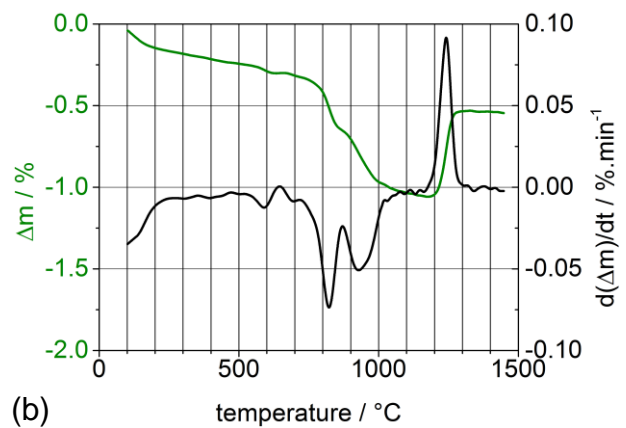


(b)

Figure 4-159: HM_Cr₂N, (a) DSC signals of the first heating and cooling cycle. (b) TG analysis of first heat-up.

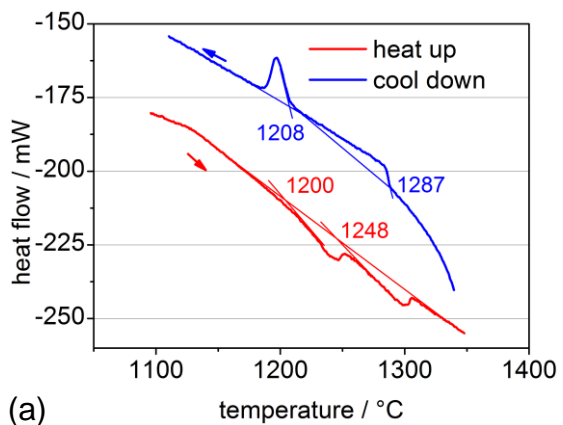


(a)

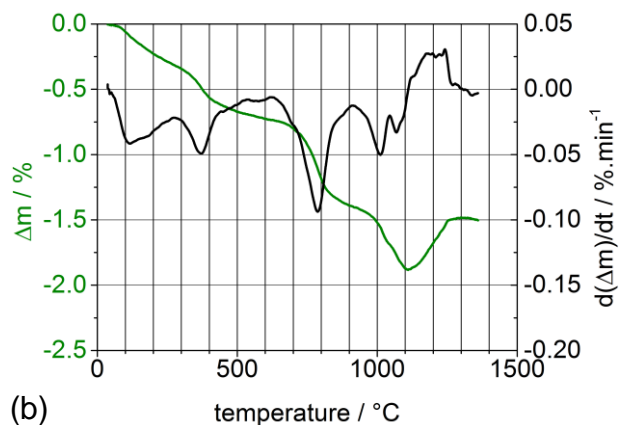


(b)

Figure 4-160: HM_Cr₂N⁺, (a) DSC signals of the first heating and cooling cycle. (b) TG analysis of first heat-up.



(a)



(b)

Figure 4-161: HM_CrB, (a) DSC signals of the first heating and cooling cycle. (b) TG analysis of first heat-up.

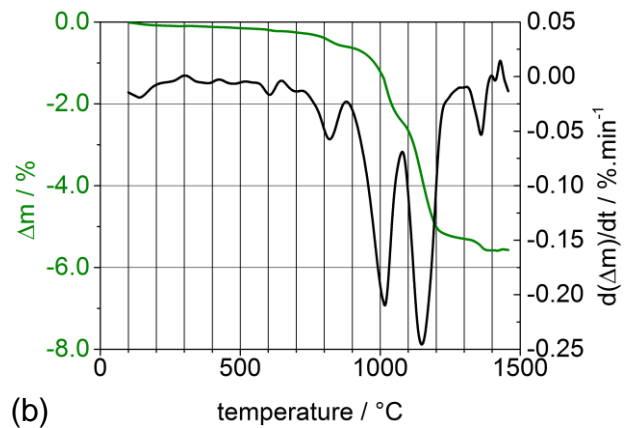
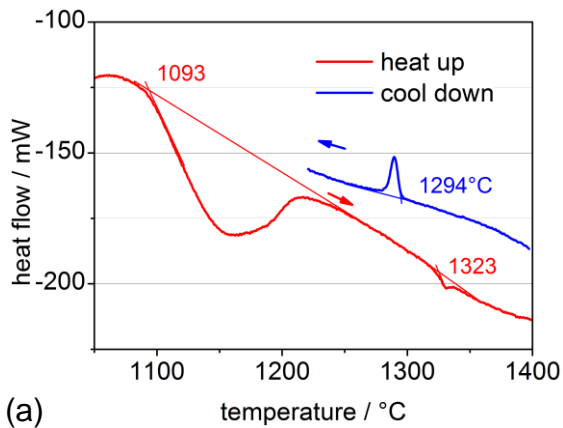


Figure 4-162: HM_Cr₂O₃, (a) DSC signals of the first heating and cooling cycle. (b) TG analysis of first heat-up.

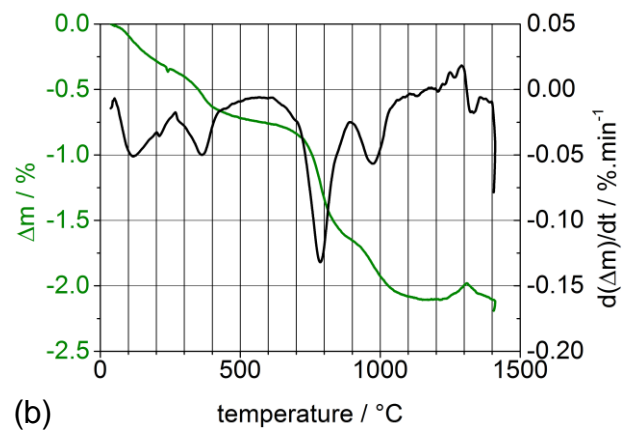
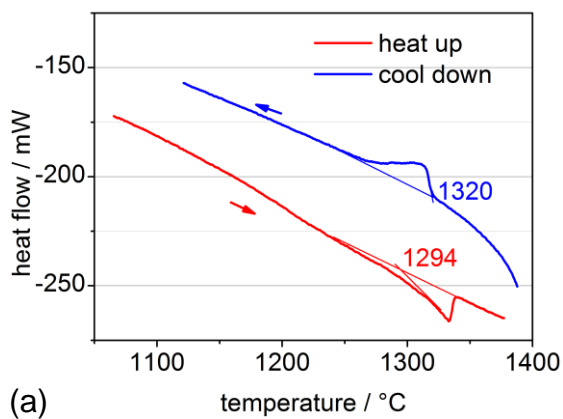


Figure 4-163: HM_VC; (a) DSC signals of the first heating and cooling cycle; (b) TG analysis of first heat-up

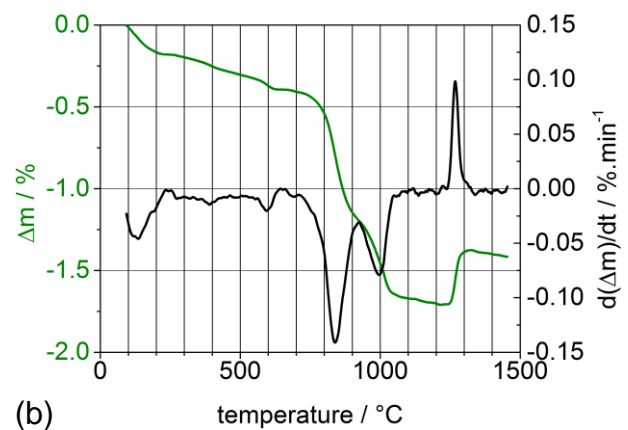
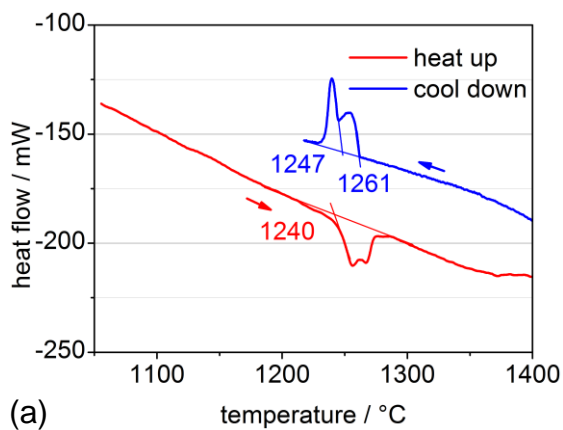


Figure 4-164: HM_V₂O₅, (a) DSC signals of the first heating and cooling cycle. (b) TG analysis of first heat-up.

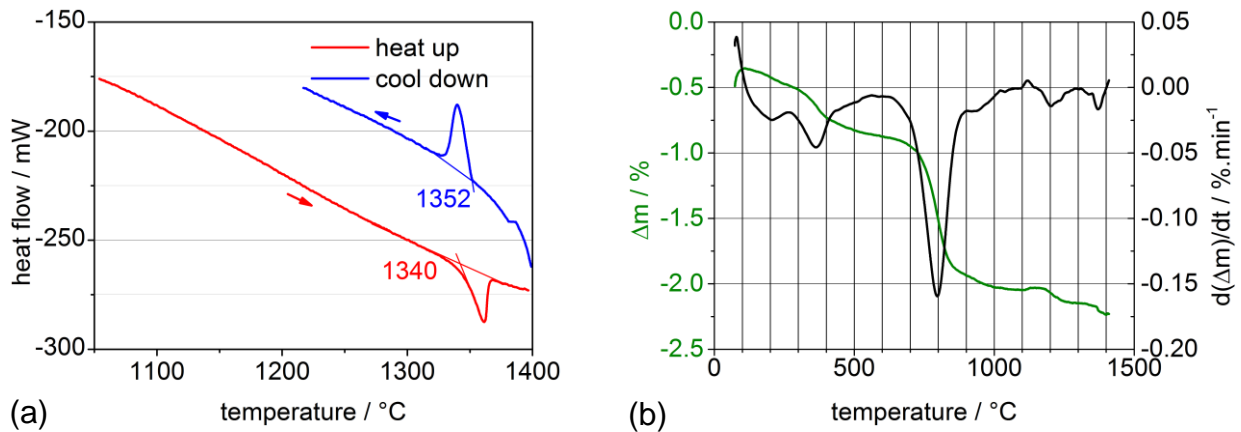


Figure 4-165: HM_MoC, (a) DSC signals of the first heating and cooling cycle. (b) TG analysis of first heat-up.

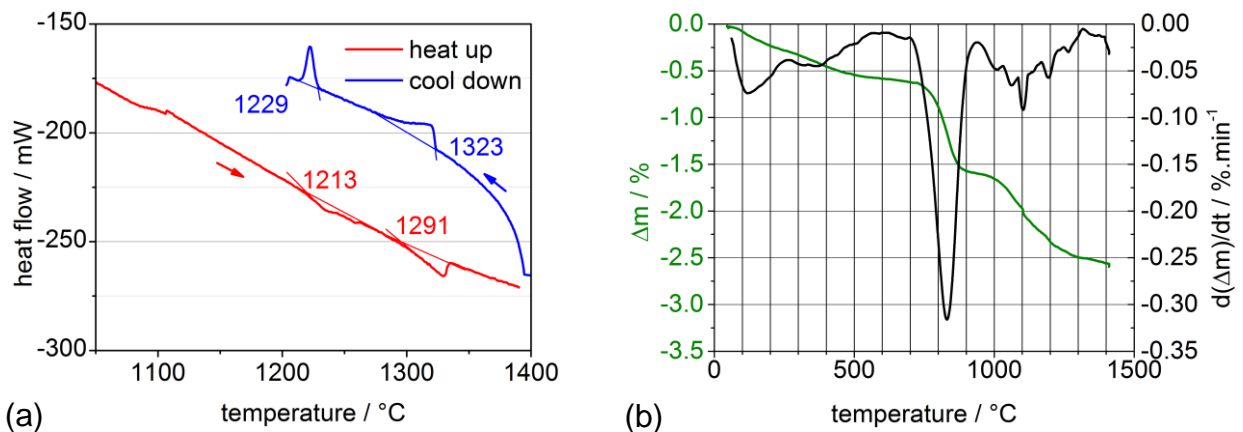


Figure 4-166: HM-1MoB, (a) DSC signals of the first heating and cooling cycle. (b) TG analysis of first heat-up.

4.7 Grain size analyses

Grain-growth inhibitors are known to not only have influence on the microstructure by retardation of WC grain growth but also to have significant impact on the microstructural evolution upon early sintering stages (see section 2.3.2). By analysis of diffusion couples it turned out that the presence of GGI has a concentration dependent influence on other microstructural parameters such as porosity or cobalt concentration. G-type diffusion couples allow direct observation of the microstructural development as a function of the GGI concentration. However, the GGI-concentrations measured in such samples were found by a factor of 5–10 higher as compared to the solubility at a given temperature in liquid-phase sintered samples.

On the other hand, such microstructures could be similar to those in the vicinity of resolving GGI grains upon heat up. In order to relate the results to “real” hardmetals interrupted sintering experiments with GGI-doped hardmetals with common concentrations <1 wt% were conducted.

If GGIs influence the microstructural evolution at early sintering stages it is likely that this influence can as well be found in fully sintered hardmetals. Furthermore it is not yet clear if the efficiency order of V>Cr>Mo is also valid at low temperatures. In order to clarify and enhance this effects hardmetals were liquid phase sintered at 1380°C with an initial 10 h plateau at 1000°C and 1150°C, respectively.

From spark plasma sintered samples the influence of GGIs on the microstructure formation and their efficiency at 1180°C was determined.

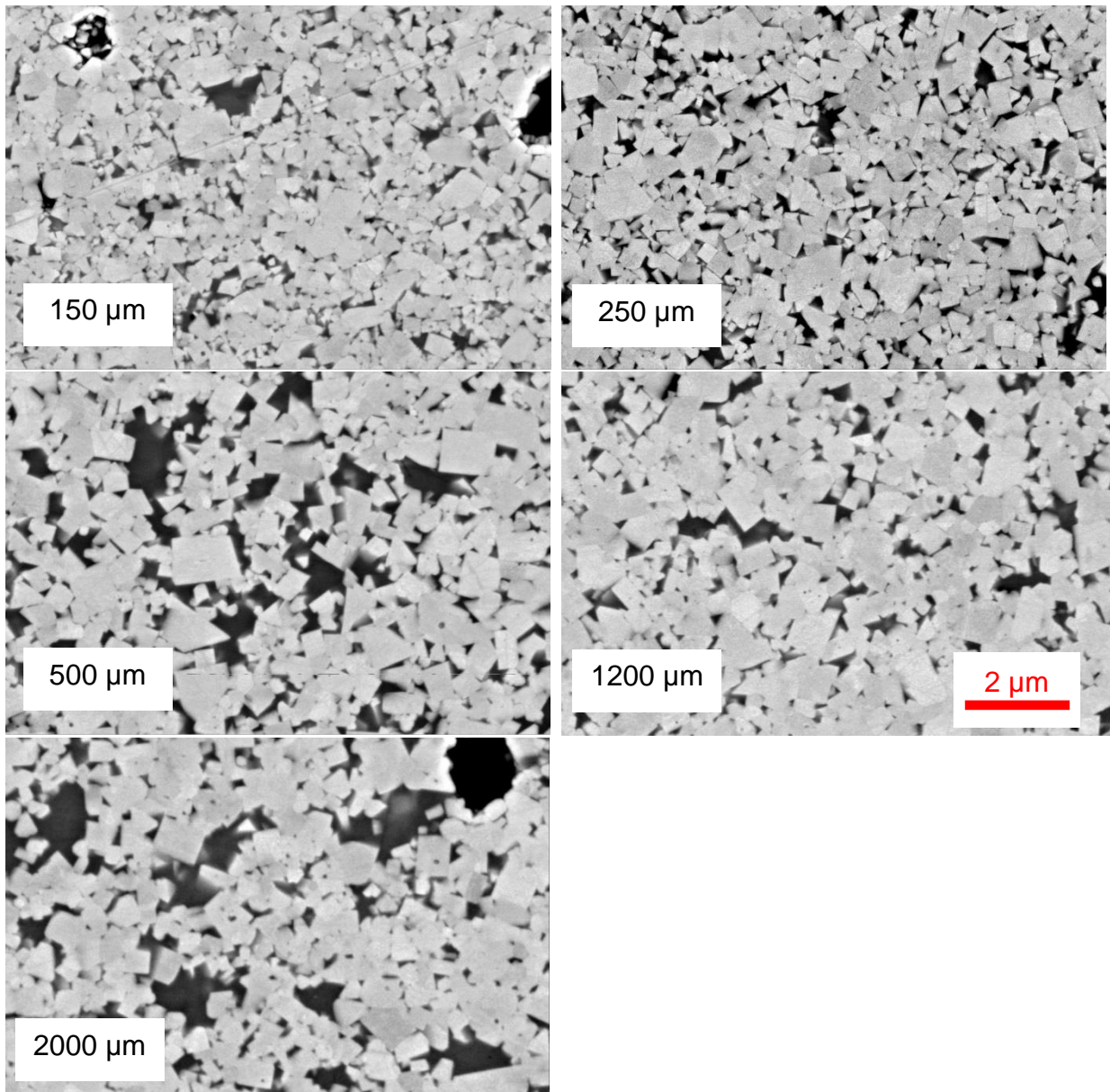
4.7.1 G-type diffusion couples

The annealing time for G-type diffusion couples were short around 15 min. However, especially diffusion couples with liquid binder phase such as CVCoG125 and CVCoG136 showed a significant grain growth as a function of the GGI-concentration. The mentioned samples were annealed for 15 min at 1250°C and 1360°C, respectively. The sample at 1250°C has the special feature of solid binder phase in the bulk while it is liquid in the presence of GGI. At 1360°C the binder phase is liquid anyway.

From both samples the WC-grain-size was analysed as a function of the distance from interface. The results are shown in Figure 4-167 for sample CVCoG125 and Figure 4-168 for sample CVCoG136. From both figures a significant growth-inhibiting effect is observed. The grain size shows indirect proportional relationship to the GGI-concentration as can be seen from the bottom right diagrams.

Interestingly for both samples a grain size of the bulk, which was not influenced by GGIs is 0.35 µm. The grain growth seems to be independent from temperature. However, only one image frame was analysed and this accordance is possibly only caused by a random error.

Another explanation can be a kinetic effect limiting the grain growth, e.g. the distribution of the cobalt phase upon the short annealing time.



Distance from interface (μm)	$d_{m,WC}$ (μm)
150	0.234
250	0.274
500	0.29
1200	0.331
2000	0.344

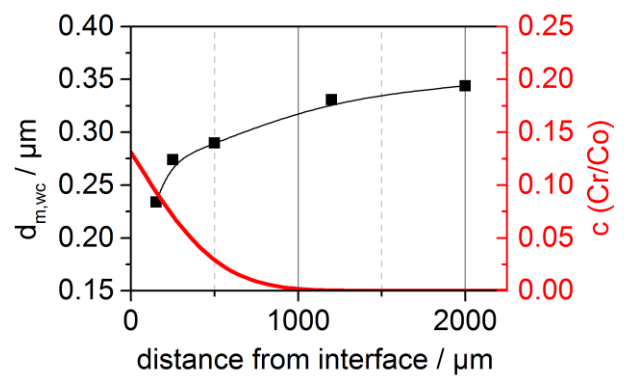
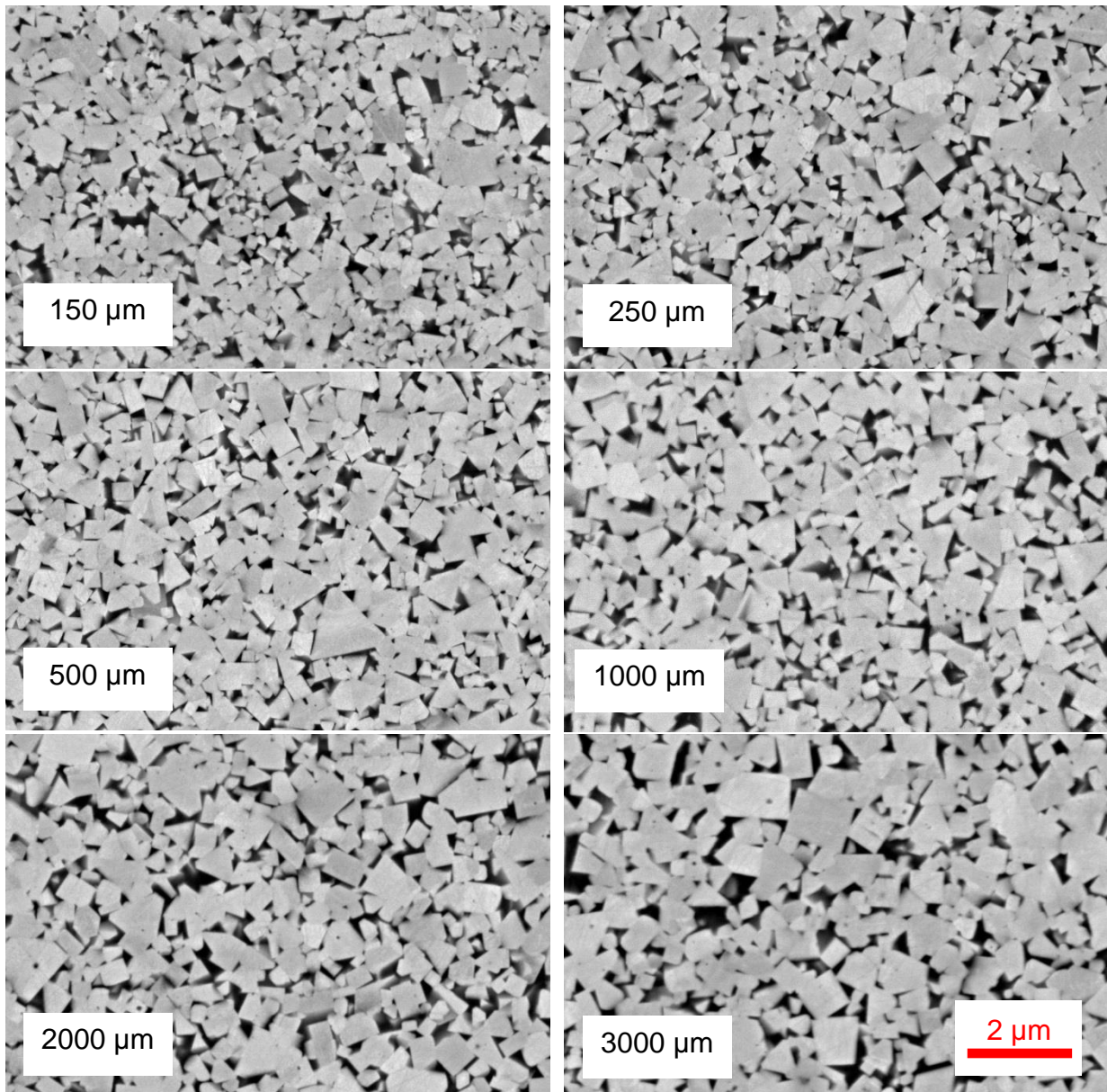


Figure 4-167: Mean WC grain-size $d_{m,WC}$ of sample CVCoG125, annealed for 15 min at 1250°C at distances of 150–2000 μm from the interface.



Distance from interface (μm)	$d_{m,WC}$ (μm)
150	0.241
250	0.283
500	0.296
1000	0.325
2000	0.329
3000	0.345

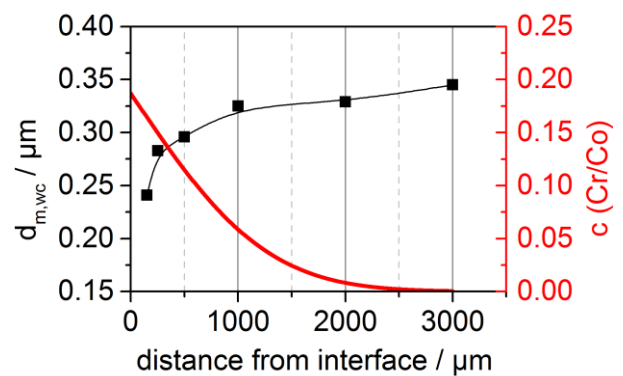


Figure 4-168: Mean WC grain-size $d_{m,WC}$ of sample CVCoG136, annealed for 15 min at 1360°C at distances of 150–3000 μm from interface.

4.7.2 GGI-doped hardmetals with varying outgassing dwells

The temperature profiles for hardmetal sintering commonly include a dwell in the temperature range of 1050-1200°C, see e.g. sintering profile in Figure 3-8. Such a dwell allows the completion of gas formation processes such as CO evolving from reduction of surface oxides. If grain-growth inhibitors are already effective upon early sintering stages the temperature and time of such a dwell should influence the grain size of liquid phase sintered hardmetals. Upon these early sintering stages initial defects within WC-grains such as dislocations are relatively unaffected due to the low homologous temperature of WC. Hence, if the effectiveness of GGIs is influenced by defects within WC grains, long dwell times should influence the final grain size distribution.

In order to detect such possible effects two types of hardmetals were prepared with WC of type DS50 or DS50m. The latter is an attritor-milled DS50 and should hence have a significantly higher number of lattice defects. From each type an undoped reference grade and three doped grades with 0.6 wt% VC, 1.0 wt% Cr₃C₂ and 0.4 wt% Cr₃C₂+ 0.4 wt% VC, respectively were prepared. These samples were liquid phase sintered at 1380°C with a varying dwell at 1000°C or 1150°C for 15 min or 600 min. The resulting grain size was analysed by line intercept using SEM-BSE images of magnification 30000x or 60000x. A minimum number of three images with a total grain number of at least 500 grains were analysed in order to get a significant mean grain size. An overview of the results of this series is listed in Table 4-37. The values listed in this table are explained in detail in section 3.8.3.

Dwell temperature 1000°C, dwell time 0.25 h, unmilled WC DS50

The microstructures and corresponding grain-size distributions determined from the sample series MGxU+100K are presented in Figure 4-169. As expected from literature chromium doping (b) shows significant inhibiting effect. The mean grain size x_m is reduced to $x_m=0.39 \mu\text{m}$ compared to $x_m=0.49 \mu\text{m}$ for the undoped sample (a). Vanadium (c) and chromium+vanadium (d) doping further decrease the grain size to $x_m=0.28 \mu\text{m}$ and $x_m=0.32 \mu\text{m}$, respectively. Interestingly, the vanadium single doping is slightly more efficient as compared to the single doping.

The fit of the logarithmic normal distribution to the experimental data is poor for both the undoped and the chromium-doped sample, as the R^2 values of 0.86 and 0.90 reveal. If vanadium is used, R^2 rises to 0.95 and further increases to 0.96 for double doping. Subsequently the grain-size is more homogeneously distributed if efficient GGIs are used. A comparison of the fitted curves of this sample series is presented in Figure 4-175(a). It is particularly striking that double doping has no benefit over vanadium single doping for hardmetals with WC of grade DS50. The vanadium single doped sample, however, contains more vanadium (0.6 wt%) as compared to the double doped (0.4 wt% VC+0.6 wt%Cr₃C₂). The reduced vanadium concentration of the double doped sample could be a reason why it is inferior to single doping. However, it will be shown below that for samples with milled WC DS50m double doping is significantly superior to single doping. The efficiency is hence dependent on the initial properties of the WC grains, which will be further discussed in section 5.7.

Dwell temperature 1000°C, dwell time 0.25 h, attritor-milled WC DS50m

The microstructures and corresponding grain-size distributions of the sample series MGx24+100K (x=ref, Cr, V, CV) are shown in Figure 4-164. The undoped sample (a) reveals an inhomogeneous grain size distribution with a large number of coarse grains. The related mean grain size is $x_m=0.42 \mu\text{m}$. By chromium doping (b) the microstructure becomes significantly finer to $x_m=0.34 \mu\text{m}$. However, particular grains are still coarse and the distribution is hence relatively wide. Vanadium (c) allows a further slight decrease of the mean grain size to $x_m=0.27 \mu\text{m}$, but the difference to chromium is within the error range of the method. The finest microstructure is achieved by Cr+V double doping (d), where a grain size of $x_m=0.18 \mu\text{m}$ was measured.

The high efficiency of the double doped sample can also be seen from the comparison of the samples in this series as illustrated in Figure 4-169(b).

This is an interesting aspect since in hardmetals with an untreated WC DS50 prepared under equal conditions, see series MGxU+100K in Figure 4-164(a). The benefit of double doping is significantly smaller.

Dwell temperature 1150°C, dwell time 0.25 h, unmilled WC DS50

The microstructures and corresponding grain size distributions measured for samples with an outgassing dwell at 1150°C for 15 min are illustrated in Figure 4-165. The undoped sample (a) shows a significant grain coarsening as compared to the doped grades. The amount of large WC grains $>1.2 \mu\text{m}$ intercept length is 4.2%. Chromium (b) reduces the amount of large grains to 1%, vanadium to 0.1% and Cr+V double doping to 0.2%. As shown from the grain-size values x_{WC} , $x_{0,WC}$ and d_{50} in Table 4-37 the finest microstructure is achieved by vanadium single doping but not by Cr+V double doping. This finding can as well be seen from a comparison of fitted logarithmic normal distributions in Figure 4-175(c).

Dwell temperature 1150°C, dwell time 0.25 h, milled WC DS50m

The sample series MGx24+115K ($x=\text{ref, C, V, CV}$) was prepared with attritor milled WC DS50m and a 15 min outgassing plateau at 1150°C. The resulting microstructures are shown in Figure 4-166, the corresponding parameters are listed in Table 4-37. In the undoped sample (a) a number of large grains $>3 \mu\text{m}$ appear. The arithmetic mean grain size is $x_m=0.43 \mu\text{m}$. Chromium (b) reduces the grain size to $x_m=0.36 \mu\text{m}$, but some relatively coarse grains can still be observed. Similar findings apply for vanadium, though the grain size $x_m=0.23 \mu\text{m}$ is significantly smaller. The finest microstructure is observed for the double-doped sample. Cr+V double doping yields the finest microstructure with $x_m=0.17 \mu\text{m}$. The effect of the various GGIs can as well be seen from the comparison of the logarithmic normal fit in Figure 4-175 (d).

All samples of this series meet the condition of the logarithmic normal distribution well as the R^2 values ranging from 0.945–0.994 shows, where the double doped sample has the best correlation.

Dwell temperature 1150°C, dwell time 10 h, unmilled WC DS50

The microstructures and grain size distributions of the sample series MGxU+115L are shown in Figure 4-167. The undoped sample (a) reveals a relatively coarse microstructure with a grain size $x_m=0.52\ \mu\text{m}$ which is significantly refined by chromium (b), vanadium (c) and Cr+V doping (d). A good correlation of experimental data and logarithmic normal fit was achieved with R^2 ranging from 0.96–0.98 with the highest correlation for the double doped and the lowest for the undoped hardmetal.

A significant fraction (2.6%) of large grains $>1.2\ \mu\text{m}$ was only found for the undoped sample, while for the single doped sample only some single grains ($<0.2\%$) and for the double doped hardmetal no larger grains were observed.

A comparison of the grain-size values in Table 4-37 and the fitted grain-size distributions in Figure 4-175(e) reveal that with long dwell times the differences between the GGIs almost disappear and the differences in the mean grain size are insignificant. This means that increasing the dwell time of the outgassing plateau can significantly enhance the inhibiting efficiency of chromium as compared to vanadium. Since chromium and vanadium have almost equal performance it is not surprising that Cr+V double doping has no further benefit.

Dwell temperature 1150°C, dwell time 10 h, attritor-milled WC DS50m

The sample series MGx24+115L (x=ref, C, V, CV) was prepared with attritor-milled WC DS50m and a 10h dwell at 1150°C prior to liquid-phase sintering. By the milling process the initial grain size is reduced and a large number of defects is introduced in WC grains. Both are known to increase the driving force for coarsening, in particular the growth of single giant grains, see e.g. [02SOM, 04SCH]. Indeed, such large grains were observed for the undoped sample, see Figure 4-168(a). Those large grains are excluded from the logarithmic normal fit, and hence not considered in the grain size value x_0 . However, they are considered in the arithmetic mean grain size x_m and the experimentally determined d_{10} , d_{50} and d_{90} values. In total, 4% of the grains exceeded an intercept length of $1.2\ \mu\text{m}$. However, this value is generally unreliable since it is unlikely to get a representative number of large grains in the $30\times 20\ \mu\text{m}$ SEM-frame. When chromium is added (b) the grain size $x_m=0.33\ \mu\text{m}$ is

drastically reduced, but 1.1% of the grains are still $>1.2 \mu\text{m}$. Vanadium (c) further reduces the grain size to $x_m=0.28 \mu\text{m}$ and the number of large grains to 0.4%.

By chromium+vanadium double doping no more large grains are observed and a fine microstructure with $x_{m,Wc}=0.020 \mu\text{m}$ was achieved. The effectiveness of the particular dopants can be compared from the fitted logarithmic normal distribution in Figure 4-175(f).

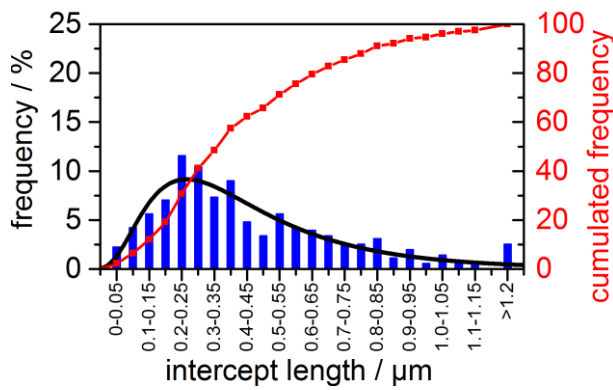
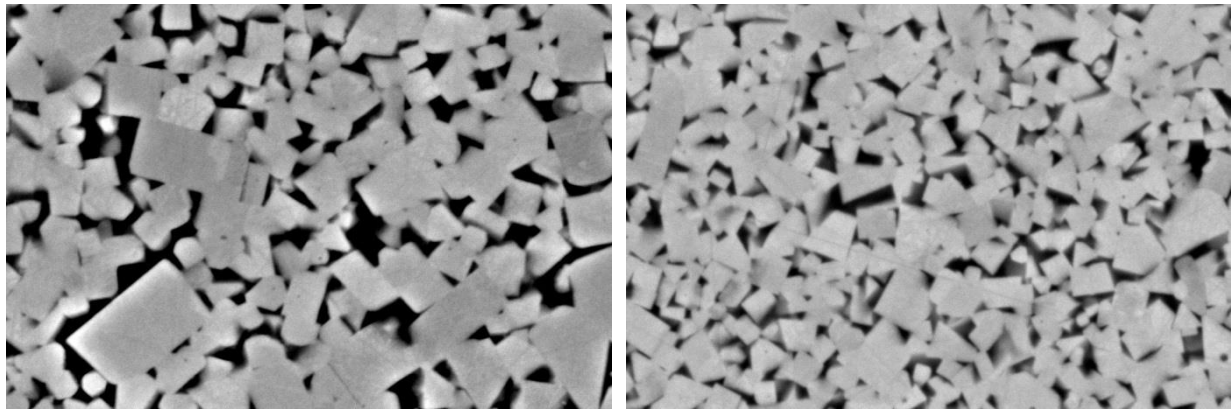
Summary of grain growth experiments

In this section the results are only presented and not discussed in depth. Such a discussion can be found in chapter 5.7. However, it may be advantageous to highlight three main findings as follows:

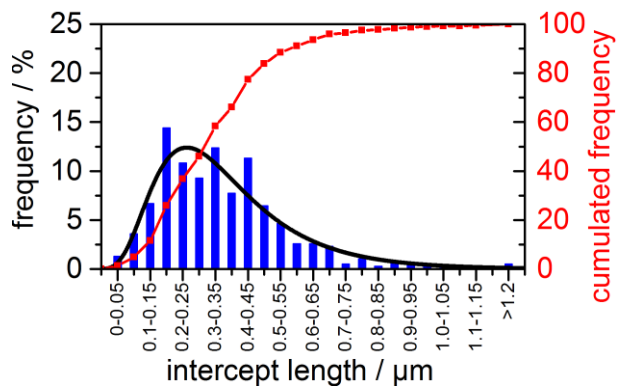
- it is particularly striking that Cr+V double doping has much higher impact on hardmetals based milled and pre-damaged WC as compared to conventional WC.
- When the green body is annealed for 10 h at 1150°C prior to liquid-phase sintering, the effectiveness of chromium and vanadium is almost identical, while vanadium is clearly superior when a short dwell time is applied such as in usual industrial sintering processes.
- When vanadium or chromium+vanadium doping is applied, the experimental data correlate well to a logarithmic normal fit ($R^2=0.960-0.994$), while the fit is relatively poor ($R^2=0.86-0.89$) for undoped samples. A long outgassing dwell increases the correlation for undoped samples when grains $>1.2 \mu\text{m}$ are excluded from the fit.

Table 4-37: Results of the grain growth experiments with different annealing temperatures and times of the outgassing plateau.

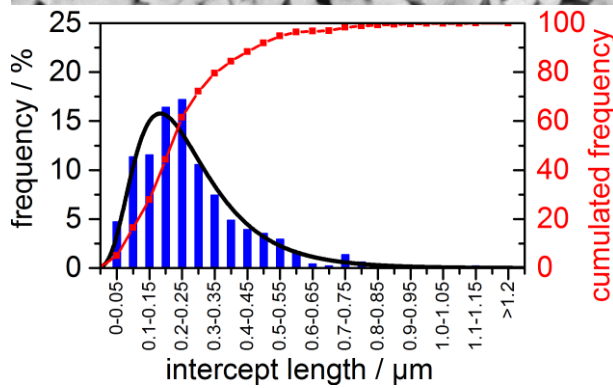
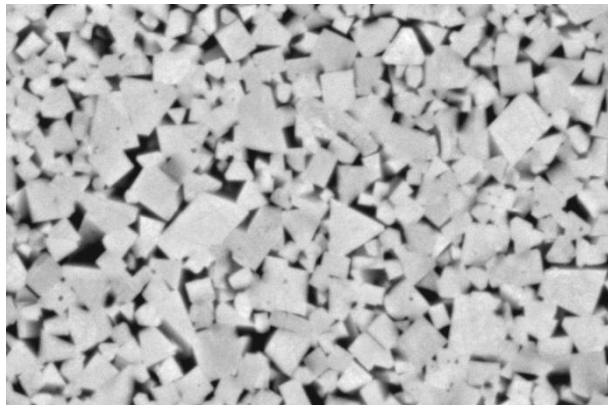
Sample	WC grade	T (plateau) (°C)	t (plateau) (h)	$x_{m,WC}$ (μm)	σ (inter) (μm)	x_0 (μm)	w (μm)	d_{10} (μm)	d_{50} (μm)	d_{90} (μm)	Grains >1.2 μm (%)	R ²
MGrefU+100K	DS50	1000	0.25	0.491	0.030	0.443	0.584	0.174	0.405	0.869	2.5	0.863
MGCU+100K				0.394	0.031	0.389	0.471	0.192	0.366	0.620	0.5	0.896
MGVU+100K				0.284	0.021	0.294	0.480	0.125	0.268	0.521	0	0.947
MGCVU+100K				0.316	0.006	0.312	0.461	0.146	0.287	0.525	0.2	0.959
MGref24+100K	DS50m	1000	0.25	0.423	0.023	0.402	0.652	0.149	0.364	0.769	1.6	0.871
MGC24+100K				0.338	0.013	0.315	0.553	0.128	0.288	0.619	0.7	0.950
MGV24+100K				0.274	0.020	0.265	0.587	0.090	0.235	0.476	0	0.979
MGCV24+100K				0.178	0.009	0.175	0.539	0.064	0.151	0.332	0	0.994
MGrefU+115K	DS50	1150	0.25	0.500	0.030	0.467	0.572	0.183	0.444	0.859	4.2	0.883
MGCU+115K				0.427	0.020	0.422	0.485	0.193	0.396	0.695	1.0	0.960
MGVU+115K				0.303	0.012	0.299	0.531	0.125	0.261	0.531	0.1	0.980
MGCVU+115K				0.325	0.009	0.328	0.486	0.116	0.290	0.531	0.2	0.984
MGref24+115K	DS50m	1150	0.25	0.430	0.027	0.391	0.577	0.161	0.366	0.814	2.8	0.945
MGC24+115K				0.356	0.034	0.272	0.581	0.110	0.267	0.552	0.2	0.961
MGV24+115K				0.231	0.010	0.215	0.508	0.091	0.192	0.433	0	0.982
MGCV24+115K				0.169	0.009	0.165	0.545	0.059	0.139	0.326	0	0.994
MGrefU+115L	DS50	1150	10	0.515	0.016	0.485	0.519	0.217	0.462	0.871	2.6	0.961
MGCU+115 L				0.338	0.032	0.330	0.578	0.117	0.300	0.595	0.2	0.977
MGVU+115 L				0.321	0.010	0.311	0.496	0.138	0.283	0.592	0.2	0.966
MGCVU+115L				0.329	0.024	0.322	0.508	0.144	0.293	0.568	0	0.981
MGref24+115L	DS50m	1150	10	0.532	0.075	0.440	0.46	0.221	0.428	0.836	4.0	0.963
MGC24+115L				0.330	0.003	0.312	0.459	0.144	0.277	0.539	1.1	0.979
MGV24+115L				0.279	0.008	0.273	0.529	0.107	0.241	0.511	0.4	0.954
MGCV24+115L				0.199	0.013	0.198	0.496	0.087	0.174	0.357	0	0.993



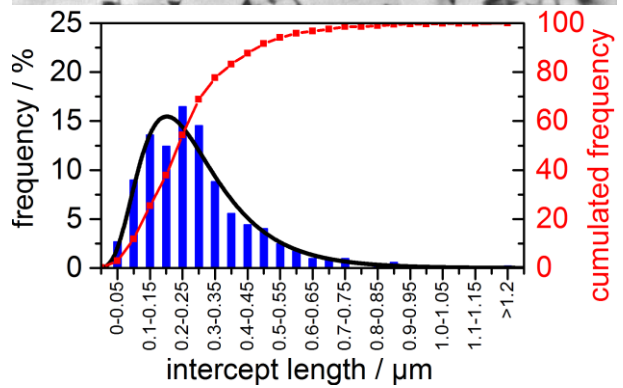
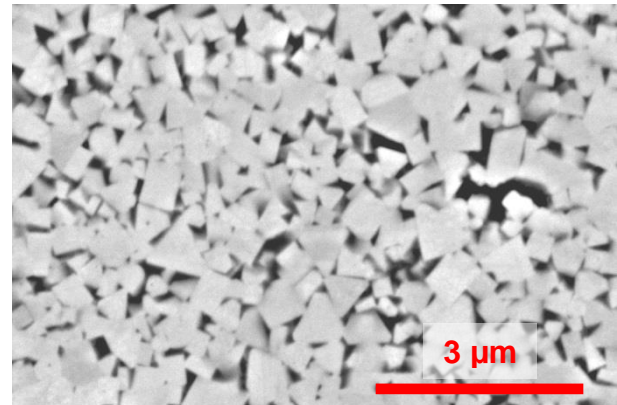
(a) undoped (MGRRefU+100K)



(b) Cr-doped (MGCU+100K)



(c) V-doped (MGVU+100K)



(d) Cr/V-doped (MGCVU+100K)

Figure 4-169: BSE Micrographs and corresponding line intercept distributions of hardmetals with WC=DS50, sintered with a 15 min outgassing plateau at 1000°C.

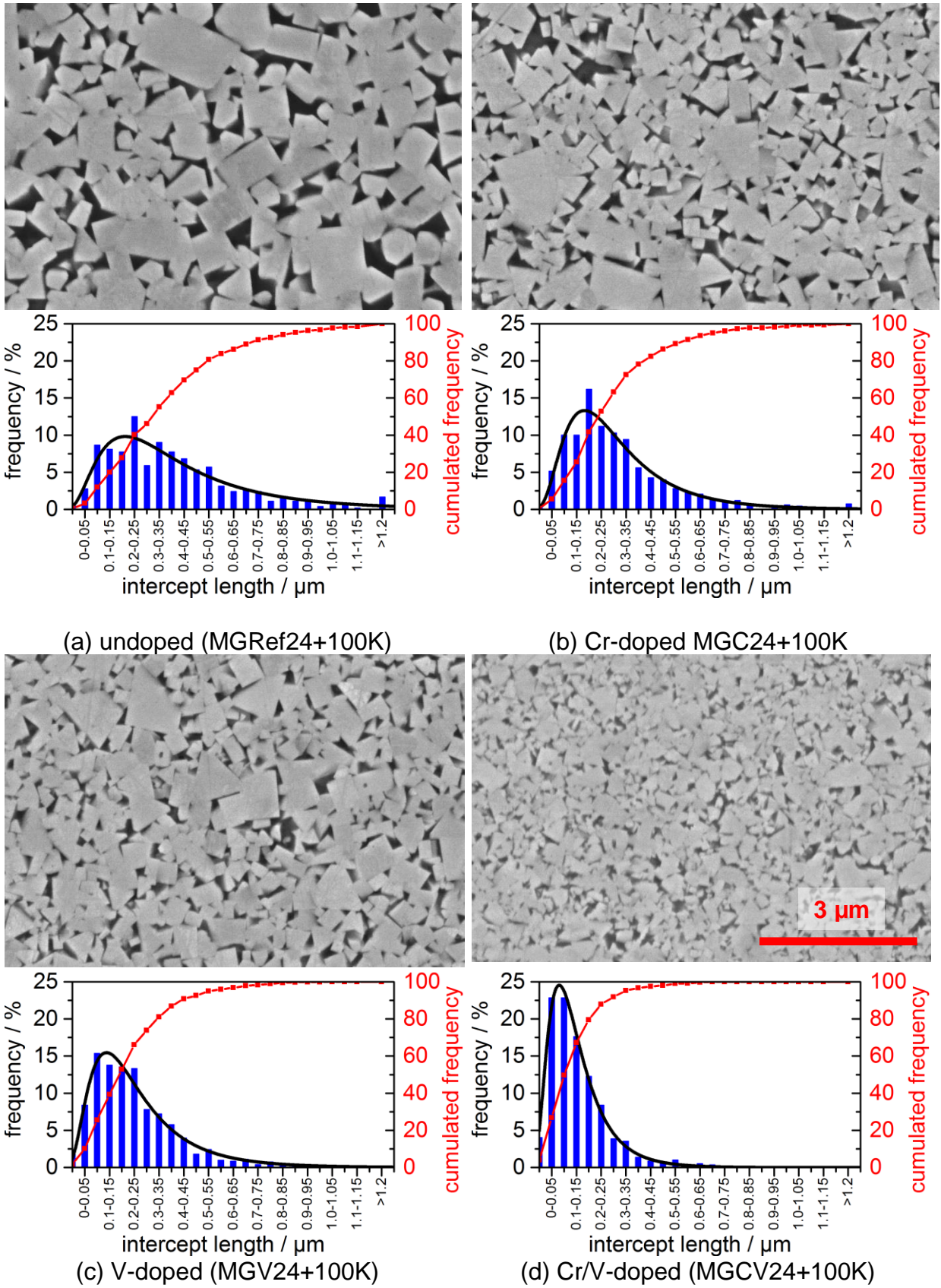
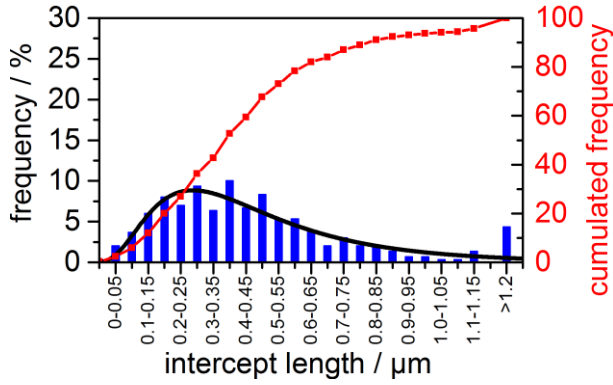
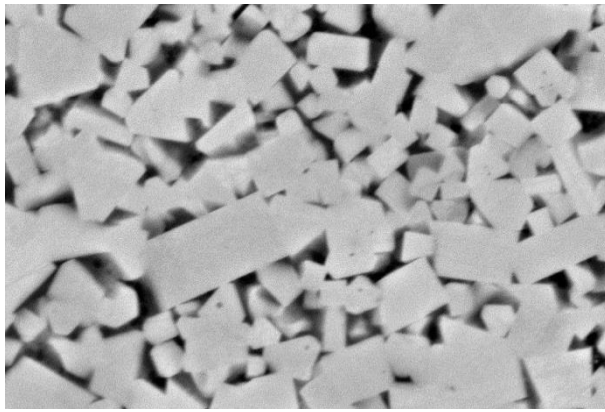
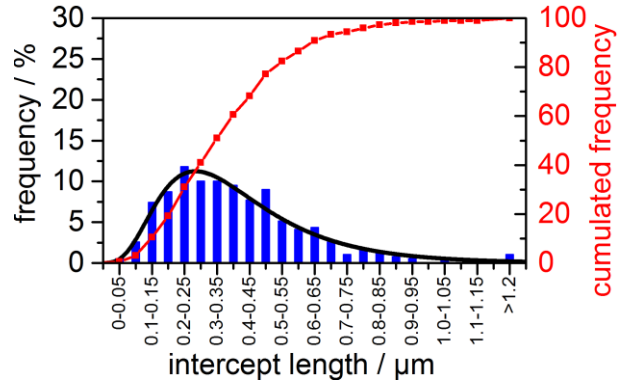
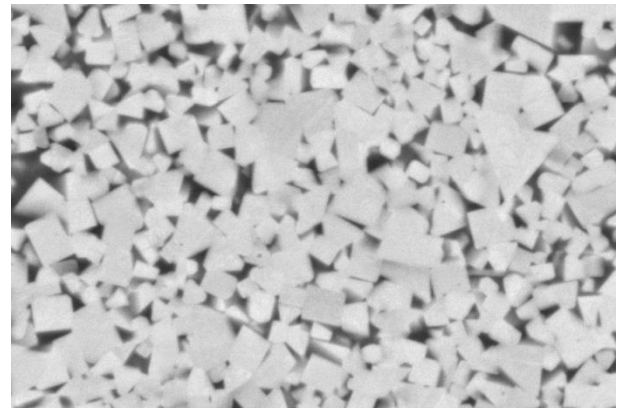


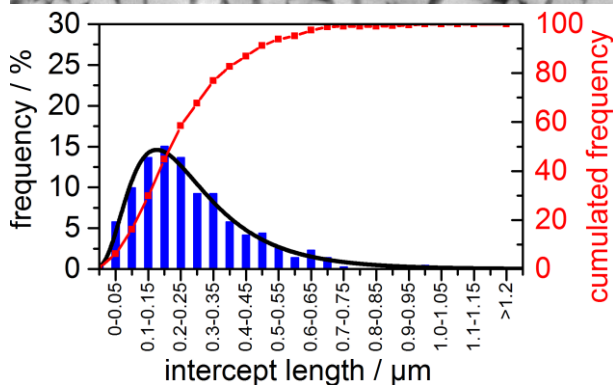
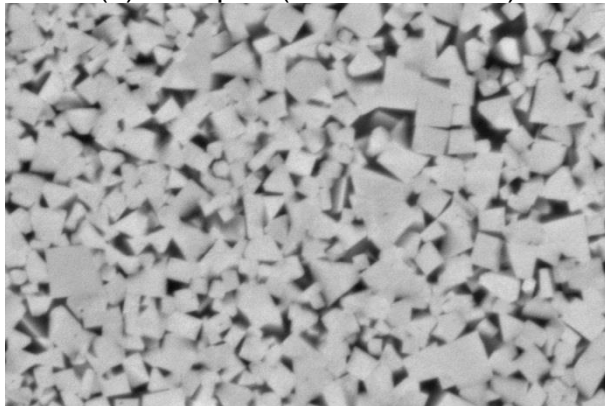
Figure 4-170: BSE Micrographs and corresponding line intercept distributions of hardmetals with WC=DS50m, sintered with a 15 min outgassing plateau at 1000°C.



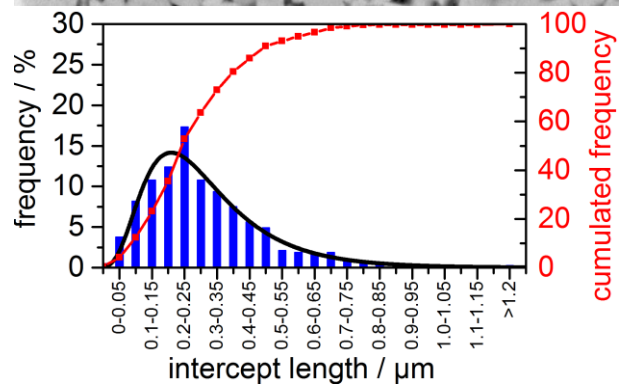
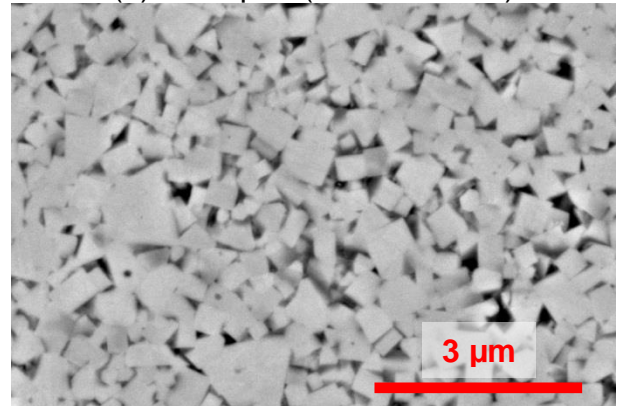
(a) undoped (MGRefU+115K)



(b) Cr-doped (MGCU+115K)



(c) V-doped (MGVU+115K)



(d) Cr/V-doped (MGCVU+115K)

Figure 4-171: BSE Micrographs and corresponding line intercept distributions of hardmetals with WC=DS50, sintered with a 15 min outgassing plateau at 1150°C.

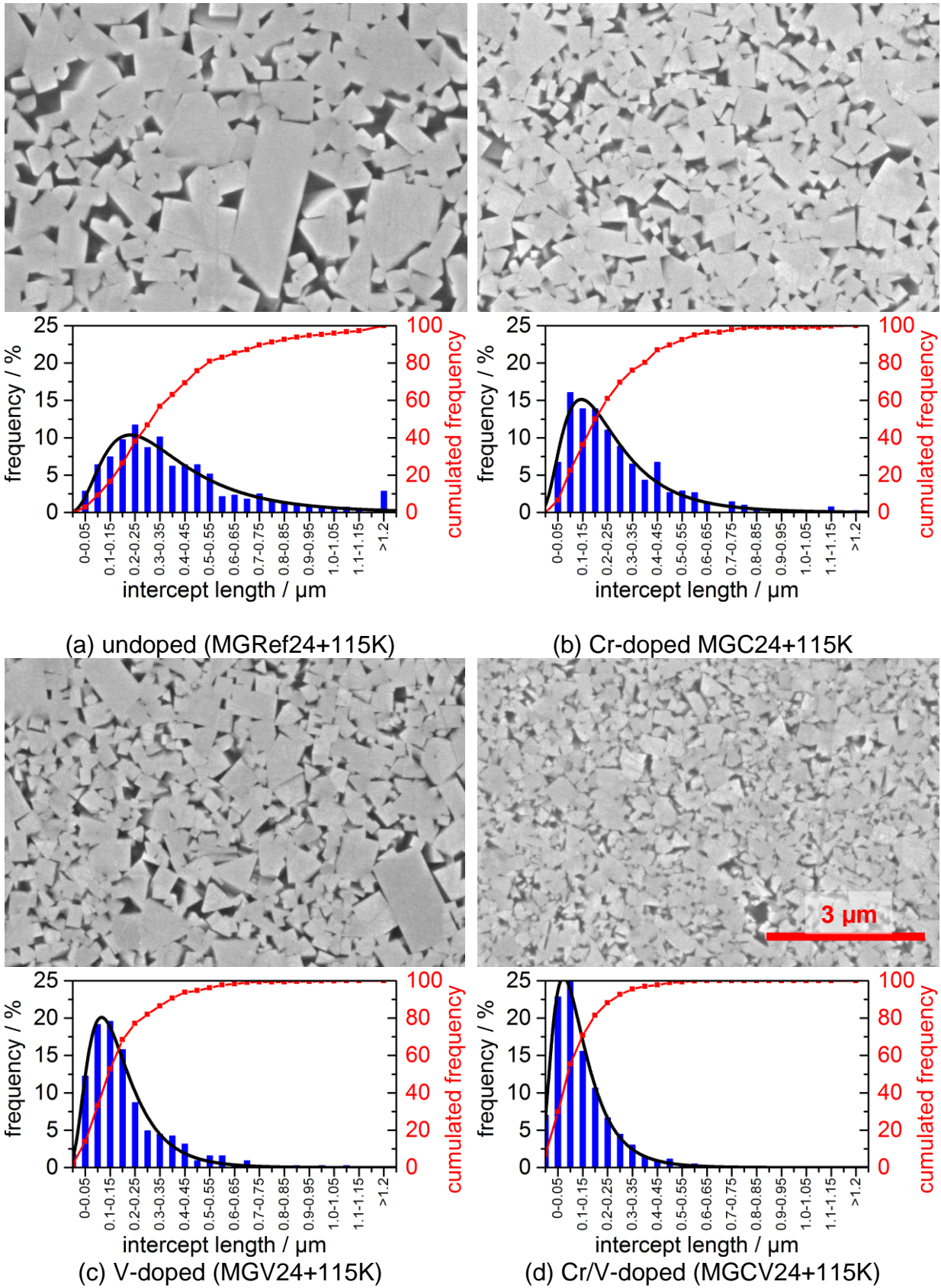


Figure 4-172: BSE Micrographs and corresponding line intercept distributions of hardmetals with WC=DS50m, sintered with a 15 min outgassing plateau at 1150°C.

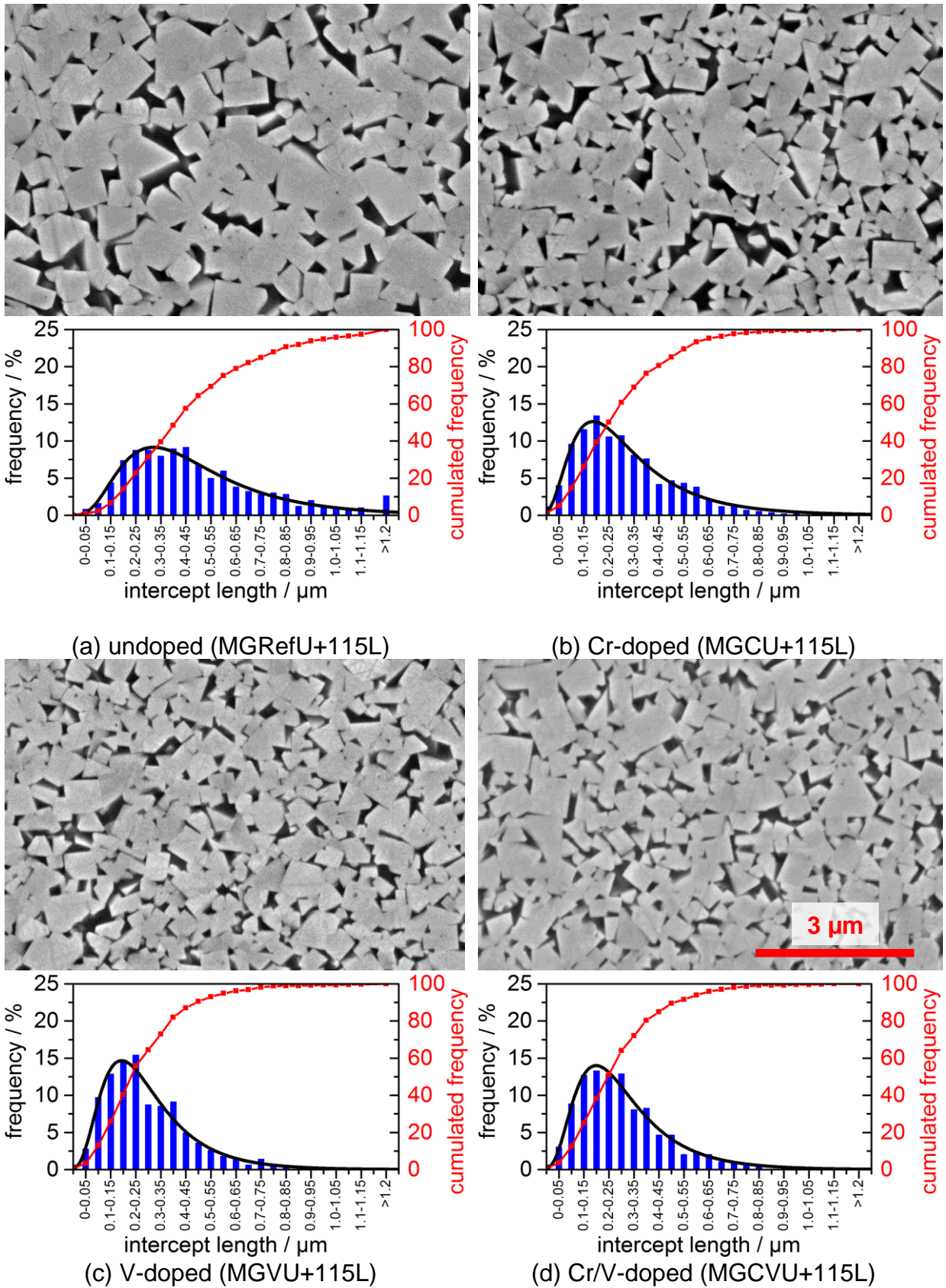


Figure 4-173: BSE Micrographs and corresponding line intercept distributions of hardmetals with WC=DS50, sintered with a 10h outgassing plateau at 1150°C.

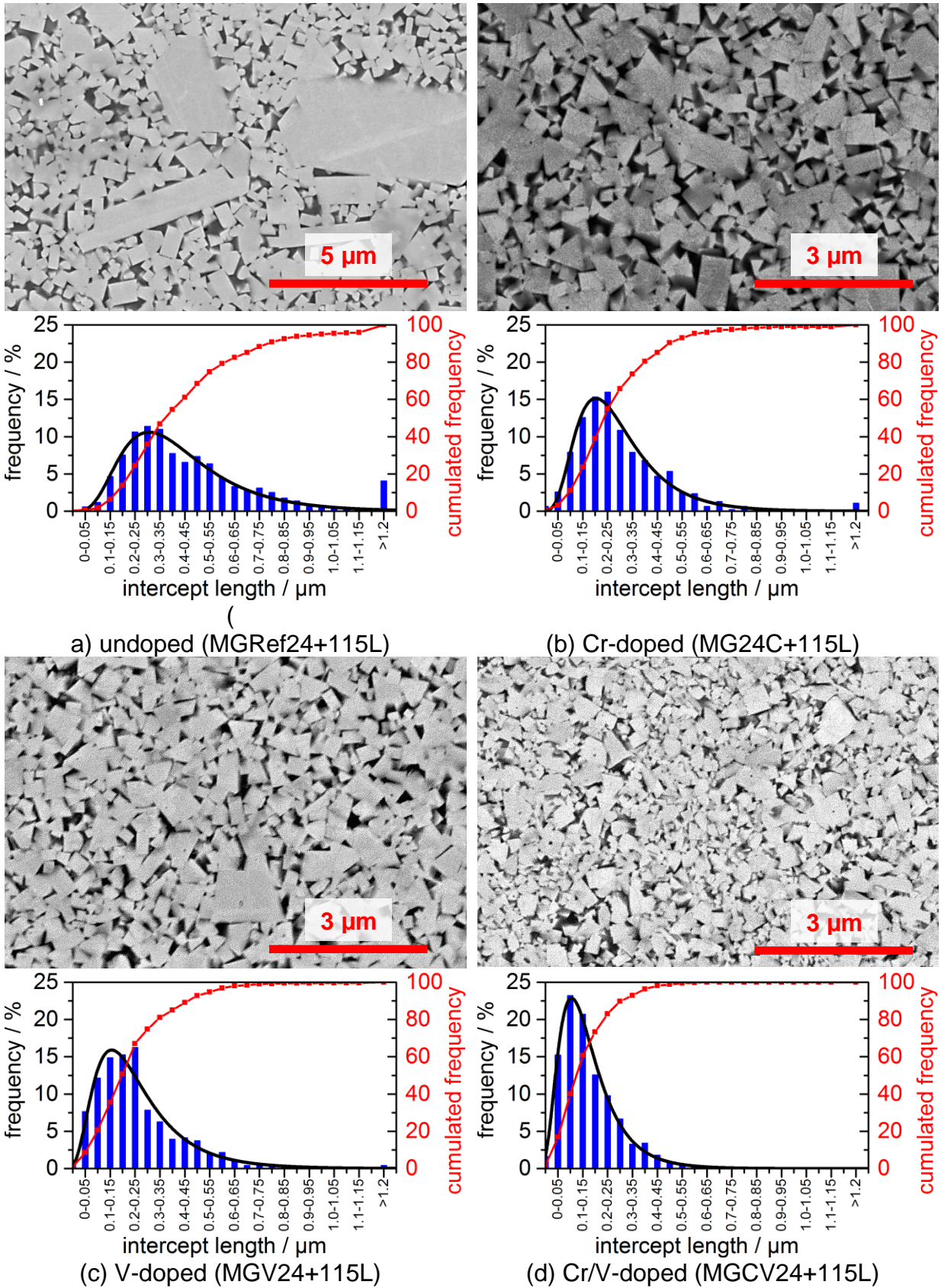


Figure 4-174: BSE Micrographs and corresponding line intercept distributions of hardmetals with WC=DS50m, sintered with a 10h outgassing plateau at 1150°C.

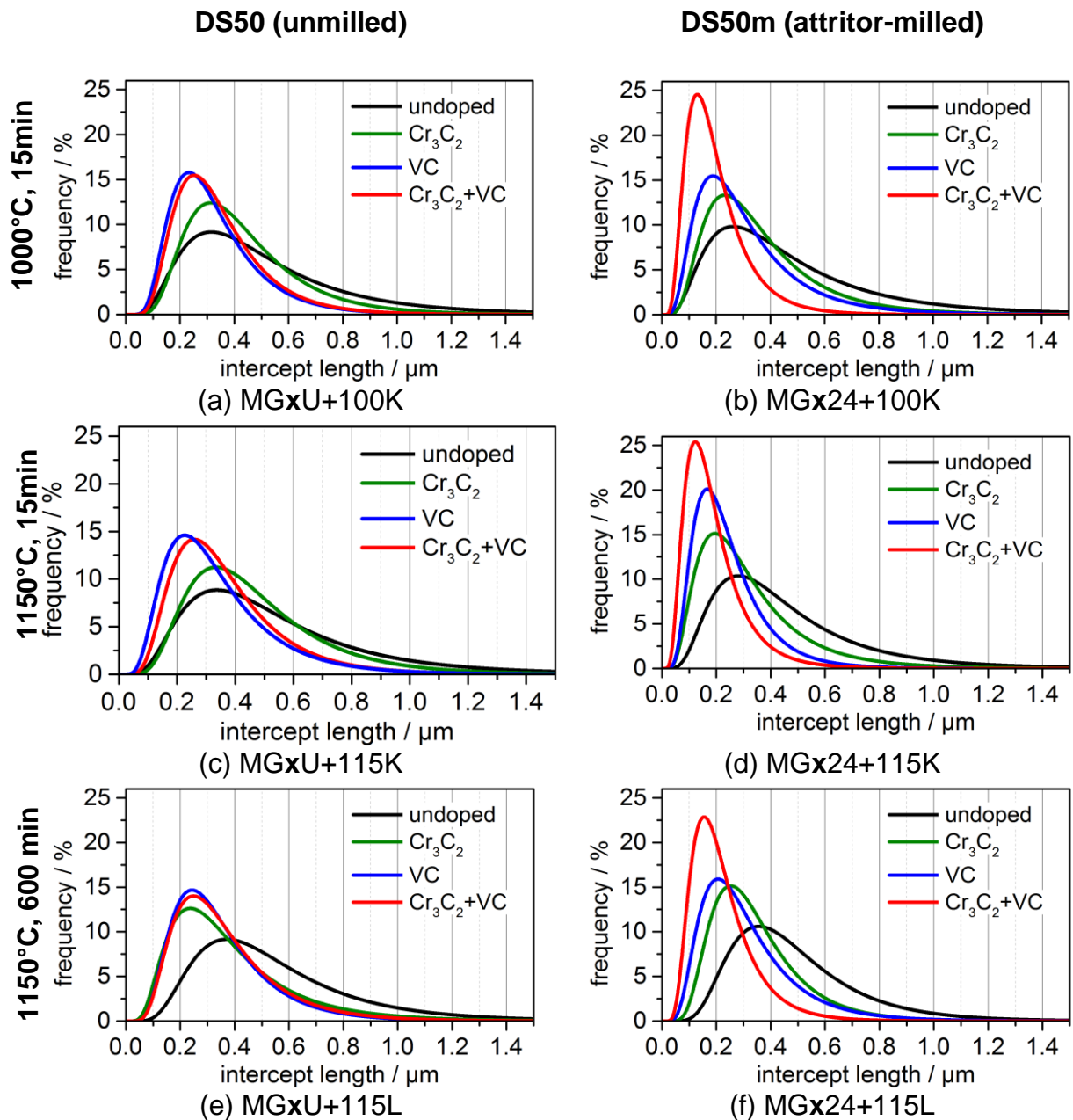


Figure 4-175: Fitted grain-size distributions (log. normal fit) of liquid-phase sintered hardmetals (1380°C) with various dopants. Annotations on the left side indicate temperature and dwell time of the outgassing plateau. Annotations in the top row refer to the WC grade. X=GGI.

4.7.3 Spark plasma sintered samples (SPS)

GGI-doped hardmetals were prepared by the SPS method at 1150°C. A specific feature of this method is that no liquid phase is present and the dwell time is short (15 min). Nevertheless, dense hardmetals are accessible due to pressure assistance. Despite the low temperature and annealing time WC grain growth is observed, since especially in near-nano grades growth initiates at ~1000°C, compare section 2.2.2. Early and fast growth inhibition is therefore essential for SPSed grades. The microstructures of the SPSed samples and the corresponding grain-size distributions are shown in Figure 4-176. Elongated binder segregations of up to 3 µm length are observed in all samples. These segregations are oriented normal to the pressing direction. Upon pressure-free sintering of hardmetals pores of up to 2–3 µm are reported to form in this temperature range [13RIC]. Their elimination requires liquid phase which allows particle rearrangement. However, upon SPS no liquid phase is present in order to trigger such rearrangement. But due to pressure assistance the binder phase is forced to fill the pores. As can be seen from the Cr+V-doped sample the GGIs are not fully resolved in the binder phase. The grain size and the magnetic properties of the samples are summarised in Table 4-38. The effects of the various dopants are discussed in detail in section 5.7, page 285.

Table 4-38: Grain size and magnetic properties of SPS samples.

Sample	GGI	$x_{m,WC}$	d_{10}	d_{50}	d_{90}	w	Ms	H _c
		µm	µm	µm	µm		µTm ³ /kg	kA/m
SP	none	0.257	0.129	0.260	0.494	0.482	17.5	21.6
SPC	Cr ₃ C ₂	0.256	0.112	0.248	0.485	0.544	18.5	24.9
SPCN	Cr ₂ N	0.238	0.110	0.235	0.459	0.523	17.9	24.7
SPV	VC	0.218	0.105	0.202	0.360	0.446	18.4	24.2
SPCV	Cr ₃ C ₂ +VC	0.217	0.098	0.213	0.421	0.531	18.8	24.5

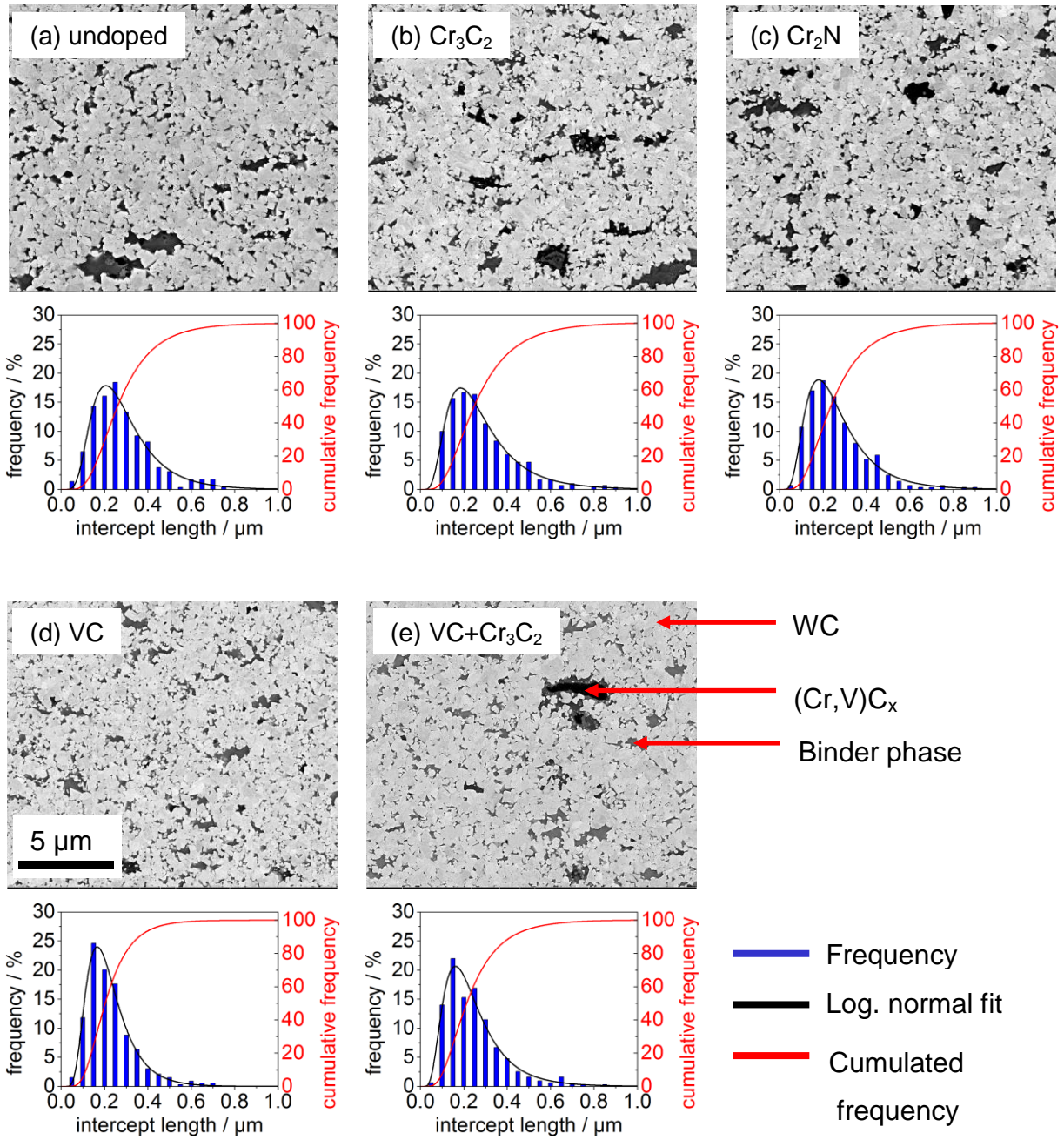


Figure 4-176: BSE micrographs of SPS samples (top row) and corresponding grain size distribution (bottom row) with various dopants

4.8 Interface chemistry

According to recent literature the inhibiting mechanism of GGIs is most likely related to the existence of $(GGI,W)C_x$ layers at the WC/Co interface, or at least a segregation at the interface within the binder phase as discussed in section 2.3.1. However, such findings were mostly concluded from liquid-phase sintered hardmetals and the layers were observed after cool-down to ambient temperature. Hence, they could have precipitated upon cooling and there is no direct proof on their existence upon sintering temperature. It is described in literature and it was shown section 4.7 that especially vanadium shows inhibiting activity at early sintering stages. Moreover, Yamamoto et al. [00YAM] found no crystalline layer but a slight segregation of vanadium appearing at the WC/Co interface of a vanadium-doped hardmetal after quenching from 1200°C, where the binder phase is in solid-state (compare solidus temperatures in Table 2-3). Thus, it is questionable whether the inhibiting effect in solid-state can be ascribed to either such layers or if other mechanisms apply.

Thus, TEM-samples were prepared from diffusion couples 20 µm from the interface. At this position, GGIs are fully soluble at the testing temperatures. Combined with the fact that samples were rapidly cooled, e.g. from 1150–800°C in 20 seconds, no precipitations are expected to form due to decreasing solubility upon cooling. From these samples, we tried to take images from the WC-Co interfaces in atomic resolution. In order to observe phases with just a few atomic layers thickness or even subatomic layers the sample has to be very thin (<200 nm) and the WC-crystal has to be oriented strictly edge on to the incident beam, otherwise diffraction phenomena appear which result in blurry images. Moreover, the sample has to keep its position extremely stable, even small drifts of 1 nm/s will deliver blurred images. These conditions were only met for sample VCoG105+. For the other samples, TEM-EDX line scans were performed in order to locate a possible presence of GGIs. However, with this method it cannot be distinguished whether the GGIs are located in a crystalline layer or segregated in the binder phase towards the interface. For more detailed description other equipment allowing higher resolution would be required, but some useful information on the interface chemistry can still be provided.

4.8.1 VWC-Co-VC, 1050°C

For the sample VCoG105+ the experimental conditions allowed an observation of the WC-Co interface with atomic resolution. The analysed sample area was prepared by FIB 10 μm from the WC-VC-Co/WC-Co interface. The corresponding vanadium concentration was measured $c(\text{V}/\text{Co})=0.03$. A TEM bright field image of the area is shown in Figure 4-177. The cobalt binder (light grey) already forms a contiguous network, but a large porosity is still remaining. This porosity made sample preparation challenging since TEM observations require thin samples with <200 nm thickness. Upon ion-Beam thinning the sample started to crumb due to the high porosity. However, a suitable TEM sample was achieved. It can be seen from the micrograph that cobalt binder already infiltrated WC/WC grain boundaries and formed thin binder lamellae. However, especially fine grains tend to form agglomerates which can subsequently cause grain growth by coalescence.

HRTEM images of two different WC/Co interfaces are shown in Figure 4-178. No vanadium rich layer was observed which would be indicated by a change of the net plane orientation at the interface. However, phases of less than a monolayer thickness can hardly be detected by this method which means the results are no 100% proof that cubic carbide layers are absent at 1050°C.

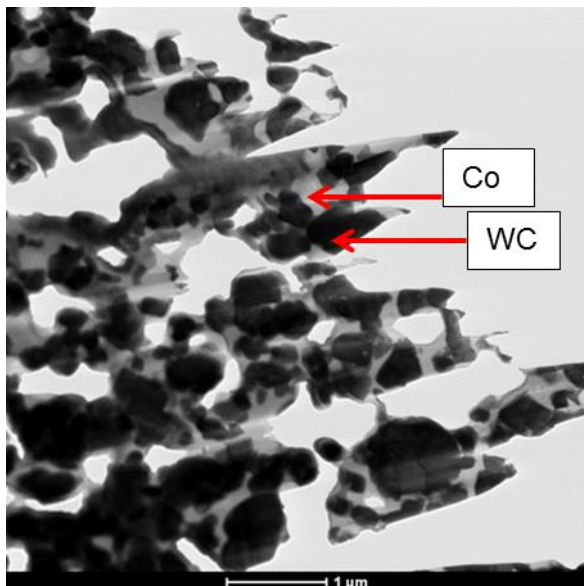


Figure 4-177: TEM darkfield image of sample VCoG105+ 10 μm from the interface.

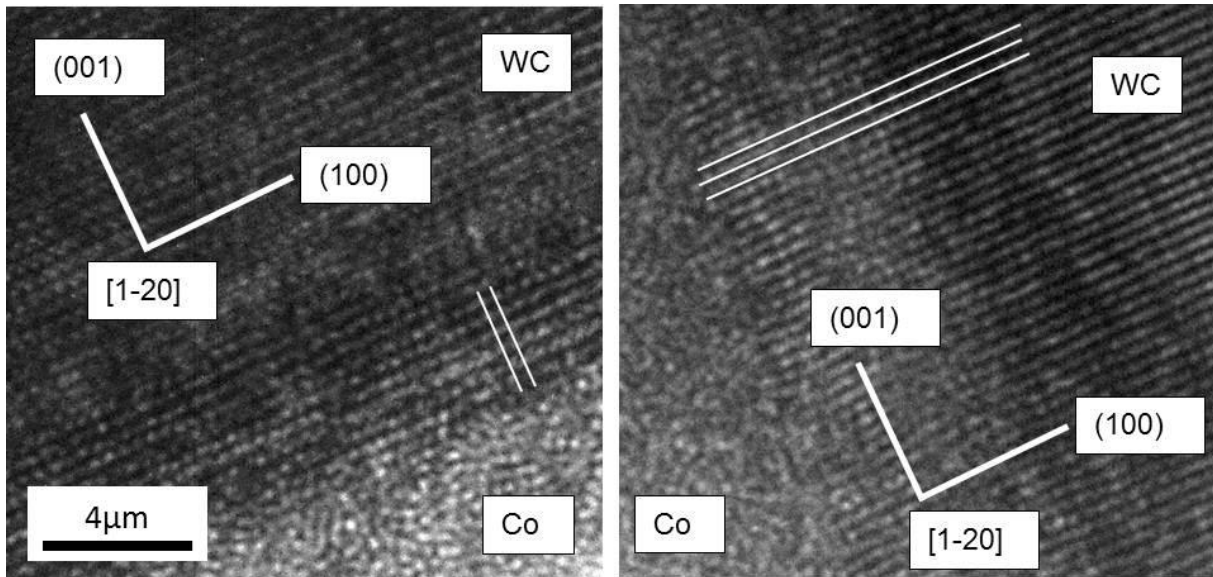


Figure 4-178: HRTEM images of WC/Co interfaces 8 μm from the interface of sample VCoG115 as published in [15BUC].

4.8.2 WC-VC-Co, 1150°C

From sample VCoG115+ which is a diffusion couple with GG1=vanadium, cobalt binder and high carbon potential, a TEM-sample was prepared 20 μm from the interface. The vanadium concentration in the hardmetal at this position was around 0.15 wt% or $c(\text{V}/\text{Co})=0.02$. From literature data in Table 2-4 a solubility of $c(\text{V}/\text{Co})=0.013$ can be interpolated. Consequently the vanadium concentration is close to the equilibrium concentration at 1150°C.

The microstructure of the sample is shown in Figure 4-179. Especially in the top left corner of the image a number of small WC grains (light grey) with “binder filled” round holes (dark grey) can be found. Such structures most likely form when agglomerates of fine grains start to coarsen by particle coalescence. In literature the latter was stated as main growth mechanism in submicron hardmetals at low temperatures, see section 2.2.2. The binder phase is already well distributed between WC grains and a number of cobalt-lamellae of just a few nanometres thickness can be found between WC grains. Such lamellae are formed upon wetting of WC/WC grain boundaries. A total number of 4 TEM-EDX line scans were conducted on this sample. They are labelled L1–L4 and their positions are illustrated in Figure 4-179. The resulting concentration profiles of V, W and Co are shown in Figure 4-180. The scan L1

originated in a WC-grain with scan direction towards the cobalt binder. The edge-on condition was met poorly since the WC-Co interface is elongated by 75 μm . The vanadium signal remains stable and no enrichment at the interface can be confirmed. Scan L2 better meets the edge-on conditions, which can be seen from the steeper W/Co gradients at the two interfaces around 50 μm and 120 μm . However, no vanadium segregation was found. The scans L3 and L4 were conducted on the same WC/Co interface but just shifted a few nanometres in position. The step width of L3 was 1 nm whereas for L4 it was 2 nm. Both show almost identical concentration profiles with clear vanadium segregation at the interface. With smaller step width the peak is slightly sharper but the difference is small. Hence, the missing peak of L1 and L2 cannot be attributed to a too coarse scanning. It was discussed in section 2.3.1 that $(\text{W},\text{V})\text{C}_x$ precipitations were only found at specific habits even in liquid-phase sintered samples while others were free of vanadium. This can be an explanation why vanadium enrichment was found only at two of four interfaces.

The vanadium concentration found in the binder phase is around 1.1 wt% for scans L2–L4 and 2.0 wt% for L1. The W concentration is around 10 wt% in samples L2–L4 but 18 wt% in L1. The reason for the higher values in L1 might be a WC grain which is hidden below the binder surface.

The vanadium solubilities found from L2–L4 are equal to those extrapolated from Table 2-4. The tungsten solubilities are slightly higher than the expected 5–6 wt%. However, this can be attributed to a non-equilibrium binder state, a local shift in carbon potential or the limited accuracy of TEM-EDX. From the present the reason cannot be clearly identified, but is most likely a combination of those three. The results of these scans are summarised in Table 4-39.

Additionally to the line scans a TEM-EDX mapping was made for sample VCoG115+. The scanned area is shown in Figure 4-181(a), (c) – (f) show the single element mappings of vanadium, cobalt, tungsten and carbon, respectively, while (b) is an overlap of all element mappings. Interestingly a few vanadium precipitations of 10–20 nm diameter were detected in the vicinity of WC/WC/Co triple points (c). These precipitations, combined with the interface segregations might be an explanation why a total vanadium concentration of $c(\text{V}/\text{Co})=0.02$ was measured in the hardmetal by EPMA but only $c(\text{V}/\text{Co})=0.012$ was found in the binder phase. As stated above, the latter is coincident with the literature solubility data.

Table 4-39: Results of TEM-EDX line scans L1-L4 of sample VCoG115+.

Scan	Length [nm]	Step width [nm]	W solubility [wt%]	V solubility [wt%]	Segregation
L1	166	2	18	2.0	✗
L2	182	2	10	1.1	✗
L3	135	1	10	1.1	✓
L4	126	2	8	1.1	✓

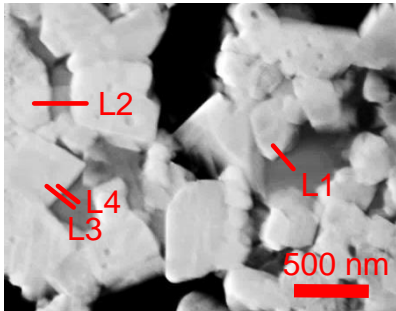


Figure 4-179: TEM microstructure of sample VCoG115+, 20 μm from interface. Red lines represent positions of EDX line scans; scan direction is towards the corresponding label L1-L4.

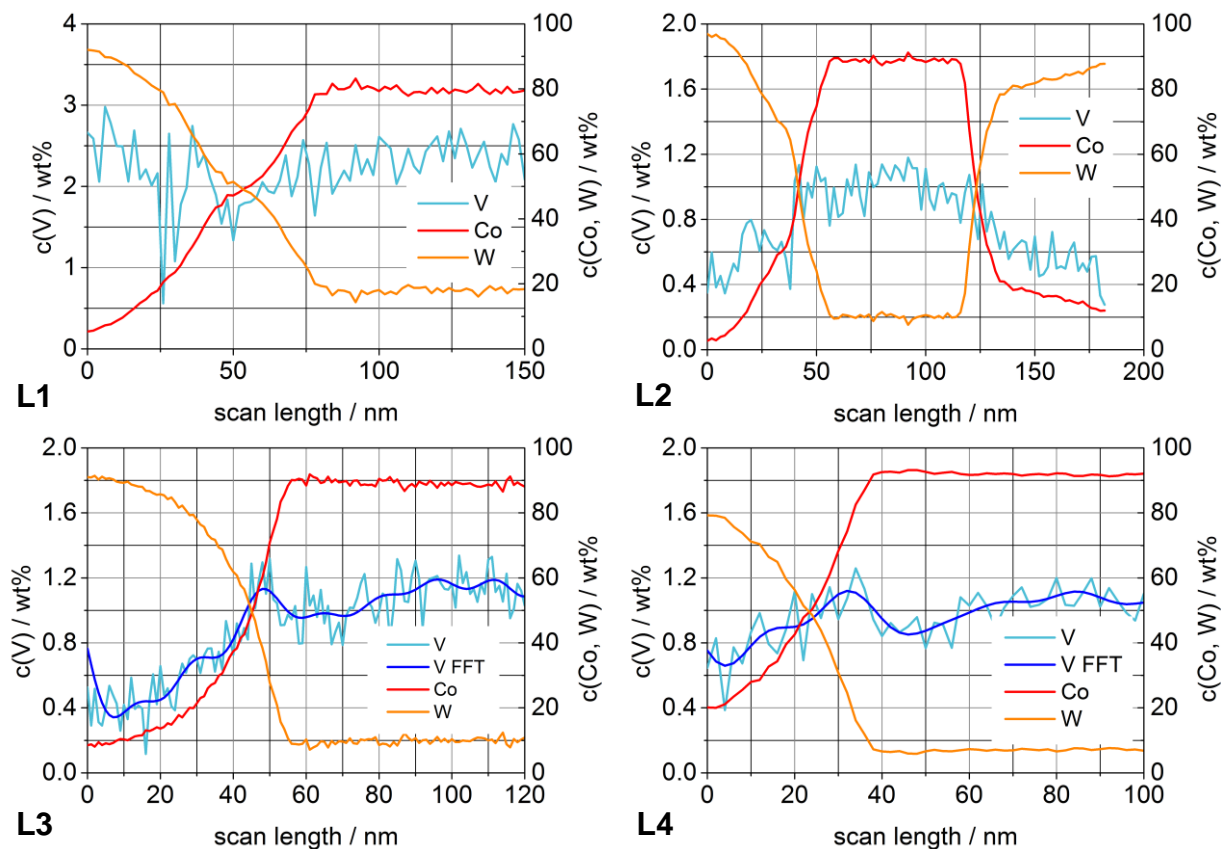


Figure 4-180: TEM-EDX line scans L1-L4 of sample VCoG115+. Refer to Figure 4-179 for scan positions.

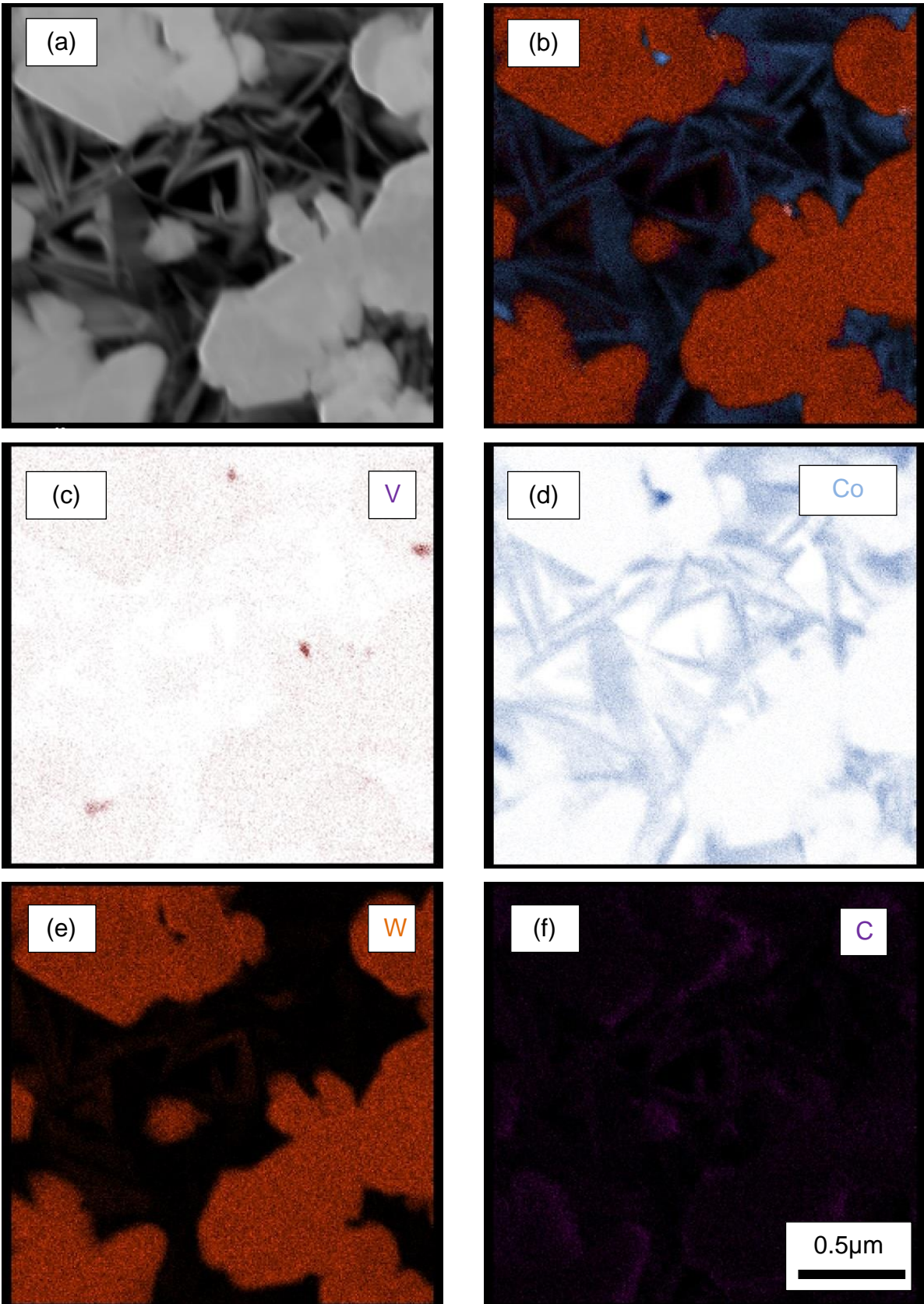


Figure 4-181: TEM-EDS mapping of the sample VCoG115+, annealed at 1150°C for 15 min with (a) the TEM darkfield image, (b) the overlay of all element mappings and (c) – (f) the single element mappings

4.8.3 WC-Co-Cr₃C₂, 1150°C

From sample CCoG115+ lamella for TEM-analyses was prepared 20 µm from the interface. The local as-measured chromium concentration in the hardmetal is $c(\text{Cr})=0.5$ wt%, the normalised concentration is $c(\text{Cr}/\text{Co})=0.052$. The corresponding microstructure is shown in Figure 4-182. A large number of WC/WC grain boundaries which are not wetted by cobalt binder appear. Such contacts can lead to grain growth by coalescence which can be an explanation for the lower efficiency of chromium as an inhibitor especially at low temperatures. A deeper discussion on this issue can be found in chapter 5.7.

A total number of 10 TEM-EDX line scans over WC/Co interfaces were conducted on this sample, their positions are indicated by the red lines in Figure 4-182. The corresponding results are shown in Figure 4-184 (L1) – (L10). Only for the scans L3–L5 chromium enrichment at the interface was found. In case of scan L3 the edge-on condition was well met for the interface at ~120 nm, where a significant enrichment of chromium was observed. In case of scan L4 there is as well a slight chromium peak at the interface at 120 nm which meets the edge-on condition suitably. However, due to the strong noise of the signal this peak cannot be considered significant. Around 50 nm a very strong and broad chromium peak was observed, similar to the one in L5. Both peaks originate from the same WC-grain. But while the L4 peak maximum is located within the cobalt phase it is located within the WC grain in L5. The L4 signal has amplitude of 15 wt% and a width of 75 nm. Such a high chromium concentration is unlikely to originate from a (W,Cr)C layer which is supported by the findings of Bounhore et al. [15BOU] who found no such layers but segregations at 1200°C. It is more likely either a strong segregation or a precipitation formed by cooling. The L5 signal has weaker amplitude of 9 wt%, is narrower and abruptly ends at the interface to cobalt. This constellation could indeed point to the presence of a (W,Cr)C layer. However, due to the absence of a microstructural proof such considerations remain speculative.

As stated above from the total number of 10 scans only one showed an enrichment of chromium at the interface (L3) and two revealed a strong signal which most likely originates from precipitations formed upon cooling (L4, L5). The others (L1, L2, L6–L10) showed no enrichment of chromium. Thus, the inhibiting mechanisms of chromium at

1150°C very likely not depend on the presence of crystalline chromium layers or segregations.

From literature data a solubility of chromium in the cobalt binder phase of $c_0(\text{Cr})=6.6 \text{ wt\%}$ or $c_0(\text{Cr/Co})=0.075$ and for tungsten of $c(\text{W})=5.5 \text{ wt\%}$ was interpolated. From the scans tungsten and chromium solubilities in the binder phase were estimated. The results are summarised in Table 4-40, but it has to be kept in mind that TEM-EDX analyses are semi-quantitative especially for low concentrations. From all scans a mean chromium concentration of $c(\text{Cr})=4.5\text{--}5 \text{ wt\%}$ or $c(\text{Cr/Co})=0.52\text{--}0.58$ was calculated. This value is in good accordance to the $c(\text{Cr/Co})=0.052$ measured by EPMA. If a significant amount of cobalt is segregated at the interfaces, the Cr/Co ratio measured in the hardmetal by EPMA would be significantly higher than measured within the binder phase by TEM. Subsequently it can be concluded that no significant interface segregations appear which is coincident with the interface analyses.

The tungsten concentration of $c(\text{W})\sim 10 \text{ wt\%}$ is by a factor of two higher than the equilibrium concentration of $c(\text{W})=5 \text{ wt\%}$ at 1150°C. Since the sample was never exposed to higher temperatures oversaturation is impossible. A local shift in carbon potential can easily happen due to the presence of a large amount of chromium in the $\text{Cr}_3\text{C}_2\text{-WC-Co}$ part of the diffusion couple and the subsequent carbon loss by reduction of the chromium surface oxides. This carbon consumption can as well affect the WC-Co part of the diffusion couple. Based on these samples it is thus likely that the carbon potential of diffusion couples locally deviates from the intended potential.

Table 4-40: Results of TEM-EDX line scans L1-L10 of sample CCoG115+.

Scan	Length (nm)	Step width (nm)	W (wt%)	Cr (wt%)	Segregation
L1	232	2	5	3	✗
L2	302	2	10	5	✗
L3	229	1	11	4.5	✓
L4	254	1	10	n.a.	✓
L5	192	1	9.5	4.5	✓
L6	261	1	10	4.5	✗
L7	265	1	9.0	5	✗
L8	275	1	11	5	✗
L9	269	1	10	5	✗
L10	269	1	10	5	✗

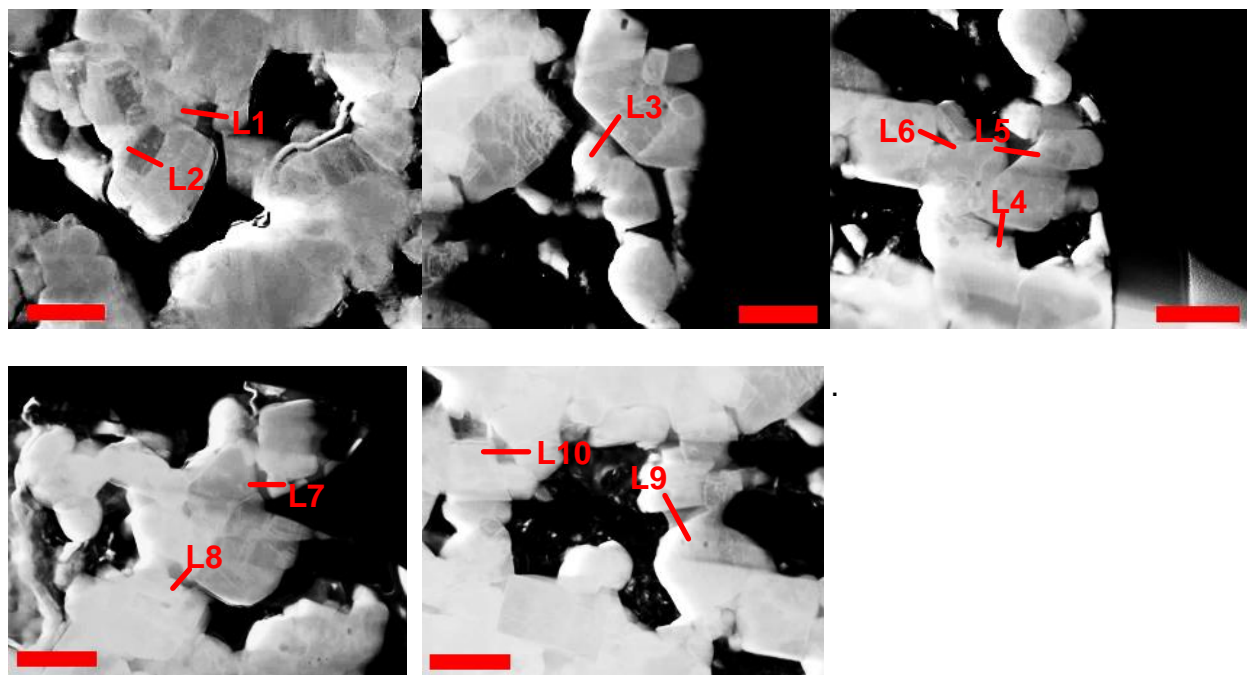


Figure 4-182: TEM microstructure of sample CCoG115+, 20 μm from interface. Red lines represent positions of EDX line scans; scan direction is towards the corresponding label

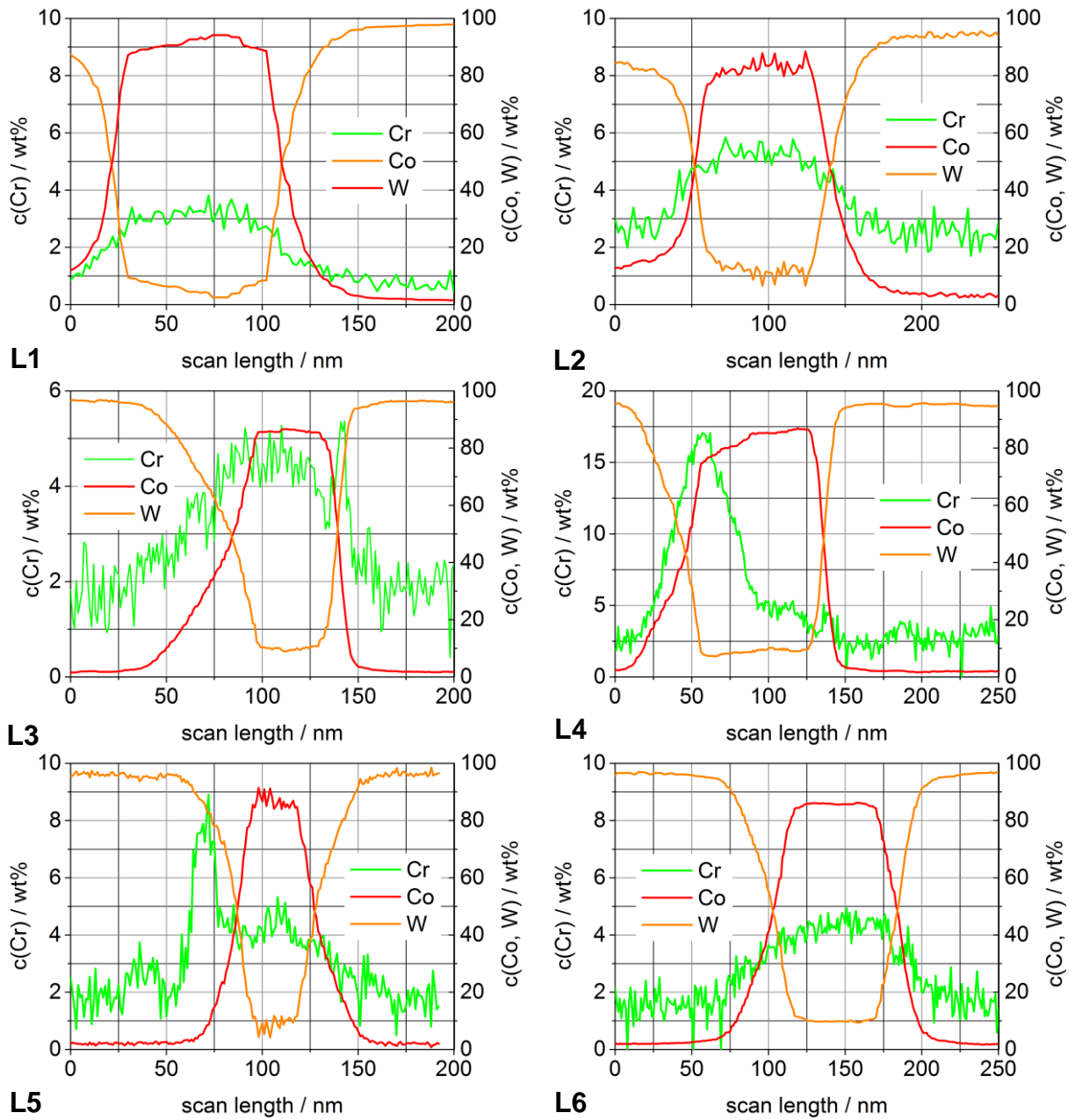


Figure 4-183: TEM-EDX line scans L1–L6 of sample CCoG115+. See Figure 4-182 for scan positions.

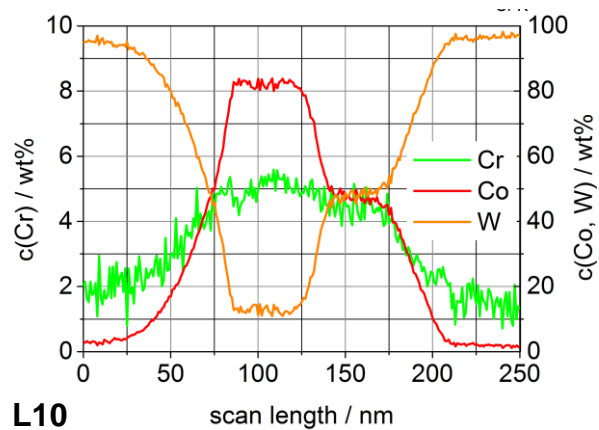
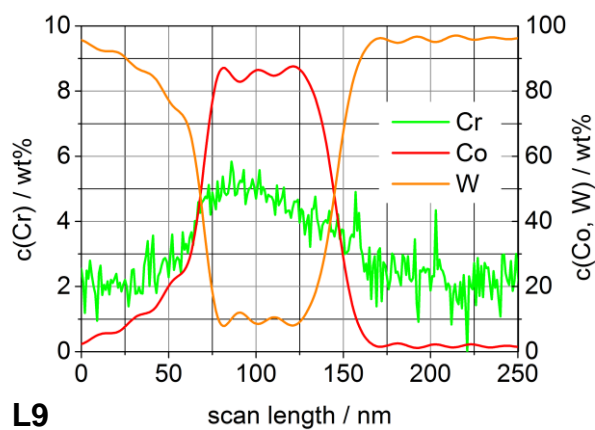
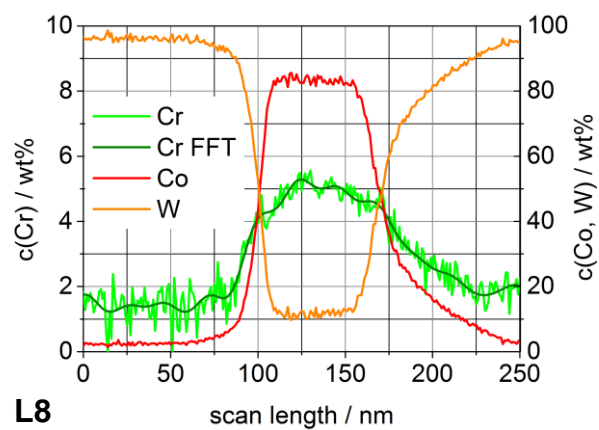
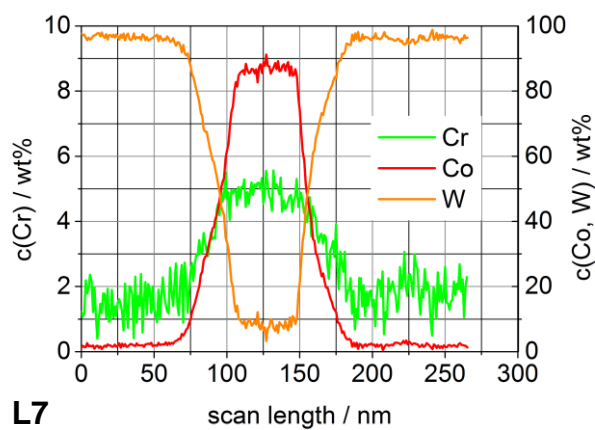


Figure 4-184: TEM-EDX line scans L7–L10 of sample CCoG115+. See Figure 4-182 for scan positions.

4.8.4 WC-Co-Cr₃C₂-VC, 1150°C

From sample CVCoG115 a TEM lamella was prepared 20 µm from the VC-Cr₃C₂-Co/WC-Co interface. The corresponding GGI concentrations are c(Cr)=0.82 wt% and c(V)=0.35 wt%. Due to a equipment failure no images were taken from this sample and a quantification of the results was not possible. Nevertheless, some information can be read from the three TEM-EDX line scans L1 – L3 in Figure 4-185. The units on the perpendicular axes refer to counts X-ray quanta. The absolute values are unrelated, hence no information on solubilities is available. The increase of the vanadium signal within the tungsten carbide as compared to cobalt binder phase derives from an overlap of the vanadium EDX-line with a tungsten line and does not refer to vanadium dissolved in WC. However, the relative trends provide some information. Scan L1 shows no enrichment of chromium or vanadium at the interface around 35 nm. The step size of this scan was 1 nm. In order to exclude the possibility that segregations may not be visible due to a too high step size the scans L2 and L3 were performed with a smaller step size of 0.1 nm. No chromium enrichment can be found in these scans as well. Vanadium, however, reveals a significant peak at the interfaces at 10 and 18 nm of samples L2 and L3, respectively. These peaks are not induced by an overlap with a tungsten line since the tungsten signal is decreasing while the vanadium signal increases. The results clearly indicate that vanadium forms a carbide layer or segregations at the WC/Co interface at 1150°C while chromium doesn't. From the fact that no chromium segregation was observed it can further be concluded that most probably the vanadium enrichment did not form by precipitation upon cooling, otherwise a chromium enrichment would as well be visible. It further means that the missing chromium signal is not caused by a too large step width or improper choice of the analysed interface. The results of the analyses are summarised in Table 4-41.

Table 4-41: Results of TEM-EDX line scans L1–L3 of sample CVCoG115+.

Scan	Length [nm]	Step width [nm]	Cr-Segregation	V-Segregation
L1	118	1	✗	✗
L2	31	0.1	✗	✓
L3	31	0.1	✗	✓

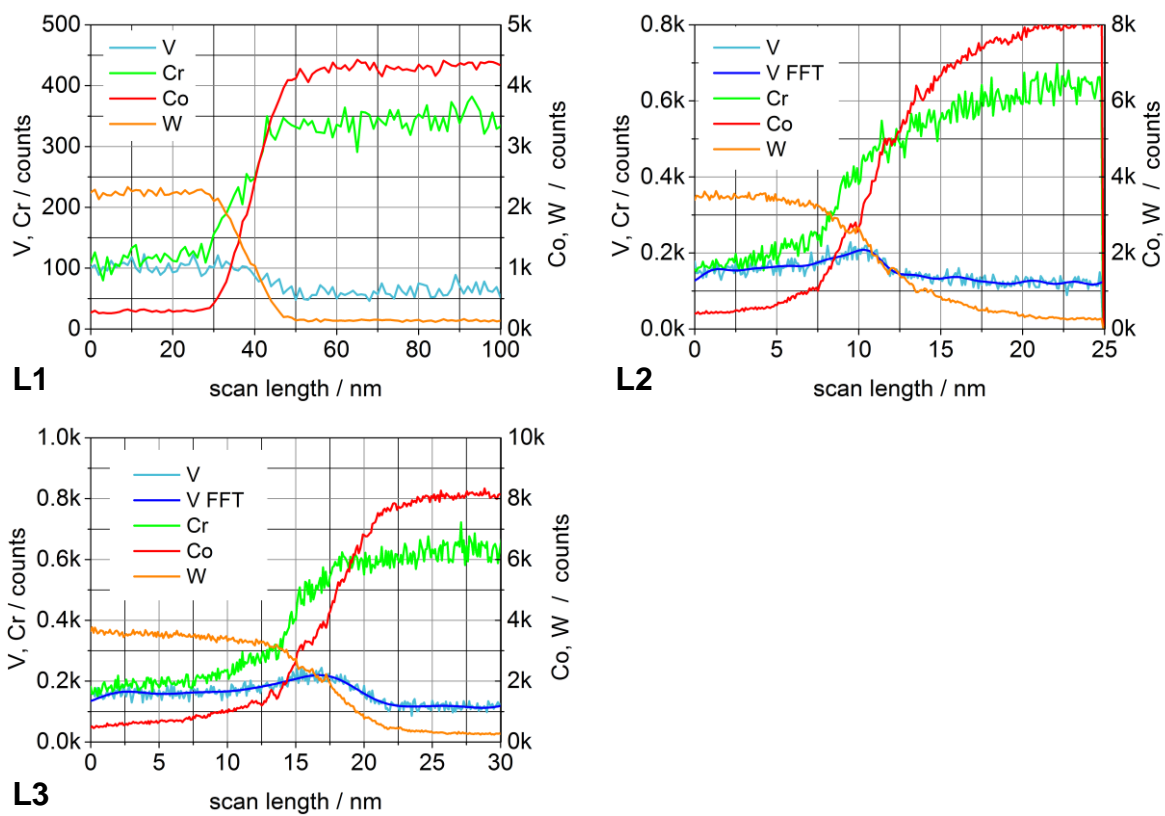


Figure 4-185: TEM-EDX line scans L1 – L3 of sample CVCoG115+.

5 Discussion

5.1 Thermal Analyses

5.1.1 Thermal analyses of the diffusion couple components

Thermal analysis of diffusion couple components was conducted in order to identify the temperatures of melt formation. The knowledge of these temperatures is of particular interest for investigation of diffusion couples since the diffusion is by two orders of magnitude faster in liquid phase as compared to solid state. Furthermore, by TG analyses information on the presence of oxides upon the diffusion experiments is accessible.

Most diffusion couples in this work were prepared with cobalt binder. The DSC data (left) and the corresponding TG data (right) of the WC-Co component WCo+, the Cr-based component CWCo+ and the V-based component VWCo+ upon the first heating cycle are shown in Figure 5-1(a). The high-carbon WC-Co sample WCo+ has a single peak at 1298°C which is in accordance to literature data (Table 2-3). In an undoped WC-Co system this temperature marks the lowest possible onset of liquid-phase formation. As shown in Table 4-30 all other diffusion couple parts with lower carbon potential have higher solidus temperatures. Regarding surface oxides it can be seen that all mass-loss events appear at $T < 950^\circ\text{C}$. Since the lowest test temperature for G-type diffusion couples was 1000°C no effect of WC or Co surface oxides on the GGI distribution is expected.

The chromium-based diffusion couple component CWCo+ of type GGI-WC-binder does not show a DSC-signal at all. In hardmetals with chromium saturated binder liquid-phase formation is expected in the range 1191–1280°C and should hence appear within the investigated temperature range. As can be seen from Table 2-4 cobalt has a certain solubility in chromium carbide. Subsequently no binder phase is available in the material at higher temperatures. This consideration is in accordance to the observation that the WC-Cr₃C₂-Co part of diffusion couples easily crack off close to the interface upon metallographic sample preparation. The absence of fcc binder phase leaves a porous, loose-sintered ceramic. However, the initial question was up to which temperature the binder in the WC-Co diffusion couple part remains fully solid. Though the WC-GGI-binder part shows no DSC signal the diffusion of

chromium into WC-binder lowers the solidus temperature. Close to the interface, the binder phase is supposed to be chromium saturated. Taking into account literature data (Table 2-3) liquid phase appears at 1191°C in a high-carbon, high-chromium hardmetal. This finding is supported by the DSC of sample WC-Co-20Cr, Figure 4-151. Subsequently, all samples prepared at $T < 1191^\circ\text{C}$ are supposed to have solid binder phase, assuming there are no binary non-equilibrium reactions.

For chromium-based diffusion couples at $T > 1191^\circ\text{C}$ the appearance of liquid phase cannot be clearly answered by means of thermal analysis. The equilibria depend on the local carbon potential and chromium concentration in the WC-Co diffusion couple part. It is discussed in section 5.5.2 that both locally change as a function of the distance from interface. Anyway, for all samples at temperatures $> 1191^\circ\text{C}$ partially liquid binder phase has to be taken into account.

Regarding an influence of surface oxides one can see a single mass loss event of sample CWCo+ setting off at $\sim 1050^\circ\text{C}$. No influence on G-type diffusion couples is hence expected. A number of M-type couples were prepared at lower temperatures of 950°C . Since they were pre-sintered all surface oxides were reduced prior to the experiment. However, before contacting the components were exposed to air. Hence, a certain amount of oxides at the interface is possible. However, the reduction peak is around 950°C , combined with long annealing time of 330 min no major influence of this oxides is assumed.

In the diffusion couples component CW424+ with Fe/Co/Ni binder alloy a small liquid-phase peak is observed, see green curve in Figure 5-1(b). Since cobalt [14KAP] and iron [98GEN] are soluble in chromium carbides the liquid phase signal is mainly caused by nickel. The onset of the liquid-phase formation appears at 1221°C . Since samples with Fe/Co/Ni binder were tested at a maximum temperature of 1150°C the binder is confirmed in solid-state. The degassing behaviour is identical to cobalt and sets off at $1000\text{--}1050^\circ\text{C}$.

Very similar findings apply for diffusion couples with Fe/Ni, see Figure 5-1(b). In contrast to cobalt-containing binder alloys a clear liquid-phase signal is observed with onset at 1241°C . Since the maximum testing temperature of Fe/Ni-based samples was 1150°C no liquid-phase is expected upon diffusion experiments. The degassing behaviour is equal to co and Fe/Co/Ni binder alloy, which can be read from a comparison in Figure 5-2(a). For all three samples only one broad peak is observed.

No binder-peak and WC-peak, which would be expected at 500–700°C and 750–850°C, respectively are observed. Due to their low content the CO forming upon their carbothermic reduction is re-uptake by chromium carbide due to an internal getter effect. This effect is confirmed and discussed in section 5.1.2.

The considerations above imply that significant reduction of the binder volume fraction occurs especially in chromium-based diffusion couples with cobalt. Since the cobalt content was chosen on order to achieve identical initial binder volume fractions, a binder concentration gradient forms upon the diffusion experiment. Such gradient may cause diffusion of cobalt from the WC-binder part towards the GGI-WC-binder part of the couple. Indeed the formation of such a concentration gradient in the WC-binder part was observed in a variety of diffusion couples with chromium as GGI. In the vanadium-based diffusion couple component VWCo the situation is more complex, see blue curve in Figure 5-1(a). Besides the liquid-phase formation peak at 1325°C a small, broad DSC signal from 1100–1200°C and a larger, narrow peak at 1201°C is observed. A similar behaviour is observed for Fe/Co/Ni binder (b) or Fe/Ni binder (c). The position of the liquid-phase peak is shifted to slightly higher temperatures of 1350°C and 1371°C for the Fe/Co/Ni and the Fe/Ni alloy, respectively. The alternative binder samples of M-, G- and H-type are all in solid binder state with maximum testing temperatures of 1150°C. Samples with cobalt binder are in liquid state in G-type samples annealed at 1360°C.

The two peaks at lower temperatures as well appear for all binder alloys. However, while the onset of the first peak shifts depending on the binder alloy in a similar order as the liquid-phase onsets, the peak at 1201°C is invariant for all three binders. Both peaks are only observed in the first heating cycle and disappear in later cycles. Thus, they are correlated to non-equilibrium events. The origin of the first signal can be clarified when comparing the DSC and the mass loss rate as shown in Figure 5-3(a) for Co, (b) for Fe/Co/Ni and (c) for Fe/Ni binder alloy. A clear correlation of the first, flat DSC signal (red) and a mass loss event (black) appears. This DSC peak is hence caused by endothermic reduction of oxides. The peak at 1201°C, however, cannot be explained by degassing and is hence dedicated to another endothermic reaction. In contrast to chromium-based diffusion couples the degassing shows a strong dependency on the binder alloy as illustrated in (b). The onset and the first degassing maximum are yet independent from the binder. However, the second maximum at

~1030°C is significantly stronger for the Fe/Ni alloy. Also the already mentioned small maximum at 1100–1200°C is somehow influenced by the binder alloy. This finding is however not of particular importance for diffusion couples, since the WC-VC-binder part should only provide a high carbon potential, which is after all the case when some traces of oxides are still present. The main degassing takes place below 1050°C and hence below the experimental temperatures. Nevertheless the dependency of vanadium-carbide degassing but the independency of chromium-carbide degassing from the presence of Fe, Co, and Ni is remarkable..

Summarising the considerations on the thermal behaviour of the diffusion couple components the following can be stated:

- Carbothermal reduction of oxides in WC-binder diffusion couple parts is finished below 950°C. No influence of oxides on GGI diffusion is hence expected.
- All H- and M-type samples are below solidus temperature.
- All diffusion couples based on alternative binder alloys are below solidus temperature.
- The chromium-based diffusion couple component CWCo+ shows no liquid – phase signal in DSC below 1400°C, whereas a small signal was found for Fe/Co/Ni and a larger one for Fe/Ni binder. The reason is an incorporation of Co and Fe in Cr-carbides.
- No evidence of an influence of surface oxides on diffusion couples at $T > 1050^\circ\text{C}$ was found in Cr-based samples.
- The degassing of chromium-based diffusion couples is independency from the binder alloy composition.
- VC-based diffusion couples show a late mass loss event at 1100–1200°C and hence in the range of diffusion couple testing.
- VC-based diffusion couple parts show a mass loss with constant rate at $T > 1000^\circ\text{C}$.
- The degassing of VC-based diffusion couples is influenced by the binder alloy composition.

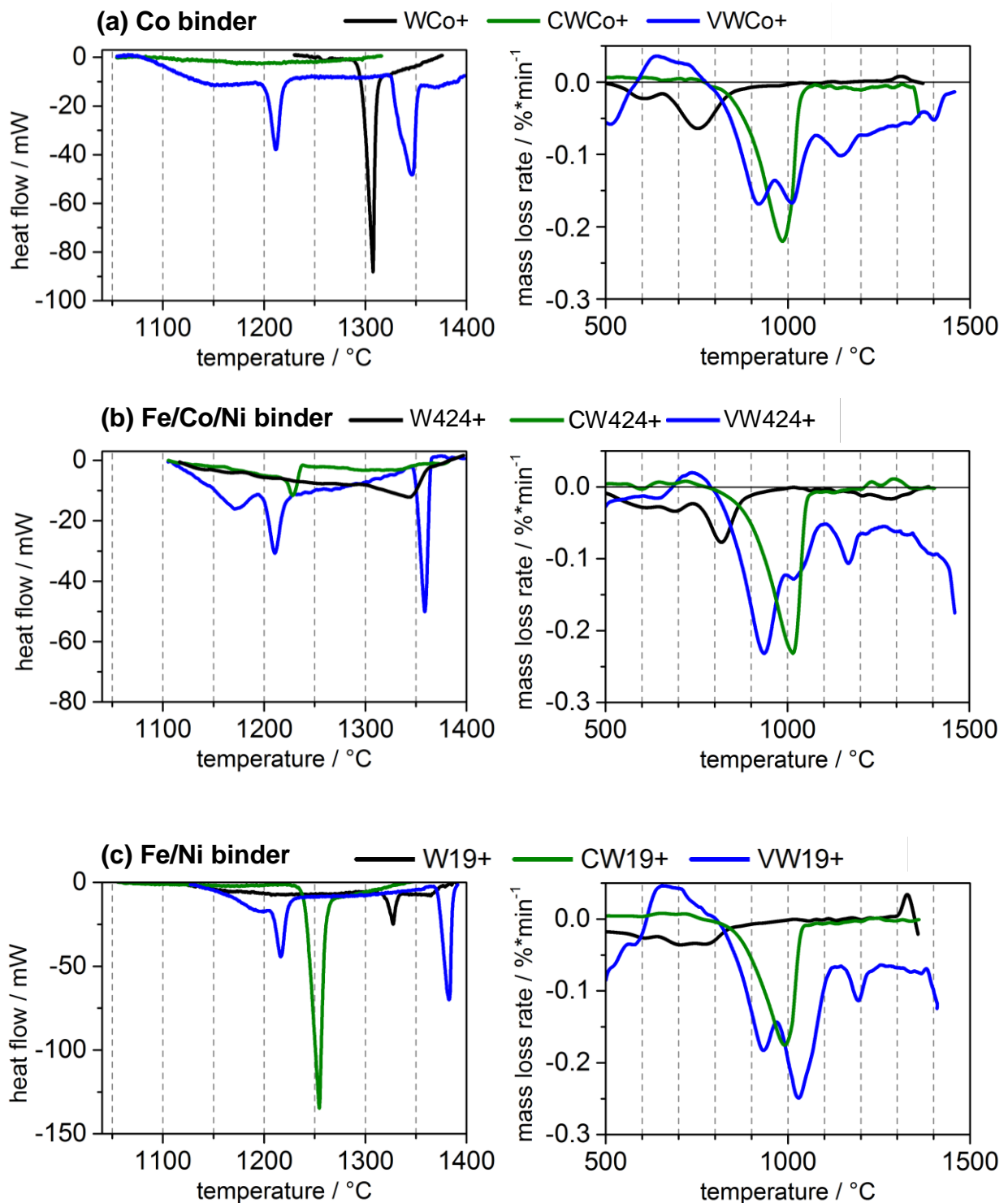


Figure 5-1: DSC (left column) and TG (right column) of diffusion couple components with (a) Co, (b) Fe/Co/Ni and (c) Fe/Ni binder. Black curves: WC-binder, green curves: Cr_3C_2 -WC-binder, blue curves: VC-WC-binder.

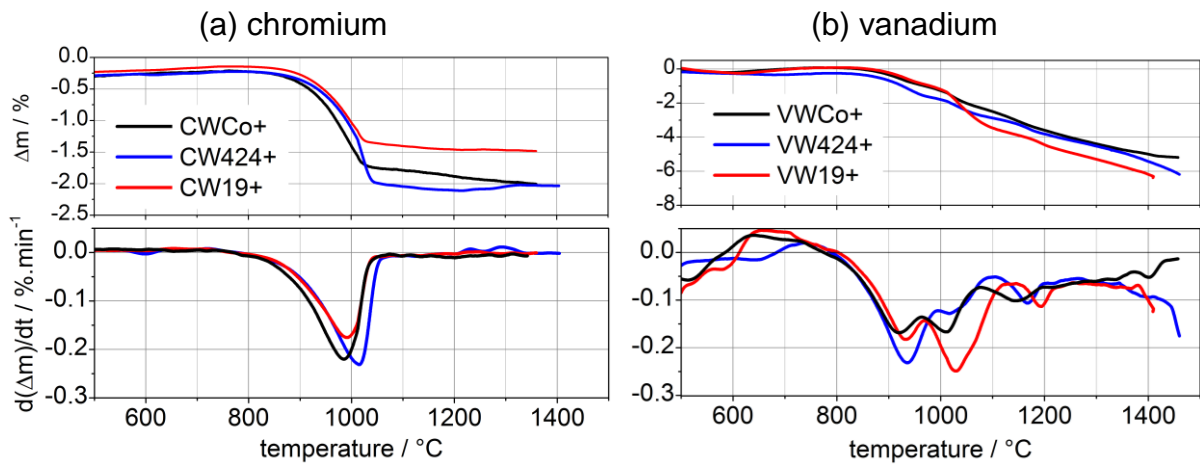


Figure 5-2: Comparison of the mass loss of (a) chromium and (b) vanadium based diffusion couple components with Co (black), Fe/Co/Ni (blue) and Fe/Ni (red) binder alloy.

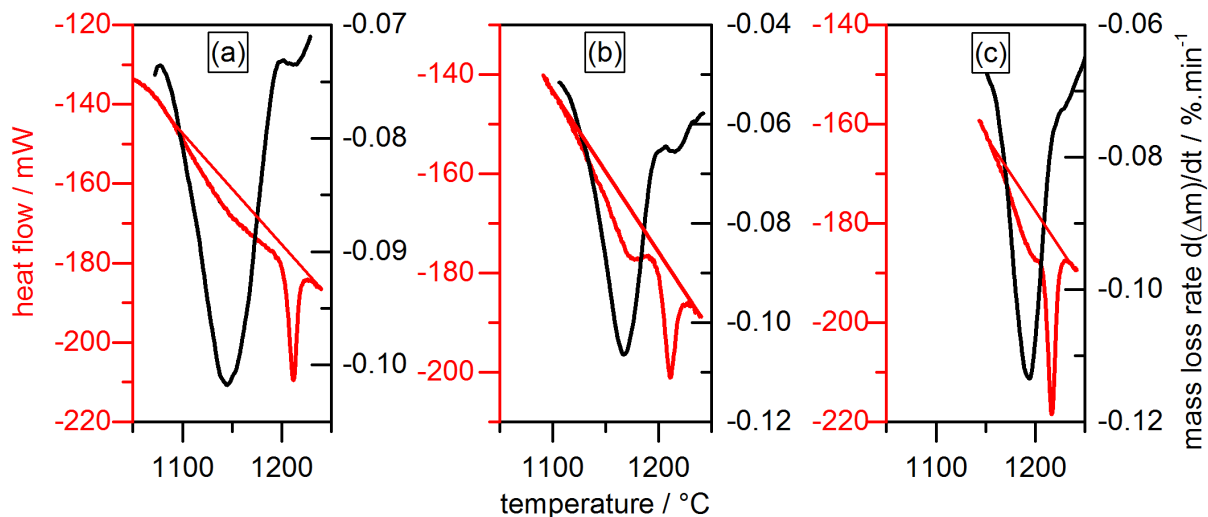


Figure 5-3: DSC signal (red curve) and corresponding TG signal (black curve) of the VC-WC-binder part of G-type couples with binder= (a) Co, (b) Fe/Co/Ni and (c) Fe/Ni.

5.1.2 Thermal reactions in chromium-doped hardmetals

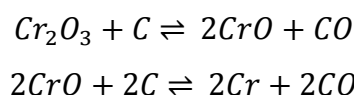
Upon sintering Cr-doped hardmetals a variety of thermochemical reactions such as phase transitions or carbothermal reductions appear. A series of WC-Cr₃C₂-Co hardmetal with varying Cr/W ratios was prepared in order to identify these reactions. A comparison of the DSC signals upon first heat-up is depicted in Figure 5-4(a) while (b) shows the mass loss rate. The DSC signals markedly depend on the Cr/W ratio. This is most likely due to a carbon potential shift. While the sample with Cr/W = 2/98 (black curve) shows a peak setting on at 1336°C the peak at Cr/W=20/80 (green

curve) appears at 1191°C. The first one fits the expectation for low carbon potential, the latter for high potential. The composition of sample 10/90 is in between them, as well as the DSC signal (green curve). However, two signals appear instead of one. A close look to the 20/80 sample however reveals as well a bimodal peak, just the height ratios are different. A comparison with the WC-Co-Cr phase diagram in Figure 2-14 shows that a melting range instead of an invariant equilibrium appears which explains the bimodal peaks. At Cr/W ratios of 50/50 and 100/0 no more liquid-phase signals are observed. The composition of the binder phase is hence no more comparable to a hardmetal, where liquid-phase should appear between 1191–1360°C.

In the tungsten-free Cr₃C₂-Co sample (CCo, 0/100) liquid-phase should appear by the eutectic reaction liquid → M₇C₃+fcc (M₃C₂ is not in equilibrium with fcc, see Figure 5-5) at around 1300°C [06STE, 14KAP1]. However, the particular composition, which is indicated by the blue dot in Figure 5-5, is located in the phase field M₇C₃+M₃C₂+C. All of these phases are in solid-state. However, carbon loss by carbothermal reduction causes an uncertainty of the sample composition which also makes the two-phase field M₇C₃+C possible. Kaplan [14KAP1] reported the invariant reaction Liquid+M₇C₃+M₃C₂+C appearing at 1506°C [14KAP1]. Experimental data by Köster et al. [55KÖS] reported the equilibrium by 100°C higher. However, the DSC experiment of sample CCo was repeated up to a maximum temperature of 1580°C. Indeed a signal was detected for this sample labelled CCo_insitu (Figure 4-135) at 1508°C which is in excellent accordance to the data of [14KAP1]. Since the sample WC-Co-50Cr shows as well no liquid-phase signal <1400°C it is to assume that cobalt is as well dissolved in the chromium carbide in presence of substantial amounts of WC. This finding is supported by the experimental observations that the WC-Cr₃C₂-Co parts of diffusion couples were extremely brittle after annealing and cracked off upon metallographic preparation. Furthermore, a comparison of the magnetic saturation of the samples WC-Co-2Cr – WC-Co-50Cr shows MS drop from 12.8 to 2.8 μTm³/kg from Cr/W=20/80 to Cr/W=50/50. However, it is surprising that the dissolution of cobalt in the chromium carbide is so fast that even upon the first heating cycle no non-equilibrium liquid-phase formation is observed.

Regarding mass loss the sample with lowest chromium concentration of $c(\text{Cr}/\text{W})=2/98$ (black) has a strong peak with maximum 880°C which is dedicated to WC reduction and a smaller one at 1050°C which is caused by chromium reduction. By increasing the chromium content to $10/90$ the WC peak height is significantly lowered and a bimodal signal with maxima at $980/1080^\circ\text{C}$ appears. By further increase to $20/80$ the WC peak disappears and a broad, single peak at 980°C forms, which is also found for $\text{Cr}/\text{W}=50/50$ and $0/100$. The reason for the absence of WC reduction signals at larger chromium concentrations is an “internal getter” effect. The CO formed by carbothermic reduction of WC-surface oxides has oxidising potential on chromium at temperatures below $\sim 1000^\circ\text{C}$. Hence the Cr_3C_2 is oxidised by the CO and no gross mass loss is observed. The signals at $1200\text{--}1250^\circ\text{C}$ are related to the liquid-phase formation.

In order to identify the reactions appearing upon heating chromium-doped hardmetals samples with varying chromium content were compared to a Cr_2O_3 doped hardmetal. The result is shown in Figure 5-6. The undoped sample (black) has a WC-reduction peak at $\sim 800^\circ\text{C}$. Addition of $0.9\text{ wt}\% \text{Cr}_2\text{O}_3$ (red) causes a slight shift of this peak. Besides WC reduction two strong peaks appear with maxima at 1010°C and 1150°C . An explanation of the bimodal peak can be either a two step reduction process or two different species of oxides such as surface and bulk oxides. The relative mass loss of the first peak between $860\text{--}1080^\circ\text{C}$ is 1.49% , the loss of the second peak is 2.97% which is a ratio of $1:2$. This ratio excludes the hypothesis of surface/bulk oxides since differently bonded surface oxides are only possible within the first atomic layers and are hence only a small fraction of the total oxides. The two step reduction is more likely since the ratio of $1:2$ almost exactly fits the reaction scheme



A comparison to the hardmetal doped with 1 wt% Cr_3C_2 (blue) shows that the Cr-related mass loss peak appears exactly at the position of the first Cr_2O_3 -reduction peak. However, the sample CWCo with 10 wt% WC and the WC-free sample CCo don't really match any of the chromium oxide reduction peaks. The presence of WC shifts the chromium reduction peak to higher temperatures. This effect gets stronger with increasing WC content as can also be seen from Figure 5-4(b). The reason might again be the internal getter effect. The CO formed by reduction of WC surface oxides fills the pores of the green body, which drastically increases the local CO potential. From the reaction equations above it can easily be seen that high CO potential shifts the chemical equilibrium to the oxide. Hence, the temperature required for the carbothermic reduction of chromium oxides increases with increasing CO potential. The more WC is present, the more CO is formed prior to chromium reduction, which explains the earlier reduction onset of the WC-free sample.

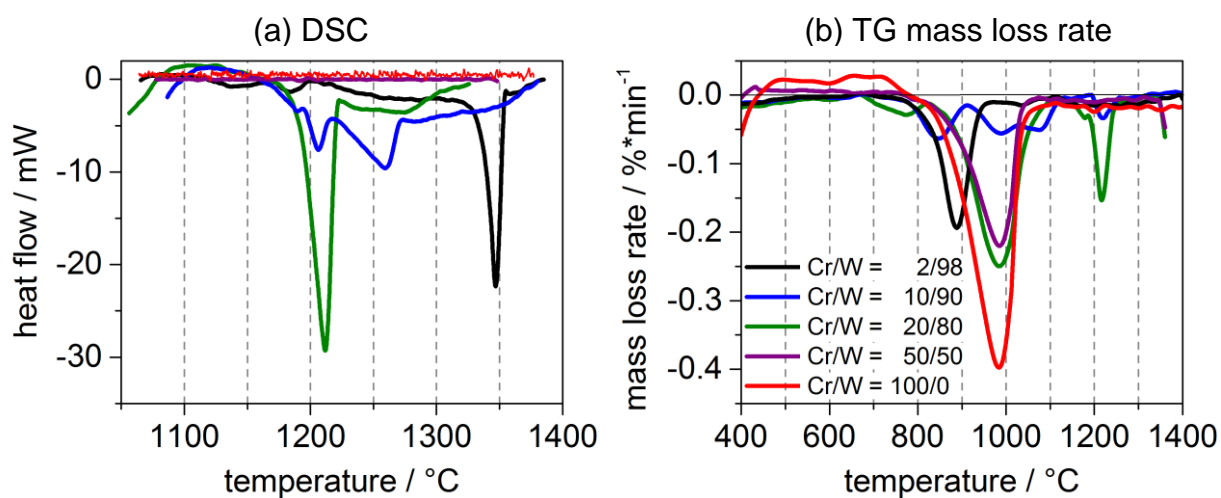


Figure 5-4: (a) DSC upon first heat up and (b) mass loss rate of WC-Cr₃C₂-Co samples with varying Cr/W atomic ratios; DSC curves are baseline-corrected.

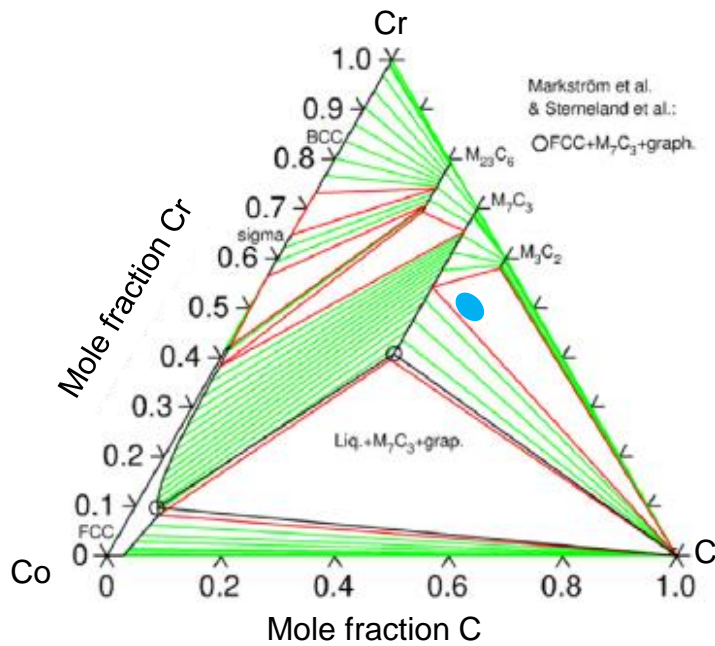


Figure 5-5: Position of sample CCo (Cr_3C_2 -20wt%Co) indicated by blue dot in the C-Co-Cr system (isothermal section at 1200°C). Phase diagram published by Kaplan et al. in Fig. 8 of ref. [14KAP1]. Area of dot indicates composition uncertainty by carbothermic carbon loss.

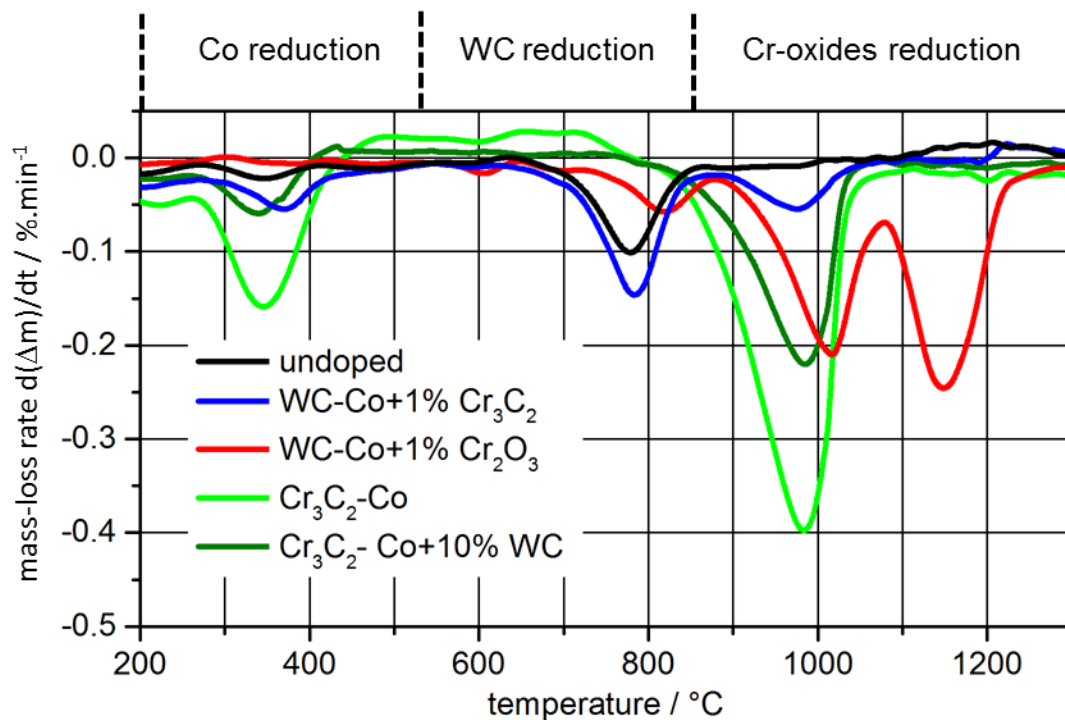


Figure 5-6: Mass loss rate of various samples of type WC- Cr_3C_2 -Co, WC- Cr_2O_3 -Co or Cr_2O_3 -Co.

5.1.3 Thermal reactions in vanadium-doped hardmetals

The DSC analysis of WC-VC-Co samples with varying atomic V/W ratio is shown in Figure 5-7(a). The W-free sample VCo (red curve) has a liquid-phase formation peak setting on at 1320°C. This is in accordance to the data published by He et al. [04He, 05HE]. The smaller peak at 1240°C could not be clarified, since it is also present in equilibrium upon the second heating cycle. According to the initial composition the sample is in the two phase area fcc+VC [05HE] and there is no equilibrium reaction at 1250°C. Even a shift in carbon would just cause the additional appearance of graphite or V₂C which would not explain the phenomenon either. The reason for the signal thus remains unclear. Anyway, this diffusion couple component was only used for some very first samples, the majority of diffusion couples was produced from the component VWC_{o+}, the effect is hence not further discussed.

The sample WC-Co-2V with V/W=2/98 (black) shows a single peak with onset 1320°C dedicated to liquid-phase formation. This temperature fits to the equilibrium at low carbon potential. The sample was intended to have high carbon potential. Carbon loss by CO formation seemed to cause a strong C shift in this sample. By increasing the V/W ratio to 10/90 (blue) or 20/80 (green) two almost identical curves with a broad signal at 1050–1150°C and a sharp signal at 1260°C were measured. The small signal is related to a mass loss event as can be seen from Figure 5-7(b). This mass loss peak grows stronger with increasing vanadium content while the WC surface oxides reduction peak at ~800°C decreases by the same ratio. The DSC peaks at 1260°C fit to liquid-phase formation at high carbon potential (compare Table 2-3).

By further vanadium-ratio increase to V/W=50/50 at% both TG and DSC show a markedly change in shape. The DSC reveals a broad peak at 1150–1250°C which is not present at lower V/W ratios. By comparison to TG the signal can be dedicated to a strong mass loss event with maximum at 1200°C. Small TG signals at this temperature were as well observed for samples with lower V/W ratio, but their heat tone was likely below the DSC detection limit. The liquid-phase signal of V/W=50/50 appears at 1340°C and the peak is similar to the low-carbon sample V/W=2/98. However, it is dissonant that an increase of VC content first shifts the C potential to high at VW=10/90 and 20/80 and then back to low at 50/50. Also, 1340°C is actually 20°C above the equilibrium of a vanadium-saturated low-carbon alloy. It can be

assumed that at this composition, an equilibrium different to $\text{Liq.}+\text{fcc}+\text{WC}+\text{MC}+\text{eta}$ appears. A possible explanation is the formation of $(\text{W},\text{V})\text{C}$. The position of the samples with varying V/W ratio in Figure 5-7 within the system $\text{W}-\text{V}-\text{C}$ as published by Obbard et al. [01OBB] is shown in Figure 5-8. The colours of the dots correspond to the colours of the key in Figure 5-7. It can be seen that the samples with $\text{V}/\text{W}=2/98$, $10/90$ and $20/80$ are in the two phase area $\text{WC}+(\text{W},\text{V})\text{C}$ while $50/50$ is at the border to the single phase field $(\text{W},\text{V})\text{C}$. Thus, this peak is most likely caused by reduction of surface oxides on $(\text{W},\text{V})\text{C}$ which formed upon heat-up. However, in the analysed sample Co is present additionally to W, V and C which changes the phase relations. Nevertheless in the W-free sample with $\text{V}/\text{W}=100/0$ (VCo , red) this peak is not observable. It is also not observed in a V-free WC-Co sample. Hence, the mass loss at 1200°C has been caused by a reaction product of W, V, C and Co. Since according to [01OBB] the sample $\text{V}/\text{W}=50/50$ with $\text{C}/(\text{W}+\text{V})=0.9$ is in the phase field $\text{fcc}+\text{WC}+(\text{W},\text{V})\text{C}+\text{C}$ a $(\text{W},\text{V})\text{C}$ related reaction is a likely explanation.

This finding basically meets considerations of Wang, Webb and Bitler [14WAN, 15WAN]. They claimed the reduction of VC happens by a preliminary formation of (W,V) -oxides and subsequent CO_2 evolution by carbothermic reduction of the latter. They found one vanadium related peak at $1000\text{--}1100^\circ\text{C}$ (see Figure 2-11 in literature section) which they dedicate to $(\text{W},\text{V})\text{C}$. However, first of all CO_2 hardly forms at these temperatures due to the Boudouard equilibrium, one would rather expect CO – but this might be attributed to their experimental setup (measurement at lower temperatures). Secondly, their argumentation is based on the consideration that according to an Ellingham diagram V_2O_3 requires temperatures of 1500°C to be carbothermally reduced. But on the one hand the reduction temperature depends on the particular CO partial pressure and on the other hand vanadium is dissolved in the binder of a hardmetal system which provides an additional driving force for the reduction. Their argument is hence not totally consistent. Furthermore, the peak temperature of $1000\text{--}1100^\circ\text{C}$ they found is significantly lower than the temperature claimed for (W,V) -oxide reduction in this work. However, the latter was found in hardmetals with high V/W ratio while [15WAN] investigated hardmetals with low VC additions which may possibly explain the difference.

In order to answer this question hardmetals doped with 0.6 wt% of VC (HM_VC) or V_2O_5 ($\text{HM_V}_2\text{O}_5$) were compared to an undoped sample (WCo+) and a W-free

VC-Co sample (VCo) as depicted in Figure 5-9. A comparison of the VC-doped (blue) and the undoped sample (black) shows identical WC reduction at $\sim 780^\circ\text{C}$ and an additional peak at $1000\text{--}1050^\circ\text{C}$ which can be related to a vanadium-specific effect. This finding is so far coincident to Wang et al. A comparison to the V_2O_5 -doped grade (red) shows a shift of WC surface-oxide reduction to higher temperatures. A second peak with maximum at 1000°C is observed, which exactly fits the signal of the VC-doped grade. Also, the W-free sample VCo (light green) shows a peak at this position. The correlation of the peak position of a VC-doped at $\sim 1000^\circ\text{C}$ sample to a V_2O_5 -doped and a W-free VC-Co sample is a strong indication that $(\text{W},\text{V})\text{C}$ does not play a significant role in the degassing behaviour and no intermediate $(\text{W},\text{V})_x\text{O}_y$ is formed. To proof this consideration the samples in Figure 5-9 are compared to VC-Co with 10 wt% WC addition (dark green, VWCo). Until a temperature of 1100°C the curve almost exactly matches the one of the W-free sample. This would not be the case if $(\text{W},\text{V})_x\text{O}_y$ degassed at 1000°C . However, at $1100\text{--}1200^\circ\text{C}$ again a peak appears which is not found in the W-free sample and also the V-free sample and is hence formed by interaction of W and V (as already concluded from Figure 5-7. This peak is then most likely dedicated to $(\text{W},\text{V})\text{C}$, but does only appear at high V/W ratios and is not found in hardmetals with usual small VC contents.

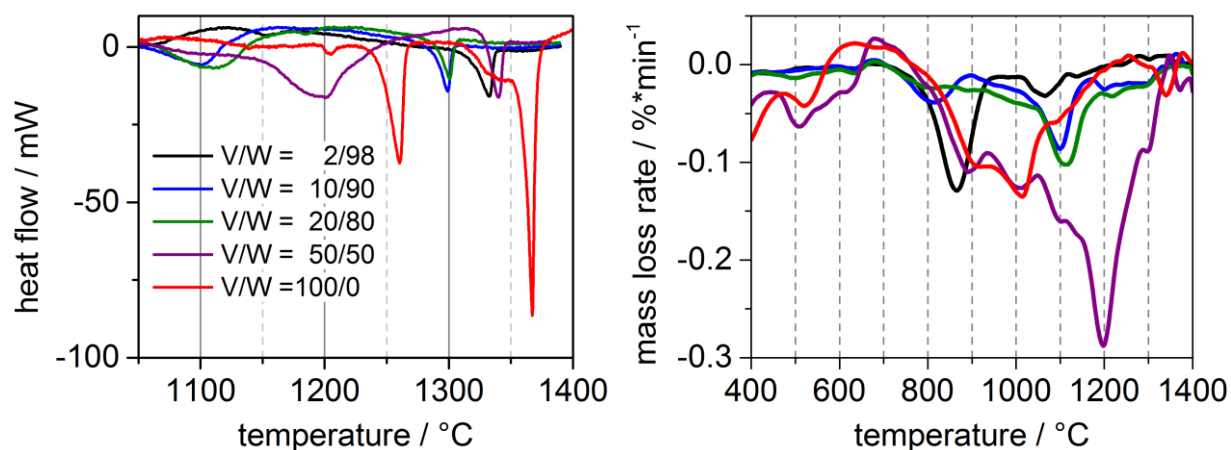


Figure 5-7: DSC (a) and TG (b) of WC-VC-Co samples with varying V/W atomic ratios.

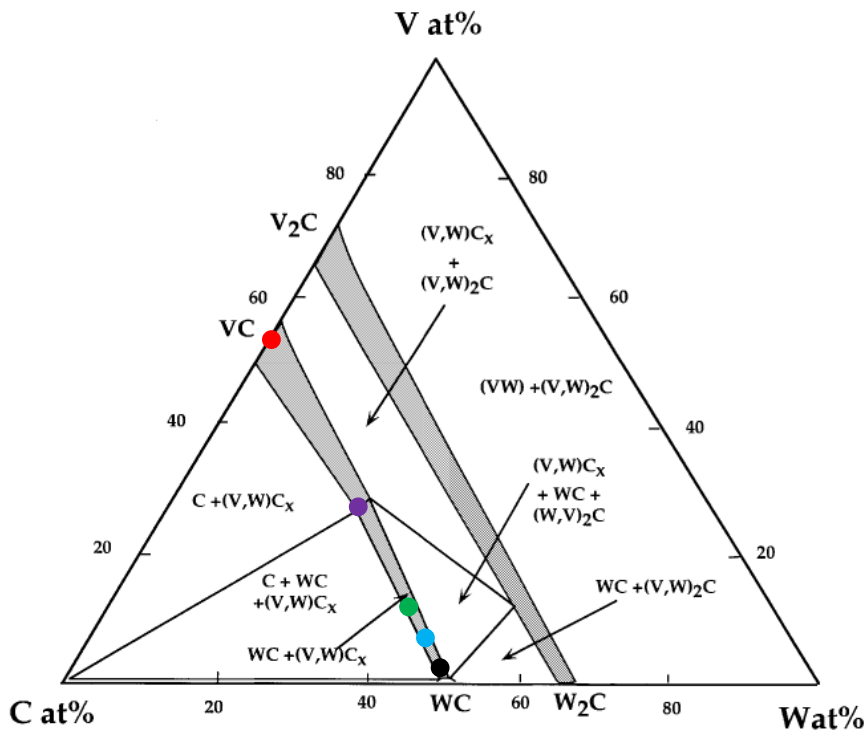


Figure 5-8: Position of hardmetal samples with varying V/W ratio in an isothermal section of the system W-V-C as published by [01OBB]. Refer to Figure 5-7 for colour key.

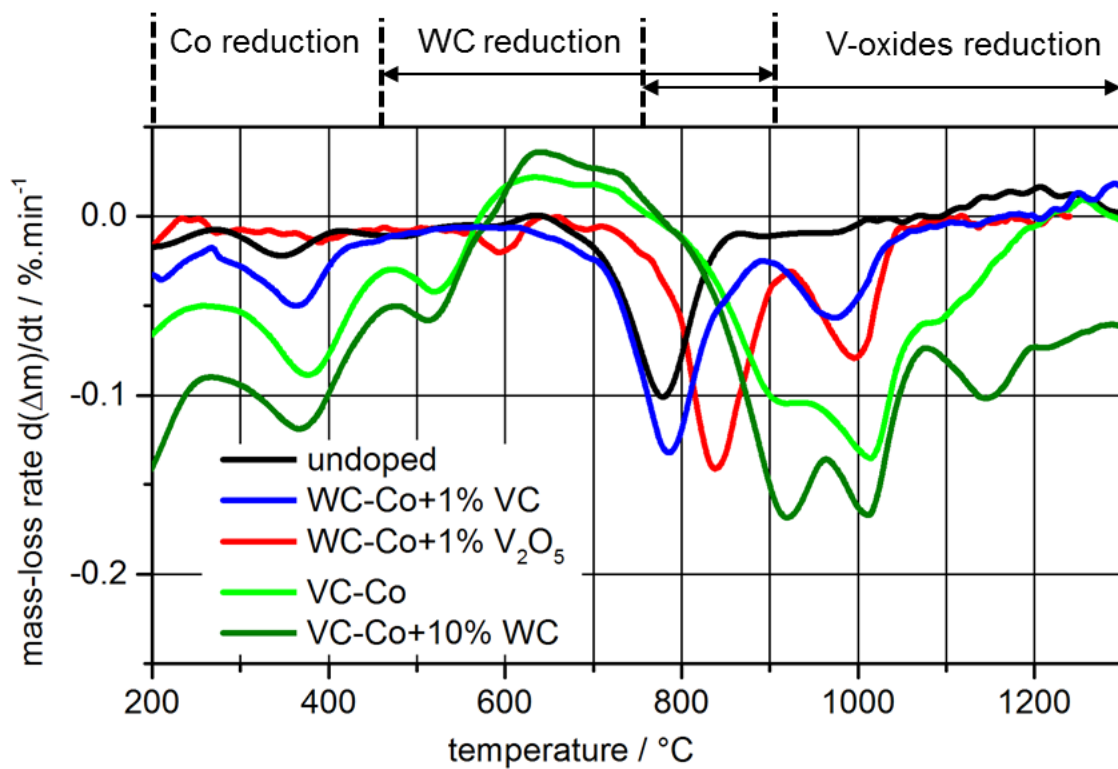


Figure 5-9: TG signals of various VC-Co, WC-VC-Co and WC-V₂O₅-Co samples.

5.2 Activation Energy

The activation energy of chromium and vanadium transport was determined from G- and M-type diffusion couples by Arrhenius plots of the transport factors. The results are listed in Table 5-1. The particular Arrhenius plots can be found in the appendix section 8.2.

It was already mentioned in section 4.1 that GGIs are not only distributed by diffusion but also spread by the migration of cobalt binder driven by wetting the WC grains. Also a variety of kinetic factors such as particle rearrangement or densification can influence the transport factors. Furthermore, the distribution and the mean free path of cobalt, and hence the main diffusion path, change as a function of temperature. The activation energies in G-type couples thus map the summarised influence of these factors and cannot be clearly dedicated to diffusion of GGIs.

The values for G-type samples are visualised in Figure 5-10. The green columns represent chromium, the blue columns vanadium. The activation energy of chromium transport is 350 kJ/mol in the +eta sample, 298 kJ/mol in the two phase sample and drops to 276 kJ/mol for high carbon potential. This is a clear trend to lower values with increasing carbon potential. The reason might be the reduced tungsten solubility in high carbon alloys. However, no such trend was found for vanadium, the values remain constant at 300–330 kJ/mol and are equal within the error range independently from the carbon potential. Furthermore, the differences in tungsten solubility as a function of the C-potential are even more promoted in Cr-doped than in V-doped hardmetals, see Table 2-4. Subsequently the different carbon dependency of chromium and vanadium transport activation is likely not caused by differences in the W concentration. It is discussed in section 5.5.2 that the carbon potential has a complex influence on the activation energies which are determined from the diffusion-couple setup used in this work.

In the sample series CVCoG both chromium and vanadium were transported simultaneously. The activation energy of 283 kJ/mol and 289 kJ/mol, respectively are identical and comparable to the values of particular samples within the 2-phase area. Since matrix effects are eliminated in this sample it can be concluded that chromium and vanadium have either almost equal activation energies for diffusion or the

activation energy is controlled by a different transport mechanism. The transport mechanisms are further discussed in 5.6.

No activation energy can be determined from samples prepared with nano-cobalt since the data does not reveal a linear relationship, see e.g. Figure 5-20(b).

Anyway, it has to be noted that the values for activation energies are not a measure for bulk diffusion in the fcc-cobalt matrix. It is discussed in detail in section 5.6 that it represents a combined measure of diffusion convolved with microstructural developments such as densification, cobalt wetting on WC and temperature dependent solubilities of matrix elements. The combination of these effects causes steeper slopes and subsequently higher values for the activation energy. This consideration is supported by the unexpectedly high pre-exponential factors as shown in Table 5-1.

In M-type samples the GGIs are transported in a fully dense, equilibrated binder phase. In contrast to G-type couples no kinetic effects such as densification or cobalt migration appear, the transport factor in this case is a real diffusion coefficient. The carbon potential for all M-type samples is fixed in the carbon-rich +C phase field.

The activation energy is around 300 ± 20 kJ/mol for all sample series, independent from the GGI or the binder alloy. This value is in good accordance to the activation energy of 282 kJ/mol for W diffusion in cobalt binder [90CER]. It will be further discussed in section 5.3 that W diffusion is rate-limiting for GGI diffusion in M-type diffusion couples.

Above findings can be summarised as follows:

- A significant effect of the carbon potential on chromium was found, decreasing from 350 kJ/mol at low carbon potential to 250 kJ/mol at high potential.
- No influence of the carbon potential on activation energy for vanadium transport was observed. The values were found around $E_a(V) = 300$ kJ/mol.
- In samples with Cr+V co-diffusion the activation energies of 280–290 kJ/mol are equal within the error range for both chromium and vanadium.
- The activation energies in G-type couples do not refer to pure diffusion but are a measure of the convolved effects of diffusion and microstructural developments as a function of temperature.

Table 5-1: Activation energies E_a and pre-exponential factors D_0 of Cr of V transport in G- and M-type diffusion couples; n.a.: no value available since no linear fit is applicable to the data.

Sample	GGI	Binder	Carbon	E_a^*	$\ln(D_0)$
				kJ/mol	$\ln(\text{cm}^2/\text{s})$
G-type					
CCoG-	Cr	Co	low (+ η)	349 ± 14	11.8 ± 1.20
CCoG	Cr	Co	2 phase	298 ± 20	7.76 ± 1.76
CCoG+	Cr	Co	high (+C)	276 ± 4	4.02 ± 0.33
VCoG-	V	Co	low (+ η)	332 ± 16	8.28 ± 1.30
VCoG	V	Co	2 phase	295 ± 25	5.24 ± 2.10
VCoG+	V	Co	high (+C)	342 ± 16	8.32 ± 0.71
CVCoG (Cr)	Cr	Co	2 phase	290 ± 20	n.a.
CVCoG (V)	V	Co	2 phase	296 ± 24	n.a.
M-type					
CCoM+	Cr	Co	high (+C)	290 ± 5	4.37 ± 0.39
VCoM+	V	Co	high (+C)	$314 \pm \text{n.a.}$	$4.90 \pm \text{n.a.}$
C424+	Cr	Fe/Co/Ni	high (+C)	300 ± 24	6.69 ± 3.35
V424+	V	Fe/Co/Ni	high (+C)	$292 \pm \text{n.a.}$	$4.39 \pm \text{n.a.}$
C19+	Cr	Fe/Ni	high (+C)	283 ± 17	3.56 ± 1.34

*The activation energies differ from those published in [13BUC, 14BUC]. The reason is these data were obtained from normalised concentration profiles, while those in [13BUC, 14BUC] were determined from as-measured profiles. Also some of them were re-measured or additional samples were added to the datasets.

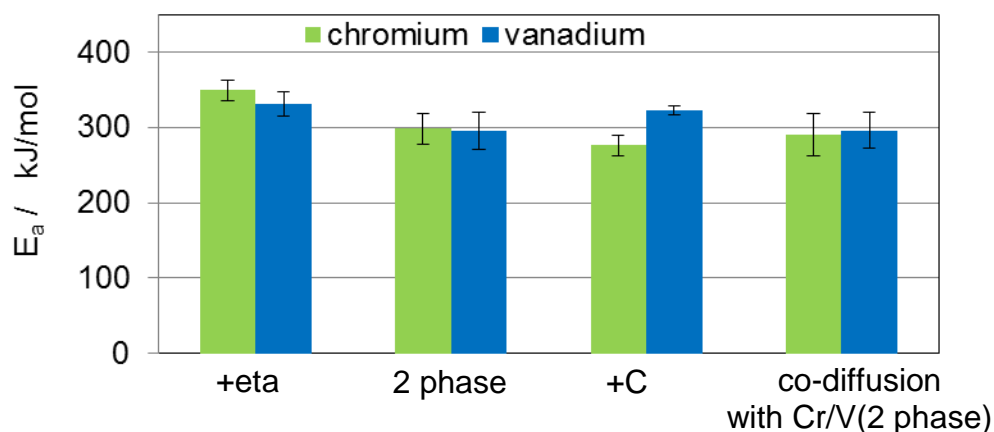


Figure 5-10: Comparison of activation energies of Cr (green bars) of V (blue bars) diffusion in G-type diffusion couples. Error bars represent the weighted error of the Arrhenius fit to the data points.

5.3 Diffusion in hardmetal binder phase (M-type)

Diffusion data of chromium and vanadium in equilibrated hardmetal binder phases was determined from model alloys with high carbon potential. Such alloys have a high volume fraction of binder phase but WC and carbon precipitates are still present. The binder phase is thus saturated with tungsten and carbon. A detailed description of the particular samples is given in section 4.4.

Arrhenius-plots of the samples with Co, Fe/Ni and Fe/Co/Ni binder are shown in Figure 5-11(a) for chromium and (b) for vanadium. The dataset for vanadium in Fe/Ni binder is missing since no experimental data was measured. No significant differences were found, the regression lines are de facto congruent. The activation energies of ~300 kJ/mol, which are proportional to the slope of the plots, are equal within the error range for both chromium and vanadium in all binder systems (compare Table 5-1). A direct comparison of the transport factors at (a) 950°C and (b) 1150°C is shown in

Figure 5-12. For vanadium in Fe/Ni binder at 950°C and chromium in cobalt binder at 1150°C no experimental data is available. The corresponding values, highlighted by an asterisk, were extrapolated from the Arrhenius fits. At both temperatures vanadium transport seems to be slightly slower, but all differences are statistically insignificant within overlapping error ranges.

This overall independency of both chromium and vanadium transport from the binder alloy composition or the GGI at any temperature seems unlikely. Indeed, in G-type couples chromium transport is significantly faster than vanadium transport (compare section 5.6). In these samples at least a slight influence of the binder alloy composition was found (compare section 5.5.4). Thus, it has to be assumed that the GGI transport is not controlled by GGI diffusion but rather limited by an additional mechanism. An influence of the dissolution kinetics is unlikely since GGIs are already dissolved in GGI-WC-binder part of the M-type diffusion couples. However, the WC-binder part of the samples is saturated with both W and C prior to the diffusion experiment. It is known that the addition of GGIs decreases the W solubility (refer to Table 2-4). Once GGI diffusion initiates, the WC-binder part is hence not in equilibrium state any more but supersaturated with tungsten. Subsequently the W-content has to be reduced simultaneously to the transport of GGIs into the WC-binder part. W diffusion may become rate controlling in such a case.

Indeed three findings support this theory. First, the activation energy of 300 ± 20 kJ/mol is in the range of W diffusion in Co (282 kJ/mol [90CER]). Second, the interface solubilities found for M-type samples are by a factor of 5–10 lower than the values estimated from literature (compare Table 2-4). This phenomenon can also occur due to an insufficient interface contact. However the diffusion couples parts were pressed together upon the diffusion experiments and a tight contact was ensured. Also such an experimental failure would not yield such a remarkable accordance as shown in Figure 4-5. Thus, the supersaturation of the binder with tungsten limits the GGI uptake. Third, a depletion of the W concentration towards the interface was observed. Figure 5-13 shows the tungsten- (top) and chromium- (bottom) concentration profiles at 950, 1050 and 1150°C. 20 μ m from the interface chromium concentration drops below the detection limit and the W concentration is around 8.5 wt%. At lower distances, and hence higher chromium contents, the tungsten concentration decreases at temperatures of 1150 and 1050°C. But at 950°C the concentration profile is almost constant. Furthermore at 1050°C a stronger gradient is formed. On a first glance this may not look like a specific trend, but it has to be considered that two contrary mechanisms influence the W diffusion. On the one hand diffusion is faster at higher temperatures and stronger gradients should form. On the other hand the solubility of W increases at higher temperatures which causes weaker gradients. The shape of the gradients may also be influenced by the fact that W has to be deposited somewhere if its content is decreased in the binder alloy. Since no nucleation of WC was observed within the binder areas the deposit may either appear at an existing WC grain in the WC-binder part or at carbide grains at the WC-GGI-binder/WC-binder interface. The distance to such grains differs from sample to sample which may influence the W diffusion.

These three findings of equal activation energies, decrease of the GGI solubility and formation of W-gradients indicate the limitation of the GG transport by W diffusion. Subsequently the information obtained from M-type couples does not provide information on specific differences of chromium and vanadium diffusion in hardmetal binder alloys in equilibrium state.

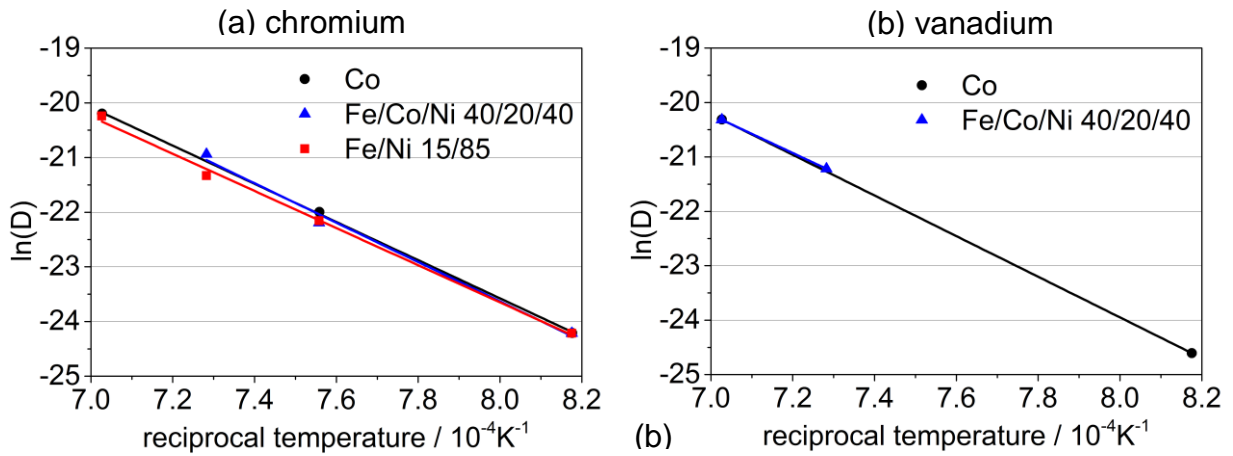


Figure 5-11: Arrhenius plots of transport factors of (a) chromium and (b) vanadium determined from M-type diffusion couples with cobalt, Fe/Co/Ni and Fe/Ni binder alloys, respectively.

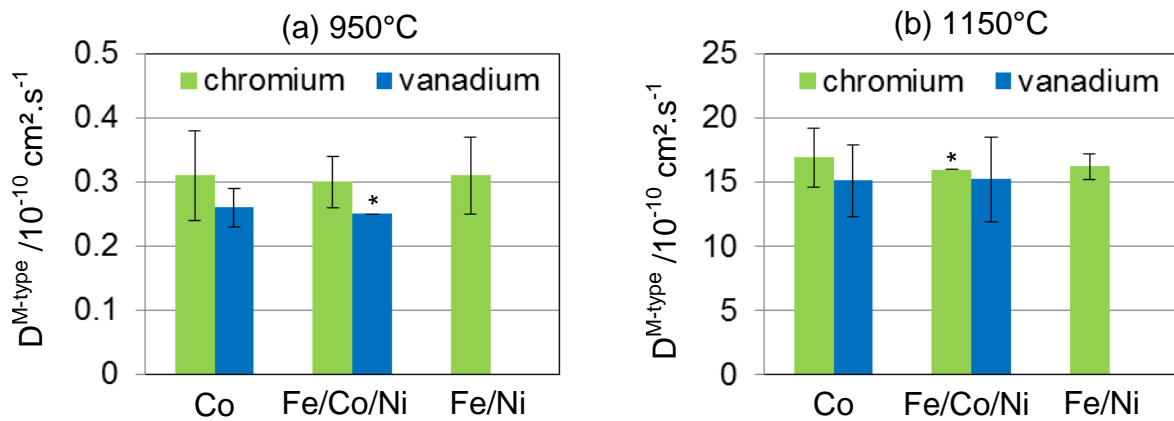


Figure 5-12: Transport factors of chromium (green columns) and vanadium (blue columns) in M-type sample at (a) 950°C and (b) 1150°C in different binder alloys
 * no experimental data available; extrapolated from Arrhenius plots.

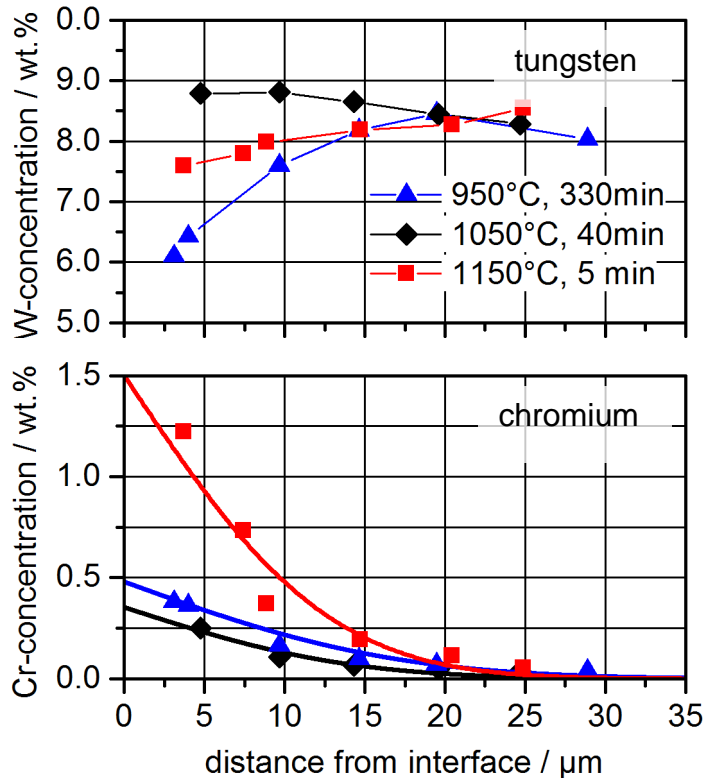


Figure 5-13: Tungsten (top) and chromium (bottom) concentration in M-type samples with cobalt binder at various temperatures.

5.4 Diffusion in sintered hardmetals (H-type)

H-type couples with high carbon potential (C-precipitations) were designed in order to gain insight to the GGI distribution in sintered hardmetals. All samples of this series were prepared at 1150°C for 5 min. The comparison to G-type couples and M-type couples was supposed to enlighten the GGI transport mechanisms upon sintering hardmetals.

In the WC-binder part of H-type couples the binder phase is saturated with tungsten and carbon. Hence, the same consequences as they were already discussed for M-type samples (section 5.3) apply: the diffusion of GGIs into the WC-binder part requires a simultaneous reduction of the W concentration in the binder phase. However, the binder mean free-path in hardmetals is $<1 \mu\text{m}$. A reduction of WC concentration by segregation on WC grains should thus be faster as compared to M-type samples. Indeed, as it will be discussed below the interface concentrations in H-

type samples are in the range of the solubilities reported in literature. Thus, the W diffusion plays a less dominant role in H- as compared to M-type samples.

Generally the diffusion depth of GGIs in all H-type samples is short around 20 μm . Since the samples were designed based on the results obtained from G-type couples the transport factors were expected to be by a factor of 10 higher and the diffusion depth subsequently by a factor of 3.2 higher. As a consequence only 3–4 data points were available for fitting the diffusion model. From such few data points and two parameters in the fitting model only one or two degrees of freedom remain for fitting. Also, a small change in the position of a particular data point causes a large error of the calculated transport factors. The latter hence possess a high uncertainty and can only be considered as a semi-quantitative estimation. Nevertheless, they can be used for a comparison with other types of diffusion couples. However, the transport factor of $D_V=2 \cdot 10^{-9} \text{ cm}^2/\text{s}$ is in good accordance to $D_V=1-2 \cdot 10^{-9} \text{ cm}^2/\text{s}$ estimated from literature data for a V_8C_7/Co diffusion couple [07HE].

In contrast to M-type couples a slight effect of the binder alloy on the GGI transport was found as shown in Figure 5-14 (a) for vanadium and (b) for chromium. In both cases the GGI transport in hardmetals with cobalt binder is significantly faster as compared to the alternative binder samples.

Regarding the interface concentrations literature data is only available for cobalt binder. For other binder alloys it can be assumed that the solubilities are at least within the same concentration range. The interface concentration of chromium in the sample with cobalt binder is $c_0(\text{Cr}/\text{Co})=0.61 \pm 0.014$, which is in good agreement to $c(\text{Cr}/\text{Co})=0.72$ estimated from literature (Table 2-4).

In samples with Fe/Co/Ni binder however, the interface concentration of $c(\text{V}/\text{Co})=0.033 \pm 0.008$ is by almost a factor three higher than $c(\text{V}/\text{Co})=0.012$ estimated from literature. Oversaturation of the binder phase can be ruled out by experimental setup. The WC-binder part of the diffusion couple was free of vanadium prior to the experiment. Thus by diffusion no concentration higher than the solubility can be achieved. Also, if it were caused by the experimental setup it should have been observed for chromium as well. From these considerations it can be assumed that a part of vanadium is not located in the binder phase. From TEM scans in samples annealed at 1150°C (section 4.8.2) and from literature (section 2.3.1) it is known that (W,V)C segregates at the WC/Co interfaces and in the vicinity of

WC/WC/Co triple-points. It can be assumed that the high vanadium concentrations are likely caused by such (W,V)C precipitates within the hardmetal.

For each binder phase the transport factors of chromium and vanadium are equal within the error range as illustrated in Figure 5-15. It can as well be seen that in nitrogen atmosphere D in hardmetals with Fe/Co/Ni binder is by 20% higher.

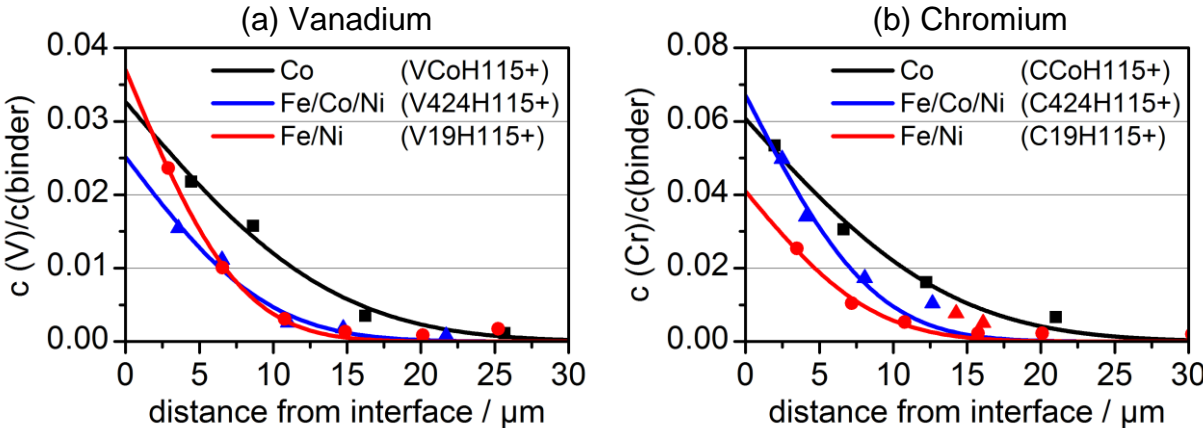


Figure 5-14: Concentration profiles of (a) vanadium and (b) chromium in H-type diffusion couples with different binder alloys after annealing 5 min at 1150°C .

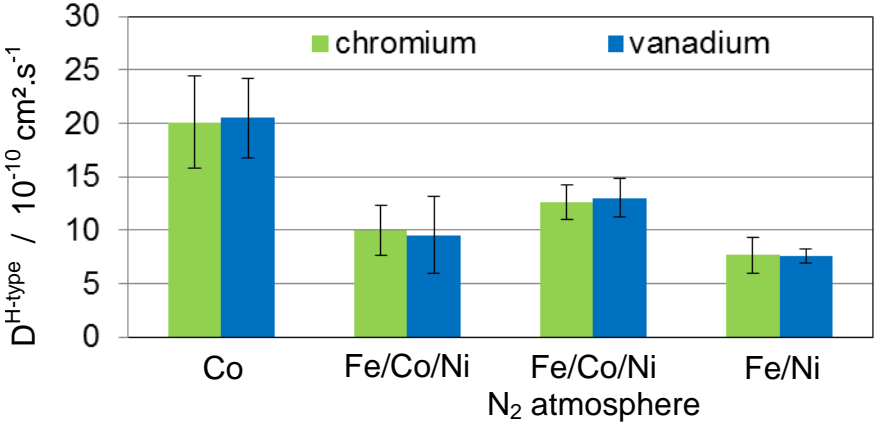


Figure 5-15: Transport factors in H-type samples with different binder alloys.

5.5 Diffusion in hardmetal green bodies (G-type)

The GGI transport in hardmetal green bodies is of great relevance for sintering ultrafine grained hardmetals. Thus, detailed investigations on a variety of parameters with possible influences on the GGI distributions were conducted. These parameters are discussed in the sections below.

5.5.1 Annealing time

The development of the GGI concentration profiles in G-type diffusion couples as a function of the annealing time was studied for both GGI=Cr and V at a temperature of 1150°C.

For chromium four annealing times of 5, 15, 30 and 60 min were applied. The resulting normalised concentration profiles are compared in Figure 5-16(a). Besides the expected increase of the diffusion depth also an increase of the interface concentration is observed. Especially at short annealing times the dissolution and degassing kinetics play a dominant role since the samples are prepared from powder mixtures. At longer times the cobalt binder of the GGI-WC-Co part is saturated with chromium and can fully provide the chromium potential. According to Equation 4 plotting of the diffusion depth vs. the square root of diffusion time should yield a linear relationship. If not, some effects appear which are not ascertained by the applied transport model. Such a plot is illustrated in Figure 5-16(b). A more or less linear relationship is found with some deviations at lower annealing times. These deviations result from the dissolution kinetics of the GGIs at the initial stages upon annealing.

For vanadium three samples with annealing times of 5, 15 and 30 min were prepared. The corresponding vanadium concentration profiles are compared in Figure 5-17(a). No sample at 60 min is available due to an insufficient contact of the diffusion couple components. In contrast to chromium all fitted curves origin from an interface concentration of $c_0(V/Co)=0.025$. However, a strong increase of the concentration 20 μm from the interface was observed. This phenomenon appears for most vanadium-based, but not for chromium-based samples in this project. This specific effect is further discussed in section 5.6. Since the vanadium solubility in cobalt at 1150°C is by a factor 5 lower than of chromium the dissolution kinetics at

the early annealing stages has less influence on the vanadium transport. Subsequently the plot of x_D vs. \sqrt{t} yields an ideal linear relationship.

The time-invariance of the transport factor of both chromium and vanadium is an important finding. It means that, except for the dissolution kinetics at low annealing times of 5 min, time dependent mechanisms do not play a significant role for the GGI transport. Kinetic side effects such as densification of the WC-Co compact appear either fast at the very early annealing stages or already upon heat-up to 1150°C. It might also be explained by densification with constant rate, but this is unlikely to remain over a time period of 30 or 60 min and can hence be excluded.

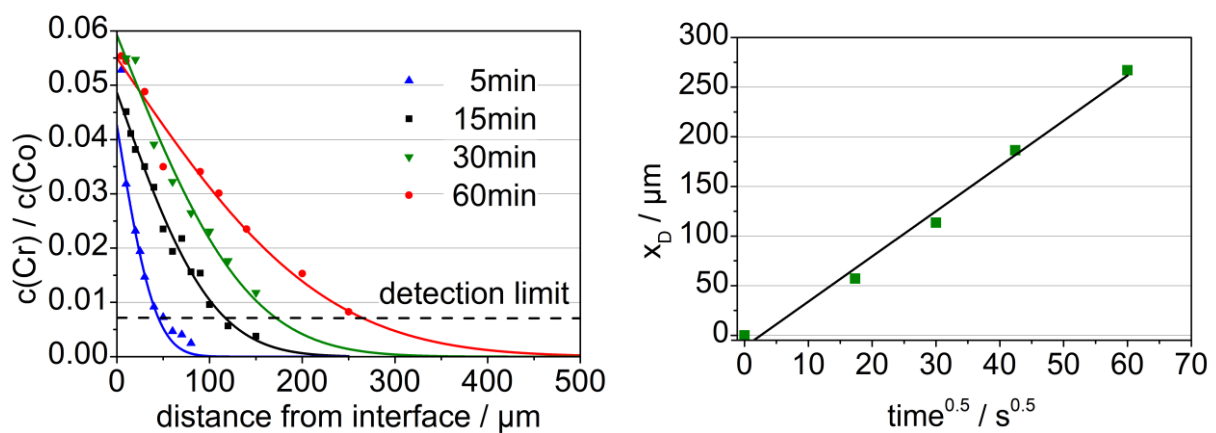


Figure 5-16: Time dependency of the chromium transport in G-type couples with high carbon potential annealed at 1150°C.

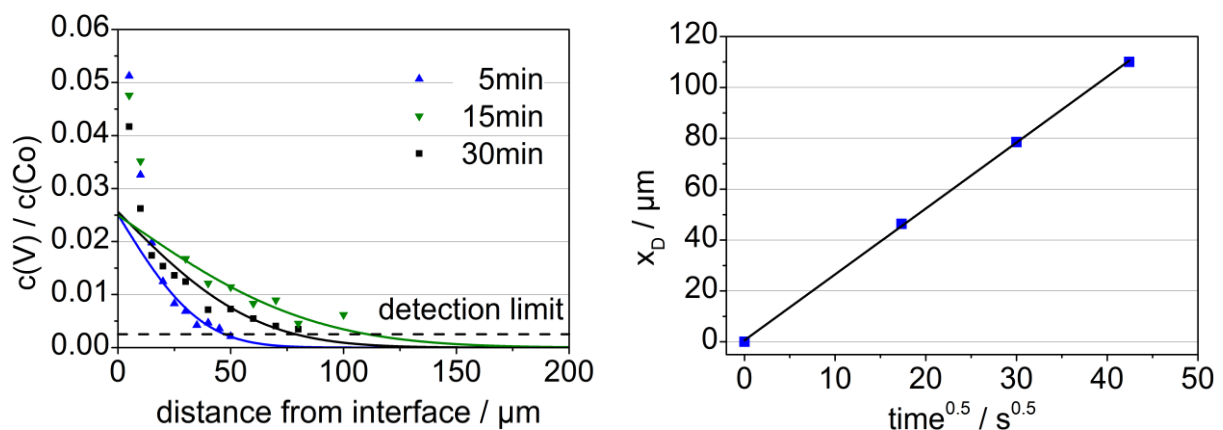


Figure 5-17: Time dependency of the vanadium transport in G-type couples with high carbon potential annealed at 1150°C.

5.5.2 Carbon potential

The carbon potential certainly has the most complex influence on the distribution of GGIs in hardmetals. Based on literature data the carbon adjustment is supposed to effect the wetting behaviour [14BOU] of Co on WC, the W solubility (see Figure 2-6), the GGI solubility [01OBB, 06LAU, 08FRI], the densification kinetics and the phase equilibria (Table 2-3). All of these parameters influence the GGI transport, subsequently a strong influence of the carbon potential on the distribution of GGIs is expected. Arrhenius plots in Figure 5-18 of (a) vanadium and (b) chromium transport in G-type samples with cobalt binder in solid-state validate this assumption.

The transport factors for vanadium increase with rising carbon potential from low (black) to high (red). The slope of the curves is proportional to the activation energy. For a further discussion of the activation energy refer to section 5.2. The difference in D between high and low carbon potential is approximately a factor of 5. High carbon potential is hence favourable for a fast distribution of vanadium in hardmetals upon sintering. However, grain growth is markedly more pronounced in high-carbon hardmetals (see section 2.2.2). A low-carbon environment is therefore generally beneficial for producing ultrafine hardmetals. The reduced grain growth is certainly of greater relevance than the slower distribution of vanadium.

For chromium the influence of the carbon potential is less distinct. At 1150°C ($7.02 \cdot 10^{-4} \text{ K}^{-1}$) the transport factors are de facto identical. With decreasing temperature the transport factors of low-carbon samples (black) become smaller as compared to the high-carbon grade (red). The slope is clearly different, resulting in higher activation energies for chromium transport in low-carbon samples. However, no difference regarding activation energy or transport factors were found for the mid- and the high-carbon samples. This is surprising at a first glance, but can be explained by considering the microstructures. Figure 5-19 shows such microstructures of chromium-based hardmetals with varying carbon adjustment at 1360°C. In the low-carbon sample (a) no C-precipitates were observed within 2 mm from the interface. However, in samples which were supposed to be in the two phase with both conventional cobalt (b) and fine cobalt (c) carbon precipitations appear around 1400 μm and 560 μm from interface, respectively which is not the case in low-carbon samples. The initial carbon potentials of the WC-Co parts of diffusion couples with either standard or fine cobalt are slightly different from each other but were confirmed

to be in the two phase field for both, see DSC in Figure 4-129 and Figure 4-131, respectively. The difference of 1500 and 560 μm might be based on the slightly different initial carbon potential. Carbon precipitates hence form upon the diffusion experiment, where the Cr_3C_2 -binder part of the diffusion couples can be considered as carbon source. When Cr_3C_2 is dissolved and chromium subsequently diffuses into the WC-Co part, the binder phase of the Cr_3C_2 -Co part saturates with carbon. Subsequently a carbon gradient forms and C diffuses into the WC-Co part. The reason why carbon precipitations are only formed at a certain distance from but not close to the interface is that at high chromium concentrations Cr-based carbides form. However, it cannot be determined whether these precipitates are formed during the diffusion experiment or by the decreasing chromium solubility upon cool down. The chromium concentrations at the border of Cr-carbides/carbon precipitations is $c(\text{Cr}/\text{Co})=0.09$ for the mid carbon alloy and $c(\text{Cr}/\text{Co})=0.4$ for the high carbon alloy. This difference might appear from the different initial carbon potential: in the high-carbon alloy the binder phase is always saturated with carbon, while the saturation is formed by diffusion in the mid carbon alloy. Nevertheless, for both alloys a high carbon potential can be considered, though the “real” potential is dependent on time and local chromium concentration.

Above considerations apply to diffusion couples with liquid binder phase. However, if they are applied to solid-state samples as well they can explain the congruence of the Arrhenius-plots for high- and mid-carbon potential: both have a high “real” potential. It might also mean that the potential of the low-carbon samples are shifted into the two phase area. If this shift is dependent on the temperature it can explain the different slopes of the Arrhenius plots for high- and low-carbon samples. As a consequence the activation energies for chromium transport in hardmetals with solid binder phase are convolved with a temperature-dependent shift of the carbon potential and are subsequently not representative for Cr diffusion at a fixed C potential.

Summarising the findings on the influence of the carbon potential in G-type diffusion couples the following conclusions can be drawn:

- The transport factors of vanadium are by a factor 5 higher in high-carbon hardmetals as compared to low-carbon potential.
- In chromium-based diffusion couples the carbon potential was found to be higher than initially adjusted by diffusion of carbon from the GGI-WC-Co part into the WC-Co part of the diffusion couples. Subsequently graphite precipitations were observed even in the mid-carbon alloy.

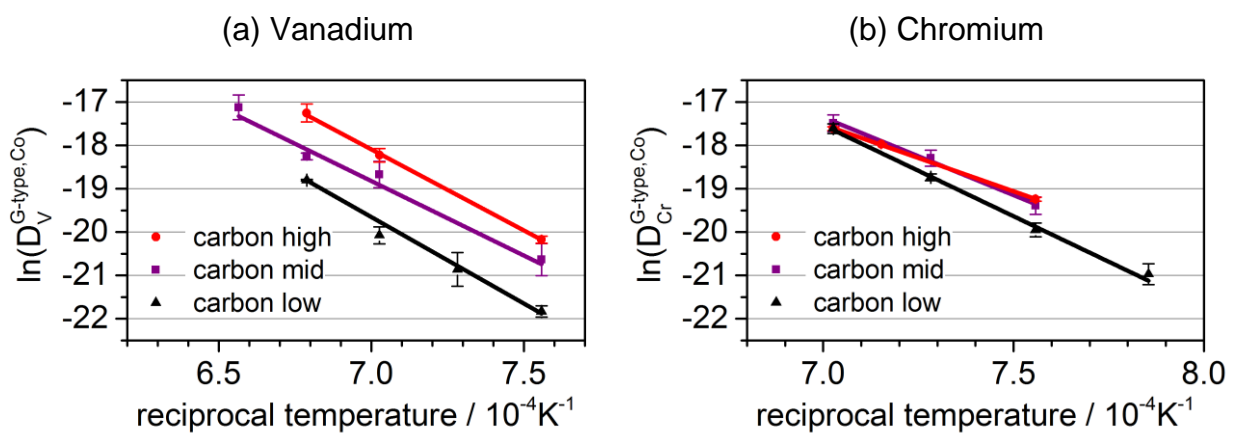


Figure 5-18: Arrhenius plots of (a) vanadium and (b) chromium transport in G-type diffusion couples with cobalt binder and varying carbon potential.

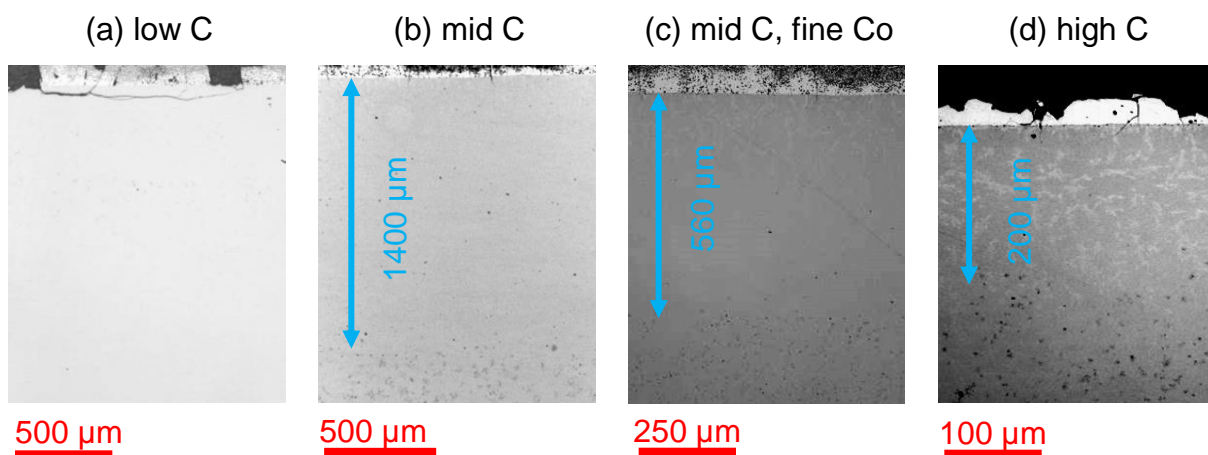


Figure 5-19: Microstructures of G-type diffusion couples at 1360°C. blue arrows indicate distance between interface and appearance of C-precipitates (black dots). (a) CCoG136-, (b) CCoG136, (c) CCo_nG136, (d) CCoG136+.

5.5.3 Initial cobalt grain-size

From literature data and preliminary works [12BRI] it can be deduced that at least the main part of the GGIs chromium and vanadium is distributed via the binder phase. A variation of the initial cobalt grain size can thus have a beneficial effect on the GGI distribution.

In a green body the cobalt is initially present as particular grains. At around 800°C wetting on WC grain initiates (see section 2.2.1), providing a continuous binder network. However, this network is rather coarse at low temperature and the cobalt is still mainly present as coarse grains, see e.g. Figure 4-100(a). The diffusion subsequently appears in a labyrinth-like network with connections between the cobalt grains acting as a bottleneck for mass transport. The idea was that finer cobalt grains might provide a finer structured, less labyrinth-like network which enhances the GGI mass transport. However a comparison of concentration profiles in G-type couples prepared from fine and standard cobalt grades at 1050°C reveals no significant improvement by the fine cobalt, see Figure 5-20(a). The concentration profiles are equal within the error range, independent from the binder grade. At 1150°C (b) the samples prepared from fine cobalt show slightly steeper concentration profiles with higher interface concentrations. The diffusion depth is however not markedly increased. The Arrhenius plot in Figure 5-21 reveals that the error ranges of the vanadium data points (blue) for fine and standard cobalt overlap in the entire temperature range. Using fine cobalt has no measurable effect on the vanadium distribution. For chromium some advantages at higher temperatures are observed, but they are still relatively small.

These findings are as well supported by microstructural features. Figure 5-22 shows the microstructure of G-type diffusion couples with fine cobalt (left column) and standard cobalt (right column). Top two rows refer to chromium, bottom two rows to vanadium. Both samples (a) and (b) at 1050°C with GGI=chromium show a brighter zone between the interface (red line) and the chromium diffusion depth (green line). Similar findings apply for vanadium (e) and (f). At 1150°C, the microstructure in the chromium based sample appears markedly brighter in fine-cobalt sample (c) as compared to the standard-cobalt grade, which can be dedicated to a higher degree of densification. Again these findings apply as well for vanadium (g) and (h). Note that the latter have a scale different to the micrographs (a)–(c). The higher densification

level explains the slight advantage of fine-grained cobalt at 1150°C by providing a more consolidated binder network for GGI transport.

However, slight advantages on GGI transport at 1150°C and no advantage at lower temperatures are no solid reason for applying fine cobalt in hardmetal production, since it has some drawbacks such as high cost and higher oxygen content. The only reason for using fine cobalt can be the finer cobalt distribution and hence improved microstructural homogeneity especially in solid-state production techniques such as SPS. The SPS samples produced in this work show some binder segregations of 2–3 µm diameter, see Figure 4-176. Such segregations can possibly be avoided by using finer cobalt grades.

The considerations regarding the application of finer cobalt grades in hardmetal production can be summarised as follows:

- At 1050°C no advantage of fine cobalt grades as compared to standard grades was observed on the distribution kinetics of both chromium and vanadium.
- A slight advantage of fine grades was observed at 1150°C for both chromium and vanadium transport. This advantage was related to a higher degree of densification of the hardmetal.
- The slight advantage of fine cobalt for GGI distribution does not justify the drawbacks of these grades.
- Fine grades might be advantageous for a more homogeneous microstructure upon solid-state sintering techniques such as SPS.

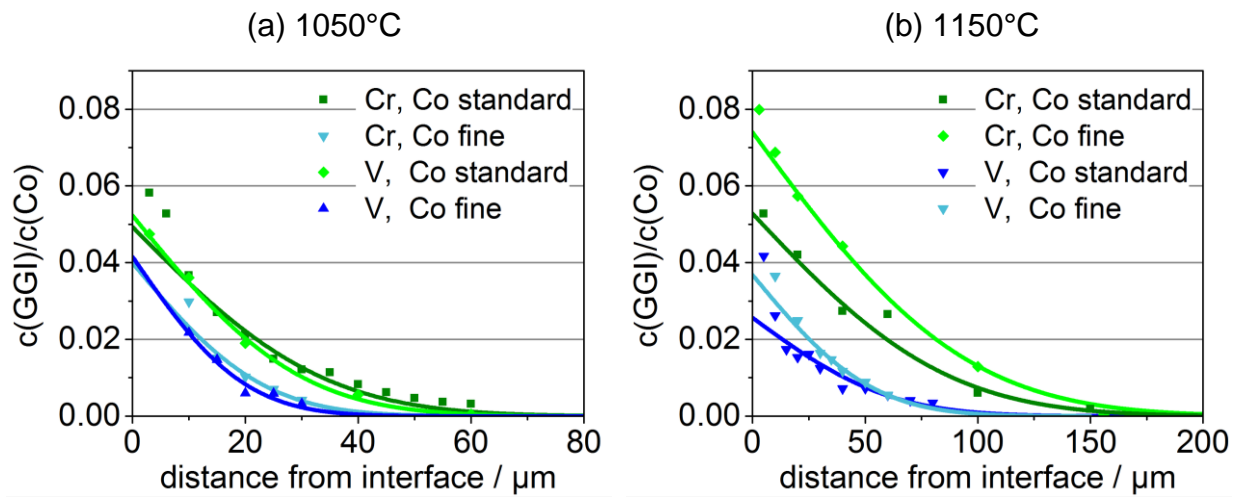


Figure 5-20: comparison of GGI concentration profiles of G-type samples with varying cobalt grain size at (a) 1050°C and (b) 1150°C.

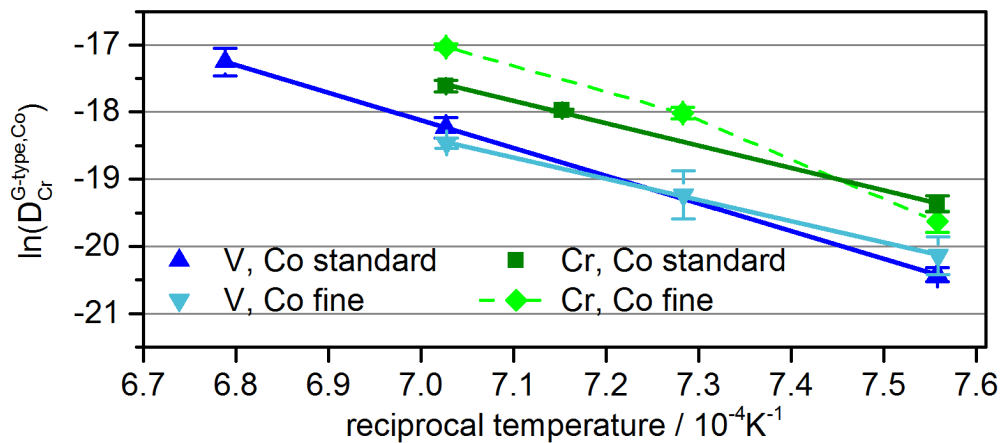


Figure 5-21: Arrhenius plot showing the dependency of Cr- and V-distribution on the initial cobalt grain size in G-type diffusion couples.

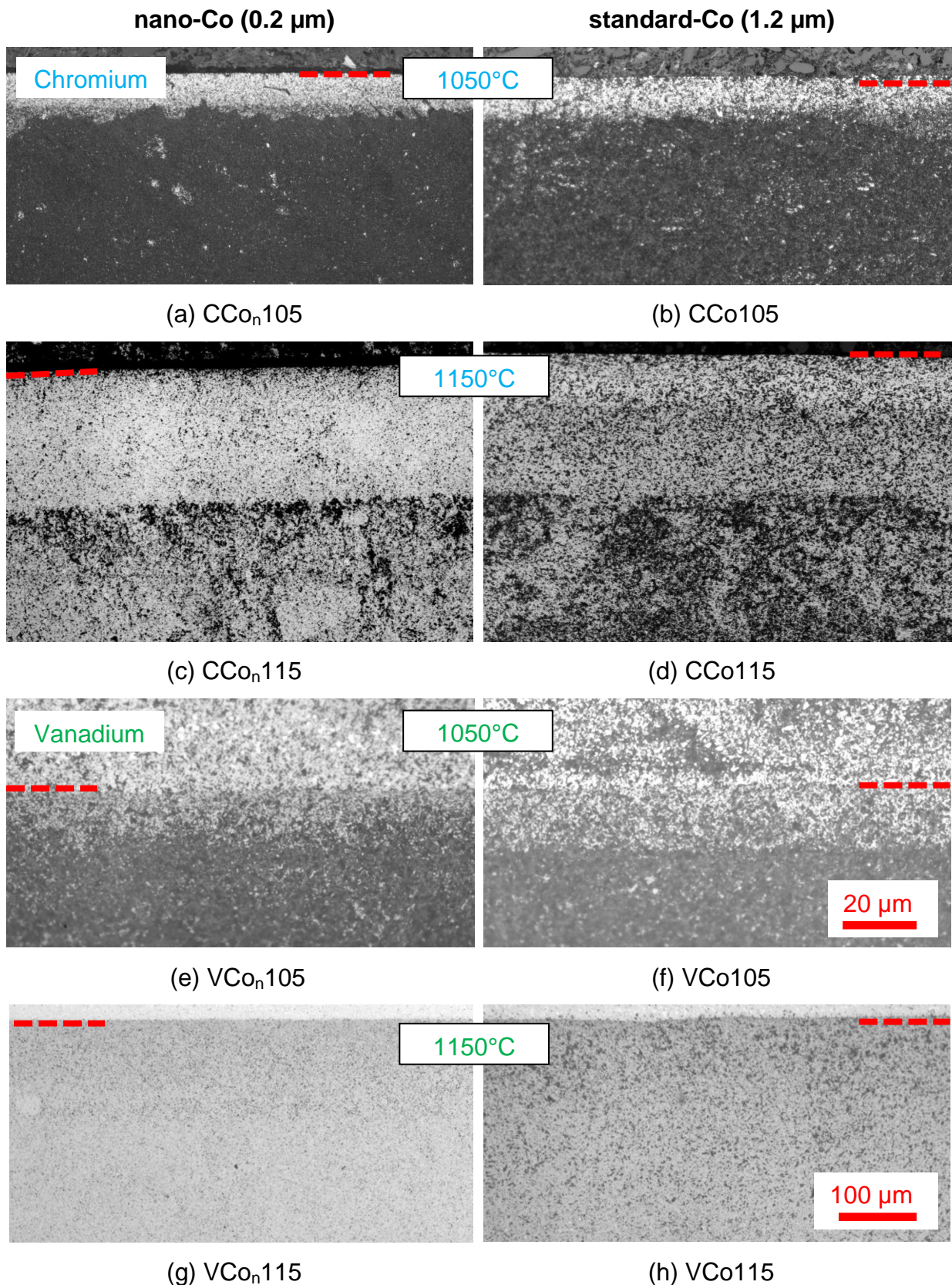


Figure 5-22: Microstructural development of G-type couples prepared with nano-cobalt (left column) or standard cobalt (right column) as a function of temperature. Dashed red lines mark the GGI-WC-Co/WC-Co interfaces.

5.5.4 Binder phase composition

Based on the results in this work it can be assumed that GGIs are distributed mainly via the binder phase. A closer look on the role of the binder phase chemistry is thus of great interest. The binder phase chemistry is on the one hand influenced by the carbon potential (W solubility) and on the other hand by the binder metal alloy. The influence of the carbon potential is discussed in section 5.5.2, the influence of the binder alloy will be discussed below. A comparison of the normalised concentration profiles of (a) chromium and (b) vanadium depending on the binder alloy is depicted in Figure 5-23. No significant influence of the binder can be observed on the distribution of both chromium and vanadium. The binder alloy hence plays a negligible role as long as it is an fcc Fe/Co/Ni binder alloy.

Though the binder does not influence the GGI transport a reversed effect is observed: The GGI influences the ratios of the binder elements in the Fe/Co/Ni binder. The weight ratios of Fe/Ni, Co/Ni and Co/Fe illustrated in Figure 5-23 (a) for GGI=chromium. Based on the initial composition of Fe/Co/Ni=40/20/40 wt% the ratios should be Fe/Co=0.5, Ni/Co=0.5 and Fe/Ni=1. The Fe/Co (black curve) ratio remains at constant at 0.5, but both the Fe/Ni and the Co/Ni ratios are significantly decreasing towards the interface. Since they are decreasing they indicate a relative enrichment of nickel at higher chromium concentrations. No such effect was observed for the vanadium based sample (b). Hence the nickel enrichment in chromium samples is caused by chromium rather than by other surface effects. A comparison to the as-measured data in

Figure 4-88 and Figure 4-90 shows that this enrichment is indeed just relative but not absolute.

The influence of the binder alloy composition on the distribution of GGIs can be summarised as follows:

- No specific effect of the composition of fcc Fe/Co/Ni binder alloys on the transport of chromium and vanadium in hardmetals was observed as compared to cobalt binder.

- A nickel relative enrichment formed at high chromium concentrations in hardmetals with Fe/Co/Ni40/20/40 wt% binder alloy. No such effect was caused by vanadium.

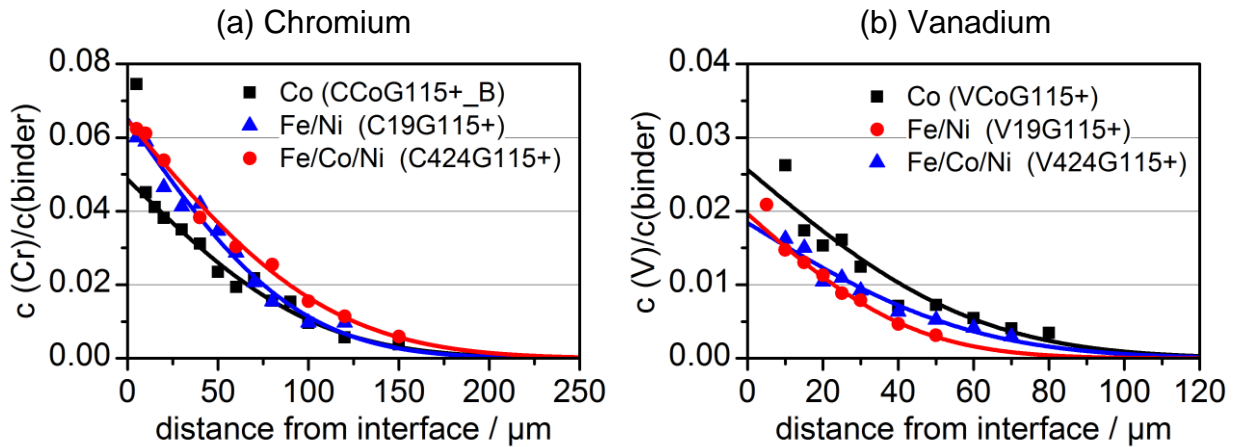


Figure 5-23: Concentration profiles of (a) chromium and (b) vanadium in G-type diffusion couples with Co, Fe/Ni and Fe/Co/Ni binder alloys annealed for 15 min at 1150°C.

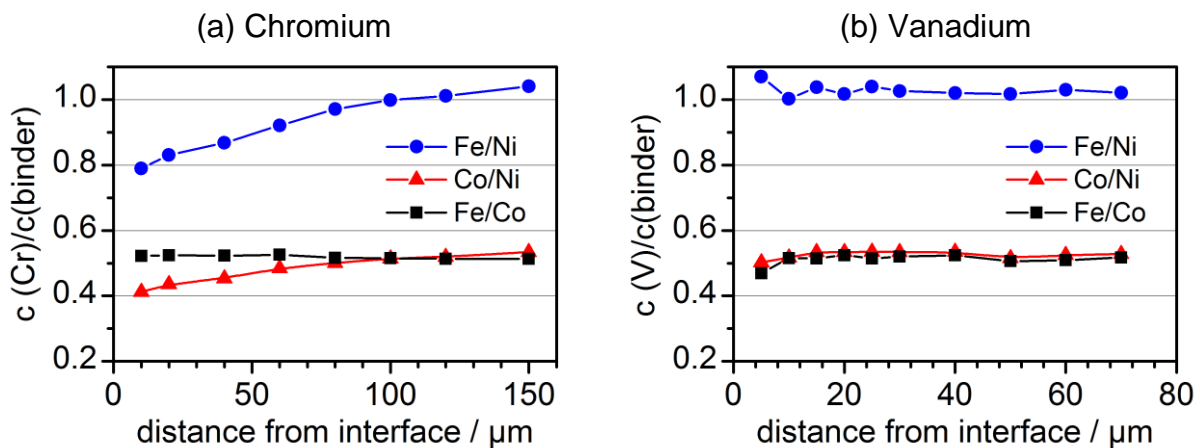


Figure 5-24: Concentration ratios of Fe, Co and Ni in G-type diffusion couples with (a) chromium and (b) vanadium annealed for 15 min at 1150°C.

5.5.5 Green density

In hardmetals GGIs may diffuse via a variety of pathways such as e.g. binder phase or WC/Co grain boundaries. Hence, an influence of the green density on the diffusion behaviour seems likely. A series of diffusion couples of type G with varying compaction pressures within the WC-binder body was prepared with the GGIs chromium and vanadium (see 3.3). The annealing time was 30 min at a temperature of 1150°C for each particular sample.

The results for chromium are illustrated in Figure 5-25. At low compaction pressures of 15 MPa or 40 MPa the chromium concentration profile does not reveal a shape which is expected upon a diffusion process, see Figure 4-41(a) and Figure 4-42(a) in section 4.3.5. Instead, a kind of a peak shape is measured. At a medium pressure of 80 MPa (Figure 4-43) this structure is already less pronounced but still observed within the first 30 μm from the interface. At higher pressures of both 160 MPa (Figure 4-44) and 240 MPa (Figure 4-28) the profile shows a steady decrease of the chromium concentration as it is expected from diffusion experiments.

The peak-shaped as-measured concentration profile for low compaction pressures seems physically impossible since it would require “uphill-diffusion” against the concentration gradient with almost no chromium at the interface. Thus a second transport mechanism is expected simultaneous to the GGI diffusion. However, normalising the chromium by the cobalt concentration yields a concentration profile without any “uphill diffusion”. The normalised concentration profiles are compared in Figure 5-25(a). A comparison of the cobalt concentration profiles is given in Figure 5-25(b). This comparison clearly shows cobalt migration off the interface towards the WC-Co body for samples prepared with low pressing forces. This effect is decreasing with increasing compaction pressures. At 240 MPa it is almost eliminated and the cobalt concentration scatters around the nominal 10 wt%.

Although the measured chromium profiles can be explained by cobalt migration it is not yet clear what the latter is caused by. It can be clarified by comparing the normalised concentration profiles of the sample series as shown in Figure 5-25(a).

Despite the normalisation by the cobalt concentration a large difference between the samples regarding the Cr/Co ratio at a given distance from the interface appears. Lower compaction pressures lead to significantly higher chromium concentrations. A Cr/Co ratio of around 0.6 close to the interface for 15 MPa corresponds to a Cr-concentration of 37 wt% within the Co phase. However, the solubility limit estimated from literature is by a factor 10 lower around $c(\text{Cr/Co})=0.07$. As it was mentioned above, the chromium concentration profile is highly correlated to the cobalt profile, thus it can be assumed that the chromium is almost quantitatively located in the binder phase. But a concentration of 37 wt% points to heavily oversaturated binder phase, which cannot be achieved by an isothermal diffusion process. Thus, there has to be a mechanism which allows concentrations much higher than the equilibrium.

The solubility of chromium in a hardmetal binder refers to an equilibrated binder which is saturated with tungsten and carbon. However the solubility of chromium in pure cobalt is around 40 at% (37 wt%) and hence at the same level as measured for the 15 MPa sample. Thus, such concentrations in a hardmetal binder phase seem only legit when almost no tungsten is present. Since G-type couples are made from green bodies, the binder phase is pure Co prior to the annealing process. Upon heating WC dissolves in the binder phase. Simultaneously the Cr diffusion from the Cr₃C₂-WC-binder part of the couple originates. As a consequence almost no W is present at the beginning of the experiment, which allows higher Cr interface concentrations as compared to the equilibrium state. During annealing an increasing amount of WC will resolve in the binder phase, causing an oversaturation of chromium. Such a high-concentration chromium profile will lead to both a tungsten and a carbon gradient, since the WC is assumed to resolve faster and in higher concentration in Cr-free cobalt as it is found in the sample bulk. A direct measurement of the gradients is not possible since it cannot be distinguished from EPMA-measurements whether is resolved in the binder phase or corresponds to WC. The reason why the effect is stronger for low pressing forces can be explained by the weaker contact pressure and the lower contact area between WC and cobalt powder particles as compared to samples compacted with high pressures. Thus the kinetic of WC-dissolving is faster and lower W-gradients will form. The Cr concentration at the interface of the 240 MPa sample of $c_0(\text{Cr/Co})=0.065$ is around the equilibrium concentration. Since all samples of this series were prepared within the same sintering cycle and from the same initial powder mixtures, the compaction pressure is the only variable.

A third consequence of a high chromium concentration might be a different wetting behaviour of the binder phase on WC grains. At 1150°C Co binder is known to wet WC grains and subsequently the green body will densify. GGIs were found to retard the wetting by shifting the onset to higher temperatures. Subsequently, the shrinkage of the WC-Co body during annealing is lower at high chromium concentrations. This effect can be seen from Figure 5-25(c) by comparing the totals of the EPMA-signals which correlate with the porosity. The totals show a general trend to lower values close to the interface and are more distinct for the samples with lower pressing forces.

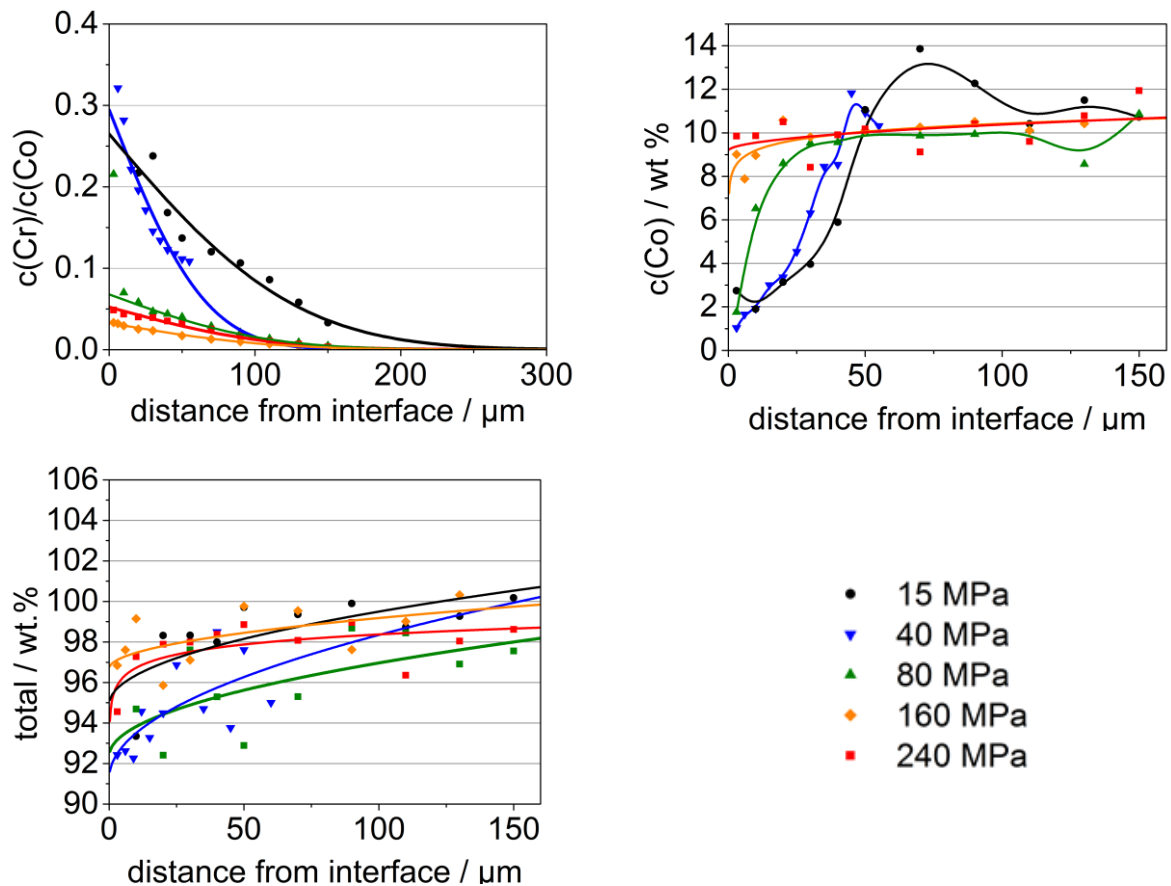


Figure 5-25: (a) Normalised chromium concentration profiles, (b) cobalt concentration profiles and (c) EPMA-totals of G-type diffusion couples prepared with varying green densities.

The concentration profiles measured for vanadium prepared with various compaction pressures of the WC-Co body are shown in Figure 5-26(a). No cobalt gradients were observed as shown in Figure 5-26(b). Apart from the data points at the interface a constant Co concentration of 10 wt% as a function of the distance from the interface is observed for all samples.

A difference in vanadium concentration is observed within the first 10 μm from the interface. At higher distances no significant difference between the samples was measured. The deviating profile at 80 MPa is considered an outlier.

Similar to chromium a decrease of the EPMA measurement totals is observed close to the interface as shown in Figure 5-26(c). Since the total can be correlated to the porosity of the green body an increase of the vanadium content causes a retardation of the shrinkage and hence the solid-state sintering process.

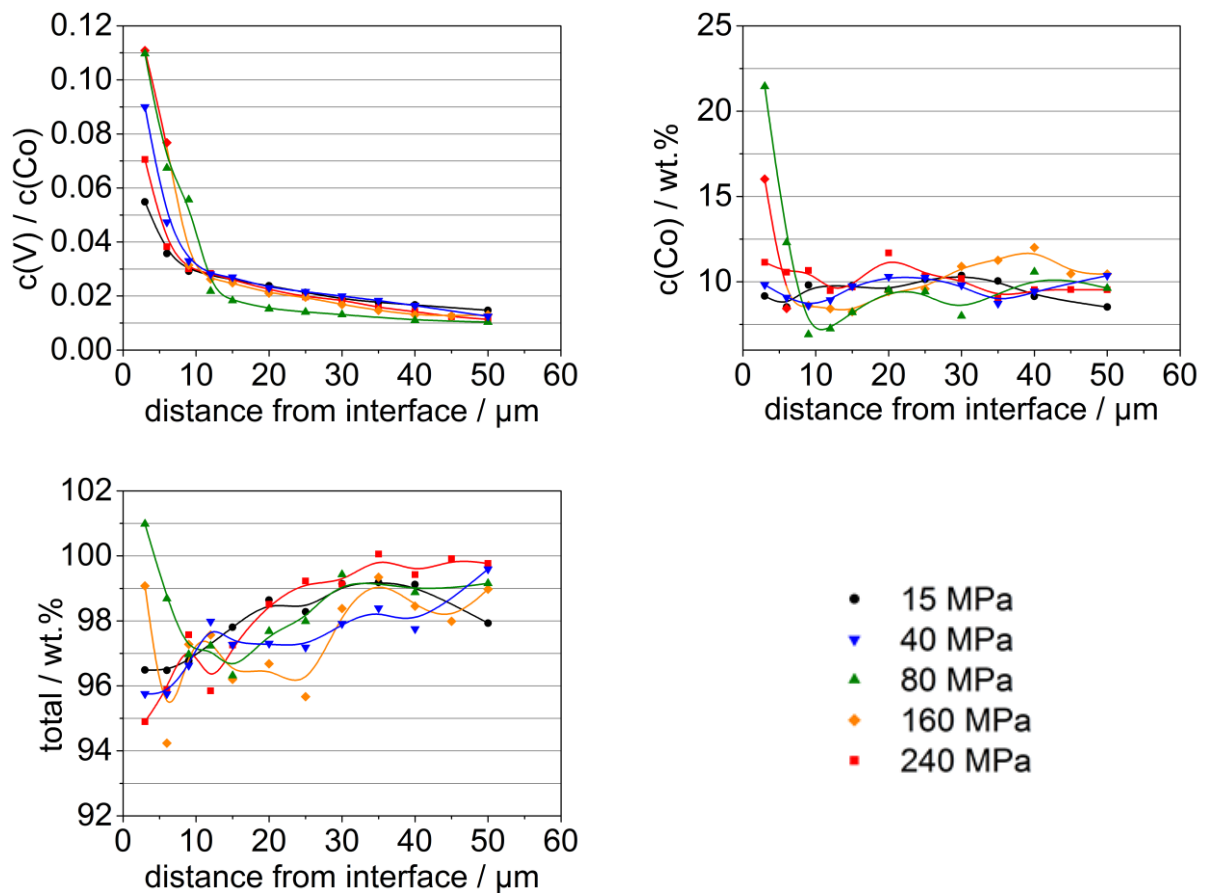


Figure 5-26: (a) Normalised vanadium concentration profiles, (b) cobalt concentration profiles and (c) EPMA-totals of G-type diffusion couples prepared with varying green densities.

5.5.6 Nitrogen and CO

It was discussed in previous sections that diffusion of both chromium and vanadium in G-type couples is affected by local non-equilibrium states which control the solubilities of the various constituents in the binder phase. Thus, an influence of reactive sintering atmospheres on the distribution of GGIs is standing to reason.

Carbon monoxide acts as a reactive gas in hardmetals since on the one hand it is oxidising to chromium and vanadium below 1000–1100°C and on the other hand it has carburising effect.

From literature [07GUS] and from previous works in our research group [12LEN] it is known that either nitrogen atmosphere, the use of GGI nitrides instead of carbides [09BRI, 10BRI1] or rim-nitrided WC powders [12WET] can affect the grain growth of

WC already at early sintering stages. Besides by atmosphere nitrogen can well be introduced by GGI-nitrides [10BRI], which was found to enhance the inhibiting effect of GGIs. In order to determine the influence of nitrogen and CO on GGI-distribution G-type diffusion couples based on Cr_3C_2 , Cr_2N or VC were annealed in either 200 mbar Ar, N_2 or CO.

In argon atmosphere no significant differences of the chromium diffusion behaviour are observed whether Cr_2N is used as a chromium donor or Cr_3C_2 , see Figure 5-27. The as-measured chromium profiles as well as the Cr/Co ratios are equal within the error range in both nitrogen and argon atmosphere. This is an important finding since Cr_2N and Cr_3C_2 have different stability and hence different dissolution kinetics. If the dissolution of GGIs in the WC-GGI-binder diffusion couple part was rate-controlling for the measured GGI-distribution significant differences in diffusion depth should have been observed. This is not the case; hence the diffusion of chromium is the rate-controlling step which is a fundamental precondition for the application of the diffusion couple technique.

It is however interesting that the application of nitrogen significantly increases the chromium interface solubility. In a high carbon potential hardmetal a solubility of $c(\text{Cr}/\text{Co})=0.06\text{--}0.07$ is estimated from literature data (see Table 2-4).

This value was found for the alloys annealed in argon as can be seen from Table 5-2. The values of $c(\text{Cr}/\text{Co})=0.09\text{--}0.13$ in nitrogen atmosphere are far above the solubility. However, at low carbon potential (presence of η) the solubility is higher around $c(\text{Cr}/\text{Co})=0.12$, which fits the measured data. The application of nitrogen thus either caused a decarburisation, which can be excluded by the use of high-purity nitrogen or it enhances the solubility of chromium (and possibly of tungsten) by replacing part of the carbon in the cobalt binder phase. The latter also would explain the grain-growth inhibiting effect of nitrogen atmosphere as reported in literature since carbon promotes WC grain growth (see section 2.3.1). However, these considerations are speculative, further works will be necessary in order to clarify the mechanisms behind. A possible setup would be the preparation of model alloys which are annealed in nitrogen atmosphere for long times at e.g. 1100°C and subsequent EPMA-measurement of W, C and GGIs in the binder phase. Alternatively, hardmetals with fixed C potential (e.g. with graphite precipitates) could be prepared in nitrogen atmosphere, characterised by magnetic properties and

compared to hardmetals sintered in argon. However, this will only provide information if the W solubility is influenced by nitrogen, but no information on the carbon content will be available. The first method is hence to be preferred .

An interesting behaviour can be expected by use of carbon monoxide. Driven by the Boudouard reaction CO has a carburising effect on hardmetals. The carburisation causes saturation of the binder phase with carbon already at relatively low temperature and subsequently affects the dissolution of WC in the cobalt, leading to a reduced W content. The latter allows higher chromium concentrations as compared to a sample annealed in inert argon atmosphere as can be seen from Figure 5-28(a) for Cr_3C_2 and (b) for Cr_2N as a chromium source.

A similar effect should be expected for vanadium. As can be seen from Figure 5-28(c) the vanadium concentration at a given distance from the interface is significantly lower in presence of CO as compared to inert Ar atmosphere. In order to explain why the vanadium distribution is affected by CO atmosphere in a different way than chromium the reduction behaviour of vanadium oxides has to be considered. It is shown in section 4.6.1.3 that full carbothermic reduction requires temperatures higher than 1230°C in inert atmosphere. This temperature is dependent on the CO partial pressure and will shift to significantly higher temperatures in CO atmosphere. At lower temperatures, such as 1150°C in case of sample VCoG115+CO, CO is not only carburising but also oxidising which has the effect that vanadium oxides are formed. Such oxides retard the dissolution of vanadium in the binder phase and subsequently the availability of the diffusing species. Interestingly, nitrogen has as well retarding effects on vanadium distribution, but the reasons are not clear yet. This behaviour can also be seen from a comparison of the transport factors as given in Table 5-2. The interface concentrations obtained from CO and N_2 atmosphere are in the range of the V solubility $c(\text{V}/\text{Co})=0.014$ at 1150°C obtained from literature. The concentration of the sample annealed in Ar is much higher which will be further discussed in section 5.6.

Table 5-2: Transport factors and interface concentrations of GGIs in G-type diffusion couples annealed at 1150°C for 15 min in 200 mbar Ar, CO or N₂.

Sample name	GGIX	Atmosphere	D (10 ⁻¹⁰ cm ² /s)	Weight ratio c(GGI)/c(Co)
CCoG115+	Cr ₃ C ₂	Ar	223 ± 47	0.052 ± 0.004
CCoG115+CO	Cr ₃ C ₂	CO	279 ± 25	0.127 ± 0.004
CCoG115+N	Cr ₃ C ₂	N ₂	73 ± 2	0.136 ± 0.005
CNCoG115+	Cr ₂ N	Ar	217 ± 23	0.058 ± 0.003
CNCoG115+CO	Cr ₂ N	CO	191 ± 8	0.101 ± 0.004
CNCoG115+N	Cr ₂ N	N ₂	90 ± 9	0.111 ± 0.006
VCoG115+	VC	Ar	121 ± 26	0.033 ± 0.004
VCoG115+CO	VC	CO	24 ± 4	0.019 ± 0.002
VCoG115+N	VC	N ₂	26 ± 7	0.017 ± 0.003

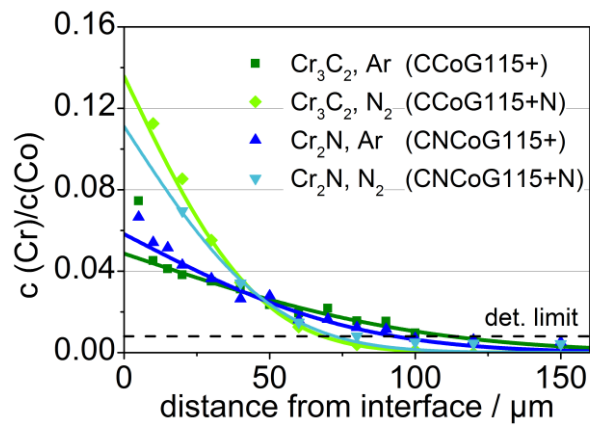


Figure 5-27: Concentration profiles of chromium in G-type diffusion couples, GGI added as Cr₃C₂ or Cr₂N, annealed for 15 min at 1150°C in 100 mbar Ar or N₂.

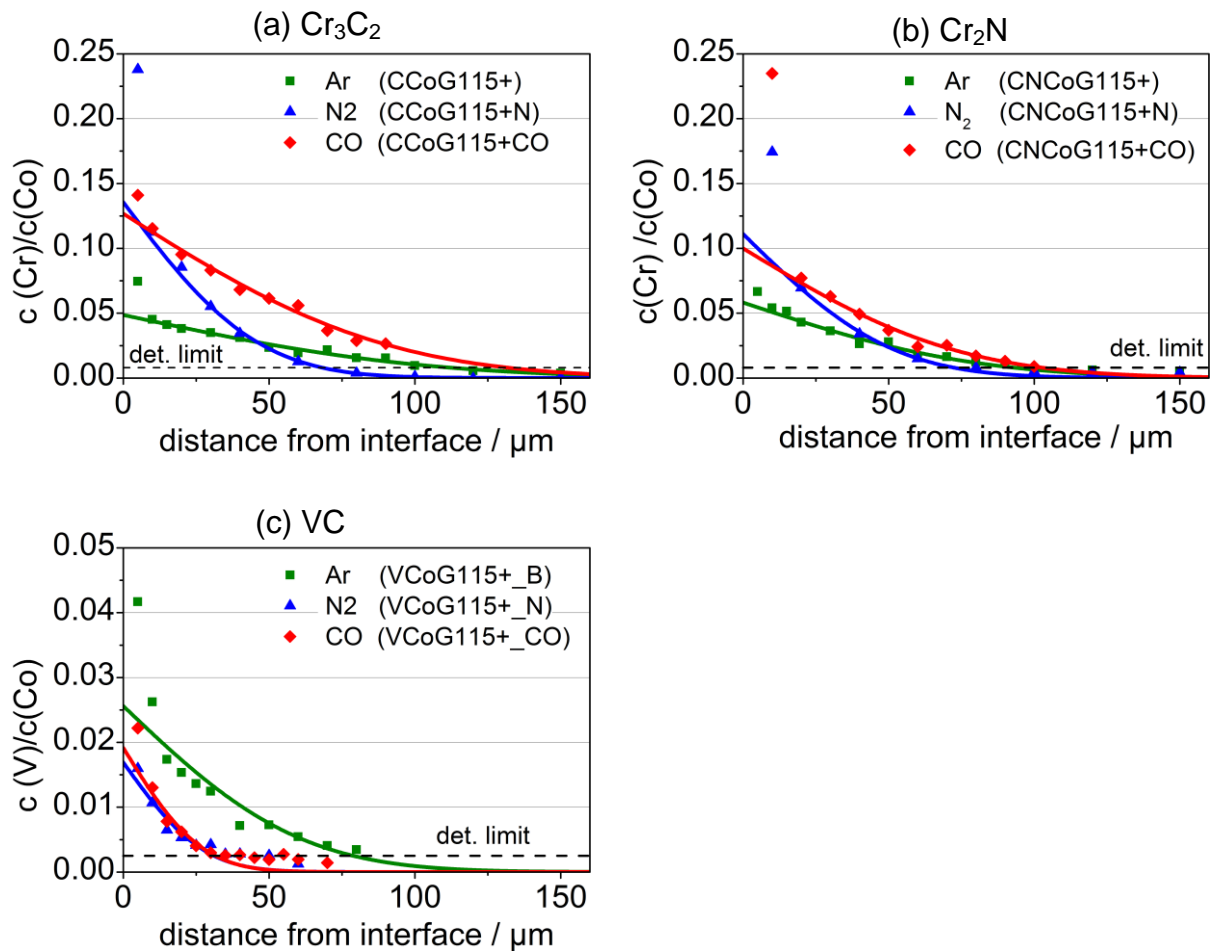


Figure 5-28: Concentration profiles of chromium or vanadium in G-type diffusion couples based on (a) Cr_3C_2 , (b) Cr_2N and (c) VC annealed varying sintering atmospheres at 1150°C for 15 min.

5.5.7 Diffusion of borides

In order to determine the influence of the presence of boron on the chromium distribution, G-type diffusion couples based on Cr_3C_2 or CrB were annealed at either 1050 or 1150°C for 15 min. From DSC analysis no phase reactions of the CrB -doped HM_CrB sample (Figure 4-161) were observed below 1212°C . No evidence for the appearance of a Co-B eutectic at 1132°C [10NPL] was found. The Cr_3C_2 -doped sample WCo (Figure 4-160) has a single melting event at 1191°C . Both samples are hence fully in solid-state at the testing temperatures of max. 1150°C .

The resulting concentration profiles for chromium at 1050°C are shown in Figure 5-29(a) for low carbon potential and (b) for high carbon potential of the WC-

Co. At low carbon potential the concentration profiles are comparable, only slightly higher concentrations were measured for the boride. Within the first 10 μm from the interface the chromium concentration is significantly higher with CrB as compared to the carbide and the corresponding fitted curve deviates significantly from the measured data. However, a variety of uncertainties influence the measured values within the first 10 μm from interface (see 4.2.1).

At high carbon potential (b) the chromium concentration is significantly higher for the boride while the difference between the profiles for the nitride and the carbide is statistically insignificant. Subsequently, especially at high carbon potential boron provides a substantial advantage for the distribution of chromium in hardmetal green bodies. However, the application of borides in hardmetals causes some specific problems. Namely, a variety of phases such as CoB, W_2B_5 or WCoB were reported to form by diffusion of boron from the surface in a WC-Co material. These phases tend to coarsen to up to some tens of micrometres even at temperatures of 900–1100°C, causing embrittlement of the material [09KÖK, 15YAH]. Though the appearance of such phases may yield advantageous surface properties e.g. for coating applications, any type of coarse phase is undesired in ultrafine hardmetals. Besides this drawback a further negative effect can be seen from the sample at 1150°C, see Figure 5-30(a). At a first glance the boride seems to have a positive effect on the chromium distribution as compared to application of carbides or nitrides. However, a look at the cobalt profile (b) reveals formation of a strong cobalt gradient with enrichment close to the interface and a drop to almost zero at 20 μm from the interface. A similar effect was observed for molybdenum at 1150°C as can be seen from Figure 5-31 (b) where boron seems to cause a cobalt gradient. Regarding the molybdenum distribution no advantage of borides was observed (a).

The formation of such a cobalt gradient does of course not apply if a hardmetal is doped with GGI-B, it is rather a specific effect of the diffusion couple setup. Nevertheless, when GGI-B is resolved in a doped hardmetal a cobalt depleted zone may form around the inhibitor grain, which causes microstructural inhomogeneities. Upon liquid-phase sintering this effect will not be relevant due to the fast homogenisation by the liquid. In solid-state sintered samples (SPS) this effect may become of relevance.

Summarising the findings on borides the following conclusions were drawn:

- At 1050°C and low carbon potential borides have no influence on the distribution of chromium.
- At high carbon potential a faster distribution and much higher solubilities of chromium were measured at both 1050°C and 1150°C if added as boride as compared to carbide.
- Formation of a strong cobalt gradient was observed at 1150°C for both chromium and molybdenum in presence of boron.

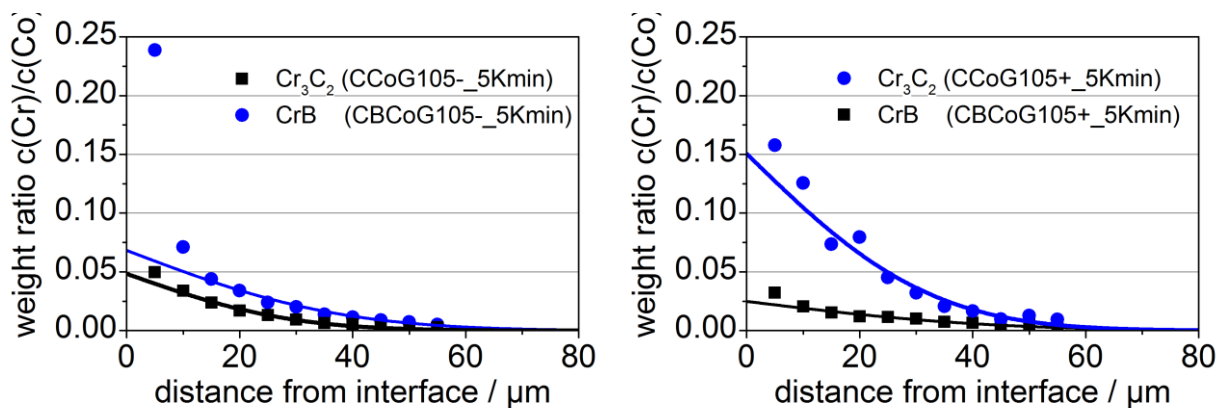


Figure 5-29: Concentration profiles of chromium in G-type diffusion couples with various chromium sources annealed for 15 min at 1050°C with (a) low and (b) high carbon potential.

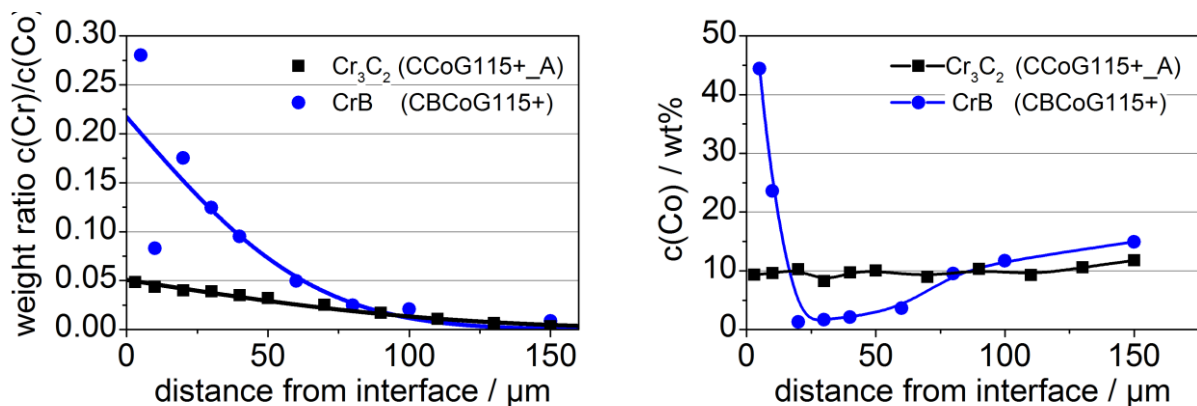


Figure 5-30: Concentration profiles of (a) chromium and (b) cobalt in G-type diffusion couples with various chromium sources annealed for 15 min at 1150°C.

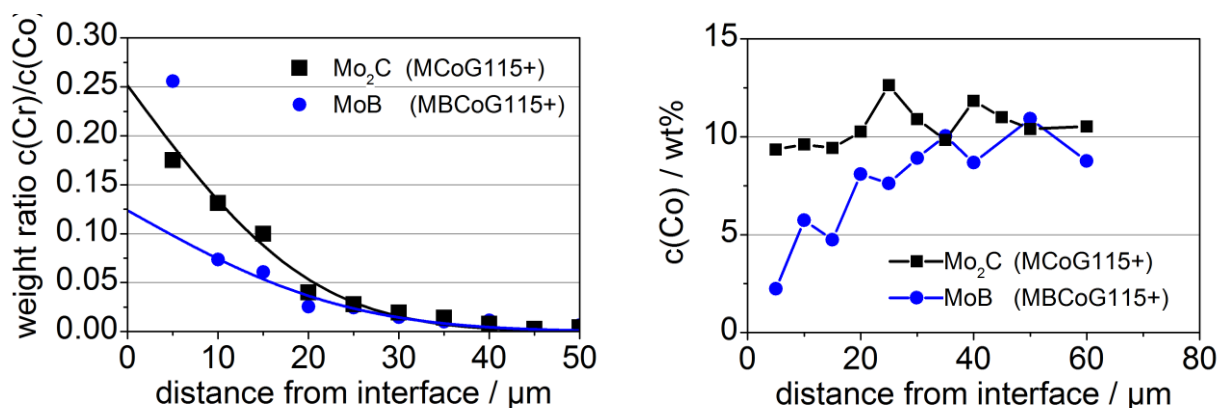


Figure 5-31: Concentration profiles of (a) molybdenum and (b) cobalt in G-type diffusion couples with various molybdenum sources annealed for 15 min at 1150°C.

5.5.8 Cr/V interdependency

Commercially available ultrafine hardmetals are nowadays most commonly double-doped with chromium and vanadium. It is hence important to gain knowledge on a possible interdependency of their distribution at early sintering stages.

As it is discussed in section 5.6 on the one hand the chromium transport is significantly faster as compared to vanadium. On the other hand vanadium is more efficient at early sintering stages as discussed in 5.7. Thus, the question arises if chromium either slows down or enhances the vanadium transport. From literature [06LAU] it is known that the presence of chromium reduces the solubility of vanadium at 1000°C from 1.1 wt% to 0.7 wt% at high carbon potential, see Table2-4.

Also from SPS samples it was shown that Cr+V double doping is less efficient than V single doping at 1150°C. Hence, the question is if chromium also somehow retards the vanadium distribution or if it just lowers the vanadium solubility. In order to find an answer the concentration profiles of both chromium and vanadium at 1150°C in a sample where they were simultaneously distributed (CVCoG115) were compared to the respective concentration profiles undisturbed by co-diffusion. The result is shown in Figure 5-32(a) where the dark green and dark blue lines represent the uninfluenced distribution of chromium and vanadium, and bright green and bright blue lines show the distribution influenced by co-diffusion, respectively. As already discussed above the interface concentrations of both chromium and vanadium are decreased in the co-diffusion sample. However, the diffusion depth of vanadium is not significantly influenced by the presence of chromium. Chromium is slightly slowed

down by presence of vanadium. However, the samples were prepared in the WC+Co two phase area and it is discussed in section 5.5.2 that a shift in carbon potential appears in such samples, especially triggered by Cr diffusion. A carbon potential shift is more likely to explain the slower Cr diffusion than the influence of vanadium, since at distances $>80\ \mu\text{m}$ no more vanadium is present.

These considerations can as well be extended to temperatures other than 1150°C as illustrated by means of the Arrhenius-plot in Figure 5-32(b). Over the entire investigated temperature range the transport factors for chromium are slightly lower in presence of vanadium. However, vanadium shows an inverse behaviour; its distribution is slightly faster in presence of chromium. The latter might be explained by a reduction of the W solubility in presence of chromium. Nevertheless, the most probable explanation is as well a shift of the carbon potential. It is not contradictory that a C-shift is an explanation for the slower chromium but the faster vanadium diffusion as compared to the reference grades though they were measured in the same sample. It was shown in section 5.5.2 that the reference grades in the two phase area have a different carbon shift. While the chromium reference grade (dark green line) is shifted to higher carbon and hence higher transport factor, no such effect was found for the vanadium grade (dark blue).

Regarding the interface chemistry no significant influence was detected as the TEM line scans in section 4.8 show. In Cr+V-doped sample an enrichment of vanadium was observed at the interface at 1150°C , but not of chromium. The same behaviour, namely segregations of vanadium but not of chromium, was as well observed in single doped samples.

The findings regarding the interdependency of Cr/V diffusion can be summarised as follows:

- No significant interdependency of the chromium and vanadium distribution at 1150°C was found in G-type couples.
- No significant interdependency on the interface chemistry at 1150°C appears.
- The maximum interface concentrations of both chromium and vanadium are decreased by presence of each other.

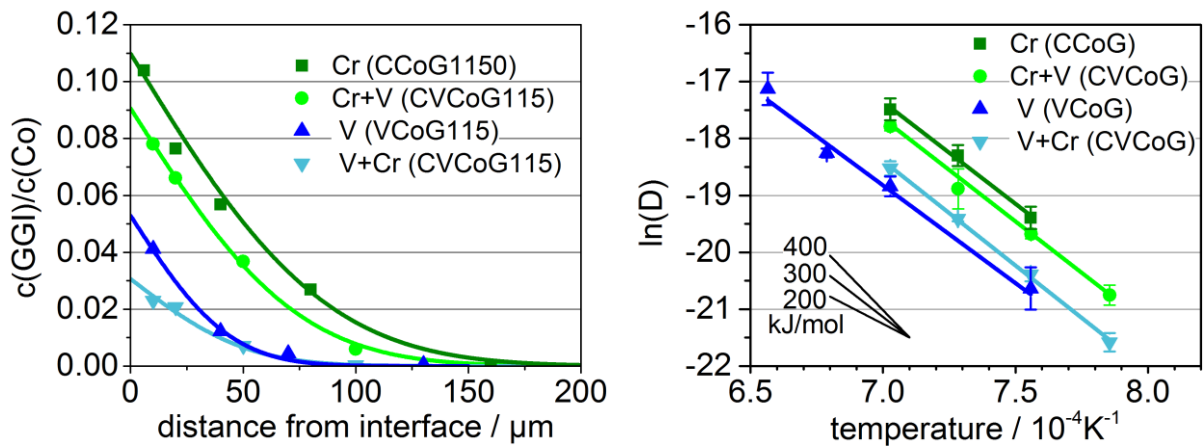


Figure 5-32: Interdependency of Cr/V transport; (a) normalised concentration profiles at 1150°C, (b) Arrhenius plots.

5.6 GGI transport mechanisms

A direct comparison of (a) chromium and (b) vanadium distribution in of G-, M- and H-type diffusion couples after 5 min at 1150°C is given in Figure 5-33. It is particularly striking that the distribution of both is significantly faster in G-type diffusion (black curves) couples than in H-type samples (green). For M-type samples (violet) markedly lower interface concentrations are observed, while those of H- and M-type samples are comparable. The reason for the different behaviour of M-type samples is that GGI diffusion is rate controlled by tungsten diffusion since the binder alloy is W-supersaturated in presence of GGIs, which is discussed in detail in section 5.3. For a deeper understanding of the transport mechanisms the focus thus lies on a comparison of G- and H-type samples. From almost equal interface concentrations it can be assumed that boundary conditions at the interface are generally equal for both sample types. This is an essential precondition for a comparison of the grades.

The transport factors obtained from G- and H-type diffusion couples at 1050°C and 1150°C are compared to literature data for GGI bulk diffusion in cobalt in Table 5-3.

The values for H-type diffusion couples are by a factor of 50–100 higher than the diffusion in bulk fcc-Co. This is at a first glance surprising. The diffusion of GGIs through WC-grains can be neglected in the investigated temperature range [08BRI]. Thus the GGIs have to diffuse via the binder phase by a labyrinth-like pathway [09GAR] which should yield lower gross diffusivities.

However, the matrix of a hardmetal is different from pure bulk cobalt metal. First of all, a hardmetal matrix has carbon and tungsten resolved. They cause a different lattice spacing which enhances the diffusivities. Second, the binder lamellae between WC are thin in an ultrafine hardmetal and usually below 1 μm . Thus, the strain field of the WC/Co grain boundaries influences a significant part of the binder volume. Grain boundary diffusion is subsequently likely to be the dominating diffusion mechanism. Bulk diffusion may be of less importance and the volume of the thin lamellae is easily filled from grain boundaries. Since grain boundary diffusion in metals is usually by 1–2 orders of magnitude faster as compared to bulk diffusion it is an explanation for the high transport factors in H-type couples.

The G-type couples have again by factor 8–10 higher transport factors as compared to H-type samples and are by up to factor 1000 higher than in bulk fcc-cobalt. The considerations on grain boundary diffusions apply as well to G-type diffusion couples. However, due to porosity in green bodies the labyrinth effect should be even more pronounced and one would expect lower transport factors as compared to H-type samples. To explain why they are higher a closer look on the distribution of the cobalt phase is required.

In the initial green body the binder appears as particular isolated grains with only occasional contact, compare Figure 2-2. At initial sintering stages cobalt wetting on WC grains initiates and a continuous cobalt network forms. This is the pathway GGIs take to distribute. The thickness of this layer is thermodynamically controlled by interface energies. At lower temperatures of 1050 or 1150°C most of the cobalt binder is still present as larger grains and with rising temperature it gets finer and more equally distributed, see e.g. Figure 2-2 or the bulk images of Figure 4-100. By this mechanism two additional effects apply which are not present in fully dense H-type couples. The first effect is that due to porosity a substantial amount of surfaces is present in the diffusion couple. Surface diffusion is even faster than grain-boundary diffusion which is one explanation for the fast GGI transport in hardmetal green bodies. The second effect is the migration of cobalt. When GGIs diffuse into the hardmetal green body they are as well dissolved in the large cobalt particles. However, when this cobalt spreads on WC grains it also further distributes the GGIs. Since the spreading is not a single, sudden event but happens over a larger time period even under isothermal conditions, the GGIs are steadily distributed. This is not

a pure diffusion process. Due to densification and WC particle rearrangement a kind of convective effect is active upon diffusion, which enables fast distribution.

The high transport factors upon sintering G-type diffusion couples can hence be understood by a combination of surface diffusion, grain boundary diffusion and migration of the cobalt phase by wetting on WC grains.

However, there is one finding in this work which disagrees with these considerations: the activation energies. As it was discussed in section 5.2 the activation energies are, depending on GGI and carbon potential, around 270–350 kJ/mol. This is significantly higher than the expected 10–100 kJ/mol if grain boundary or surface diffusion is rate controlling. It is even higher than for bulk diffusion in pure cobalt which is 260–275 kJ/mol for both vanadium and chromium. To solve this contradiction one again has to look at the processes appearing upon solid-state sintering. The calculation of activation energies from Arrhenius plots is based on the implicit assumption of constant matrix conditions upon sintering. This assumption is not fulfilled in hardmetals. A temperature increase causes:

- Higher solubilities of carbon and tungsten in the matrix
- Densification and subsequent reduction of surfaces and pores
- A reduction of the amount of “coarse” initial cobalt particles and more equal distribution of cobalt with subsequent higher amount of cobalt “channels”
- A reduction of the labyrinth effect by pore elimination

The reduction of surfaces will slow down GGI diffusion, but all other effects will accelerate it. Their summarised effect will overrule the effect of surface reduction. Hence, the GGI transport at increasing temperature is not only faster by thermal activation of diffusion but also by additional effects due to a changing matrix. This will cause a steeper slope in the Arrhenius plot as if it would be by pure diffusion. Since the slope is proportional to the activation energies the latter are overestimated.

Nevertheless, the activation energies in this work are not a measure for GGI diffusion but they are a measure for the thermal dependency of GGI distribution in hardmetal green bodies, which combines the effects of diffusion and of microstructural developments.

Two further aspects to be considered are the interface concentration c_0 obtained from the fits to the experimental concentration profiles and the quality of these fits.

Essential differences between chromium on the one hand and vanadium on the other hand appeared.

The interface concentrations $c_0(\text{GGI/Co})$ of chromium are, within the error range, not significantly different from the solubilities estimated from literature, as can exemplarily be seen from sample CCoG115+_A in Figure 5-34(a). This sample is representative for all G-type diffusion couples based on Cr_2C_3 as can be seen in section 4, though some particular samples can deviate from these findings due to measurement errors. Also the model fits quite well to the data as can be seen from the residual plot in (b). The randomly distributed residues are also characteristic for chromium-based samples. From (a) it can further be observed that normalising the as-measured data by the cobalt content yields significant smoothing of the data. The combination of these findings indicates that chromium is almost quantitatively located in the binder phase.

In contrast, vanadium reveals a different behaviour. The interface concentrations c_0 obtained from the fit were generally by a factor 2–3 higher than the binder-phase solubilities estimated from literature, depending on the temperature. However, within the first 10–20 μm the measured concentrations were significantly higher than estimated by the fit curve. Consequently, the real concentrations were even higher than the calculated c_0 values. This behaviour is exemplarily illustrated by the representative sample VCoG115+_A in Figure 5-34(c) but was observed in a similar manner for most vanadium containing samples. The residues plot (d) reveals a systematic deviation of the modelled and the measured data which means the model does not sufficiently describe the vanadium transport. However, when ignoring the first 10–20 μm the model still has good correlation and the value D was introduced as a measure of total vanadium transport phenomena, for which it is still suitable.

Anyway, taking into account these findings it has to be assumed that not all of the vanadium is located within the binder phase. Indeed, from TEM analyses an enrichment of vanadium at the WC/Co interface was detected at 1150°C. It was not possible to determine if these segregations can quantitatively explain the observed concentrations. Anyway, it is certainly an interesting topic for future investigations.

Summarising the findings on the transport mechanisms of GGIs in hardmetals the following can be stated:

- There is evidence that substantial amounts of GGIs diffuse via grain boundaries and surfaces by the thin binder layers at initial sintering stages.
- Besides diffusion microstructural changes such as densification and cobalt wetting on WC further enhance the GGI transport.
- The transport factors at 1150°C in hardmetal green bodies are by a factor of 500–1000 higher than GGI diffusion in pure bulk fcc-cobalt.
- The activation energies calculated in this project are a convolved measure for thermal activation of diffusion and temperature dependent microstructural changes.
- The interface concentrations c_0 obtained from fitting the diffusion model and the experimental data for chromium diffusion are identical to the solubilities of chromium in hardmetals. Evidence was found that chromium is quantitatively located in the binder phase.
- For vanadium the measured concentrations $c(V/Co)$ are much higher than expected from literature data. It was assumed that a part of vanadium is not located in the binder phase but at the WC/Co interfaces.

Table 5-3: Transport factors in G- and H-type diffusion couples and comparison to literature data of GGI diffusion in fcc-Co (compare Table 2-5).

Matrix	D(Cr) [cm ² /s]		D(V) [cm ² /s]	
	1050°C	1150°C	1050°C	1150°C
G-type, high C	44.6	178	20	114
G-type, low C	21.6	53.4	3.3	13.5
H-type, high C	n.a.	20.5	n.a.	20.1
GGI in fcc-Co	0.14	0.27	0.096	0.57

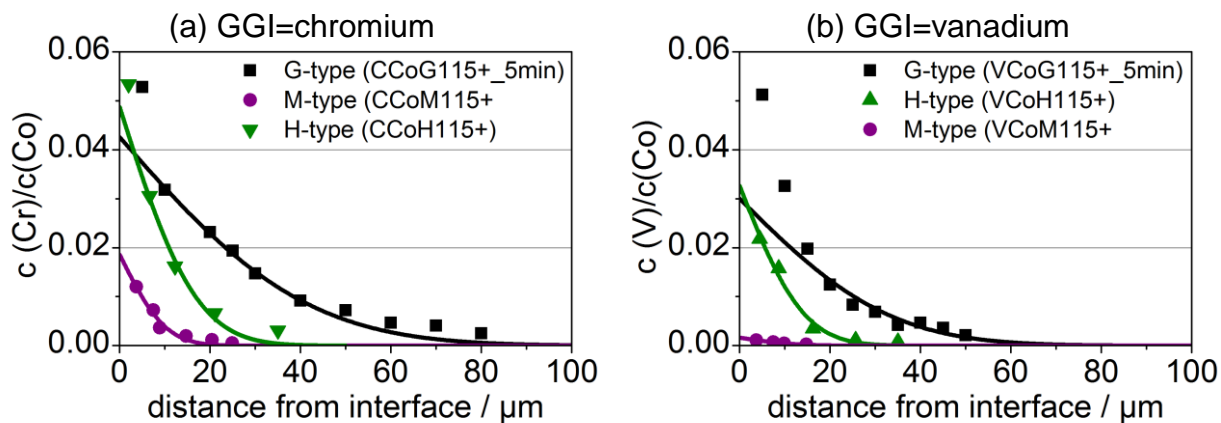


Figure 5-33: Comparison of G-, M- and H-type diffusion couples with cobalt binder and annealed at 1150°C for 5 min.

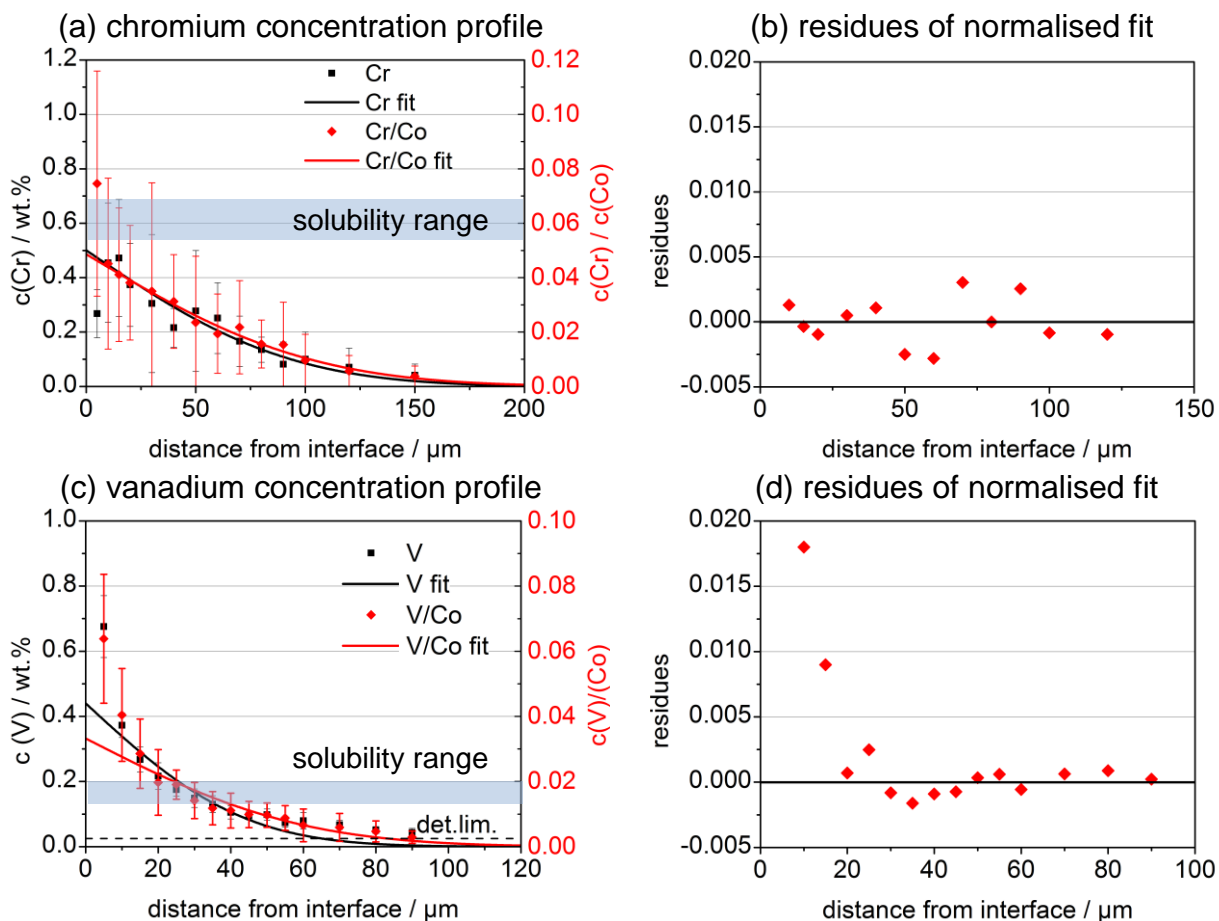


Figure 5-34: Concentration profiles (left) and corresponding residues (right) of G-type diffusion couples with chromium (top) and vanadium (bottom) annealed at 1150°C for 15 min.

5.7 Effectiveness of GGIs at early sintering stages

A sufficient distribution of GGIs upon the initial sintering stages is a necessary, but not a sufficient condition for producing ultrafine hardmetals. Of course GGIs also have to be effective at low temperatures. The efficiency order of $V > Cr > Mo$ (see 2.3) was determined from liquid-phase sintered hardmetals. However, on the one hand substantial WC grain growth appears already at temperatures around 1000°C in ultrafine grades, on the other hand sophisticated sintering techniques such as SPS operate in the temperature range of solid binder phase. Both cases, and especially the combined case of SPSed ultrafine grades, require fast available GGIs with high inhibiting potential at initial sintering stages.

A comparison of the cumulated frequencies of SPSed samples can be read from Figure 5-35. It is particularly striking that the curves of the undoped and the Cr_3C_2 -doped samples are more or less congruent, the difference is within the error range. On the other hand a slight benefit appears when Cr_2N is used as a chromium source. The nitride is supposed to have faster dissolution kinetic due to its thermal decomposition. This is in accordance to literature data (e.g. [10BRI], see section 2.3) where the use of Cr_2N instead of Cr_3C_2 turned out as advantageous for liquid-phase sintered hardmetals by reduction of abnormal grain growth. The latter is reported to initiate already upon early sintering stages [02SOM]. The benefit of Cr_2N for liquid-phase sintered hardmetals might thus origin from the higher efficiency at the early sintering stages due to faster dissolution.

VC turned out to be the most efficient inhibitor for SPSed hardmetals, which was already reported by various authors (e.g. [13RIC] see section 2.3). However, for liquid-phase sintered hardmetals a combined doping of $Cr_3C_2 + VC$ was reported to further improve the inhibiting effect [09BRI]. From the present data the combined doping of 0.6 wt% $Cr_3C_2 + 0.4$ wt% VC is inferior to 0.6 wt% VC single doping. If Cr_3C_2 has no significant effect on SPS samples of this series the reduced efficiency of the co-doping can be explained by the reduced VC concentration.

The inefficiency of Cr_3C_2 for SPS disagrees with literature data. This may have two reasons. First of all in present work an ultrafine hardmetal was chosen while most publications are subject to near-nano grades < 100 nm. For such fine grades chromium might have an effect since the driving force for coarsening is substantially larger. Second, the present work was conducted at 1150°C with solid binder phase.

The works proving the efficiency of Cr_3C_2 such as [14ALA, 07HUA] operate in a temperature range of 1200–1300°C and with chromium concentrations where the binder phase is, depending on the carbon potential, partially liquid. Hence chromium is significantly faster distributed and interface energies are different which might explain the difference.

From TEM-analyses at 1150°C no segregations of chromium were found at the WC/Co interface (see section 4.8.3) while they were found for vanadium (4.8.1) at least at some WC/Co interfaces. In a Cr+V-doped sample (4.8.4) a clear enrichment of vanadium at the interface was observed, but not of chromium. This might be an explanation for the significantly higher efficiency of vanadium at 1150°C.

If chromium is really not efficient at a temperature of 1150°C this effect should also be detectable in liquid-phase sintered sample with varying outgassing dwell time. In particular, doped hardmetals were liquid-phase sintered at 1380°C with varying outgassing dwells at 1000°C for 15 min, at 1150°C for 15 min and at 1150°C for 600 min. In case chromium is not effective at 1150°C or lower, the grain-size ratio of the Cr-doped and the undoped sample should be independent from the temperature and time of the outgassing dwell. If chromium is efficient at these temperatures, the grain-size increase of the undoped sample should be significantly larger after 10 h than of the chromium-doped sample.

A comparison of the mean grain size of the SPS samples and the liquid-phase sintered samples based on WC of grade DS50 is shown in Figure 5-36(a). As expected the grain size of the SPSed samples is significantly smaller than of the liquid-phase sintered samples. The mean grain size of the undoped samples (black bars) is only slightly increasing, but is not really influenced by a long dwell time. Similar findings apply for vanadium (blue bar). Interestingly, as it was already found in SPSed samples, $\text{Cr}_3\text{C}_2+\text{VC}$ doping has no benefit over VC single doping.

For chromium (green bars) however, a significant reduction of the grain growth by applying a long sintering plateau was observed. At first glance this is contradictory since longer sintering times cannot cause smaller grains. But a comparison with SPS samples shows that the main grain growth does not occur during but after the degassing dwell. This means the long degassing dwell leads to a certain interaction between GGI and WC which hinders grain growth upon the subsequent liquid-phase sintering.

The independency of the grain growth in the undoped sample from the time of the degassing dwell is a hint that no substantial grain growth appears upon the dwell. The ultrafine grade DS50 is maybe too coarse to promote growth at low temperatures. Thus a second series was prepared with the attritor-milled WC DS50m. The attritor milling further generates a large number of lattice defects in the WC powder. These defects may have an activation effect on the growth and also influence the effects of GGIs. The results of this series are shown in Figure 5-36(b). The grain sizes are generally smaller as compared to the samples prepared from unmilled DS50. The absolute grain size of the chromium-doped sample is more or less independent from the degassing plateau; same applies to VC or VC+Cr₃C₂ doping. The grain size of the undoped sample significantly increases after the 10h dwell. Relative to the undoped sample the efficiency of chromium is again higher if a long plateau is applied, though no absolute difference was found as a function of the dwell parameters.

The most important finding is that, in contrast to the unmilled grades the combination of Cr+V is by far the most efficient inhibitor. The mechanism behind this effect cannot be clarified from the present data. However, it might be correlated to the enhanced defect density of WC grains and the smaller initial grain size.

Summarising these considerations, the following conclusions can be drawn:

- The temperature range <1150°C generally has a negligible influence on the grain growth in liquid-phase sintered hardmetals.
- Double-doping of Cr+V has no benefit over VC single doping in SPSed samples or samples prepared from conventional WC DS50. However, a substantial benefit could be found if an attritor-activated WC was used.
- Doping of chromium carbide has no advantage in SPS at 1150°C over undoped samples. An inhibiting effect was found by the use of Cr₂N as a chromium source.
- The relative inhibiting effect of chromium on liquid-phase sintered hardmetals increases with increasing dwell time at 1150°C, indicating a reaction between Cr and WC.

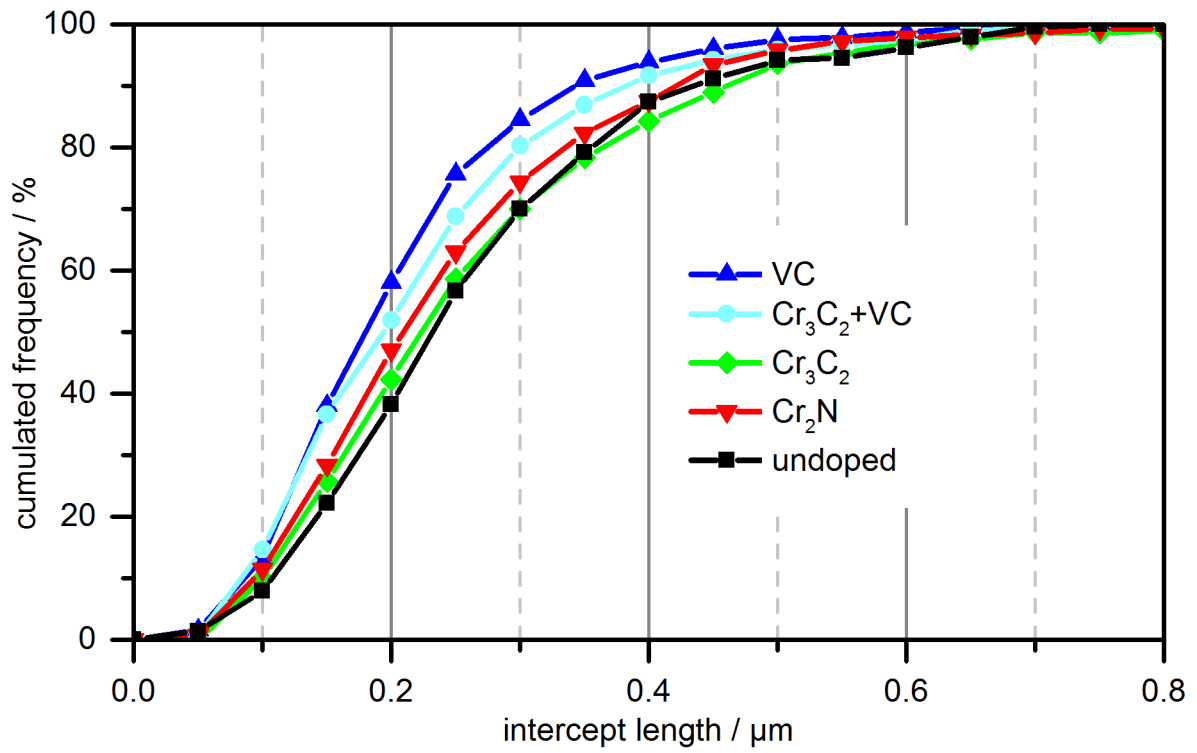


Figure 5-35: SPS samples with various GGI dopants: cumulated frequency of the grain-size distribution.

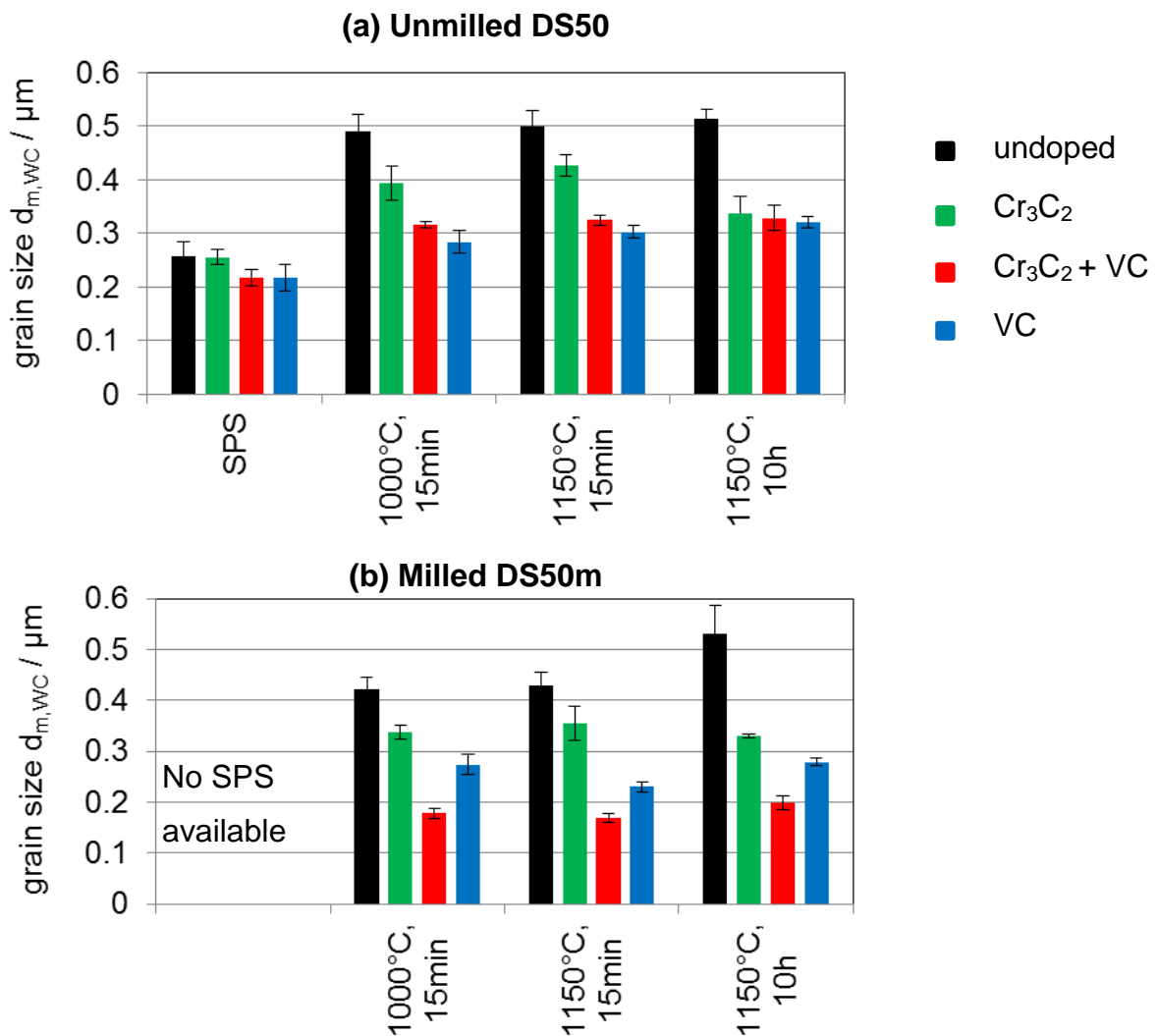


Figure 5-36: Mean grain size $d_{m,WC}$ of hardmetals based on (a) unmilled and (b) milled WC. Horizontal axes indicate SPS or otherwise the temperature and length of the dwell prior to liquid-phase sintering. No SPS was made for the milled samples DS50m. For detailed grain size analyses of particular samples refer to Table 4-37 in section 4.7.1.

5.8 Impact of results on hardmetal production

A number of possible influence factors on the distribution of GGIs were investigated upon early sintering stages. The following conditions were found advantageous for GGI-distribution:

- High carbon potential
- CO-atmosphere
- N₂ atmosphere
- Low green density
- Use of borides instead of carbides

However, high carbon potential and subsequently also CO atmosphere promote grain growth which is disadvantageous for ultrafine-grained hardmetals. The negative effect of pronounced growth is certainly stronger than the positive effect of faster distribution. Borides are also disadvantageous due to the formations of coarse boride phases. Low green densities are as well disadvantageous. This means that nitrogen atmosphere is the only parameter which is advantageous for distribution without strong negative side effects. Further, the application of nitrides instead of carbides was found to have advantages on grain growth upon SPS which are not dedicated to the distribution but to the dissolution behaviour or possibly also to the presence of nitrogen in the pores of the green body.

Anyway, one question which is most relevant for hardmetal production is about a suitable initial grain size of GGI powders in hardmetal mixtures. On the one hand, with finer powders a better initial distribution of GGIs can be achieved and they resolve faster. The pores left back after their dissolution are as well smaller. On the other hand finer powders are cost-intensive and may be difficult to mix due to agglomeration effects. Based on the distribution data in this work it is now possible to give a quantitative answer on how fine GGIX powders have to be added in order to ensure a sufficient GGI distribution in the hardmetal upon early sintering stages.

From the diffusion behaviour a critical grain-size $d_{GGI,c}$ of GGIX (X=carbides, nitrides,...) powders can be calculated. The GGIs used for producing hardmetals have to be smaller than this critical grain size to achieve a suitable diffusion and distribution of GGIs already upon heat-up to sintering temperature. Suitable distribution is defined by a minimal concentration $c_{GGI,min}$ which is available within the entire material by using GGI-X grades of critical diameter $d_{GGI,c}$.

The basic idea is to estimate the spacing x_{GGI} of particular GGIX particles in a hardmetal green body. For a weight ratio of GGIX in the mixture this spacing becomes larger when coarser grains are added and smaller for finer grains. Thus, the

distance GGIs have to diffuse in order to ensure a certain concentration of GGIs within the entire green body increases for coarser grains. If the critical grain size $d_{GGI,C}$ is exceeded, the spacing x_{GGI} gets too large and grain growth may initiate before GGIs are distributed.

For calculating the spacing x_{GGI} the GGIX particles can in a first approximation be considered to be distributed in a cubic grid. The spacing farthest distance from an inhibitor particle is then given by the half of the cubic diagonal. A WC grain located at this position will be the last one to “see” GGIs. This WC grain is located at the distance x_{GGI-WC} . The relation of x_{GGI} and x_{GGI-WC} is thus given by

$$x_{GGI} = 2 * x_{GGI-WC} / \sqrt{3} \quad \text{Equation 11}$$

From the total volume fraction V_{tot} of GGI-X in the starting material the volume of a single GGICarbide grain can be calculated. In a normalised volume element the number of grains n is given by

$$n = (1/x_{GGI})^3 \quad \text{Equation 12}$$

From which the volume of a single grain is given by

$$V_{GGI,C} = V_{tot}/n \quad \text{Equation 13}$$

Assuming ball-shaped grains the critical diameter d_{GGIX} is then calculated by

$$d_{GGI,C} = \sqrt[3]{\frac{6 * V_{GGI,C}}{\pi}} \quad \text{Equation 14}$$

The relations of all parameters defined above are depicted in the sketch in Figure 5-37.

However some assumptions were made for these considerations which cause errors as follows:

- GGIX are estimated as a point source for GGI diffusion.
- Distribution in a cubic grid: In reality the distribution is not that homogeneous and agglomeration appears.
- GGIX particles provide a steady source for GGIs. This assumption is true for very initial sintering stages since common dopant concentrations of

0.1–0.4 wt% VC and up to 0.6–1.0 wt% Cr₃C₂ are above solubility limit at initial sintering stages.

- One-dimensional diffusion. The kinetic data estimated one-dimensional diffusion from one GGIX grain via the distance $x_{\text{GGI-WC}}$. However, at this distance the diffusion spheres of eight GGI-X grains overlap. The calculations hence underestimate $c_{\text{GGI,min}}$.
- Shrinkage: no densification is considered in the model. This is however not necessary since densification kinetics is already included in the transport factors.

With exception of agglomeration all of these errors will lead to an underestimation of the critical diameter d_{GGI} . As a consequence in reality even coarser grains are sufficient than calculated in this work. Anyway, the real critical grain size is certainly within the same order of magnitude.

One parameter which is hard to determine is which minimal concentration $c_{\text{GGI,min}}$ is required to enable growth inhibition at low temperatures. For vanadium there is evidence that a (W,V)C layer plays a certain role for inhibition. In this work no such layer was observed at 1050°C, but enrichment at the WC/Co interface at 1150°C was detected. The question is which amount of VC is required. It was shown that GGIs distribute mainly via the grain boundaries, thus small amounts of VC should be sufficient, but larger amounts likely improve the effect. For chromium a different inhibiting mechanism has to apply since no evidence for interface segregations was found at 1150°C. Chromium most likely inhibits grain growth by an adjustment of the binder phase chemistry. In this case no critical value exists, it is rather “the more the better”. Hence it should be at the solubility limit.

The transport parameters used for the following calculations were those of high-carbon alloys, where GGI are of greatest importance due to the higher grain growth. Commercially available hardmetals are produced in the WC+Co two phase area mostly with magnetic saturation of 82–85% which is close to the high-carbon boundary of ~91% to achieve optimised bending strength. Diffusion profiles upon usual industrial heating rates of 5 K/min were calculated using Equation 8 – Equation 10. From these concentration profiles the critical GGI-C grain sizes $d_{\text{GGI,C}}$ were estimated to ensure a certain GGI-concentration at a given temperature. The results

are shown in Figure 5-38(a) for vanadium and (b) for chromium. These diagrams are to be read in the following manner: To ensure a vanadium (a) concentration of $c(V/Co)=0.02$ at 1050°C everywhere in the material a GGI-X grain-size of $6\ \mu\text{m}$ is sufficient. If $c(V/Co)=0.03$ is required, finer powders of $4\ \mu\text{m}$ should be used.

From literature it is known that grain growth in ultrafine materials initiates around 1000°C . Taking into account the solubility limits, indicated by the black circle in Figure 5-38, it can be seen that a grain size of $\sim 5\ \mu\text{m}$ is sufficient for a suitable distribution of both vanadium and chromium. However, it was found from diffusion couples that vanadium concentrations can even form above solubility limit by diffusion processes due to grain-boundary segregations.

These calculations clearly reveal that from the distribution point of view GGIX grain sizes of several micrometres are sufficient. However, as already discussed by Richter et al. [13RIC] a reasonable upper limit of GGIX grain size can be defined by the pore size of the hardmetal. Upon sintering a hardmetal the densification process is not uniform. While most of the material densifies, pores of several micrometres diameter are formed which can even grow upon heat-up by coalescence or ripening mechanisms. Microstructural investigations (Figure 4-100) in this work support these findings. In doped hardmetals additional pores are formed by the dissolution of GGIs. If GGI-induced pores are not larger than the pores naturally appearing in undoped hardmetals they will very likely not influence the mechanical properties of the sintered material [13RIC]. Summarising these considerations a reasonable GGIX grain size is not limited by GGI diffusion. Instead, the upper limit is set by the pore formation and subsequent microstructural inhomogeneities.

These findings however apply to ultrafine hardmetals which are sintered by conventional liquid-phase sintering techniques with usual low heating rates. For fast solid-state techniques such as SPS they have to be modified. The heating rates are fast around $100\ \text{K/min}$. GGIs have hardly time to resolve and distribute before common sintering temperatures of $1150\text{--}1250^{\circ}\text{C}$ are reached. From the diffusion couples in this work, which were prepared under similar conditions, it was shown that GGIs still distribute fast. Chromium e.g. is transported up to $60\ \mu\text{m}$ within the first 5 minutes at 1150°C . The salient point for producing nano-grained materials is not the distribution but rather the microstructural homogeneity. It was shown that the presence of GGIs can cause some local changes of the carbon potential or of the

cobalt content at the interface of diffusion couples. The same mechanisms are likely to apply in the vicinity of a dissolving GGIX grain upon sintering. In liquid-phase sintered hardmetals the homogenising effect of the liquid phase equalises these effects. In SPS no liquid phase is present. Subsequently for these techniques significantly finer GGIS should be used, also with respect to dissolution kinetics. The best method, however, would be the application of pre-alloyed binder metals or WC powder as they are already reported and available, see e.g. [11WEI, 15WEI].

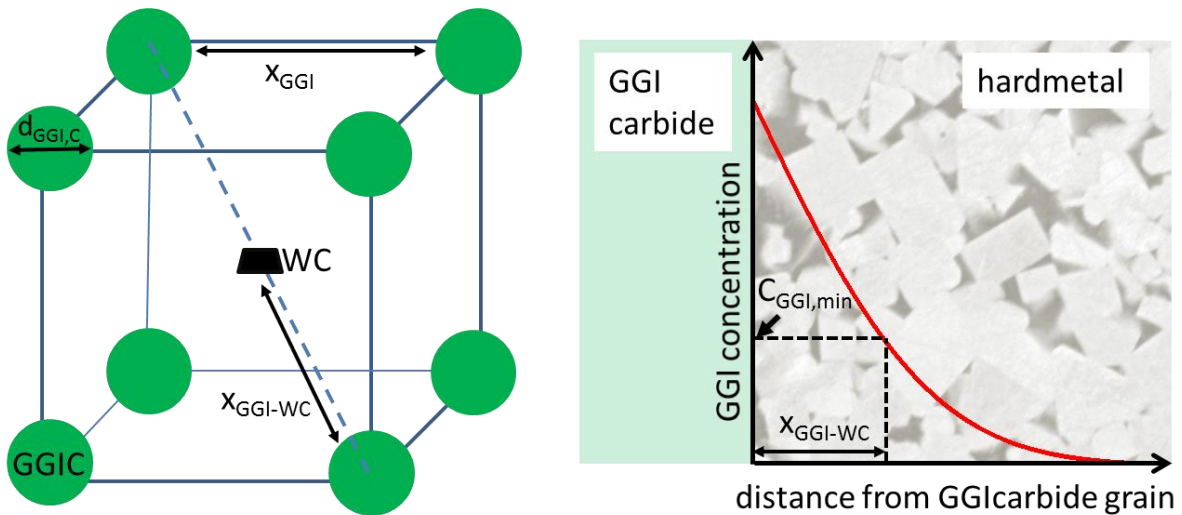


Figure 5-37: Illustration of the parameters introduced in this section required to determine the critical GGI-X grain size $d_{GGI,C}$.

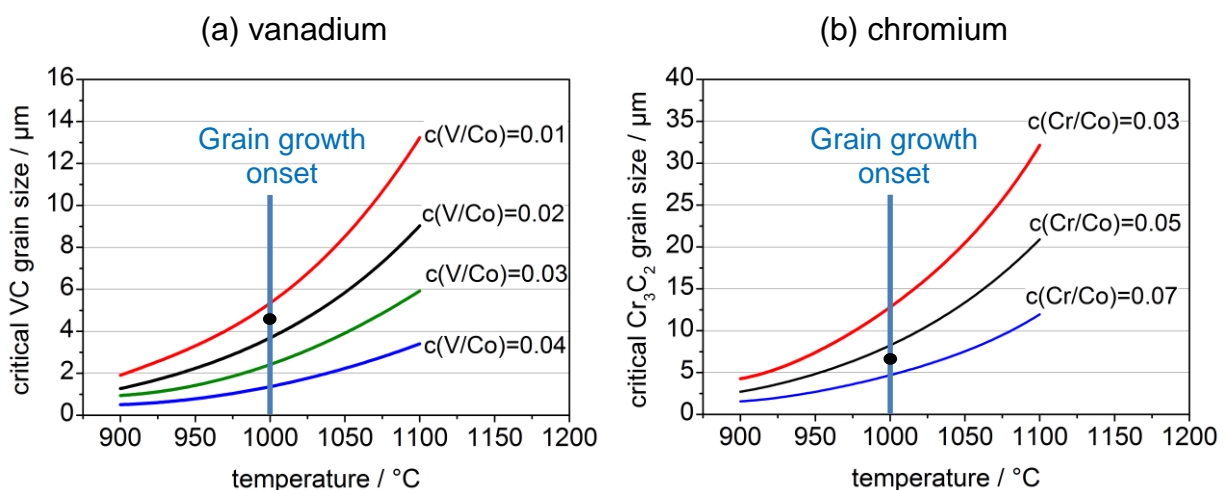


Figure 5-38: Estimation of critical grain size $d_{GGI,c}$ of (a) VC and (b) Cr_3C_2 at a constant heating rate of 5 K/min in a high-carbon hardmetal. Black circle marks solubility at 1000°C.

6 Summary

6.1 General Aspects

This work aims to gain insight into fundamentals of the distribution of the grain-growth inhibitors vanadium and chromium, and to less extent molybdenum, in hardmetals upon the initial solid-state sintering stages. While in conventional hardmetal grades with grain sizes ranging from 1–10 μm solid-state grain growth can be neglected, it plays a substantial role in the production of modern ultrafine and near-nano grades. Growth onset was reported at temperatures around 1000°C in near-nano grades. Thus, a sufficient distribution of grain-growth inhibitors (GGIs) is essential already at initial sintering stages. Sintering hardmetals is a complex process with a variety of thermochemical reactions and microstructural developments appearing simultaneously. In this thesis a number of key parameters were identified to have possible influence on the distribution of GGIs and systematically analysed:

- The carbon potential
- The initial cobalt grain size
- The green density
- By which compound GGIs are introduced in the powder mixtures
- Sintering atmosphere (inert, CO, N₂)
- Binder phase composition
- The heating rate
- The shrinkage upon sintering
- Possible interdependencies of Cr/V diffusion
- Migration of cobalt by surface wetting on WC
- Grain boundary diffusion along WC/Co grain boundaries
- Carbothermic reduction of surface oxides

In order to clarify the influence of these effects a number of analytical methods was applied. Simultaneous Differential Scanning Calorimetry/Thermogravimetric Analysis (DSC/TG) allowed insight into liquid-phase formation processes, non-equilibrium reactions upon heat-up and carbothermic reactions.

Influences on the distribution of GGIs were investigated by means of the diffusion couple technique. Such diffusion couples are composed from two parts: A WC-binder body of 1 cm thickness and a GGIX-WC-binder (X =carbide, nitride, boride) layer of 100 – 200 μm thickness. After contacting the two parts the samples were annealed at various temperatures ranging from 950 – 1360°C for annealing times of range 5–330 min. Upon the annealing process the GGIs were transported from the GGI-WC-binder to the WC-binder part following the chemical potential gradient. The resulting concentration profiles were analysed by means of Electron-Probe Microanalysis (EPMA). Microstructural Analyses using Light-Optical Microscopy (LOM), Transmission-Electron Microscopy (TEM) and Scanning-Electron Microscopy (SEM) delivered complementary information on microstructural development. Three different types of diffusion couples were prepared as follows:

- **G-type** couples were prepared from hardmetal Green bodies
- **H-type** couples were prepared from pre-sintered Hardmetals
- **M-type** couples were prepared from pre-sintered Model alloys

Combining the information obtained from these samples allowed deeper insight into the distribution mechanisms of GGIs upon sintering doped hardmetals.

Hardmetals doped with various GGIs of weight ratio $c(\text{GGI}/\text{binder})=0.05$ were liquid-phase sintered with prior dwells varying from 10 min – 10h within the solid-state regime in order to gain information on the efficiency of GGIs at the initial sintering stages. Additionally a set of samples was Spark-Plasma-Sintered (SPS) at 1150°C. The samples were characterised with respect to their grain-size distribution using linear-intercept method to SEM-BSE samples.

6.2 Thermal analyses

Thermal analysis aimed to gain insight into thermal processes upon heating up WC-GGIX-binder hardmetals. WC-Co hardmetals doped with Cr_3C_2 and Cr_2O_3 with common concentrations of $c(\text{Cr}/\text{Co})=0.05$ (weight ratio) were compared to hardmetals with high chromium concentrations of $c(\text{Cr}/\text{W})=2/98\text{--}100/0$ at%. The results are depicted in Figure 6-1. It can be seen that the chromium-specific TG signals with maximum $\sim 1000^\circ\text{C}$ correlate well to a reduction step in a Cr_2O_3 -doped

hardmetals. The WC reduction signal at 800–900°C disappears at higher chromium concentrations which is related to an internal getter effect. For a detailed discussion of thermal analysis of chromium-doped hardmetals please refer to 5.1.2, page 237. In the same manner the thermal reactions of vanadium-doped hardmetals was analysed. The results are depicted in Figure 6-2. The vanadium specific TG signal at 1050–1150°C correlates well to a reduction step of V₂O₅-doped hardmetals. At higher vanadium concentrations a specific interaction between WC and vanadium oxides was detected. For detailed discussion of thermal analysis of vanadium-doped hardmetals please see section 5.1.3, page 242.

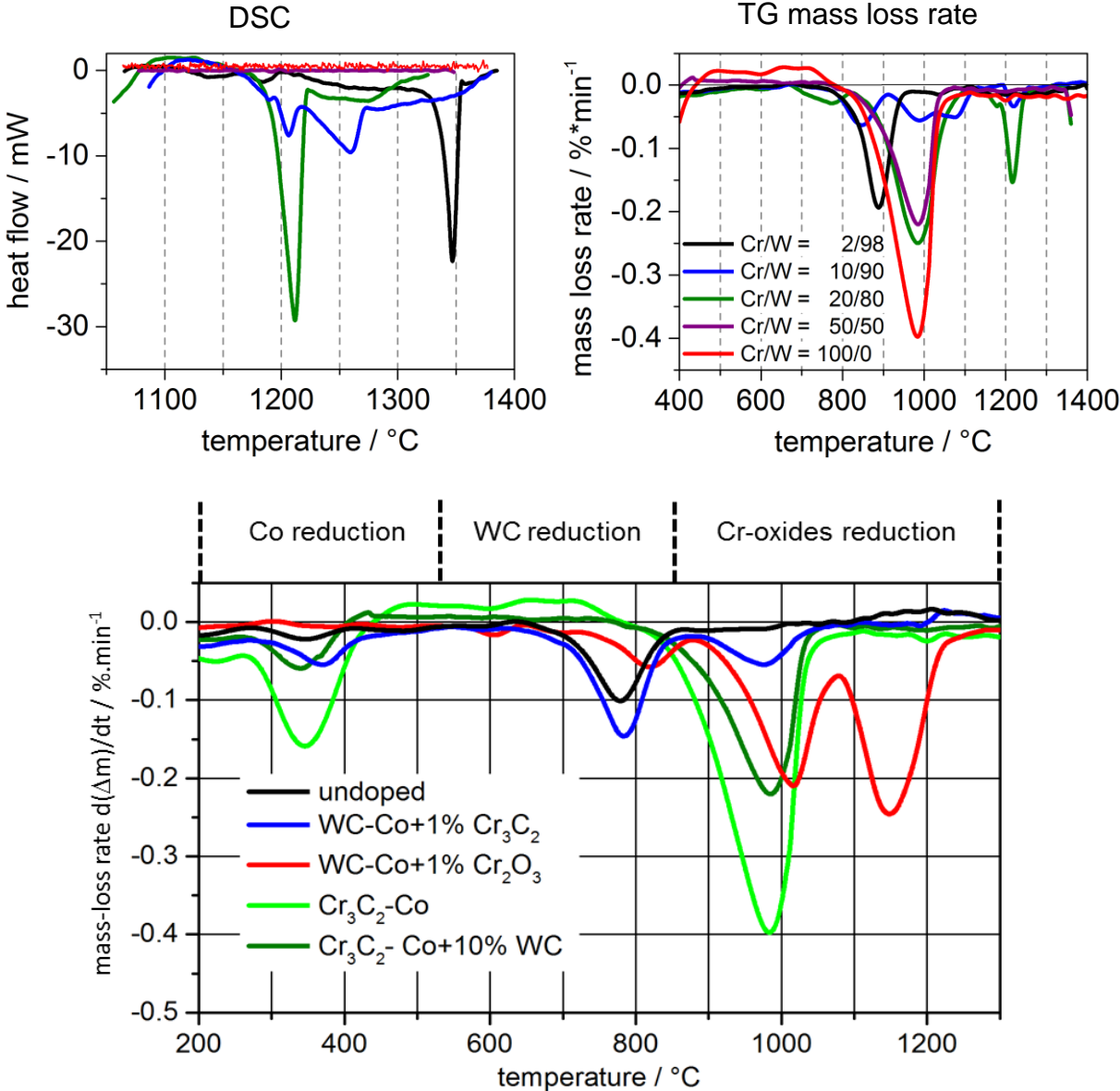


Figure 6-1: DSC upon first heat up and (top left) and mass loss rate (top right) of WC-Cr₃C₂-Co samples with varying Cr/W atomic ratios and 16.3 vol% binder. Bottom: Comparison of mass loss rate of WC-CrX-Co hardmetals.

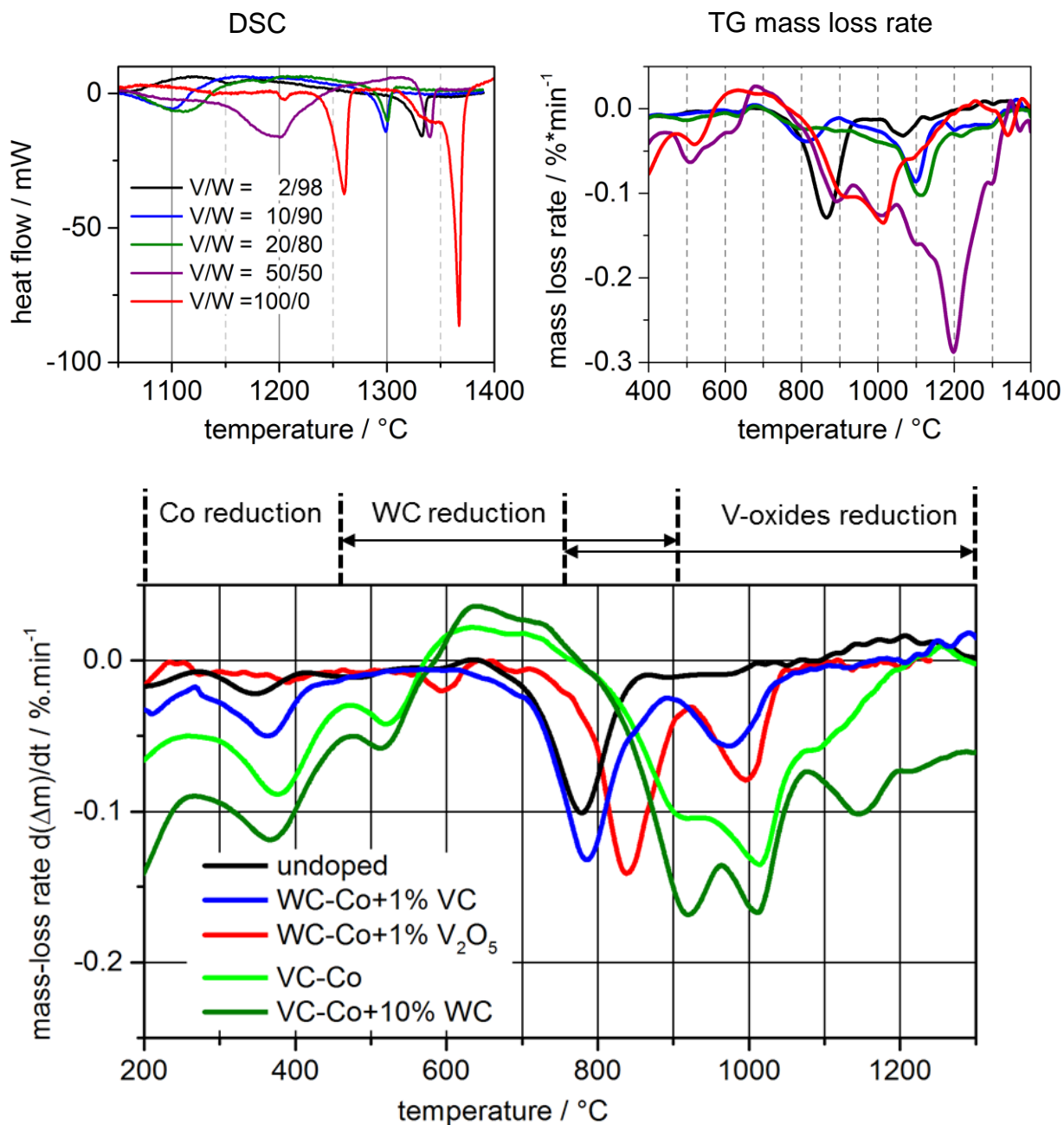


Figure 6-2: DSC upon first heat up and (top left) and mass loss rate (top right) of WC-VC-Co samples with varying V/W atomic ratios and 16.3 vol% binder. Bottom: Comparison of mass loss rate of WC-VX-Co hardmetals, X= oxide or carbide.

6.3 Parameters influencing GGI distribution

Carbon potential

The carbon potential was found to have a rather complex influence on the distribution of GGIs in hardmetal green bodies. Carbon not only influences GGI diffusion but also has impact on a variety of microstructural processes appearing upon sintering hardmetals. The transport factors calculated from concentration profiles are determined by a convolution of GGI diffusion and microstructural development. Conclusions on a specific influence of carbon on GGI diffusion were thus not possible. However, the overall influence on the GGI transport was determined. Arrhenius plots of the chromium or vanadium transport depending on the carbon potential are shown in Figure 6-3. Generally high carbon potential was found to enhance GGI transport. However, in chromium-based diffusion couples a shift to higher carbon potential was observed due to a co-diffusion of chromium and carbon. For a detailed discussion please refer to section 5.5.2, page 257.

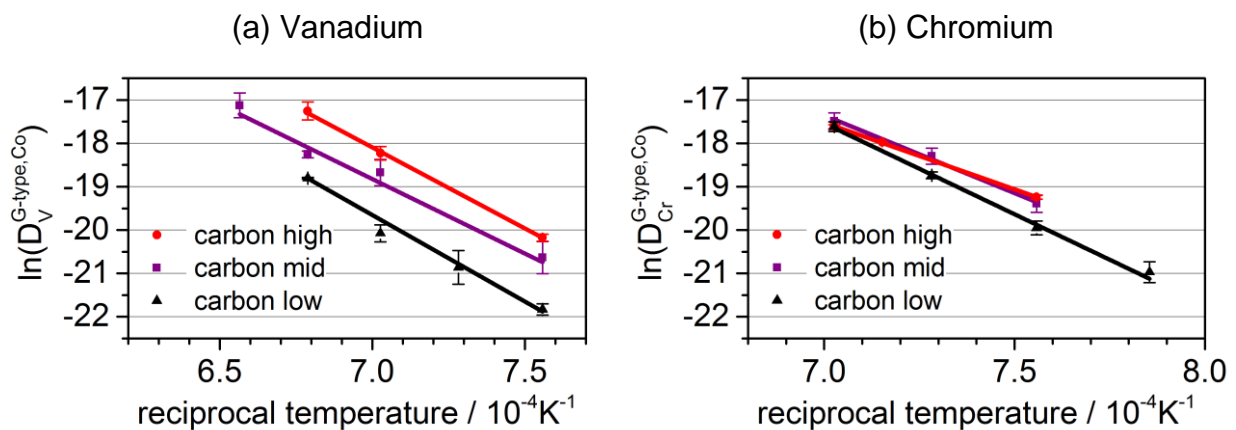


Figure 6-3: Arrhenius plots of (a) vanadium and (b) chromium transport in G-type diffusion couples with cobalt binder and varying carbon potential.

Binder alloy

A series of diffusion couples was prepared with austenitic Fe/Ni and Fe/Co/Ni binder alloys. At a temperature of 1150°C no significant influence of the binder alloy composition on the distribution of chromium and vanadium was observed, in green-body based G-type diffusion couples. In H-type couples prepared from pre-sintered

hardmetals slightly faster distribution in cobalt binder was observed as compared to hardmetals with alternative binders. For a detailed discussion on the influence of the binder alloy in H-type samples refer to section 5.4, page 252. Green-body based G-type diffusion couples are discussed in section 5.5.4, page 264.

Initial cobalt grain size

G-type diffusion couples based on either chromium or vanadium with high carbon potential were prepared with two different cobalt grain sizes. Besides the conventional grade an ultrafine grade with 0.2 μm grain size was used. Anyway, as can be seen from an Arrhenius-plot in Figure 6-4 there is no significant influence of the initial cobalt grain size on the GGI distribution. This is coincident with the findings that upon the early sintering stages GGIs are mainly distributed via the WC/Co grain boundaries and the thin layers binder layers formed by wetting of cobalt on WC grains. Their thickness is determined by thermodynamic and kinetic processes and is – within certain boundary conditions – independent from the size of the initial cobalt particles.

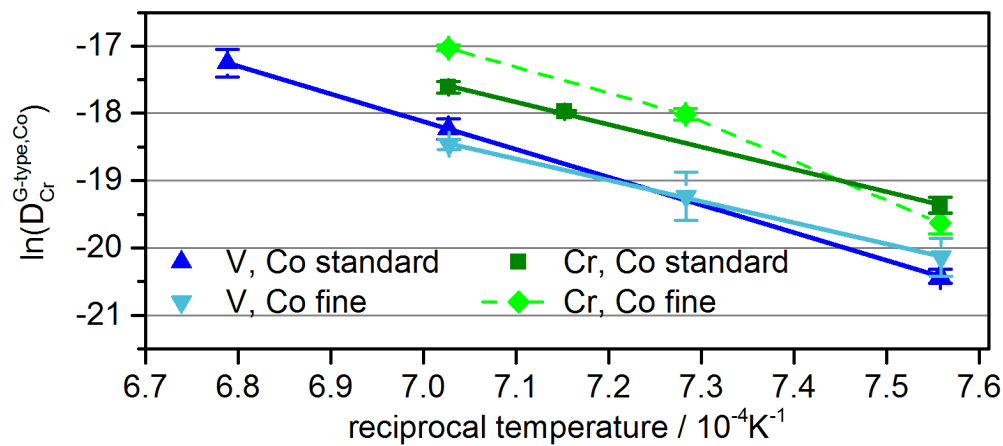


Figure 6-4: Arrhenius plot showing the dependency of chromium and vanadium distribution on the initial cobalt grain size in G-type diffusion couples.

Green density

Regarding the green density a significantly faster distribution in low-density hardmetals was detected. This effect was accompanied by formation of a cobalt gradient. The results indicate that densification processes and subsequently the wetting of binder on WC grains play a significant role on the GGI distribution in hardmetals at initial sintering stages. The particular discussion can be found in section 5.5.5, page 265.

Addition of borides

Borides were found to have a positive effect on the distribution of chromium at temperatures of 1050 and 1150°C in WC-Co hardmetals with high carbon potential. No significant influence was observed in low-carbon hardmetals. The presence of borides caused the formation of a strong cobalt gradient. Close to the interface of the diffusion couples the cobalt concentration dropped to almost zero. A detailed discussion can be found in section 5.5.7, page 274.

Sintering atmosphere

The sintering atmosphere has a strong influence on the GGI distribution at initial sintering stages. The concentration profiles of chromium within the WC-Co part of a Cr_3C_2 -WC-Co/WC-Co diffusion couple (a), a Cr_2N -WC-Co/WC-Co diffusion couple (b) and of vanadium in a VC-WC-Co/WC-Co diffusion couple (c) are depicted in Figure 6-5. For chromium a positive effect of CO but a negative effect of N_2 at 1150°C was found. This is in accordance to the finding that distribution is faster in high-carbon hardmetals, since CO is carburising. For vanadium both CO and N_2 are disadvantageous as compared to argon. In case of CO this can be attributed the oxidising effect of CO on vanadium at 1150°C. A detailed discussion can be found in section 5.5.6, page 269.

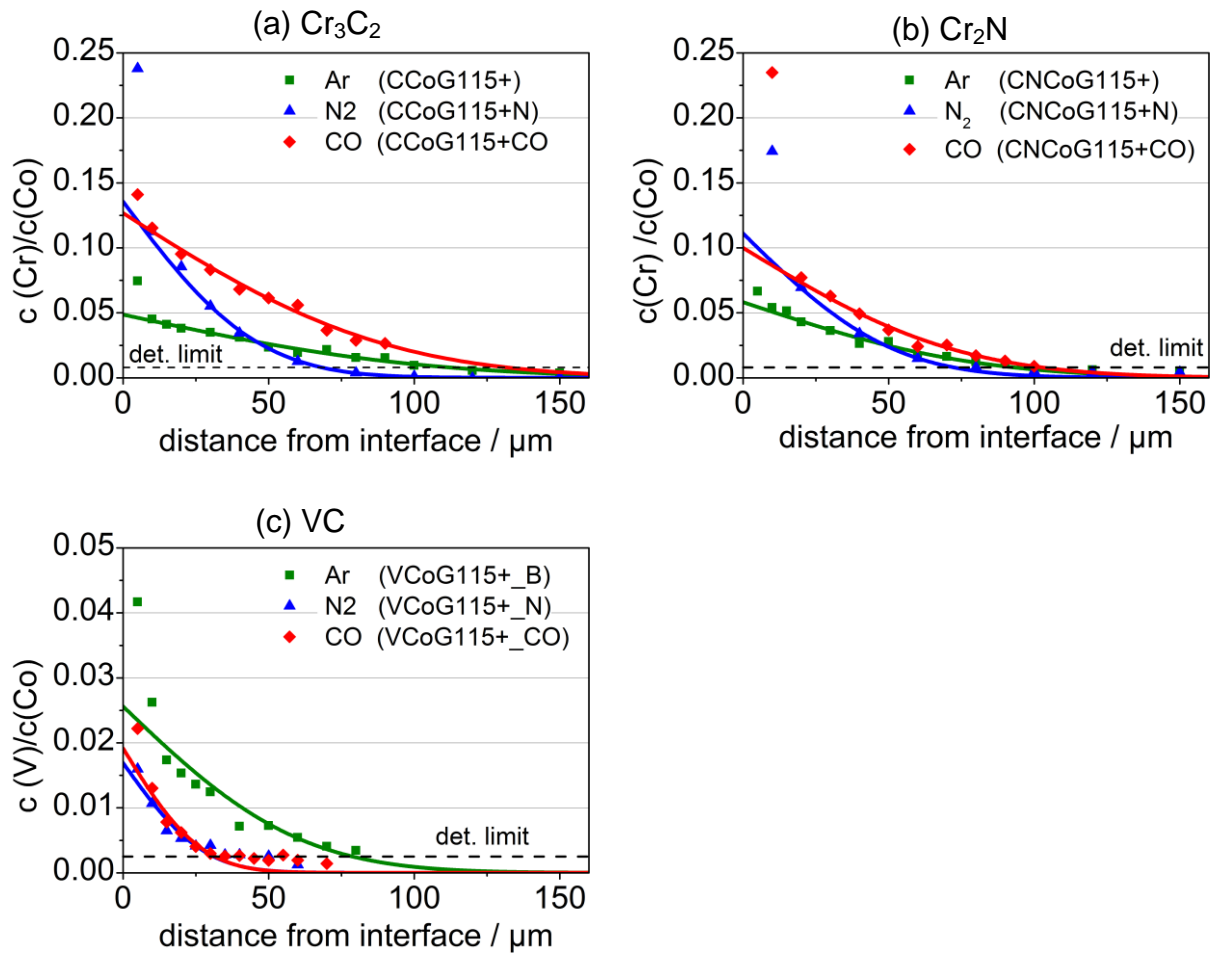


Figure 6-5: Concentration profiles of chromium or vanadium in G-type diffusion couples based on (a) Cr₃C₂, (b) Cr₂N and (c) VC annealed varying sintering atmospheres at 1150°C for 15 min.

6.4 Efficiency of GGIs at initial sintering stages

The efficiency of GGIs at the initial sintering stages was investigated by means of two different samples series. The first series was based on GGIX doped SPS samples. The second series is based on liquid-phase sintered, doped hardmetals. Prior to the appearance of liquid phase a dwell time at 1000–1150°C for 10 min–10 h was applied. Both series had fixed carbon potential (graphite <precipitations) and were analysed by means of SEM-BSE micrographs. The following conclusions were drawn:

- The temperature range <math><1150^{\circ}\text{C}</math> generally has a rather small influence on the grain growth in liquid-phase sintered ultrafine hardmetals with high carbon potential
- In hardmetals prepared from conventional WC DS50 no substantial benefit of 0.6 wt%Cr₃C₂ + 0.4 wt% VC double-doping as compared 0.6 wt% VC single doping in samples SPSed at 1150°C as well as samples liquid-phase sintered at 1380°C was found. However, a substantial benefit of double doping was found if an WC DS50m (DS50 attritor-milled for 24h) is used.
- Doping of chromium carbide has no advantage upon SPS at 1150°C as compared to undoped samples. An inhibiting effect was found by the use of Cr₂N as a chromium source.
- The relative inhibiting effect of chromium as compared to undoped sample in liquid-phase sintered hardmetals increases with increasing dwell time at 1150°C, indicating a reaction between Cr and WC.
- From TEM analysis a clear segregation of vanadium at the WC/Co interface was observed, but not of chromium. V-rich precipitates of 10–20 nm size were observed at particular WC/WC/Co triple junctions.

The particular results from SPS-experiments are discussed in section 4.7.3, page 217. The results for doped, liquid-phase sintered hardmetals are shown in section 4.7.2, page 204. The detailed discussion on the efficiency of GGIs upon solid state sintering can be found in section 5.7, page 285.

6.5 Transport mechanisms of GGIs upon sintering

By combining the data obtained from G-, M- and H-type samples and the findings from TEM-analysis conclusions on the transport mechanisms of GGIs at initial sintering stages were drawn. The main finding is that GGI transport in hardmetal green bodies is substantially faster than GGI diffusion in fcc binder metals. The formation of a thin, continuous binder network by wetting on WC grains seems to be the critical process. The particular conclusions on the GGI distributions can be summarised as follows:

- There is evidence that substantial amounts of GGIS diffuse via grain boundaries and surfaces by the thin binder layers covering WC grains at initial sintering stages.
- Besides diffusion, microstructural changes such as densification and binder wetting on WC further enhance the GGI transport.
- The transport factors at 1150°C in hardmetal green bodies are by a factor of 500–1000 higher than GGI diffusion in pure bulk fcc-cobalt
- The activation energies of 300 ± 50 kJ/mol calculated in this project are a convolved measure for thermal activation of diffusion and temperature dependent microstructural changes.
- The interface concentrations $c_0(\text{Cr/Co})$ obtained from fitting the diffusion model the experimental data for chromium transport are identical to the solubilities of chromium in hardmetals. Evidence was found that chromium is quantitatively located in the binder phase
- For vanadium the measured interface concentrations $c_0(\text{V/Co})$ are much higher than expected from literature data. It was assumed that a part of vanadium is not located in the binder phase but at the WC/Co interfaces.

For a detailed discussion on the GGI transport please refer to section 5.6, page 279.

6.6 Conclusions for hardmetal production

In industrial hardmetal production grain-growth inhibitors are commonly added as carbide or nitride powders. For ultrafine grained hardmetals, usual GGIX grain sizes are around 1–2 μm and thus by a factor 5–10 larger than the WC grain size. From the distribution data obtained in this work it was found that for liquid-phase sintered hardmetals these grain sizes are in any case sufficient, no benefit is expected from finer powders. The distribution mainly appears via surface and interface diffusion and is fast already at relatively low temperatures around 1000°C. An upper limit of the GGIX grain size is determined by pores left back after GGIX dissolution and is around 2–3 μm . These considerations do not apply for SPSed near-nano hardmetals with short sintering times. For such materials fine GGI powders are beneficial. A detailed discussion on this topic can be found in section 5.8, page 289.

7 Literature

- [55KÖS] W. Köster and F. Sperner
Das Dreistoffsystem Kobalt–Chrom–Kohlenstoff
Arch. Eisenhüttenwesen 26: 555–559 (1955)
- [72HAY] K. Hayashi, Y. Fuke and H. Suzuki
Effects of Addition Carbides on the Grain Size of WC-Co Alloy
Journal of the Japanese Society of Powder and Powder Metallurgy, 19, 67-71 (1972)
- [73GRE] H. Grewe, H. E. Exner and P. Walter
Inhibiting of Grain Coarsening in Cemented Carbides of the ISO-K 10 Type by Carbide Additions
Zeitschrift fuer Metallkunde/Materials Research and Advanced Techniques, 64[2]: 85-93 (1973)
- [79PRA] L. Prakash
Dissertation: Weiterentwicklung von Wolframcarbid Hartmetallen unter Verwendung von Eisenbasis-Bindelegierungen (Development of WC-Co hardmetals based on iron-nickel binder alloys), Universität Karlsruhe, (1979)
- [85SHE] D. K. Shetty, I. G. Wright, P. N. Mincer and A. H. Clauer
Indentation Fracture of WC-Co Cermets
Journal of Materials Science, 20[5]: 1873-82 (1985)
- [86SHE] D. K. Shetty and I. G. Wright
On Estimating Fracture-Toughness of Cemented Carbides from Palmqvist Crack Sizes
Journal of Materials Science Letters, 5[3]: 365-68 (1986)
- [87ALM] A. Almond and B. Roebuck
Very-fine-grained hardmetals
International Journal of Refractory Metals and Hard Materials, 6[3]: 137–44 (1987)
- [87GUI] A. F. Guillermet
Thermodynamic Analysis of the Co-C System
Zeitschrift Für Metallkunde 78[10]: 700–09 (1987)
- [88GUI] A .F. Guillermet
Study of the Thermodynamic Properties of the Co-Fe-Ni-W-C System Using CALPHAD Techiques
Thesis, Royal Institute of Technology, Stockhol, Sweden (1988)
- [90CER] J. Cermák, F. Rollert, H. Mehrer
Diffusion of carbon-14 in fcc cobalt
Zeitschrift Metallkunde 81: 81 (1990)

- [91FUK] T. Fukatsu, K. Kobori and M. Ueki
Micro-grained cemented carbide with high strength
International Journal of Refractory Metals and Hard Materials, 10[2]: 57-60
(1991)
- [95FAN] Z. G. Fang and J. W. Eason
Study of Nanostructured WC-Co Compositea
International Journal of Refractory Metals & Hard Materials, 13[5]: 297-303
(1995)
- [95ROE] B. Roebuck
Terminology, Testing, Properties, Imaging and Models for Fine-Grained
Hardmetals
International Journal of Refractory Metals & Hard Materials, 13[5]: 265-79
(1995)
- [95SCH] W. D. Schubert, A. Bock and B. Lux
General Aspects and Limits of Conventional Ultrafine WC Powder
Manufacture and Hard Metal Production
International Journal of Refractory Metals & Hard Materials, 13[5]: 281-96
(1995)
- [95SPR] G. E. Spriggs
A History of Fine-Grained Hardmetal
International Journal of Refractory Metals & Hard Materials, 13[5]: 241-55
(1995)
- [96POR] R. Porat, S. Berger, A. Rosen
Dilatometric study of the Sintering mechanisms of Nanocrystalline Cemented
Carbides
Nanostructured Materials 7[4]: 129–36 (1996)
- [97GIL] G. Gille, B. Szesny and G. Leitner
A new 0.4 μm WC powder as well as powder related properies and sintering
behaviour of 0.6-3 μm WC-Co hardmetals
Proceedings of the 14th Plansee Seminar, Reutte, Austria, 2, 163-67 (1997)
- [98ARA] P. Arato, L. Bartha, R. Porat, S. Berger and A. Rosen
Solid or liquid phase sintering of nanocrystalline WC/Co hardmetals
Nanostructured Materials, 10[2]: 245-55 (1998)
- [98GEN] M.E. Generalov, V.A. Naumov, A.V. Mokhov, N.V. Trubkin
Isovite (Cr,Fe)₂₃C₆ - a new mineral from the gold-platinum bearing placers of
the Urals", Zapiski Vserossiyskogo mineralogicheskogo obshchestva. 127,
26–37(1998)
- [98HAG] S. Haglund, J. Ågren and B. Uhrenius
Solid state sintering of cemented carbides - An experimental study
Zeitschrift Fur Metallkunde, 89[5]: 316-22 (1998)
- [98HAG1] S. Haglund, J. Ågren
W Content in Co binder During Sintering of WC-Co
Acta Metallurgica 46[8]: 2801–7 (1998)

- [98ZAC] J. Zackrisson, B. Jansson, G.S. Uphadyaya, H.O. Andrén
WC-Co based cemented carbides with large Cr₃C₂ additions
International Journal of Refractory Metals and Hard Materials 16: 417–22
(1998)
- [99CAR] D. F. Carroll
Sintering and microstructural development in WC/Co-based alloys made with
superfine WC powder
International Journal of Refractory Metals & Hard Materials, 17[1-3]: 123-32
(1999)
- [00ROE] B. Roebuck
Measurement of grain size and size distribution in engineering materials
Materials Science and Technology, 16[10]: 1167-74 (2000)
- [00YAM] T. Yamamoto, Y. Ikuhara and T. Sakuma
High resolution transmission electrom microscopy study in VC-doped WC-Co
compound
Science and Technology of Advanced Materials, 1[97-104] (2000)
- [01ALL] C. H. Allibert
Sintering features of cemented carbides WC-Co processed from fine powders
International Journal of Refractory Metals & Hard Materials, 19[1]: 53-61
(2001)
- [01CHA] S. I. Cha, S. H. Hong, G. H. Ha and B. K. Kim
Microstructure and mechanical properties of nanocrystalline WC-10Co
cemented carbides
Scripta Materialia, 44[8-9]: 1535-39 (2001)
- [01OBB] E.G. Obbard, S. Luyckx, S. Hamar-Thibault, C.H. Allibert
Determination of the composition range suitable to the formation of WC-
(V,W)_x-Co materials
International Journal of Refractory Metals and Hard Materials 19, 349–57
(2001)
- [01SAI] T. Sailer, M. Herr, H.G. Sockel, R. Schulte, H. Feld, L.J. Prakash
Microstructure and mechanical properties of ultrafine-grained hardmetals
International Journal of Refractory Metals & Hard Materials, 19: 553–59
(2001)
- [01SIL] A. G. P. da Silva, W. D. Schubert and B. Lux
The role of the Binder Phase in WC-Co Sintering
Materials Research, 4[2]: 59-62 (2001)
- [01LAY] S. Lay, S. Hamar-Thibault and A. Lackner
HREM characterisation of VC in doped WC-Co Cermets
Proceedings of the 15th International Plansee Seminar, Reutte, Austria, 50-64
(2001)

- [01YAM] T. Yamamoto, Y. Ikuhara, T. Watanabe, T. Sakuma, Y. Taniuchi, K. Okada and T. Tanase
High resolution microscopy study in Cr₃C₂-doped WC-Co
Journal of Materials Science, 36[3]:885-90 (2001)
- [02GIL] G. Gille, B. Szesny, K. Dreyer, H. van den Berg, J. Schmidt, T. Gestrich and G. Leitner
Submicron and ultrafine grained hardmetals for microdrills and metal cutting inserts
International Journal of Refractory Metals & Hard Materials, 20[1]: 3-22 (2002)
- [02LAY] S. Lay, S. Hamar-Thibault and A. Lackner
Location of VC in VC, Cr₃C₂ codoped WC-Co cermets by HREM and EELS
International Journal of Refractory Metals & Hard Materials, 20[1]: 61-69 (2002)
- [02SAI] T. Sailer
Dissertation: Ultrafeinkörnige Hartmetalle mit Co-Binder und alternativen Bindersystemen -Korrelation von Mikrostruktur und mechanischem Verhalten unter monoton ansteigender und zyklisch wechselnder Beanspruchung
Universität Erlangen-Nürnberg, (2002)
- [02SOM] M. Sommer, W.D. Schubert, E. Zobetz and P. Warbichler
On the formation of very large WC crystals during sintering of ultrafine WC-Co alloys
International Journal of Refractory Metals & Hard Materials, 20[1]: 41-50 (2002)
- [02WIT] B. Wittmann, W. D. Schubert and B. Lux
WC grain growth and grain growth inhibition in nickel and iron binder hardmetals
International Journal of Refractory Metals & Hard Materials, 20[1]: 51-60 (2002)
- [03MAC] H. R. de Macedo, A. G. P. da Silva and D. M. A. de Melo
The spreading of cobalt, nickel and iron on tungsten carbide and the first stage of hard metal sintering
Materials Letters, 57[24-25]: 3924-32 (2003)
- [03CHA] V. Chabretou, C. H. Allibert and J. M. Missiaen
Quantitative analysis of the effect of the binder phase composition on grain growth in WC-Co sintered materials
Journal of Materials Science 38[12]: 2581-90 (2003)
- [03LAY] S. Lay and M. Loubradou
Characteristics and origin of clusters in submicron WC-Co cermets
Philosophical Magazine, 83[23]: 2669-79 (2003)
- [03LAY1] S. Lay, J. Thibault and S. Hamar-Thibault
Structure and role of the interfacial layers in VC-rich WC-Co cermets
Philosophical Magazine, 83[10]: 1175-90 (2003)

- [03LEE] H. R. Lee, D. J. Kim, N. M. Hwang and D. Y. Kim
Role of vanadium carbide additive during sintering of WC-Co: Mechanism of grain growth inhibition
Journal of the American Ceramic Society, 86[1]: 152-54 (2003)
- [04DEL] A. Delanoe, M. Bacia, E. Pauty, S. Lay and C. H. Allibert
Cr-rich layer at the WC/Co interface in Cr-doped WC-Co cermets: segregation or metastable carbide?
Journal of Crystal Growth, 270[1-2]: 219-27 (2004)
- [04HUA] S. Huang, L. Li, O. van der Biest and J. Vlugels
Thermodynamic assessment of the Co-V and Co-V-C System
Journal of Alloys and Compounds 385: 114–18 (2004)
- [04KAW] M. Kawakami, O. Terada and K. Hayashi
Effect of sintering Cooling Rate on V Segregation Amount at WC/Co Interface in VC-doped WC-Co Fine-Grained Hardmetal
Journal of the Japanese Society of Powder and Powder Metallurgy, 51[8]: 576-85 (2004)
- [04LEI] G. Leitner, T. Gestrich and K. J. Rößler
Sintern von Hartmetallen – Thermoanalytische Simulation
Pulvermetallurgie – Kompetenz und Perspektive 20: 97-116 (2004)
- [05COL] M. Collin and S. Norgren
Hardness Gradients in WC-Co created by local addition of Cr₃C₂
Proceedings of the 16th Plansee Seminar, Reutte, Austria, [HM5], 227–40 (2005)
- [05DEL] A. Delanoe, J. M. Missiaen, C. H. Allibert, S. Lay and E. Pauty
Effects of the C-potential and Cr doping on the densification of alloys WC-Co
Proceedings of the 16th Plansee Seminar, Reutte, Austria, [HM43], 642–52 (2005)
- [05ELF] M. Elfving and S. Norgren
Study of solid-state sintered fine-grained cemented carbides
International Journal of Refractory Metals & Hard Materials, 23[4-6]: 242–48 (2005)
- [05FAN] Z. Fang, P. Maheshwari, X. Wang, H. Y. Sohn, A. Griffo and R. Riley
An experimental study of the sintering of nanocrystalline WC-Co powders
International Journal of Refractory Metals & Hard Materials, 23[4-6]: 249–57 (2005)
- [05HUA] S. Huang, L. Li, J. Vlugels and O. van der Biest
Thermodynamics and Microstructures of Co-V₈C₇ Alloy
Materials Science Forum 492: 523–30 (2005)
- [05KAW] M. Kawakami, O. Terada and K. Hayashi
Segregation amount of dopants at WC/Co Interface in Cr₃C₂ and VC+Cr₃C₂-Doped WC-Co Submicro-Grained Hardmetals
Proceedings of the 16th Plansee Seminar, Reutte, Austria, [HM44], 653–67 (2005)

- [05LIN] C. Lin and G. Yuan
Effects of Rare Earths on the Microstructure of Nanocrystalline WC-VC-10Co Hardmetals
Proceedings of the 16th Plansee Seminar, Reutte, Austria, 2, 363–77 (2005)
- [05MOR] C. W. Morton, D. J. Wills and K. Stjernberg
The temperature ranges for maximum effectiveness of grain growth inhibitors in WC-Co alloys
International Journal of Refractory Metals & Hard Materials, 23[4–6]: 287–93 (2005)
- [05PET] A. Petersson and J. Ågren
Rearrangement and pore size evolution during WC-Co sintering below the eutectic temperature
Acta Materialia, 53[6]: 1673–83 (2005)
- [05SAN] J. M. Sanchez, A. Ordonez, R. Gonzalez
HIP after sintering of ultrafine WC-Co hardmetals
International Journal of Refractory Metals and Hard Materials, 23[3]: 193–98 (2005)
- [05WAN] H.-T. Wang, X. Wang and Y.-N. Yu
Study of Grain Growth of Nanocrystalline WC/Co Powder in the Early Stage of Sintering [J]
Rare Metals and Cemented Carbides, 1[6] (2005)
- [06ADO] A. Adorjan, W. D. Schubert, A. Schön, A. Bock and B. Zeiler
WC grain growth during the early stages of sintering
International Journal of Refractory Metals and Hard Materials, 24[5]: 365–73 (2006)
- [06GES] T. Gestrich, K. Jaenicke-Roessler and G. Leitner
Investigation of Processes During Sintering of Hardmetal by Means of Thermal Analysis
Proceedings of the EURO PM2006 Congress & Exhibition, Ghent, Belgium, 1: Hard Materials, 145-50 (2006)
- [06KAW] M. Kawakami, O. Terada and K. Hayashi
HRTEM Microstructure and Segregation Amount of Dopants at WC/Co Interfaces in TiC and TaC Mono-doped WC-Co Submicro-grained Hardmetals
Journal of the Japanese Society of Powder and Powder Metallurgy, 53[2]: 166–71 (2006)
- [06LAU] L. Lauter
Dissertation: Einfluss von Dotierungselementen auf das Gefüge und die Eigenschaften von WC-Co-Hartmetallen (Influence of dopants on the microstructure and properties of WC-Co hardmetals)
Institute of Chemical Technologies and Analytics, Faculty of Technical Chemistry, Vienna University of Technology (2006)
- [06LIU] S. Liu, Z. L. Huang, G. Liu and G. B. Yang
Preparing nano-crystalline rare earth doped WC/Co powder by high energy ball milling
International Journal of Refractory Metals & Hard Materials, 24[6]: 461–64 (2006)

- [06SEO] O. Seo and S. Kang
On the dissolution of WC in WC-Co alloys
Science of Engineering Ceramics III, 317-318[2]63-66 (2006)
- [06STE] T. Sterneland, A. Markström, R. Aune, S. Norgren and S. Seetharaman
Investigation of (Cr,Co)₇C₃-graphite equilibrium in the temperature interval
1373–1473K,
Metallurgical and Materials Transactions A 37[A]: 3023–28 (2006)
- [06VIL] M. Viljus, J. Pirso and S. Letunovits
Low Temperature Synthesized WC and Its Usability for Fine-Grained
Hardmetal
Proceedings of the EURO PM2006 Congress & Exhibition, Ghent, Belgium, 1,
281–86 (2006)
- [07HE] Y He, L. Li, S. Huang, J. Vleugels and O. Van der Biest
Computer simulating the diffusion behaviour of V and W in Co binder layer of
WC–Co cemented carbide
Journal of Alloys and Compounds 436: 146–49 (2007)
- [07LI] N. Li, Y. Qiu, W. Zhang, Y. Wen, Y. Zhang, Y. Zhou
Influence and function of inhibitor VC/Cr₃C₂ on the grain growth in super fine
WC-Co cermets
Xiyou Jinshu Cailiao Yu Gongcheng/Rare Metal Materials and Engineering
36[10]: 1763–66 (2007)
- [07FU] L. Fu, F. Qu and H. Chen
Mechanical drilling of printed circuit boards: the state-of-the-art
Circuit World, 33[4]: 3–8 (2007)
- [07GRI1] B. Gries and L. Prakash
Iron bonds to curb hardmetal's more lethal tendencies
Metal Powder Report, 62[11]: 15–17 (2007)
- [07GUS] P. Gustafson, M. Waldenström, S. Norgren
Method of making a fine grained cemented carbide
Patent EP1500713 B1 (2007)
- [07HUA] S.G. Huang, L. Li, K. Vanmeensel, O. Van der Biest and J. Fluegels
VC, Cr₃C₂ and NbC doped WC-Co cemented carbides prepared by pulsed
electric current sintering
International Journal of Refractory Metals & Hard Materials, 25[5–6]: 417–22
(2007)
- [07MAH] P. Maheshwari, Z. G. Z. Fang and H. Y. Sohn
Early-stage sintering densification and grain growth of nanosized WC-Co
powders
International Journal of Powder Metallurgy, 43[2]: 41–47 (2007)

- [07MEH] H. Mehrer
Diffusion in Solids: Fundamentals, Methods, Materials, Diffusion-Controlled Processes
Springer Series in Solid State Science 155, Springer Verlag Berlin Heidelberg (2007)
- [07SCH] G. K. Schwenke and J. V. Sturdevan
Magnetic saturation & coercivity measurements on chromium-doped cemented carbides
International Journal of Powder Metallurgy, 43[2]: 21-31 (2007)
- [07SUN] L. Sun, C. C. Ha and M. Xian
A research on the grain growth of WC-Co cemented carbide
International Journal of Refractory Metals & Hard Materials, 25[2]: 121–24 (2007)
- [07SUN1] I. Sun, C-C. Jia, A-G. Lin, R-J. Cao
VC addition prepared ultrafine WC-11Co composites by spark plasma sintering
Journal of Iron and Steel Research, International 14[5]: 85–89 (2007)
- [08FRI] K. Frisk and A. Markström
Effect of Cr and V on phase equilibria in Co-WC based hardmetals
International Journal of Materials Research, 99[3]: 287–93 (2008)
- [08WAN] X. Wang, Z. Z. Fang and H. Y. Sohn
Grain growth during the early stage of sintering of nanosized WC-Co powder
International Journal of Refractory Metals and Hard Materials, 26[3]: 232–41 (2008)
- [09BOU] V. Bounhoure, J. M. Missiaen, S. Lay and E. Pauty
Discussion of Nonconventional Effects in Solid-State Sintering of Cemented Carbides
Journal of the American Ceramic Society, 92[7]: 1396–402 (2009)
- [09BRI] M. Brieseck, I. Hünsche B. Caspers, B. Szesny, G. gille and W. Lengauer
Optimised sintering and Grain-Growth Inhibition of Ultrafine and Near-Nano Hardmetals
Proceedings of the Euro PM2009, Copenhagen, Denmark, Vol.1: Hardmetals and Cermets (2009)
- [09DEL1] A. Delanoe and S. Lay
Evolution of the WC grain shape in WC-Co alloys during sintering: Cumulated effect of the Cr addition and of the C content
International Journal of Refractory Metals & Hard Materials, 27[2]: 189–97 (2009)

- [09FAN] Z. Z. Fang, X. Wang, T. Ryu, K. S. Hwang and H. Y. Sohn
Synthesis, sintering, and mechanical properties of nanocrystalline cemented tungsten carbide - A review
International Journal of Refractory Metals and Hard Materials, 27[2]: 288–99 (2009)
- [09HAS] M. Hashiya, Y. Kubo, C. Gierl and W. D. Schubert
The influence of Carbon content and Additions of Growth inhibitors (V,Cr) on the formation of melt in WC-Co and WC-Ni alloys
Proceedings of the 17th Plansee Seminar, Reutte, Austria, 2, [HM55/1], (2009)
- [09KON] I. Konyashin, S. Hlawetschek, B. Ries and F. Lachmann
Gradient WC-Co Structures Obtained by Regulated WC Re-Crystallization without using Grain Growth Inhibitors.
Proceedings of the 17th Plansee Seminar, Reutte, Austria, 6/1–6/12 (2009)
- [09KÖK] S. Köksal
The Characterization of WC-Co Based Materials Boronized within Molten Salt Bath
Solid State phenomena 144: 261–66 (2009)
- [09NEU] G. Neumann, and C. Tujin
Self-Diffusion and Impurity Diffusion in pure Metals: Handbook of Experimental Data
Pergamon Materials Series 14, Elsevier (2009)
- [09PRA] L. Prakash and B. Gries
WC Hardmetals with Iron Based Binders
Proceedings of the 17th Plansee Seminar, Reutte, Austria, 2, [HM5], (2009)
- [09WAN] X. Wang, Z.Z. Fang, H. Zhang, V. Kumar and H.Y. Sohn
WC Grain Growth During Heat-Up of Nanocrystalline WC-Co
Proceedings of the 17th Plansee Seminar, Reutte, Austria, 2 [HM12] (2009)
- [10BRI] M. Brieseck, M. Bohn and W. Lengauer
Diffusion and solubility of Cr in WC
Journal of Alloys and Compounds, 489[2]: 408–14 (2010)
- [10BRI1] M. Brieseck
Dissertation: Der Effekt von Kornwachstumshinhibitoren auf die Sinterverdichtung, Gefügeentwicklung und mechanischen Eigenschaften nanoskaliger und ultrafeinkörniger WC-Co-Hartmetalle (The effect of grain-growth inhibitors on the mechanical properties of near-nano and ultrafine WC-Co hardmetals)
Insitute of Chemical Technologies and Analytics, Vienna University of Technology, (2010)
- [10CAS] B. Caspers, T. Säuberlich and M. Zumdick
Early stage of sintering in near-nano WC/Co hardmetals
Proceedings of the World Powder Metallurgy Congress and Exhibition, World PM 2010, Florenz, Italy, 3, (2010)

- [10JOH] S. A. E. Johansson and G. Wahnstrom
Theory of ultrathin films at metal-ceramic interfaces
Philosophical Magazine Letters, 90[8]: 599-609 (2010)
- [10KOO] R. Koos
Master Thesis: Eigenschaften von Hartmetallen mit Fe/Co/Ni Bindern
(Properties of hardmetals with Fe/Co/Ni binder alloys)
Vienna University of Technology (2010)
- [10KON] I. Konyashin, S. Hlawatschek, B. Ries, F. Lachmann, A. Sologubenko and
T. Weirich
A New Approach to Fabrication of Gradient WC-Co Hardmetals
International Journal of Refractory Metals and Hard Materials 18: 228–37
(2010)
- [10LEN] W.Lengauer, M.Bohn, H.Hochenauer and L.Lauter
Binder phase analysis for property improvement of WC-Co and
WC-TiC-(Ta,Nb)C-Co hardmetals
Proceedings of the World PM 2010, Florence (I), Vol.3, paper 513, CD-ROM
Edition, EPMA, Shrewsbury UK (2010)
- [10NPL] Web Resource provided by NPL
Calculated B-Co phase diagram
<http://resource.npl.co.uk/mtdata/phdiagrams/bfe.htm>.
Website update: 11.09.2010. Download: 5.7.2015
- [10WEI] J. Weidow and H. O. Andr en
Grain and phase boundary segregation in WC-Co with small V, Cr or Mn
additions
Acta Materialia, 58[11]: 3888-94 (2010)
- [11BON] V. Bonache, M. D. Salvador, A. Fern andez and A. Borell
Fabrication of full density near-nanostructured cemented carbides by
combination of VC/Cr₃C₂ addition and consolidation by SPS and HIP
technologies
International Journal of Refractory Metals and Hard Materials 29[2]:202–08
(2011)
- [11GAR] J. Garcia and O. Prat
Experimental investigations and DICTRA simulations on formation of
diffusion-controlled fcc-rich surface layers on cemented carbides
Applied Surface Science 257[21]: Pages 8894–900 (2011)
- [11SUN] L. Sun, T. Yang, C. Jia and J. Xiong
VC, Cr₃C₂ doped ultrafine WC-Co cemented carbides prepared by spark
plasma sintering
International Journal of Refractory Metals and Hard Materials 29[2]:147–52
(2011)

- [11WAG] S. Wagner
Dissertation: Hartmetalle mit alternativen Bindern: Aufbau und Eigenschaften (Hardmetals with alternative binder alloys: structure and properties)
Institute of Chemical Technologies and Analytics, Vienna University of Technology (2011)
- [11WEI] J. Weidow, S. Johansson, H.O. Andr en, G. Wahnstr m
Transition metal solubilities in cemented carbide materials
Journal of the American Ceramic Society 94[2]: 605–10 (2011)
- [12BRI] M. Brieseck, I. Hunsche, B. Caspers, G. Gille, M. Bohn and W. Lengauer
Diffusion Behaviour of the Grain-Growth Inhibitor VC in Hardmetals
Diffusion in Materials - Dimat 2011, 323-325[509-14 (2012)
- [12BUC] C. Buchegger
Diploma Thesis: Eigenschaften von Hartmetallen mit alternativen Bindern (Properties of hardmetals with alternative binder alloys)
Institute for Chemical Technologies and Analytics, Vienna University of Technology, (2012)
- [12JOH] S. A. E. Johansson and G. Wahnstrom
First-principles study of an interfacial phase diagram in the V-doped WC-Co system
Physical Review B, 86[3] (2012)
- [12KON] I. Konyashin, S. Hlawetschek, B. Ries and A.T. Fry
A novel sintering technique for fabrication of functionally graded WC-Co cemented carbides
Journal of Materials Science 47: 7072–84 (2012)
- [12LAY] S. Lay, M. Loubradou, S. A. E. Johansson and G. Wahnstr m
Interface structure in a WC–Co alloy co-doped with VC and Cr₃C₂
Journal of Materials Science 47:1588–93 (2012)
- [12RIC] V. Richter, J. Poetschke, R. Holke
Development of the Microstructure of Nanostructures Materials during Sintering
Proceedings of the World PM2012, Yokohama, Japan: 18C-S2-33 (2012)
- [12SUG] I. Sugiyama, Y. Mizumukai, T. Taniuchi, K. Okada, F. Shirase, T. Tanase, Y. Ikuhara and T. Yamamoto
Formation of (W,V)C-x layers at the WC/Co interfaces in the VC-doped WC-Co cemented carbide
International Journal of Refractory Metals & Hard Materials, 30[1]: 185-87 (2012)
- [12WET] M. Wetzel, S. Wawrzik, C. Buchegger, C. Gierl and W. Lengauer
Interaction of nitrogen with WC and nitrogen-assisted sintering of hardmetals
Proceedings of the International Euro Powder Metallurgy Congress and Exhibition, Euro PM2012, 2 (2012)

- [13BUC] C. Buchegger, J. Langlade and W. Lengauer
Interdependencies of Grain-Growth Inhibitor Diffusion in WC-Co hardmetals
Proceedings of the 18th Plansee Seminar, Reutte, Austria, HM73, 1587-97
(2013)
- [13BUC2] C. Buchegger and W. Lengauer
Creep Behaviour of Hardmetals with Alternative Binder Alloys at Elevated
Temperatures
Proceedings of the 18th Plansee Seminar, Reutte, Austria, HM85, 1685–93
(2013)
- [13ESP] L. Espinosa-Fernández, A. borelli, M.D. Salvador and C. F. Gutierrez-
Gonzalez
Sliding wear behaviour of WC-Co-Cr₃C₂-VC composites fabricated by
conventional and non-conventional techniques
Wear 307[1–2]: 60–67 (2013)
- [13GEN] R. Genga, L. A. Cornish and G. Akdogan
Optimization of WC Particle Size, Ni Binder Content and Mo₂C Addition for
Improved SPS WC-TiC-Ni Cemented Carbides
Proceedings of the 18th Plansee Seminar, Reutte, Austria, (2013)
- [13RIC] V. Richter, J. Poetschke, R. Hole and A. Michaelis
Nanoscaled Hardmetals - Fiction or Reality?
Proceedings of the 18th Plansee Seminar, Reutte, Austria, (2013)
- [13TOU] C. Toufar, W. D. Schubert, M. Hashiya and Y. Kubo
On the Formation of Precipitations in Highly (Cr,V)-doped Cemented Carbides
Proceedings of the 18th Plansee Seminar, Reutte, Austria, HM66, (2013)
- [14ALA] N. Al-Aqeeli, K. Mohammed, T. Laoui, N.Saheb
VC and Cr₃C₂ doped WC-based nano-cermets prepared by MA and SPS
Ceramics International 40[8]: 11759–65 (2014)
- [14BOU] V. Bounhoure, S. Lay, F. Charlot, A. Antoni-Zdziobek, E. Pauty and J. M.
Missiaen
Effect of C content on the microstructure evolution during early solid state
sintering of WC-Co alloys
International Journal of Refractory Metals & Hard Materials, 44, 27-34 (2014)
- [14DAL] V. Dalbauer and T. Jewett
Effect of Mo and Mo₂C Additions on the Microstructure of Sintered WC-Co
Components
Proceedings of the Euro PM2014 Congress and Exhibition, Salzburg, Austria,
(2014)
- [14KAP] B. Kaplan, A. Markström, S. Norgren and M. Selleby
Experimental Determination of the Solubility of Co in the Cr-Based Carbides
Cr₂₃C₆, Cr₇C₃, and Cr₃C₂
Metallurgical and Materials Transactions a-Physical Metallurgy and Materials
Science, 45A[11]: 4820–28 (2014)

- [14KAP1] B. Kaplan, A. Markstrom, A. Blomqvist, S. Norgren and M. Selleby
Thermodynamic analysis of the Co-Cr-C system
Calphad-Computer Coupling of Phase Diagrams and Thermochemistry, 46,
226-36 (2014)
- [14PRA] L. Prakash
Properties and applications of WC hardmetals with iron based binders
Advances in Tungsten, Refractory and Hardmaterials IX - Proceedings of the
9th International Conference on Tungsten, Refractory and Hardmaterials, 113–
25 (2014)
- [14WAN] H. Wang, T. Webb and J.W. Bitler
Different Effects of Cr₃C₂ and VC on Sintering Behavior of WC-Co Materials
Proceedings of the tungsten, refractory & hardmaterials conference,
Orlando, USA: 153–61 (2014)
- [14XIE] H. Xie, Y. Liu, J. Ye, M. Li, Y. Zhu and H. Fan
Effect of (Cr_{0.8}V_{0.2})₂(C,N) addition on microstructure and mechanical
properties of WC-8Co cemented carbides
International Journal of Refractory Metals and Hard Materials, 47, 145–49
(2014)
- [15ALA] N. Al-Aqeeli
Characterization of nano-cemented carbides Co-doped with vanadium and
chromium carbides
Powder Technology, 273, 47–53 (2015)
- [15ALA1] N. Al-Aqeeli, K. Mohammad, T. Laoui, N. Saheb
The effect of variable binder content and sintering temperature on the
mechanical properties of WC-Co-VC/Cr₃C₂ nanocomposites
Materials and Manufacturing Processes 30[4]: 327-334 (2015)
- [15BON] A. E. A. Bondar
Carbon-Cobalt-Tungsten
The Landolt-Börnstein Database; Group IV Physical Chemistry, 11E2, M.
Material Science International Team, Springer-Verlag Berlin Heidelberg
(2015)
- [15BUC] C. Buchegger, W. Lengauer, J. Bernardi, J. Gruber, T. Ntaflos, F. Kiraly and J.
Langlade
Diffusion parameters of grain-growth inhibitors in WC based hardmetals with
Co, Fe/Ni and Fe/Co/Ni binder alloys
International Journal of Refractory Metals and Hard Materials, 49[1]: 67-74
(2015)
- [15BOU] V. Bounhour, S. Lay, S. Coindeau, S. Norgren, E. Pauty, J.M. Missiaen
Effect of Cr addition on solid state sintering of WC-Co alloys
International Journal of Refractory Metals and Hard Materials, 52, 21-28
(2015)

- [15KAP] B. Kaplan, S. Norgren, M. Schwind and M. Selleby
Thermodynamic calculations and experimental verification in the WC-Co-Cr cemented carbide system (Reprint of Int. Journal of Refractory Metals and Hard Materials vol 48, pg 257-262, 2015)
International Journal of Refractory Metals & Hard Materials, 49[4] 00-05 (2015)
- [15KAW] M. Kawakami and K. Kitamura
Segregation layers of grain growth inhibitors at WC/WC interfaces in VC-doped submicron-grained WC-Co cemented carbides
International Journal of Refractory Metals and Hard Materials, 52[229-34 (2015)
- [15SCH] W. D. Schubert, M. Fugger, B. Wittmann and R. Useldinger
Aspects of sintering of cemented carbides with Fe-based binders
International Journal of Refractory Metals and Hard Materials, 49[1]: 110-23 (2015)
- [15WAN] H. Wang, T. Webb and J. W. Bitler
Different Effects of Cr₃C₂ and VC on the Sintering Behavior of WC-Co Materials
International Journal of Refractory Metals and Hard Materials, in press, (2015)
- [15WEI] J. Wiedow, E. Halwax, W.D. Schubert
Analysis of WC with increased Ta doping
International Journal of Refractory Metals and Hard Materials, 49:36–41 (2015)
- [15WEI1] J. Weidow, A. Blomqvist, J. Salomonsson, S. Norgren
Cemented Carbides based on WC pre-alloyed with Cr or Ta
International Journal of Refractory Metals and Hard Materials, 47, 145–49 (2014)
- [15WOY] M. Woydt and H. Mohrbacher
The use of niobium carbide (NbC) as cutting tools and for wear resistant tribosystems
International Journal of Refractory Metals and Hard Materials, 49[1]: 212-18 (2015)
- [15YAH] M. Yahiaoui, J.-Y. Paris, J. Denape, C. Colin, O. Ther, A. Dourfay
Wear mechanisms of WC-Co drill bit inserts against alumina counterface under dry friction Part 2 — Graded WC-Co inserts.
International Journal of Refractory Metals and Hard Materials 48:65–73 (2015)
- [16FAB] T. A. Fabijanić, Ž. Alar and D. Ćorić
Influence of consolidation process and sintering temperature on microstructure and mechanical properties of near nano- and nano-structured WC-Co cemented carbides
International Journal of Refractory Metals and Hard Materials, 54, 82-89 (2016)

- [16ZHO] P. Zhou, Y. Peng, C. Buchegger, Y. Du and W. Lengauer
Experimental investigation and thermodynamic assessment of the C–Co–Fe–
Ni–W system
International Journal of Refractory Metals and Hard Materials, 54, 60–69
(2016)

8 Annex

8.1 Device settings for EPMA

Setup Set_1a_def5

Location: Vienna
Elements: V, Cr, Co, W; Carbon calculated stoichiometric to W
Beam current: 25 nA
Beam voltage: 20 keV
Overlap correction: Cr $K\alpha$ / V $K\beta$
Filename:: okt1222_Set1a_def5.qtiSet
Date: October 22, 2012

Table 8-1: Detector settings for EPMA-Setup file Set_1a _def5

Element	Line	Standard	Detector	Mode	Peak Position	Background	Bias
V	$K\alpha$	VC	PET	Int.	28629	-350/250	1287
Co	$K\alpha$	Co	LIF	Int.	44412	-300/350	1334
Cr	$K\alpha$	Cr	LLIF	Int.	56843	-300/400	1800
W	$M\alpha$	WC	PET	Diff.	79778	-900/700	1280

Setup Fe_Ni

Location: Vienna
Elements: V, Cr, Co, Ni, Fe, W; C calculated stoichiometric to W (=WC)
Beam current: 25 nA
Beam voltage: 20 keV
Overlap correction: Cr $K\alpha$ / V $K\beta$, V $K\alpha$ / W $L\beta$
Filename:: Nov1311_fe_ni.qtiSet
Date: November 11, 2013

Table 8-2: Detector settings for EPMA-Setup file Fe_Ni

Element	Line	Standard	Detector	Mode	Peak Position	Background	Bias
V	$K\alpha$	VC	PET	Int.	28633	-350/250	1287
Cr	$K\alpha$	Cr	LLIF	Int.	56848	-300/400	1800
Co	$K\alpha$	Co	LIF	Int.	44411	-300/350	1334
Fe	$K\alpha$	Fe	LIF	Int.	48089	-450/450	1334
Ni	$K\alpha$	Ni	LLIF	Int.	41171	-300/350	1800
W	$M\alpha$	WC	PET	Diff.	79785	-900/700	1280

Setup TU_2015-03-23

Location: Vienna
Elements: V, Cr, Co,W C calculated stoichiometric to W (=WC)
Beam current: 30 nA
Beam voltage: 20 keV
Overlap correction: V $K\alpha$ / W $L\beta$
Filename:: TU_2015-03-23.qtiSet
Date: March 23, 2015

Table 8-3: Detector settings for EPMA-Setup file TU_2015-03-23

Element	Line	Standard	Detector	Mode	Peak Position	Background	Bias
V	$K\alpha$	VC	PET	Int.	28625	-350/250	1300
Cr	$K\alpha$	Cr	LLIF	Int.	56847	-300/400	1800
Co	$K\alpha$	Co	LIF	Int.	44409	-300/350	1339
W	$M\alpha$	WC	PET	Diff.	79768	-800/550	1287

8.2 Activation energies

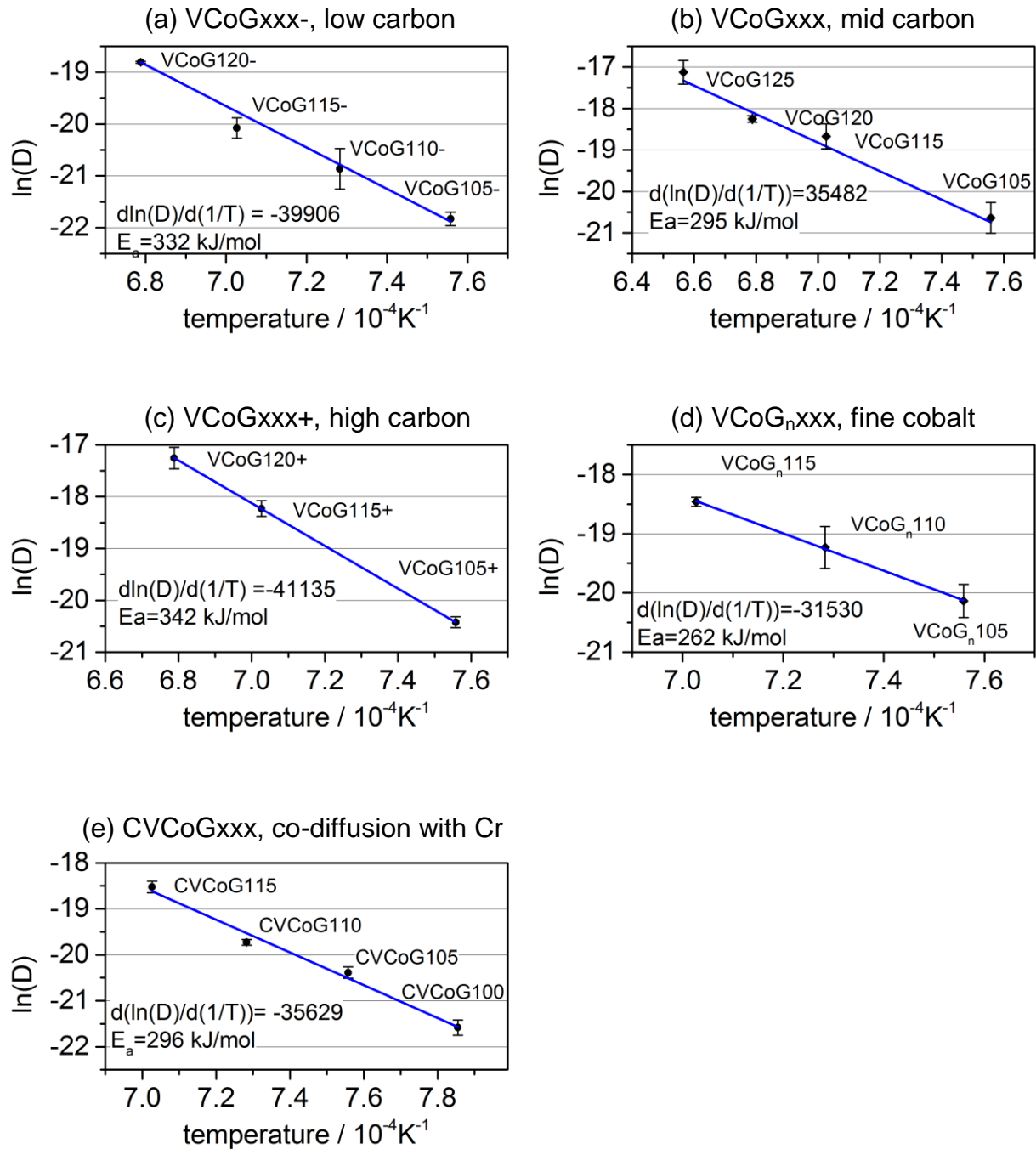


Figure 8-1: Arrhenius plots and activation energies of vanadium transport in G-type diffusion couples. The placeholder xxx refers to the temperature key according to sample nomenclature as described in Table 3-5, page 40.

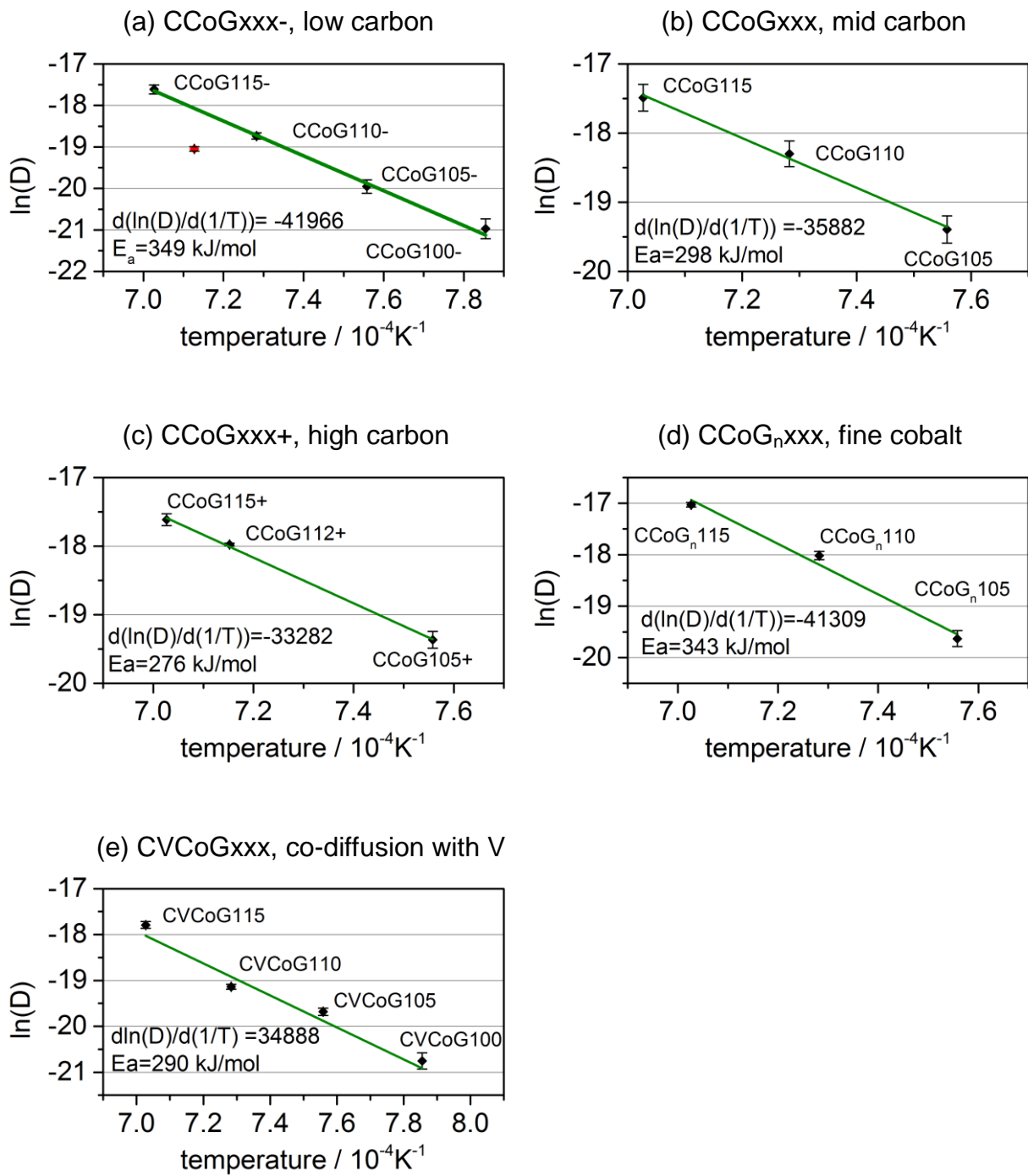


Figure 8-2: Arrhenius plots and activation energies of chromium transport in G-type diffusion couples. The placeholder xxx refers to the temperature key according to sample nomenclature as described in Table 3-5, page 40.

8.3 DSC and TG analyses

8.3.1 Diffusion couple components with cobalt binder

WCo-: WC-10wt%Co, low carbon

Peak No.	1 st heat-up	1 st cool-down	2 nd heat-up	2 nd cool-down
	H1	C1	H2	C2
Onset	1366	1360	1368	1362
Maximum	1376	1348	1375	1349

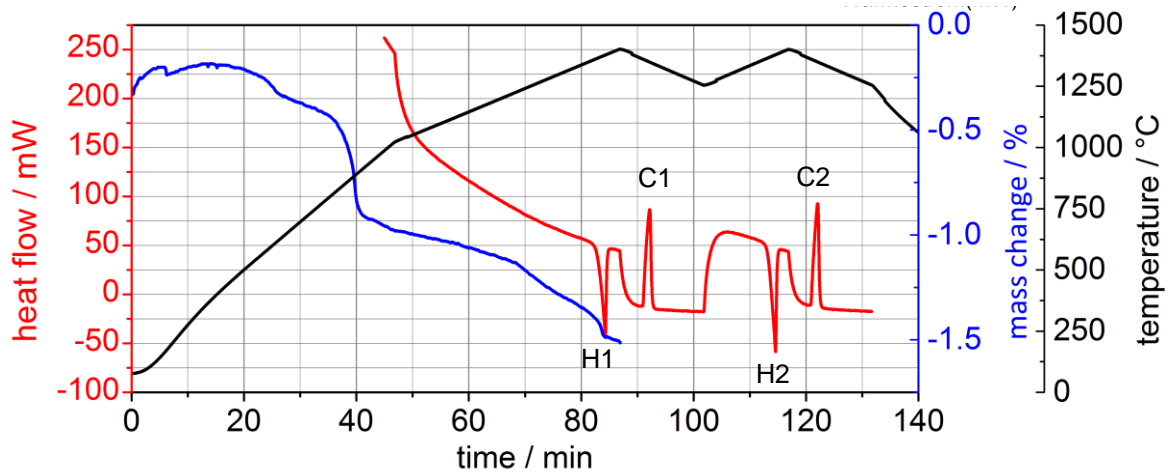


Figure 8-3: STA of WCo-.

WCo+: WC-10wt%Co, high carbon

Peak No.	1 st heat-up	1 st cool-down	2 nd heat-up	2 nd cool-down
	H1	C1	H2	C2
Onset	1298	1295	1298	1295
Maximum 1	1308	1286	1307	1286

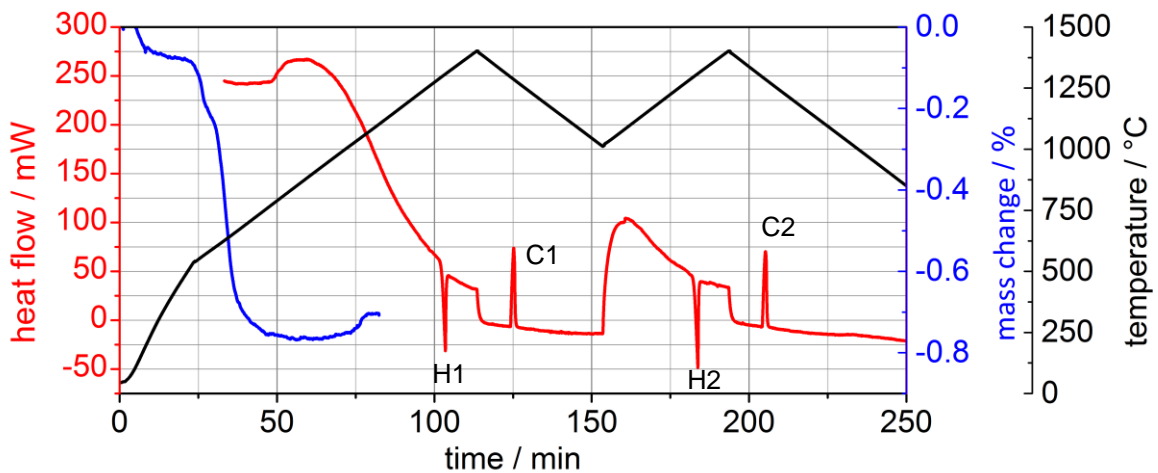


Figure 8-4: STA of WCo+.

WCo_n: WC-10wt%Co, fine cobalt

Peak No.	1 st heat-up	1 st cool-down	2 nd heat-up	2 nd cool-down
	H1	C1	H2	C2
Onset	1311	1338	1313	1337
Maximum 1	1327	1325	1329	1325

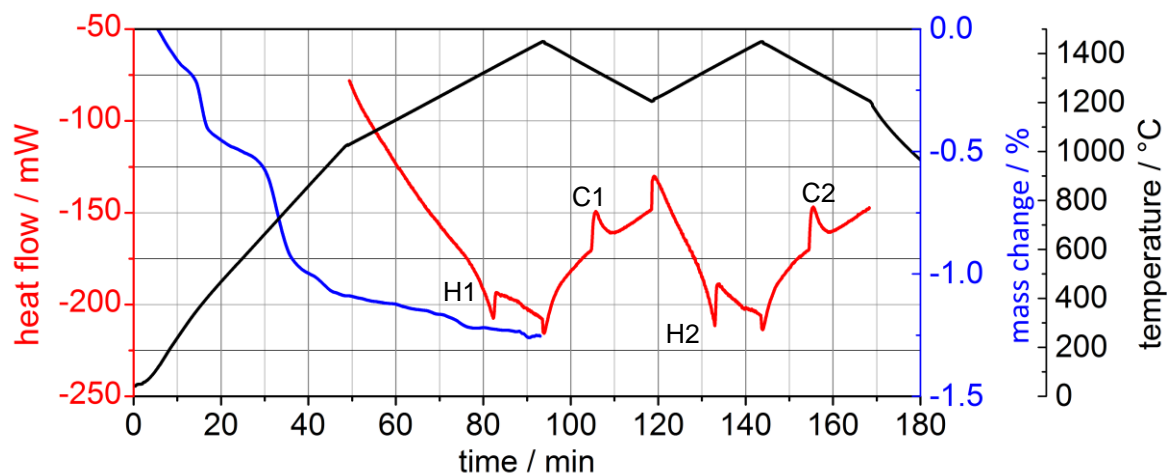


Figure 8-5: STA of WCo_n.

CWCo+: Cr₃C₂-WC-10wt%Co

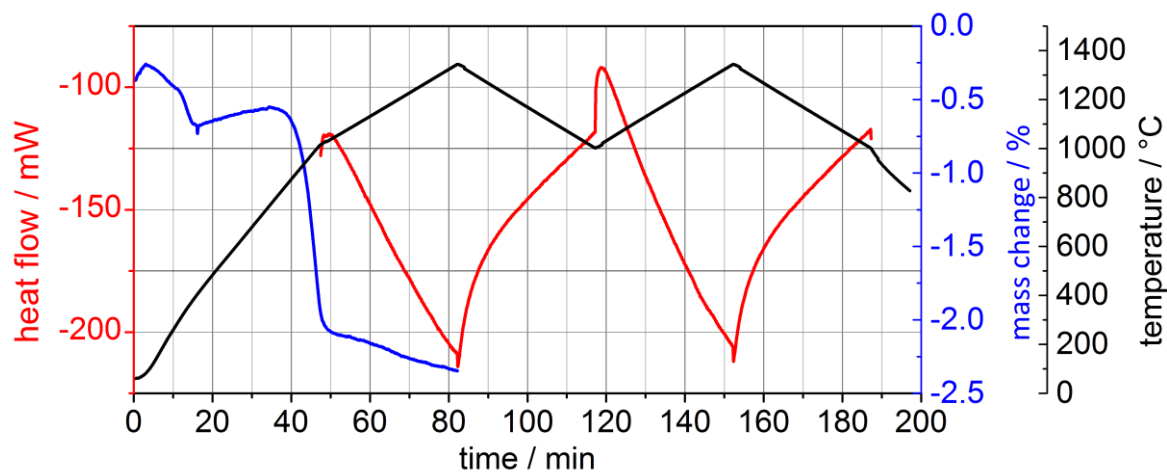


Figure 8-6: STA of CWCo. Filename in database: WC+C-Ar

CCo+: Cr₃C₂-Co

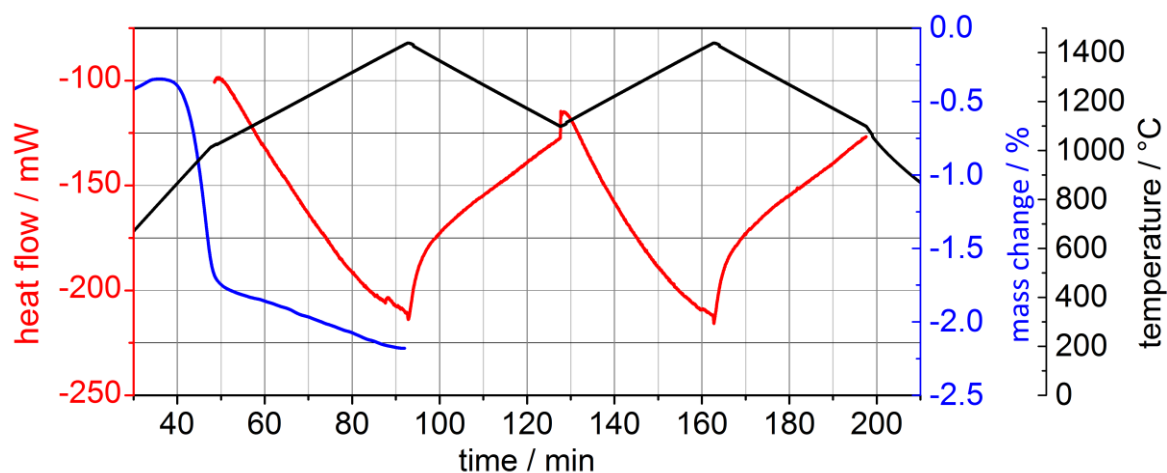


Figure 8-7: STA of CCo+. Filename in database: CA-Ar

VWCo+: VC-WC-Co

Peak No.	1 st heat-up		1 st cool-down	2 nd heat-up	2 nd cool-down
	H1a	H1b	C1	H2	C2
Onset	1201	1325	1315	1312	1309
Maximum	1211	1346	1303	1328	1298

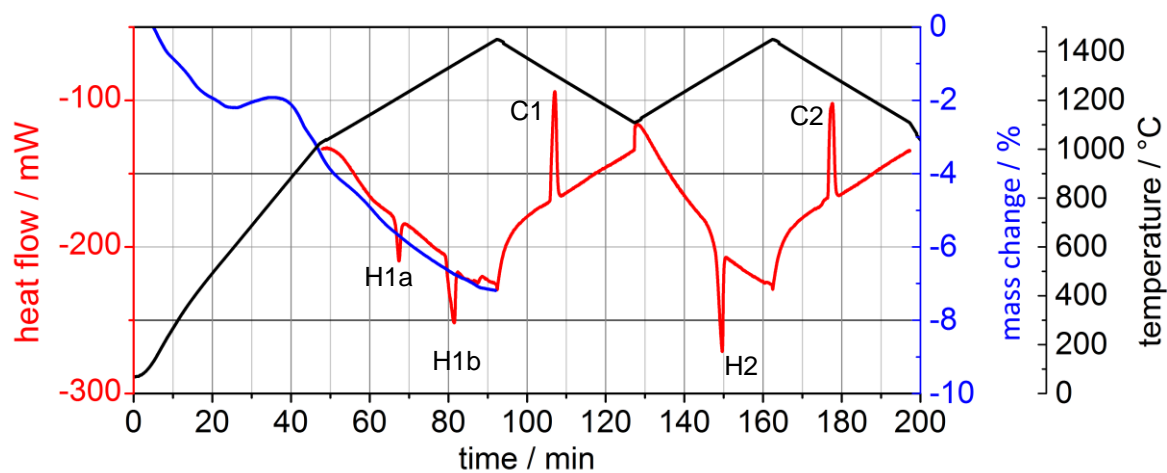


Figure 8-8: STA of VWCo+. Filename in database: WV+C-Ar-2

VCo+: VC-Co

Peak No.	1 st heat-up		1 st cool-down		2 nd heat-up		2 nd cool-down	
	H1a	H1b	C1a	C1b	H2a	H2b	C2a	C2b
Onset	1246	1356	1352	1207	1226	1357	1352	1205
Maximum	1260	1367	1343	1193	1242	1366	1343	1194

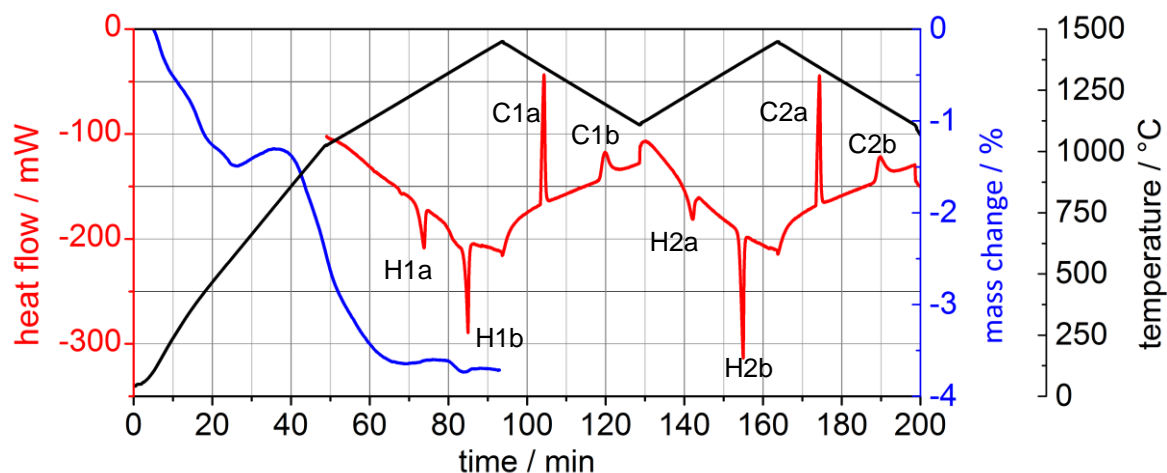


Figure 8-9: STA of VCo+. Filename in database: VA-Ar

CVCo: Cr₃C₂-VC-Co

Peak No.	1 st heat-up	1 st cool-down	2 nd heat-up	2 nd cool-down
	H1	C1	H2	C2
Onset	1254	1250	1257	1248
Maximum 1	1264	1243	1268	1243

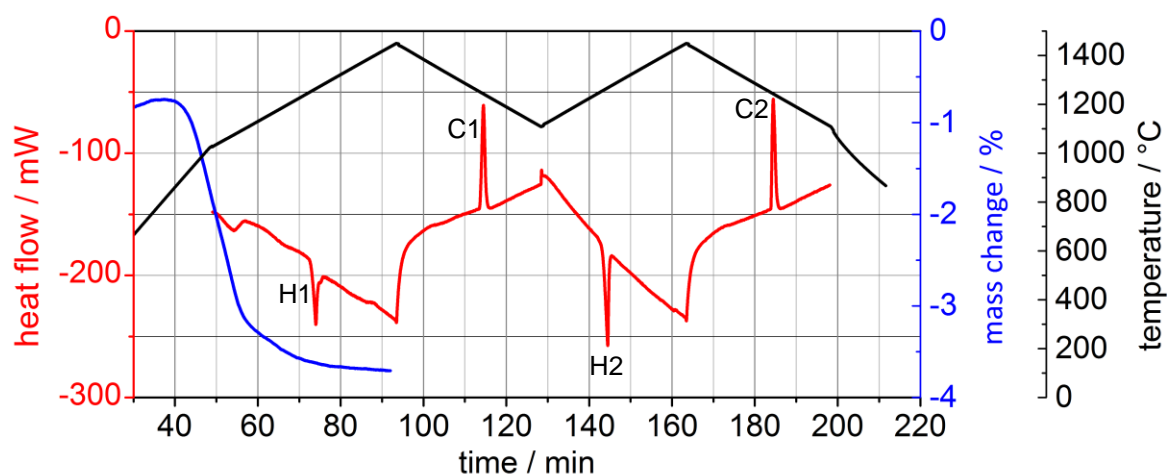


Figure 8-10: STA of CVCo. Filename in database: CVA-Ar

8.3.2 Diffusion couple components with Fe/ Ni 15/85wt% binder

W19+: WC-Fe/Ni 15/85wt%

Peak No.	1 st heat-up	1 st cool-down	2 nd heat-up	2 nd cool-down
	H1	C1	H2	C2
Onset	1320	1314	1318	1313
Maximum 1	1327	1311	1329	1312
Maximum 2	1363	1305	1365	1303

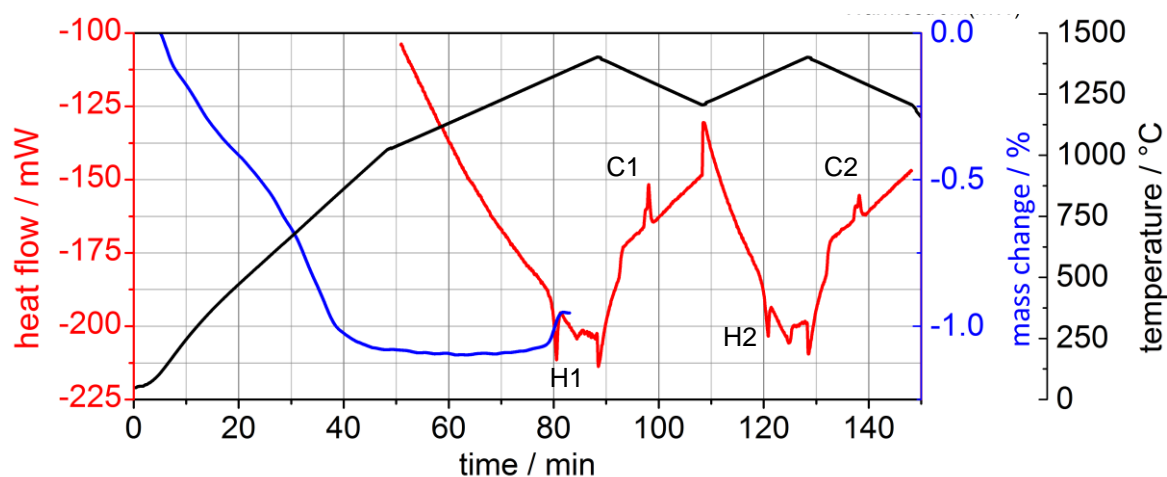


Figure 8-11: STA of W19+. Filename in database: WC-19+ Ar

VW19+: VC-WC-Fe/Ni 15/85wt%

Peak No.	1 st heat-up		1 st cool-down	2 nd heat-up	2 nd cool-down
	H1a	H1b	C1	H2	C2
Onset	1206	1371	1351	1358	1349
Maximum 1	1216	1383	1340	1371	1338

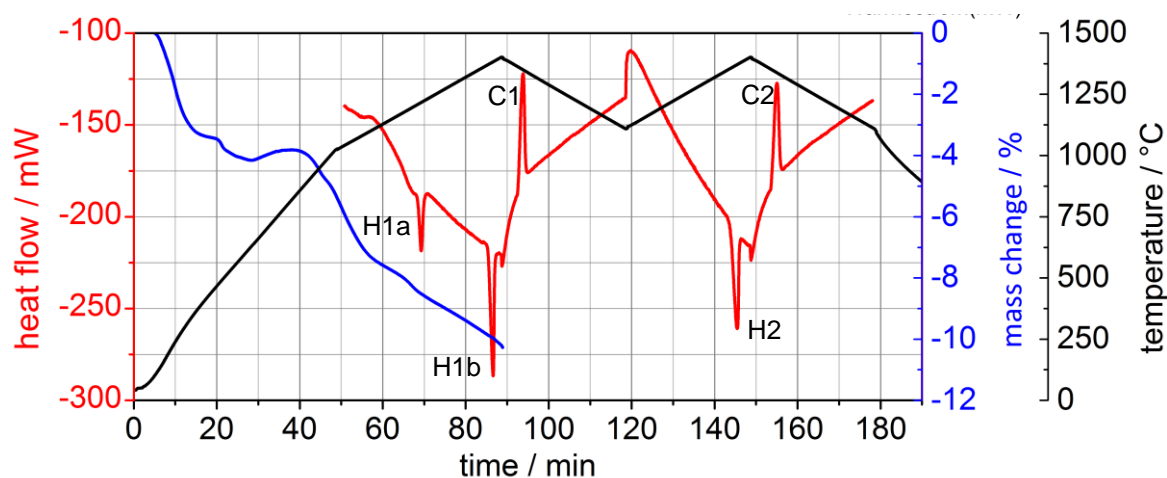


Figure 8-12: STA of VW19+. Filename in database: V19+ Ar

CW19+: Cr₃C₂-WC-Fe/Ni 15/85wt%

Peak No.	1 st heat-up	1 st cool-down	2 nd heat-up	2 nd cool-down
	H1	C1	H2	C2
Onset	1241	1238	1243	1243
Maximum 1	1256	1231	1257	1231

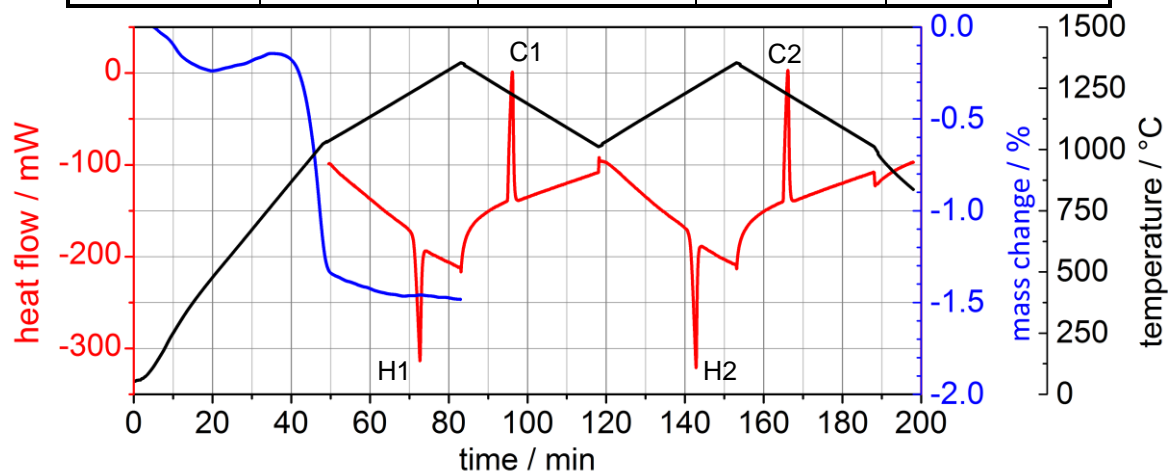


Figure 8-13: STA of CW19+. Filename in database: C19+ Ar

8.3.3 Diffusion couple components with Fe/Co/Ni 40/20/40wt% binder

W424+: WC-Fe/Co/Ni 40/20/40wt%

Peak No.	1 st heat-up	1 st cool-down	2 nd heat-up	2 nd cool-down
	H1	C1	H2	C2
Onset	1290	1345	1335	1351
Maximum 1	1345	1330	1351	1340

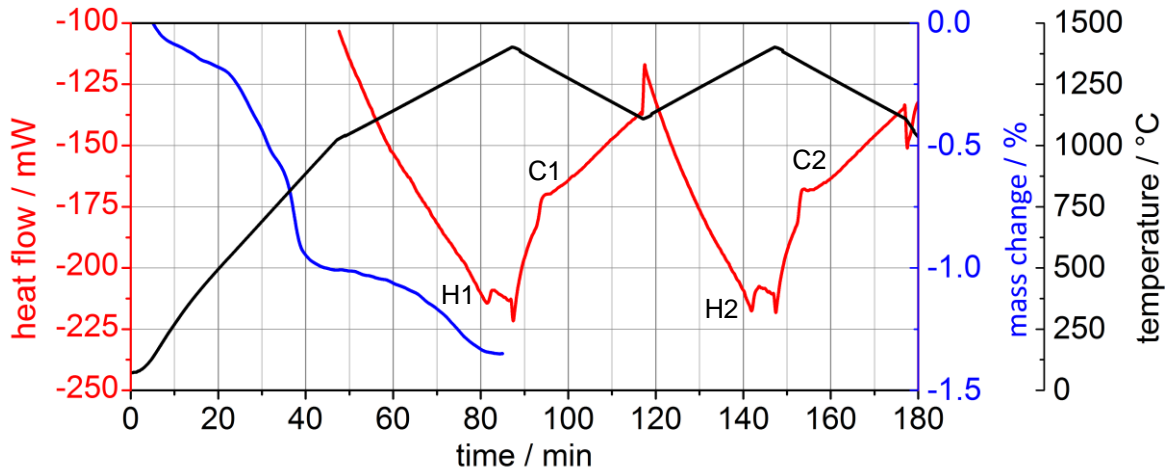


Figure 8-14: STA of W424+. Filename in database: WC-424+ Ar.+

VW424+: VC-WC-Fe/Ni 15/85wt%

Peak No.	1 st heat-up			1 st cool-down	2 nd heat-up	2 nd cool-down
	H1a	H1b	H1c	C1	H2	C2
Onset	1148	1201	1350	1314	1308	1297
Maximum	1169	1210	1359	1303	1325	1287

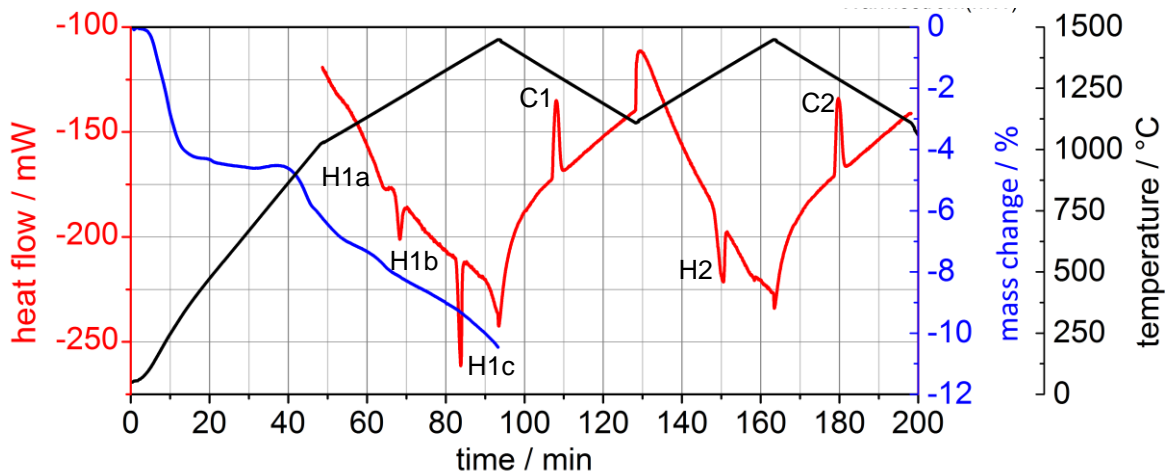


Figure 8-15: STA of VW424+. Filename in database: V424+ Ar.

CW424+: Cr₃C₂-WC-Fe/Ni 15/85wt%

Peak No.	1 st heat-up	1 st cool-down	2 nd heat-up	2 nd cool-down
	H1	C1	H2	C2
Onset	1215	1221	1220	1218
Maximum 1	1226	1214	1231	1213

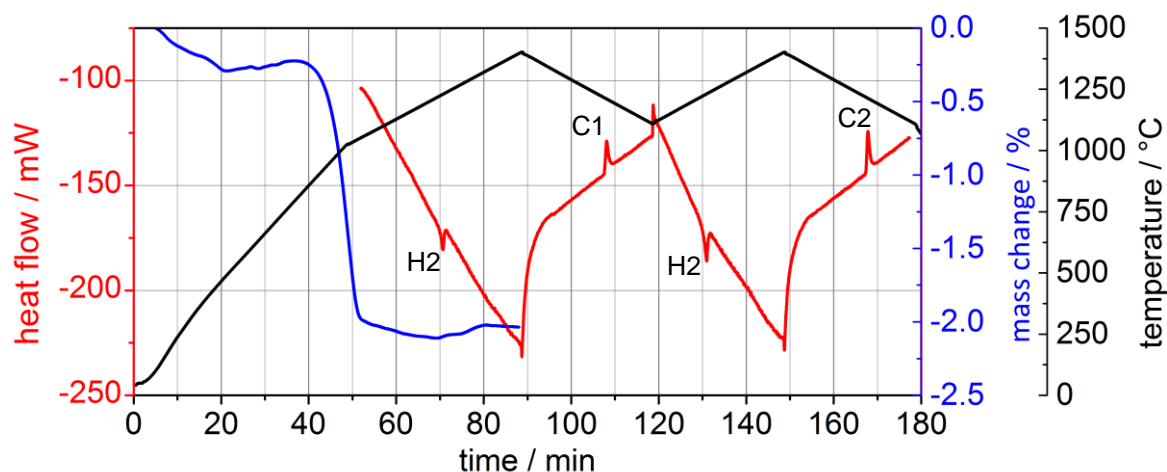


Figure 8-16: STA of CW424+. Filename in database: C424+ Ar.

8.3.4 Varying Cr/W ratio

WC-Co-50Cr: Cr/W=50/50 at%, WC-Cr₃C₂-Co

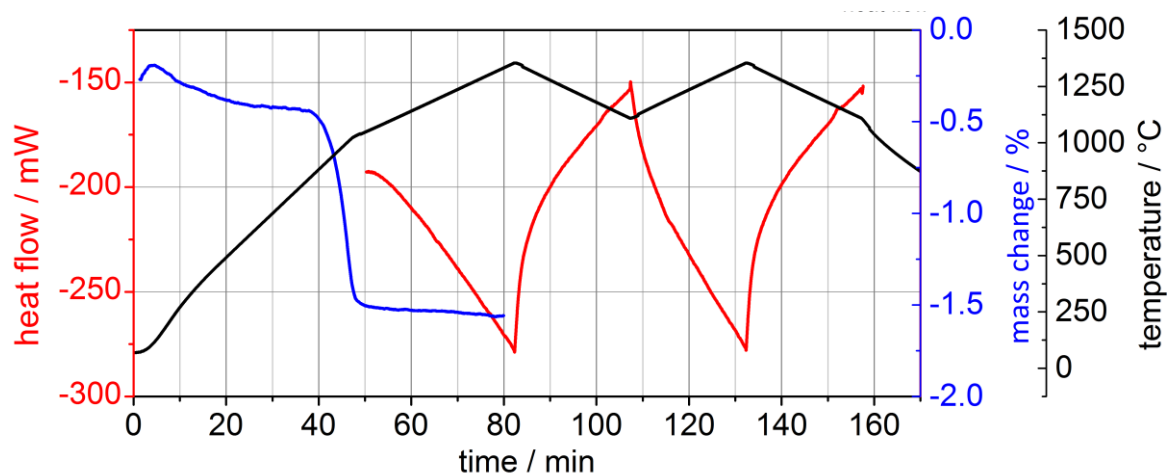


Figure 8-17: STA of WC-Co-50Cr. Filename in database: WC-Co-50Cr.

WC-Co-20Cr: Cr/W=20/80 at%, WC-Cr₃C₂-Co

Peak No.	1 st heat-up		1 st cool-down		2 nd heat-up		2 nd cool-down	
	H1		C1a	C1b	H2		C2a	C2b
Onset	1203		1255	1207	1215		1250	1210
Maximum	1222		1247	1195	1232		1245	1197

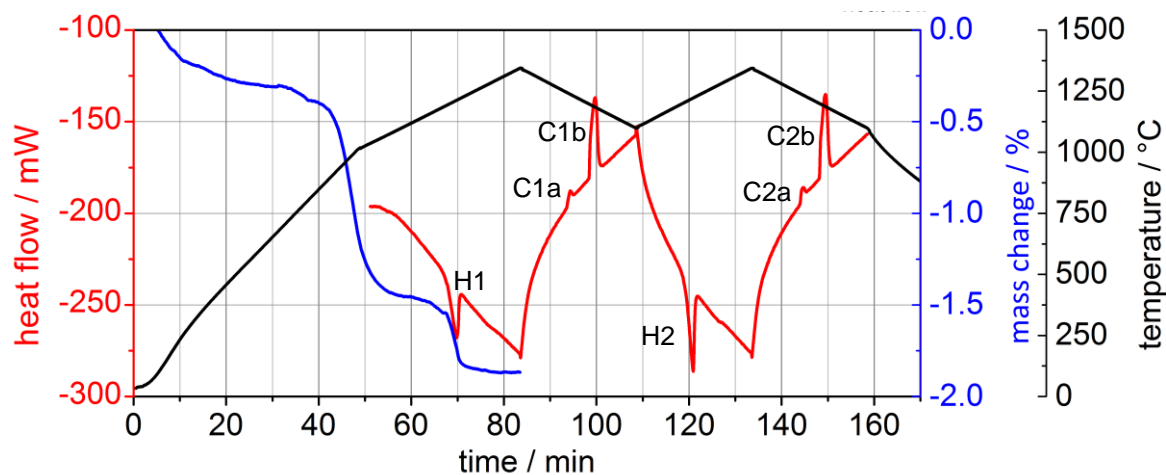


Figure 8-18: STA of WC-Co-20Cr. Filename in database: WC-Co-20Cr.

WC-Co-10Cr: Cr/W=10/90 at%, WC-Cr₃C₂-Co

Peak No.	1 st heat-up		1 st cool-down		2 nd heat-up		2 nd cool-down	
	H1a	H1b	C1a	C1b	H2a	H2b	C2a	C2b
Onset	1203	1243	1259	1184	1211	1237	1260	1182
Maximum	1216	1269	1255	1179	1219	1270	1256	1176

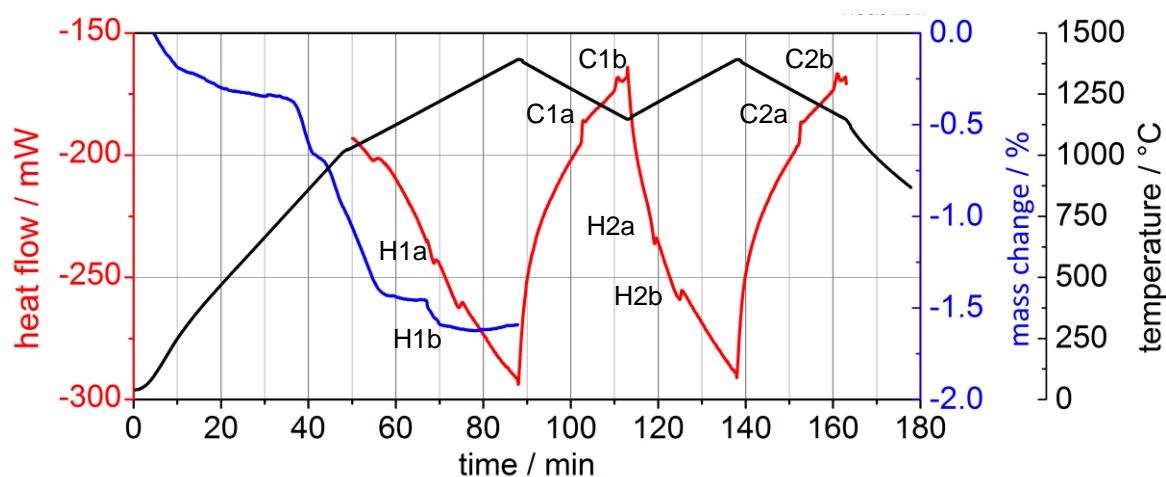


Figure 8-19: STA of WC-Co-10Cr. Filename in database: WC-Co-10Cr.

WC-Co-2Cr: Cr/W=2/98 at%, WC-Cr₃C₂-Co

Peak No.	1 st heat-up		1 st cool-down		2 nd heat-up		2 nd cool-down	
	H1		C1		H2		C2	
Onset	1348		1348		1348		1348	
Maximum	1360		1334		1360		1336	

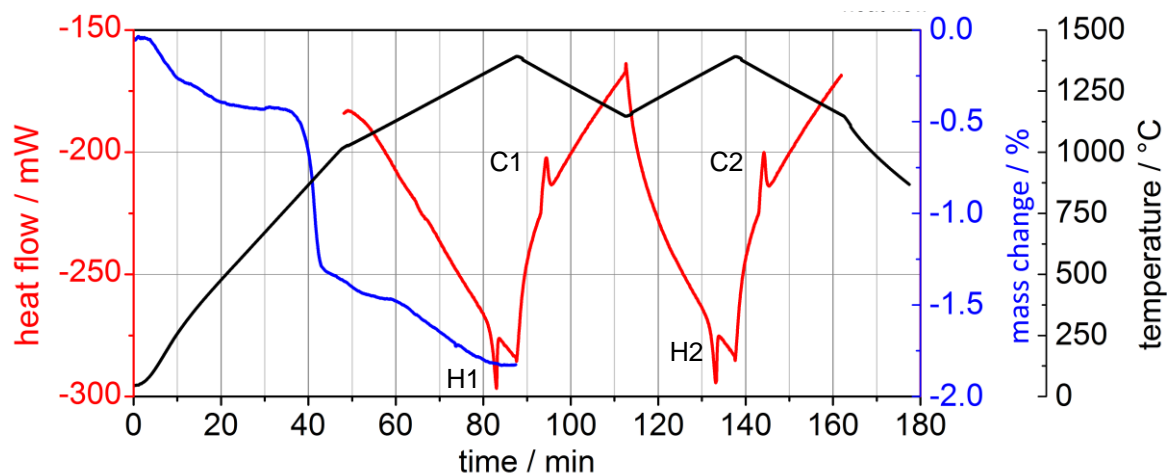


Figure 8-20: STA of WC-Co-2Cr. Filename in database: WC-Co-2Cr.

8.3.5 Varying V/W ratio

WC-Co-50V: V/W=50/50 at%, WC-VC-Co

Peak No.	1 st heat-up		1 st cool-down		2 nd heat-up		2 nd cool-down	
	H1a	H1b	C1		H2		C2	
Onset	1146	1326	1304		1309		1306	
Maximum	1210	1341	1300		1315		1301	

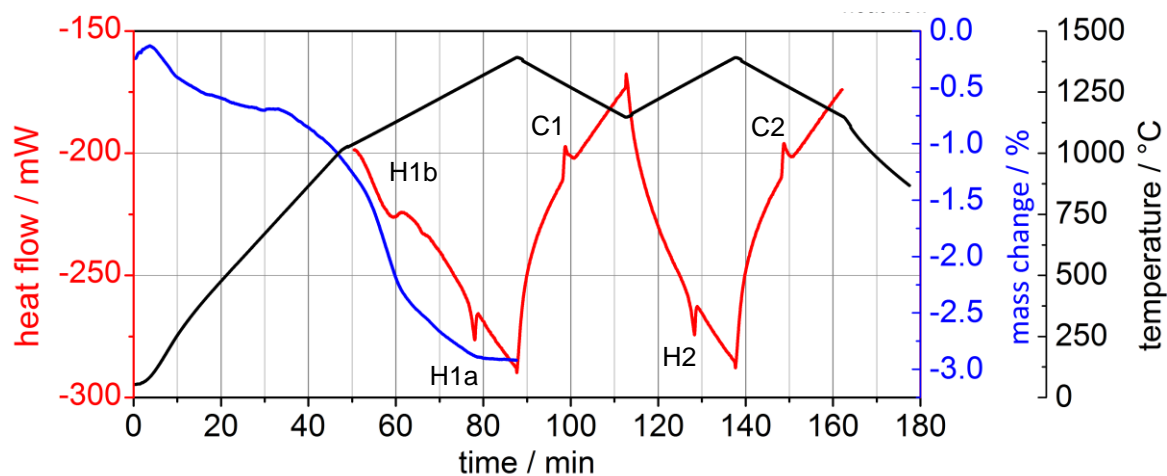


Figure 8-21: STA of WC-Co-50V. Filename in database: WC-Co-50V.

WC-Co-20V: V/W=20/80 at%, WC-VC-Co

Peak No.	1 st heat-up			1 st cool-down	2 nd heat-up	2 nd cool-down
	H1a	H1b	H1c	C1	H2	C2
Onset	1055	1176	1289	1296	1300	1296
Maximum	1120	1195	1310	1291	1312	1291

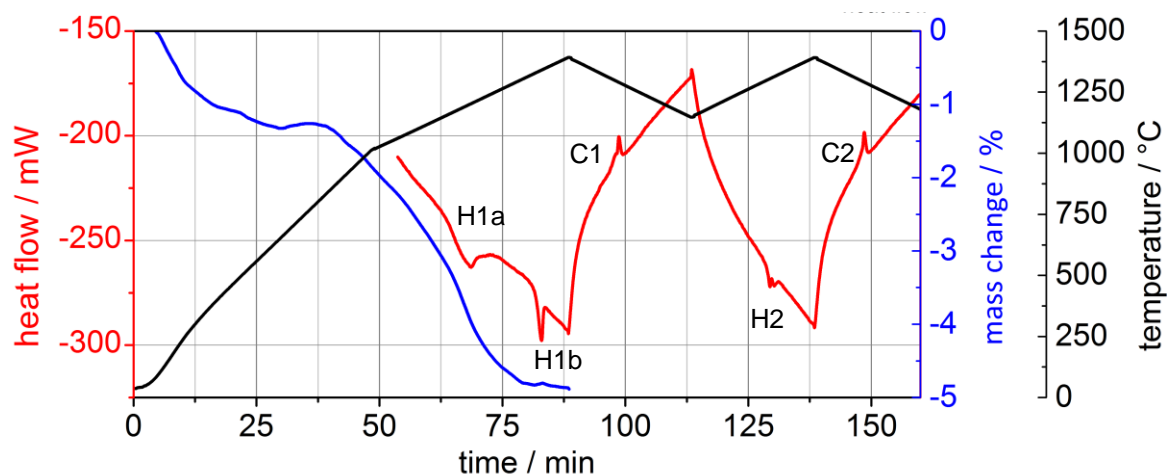


Figure 8-22: STA of WC-Co-20V. Filename in database: WC-Co-20V.

WC-Co-10V: V/W=10/90 at%, WC-VC-Co

Peak No.	1 st heat-up		1 st cool-down	2 nd heat-up	2 nd cool-down
	H1a	H1b	C1	H2	C2
Onset	1052	1285	1293	1299	1293
Maximum	1110	1309	1288	1311	1288

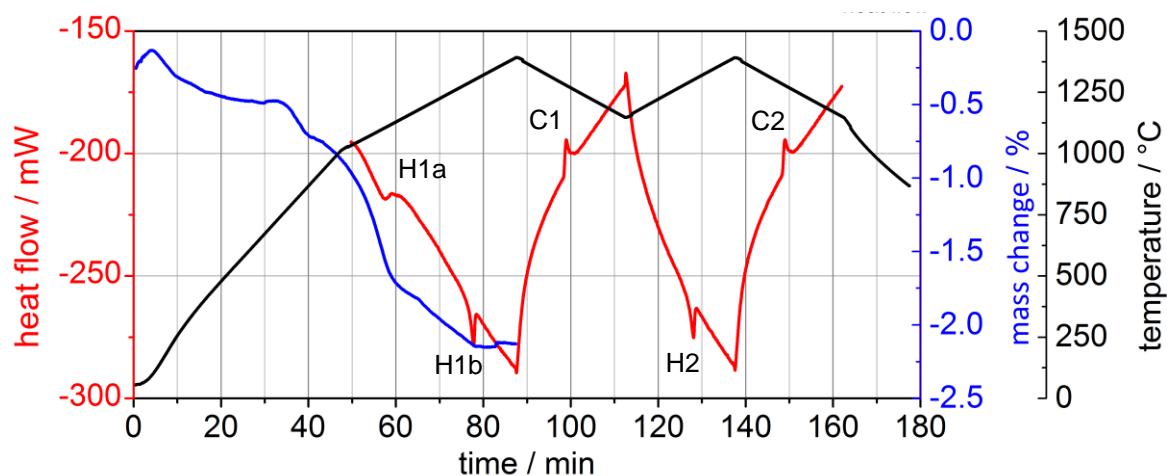


Figure 8-23: STA of WC-Co-10V. Filename in database: WC-Co-10V.

WC-Co-2V: V/W=2/98 at%, WC-VC-Co

Peak No.	1 st heat-up		1 st cool-down	2 nd heat-up	2 nd cool-down
	H1a	H1b	C1	H2	C2
Onset	1141	1316	1328	1326	1328
Maximum	1163	1342	1313	1343	1313

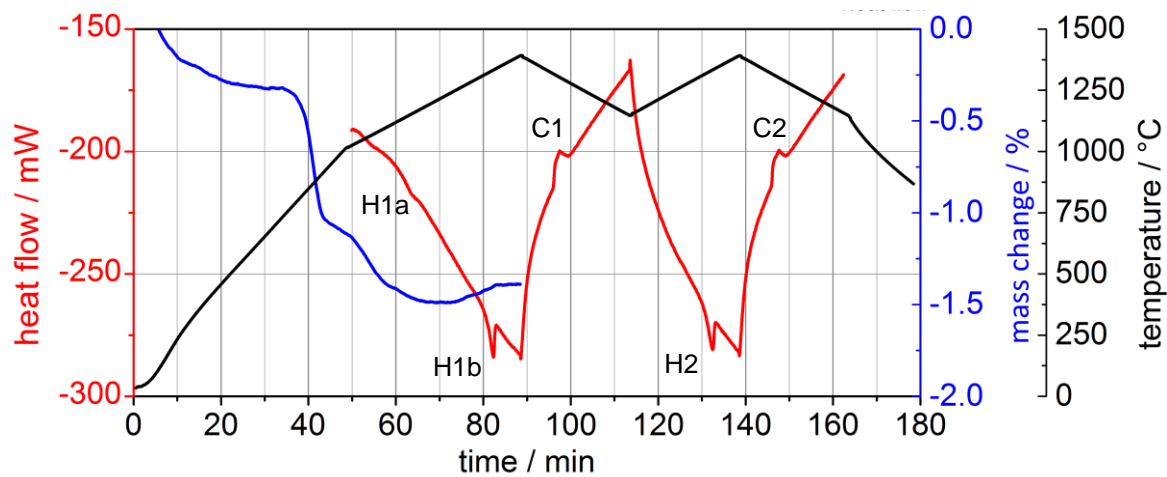


Figure 8-24: STA of WC-Co-2V. Filename in database: WC-Co-2V.

8.3.6 Varying Mo/W ratio

WC-Co-50Mo: Mo/W=50/50 at%, WC-Mo₂C-Co

Peak No.	1 st heat-up		1 st cool-down		2 nd heat-up		2 nd cool-down	
	H1	C1a	C1b	H2	C2a	C2b		
Onset	1183	1334	1216	1221	1366	1223		
Maximum	1214	1319	1209	1247	1357	1207		

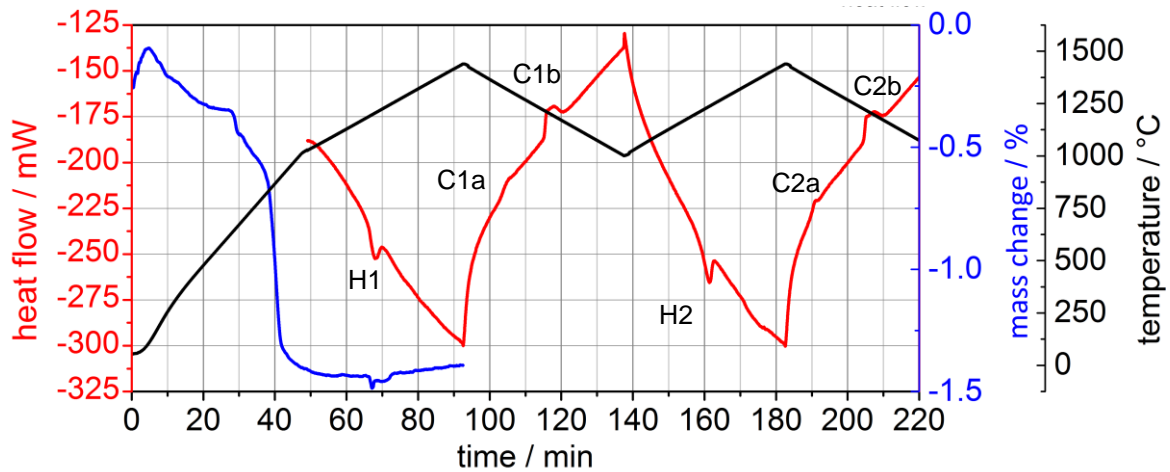


Figure 8-25: STA of WC-Co-20Mo. Filename in database: WC-Co-50Mo.

WC-Co-20Mo: Mo/W=20/80 at%, WC-Mo₂C-Co

Peak No.	1 st heat-up		1 st cool-down		2 nd heat-up		2 nd cool-down	
	H1	C1	H2	C2				
Onset	1301	1315	1311	1309				
Maximum	1318	1295	1325	1298				

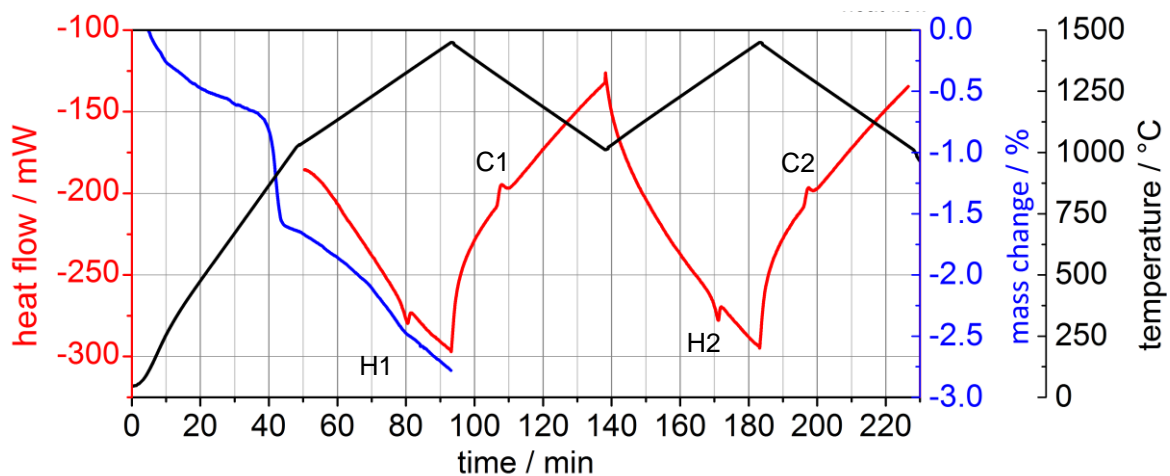
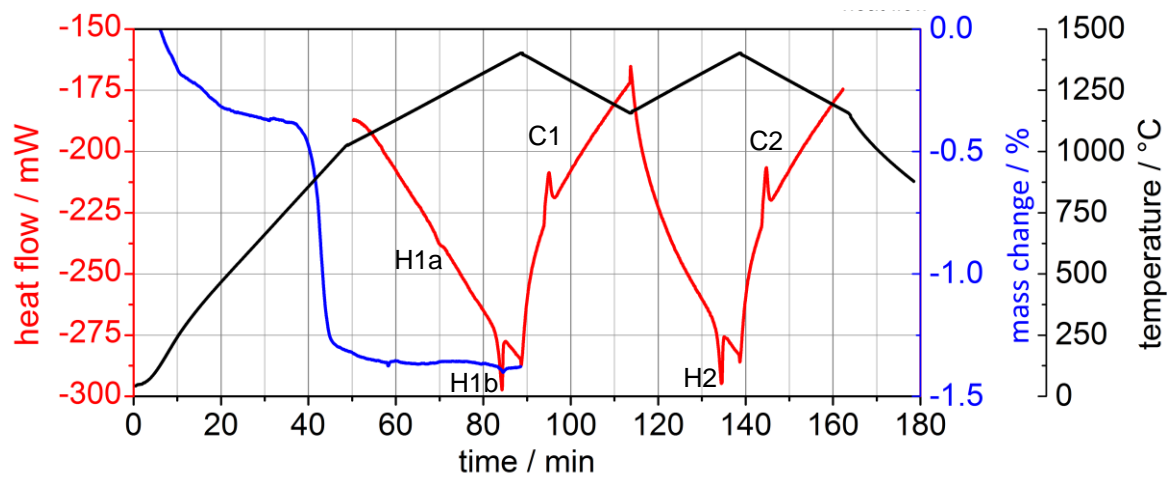


Figure 8-26: STA of WC-Co-20Mo. Filename in database: WC-Co-20Mo.

WC-Co-2Mo: Mo/W=2/98 at%, WC-Mo₂C-Co

Peak No.	1 st heat-up		1 st cool-down	2 nd heat-up	2 nd cool-down
	H1a	H1b	C1	H2	C2
Onset	1212	1347	1348	1343	1351
Maximum	1223	1361	1338	1362	1341



8.3.7 Chromium-doped hardmetals

HM Cr_3C_2 : $c(\text{Cr}/\text{Co})=0.05$, WC-Co- Cr_3C_2

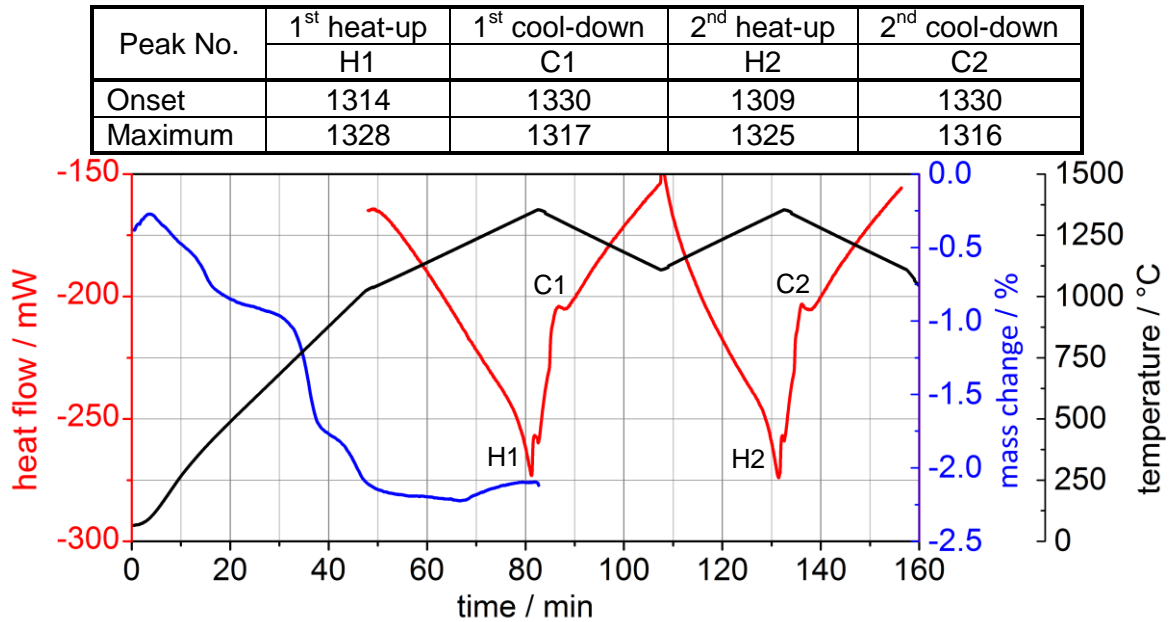


Figure 8-27: STA of HM_ Cr_3C_2 . Filename in database: WC-Co- Cr_3C_2 -C Ar.

HM Cr_2N -. $c(\text{Cr}/\text{Co})=0.05$, WC-Co- Cr_2N , low carbon

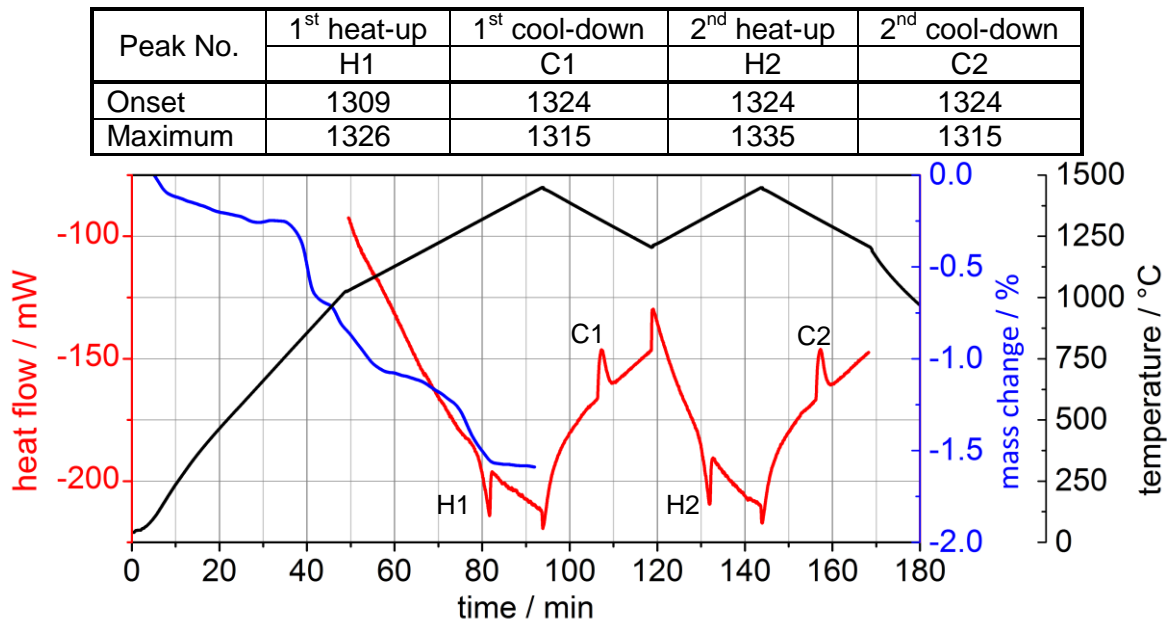


Figure 8-28: STA of HM_ Cr_2N -. Filename in database: CrN-10- Ar.

HM_Cr₂N+: c(Cr/Co)=0.05, WC-Co-Cr₂N, high carbon

Peak No.	1 st heat-up		1 st cool-down	2 nd heat-up		2 nd cool-down
	H1		C1	H2		C2
Onset	1201		1253	1244		1254
Maximum	1248		1245	1261		1244

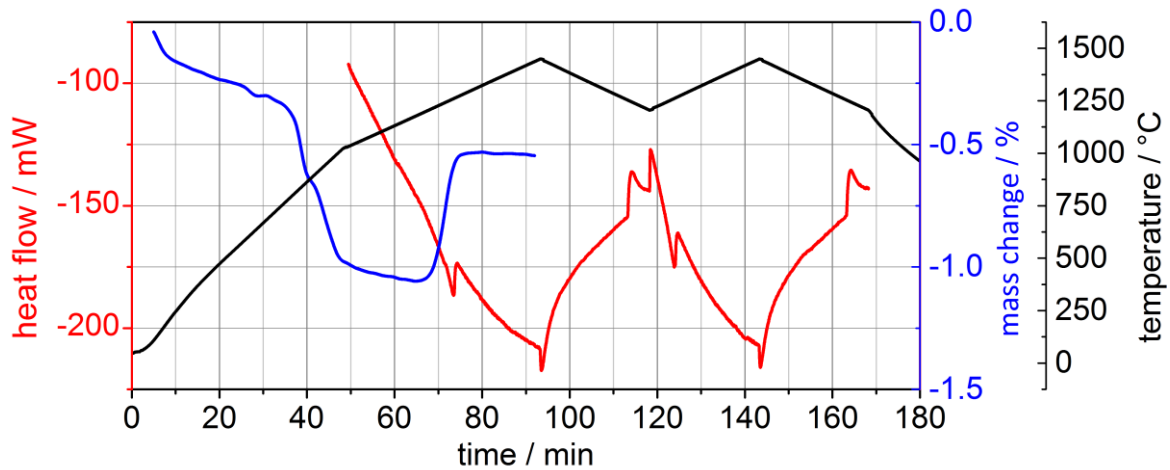


Figure 8-29: STA of HM_Cr₂N+ . Filename in database: CrN+10- Ar.

HM_Cr₂O₃: c(Cr/Co)=0.05, WC-Co-Cr₂O₃

Peak No.	1 st heat-up		1 st cool-down	2 nd heat-up	2 nd cool-down
	H1a	H1b	C1	H2	C2
Onset	1093	1323	1294	1329	1294
Maximum	1151	1331	1289	1337	1289

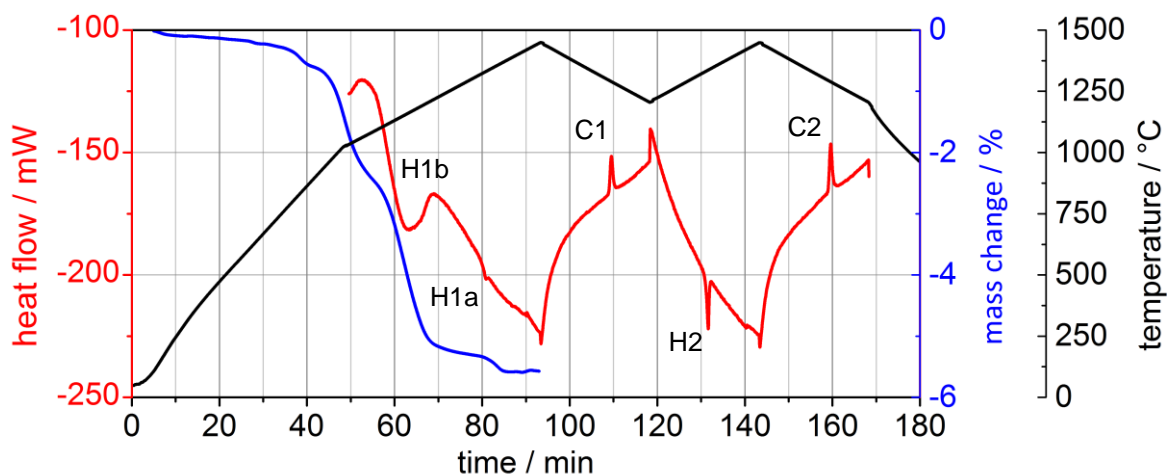


Figure 8-30: STA of HM_Cr₂O₃. Filename in database: COx+ Ar.

HM_CrB: c(Cr/Co)=0.05, WC-Co-CrB

Peak No.	1 st heat-up		1 st cool-down		2 nd heat-up		2 nd cool-down	
	H1a	H1b	C1a	C1b	H2a	H2b	C2a	C2b
Onset	1200	1248	1287	1208	1219	1280	1289	1205
Maximum	1239	1298	1283	1197	1236	1297	1283	1201

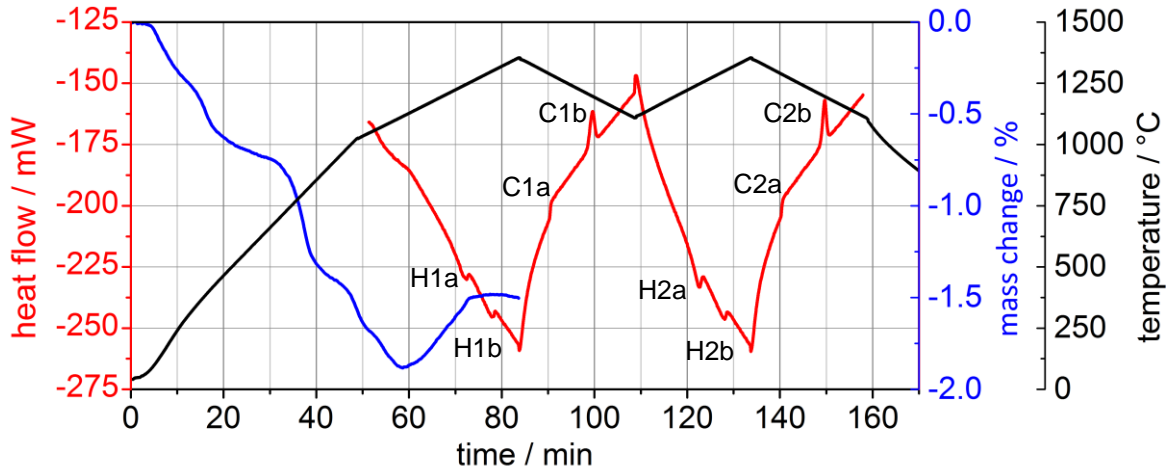


Figure 8-31: STA of HM_CrB. Filename in database: WC-Co-CrB-C-Ar.

HM_VC: c(V/Co)=0.05, WC-Co-VC

Peak No.	1 st heat-up	1 st cool-down	2 nd heat-up	2 nd cool-down
	H1	C1	H2	C2
Onset	1294	1320	1311	1321
Maximum	1334	1311	1336	1312

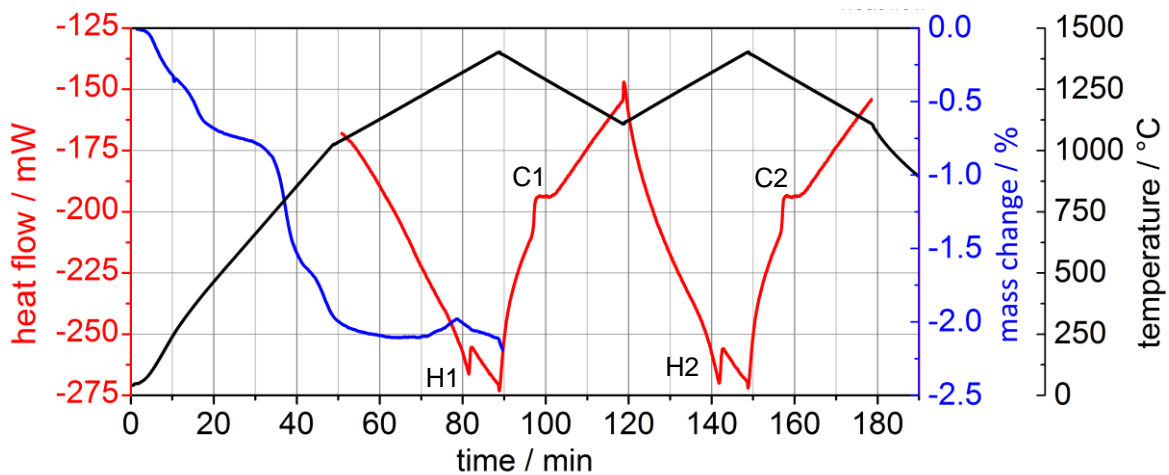


Figure 8-32: STA of HM_VC. Filename in database: WC-Co-VC-C-Ar.

HM V_2O_5 : c(V/Co)=0.05, WC-Co- V_2O_5

Peak No.	1 st heat-up	1 st cool-down	2 nd heat-up	2 nd cool-down
	H1	C1	H2	C2
Onset	1240	1261	1253	1263
Maximum 1	1256	1255	1260	1255
Maximum 2	1268	1239	1271	1239

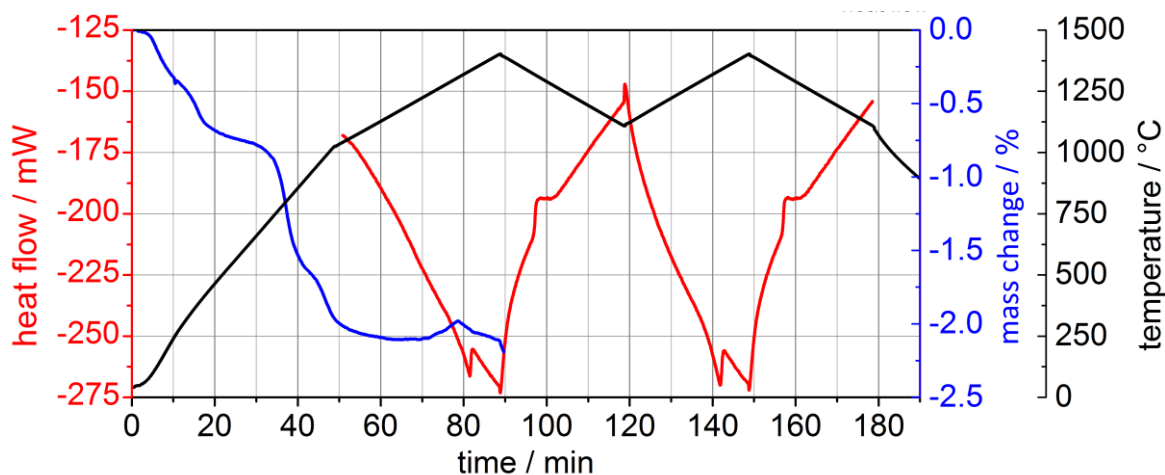


Figure 8-33: STA of HM_ V_2O_5 . Filename in database: VOx09+ Ar.

HM Mo_2C : c(Mo/Co)=0.05, WC-Co- Mo_2C

Peak No.	1 st heat-up	1 st cool-down	2 nd heat-up	2 nd cool-down
	H1	C1	H2	C2
Onset	1340	1352	1354	1353
Maximum	1362	1340	1367	1342

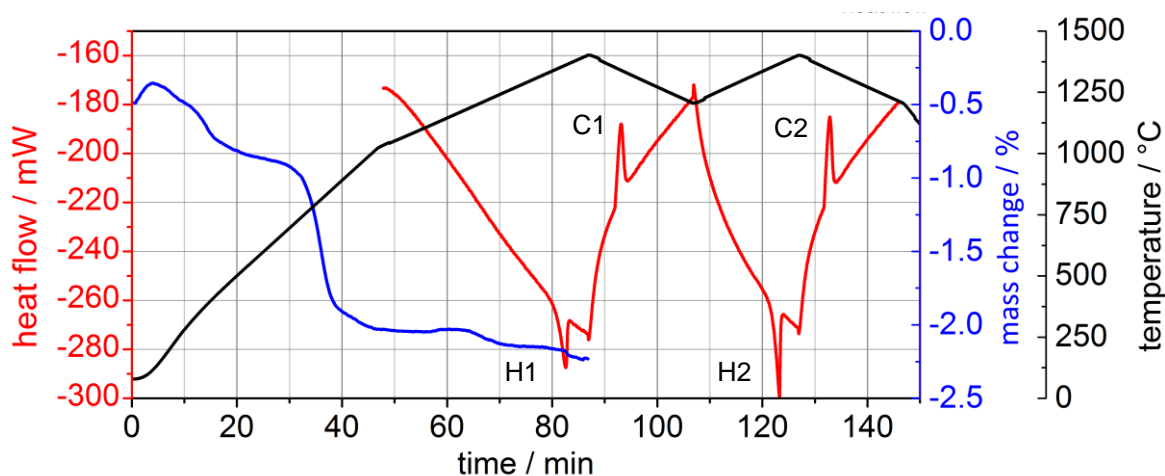


Figure 8-34: STA of HM_ Mo_2C . Filename in database: WC- Mo_2C -Co-C-Ar.

HM_MoB: c(Mo/Co)=0.05, WC-Co-MoB

Peak No.	1 st heat-up		1 st cool-down		2 nd heat-up		2 nd cool-down	
	H1a	H1b	C1a	C1b	H2a	H2b	C2a	C2b
Onset	1213	1291	1229	1323	1247	1315	1227	1324
Maximum	1235	1329	1211	1303	1260	1332	1222	1320

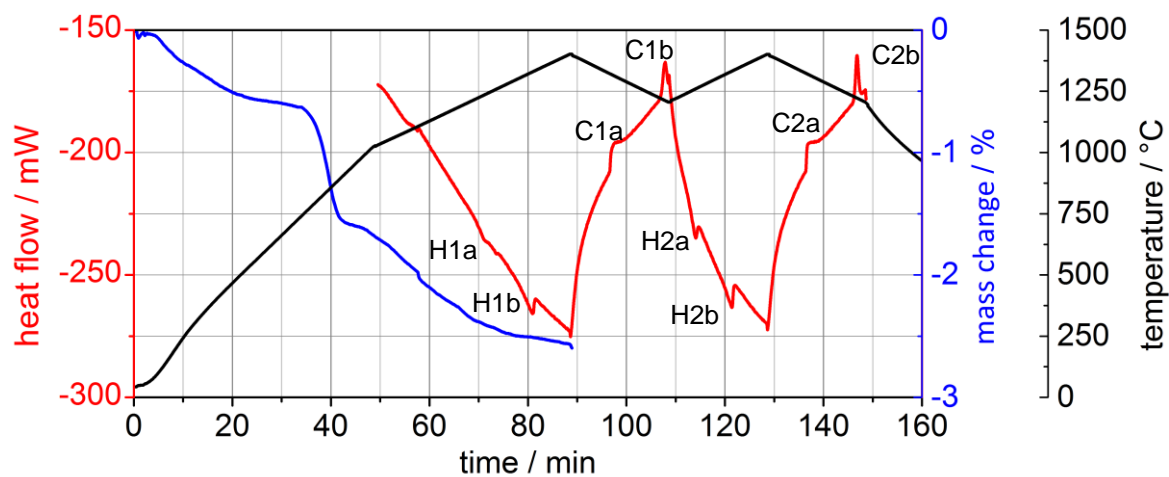


Figure 8-35: STA of HM_MoB. Filename in database: WC-MoB-Co-C-Ar

Lebenslauf

Persönliche Daten

Titel	Dipl.-Ing., BSc.
Geburtsdatum	02.04.1985
Staatbürgerschaft	Österreich
Familienstand	Verheiratet
Kinder	Keine
Präsenzdienst	Abgeleistet



Ausbildung

Seit 07.2012	Doktoratsstudium Technische Chemie; TU Wien Thema: Diffusion von Kornwachstumsinhibitoren in Hartmetallen Abschluss voraussichtlich Herbst 2015
02.2010 – 06.2012	Masterstudium Werkstofftechnologie und Werkstoffanalytik; TU Wien Diplomarbeit: Eigenschaften von Hartmetallen mit alternativen Bindern <i>Mit Auszeichnung abgeschlossen</i>
09.2006 – 02.2010	Bachelorstudium Technische Chemie; TU Wien Bachelorarbeit: Optimierung der Formkörperherstellung polymer-abgeleiteter Keramiken <i>Mit Auszeichnung abgeschlossen</i>
09.2001 – 06.2005	Höhere technische Bundeslehranstalt (HTL) Wels, Österreich Fachrichtung Chemieingenieurwesen

Praktika

08–09.2012	Hong-Kong Polytechnic University , China; Department of Applied Physics Entwicklung seltenerd-dotierter Oxide für Infrarotlaser
2012–2015	Projektzusammenarbeit mit Partnerfirmen, u.a. Arbeitskreis Hartmetall, im Rahmen diverser Projekte an der TU Wien
07 – 08.2008	Lenzing AG, Lenzing, Österreich: Qualitätssicherung
08.2007	Mineralka d.o.o., Amstetten, Österreich: Qualitätssicherung
08 – 09.2003	Thermax GesmbH, Amstetten, Österreich: Produktentwicklung
07.2002	Fa. Bluhm-Systeme GesmbH, Schwanenstadt, Österreich: Lagerist
2001–2006	Dachdeckerei Schmid, Attnang-Puchheim, Österreich: Mehrere Ferialjobs

Zusatzqualifikationen und Soft Skills

Kommunikation	Die Erfolgsschmiede: Präsentieren-Moderieren- Kommunizieren als Erfolgsfaktor (Kurzlehrgang 2010, Corporate Consult)
Sprachen	Englisch: Fließend in Wort und Schrift Indonesisch: Basiskenntnisse
Software	MS Office Origin 9.1 Matlab: Basiskenntnisse
Führerschein	Klasse B

Auszeichnungen

2013	Diplomarbeitspreis der Stadt Wien
2011	Teilnahme an TUTHETOP: das High-Potential Programm der TU Wien
2008	Leistungsstipendium der TU Wien

Freizeitinteressen

Elektronische Basteleien, Science-Fiction Romane, Badminton, Laufen